

# nature

## OMICRON & ANTIBODIES

Insights into vaccine response  
to the SARS-CoV-2 variant

**Charting diversity**  
Publishers gear up to  
track bias at scholarly  
journals

**Public health**  
Government sloth not  
personal hesitancy is  
slowing vaccine uptake

**What lies beneath**  
Quantum sensing  
maps large structures  
below Earth's surface

Vol 596 No. 7401  
24 February 2022

# Nature.2022.02.26

[Sat, 26 Feb 2022]

- [This Week](#)
- [News in Focus](#)
- [Books & Arts](#)
- [Opinion](#)
- [Work](#)
- [Research](#)
- [Amendments & Corrections](#)

# This Week

- **[Female scientists in Africa are changing the face of their continent](#)** [ 22 February 2022]  
Editorial • Why international researchers should be lining up to collaborate with women working in science across Africa.
- **[Keep science out of Europe's post-Brexit arguments](#)** [ 23 February 2022]  
Editorial • Scientific collaboration has become a casualty of Switzerland's and the United Kingdom's tussles with the European Union.
- **[Commit to transparent COVID data until the WHO declares the pandemic is over](#)** [ 22 February 2022]  
World View • Governments and organizations responsible for crucial COVID data must do more not less.
- **[Soft X-rays capture the dance of the organelles](#)** [ 14 February 2022]  
Research Highlight • A CT-like scan images what's inside a live cell in 3D — including the interactions of its components.
- **[Gender pay gap closes after salary information goes public](#)** [ 16 February 2022]  
Research Highlight • Study of tens of thousands of academics links transparency in compensation with greater pay equality.
- **[Nature's first known solid 'nanofoam' helps pollen to ride the wind](#)** [ 16 February 2022]  
Research Highlight • A porous layer gives pollen grains extraordinary toughness while allowing them to float on the breeze.
- **[The Black Death devastated parts of Europe — but spared others](#)** [ 16 February 2022]  
Research Highlight • Analysis of fossil pollen suggests that populations in some areas grew despite the plague's rampage.
- **[The plastic littering a beach can be tracked to its source](#)** [ 15 February 2022]  
Research Highlight • Efforts to clean up beaches could be aided by a model that traces the movement of floating plastic debris.

- **How a space rock became King Tut's dagger** [ 15 February 2022]  
Research Highlight • An X-ray scan helps to show how the pharaoh's knife was forged — and suggests a prestigious pedigree.
- **A drug tames a common-cold virus that's also a killer** [ 16 February 2022]  
Research Highlight • Therapy reduces study participants' levels of respiratory syncytial virus — and 'mucus weight'.

---

| [Next section](#) | [Main menu](#) |

- EDITORIAL
- 22 February 2022

# Female scientists in Africa are changing the face of their continent

Why international researchers should be lining up to collaborate with women working in science across Africa.



Chemist Veronica Okello at Machakos University in Kenya is urging younger researchers to be less timid, air their views and approach professors for professional opportunities. Credit: Esther Sweeney for *Nature*

Female scientists in Africa are entrepreneurial and resourceful. They are finding innovative solutions to problems that affect their communities, and

many are actively seeking to engage others in their work. But for more women on the continent to achieve in science, they need policies that help to lower the barriers to their success and that incentivize international collaborations. These are among the findings of a special series of articles in *Nature*, as well as a poll that received responses from 249 African researchers. The majority (217) work in African countries, and 103 identified as female.

Our series shows that women working in research in African countries are thriving — founding businesses, launching non-profit science-education efforts, training the next generation of scientists and joining their countries' health, agricultural and space ministries.

They include [Khady Sall](#) in Senegal, who in 2020 led a project to manufacture face shields against COVID-19, and [Veronica Okello](#) in Kenya, who is researching green approaches to cleaning up heavy metals such as chromium and arsenic. We also profile [Aster Tsegaye](#), an HIV/AIDS researcher helping to train researchers in Ethiopia, and [Elizabeth Kimani-Murage](#), who studies malnutrition in Nairobi's urban communities.

[Pontsho Maruping](#) has switched from working in South Africa's mining sector to helping to develop the country's astronomy and space programme. Meanwhile, [Angela Tabiri](#) in Ghana studies quantum algebra and founded a network of female mathematicians. [Adidja Amani](#) helps to run vaccination programmes at Cameroon's public-health ministry, and Nigerian microbiologist [Amina Ahmed El-Imam](#) researches the production of fuels from microorganisms.

Many also [work in community empowerment](#), are helping to communicate science to wider audiences or are working to boost science education. And their achievements have often come after a period of study or research abroad — a finding echoed in our poll. Of our poll's 103 female respondents, 59 had studied abroad; their reasons for doing so included gaining international experience, building professional networks and bringing back specific expertise.

It is also clear from the profiles that many of the women made huge personal sacrifices to obtain their PhDs — those who studied overseas and are

mothers, for example, often spent months at a time away from their children, leaving them in the care of others, such as fathers and grandparents.

Women in Africa experience greater barriers to developing careers in science, technology, engineering and mathematics (STEM) than do women in high-income countries, with lack of funding a particular problem. Some challenges, however, will be familiar to women the world over. Many women need to take time out for pregnancy, maternity leave and breastfeeding, and women also tend to do a higher share of childcare and domestic duties.

Moreover, some women told *Nature* that they have not been promoted as quickly as their male counterparts, even though they are publishing at the same rate and bringing in as much research funding and equipment to their institutions as men. The reasons vary, but include being evaluated according to outdated criteria. Often, for example, adjustments are not made for the gaps in publication and funding records that result from women taking parental leave. Although the gender gap is closing, the World Economic Forum forecasts that, at current rates, this could take 95 years in sub-Saharan Africa ([go.nature.com/3i9oxb9](http://go.nature.com/3i9oxb9)).

Our series also illustrates the impacts of chronic funding shortages in Africa, and the resourcefulness needed to push many projects forwards. In countries where universities lack access to national grant programmes, some researchers and students pool funds from their salaries to buy reagents and small items of equipment. They are willing to make these and other sacrifices, knowing that research experience will both make them valuable and benefit their communities.

Africa's researchers badly need long-term, stable investment from internal and external funding sources, including venture capital. In our poll, 56% of respondents (122 of 217) working in science in Africa cited a lack of funding as their greatest career challenge, and it was the top concern for both men and women. Work-life balance was the second-most mentioned concern for women. If only Africa's governments and the international donor community could do more to help scientists to realize their ambitions: even modest funding increases could go a long way towards accelerating nation-building.

That said, some continent-wide initiatives are helping to address systemic challenges for female scientists in Africa. Since 2011, the Consortium for Advanced Research Training in Africa (CARTA), based in Nairobi, has sponsored 228 doctoral and postdoctoral fellows, 57% of whom were women, across a number of countries. CARTA has two women at its helm: co-directors Catherine Kyobutungi and Sharon Fonn.

Similarly, the African Institute for Mathematical Sciences (AIMS) is a pan-African network of centres that has trained almost 2,500 students in intensive, residential mathematics master's programmes, with more than 800 going on to get PhDs. AIMS is led by the educationalist Lydie Hakizimana, and its main goals include increasing the continent's number of maths students and the representation of women in STEM fields. One-third of its alumni are women.

Such networks are further strengthened when researchers in high-income countries, which tend to have more-mature scientific infrastructures, get involved. Researchers in such countries have an important part to play by collaborating with researchers in Africa.

Such partnerships would benefit scientists not just in Africa, but throughout the world. African researchers include leaders in their fields; scientists on the continent can also bring fresh perspectives, informed by their knowledge and experiences, to research projects. International collaboration needs to be more common. As the COVID-19 pandemic has shown, such exchanges can happen seamlessly on virtual platforms. Africa's female scientists are on the rise — and partnering with them could give sky-high returns.

*Nature* **602**, 547–548 (2022)

*doi:* <https://doi.org/10.1038/d41586-022-00492-x>

---

This article was downloaded by **calibre** from <https://www.nature.com/articles/d41586-022-00492-x>

- EDITORIAL
- 23 February 2022

# Keep science out of Europe's post-Brexit arguments

Scientific collaboration has become a casualty of Switzerland's and the United Kingdom's tussles with the European Union.



UK science minister George Freeman says funds will be available if the United Kingdom cannot associate to Horizon Europe. But collaboration is about more than money. Credit: Tayfun Salci/ZUMA/Shutterstock

A year ago, researchers from across Europe breathed sighs of relief when the United Kingdom and the European Union agreed the terms of their relationship after Brexit.

Although a majority of UK researchers did not support their country's exit from the EU, there was relief that they would still be permitted to participate in the EU's €95.5-billion (US\$107-billion) collaborative research programme, Horizon Europe, through a category of membership called association.

The UK government would pay the EU a total of around £15 billion (US\$20.4 billion) over 7 years. In exchange, UK researchers would be able to apply for prestigious grants from the European Research Council (ERC), and participate in Horizon Europe collaborations, including taking leadership roles. The United Kingdom would no longer have the right to contribute to governance decisions, but UK representatives could sit on committees as observers.

That was then. A year later, [it all seems very different](#). Some 46 researchers in the United Kingdom who have been selected for ERC grants are being prevented from accessing their funding because of an ongoing Brexit-linked dispute over trade and borders with Northern Ireland. Furthermore, Switzerland — which is not an EU member but has associated to EU science programmes in the past — has not had its association renewed. This is because of unresolved negotiations over the country's wider relations with the EU.

The EU says that these outstanding disagreements need to be fixed before UK and Swiss participation can resume. For now, a swift resolution is not looking likely.

This is a concern for researchers on all sides, not least because EU schemes are time-limited. Horizon Europe, which began last year, is due to end in 2027. Unless the wider disagreements can be resolved quickly, grant winners will remain in limbo. Already, there are reports that some UK grant recipients might choose to relocate to an EU country to take up their funding, instead of risking losing it. Looking further ahead, there might be fewer opportunities for EU researchers to collaborate with UK and Swiss colleagues.

These delays are worrying in another sense: it seems to be a farewell to the principle that nations should not let political or policy disagreements prevent

their scientists working together. Linking science funding to the outcomes of international disputes makes little sense when the funding schemes have nothing to do with the disagreements, and when the countries have paid, or agreed to pay, into a joint fund.

Researchers are being used as “a bargaining chip on both sides” of the English Channel, explained Kurt Deketelaere, head of the secretariat of the League of European Research Universities in Leuven, Belgium, to a UK parliamentary committee during hearings earlier this month. And the damage to science could be considerable.

Frustrated researchers from across the continent have launched the [Stick to Science](#) campaign, with the subtitle: ‘Put science collaboration before politics’. So far, it has gathered around 4,000 signatures. “Every month’s delay weakens European science,” says Jan Palmowski, secretary-general of the Guild of European Research-Intensive Universities in Brussels.

UK science minister George Freeman is trying to reassure researchers that extra funds will be available for international collaborations if association to Horizon Europe doesn’t work out. But collaborative projects are about much more than money. Materials physicist Robin Grimes, a former science adviser to the UK foreign-affairs department, told this month’s parliamentary committee that Europe’s researchers have been able to make advances in their fields because of long-standing relationships, which often transcend a single funding cycle.

It is true that, for decades, research has been one of the ways in which Europe’s people have been able to work together. Relations between previous UK governments and the EU hit rocky periods long before Brexit, but governments on all sides agreed that, regardless of the state of wider relations, science links needed to remain an important priority. Joint European funding schemes (previously known as the Framework programmes) have been part of the EU and its predecessor bodies since at least the 1980s.

More than a year ago, *Nature* warned about a creeping anti-research narrative across all of Europe (see [Nature 588, 370; 2020](#)); now, divisions between nations are spilling over into science. EU officials, together with

their counterparts from Switzerland and the United Kingdom, should reflect on the implications of what they are doing. Both Switzerland and the United Kingdom should be allowed to associate to EU funding schemes, regardless of ongoing political disagreements. Dragging research and scholarship into international disputes helps no one.

*Nature* **602**, 548 (2022)

*doi:* <https://doi.org/10.1038/d41586-022-00410-1>

---

This article was downloaded by **calibre** from <https://www.nature.com/articles/d41586-022-00410-1>

| [Section menu](#) | [Main menu](#) |

- WORLD VIEW
- 22 February 2022

# Commit to transparent COVID data until the WHO declares the pandemic is over



Governments and organizations responsible for crucial COVID data must do more not less.

- [Edouard Mathieu](#) 0

Rich countries are now winding up intense COVID-19 vaccination campaigns, de-emphasizing public-health interventions and reporting data less frequently, even with three billion people still unvaccinated. I worry that governments and organizations responsible for crucial data-gathering efforts will fail to focus on what's truly needed to navigate out of the pandemic.

When the pandemic first surged in 2020, a few people at Johns Hopkins University in Baltimore, Maryland, took the initiative to start counting each country's confirmed cases and reported deaths. Meanwhile, Our World in Data, a data publisher in Oxford, UK, started painstakingly assembling country-by-country data on testing. I quit my job at a digital-services company to join that effort.

Data publishers — whether they are national governments, international organizations or online publications — should make a frank commitment to provide the public and researchers with transparent data on the pandemic until the World Health Organization (WHO) declares that it is over, and the WHO should coordinate this effort.

There are huge inequalities in data reporting around the world. Most of my time over the past two years has been spent digging through official websites and social-media accounts of hundreds of governments and health authorities. Some governments still report official statistics in low-resolution images on Facebook or infrequent press conferences on YouTube — often because they lack resources to do better. Some countries, including China and Iran, have provided no files at all.

Sometimes, it's a lack of awareness: government officials might think that a topline figure somewhere in a press release is sufficient. Sometimes, the problem is reluctance: publishing the first file would mean a flood of requests for more data that authorities can't or won't publish.

Some governments rushed to launch pandemic dashboards, often built as one-off jobs by hired contractors. Civil servants couldn't upgrade them as the pandemic shifted and new metrics and charts became more relevant. I started building our global data set on COVID-19 vaccinations in 2021, but many governments didn't supply data for weeks — sometimes months — after roll-outs because their dashboards couldn't accommodate the data. Worse, they rarely supplied underlying data essential for others to download and produce their own analyses. (My team asked repeatedly.)

Over and over, I've seen governments emphasize making dashboards look good when the priority should be making data available. A simple text file would do. After all, research groups like mine and citizens with expertise in

data-visualization tools are more than willing to create a useful website or mobile app. But to do so, we need the raw material in a machine-readable format.

There are many good examples of governments making their data available for others to make visible. The open-access GitHub repositories of the Malaysian and Chilean governments are prime examples of how to do this. Where governments haven't done it, volunteer groups have stepped in: the Sledilnik project in Slovenia, the COVID LIVE and CovidBase websites in Australia, and the COVID Tracking Project in 2020 in the United States are heroic efforts.

Such organizations have taken on this job for the past two years, but the world should not rely on a private university to tally the pandemic's death toll or announce when 60% of the global population is vaccinated. The WHO should collect and aggregate national figures into an international data set.

Yes, this will take a (modest) commitment of resources. More than that, it will take agility. In an ever-evolving situation, it's impossible to produce useful data if it takes six months to add or update a data field. Our team added a metric for boosters in August 2021, as soon as countries such as Israel rolled them out. The WHO still doesn't track them.

Great shifts are possible. After making a concerted effort over the past decade, the World Bank now publishes some of the best open-access, clean and reliable data sets on global development. The WHO could have a similar role for the world's public-health data.

The WHO and international health leaders can do more to encourage a holistic approach to managing long-term pandemic data. That would allow national authorities both to keep counting cases, hospitalizations and more, and to become better at doing so. Many essential data are still unavailable. The distinction between hospital admissions directly due to COVID-19 and cases detected incidentally is now crucial as the latter fraction increases. But few countries supply those breakdowns.

Another bigger problem is the lack of all-cause mortality data. Without that, it is impossible to know the true toll of the pandemic. When we look at the rare all-cause mortality data available across Africa — in Egypt and South Africa, for example — the death toll seems much higher than headline figures suggest.

National and international authorities and the public have relied on online publications — including media organizations and Our World in Data — to track pandemic metrics and make sense of all the data. But those authorities, too, bear a responsibility, especially to countries that would otherwise fly the rest of the pandemic blind and be too quickly forgotten by rich countries that are eager to move on.

*Nature* **602**, 549 (2022)

*doi:* <https://doi.org/10.1038/d41586-022-00424-9>

---

This article was downloaded by **calibre** from <https://www.nature.com/articles/d41586-022-00424-9>

| [Section menu](#) | [Main menu](#) |

- RESEARCH HIGHLIGHT
- 14 February 2022

# Soft X-rays capture the dance of the organelles

A CT-like scan images what's inside a live cell in 3D — including the interactions of its components.

 Soft X-ray tomography combines rapid collection and high-resolution visualization to understand subcellular reorganization.

An X-ray-based imaging method unveils a cell's substructures, including the nucleus, mitochondria and insulin vesicles (blue, magenta and yellow, respectively; artificially coloured). Credit: V. Loconte *et al./Structure*

An imaging technique that uses X-rays can reveal in 10 minutes not only the 3D structure inside a cell, but also how its organelles interact with each other<sup>1</sup>.

## Access options

Subscribe to Nature+

Get immediate online access to the entire Nature family of 50+ journals

\$29.99

monthly

[Subscribe](#)

Subscribe to Journal

Get full journal access for 1 year

\$199.00

only \$3.90 per issue

[Subscribe](#)

All prices are NET prices.

VAT will be added later in the checkout.

Tax calculation will be finalised during checkout.

Buy article

Get time limited or full article access on ReadCube.

\$32.00

[Buy](#)

All prices are NET prices.

### **Additional access options:**

- [Log in](#)
- [Learn about institutional subscriptions](#)

*Nature* **602**, 550 (2022)

*doi:* <https://doi.org/10.1038/d41586-022-00420-z>

## **References**

1. Loconte, V. et. al. *Structure* <https://doi.org/10.1016/j.str.2022.01.006> (2022).

| [Section menu](#) | [Main menu](#) |

- RESEARCH HIGHLIGHT
- 16 February 2022

# Gender pay gap closes after salary information goes public

Study of tens of thousands of academics links transparency in compensation with greater pay equality.



Pay transparency was associated with more pay equality in academic workplaces in eight US states. Credit: Getty

The pay gap between men and women tends to shrink after workers learn what their colleagues earn<sup>1</sup>.

## Access options

Subscribe to Nature+

Get immediate online access to the entire Nature family of 50+ journals

\$29.99

monthly

[Subscribe](#)

Subscribe to Journal

Get full journal access for 1 year

\$199.00

only \$3.90 per issue

[Subscribe](#)

All prices are NET prices.

VAT will be added later in the checkout.

Tax calculation will be finalised during checkout.

Buy article

Get time limited or full article access on ReadCube.

\$32.00

[Buy](#)

All prices are NET prices.

### **Additional access options:**

- [Log in](#)
- [Learn about institutional subscriptions](#)

*Nature* **602**, 550 (2022)

*doi:* <https://doi.org/10.1038/d41586-022-00434-7>

## **References**

1. Obloj, T., & Zenger, T. *Nature Hum. Behav.* <https://doi.org/10.1038/s41562-022-01288-9> (2022).

---

This article was downloaded by **calibre** from <https://www.nature.com/articles/d41586-022-00434-7>

- RESEARCH HIGHLIGHT
- 16 February 2022

# Nature's first known solid 'nanofoam' helps pollen to ride the wind

A porous layer gives pollen grains extraordinary toughness while allowing them to float on the breeze.

3D reconstruction lateral view of the full grain of a modern pine pollen specimen from x-ray nanotomography data.

The foamy structure of a pollen grain's outer wall is visible in a reconstructed image of pollen from a modern pine tree (family Pinaceae).  
Credit: R. Cojocaru *et al.*/*Sci. Adv.*

Tasked with the survival of their species, many pollen grains must drift with the wind and endure harsh conditions. Advanced imaging techniques reveal that they do so thanks to exterior shells made of a tough material riddled with nanometre-sized pores — the first known example of a solid biological 'nanofoam'<sup>1</sup>.

## Access options

Subscribe to Nature+

Get immediate online access to the entire Nature family of 50+ journals

\$29.99

monthly

## Subscribe

Subscribe to Journal

Get full journal access for 1 year

\$199.00

only \$3.90 per issue

## Subscribe

All prices are NET prices.

VAT will be added later in the checkout.

Tax calculation will be finalised during checkout.

Buy article

Get time limited or full article access on ReadCube.

\$32.00

## Buy

All prices are NET prices.

## **Additional access options:**

- [Log in](#)
- [Learn about institutional subscriptions](#)

*Nature* **602**, 550 (2022)

*doi:* <https://doi.org/10.1038/d41586-022-00437-4>

## **References**

1. Cojocaru, R. *et al.* *Sci. Adv.* **8**, eabd0892 (2022).

---

This article was downloaded by **calibre** from <https://www.nature.com/articles/d41586-022-00437-4>

| [Section menu](#) | [Main menu](#) |

- RESEARCH HIGHLIGHT
- 16 February 2022

# The Black Death devastated parts of Europe — but spared others

Analysis of fossil pollen suggests that populations in some areas grew despite the plague's rampage.

The Bagno Kusowo peatland is one of best-preserved Baltic raised bogs in Northern Poland.

Ancient pollen collected from this peat bog in northern Poland hints that the Black Death did not ravage the local population. Credit: Mariusz Lamentowicz

The fourteenth-century pandemic known as the Black Death might not have been as devastating as was previously thought, an analysis of ancient pollen suggests<sup>1</sup>.

## Access options

Subscribe to Nature+

Get immediate online access to the entire Nature family of 50+ journals

\$29.99

monthly

[Subscribe](#)

Subscribe to Journal

Get full journal access for 1 year

\$199.00

only \$3.90 per issue

[Subscribe](#)

All prices are NET prices.

VAT will be added later in the checkout.

Tax calculation will be finalised during checkout.

Buy article

Get time limited or full article access on ReadCube.

\$32.00

[Buy](#)

All prices are NET prices.

### **Additional access options:**

- [Log in](#)
- [Learn about institutional subscriptions](#)

*Nature* **602**, 550 (2022)

*doi:* <https://doi.org/10.1038/d41586-022-00435-6>

## **References**

1. Izdebski, A. *et al.* *Nature Ecol. Evol.* <https://doi.org/10.1038/s41559-021-01652-4> (2022).

| [Section menu](#) | [Main menu](#) |

- RESEARCH HIGHLIGHT
- 15 February 2022

# The plastic littering a beach can be tracked to its source

Efforts to clean up beaches could be aided by a model that traces the movement of floating plastic debris.

 Plastic trash covers the beach in Jimbaran, Bali, Indonesia on January 27, 2021.

Paradise lost: plastic fouls a beach in Bali, Indonesia. A new model can identify the sources of such rubbish. Credit: Agung Parameswara/Getty

Simulations of plastic particles' travels on ocean currents can help scientists to identify sources of coastal pollution<sup>1</sup>.

## Access options

Subscribe to Nature+

Get immediate online access to the entire Nature family of 50+ journals

\$29.99

monthly

[Subscribe](#)

Subscribe to Journal

Get full journal access for 1 year

\$199.00

only \$3.90 per issue

## Subscribe

All prices are NET prices.

VAT will be added later in the checkout.

Tax calculation will be finalised during checkout.

Buy article

Get time limited or full article access on ReadCube.

\$32.00

## Buy

All prices are NET prices.

## **Additional access options:**

- [Log in](#)
- [Learn about institutional subscriptions](#)

*Nature* **602**, 551 (2022)

*doi:* <https://doi.org/10.1038/d41586-022-00433-8>

## **References**

1. Van Duinen, B., Kaandorp, M. L. A. & Van Sebille, E. *Geophys. Res. Lett.* <https://doi.org/10.1029/2021GL097214> (2022).

---

This article was downloaded by **calibre** from <https://www.nature.com/articles/d41586-022-00433-8>

- RESEARCH HIGHLIGHT
- 15 February 2022

# How a space rock became King Tut's dagger

An X-ray scan helps to show how the pharaoh's knife was forged — and suggests a prestigious pedigree.

 Top two photos of Tutankhamen's dagger at the Egyptian Museum of Cairo, 2020. Bottom photo, the dagger from the 1925 discovery.

The pattern of nickel atoms in its blade reveal the relatively low temperatures at which King Tut's dagger was forged (top and middle, both sides of the object; bottom, the dagger on discovery in 1925). Credit: T. Matsui *et al.*/*Meteorit. Planet. Sci.*

Chemical analysis of an iron dagger found in King Tutankhamen's tomb has identified the type of meteorite from which the metal was derived — and suggests the knife might have been a gift from another ruler<sup>1</sup>.

## Access options

Subscribe to Nature+

Get immediate online access to the entire Nature family of 50+ journals

\$29.99

monthly

[Subscribe](#)

Subscribe to Journal

Get full journal access for 1 year

\$199.00

only \$3.90 per issue

[Subscribe](#)

All prices are NET prices.

VAT will be added later in the checkout.

Tax calculation will be finalised during checkout.

Buy article

Get time limited or full article access on ReadCube.

\$32.00

[Buy](#)

All prices are NET prices.

### **Additional access options:**

- [Log in](#)
- [Learn about institutional subscriptions](#)

*Nature* **602**, 551 (2022)

*doi:* <https://doi.org/10.1038/d41586-022-00436-5>

## **References**

1. Matsui, T., Moriwaki, R., Zidan, E., & Arai, T. *Meteorit. Planet. Sci.* <https://doi.org/10.1111/maps.13787> (2022).

| [Section menu](#) | [Main menu](#) |

- RESEARCH HIGHLIGHT
- 16 February 2022

# A drug tames a common-cold virus that's also a killer

Therapy reduces study participants' levels of respiratory syncytial virus — and 'mucus weight'.

 Respiratory syncytial virus virions (blue) and anti-RSV antibodies (yellow) on the surface of cultured human lung cells.

Human lung cells release particles of respiratory syncytial virus (blue), which can be inhibited with a compound that interferes with viral replication. Credit: National Institute of Allergy and Infectious Diseases/National Institute of Health/Science Photo Library

In a small trial in humans, an easily taken drug tamped down levels of a common respiratory virus that can prove deadly for infants and older people<sup>1</sup>.

## Access options

Subscribe to Nature+

Get immediate online access to the entire Nature family of 50+ journals

\$29.99

monthly

[Subscribe](#)

Subscribe to Journal

Get full journal access for 1 year

\$199.00

only \$3.90 per issue

[Subscribe](#)

All prices are NET prices.

VAT will be added later in the checkout.

Tax calculation will be finalised during checkout.

Buy article

Get time limited or full article access on ReadCube.

\$32.00

[Buy](#)

All prices are NET prices.

### **Additional access options:**

- [Log in](#)
- [Learn about institutional subscriptions](#)

*Nature* **602**, 551 (2022)

*doi:* <https://doi.org/10.1038/d41586-022-00455-2>

## **References**

1. Ahmad, A. *et al.* *N. Engl. J. Med.* **386**, 655-666 (2022).

| [Section menu](#) | [Main menu](#) |

# News in Focus

- **[Earth-like planet, neutrino's mysterious mass and disease eradication](#)** [ 23 February 2022]  
News Round-Up • The latest science news, in brief.
- **[Ukrainian scientists fear for their lives and future amid Russian threat](#)** [ 19 February 2022]  
News • Researchers say that conflict will hinder progress made since Ukraine's revolution in 2014.
- **[Why does the Omicron sub-variant spread faster than the original?](#)** [ 16 February 2022]  
News • Early studies suggest that the BA.2 lineage might prolong the Omicron wave, but won't necessarily cause a fresh surge of COVID infections.
- **[NIH issues a seismic mandate: share data publicly](#)** [ 16 February 2022]  
News • The data-sharing policy could set a global standard for biomedical research, scientists say, but they have questions about logistics and equity.
- **[China's approval of gene-edited crops energizes researchers](#)** [ 11 February 2022]  
News • Scientists say newly published guidelines will spur research into crops that have increased yields and greater resilience to climate change.
- **[Heart-disease risk soars after COVID — even with a mild case](#)** [ 10 February 2022]  
News • Massive study shows a long-term, substantial rise in risk of cardiovascular disease, including heart attack and stroke, after a SARS-CoV-2 infection.
- **[Cancer 'moonshot' has lofty new goal: halve deaths in 25 years](#)** [ 10 February 2022]  
News • Researchers take stock of the US\$1.8-billion initiative's first five years as Biden announces ambitious target.
- **[A supernova could light up the Milky Way at any time. Astronomers will be watching](#)** [ 21 February 2022]

News Feature • When a star from our Galactic neighbourhood explodes, it could outshine the Moon. Researchers are racing to get ready for the fireworks.

- **The giant plan to track diversity in research journals** [ 23 February 2022]

News Feature • Efforts to chart and reduce bias in scholarly publishing will ask authors, reviewers and editors to disclose their race or ethnicity.

- NEWS ROUND-UP
- 23 February 2022

# Earth-like planet, neutrino's mysterious mass and disease eradication

The latest science news, in brief.



An artist's impression of the newly discovered planet orbiting Proxima Centauri. Credit: ESO/L. Calçada

**Earth-like planet spotted orbiting sun's closest star**

Astronomers have [discovered a third planet orbiting Proxima Centauri](#), the star closest to the Sun. Called Proxima Centauri d, the newly spotted world is probably smaller than Earth, and could have oceans of liquid water.

Astronomer João Faria and his collaborators detected Proxima Centauri d by measuring tiny shifts in the spectrum of light emitted by the star as the planet's gravity pulled at it during orbit. The team used a state-of-the art instrument called the Echelle Spectrograph for Rocky Exoplanets and Stable Spectroscopic Observations at the Very Large Telescope, a system of four 8.2-metre telescopes at the European Southern Observatory in Cerro Paranal, Chile. The results were published on 10 February ([J. P. Faria et al. Astron. Astrophys. 658, A115; 2022](#)).

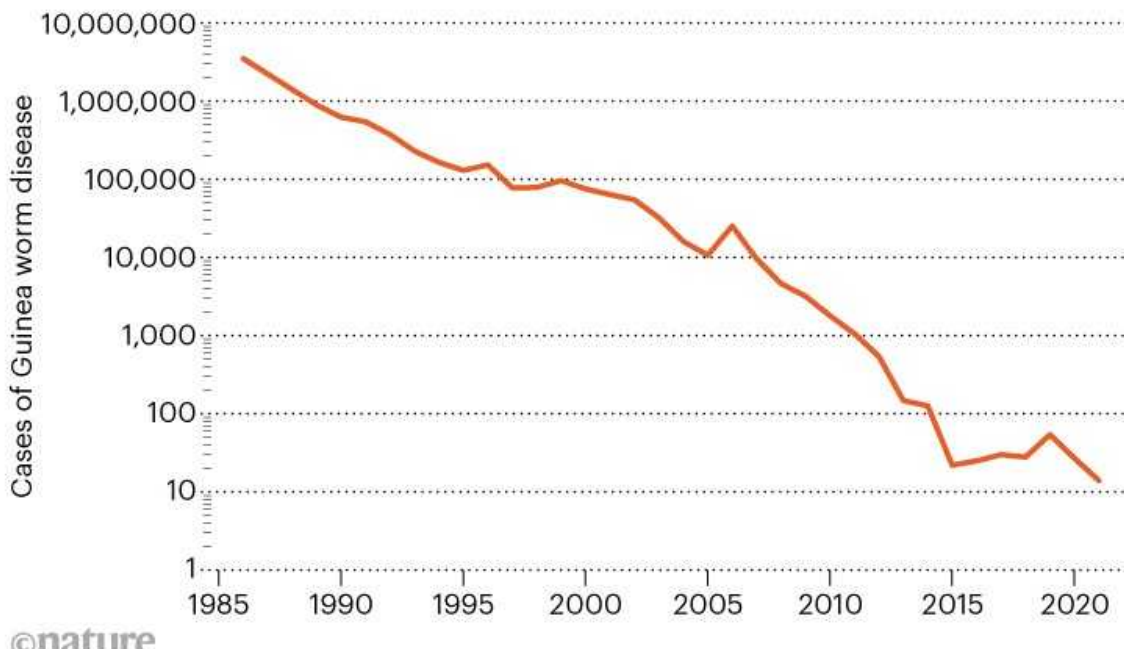
“It is fascinating to know that our Sun’s nearest stellar neighbour is the host to three small planets,” says Elisa Quintana, an astrophysicist at NASA’s Goddard Space Flight Center in Greenbelt, Maryland. “Their proximity make this a prime system for further study, to understand their nature and how they likely formed.”

## Guinea worm disease nears eradication

Only 14 cases of infection with Guinea worm — a parasite that causes painful skin lesions — were reported in humans in 2021, [sparking hope that the disease could soon be eradicated](#). The tally is the lowest ever for an infection that, as recently as the 1980s, was found in more than 20 countries and infected 3.5 million people a year (see ‘On the way out’). “It’s pretty amazing,” says Adam Weiss, director of the Guinea Worm Eradication Program of the Carter Center, which is headquartered in Atlanta, Georgia. The centre announced the numbers in late January.

## ON THE WAY OUT

Guinea worm disease is one of eight conditions that the International Task Force for Disease Eradication thinks could be eradicated in coming decades, considerably improving quality of life for millions of the world's poorest people.



©nature

Source: The Carter Center

The reduction — a drop of close to 50% compared with the 27 cases reported in 2020 — is the result of a near 40-year effort by international organizations and national governments to rid the world of Guinea worm, says Weiss. If the initiative succeeds, the condition will join smallpox and rinderpest (a virus that infected mainly cattle and buffalo) as the only diseases to have been purposefully eradicated in human history.

There is no recognized treatment or vaccine for the parasite. Instead, eradication campaigns have focused on preventing transmission. But, a remaining reservoir for the parasite in animals means eradication could be a while off, if indeed it is possible, say some scientists.



The Karlsruhe Tritium Neutrino (KATRIN) experiment has produced the most precise measurement of the neutrino's mass yet. Markus Breig

## New upper limit for elusive neutrino's mass

Physicists are one step closer to [nailing down the mass of the neutrino](#), perhaps the most mysterious of all elementary particles.

The team at the Karlsruhe Tritium Neutrino (KATRIN) experiment in Germany reports that neutrinos have a maximum mass of 0.8 electronvolts ([The KATRIN Collaboration \*Nature Phys.\* \*\*18\*\*, 160–166; 2022](#)). There is indirect evidence that the particles should be lighter than 1 electronvolt, but this is the first time that this has been shown in a direct measurement.

KATRIN (pictured) weighs neutrinos produced by the nuclear decay of tritium, a radioactive isotope of hydrogen. When a tritium nucleus decays into a helium one, it ejects an electron and a neutrino. The neutrino is lost, but the electron is channelled into a 23-metre-long, blimp-shaped steel vacuum chamber, where its energy is measured precisely.

The electron carries almost all of the energy released during the tritium's decay, but some is lost with the neutrino. The value of this shortfall can be used to calculate the particle's mass.

KATRIN has so far been able to put only an upper bound on the neutrino's mass. But researchers say that it might be able to make a definitive measurement once it finishes collecting data in 2024.

*Nature* **602**, 553 (2022)

*doi:* <https://doi.org/10.1038/d41586-022-00494-9>

---

This article was downloaded by **calibre** from <https://www.nature.com/articles/d41586-022-00494-9>

| [Section menu](#) | [Main menu](#) |

- NEWS
- 19 February 2022

# Ukrainian scientists fear for their lives and future amid Russian threat

Researchers say that conflict will hinder progress made since Ukraine's revolution in 2014.

- [Holly Else](#) &
- [Nisha Gaind](#)



Ukrainian soldiers stationed in the eastern region of Donetsk. Credit: Tyler Hicks/The New York Times/Redux/eyevine

As Ukraine braces for the possibility of an imminent invasion by Russia, several Ukrainian scientists have told *Nature* that they and their colleagues are taking measures to protect themselves and their work, including gathering items for self-defence and preparing to flee. The escalating tensions come eight years after a [revolution that pushed Ukraine to cut ties with Russia](#) — including those related to research — and forge closer links with the European Union. Researchers fear that fresh conflict will plunge Ukraine into turmoil and halt the progress that it has since made in science.

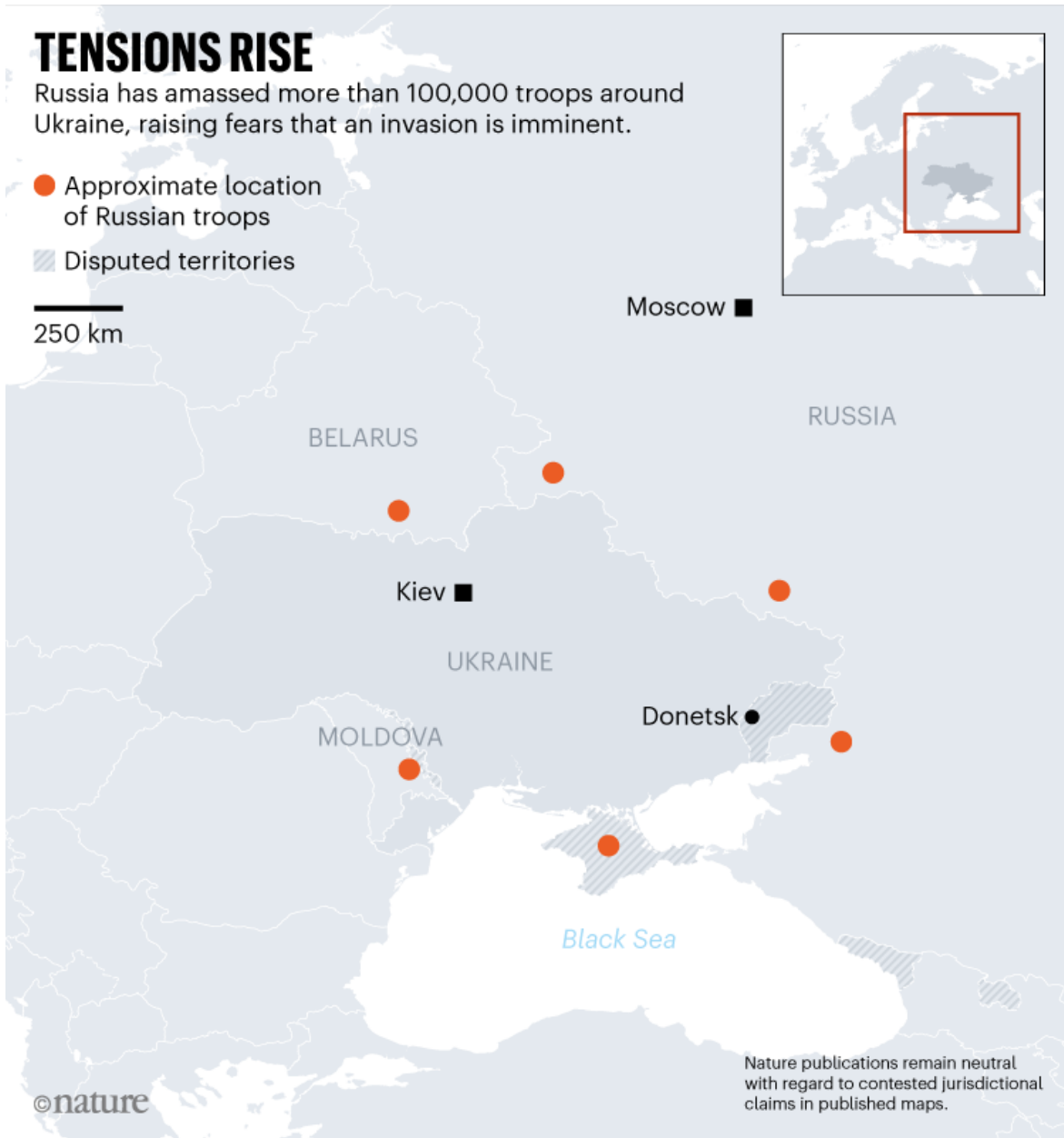
“At the moment, I am sitting in a warm place and the Internet is available. I don’t know if that will be the case tomorrow,” says Irina Yegorchenko, a mathematician at the Institute of Mathematics in Kiev, which is near Ukraine’s border with Belarus.

In the past few weeks, Russia’s massive military build-up at its border with Ukraine and inside Belarus has marked a rapid intensification of tensions that have been rumbling on since 2013. Then, [a wave of protests and civil unrest](#) ousted Ukraine’s Russian-leaning leader in early 2014 and the country elected a pro-European government. That year, Russia invaded Ukraine and seized the Crimean peninsula.

Research institutions in Crimea, previously run by the National Academy of Sciences of Ukraine, [were transferred to Russian control](#). Fighting in the eastern Ukrainian regions of Luhansk and Donetsk continues to this day. The conflict led to 18 universities relocating out of Luhansk and Donetsk to other parts of the country, with many researchers losing their homes and laboratories. Most of the academic staff at one displaced university — Vasyl’ Stus Donetsk National University, now in Vinnytsia — are people who were forced to leave and who lost their property, livelihoods and family ties, says Roman Fedorovich Hryniuk, the institution’s rector.

As a result of the conflict, many Ukrainian researchers cut links with Russia and formed new ties with their peers in Europe, the United States and China. “It was painful to lose established relations and build-up new ones, but it gave us a new point of view,” says Illya Khadzhynov, vice-rector of

scientific work at the university. In 2015, [Ukraine joined the EU's flagship research-funding programme](#), giving its scientists the same rights to apply for grants as EU members.



Source: European Council on Foreign Relations

## Troop movements

Now, some 130,000 Russian troops are at the border with Ukraine and inside Belarus, which commentators in the West see as an act of aggression (see ‘Tensions rise’). Russia says that it has no plans to invade, but some scientists are feeling the strain.

“There is a very certain threat of war. I feel like I could die tomorrow, or in two days, but I can’t do anything about that,” says Yegorchenko. Although she feels that it is useless to prepare, she is keeping electronic devices such as phones and power banks charged, and is in constant contact with her family. “All scientists do that,” she adds.

“In general, this Russian tension is aiming to create chaos in Ukraine, and harm to the economic situation. We know that we will have less funding for research, less opportunities to travel and zero chances of internal conferences in Ukraine,” she says. But overall, she is trying not to worry and is working more than usual to help cope with the situation. “Mathematics is a good therapy,” she says.

At the Sumy National Agrarian University, which is 30 kilometres from the border with Russia, staff have been trained in how to behave in the event of hostility. The university has drawn up plans for employees to evacuate from the building to bomb shelters. There are also plans to move unique scientific equipment and biological specimens out of the region.

“In private conversations, scientists say that they have collected ‘alarming suitcases’ with documents and essentials,” says Yurii Danko, an economist at the institution. The bags contain clothes, medicines, tools, self-defence items and food, he says. Danko does not believe that Russia will invade, but says that if it did, many scientists would be forced to move from their homes to areas controlled by Ukraine to continue working — or might have to go abroad. “In case of the occupation, scientists will not work for the enemy,” he adds.

## Trying to keep calm

Further west, in the city of Lviv, near the Polish border, computer scientist Oleksandr Berezko says that many feel the tension but are trying to keep

calm. “It might sound strange, but the war has started eight years ago; it hasn’t started now,” he says.

Berezko, who works at Lviv Polytechnic National University, was planning a small meeting for around 20 early-career researchers to discuss open science at the end of March; he says it is now likely to be cancelled.

“Ukrainian research is not in the best shape and many people are trying to develop our research system to bring it close to European and worldwide standards,” he says. If there is war, the government’s priority will be the armed forces and helping people to survive.

Vladimir Kuznetsov, a plant biologist at the K. A. Timiryazev Institute of Plant Physiology in Moscow, says that the situation between his country and Ukraine is highly undesirable and unacceptable. “They won’t give money to researchers. Many researchers will leave Ukraine and that will be very bad,” says Kuznetsov. He thinks that there won’t be an invasion, and hopes that the situation will stabilize soon. Although scientific collaboration between the two nations has dwindled, scientists in Ukraine try not to show that they are in contact with Russian peers, “so as not to put themselves and their families at risk”, says Kuznetsov.

*Nature* **602**, 555-556 (2022)

*doi:* <https://doi.org/10.1038/d41586-022-00505-9>

---

This article was downloaded by **calibre** from <https://www.nature.com/articles/d41586-022-00505-9>

- NEWS
- 16 February 2022

# Why does the Omicron sub-variant spread faster than the original?

Early studies suggest that the BA.2 lineage might prolong the Omicron wave, but won't necessarily cause a fresh surge of COVID infections.

- [Ewen Callaway](#)



The Philippines is one of the nations in which the BA.2 sub-variant of Omicron has spread quickly. Credit: Lisa Marie David/Reuters

COVID-19 researchers are rushing to understand why a relative of the main Omicron variant is displacing its sibling in countries around the world.

The variant, known as BA.2, has spread rapidly in countries including Denmark, the Philippines and South Africa in the past few weeks. It follows the initial spread of the BA.1 Omicron variant of the virus SARS-CoV-2, which was first identified in southern Africa in late November and quickly spread worldwide.

A laboratory study<sup>1</sup> of BA.2 suggests that its rapid ascent is probably the result of it being more transmissible than BA.1. And other preliminary studies suggest that BA.2 can readily overcome immunity from vaccination and previous infection with earlier variants, although it is not much better than BA.1 at doing so.

If real-world epidemiological studies support these conclusions, scientists think that BA.2 will be unlikely to spark a second major wave of infections, hospitalizations and deaths after Omicron's initial onslaught.

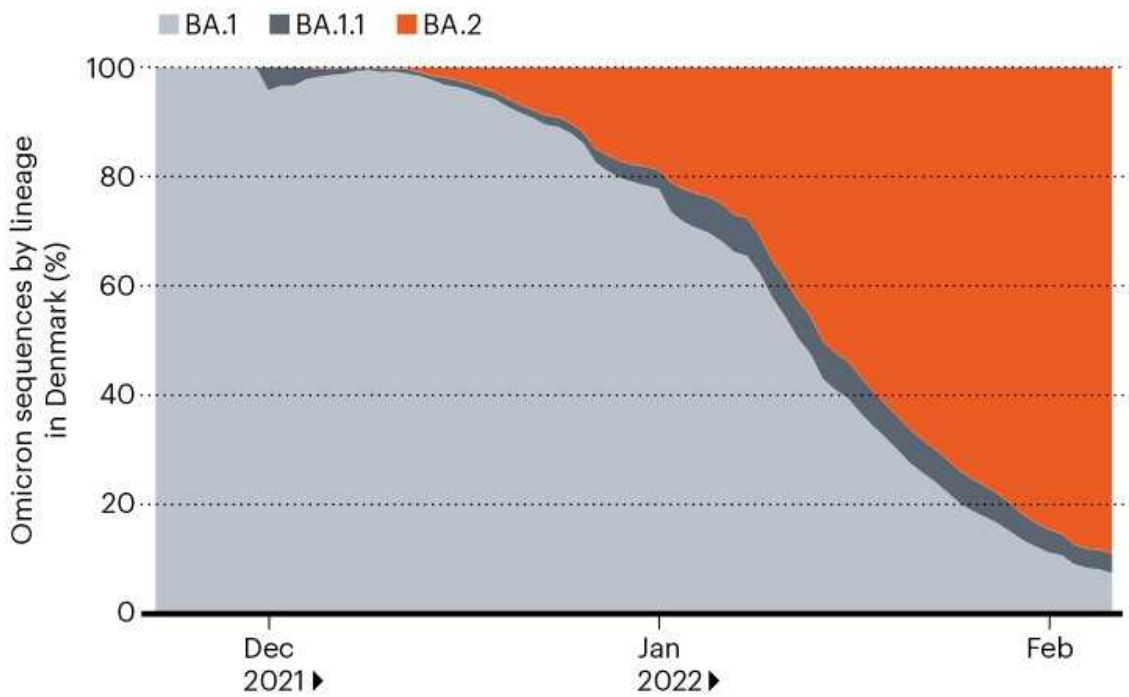
"It might prolong the Omicron surge. But our data would suggest that it would not lead to a brand-new additional surge," says Dan Barouch, an immunologist and virologist at Beth Israel Deaconess Medical Center in Boston, Massachusetts, who led the laboratory study, posted on the medRxiv preprint server on 7 February.

## Growth advantage

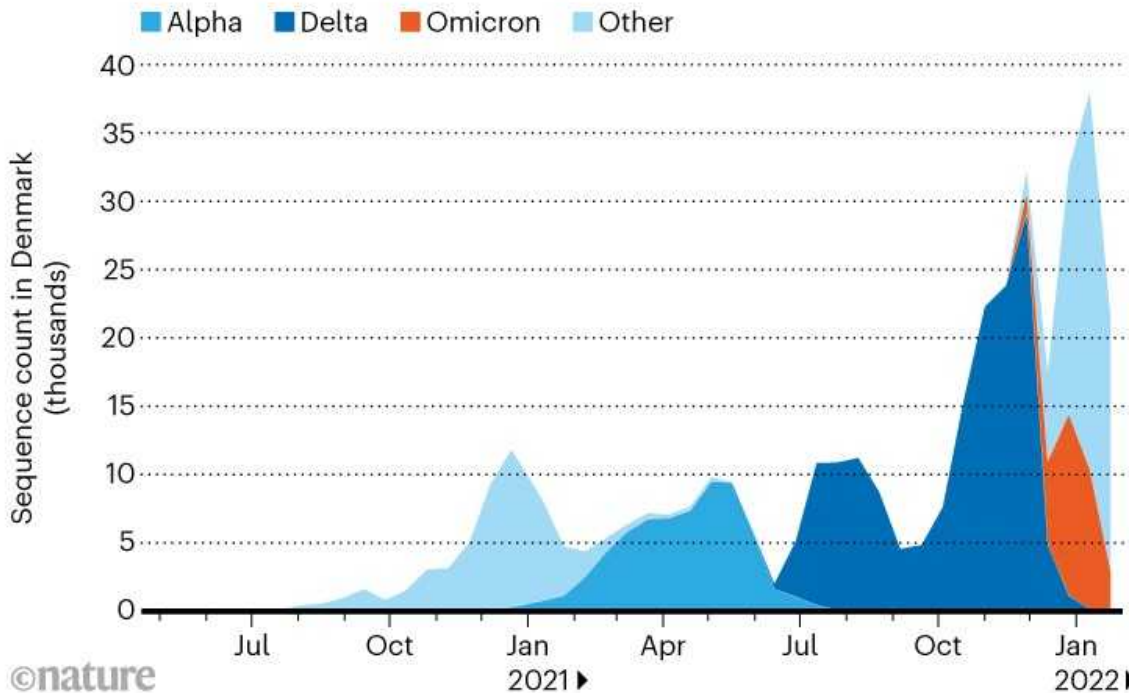
BA.2's steady rise in prevalence in multiple countries suggests that it has a growth advantage over other circulating variants, says Mads Albertsen, a bioinformatician at Aalborg University in Denmark. That includes other forms of Omicron, such as a less-prevalent lineage called BA.3 (see 'Omicron's many variants').

## OMICRON'S MANY VARIANTS

The BA.2 lineage of Omicron spreads faster than the original BA.1 variant, and it has now become the prevalent Omicron lineage in Denmark.



Omicron emerged last November and quickly overtook the Delta variant.



Source: [outbreak.info](#) (top); [covariants.org](#) (bottom).

“From a scientific perspective, the question is why,” says Barouch. Researchers think that a large part of the reason Omicron quickly replaced the Delta variant is its ability to infect and spread among people who had been immune to Delta. So one possibility for BA.2’s rise is that it’s even better than BA.1 at overcoming immunity — potentially including the protection gained from a BA.1 infection.

The variants’ differing behaviours could be explained by their many genetic differences. Dozens of mutations distinguish BA.1 from BA.2 — particularly at key portions of the virus’s spike protein, the target of potent antibodies that can block infection. “BA.2 has a whole mess of new mutations that no one has tested,” says Jeremy Luban, a virologist at the University of Massachusetts Chan Medical School in Worcester.

To assess any differences between BA.1 and BA.2, Barouch’s team measured how well ‘neutralizing’, or virus-blocking, antibodies in people’s blood protected cells from infection by viruses with either variant’s spike protein<sup>1</sup>. The study looked at 24 people who had received three doses of the RNA vaccine made by Pfizer in New York City; they produced neutralizing antibodies that were slightly better at fending off infection by viruses with BA.1’s spike than those with BA.2’s. The same was true for a smaller group of people who had gained immunity from infection during the initial Omicron surge, and in some cases also from vaccination.

The small difference in overall potency against the two variants means that an ability to evade immunity is unlikely to explain BA.2’s ascent worldwide, says Barouch.



In Denmark, where vaccination rates are high, BA.2's rise is so far not causing significant problems. Credit: Carsten Snebjerg/Bloomberg via Getty

## Comparing variants

The results chime with those from a 9 February preprint<sup>2</sup> led by virologist David Ho at Columbia University in New York City, which found that BA.2 and BA.1 had similar abilities to resist neutralizing antibodies in the blood of people who had been vaccinated or previously infected.

But Ho's team also found signs that genetic mutations unique to BA.2 affect how some antibodies recognize the variant. The researchers found that one family of antibodies that attach to a part of the spike protein that binds to host cells was much less effective at neutralizing BA.2 than BA.1, and another type of spike antibody tended to be more active against BA.2. And a 15 February preprint<sup>3</sup> led by virologist Kei Sato at the University of Tokyo

found that hamsters and mice infected with BA.1 produced antibodies that were less potent against BA.2 than BA.1.

It's not yet clear what the latest lab studies mean for immune protection against BA.2 in the real world. Barouch says his team's study cannot indicate whether people who have recovered from BA.1 are susceptible to BA.2 reinfection. But he thinks his team's data suggest that such risks are unlikely to be much higher for BA.2 than for BA.1.

According to news reports, researchers in Israel have identified a handful of cases in which people who had recovered from BA.1 became infected with BA.2. Meanwhile, Danish researchers have begun a study to determine how frequently such reinfections occur, says Troels Lillebaek, a molecular epidemiologist at the State Serum Institute in Copenhagen and chair of Denmark's SARS-CoV-2 Variants Risk Assessment Committee. "If there was no protection, that would be a surprise and, I think, unlikely. We will know for sure within a few weeks."

## Viral properties

Another study, of Omicron spread in more than 8,000 Danish households, suggests that BA.2's rise results from a mix of factors<sup>4</sup>. Researchers including Lillebaek found that unvaccinated, double-vaccinated and boosted individuals were all more susceptible to BA.2 infection than to BA.1 infection.

That unvaccinated people are also at heightened risk of BA.2 infection suggests that properties of the virus other than immune evasion are at least partly behind its enhanced transmissibility, says Lillebaek.

In Denmark, where vaccination rates are high, BA.2's ascent is so far not causing significant problems, says Lillebaek. A [preliminary study](#) found that the variant seems to cause no more severe illness than does BA.1, including in children.

But BA.2 could pose greater challenges in places that have lower vaccination rates, says Lillebaek. The variant's growth advantage over BA.1

means that it could extend Omicron peaks, increasing the odds of infection for older people and other groups at high risk of severe disease. “I think the main problem with BA.2 is even more transmission,” Lillebaek adds. “You risk even more people testing positive within a short time, putting strain on the hospital system.”

## Mutation, mutation, mutation

There are also hints that BA.2 could limit treatment options. In laboratory experiments, Ho’s team found<sup>2</sup> that the variant was resistant to a therapeutic monoclonal antibody, called sotrovimab, that was effective against BA.1. However, the drug’s manufacturer, Vir Biotechnology in San Francisco, California, said in a press release on 9 February that its own unpublished experiments suggest that sotrovimab remains effective against BA.2.

Identifying the specific properties of BA.2 and the genetic mutations responsible for its growth advantage will be no simple matter, says Luban. In other fast-spreading variants, including Alpha and Delta, researchers have spotted mutations that seem to speed transmission, but these are unlikely to fully explain those variants’ behaviour.

And molecular mechanisms that seem important for other variants’ advantages — such as those that control the virus’s ability to bind tightly to human cells or to quickly fuse its membrane with those of infected cells — might be less crucial in distinguishing between BA.1 and BA.2, adds Luban. “Omicron really slapped a lot of people in the face who thought everything was clear,” he says. “It’s a puzzle.”

*Nature* **602**, 556-557 (2022)

*doi:* <https://doi.org/10.1038/d41586-022-00471-2>

## References

1. Yu, J. *et al.* Preprint at medRxiv  
<https://doi.org/10.1101/2022.02.06.22270533> (2022).

2. Iketani, S. *et al.* Preprint at bioRxiv  
<https://doi.org/10.1101/2022.02.07.479306> (2022).
  3. Yamasoba, D. *et al.* Preprint at bioRxiv  
<https://doi.org/10.1101/2022.02.14.480335> (2022).
  4. Lyngse, F. P. *et al.* Preprint at medRxiv  
<https://doi.org/10.1101/2022.01.28.22270044> (2022).
- 

This article was downloaded by **calibre** from <https://www.nature.com/articles/d41586-022-00471-2>

| [Section menu](#) | [Main menu](#) |

- NEWS
- 16 February 2022
- Correction [16 February 2022](#)

# NIH issues a seismic mandate: share data publicly

The data-sharing policy could set a global standard for biomedical research, scientists say, but they have questions about logistics and equity.

- [Max Kozlov](#)



The US National Institutes of Health, located in Bethesda, Maryland, is the world's largest funder of biomedical research. Credit: Grandbrothers/Alamy

In January 2023, the US National Institutes of Health (NIH) will begin requiring most of the 300,000 researchers and 2,500 institutions it funds annually to include a data-management plan in their grant applications — and to eventually make their data publicly available.

Researchers who spoke to *Nature* largely applaud the open-science principles underlying the policy — and the global example it sets. But some have concerns about the logistical challenges that researchers and their institutions will face in complying with it. Namely, they worry that the policy might exacerbate existing inequities in the science-funding landscape and could be a burden for early-career scientists, who do the lion's share of data collection and are already stretched thin.

The mandate, in part, aims to tackle the reproducibility crisis in scientific research. Last year, a US\$2-million, eight-year attempt to replicate influential cancer studies [found that fewer than half of the assessed experiments](#) stood up to scrutiny. Efforts to tally the cost of irreproducible research in the United States [have found that \\$10 billion to \\$50 billion is spent](#) on studies that use deficient methods, a cost that is mostly fronted by public funding agencies.

Irreproducible studies not only waste taxpayers' money, says Lyric Jorgenson, the acting associate director for science policy at the NIH, but also undermine public trust in science. "We want to make sure that we're making good on the nation's investment and fostering transparency and accountability in research," she says.

Joseph Ross, a health-policy researcher at Yale School of Medicine in New Haven, Connecticut, says the mandate's effects will be felt far beyond US borders because the NIH is the world's largest public funder of biomedical research. Ensuring that the policy sets the right tone is important, Ross says, because it will signal to scientists all over the world how biomedical research should be done.

## A seismic shift

Under the new policy, which will go into effect on 25 January, all NIH grant applications for projects that collect scientific data must include a ‘data management and sharing’ (DMS) plan that contains details about the software or tools needed to analyse the data, when and where the raw data will be published and any special considerations for accessing or distributing that data.

Such a seismic shift in practice has left some researchers worried about the amount of work that the mandate will require when it becomes effective.

Jenna Guthmiller, an immunologist at the University of Chicago in Illinois, can attest that more work will probably be required. She is one of a handful of researchers funded through a US National Institute of Allergy and Infectious Diseases (NIAID) programme that has enacted a policy similar to the NIH-wide plan, she says. For Guthmiller, that meant tracking down information on long-gone reagents and experimental conditions for a project that’s been running for four years. That took 15 hours, she says, “and I was fortunate enough to work with a data manager”.

Because the vast majority of laboratories and institutions don’t have data managers who organize and curate data, the policy — although well-intentioned — will probably put a heavy burden on trainees and early-career principal investigators, says Lynda Coughlan, a vaccinologist at the University of Maryland School of Medicine in Baltimore, who has been leading a research team for fewer than two years and is worried about what the policy will mean for her.

Jorgenson says that, although the policy might require researchers to spend extra time organizing their data, it’s an essential part of conducting research, and the potential long-term boost in public trust for science will justify the extra effort.

Others worry that data-management activities will further sap funds from under-resourced labs. Although the policy outlines certain fees that researchers can add to their proposed budgets to offset the costs of compliance with the mandate, it doesn’t specify what criteria the NIH will use to grant these requests.

For the policy to be successful, Ross says that the NIH needs to be clear about how it will award these resources — especially to early-career researchers and to underfunded institutions — so as not to exacerbate existing inequities in the research community.

Jorgenson responds that the agency is evaluating the costs of compliance and hopes to prepare more guidance and information.

## Potential pitfalls

As part of the data-sharing policy, when a research project is complete or when its grant expires — whichever comes first — NIH programme officers will review the DMS plan to ensure that researchers have adhered to it. At that time, the policy stipulates that researchers must share any ‘scientific data’ needed to “validate and replicate research findings, regardless of whether the data are used to support scholarly publications” — although it makes an exception in cases where data sharing would pose a significant legal, ethical or technical burden. The NIH recommends that this data be shared only in a reputable repository; ultimately, researchers will decide where to upload the information.

The broad term ‘scientific data’ has left some researchers confused about exactly what information they’ll be required to share. It’s hard to predict which data might be useful for other researchers, or whether that data will ever be accessed by anyone, Coughlan says.

In response to an early draft of the policy, the American Association for Universities, an organization based in Washington DC that represents 66 universities, [wrote in 2020](#) that the NIH’s definition of scientific data needed to be narrowed, and suggested that the agency limit it to include only data underlying scholarly publications.

Jorgenson says that data collected when experiments don’t work — and therefore that are not in publications — are just as important to communicate, because they include information that could help other researchers to understand the full context of an experiment’s success. The

ambiguity in the policy offers researchers flexibility in determining which data are truly necessary to reproduce research findings, she says.

Brian Nosek, executive director of the Center for Open Science, based in Charlottesville, Virginia, points out that it will be a major challenge for the NIH to ensure that all relevant data have been shared at the conclusion of a project. Although the policy is an “important milestone of maturing the open-science movement beyond just thinking about open access”, Nosek worries that some applicants might not take it seriously if there are no consequences for non-compliance. Jorgenson responds that if the policy is not followed, future funding awards for researchers or institutions could be jeopardized.

Despite its potential pitfalls, Ross thinks that the policy will have a ripple effect that will persuade smaller funding agencies and industry to adopt similar changes. “This policy establishes what people expect from clinical research,” he says. “It’s essentially saying the culture of research needs to change.”

*Nature* **602**, 558-559 (2022)

*doi:* <https://doi.org/10.1038/d41586-022-00402-1>

## Updates & Corrections

- **Correction 16 February 2022:** In an earlier version of this story, Lyric Jorgenson's surname was spelled incorrectly.

---

This article was downloaded by **calibre** from <https://www.nature.com/articles/d41586-022-00402-1>

- NEWS
- 11 February 2022

# China's approval of gene-edited crops energizes researchers

Scientists say newly published guidelines will spur research into crops that have increased yields and greater resilience to climate change.

- [Smriti Mallapaty](#)



Powdery mildew, seen here growing on wheat, reduces the yield and quality of crops. Credit: Nigel Cattlin/Alamy

Researchers in China are excited by their government's approval of gene-edited crops, which they say clears the way for the plants' use in agriculture and should boost research into varieties that are tastier, pest-resistant and better adapted to a warming world.

Since China's agriculture ministry released preliminary guidelines on 24 January, researchers have been hurrying to submit applications for the use of their gene-edited crops. These include the development of wheat varieties

resistant to a fungal disease called powdery mildew, which are described in a paper in *Nature* this week<sup>1</sup>.

“This is very good news for us. It really opens the door for commercialization,” says plant biologist Caixia Gao at the Chinese Academy of Sciences’ Institute of Genetics and Developmental Biology in Beijing, who is a co-author of the paper.

“The decision is a big step forward for China,” and will take research from theory into the field, says Jin-Soo Kim, who heads the Center for Genome Engineering at the Institute for Basic Science in Daejeon, South Korea.

China’s new rules are more conservative than those in the United States — which does not regulate gene-edited crops that incorporate small changes similar to those that could occur naturally — but are more lenient than the tough European Union stance of treating all gene-edited crops as genetically modified (GM) organisms.

## No foreign genes

Gene-edited crops are developed using technologies such as CRISPR–Cas9 that can make small tweaks to DNA sequences. They differ from crops obtained by genetic modification because this typically involves the insertion of entire genes or DNA sequences from other plant or animal species. However, until now, in China they have come under the same legislation as that covering GM organisms.

Currently, it can take up to six years to get biosafety approval for a GM crop in China. But researchers say the new guidelines — which lay out the process for receiving a biosafety certificate for gene-edited crops — could reduce the approval time to one to two years.

GM crops require extensive, large-scale field trials before they are approved for use. The new guidelines stipulate that, for gene-edited crops deemed to pose no environmental or food-safety risks, developers need only provide laboratory data and conduct small-scale field trials.

However, researchers say that some of the guidelines are ambiguous. They apply to crops in which gene-editing technology is used to remove genes or make single-nucleotide changes, but it is not clear whether they also apply to crops that have had DNA sequences introduced from other varieties of the same species.

“We will have to confirm whether these are allowed,” because it is important to have clarity around the rules, says Chengcai Chu, a rice geneticist at South China Agricultural University in Guangzhou.

Already, researchers are planning to focus more of their work on developing new crops that will be valuable to farmers. For example, Jian-Kang Zhu, a plant molecular biologist at the Southern University of Science and Technology in Shenzhen, says he wants to develop gene-edited varieties that have increased yields, resilience against climate change and a better response to fertilizer.

Others are preparing applications for rice that is particularly aromatic, and soya bean that has a high content of oleic fatty acids, which could produce oil low in saturated fats.

## Resistance and growth

Gao’s powdery mildew-resistant wheat could be one of the first to be approved. In 2014, she and her team used gene editing to knock out a gene that make wheat susceptible to the fungal disease, but found that these changes also stunted the plant’s growth<sup>2</sup>. However, one of their edited plants grew normally, and the researchers found that this was due to deletion of a portion of chromosome that meant the expression of a gene involved in sugar production was not repressed.

Since then, the researchers have been able to remove that same portion of the chromosome, in addition to the gene that makes the plant susceptible to powdery mildew, creating fungus-resistant wheat varieties that don’t suffer from restricted growth.

“This is a very comprehensive and beautifully done piece of work,” says Yinong Yang, a plant biologist at Pennsylvania State University in University Park. It also has broad implications for almost all flowering plants, he says, because powdery mildew can infect some 10,000 plant species.

“It is really exciting work,” adds David Jackson, a plant geneticist at Cold Spring Harbor Laboratory in New York, although he cautions that the data on how well the wheat grew were based on relatively few plants largely grown in greenhouses and will need to be confirmed with larger field trials.

Studies such as this are evidence of China’s strong track record of research into gene-edited crops, and the new regulations “are set to see China take full advantage of their academic lead”, says Penny Hundleby, a plant scientist at the John Innes Centre in Norwich, UK.

*Nature* **602**, 559-560 (2022)

*doi:* <https://doi.org/10.1038/d41586-022-00395-x>

## References

1. Li, S. *et al.* *Nature* <https://doi.org/10.1038/s41586-022-04395-9> (2022).
2. Wang, Y. *et al.* *Nature Biotechnol.* **32**, 947–951 (2014).

---

This article was downloaded by **calibre** from <https://www.nature.com/articles/d41586-022-00395-x>

- NEWS
- 10 February 2022

# Heart-disease risk soars after COVID — even with a mild case

Massive study shows a long-term, substantial rise in risk of cardiovascular disease, including heart attack and stroke, after a SARS-CoV-2 infection.

- [Saima May Sidik](#)



The risk of 20 diseases of the heart and blood vessels is high for at least a year after a COVID-19 diagnosis.Credit: Living Art Enterprises/Science Photo Library

Even a mild case of COVID-19 can increase a person's risk of cardiovascular problems for at least a year after diagnosis, a new study<sup>1</sup> shows. Researchers found that rates of many conditions, such as heart failure and stroke, were substantially higher in people who had recovered from COVID-19 than in similar people who hadn't had the disease.

What's more, the risk was elevated even for those who were under 65 years of age and lacked risk factors, such as obesity or diabetes.

"It doesn't matter if you are young or old, it doesn't matter if you smoked, or you didn't," says study co-author Ziyad Al-Aly at Washington University in St. Louis, Missouri, and the chief of research and development for the Veterans Affairs (VA) St. Louis Health Care System. "The risk was there."

Al-Aly and his colleagues based their research on an extensive health-record database curated by the United States Department of Veterans Affairs. The researchers compared more than 150,000 veterans who survived for at least 30 days after contracting COVID-19 with two groups of uninfected people: a group of more than five million people who used the VA medical system during the pandemic, and a similarly sized group that used the system in 2017, before SARS-CoV-2 was circulating.

## Troubled hearts

People who had recovered from COVID-19 showed stark increases in 20 cardiovascular problems over the year after infection. For example, they were 52% more likely to have had a stroke than the contemporary control group, meaning that, out of every 1,000 people studied, there were around 4 more people in the COVID-19 group than in the control group who experienced stroke.

The risk of heart failure increased by 72%, or around 12 more people in the COVID-19 group per 1,000 studied. Hospitalization increased the likelihood

of future cardiovascular complications, but even people who avoided hospitalization were at higher risk for many conditions.

“I am actually surprised by these findings that cardiovascular complications of COVID can last so long,” Hossein Ardehali, a cardiologist at Northwestern University in Chicago, Illinois, wrote in an e-mail to *Nature*. Because severe disease increased the risk of complications much more than mild disease, Ardehali wrote, “it is important that those who are not vaccinated get their vaccine immediately”.

Ardehali cautions that the study’s observational nature comes with some limitations. For example, people in the contemporary control group weren’t tested for COVID-19, so it’s possible that some of them actually had mild infections. And because the authors considered only VA patients — a group that’s predominantly white and male — their results might not translate to all populations.

Ardehali and Al-Aly agree that health-care providers around the world should be prepared to address an increase in cardiovascular conditions. But with high COVID-19 case counts still straining medical resources, Al-Aly worries that health authorities will delay preparing for the pandemic’s aftermath for too long. “We collectively dropped the ball on COVID,” he said. “And I feel we’re about to drop the ball on long COVID.”

*Nature* **602**, 560 (2022)

doi: <https://doi.org/10.1038/d41586-022-00403-0>

## References

1. Xie, Y., Xu, E., Bowe, B. & Al-Aly, Z. *Nature Med.* <https://www.nature.com/articles/s41591-022-01689-3> (2022).

- NEWS
- 10 February 2022

# Cancer ‘moonshot’ has lofty new goal: halve deaths in 25 years

Researchers take stock of the US\$1.8-billion initiative’s first five years as Biden announces ambitious target.

- [Heidi Ledford](#)



Biden announced the Cancer Moonshot Initiative’s new target on 2 February.Credit: Anna Moneymaker/Getty

Pathologist and cancer researcher Michael Becich has two criteria for setting goals: they should be measurable, and they should lofty, even if that means they border on unattainable. “By trying to hit a lofty goal, we start to measure ourselves against that,” he says. “And what gets measured gets done.”

US President Joe Biden announced on 2 February that he would renew the US Beau Biden Cancer Moonshot Initiative — a \$1.8-billion cancer research programme that began 5 years ago and was slated to run for another 2 — with a fresh target of decreasing cancer deaths by at least 50% in the next 25 years. Becich saw a goal, albeit a lofty one, that he could get behind. “Here’s a politician trying to understand the science,” he says. “And I applaud him for what he wants to do with it.”

For Becich, who works at the University of Pittsburgh in Pennsylvania, and other cancer researchers, that’s a welcome change. For decades, they have been tethered to unrealistic political promises. In 1971, former president Richard Nixon aimed for cancer to be cured in five years. In 2016, then-vice-president Biden declared that the moonshot would achieve ten years of cancer research in only five years — a target that Becich considers worthy, but too subjective and difficult to measure. Even now, as researchers hope the renewal of the programme will come with a fresh influx of funds — Biden has yet to say how much — it will take years to determine whether the first five years has met that original target.

Congress awarded the moonshot’s first \$1.8 billion over seven years. Although this sounds like a dazzling sum, it constituted a relatively small annual investment, says epidemiologist Cary Gross at Yale School of Medicine in New Haven, Connecticut. The funds amounted to a yearly increase of only about 5% to the budget of the US National Cancer Institute (NCI), which funds moonshot programmes. “What was conveyed to the public with great excitement was that we’re going to reshape the way we do cancer research,” says Gross. “They said, ‘We’re going to revolutionize everything: you were getting \$100, now we’re going to give you \$105.’”

Still, the NCI found room to launch more than 240 projects covering a wide spectrum of cancer research. Moonshot programmes are studying therapies that stimulate the immune system to fight paediatric cancers, and are

compiling 3D atlases of tumour cells as they progress from precancerous lesions to advanced disease. There are programmes to address disparities in access to health care, and to improve the implementation of best clinical practices after they have been identified in clinical trials. And the NCI built data-sharing infrastructure, such as the Cancer Research Data Commons, to maximize the use of the generated data — a crucial way to amplify the impact of moonshot programmes, says Gross.

## Accelerated progress?

Despite the moonshot's achievements, it will be difficult to determine whether the programme has delivered on Biden's initial pledge to accomplish ten years' worth of progress in five. At a December meeting of the National Cancer Advisory Board, NCI deputy director Dinah Singer said that moonshot programmes had already yielded 1,212 publications, 14 supported patents and 22 clinical trials. On average, moonshot publications tended to be more heavily cited than other NCI-funded research, but Singer noted that this could be a by-product of the moonshot's focus on large collaborations, which tend to draw more citations. "We're struggling to identify what the right metrics are," Singer said.

That struggle will be compounded by an explosion in cancer research that began well before the moonshot's start date, says biomedical informaticist Jeremy Warner at Vanderbilt University in Nashville, Tennessee. Fuelled by advances in genomics, genome editing, diagnostics and biomarker discoveries, researchers have been pouring into the field. "It's even harder to ascertain if the moonshot itself accelerated progress," Warner says. "Because progress was already on a steep, non-linear climb."

Over the years, the NCI has worked hard to attract researchers from other fields to cancer research, says Anna Barker, chief strategy officer at the Ellison Institute for Transformative Medicine at the University of Southern California in Los Angeles and a former NCI deputy director. But the influx of applicants for funding combined with US budget uncertainty has led to low rates of awarded grants, she notes. Only about 9% of grant applications to the NCI are funded, and the NCI will struggle to keep that from dropping any lower, she says. "Recent advances are dragging all of these great people

from other disciplines, which was the goal,” Barker says. “We’ve been successful in doing that, but now we’ve got lots of applications.”

Biden’s decision to renew the moonshot — if it is accompanied by significant funding — could allow the NCI to delay the difficult task of shutting down projects linked to the initiative. As of December, about two-thirds of the funded projects had expressed interest in continuing past the original end of the moonshot, Singer told NCI advisers. Not all of these programmes were likely to win continued funding, she said — but if they did, the NCI would need an additional \$100 million each year to allow them to continue without taking funds from other NCI grant pools. “It’s really easy to start programmes,” says Barker. “And very difficult to stop them.”

## Earlier diagnosis

Details of the next iteration of the moonshot and its priorities are unclear at present, but Biden’s statement included references to advancing technologies that can lead to earlier diagnosis of cancers, and harnessing mRNA vaccines to target tumours. It also reiterated a commitment to data sharing.

For oncologist Bishal Gyawali at Queen’s University in Ontario, Canada, Biden’s renewed emphasis on ensuring access to cancer screening and early detection could represent a key moment for the field. In 2017, Gyawali called for a cancer ‘groundshot’ initiative that would focus on ensuring access to available treatments rather than hunting for the next cure. “All the fuss was about how wonderful the new innovations will be,” he says. “But that did not acknowledge the fact that we already have so many interventions in oncology that we already have proven to work, and most of the patients of the world don’t have access to these treatments.”

Lack of access is also a problem in the United States itself, says Amelie Ramirez, who studies population health at the University of Texas Health Science Center at San Antonio, Texas. For example, cancer is the number-one killer in the US Latinx community, she says. Many in this group lack access to early cancer screening — so they are diagnosed later in the disease course, she notes. “I was heartened to hear the specific words ‘to address

inequities' as its own goal in the renewed moonshot," she says. "The call to action for cancer screening is desperately needed."

For any moonshot effort, data sharing will be pivotal to ensure that the programmes maximize their impact, says Becich. Researchers in the first generation of moonshot programmes have been slower than he expected to upload their data to the Cancer Research Data Commons and other platforms, and he worries that they might not do so before the original moonshot comes to an end in two years.

"Instead of making the moonshot more complex, what we need to do is make sure that the central goal of sharing data [happens] as quickly as possible," Becich says. "Let's not just talk about doing it, let's measure the data-sharing. Let's make that a central part of where the moonshot goes."

*Nature* **602**, 561 (2022)

*doi:* <https://doi.org/10.1038/d41586-022-00376-0>

---

This article was downloaded by **calibre** from <https://www.nature.com/articles/d41586-022-00376-0>

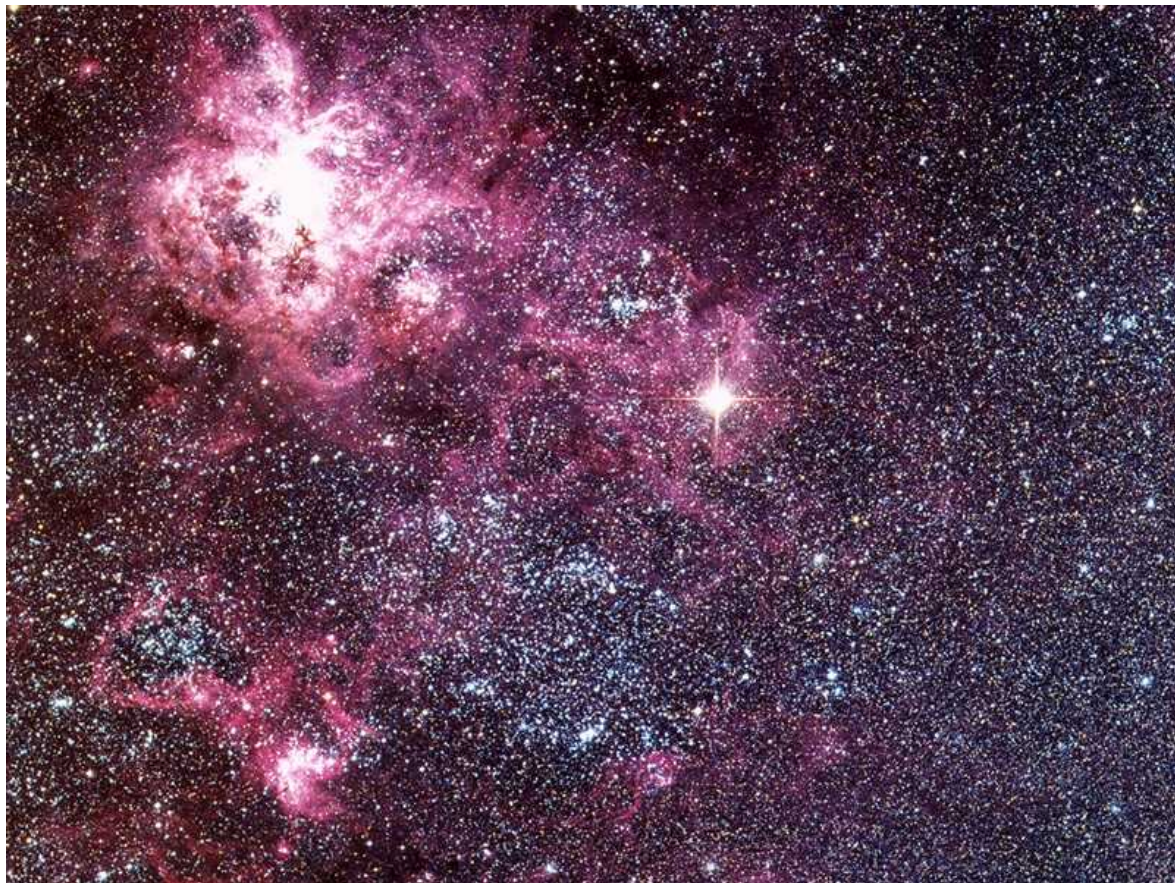
| [Section menu](#) | [Main menu](#) |

- NEWS FEATURE
- 21 February 2022

# A supernova could light up the Milky Way at any time. Astronomers will be watching

When a star from our Galactic neighbourhood explodes, it could outshine the Moon. Researchers are racing to get ready for the fireworks.

- [Davide Castelvecchi](#)



Supernova 1987A appears as a bright spot near the centre of this image of the Tarantula nebula, taken by the ESO Schmidt Telescope.Credit: ESO

Masayuki Nakahata has been waiting 35 years for a nearby star to explode.

He was just starting out in science the last time it happened, in February 1987, when a dot of light suddenly appeared in the southern sky. This is the closest supernova seen during modern times; and the event, known as SN 1987A, gained worldwide media attention and led to dramatic advances in astrophysics.

Nakahata was a graduate student at the time, working on what was then one of the world's foremost neutrino catchers, the Kamiokande-II detector at the Kamioka Underground Observatory near Hida, Japan. He and a fellow student, Keiko Hirata, spotted evidence of neutrinos pouring out of the supernova — the first time anyone had seen these fundamental particles originating from anywhere outside the Solar System.

Now, Nakahata, a physicist at the University of Tokyo, is ready for when a supernova goes off. He is head of the world's largest neutrino experiment of its kind, Super-Kamiokande, where upgrades to its supernova alert system were completed late last year. The improvements will enable the observatory's computers to recognize when it is detecting neutrinos from a supernova, almost in real time, and to send out an automated alert to conventional telescopes worldwide.

Astronomers will be waiting. "It's gonna give everybody the willies," says Alec Habig, an astrophysicist at the University of Minnesota, Duluth. Early warning from Super-Kamiokande and other neutrino observatories will trigger robotic telescopes — in many cases responding with no human intervention — to swivel in the direction of the dying star to catch the first light from the supernova, which will come after the neutrino storm.

But when the light arrives, it could be too much of a good thing, says Patrice Bouchet, an astrophysicist at the University of Paris-Saclay who made crucial observations of SN 1987A, from the La Silla Observatory in Chile. The brightest events, which would shine brighter than a full Moon and be

visible during the day, would overwhelm the ultra-sensitive but delicate sensors in the telescopes used by professional astronomers.

And some of the instruments Bouchet used back then no longer exist. “If η Carinae or Betelgeuse explode,” says Bouchet, referring to two well-known stars, “we are not ready to observe it as we did with ’87A.” Researchers will scramble to adapt their instruments on the fly, but the lion’s share of the observations could fall on amateur astronomers, who have smaller telescopes and are in many cases very proficient at using them.

The scientific pay-off will nevertheless be immense. Supernovae have rarely been observed up close, but they are crucial for understanding how the chemical elements that were forged inside stars by nuclear fusion disperse across galaxies. And the stellar explosions themselves synthesize elements that would not exist otherwise. The neutrinos that Nakahata and others hope to capture will provide a unique window into the extreme physics that goes on inside an exploding star, and could lead to important discoveries about the fundamental forces and particles of nature.

## New light

It was early in the morning of 24 February 1987, when Ian Shelton, the staff telescope operator at a Canadian observatory in Las Campanas, Chile, spotted an unexpected dot of light. It appeared on some routine exposures he had just taken of the Large Magellanic Cloud, a small galaxy that orbits the Milky Way and is visible in the southern sky.

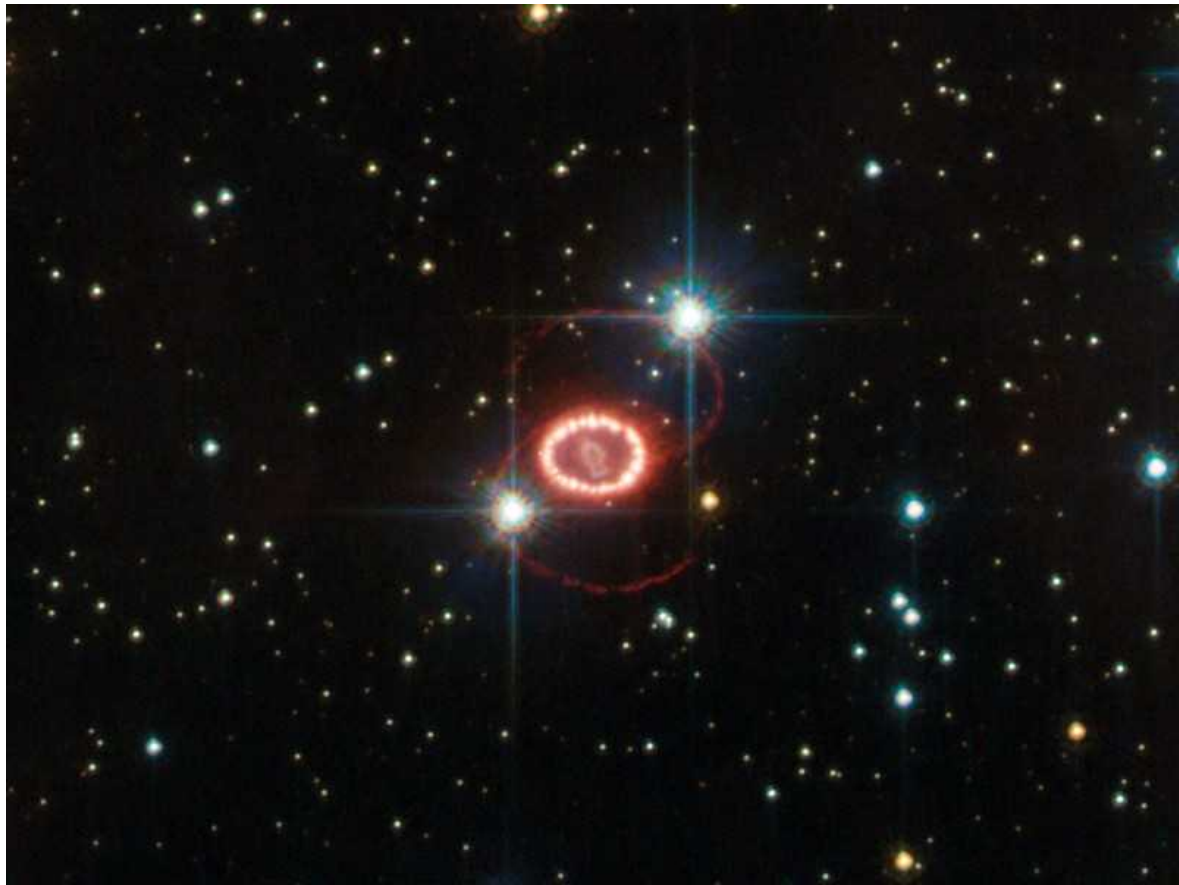
Shelton immediately realized that this could be a significant event. He stepped outside to look with his own eyes and, sure enough, noticed a bright star that had not been there before. It was the first such stellar object to be visible with the naked eye since the German astronomer Johannes Kepler recorded one in 1604.

Supernovae are among the most energetic cataclysms in the cosmos, shining for a period of weeks or months, and in some rare cases emitting more light than an entire galaxy. Supernova explosions comprise several types, but the

most common occurs at the end of the life of a very large star — one somewhere between 8 and 140 times the mass of the Sun.

The star runs out of fuel for the nuclear fusion that had been powering it, leaving behind an inert core of iron and nickel in a state of plasma. The outer layers of the star begin to fall inwards, and the core starts to collapse. In a span of milliseconds, most of the matter in the core gets so compressed that protons and electrons combine to form neutrons. The core's density suddenly rises by several orders of magnitude, because neutrons take up much less space than plasma. The neutrons pack into a denser ball — as dense as the laws of physics permit, forming what Habig calls a proto-neutron star inside the core.

The formation of each neutron releases a neutrino, and so the core's collapse releases a brief initial burst of neutrinos. But the cataclysm has only just begun. “The rest of the star is raining down on that proto-neutron star,” says Habig. After falling for thousands of kilometres in an intense gravitational field, the material hits the hard surface of the neutron core, bouncing back with a shock wave that propagates outwards. The shock wave is so violent that the rest of the star disintegrates, leaving only the neutron star as a remnant, which weighs around twice as much as the Sun.



The Hubble Space Telescope captured SN 1987A in 2011 surrounded by a set of glowing rings.Credit: ESA/Hubble & NASA

During the collapse itself, the energy released by the falling matter smashes elementary particles together as happens in a high-energy collider, continuously turning energy into new particles of all kinds. “It’s so incredibly hot and dense, everything is happening,” says Kate Scholberg, an astrophysicist at Duke University in Durham, North Carolina.

Most of those particles have nowhere to go and keep bumping into each other — with one exception. When a collision produces a neutrino, that particle will have a high chance of escaping into outer space without hitting anything else. As a result, many neutrinos are produced over a period of ten seconds or more. Researchers estimate that SN 1987A ejected  $10^{58}$  of these particles.

On these time scales, neutrinos are by far the dominant way in which the supernova dissipates energy. Although the shock wave can take many hours

to make it through the outer layers of the star and to become visible, neutrinos come out right away, practically at the speed of light. More than 99% of the energy from a core-collapse supernova escapes not as light, but as neutrinos.

Eventually, most of the star's original mass disperses into interstellar space. Over the following eons, it will trigger the formation of new stars and planets; our Solar System might have formed that way, some 5 billion years ago.

## The centre cannot hold

On average, one or two Milky Way stars per century undergo core collapse, according to the most recent estimates<sup>1</sup>. Yet throughout history, only five supernovae have been recorded as being visible with the naked eye, with two thought to be of the core-collapse type<sup>2</sup>. There are various reasons for this discrepancy. If enough mass concentrates in the collapsing core, it forms a black hole without producing much of a light show. In perhaps the majority of cases, an explosion does happen, but remains hidden from view by thick interstellar dust in the plane of the Milky Way, where massive stars reside.

Fortunately, the same physics that lets neutrinos escape a star's core will also let them cross the dusty Galactic Centre unimpeded. This means that neutrino detectors on Earth will pick up a shower of neutrinos no matter what, and so will record collapsing stars that would not have been detected by any other means.

And what a shower it will be. In 1987, Kamiokande-II was one of the world's largest neutrino detectors. Its 3,000 tonnes of water picked up 11 neutrinos; experiments in Ohio and Russia captured a handful, too. If a similar event were to occur today, Super-Kamiokande, which opened in 1996 and holds 50,000 tonnes of water, would spot at least 300 of the particles — and many more if the supernova occurs in our Galaxy, as opposed to in the Large Magellanic Cloud.

Beginning in 2018, Super-K, as the observatory is known, [had an upgrade that has vastly improved its ability to study supernovae](#). In particular, the Super-K collaboration, which includes Japanese and US physicists, added the rare-earth metal gadolinium to the detector's water. Its presence will enable the detector to clearly distinguish two types of supernova neutrino. One type produces flashes inside the detector that propagate in a random direction. But the flashes from the other type point straight back at the direction in which the neutrino was travelling.

Being able to tell the two apart in real time means that Super-K's software will rapidly calculate where in the sky astronomers should point their telescopes, within an angle of less than 3 degrees. "Using this information, Super-K is the world's best detector for determining the direction to a supernova," says Nakahata.

The supernova alert system, called SNWatch, is programmed to notify senior collaboration members about a possible sighting. At the same time, it sounds an alarm in the detector's cavernous underground hall and control room. Sara Sussman, a physicist now at Princeton University in New Jersey, spent time working at Super-K in 2017 during her undergraduate studies, and experienced the alarm in person. It went off during her first stint as the shift operator in the Super-K control room, and Sussman didn't know it was a drill. "I'm never gonna forget that moment for the rest of my life," she says.

Until recently, the Super-K procedures in case of a supernova prescribed that a senior team would hold an emergency meeting to decide whether the signal was genuine, and whether to send the news out. Starting last December, the collaboration removed any need for human intervention. In case of a neutrino shower, SNWatch will send an automated alert — including the event's coordinates in the sky — to astronomers within 5 minutes, Nakahata says. Future improvements in the software should bring that down to 1 minute, he adds.

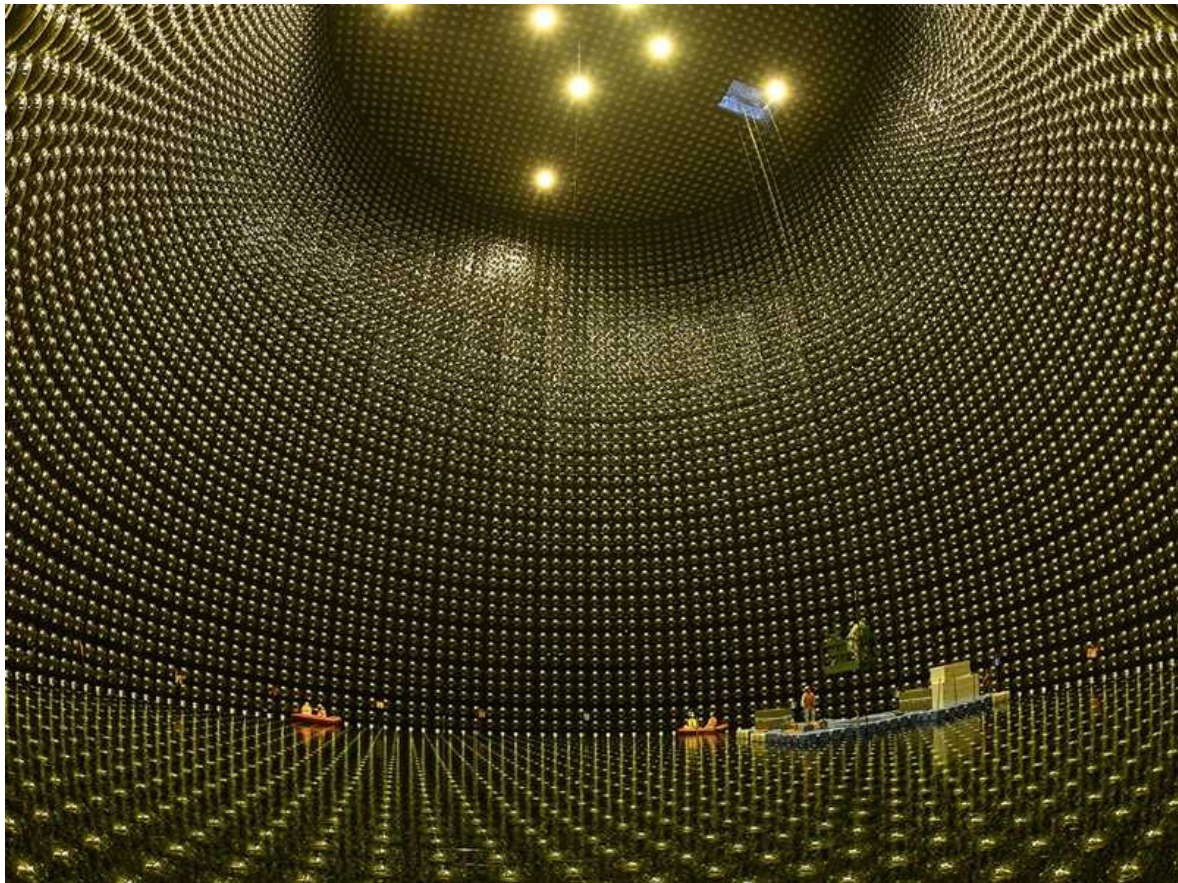
This will be a far cry from how information spread following the discovery of SN 1987A. The Chilean mountaintop of Las Campanas where Shelton worked did not even have a telephone line, and its radio telephone rarely worked. To alert other researchers to the scientific treasure that had just

appeared, observatory staff had to drive to the nearest town, two hours away, and send a telegram.

## On alert

Neutrino alert systems are not new: one has existed for nearly two decades. The Supernova Early Warning System (SNEWS) is a network involving Super-K and several other neutrino observatories. It includes IceCube, an array of light sensors embedded in a cubic kilometre of Antarctica's ice, and KM3NeT, a similar array submerged in the Mediterranean Sea. Large neutrino facilities now under construction in the United States and China are expected to join in the next few years, and Japan is building Hyper-Kamiokande, which will be five times larger than Super-K. "We expect 54,000–90,000 neutrinos if a supernova explodes in the centre of the Galaxy," says Francesca Di Lodovico, co-spokesperson for the Hyper-Kamiokande detector.

The main idea of SNEWS is to combine signals to improve the confidence in a detection, even if the individual ones look marginal at best. Each detector runs software that notifies a central SNEWS server of any unusual activity. SNEWS sends an alert to astronomers only if neutrino detectors in two separate geographical areas see a spike in activity within 10 seconds of each other. "If two see something and are not in the same lab, then it would be really hard for something random to happen in Japan and Italy, say," says Habig.



A team uses boats to work inside the Super-Kamiokande detector near Hida, Japan.Credit: Kamioka Observatory/Institute for Cosmic Ray Research/The University of Tokyo

Scholberg and Habig began working on SNEWS in the 1990s, a few years after SN 1987A made researchers realize the importance of getting neutrino alerts out quickly. Kamiokande-II had no live reporting system at the time. Nakahata and Hirata were charged with looking for supernova neutrinos after the fact; they printed out several days' worth of the detector's raw data — hundreds of pages of continuous-feed paper, the type with perforated edges — and [inspected it visually to find the bump](#).

Since SNEWS went live in 2005, it has not had the opportunity to send out a single alert. “You’ve got to admire the tenacity and the endurance,” says Robert Kirshner, an astronomer at Harvard University in Cambridge, Massachusetts. “They know they’re right, they know it’s important — but they’re not getting rewarded a lot.”

Now, SNEWS is about to roll out its first major upgrade, called SNEWS 2.0<sup>3</sup>. One goal is to produce alerts on the basis of lower-confidence sightings of possible supernova neutrinos. Observatories used to be conservative about sending out alerts, wanting to avoid any risk of false alarms. But in recent years, the culture has changed, and researchers are more comfortable exchanging lower-confidence alerts, just in case.

“The attitude has flipped 180 degrees,” Habig says. This change was brought in part by the advent of gravitational-wave astronomy, which yields weekly or even daily signals that many astronomers follow up using ordinary telescopes. That way, the same event can be studied using different astronomical phenomena, a trend called multi-messenger astronomy.

Another innovation of SNEWS 2.0 is that when multiple observatories record a neutrino shower, it will compare the exact timings of the particles’ arrival, and use those to triangulate back to the source. The pointing will be vastly less precise than that provided by Super-K alone, but the triangulation might end up being even faster, Habig says.

## Too much light

When Shelton spotted SN 1987A, Bouchet was in the right place at the right time. He had been working at the European Southern Observatory in La Silla, where he used a special device that could make infrared measurements of stars during the daytime. This meant that Bouchet could continue to measure the supernova’s brightness even when daylight in the sky drowned out the visible light from stars. But the telescope Bouchet used has been decommissioned, and no modern observatory has the right equipment to make daytime infrared measurements.

What’s worse, Bouchet adds, is that most large observatories have decommissioned their smaller visible-light telescopes, focusing on the largest, most sensitive instruments, which could be useless for observing a bright event. But Danny Steeghs, an astronomer at the University of Warwick, UK, is more optimistic. There has been a renaissance in ‘small astronomy’, he says, spurred in part by multi-messenger astronomy. “Now we have a new generation of more-bespoke, smaller telescopes,” Steeghs

says. When a supernova happens, he says, “we might miss the very first stages, but I am sure everyone will be creative.” Steeghs runs the Gravitational wave Optical Transient Observer, a system that can rapidly cover a large part of the sky to chase after possible light associated with gravitational waves.

“Even in the case of a really bright one, astronomers are clever and will find a way,” says Andy Howell, senior scientist at the Las Cumbres Observatory. Las Cumbres is an organization based near Santa Barbara, California, which runs a network of robotic telescopes that together give global coverage of the sky. “We could observe the supernova around the clock, since we always have telescopes in the dark.”

To observe extra bright objects, astronomers might use tricks such as taking short exposures, or partially blacking out the telescope’s mirror so that it reflects less light. But one of the most crucial observations — measuring the supernova’s brightness and how it evolves over time — will be difficult to do precisely. Astronomers usually measure a star’s brightness by calibration, by comparing it to that of another, well-known object in the same field of view. But calibration is difficult when the object of study is so bright that no other star can be seen in the same shot.

If professional astronomers stumble, an army of serious hobbyists might come to the rescue, Bouchet says. The American Association of Variable Star Observers (AAVSO), headquartered in Cambridge, Massachusetts, will help to coordinate the efforts of amateur astronomers, many of whom will be eager to jump in. “They would be on it — some of them within minutes,” says Elizabeth Waagen, an astronomer who has been on the AAVSO staff for 40 years and helps to coordinate observer campaigns.

“We are everywhere,” says Arto Oksanen, an IT professional based in Jyväskylä, Finland, who is a celebrity in the world of amateur astronomy. “At any given time, there is someone that can observe under clear skies.” Oksanen is the chair of a club of observers that built and runs its own remotely operated observatory, with a 40-centimetre reflector telescope and an automatic dome, some 300 kilometres north of Helsinki.

To take measurements of a very bright supernova, even smaller telescopes will do. Oksanen says that if the object is extremely bright — and assuming it is visible in the Finnish sky — the first thing he would probably do is take pictures with his Nikon digital SLR camera. With a supernova, time is of the essence, and even this rough method would record invaluable information about how the explosion varies in brightness.

But Tom Calderwood, an amateur astronomer in Bend, Oregon, says that few serious hobbyists have made such contingency plans to prepare for a possible supernova. “It’s definitely worth it for the amateur community to sit down and think what they would do,” he says.

The supernova of 1987 changed many lives overnight. Shelton decided to pursue a PhD in astronomy. Bouchet spent much of the next year on the Chilean mountaintop and has been studying the supernova and its remnants ever since, as has Kirshner, who has been involved in the search for SN 1987A’s neutron-star remnant. That’s something he could soon help to nail down using NASA’s recently launched [James Webb Space Telescope](#), which might be able to detect infrared radiation from the remnant that makes it through the surrounding shroud of dust. Nakahata’s boss at the time, the late Masatoshi Koshiba, shared a Nobel physics prize in 2002 for his work using Kamiokande-II, in large part for detecting the 11 supernova neutrinos.

Waagen says that many young people can trace the time when they became interested in astronomy — or science in general — to a specific day, when “some spectacular event caught their imagination and changed the course of their lives”. The next supernova will change a lot of lives, too, she says. “It will connect them to the sky in a new way.”

“It will be wild,” says Ed Kearns, a particle physicist at Boston University in Massachusetts. “I don’t know exactly what’s going to happen, because there’s so much human nature involved.” No supernova neutrinos have been detected since 1987, but it could happen any time, he adds. “Every year is a fresh year, every day is a fresh day for a chance at a supernova.”

*Nature* **602**, 562-565 (2022)

doi: <https://doi.org/10.1038/d41586-022-00425-8>

# References

1. Rozwadowska, K., Vissani, F. & Cappellaro, E. *N. Astron.* **83**, 101498 (2021).
2. Murphey, C. T., Hogan, J. W., Fields, B. D. & Narayan, G. *Mon. Not. R. Astron. Soc.* **507**, 927–943 (2021).
3. Al Kharusi, S. *et al.* *N. J. Phys.* **23**, 031201 (2021).

---

This article was downloaded by **calibre** from <https://www.nature.com/articles/d41586-022-00425-8>

| [Section menu](#) | [Main menu](#) |

- NEWS FEATURE
- 23 February 2022

# The giant plan to track diversity in research journals

Efforts to chart and reduce bias in scholarly publishing will ask authors, reviewers and editors to disclose their race or ethnicity.

- [Holly Else](#) &
- [Jeffrey M. Perkel](#)

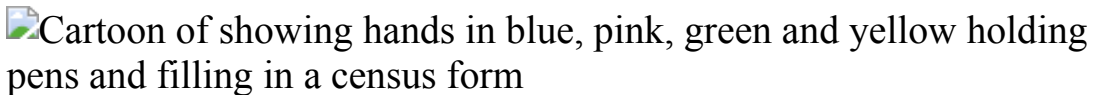


Illustration by Camelia Pham/Folio Art

In the next year, researchers should expect to face a sensitive set of questions whenever they send their papers to journals, and when they review or edit manuscripts. More than 50 publishers representing over 15,000 journals globally are preparing to ask scientists about their race or ethnicity — as well as their gender — in an initiative that's part of a growing effort to analyse researcher diversity around the world. Publishers say that this information, gathered and stored securely, will help to analyse who is represented in journals, and to identify whether there are biases in editing or review that sway which findings get published. Pilot testing suggests that many scientists support the idea, although not all.

The effort comes amid a push for a [wider acknowledgement of racism and structural racism in science and publishing](#) — and the need to gather more information about it. In any one country, such as the United States, ample data show that minority groups are under-represented in science, particularly at senior levels. But data on how such imbalances are reflected — or intensified — in research journals are scarce. Publishers haven't

systematically looked, in part because journals are international and there has been no measurement framework for race and ethnicity that made sense to researchers of many cultures.

“If you don’t have the data, it is very difficult to understand where you are at, to make changes, set goals and measure progress,” says Holly Falk-Krzesinski, vice-president of research intelligence at the Dutch publisher Elsevier, who is working with the joint group and is based in Chicago, Illinois.

In the absence of data, some scientists have started measuring for themselves. Computational researchers are scouring the literature using software that tries to estimate racial and ethnic diversity across millions of published research articles, and to examine biases in who is represented or cited. Separately, over the past two years, some researchers have criticized publishers for not having diversity data already, and especially for being slow to collate information about small groups of elite decision makers: journal editors and editorial boards. At least one scientist has started publicizing those numbers himself.

After more than 18 months of discussion, publishers are now close to agreeing on a standard set of questions — and some have already started gathering information. Researchers who have pushed to chart racial and ethnic diversity at journals say that the work is a welcome first step.

“It is never too late for progress,” says Joel Babdor, an immunologist at the University of California, San Francisco. In 2020, he co-founded the group Black in Immuno, which supports Black researchers in immunology and other sciences. It urges institutions to collect and publish demographic data, as part of action plans to dismantle systemic barriers affecting Black researchers. “Now we want to see these efforts being implemented, normalized and generalized throughout the publishing system. Without this information, it is impossible to evaluate the state of the current system in terms of equity and diversity,” the group’s founders said in a statement.



Immunologist Joel Babdor, who co-founded the group Black in Immuno. Credit: Noah Berger for UCSF

## Lacking data

The effort to chart researcher diversity came in the wake of protests over the killing of George Floyd, an unarmed Black man, by US police in May 2020. That sparked wider recognition for the Black Lives Matter movement and of the structural racism that is embedded in society, including scientific institutions. The following month, the Royal Society of Chemistry (RSC), a learned society and publisher in London, led 11 publishers in signing a joint commitment to track and reduce bias in scholarly publishing (see [go.nature.com/36gqrtp](https://go.nature.com/36gqrtp)). This would include an effort to collect and analyse anonymized diversity data, as reported by authors, peer reviewers and editorial decision makers at journals. That group has now grown to 52 publishers. (Springer Nature, which publishes this journal, has joined the group; *Nature*'s news team is editorially independent of its publisher.)

But publishers had a problem: they were lacking data. Many had made a start collecting and analysing information on gender, but few had tried to chart the ethnic and racial make-up of their contributors. Some that had done so had relied on their links to scholarly societies to gather regionally limited data.

The American Geophysical Union (AGU) in Washington DC, for instance, which is both a scientific association and a publisher, held information about some US members who had disclosed their race or ethnicity. In 2019, researchers used these data to study manuscripts submitted to AGU journals<sup>1</sup>. They cross-checked author information with the AGU member data set, and found that papers with racially or ethnically diverse author teams were accepted and cited at lower rates than were those that had homogenous teams. But the scientists were able to check the race or ethnicity of author teams for only 7% of the manuscripts in their sample.

The UK Royal Society in London, meanwhile, had [used annual surveys to collect data for its journals](#). But by mid-2020, its most recent report (covering 2018) had responses from just 30% of editors and 9% of authors and reviewers, in the categories ‘White British’, ‘White other’ and ‘Black and minority ethnic’. (Here, and throughout this article, the categories listed are terms chosen by those who conducted a particular survey or study.)



Holly Falk-Krzesinski.Credit: Elsevier

The joint commitment group decided that it would ask scientists about their gender and race or ethnicity when they authored, reviewed or edited manuscripts. The group started by agreeing on a standard schema, or structured list, of questions about gender — although even this wasn't simple, requiring detailed explanatory notes. But what to ask researchers globally about race and ethnicity was a tougher problem, as publishers such as Elsevier had discussed before they joined the group. "It almost seemed an insurmountable challenge when we were working on it on our own," says Falk-Krzesinski.

Cultural understanding of race and ethnicity differs by country: social categories in India or China, for instance, are different from those in the United States. The historical associations of asking people to disclose these personal descriptors pose another set of problems, and could, if not sensitively handled, intensify concerns about how these data will be used. In countries such as the United States, people might be accustomed to sharing the information with their employers; some companies are required to report this to the federal government by law. But in others, such as Germany, authorities do not collect race or ethnicity data. Here, there is extreme sensitivity around racial classification — rooted in revulsion at the way such information was used in the 1930s and 1940s to organize the Holocaust. Race and ethnicity data must also be carefully processed during collection and storage under Europe's data-protection laws.

## Computational audits

In the absence of comprehensive data, many studies in the past decade have used computational algorithms to measure gender diversity. Processes that estimate gender from names are far from perfect (particularly for Asian names), but seem statistically valid across large data sets. Some of this work has suggested signs of bias in peer review. An analysis of 700,000 manuscripts that the RSC published between 2014 and 2018, for instance<sup>2</sup>, pointed the organization to biases against women at each stage of its publishing process; in response, it developed a guide for reducing gender bias. Collecting those data was crucial, says Nicola Nugent, publishing

manager at the RSC in Cambridge, UK — without the baseline numbers, it was hard to see where to make changes.

Some researchers have also developed algorithms to estimate ethnicity or geographical origin from names. That idea goes back decades, but has become easier with massive online data sets of names and nationalities or ethnicities, together with growing computer power. Such algorithms can only ever provide rough estimates, but can be run across millions of papers.

US computational biologist Casey Greene at the University of Colorado Anschutz Medical Campus in Aurora argues that publishers could glean insights from these methods, if they apply them to large numbers of names and limit analysis to broad ethnicity classes — especially when examining past papers, for which it might not be possible to ask authors directly.

In 2017, for instance, a team led by computer scientist Steven Skiena at Stony Brook University in New York used millions of e-mail contact lists and data on social-media activity to train a classifier called NamePrism. It uses people's first and last names to estimate their membership of any of 39 nationality groups — for example, Chinese, Nordic or Portuguese — or six ethnicities, corresponding to categories used by the US Census Bureau<sup>3</sup>. NamePrism clusters names into similar-seeming groups, and uses curated lists of names with known nationalities to assign nationalities to those groups. It is more accurate for some categories than for others, but has been cited in a few dozen other studies.

Some studies use these kinds of tools to analyse representation. In 2019, Ariel Hippen, a graduate student in Greene's lab, scraped biographical pages from Wikipedia to train a classifier that assigns names to ten geographical regions. A team including Greene, Hippen and data scientist Trang Le at the University of Pennsylvania, Philadelphia, then used the tool to document under-representation of people from East Asia in honours and invited talks awarded by the International Society for Computational Biology<sup>4</sup>. Last year, Natalie Davidson, a postdoc in the Greene lab, [used the same tool to quantify representation in \*Nature\*'s news coverage](#), finding fewer East Asian names among quoted sources, compared with their representation in papers<sup>5</sup>.

Other studies analyse citation patterns. For instance, one analysis<sup>6</sup> of US-based authors found that papers with authors of different ethnicities gained 5–10% more citations, on average, than did papers with authors of the same ethnicity, a finding that has been [interpreted as a benefit of diverse research groups](#). And a 2020 preprint<sup>7</sup> from a team led by physicist Danielle Bassett at the University of Pennsylvania found that authors of colour in five neuroscience journals are undercited relative to their representation; the team’s analysis suggests that this is because white authors preferentially cite other white authors.

Instead of training a classifier, a different idea is to estimate ethnicity directly from census information — although this approach is limited to names from the country that did the census. In January, a team used<sup>8</sup> US Census Bureau data to assign US names a probability distribution of being associated with any of four categories: Asian, Black, Latinx or White. The researchers then studied papers by 1.6 million US-based authors, and found that work from what they describe as minoritized groups is over-represented in topics that tend to receive fewer citations, and that their research is less cited within topics.

Still, Cassidy Sugimoto, an information scientist at the Georgia Institute of Technology in Atlanta who worked on that study, says computational methods are largely incapable of addressing the most pressing questions about racial diversity and inclusion in science. This is because ethnicity is only loosely associated with family name (most obviously in the case of surname changes after marriage), and has many more dimensions than gender. “Race and ethnicity classification is infinitely more complicated than gender disambiguation,” she says.

Given those complex dimensions, the best option for collecting data is simply to invite scientists to self-identify, says Jory Lerback, a geochemist at the University of California, Los Angeles, who worked with the AGU on its studies of academic diversity.

Hippen, Davidson and Greene agree. In a correspondence article<sup>9</sup> this year, they advise those using automated tools to be transparent, to share results with affected communities and to ask people how they identify, if possible.

## Called out for inaction

As publishers discussed how to follow up their June 2020 commitment, they faced outside pressure. An increasing number of scientists began calling out the publishing industry for its inaction on providing diversity data.

In October 2020, *The New York Times* reported how several US scientists, including Babdor, were unhappy that publishers, despite their commitment, had no idea of how many Black researchers were among their authors.

That same month, Raymond Givens, a cardiologist at Columbia University Irving Medical Center in New York City, had begun privately tallying editors' ethnicities himself. He counted the number of what he classed as Black, brown, white and Hispanic people on the editorial boards of two leading medical journals, *The New England Journal of Medicine (NEJM)* and *JAMA*, after reading a now-retracted article<sup>10</sup> on affirmative-action programmes, published in a different society journal. Givens categorized the editors by looking at their photographs online, together with other contextual clues, such as surname and membership of associations that might indicate identity, and determined that just one of *NEJM*'s 51 editors was Black and one was Hispanic. At *JAMA*, he found that 2 of 49 editors were Black and 2 were Hispanic. Givens e-mailed the journals his data; he had no response from *JAMA* and got an acknowledgement from *NEJM*, but editors there didn't get back to him.



Cardiologist Raymond Givens tallied data on editors at leading medical journals. Credit: Nathan Bajar/NYT/Redux/eyevine

Within months, *JAMA* had become embroiled in controversy after a deputy editor, Edward Livingston, hosted a podcast in which he questioned whether structural racism could exist in medicine if it was illegal. More than 10,000 people have now signed a petition calling for *JAMA* to take measures to review and restructure its editorial staff and processes, as well as to commit to a series of town-hall conversations with health-care staff and patients who are Black, Indigenous and people of colour (BIPOC). Livingston, and Howard Bauchner, the then-editor-in-chief of *JAMA*, have also stepped down from their posts.

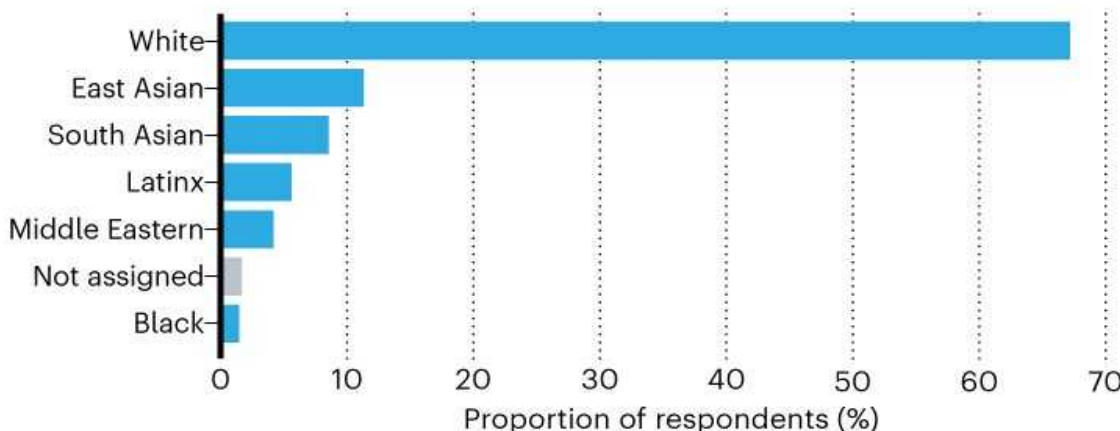
Givens' efforts became public in April 2021, when [news website STAT reported his findings](#). "A lot of journals have all of a sudden been shocked by being confronted in this way," says Givens. But it's important to ask why it has taken them so long to start thinking about how to collect this kind of information, he says. He acknowledges that making his own categorizations is an "imperfect" method, but says someone had to undertake the project to confront journals with the problem.

Both *JAMA* and *NEJM* say they have added BIPOC editors to their boards, although *NEJM* did not provide a breakdown of editorial staff ethnicities when asked. *JAMA*, meanwhile, has published aggregate data only on editors and editorial board members across its 13 JAMA Network journals.

Givens still has concerns that those who have joined editorial boards have peripheral influence compared with white men who retain central, powerful positions. He has continued his work, gathering gender and race data by eye on more than 7,000 editors at around 100 cardiology journals — finding that fewer than 2% are Black and almost 6% are Latinx — and looking at networks between the editors ('A view of cardiology editors' diversity').

## A VIEW OF CARDIOLOGY EDITORS' DIVERSITY

Cardiologist Raymond Givens conducted his own analysis of race or ethnicity of more than 7,000 editors at around 100 cardiology journals. He reports that less than 2% were Black.



©nature

\*Categories listed are those used by Givens, who assigned identities himself.

Source: R. Givens

“When you look at the networks, white men are central: they are the hub from which all the spokes emanate,” he says. “Sometimes you really have to shake the system to force it to change. Until you are going to reshape the system, we will still be having this conversation a decade from now.”

When it comes specifically to information on editorial board members, Givens says that’s not difficult to collect — if publishers truly put in the effort. He says it took him only a few months to do it. “It’s just counting,” he says. “When people say you have to start with collecting the data, I never have confidence that it will lead to anything. There needs to be intense pressure on them.”

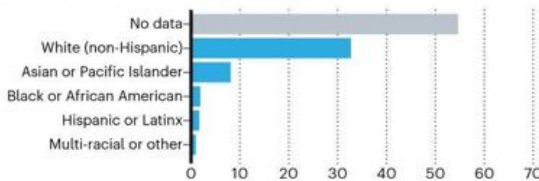
*Nature*'s news team asked seven high-profile journals besides *JAMA* and *NEJM* (including *Nature*) for information about the diversity of editorial board members and professional staff. None provided it at the journal level, but some shared information about the make-up of staff across their entire company, or wider family of journals (see ‘Editors at high-profile journals’ and supplementary information). These broader metrics might not reflect diversity at any one journal.

## EDITORS AT HIGH-PROFILE JOURNALS

Nature journalists asked publishers of nine scientific journals for data on the diversity of their editors or professional staff. None provided race or ethnicity data at the journal level, although some did across a family of journals. For detailed responses, see Supplementary information<sup>a</sup>.

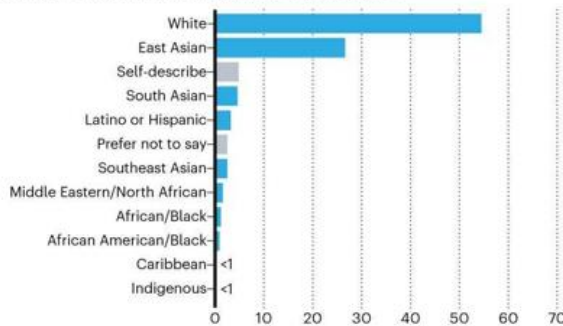
### Science

Provided gender and race or ethnicity data for editors and advisers across the Science family of journals.



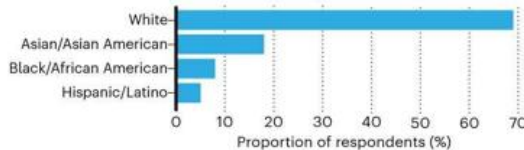
### Journal of the American Chemical Society

Provided gender data for ACS editorial board and race or ethnicity data across editors at American Chemical Society journals<sup>b</sup>.



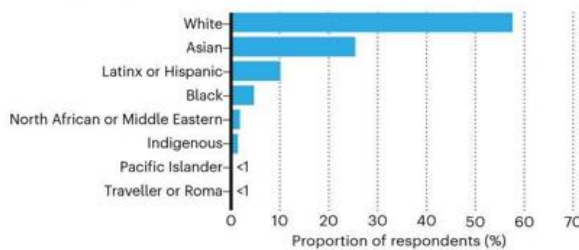
### JAMA

Provided data for editors or editorial board members for all JAMA network journals.



### Nature

Provided gender and race or ethnicity data for staff across entire company (Springer Nature), for 62% who took part in survey<sup>c</sup>.



### Proceedings of the National Academy of Sciences USA (PNAS)

Provided gender data for the PNAS editorial board.

### The Lancet

Provided gender data for international editorial advisers across all Lancet journals.

### Cell

Does not currently request personal data from staff.

### The New England Journal of Medicine

Provided gender and some ethnicity information only for new additions among editors and editorial board since 2019.

### Angewandte Chemie

Provided geographical (but not gender, race or ethnicity) data for an international advisory board, and gender data for a scientific advisory committee that is "helping to shape the scientific profile" of the journal.

<sup>a</sup>Categories listed are those used by the publishers that collected the data.

<sup>b</sup>Respondents could select more than one category.

Sources: AAAS/ACS/JAMA/Springer Nature/PNAS/The Lancet/Cell/NEJM/Angew. Chem.

## Ethnicity surveys

While the joint group of publishers started work on its race and ethnicity schema, some US publishers — who were not all in the group at the time — raced ahead with data collection.

As far back as 2018, the American Association for the Advancement of Science (AAAS) in Washington DC had begun working on how best to ask manuscript authors and reviewers about their race and ethnicity. It decided to use categories that closely followed US census descriptions, because that is a vetted system familiar to those in the United States, a spokesperson says.

In October 2020, [the AAAS published data it had collected over the past year](#). The respondents covered only 12% of authors and reviewers in the Science family of journals. [A report covering the subsequent year](#), released in January 2022, upped that coverage to 33%, because, the publisher said, it had improved the way it collected information using its electronic submission system for manuscripts and peer review. But data are still limited, and the AAAS is concerned that some researchers might not feel confident disclosing their ethnicity, its spokesperson says. The overall proportion identifying as African American or Black was less than 1%. Of the proportion who did report ethnicity, 57% identified as white (non-Hispanic) and 34% as Asian or Pacific Islander (which the AAAS grouped together in its reporting). The publisher is refining its race and ethnicity questions and last month added its name to the joint commitment. It is now looking at whether to adopt that group's schema, when the framework is ready.

Another publisher that raced ahead was the American Chemical Society (ACS) in Washington DC, an early signatory of the joint commitment. It also pledged in June 2020 to collect demographic data to make its journals more representative of the communities it serves. From February to September 2021, it started to ask authors and reviewers across its more than 75 journals for their gender and racial or ethnic identities (with a choice of

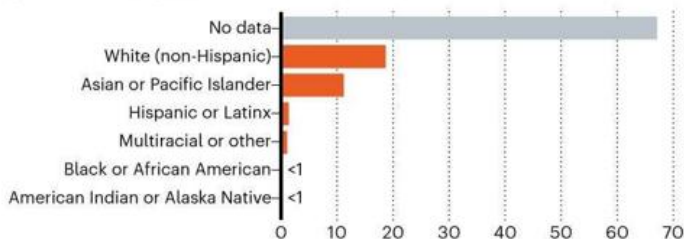
ten categories), among other questions. Designing the categories required some market research, with a goal of being inclusive and crafting questions that are clear and easy to answer, says Sarah Tegen, a senior vice-president in the ACS journals publishing group. In December 2021, the ACS announced [aggregate results from more than 28,000 responses](#); only around 5% of respondents chose not to disclose race or ethnicity. It noted that, among authors who gained their PhD more than 30 years ago, just under two-thirds identified as white — but among those who gained it less than 10 years ago, only about one-quarter did. Among editors of all ACS journals, 55% were white, 27% East Asian and 1.2% African/Black. Tegen says the data are a useful baseline for understanding the demographics of ACS journals (see ‘Early data on race and ethnicity from journals’).

## EARLY DATA ON RACE AND ETHNICITY FROM JOURNALS

Publishers are still discussing how to collect global data on the race or ethnicity of authors, editors or reviewers at their journals. Some have already published information — but differ in the categories they report\*.

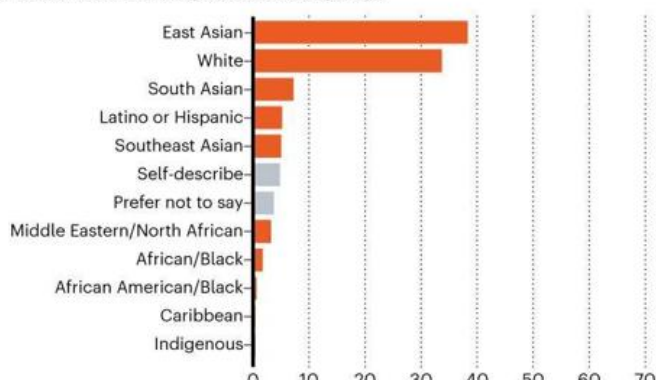
### American Association for the Advancement of Science (AAAS)

Science family authors and reviewers. (For further AAAS data, see [go.nature.com/3syj35b](https://go.nature.com/3syj35b).)

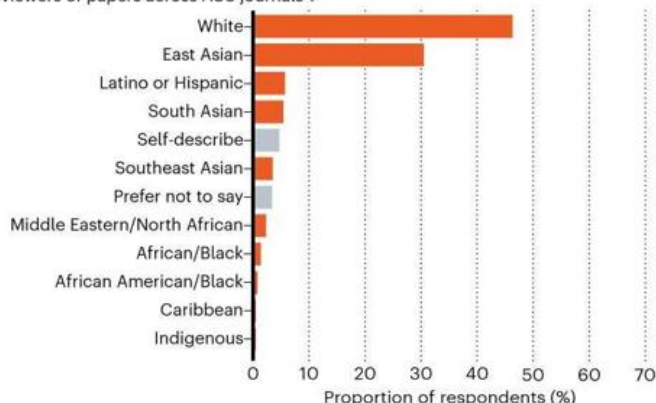


### American Chemical Society (ACS)

Corresponding authors submitting across ACS journals\*. (For further ACS data, see [go.nature.com/3gx7zqj](https://go.nature.com/3gx7zqj).)

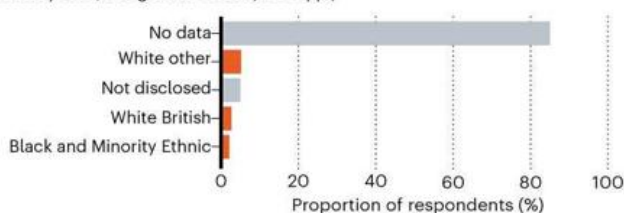


Reviewers of papers across ACS journals†.



### Royal Society

Authors across Royal Society journals. (For further Royal Society data, see [go.nature.com/3bu7qtp](https://go.nature.com/3bu7qtp).)



\*Categories listed are those used by the publishers that collected the data.

†Respondents could select more than one category.

Sources: AAAS/ACS/R. Soc.

For its part, the joint group of publishers was ready in February 2021 to consult a specialist — demographer Ann Morning at New York University — about its draft framework for asking about race and ethnicity. “It was a neat challenge,” says Morning, who advises the US government on its census process. She was intrigued by the difficulty of coming up with a standard schema that could apply across cultures. At that time, she says, publishers had thrown together a list of terms describing race and ethnicity, but they had not thought about how it would all fit together. “It was immediately obvious it was very confused.” She advised separating ethnicity and race into two questions. The first covered geographical ancestry and provided 11 options, including illustrative examples. The second covered race, in six options. (In both cases, respondents can choose not to answer.)



Ann Morning.Credit: Miller/NYU Photo Bureau

The draft was then sent to researchers for pilot testing, with a short accompanying survey. Of more than 1,000 anonymous respondents, greater

than 90% reported their race and ethnicity, and more than two-thirds said they felt well represented in the schema. About half said they would be comfortable providing this information when submitting a paper.

The results suggest that some respondents were not willing to give information. But Falk-Krzesinski, who led the market research on behalf of the joint group, says that the response rate was much higher than expected. “Even if people didn’t feel entirely well represented, they were willing to answer. They didn’t need perfection,” she says.

Some respondents who were concerned about giving their race or ethnicity said they didn’t feel it necessary to disclose because they believed science was a meritocracy; others, however, worried about how the data would be used. The publisher group has since changed the wording of its questions to make clearer why it is collecting the data and how they will be used and stored. The information will not be visible to peer reviewers, and although collected through editorial management systems, will be stored separately, with tightly controlled access, Falk-Krzesinski says.

Publishers will meet next month to vote on endorsing the schema to roll it out into editorial management systems; they declined to share the final list of questions and categories publicly until they had reached a consensus.

The American Psychological Association (APA) in Washington DC, which publishes 90 journals, has forged its own path outside the joint group. Last year, it updated its electronic manuscript system, which had previously only invited users to give gender information and the option to answer ‘yes’ or ‘no’ for minority or disability status. Now, users can choose from 11 options describing race and ethnicity (similar to, but not the same as, US census categories), and from a wider slate of descriptors around gender identity. A blog post on this initiative noted that the data will help to set goals to develop more representative pools of authors and editorial board members (see [go.nature.com/3uwkab7](https://go.nature.com/3uwkab7)). In the longer term, researchers hope to study acceptance rates for authors with various demographics to examine potential biases in peer review.

## From data to policy

Babdor is not surprised it has taken publishers so long to agree on standards to collect data, because of the complexity and the fact that it has not been done before. “Every country has its own rules about how to talk about these issues,” he says.

He says that the data should be freely available so that everyone can analyse and discuss them — and that it will be crucial to look at the compounding effects of intersectionality, such as how disparity affects Black women and Black disabled individuals.

Keletso Makofane, a public-health researcher and activist at the Harvard T.H. Chan School of Public Health in Boston, Massachusetts, says that the efforts of publishers are a fantastic start. He sees a use for the data in his work — a project to track the networks of researchers who are studying structural racism. Understanding the race and ethnicity of the scientists involved in this type of work is important, he says. But it’s not just about authors and reviewers. “It’s important to look at the people who make the higher-level decisions about policies of the journals,” he says.

To engage the historically marginalized populations they hope to reach, Lerback says, publishers (and researchers studying how ethnicity affects scholarly publishing) must commit to engaging with these groups beyond simply asking for data. Most importantly, she adds, they should build trust by following up findings with action.

In the wake of her AGU study, for instance, the organization changed its article submission system with the aim of increasing the diversity of peer reviewers. It now points out to both authors and editors that the process of recommending or finding reviewers can be biased — and invites them to expand their peer-review networks.

“Data is the currency of which policy gets implemented,” Lerback says.

*Nature* **602**, 566-570 (2022)

*doi:* <https://doi.org/10.1038/d41586-022-00426-7>

## References

1. Lerback, J. C., Hanson, B. & Wooden, P. *Earth Space Sci.* **7**, e2019EA000946 (2020).
2. Day, A. E., Corbett, P. & Boyle, J. *Chem. Sci.* **11**, 2277–2301 (2020).
3. Ye, J. *et al.* *Proc. 2017 ACM Inf. Knowl. Mgmt* 1897–1906 (2017).
4. Le, T. T. *et al.* *Cell Syst.* **12**, 900–906 (2021).
5. Davidson, N. R. & Greene, C. S. Preprint at bioRxiv  
<https://doi.org/10.1101/2021.06.21.449261> (2021).
6. Freeman, R. B. & Huang, W. *Nature* **513**, 305 (2014).
7. Bertolero, M. A. *et al.* Preprint at bioRxiv  
<https://doi.org/10.1101/2020.10.12.336230> (2020).
8. Kozlowski, D., Larivière, V., Sugimoto, C. R. & Monroe-White, T. *Proc. Natl Acad. Sci. USA* **119**, e2113067119 (2022).
9. Hippen, A. A., Davidson, N. R. & Greene, C. S. *Nature Hum. Behav.*  
<https://doi.org/10.1038/s41562-021-01279-2> (2022).
10. Wang, N. C. *J. Am. Heart Assoc.* **9**, e015959 (2020); retraction **9**, e014602 (2020).

---

This article was downloaded by **calibre** from <https://www.nature.com/articles/d41586-022-00426-7>

## Books & Arts

- **Lies of the land: how eugenicists tried to hijack the north**

[ 21 February 2022]

Book Review • There's so much more to the Arctic than tundra, explorers and pseudoscience.

- **Origins of consciousness, and sustainable cities: Books in brief** [ 07 January 2022]

Book Review • Andrew Robinson reviews five of the week's best science picks.

- BOOK REVIEW
- 21 February 2022

# Lies of the land: how eugenicists tried to hijack the north

There's so much more to the Arctic than tundra, explorers and pseudoscience.

- [Josie Glausiusz](#) 0



Hunter Henrik Josvasson navigates through ice near Tasiilaq, Greenland. Credit: Lucas Jackson/Reuters/Alamy

## **Extreme North: A Cultural History** Bernd Brunner (*transl. Jefferson Chase*) WW Norton (2022)

In *The Idea of North*, a 1967 radio documentary by pianist Glenn Gould, a series of interwoven voices muse on travels in the Canadian Arctic. To the clickety-clack of train wheels rolling over tracks, the speakers ruminate on solitude, shattered illusions, the improbability of future “gigantic plastic bubbles surrounding Arctic villages with a cloak of warm air”, and what Gould calls an “incredible tapestry of tundra and taiga”.

German historian of culture and science Bernd Brunner, in his book *Extreme North*, weaves a darker tapestry, layering legends over the science and history of the north to describe a place that is real, remote, inscrutable and cold. Indigenous peoples of the Arctic — including the Sámi of Finland, Norway and Sweden, the Chukchi and Nenets of Russia and the Inuit of Alaska, Canada and Greenland — have lived in the north for thousands of years. For others, especially racist eugenicists of the nineteenth and twentieth centuries, the north symbolized Utopia, the incubator of a ‘master race’. Brunner untangles the origin of these pseudoscientific ideas, from the veneration of the Vikings and Old Norse sagas to the doctrine of ‘Nordic’ superiority promoted by Nazi ideologues.

Where the north begins depends on the eye of the beholder. The volcanic, ice-covered Bouvet Island is claimed by Norway, but lies in the north “only from the perspective of the South Pole”, Brunner writes. Located between South Africa and Antarctica, it is a 49-square-kilometre nature reserve dominated by seals, along with penguins and other seabirds.

For Europeans of antiquity, “the North was a phantasmagoric dark spot beyond the border of the Greco-Roman universe”, Brunner explains. In the fourth century bc, Greek astronomer Pytheas of Massalia claimed he had discovered the legendary far-north island of Ultima Thule, later identified as Iceland, Greenland or the Faroe Islands, among other places.

Ultima Thule was also the nickname of a distant object in the Kuiper belt beyond Neptune — 6.5 billion kilometres from Earth — explored in 2019 by NASA’s New Horizons craft. It was eventually renamed Arrokoth, meaning ‘sky’ in the Powhatan/Algonquian language spoken by Native Americans of

the Chesapeake Bay region, after it was pointed out that ‘Ultima Thule’ had been co-opted in the nineteenth century to refer to the mythological homeland of the supposed Aryan people. Brunner traces this malignant myth back to mid-eighteenth-century French, German and US thinkers, who began to classify humanity into ‘races’ and rethink the then-common idea that humans had emerged in the biblical lands of the Middle East.

## Shameful history

Nineteenth-century French diplomat Joseph Arthur de Gobineau developed the idea of a superior race he called Aryans (from the Sanskrit *arya*); he claimed that the Baltic coast and the Scandinavian Peninsula were the “maternal lap of nations”. In 1922, German linguist Hans Friedrich Karl Günther published his study *Racial Science of the German People*. He classified Germans as one of six ‘Nordic’ peoples, alongside Danes, Icelanders, Norwegians, Swedes and Finns; Jews were to him “a thing of ferment and disturbance”. His writings provided the foundation of the Nazi Party’s racial theories.



Three women in Selawik, Alaska, pictured in the 1920s.Credit:  
Buyenlarge/Getty

In the United States, William Warren, first president of Boston University in Massachusetts, described how “man was created in an Arctic Paradise with the Tree of Life at the North Pole”, according to a *Nature* review of his 1885 book *Paradise Found* ([Nature 32, 28; 1885](#)). Brunner also tells how eugenicist Madison Grant’s *The Passing of the Great Race*, published in 1916, “promoted the ‘Nordic race’ as superior and responsible for Western civilization’s greatest achievements”. The book sold millions in the United States, and Grant became a key proponent of the US eugenics movement. His book, which was praised by both former president Theodore Roosevelt and Adolf Hitler, led US politicians to enact state laws that banned interracial marriage. These were finally overturned only in 1967, by the US Supreme Court in the case *Loving v. Virginia*.

The eugenicists’ theories about northern superiority did not include Indigenous peoples of the Arctic. Nineteenth-century anthropologists considered Inuit to be living in Stone Age cultures, even as European, US and Russian explorers forced Inuit guides to assist in their forays into frozen climes. Explorers also kidnapped Indigenous people. In 1897, for example, polar researcher Robert Peary transported six Greenland Inuit, including a man named Qisuk and his young son Minik, to the American Museum of Natural History in New York City, where visitors were invited to ogle them. Four, including Qisuk, died of tuberculosis. Despite Minik’s lifelong quest to retrieve his father’s remains, the museum stored the bones of these four people until 1993, when they were returned for traditional burial in Qaanaaq, the northernmost town in Greenland.

## The melting north

Today, Qaanaaq is succumbing to the effects of climate change as the permafrost melts, causing houses to crack and sink. That’s a key part of the Arctic story, to which Brunner gives scant attention. Likewise, he expends little space on Indigenous people’s own knowledge and adaptation to their environment, their myriad languages (at least 20 in Alaska alone) or their sacred traditions.

Northern Indigenous peoples might be forced to adapt to their changing environment. According to the 2021 Arctic Report Card published by the US National Oceanographic and Atmospheric Administration, the Arctic is warming more than twice as fast as the rest of the planet. On 14 August 14 2021, rain — rather than snow — was observed at Greenland's 3,200-metre-altitude Summit Station for the first time. In June 2021, snow cover in the Eurasian Arctic was its third-lowest since records began in 1967. The Arctic, says the report, “is disappearing before our eyes” due to “unrelenting human-caused climate change”.

As the North warms and microplastics contaminate Arctic snow, sea ice, sea water and beaches, it seems that those “giant plastic bubbles surrounding Arctic villages with a cloak of warm air”, are no longer mere fantasy. As one speaker notes in *The Idea of North*: “Our number one enemy, instead of being Mother Nature, is, of course, human nature.”

*Nature* **602**, 571-572 (2022)

*doi:* <https://doi.org/10.1038/d41586-022-00427-6>

---

This article was downloaded by **calibre** from <https://www.nature.com/articles/d41586-022-00427-6>

| [Section menu](#) | [Main menu](#) |

- BOOK REVIEW
- 07 January 2022

# Origins of consciousness, and sustainable cities: Books in brief

Andrew Robinson reviews five of the week's best science picks.

- [Andrew Robinson](#) 0



ASTRONAUT  
**NICOLE STOTT**

# BACK TO **EARTH**

WHAT LIFE IN SPACE TAUGHT ME  
ABOUT OUR HOME PLANET—  
AND OUR MISSION TO PROTECT IT

## **Back to Earth**

Nicole Stott *Seal* (2021)

NASA astronaut Nicole Stott says that “you are grounded” are “the worst and the best three words” an astronaut can hear — signifying either that the astronaut is forbidden to fly, or that they have an attribute crucial for success. The words also suggest her book’s down-to-earth purpose: to explain how space flight enriches life on Earth. She recalls her own “Earthrise moment” on first looking out of the Space Shuttle — the sudden realization that we live on a planet that must be preserved from human destruction.

# FEELING & KNOWING

## Making Minds Conscious



**ANTONIO DAMASIO**

Author of *The Strange Order of Things*

## **Feeling & Knowing**

Antonio Damasio *Pantheon* (2021)

According to neuroscientist Antonio Damasio, the origin of consciousness — “the intriguing pirouette that allows the physical body to harbour mental experiences” — is often considered impossible to explain, despite the efforts of brilliant minds ranging from Sigmund Freud to Francis Crick. This intentionally short book for the general reader provides no explanation of consciousness as such, but much elegant prose to provoke thought, including ideas from biology, neuroscience, philosophy and psychology.

# CORRUPT CULTURES

## Cheating in Science and Society

Roy Yorke Calne

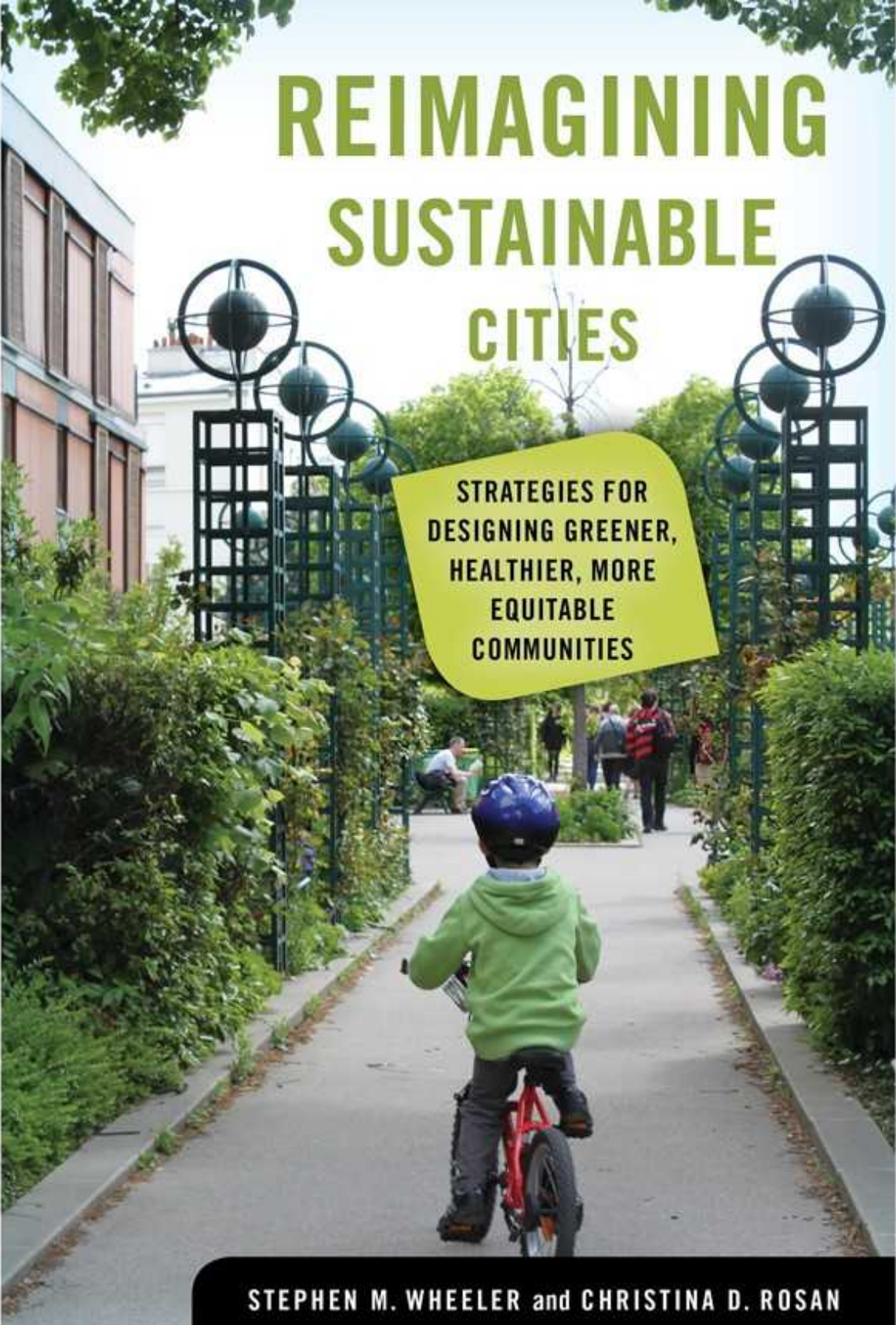


 World Scientific

## **Corrupt Cultures**

Roy Yorke Calne *World Scientific* (2021)

Organ-transplant pioneer Roy Calne draws on a long career in his brief, straightforward reflection on how to reduce cheating in science. It focuses on three accepted cases of fraud — by dermatologist William Summerlin, biologist Haruko Obokata and surgeon Paolo Macchiarini — implicating major institutions. He suggests ways to minimize misconduct, and admits that it is “immensely difficult”. He ends with advice from the Buddha: “Believe nothing, even if I have said it, unless it agrees with your own reason and common sense.”



# REIMAGINING SUSTAINABLE CITIES

STRATEGIES FOR  
DESIGNING GREENER,  
HEALTHIER, MORE  
EQUITABLE  
COMMUNITIES

STEPHEN M. WHEELER and CHRISTINA D. ROSAN

## **Reimagining Sustainable Cities**

Stephen M. Wheeler & Christina D. Rosan *Univ. California Press* (2021)

“Go to the city/See the crazy people there./Like lambs to the slaughter,/They’re drinking the water,/And breathing [cough] the air!” sang Tom Lehrer in ‘Pollution’ in 1965. The concept of sustainable development was pioneered in a 1972 report. Half a century on, drastic change is still needed, warn urban ecologists Stephen Wheeler and Christina Rosen in their enlightening survey of today’s cities. They offer practical, if challenging, strategies for promoting “ecological health, social equity, quality of life, cooperation and compassion”.

NICOLE

STARO

SIELSKI

MEDIA

HOT

&

COLD



## **Media Hot & Cold**

Nicole Starosielski *Duke Univ. Press* (2021)

The intense media focus on climate change makes this meditation on the cultural significance of temperature coolly topical. Nicole Starosielski's background is in media, culture and communication; despite references to science and technologies such as thermostats and infrared cameras, she mainly considers heat's social effects. She cites the Ford Motor Company's history of giving the hot, dangerous jobs in its foundry to Black workers, which reinforced racial stereotypes about suitability for certain types of labour.

*Nature* **602**, 572 (2022)

*doi:* <https://doi.org/10.1038/d41586-022-00032-7>

---

This article was downloaded by **calibre** from <https://www.nature.com/articles/d41586-022-00032-7>

| [Section menu](#) | [Main menu](#) |

# Opinion

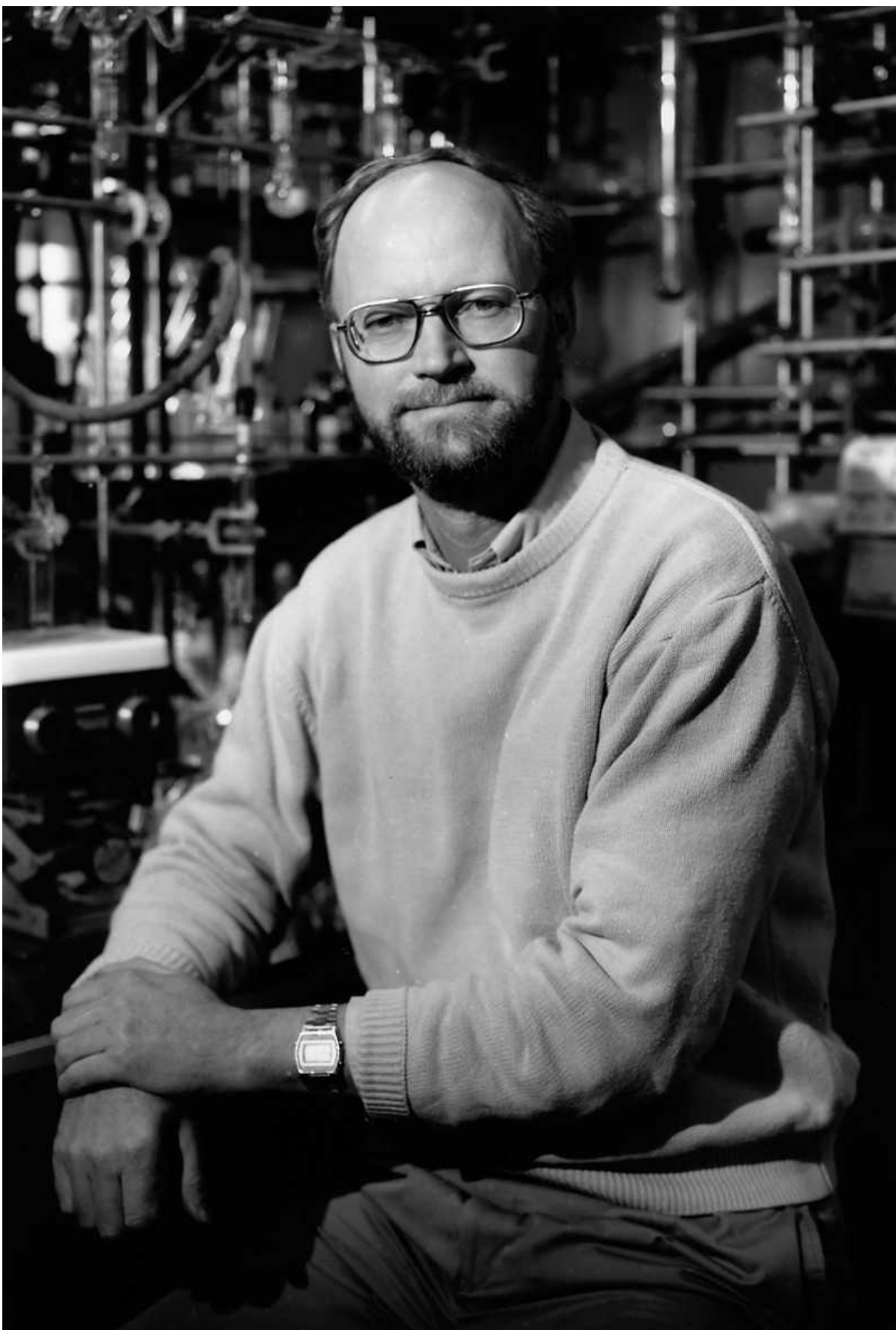
- **[Robert Grubbs \(1942–2021\)](#)** [ 18 February 2022]  
Obituary • Nobel prizewinner whose universal catalysts transformed chemistry.
- **[COVID-19: talk of ‘vaccine hesitancy’ lets governments off the hook](#)** [ 22 February 2022]  
Comment • Go beyond the attitudes of individuals and focus more on what governments must do to build people’s trust and ensure easy access to vaccines for all.
- **[Apply Singapore Index on Cities’ Biodiversity at scale](#)** [ 22 February 2022]  
Correspondence •
- **[Europe reforms its research evaluation and management](#)**  
[ 22 February 2022]  
Correspondence •
- **[Don’t just mandate open data, fund it](#)** [ 22 February 2022]  
Correspondence •
- **[Global Disability Summit demands health equity](#)** [ 17 February 2022]  
Correspondence •

- OBITUARY
- 18 February 2022

# Robert Grubbs (1942–2021)

Nobel prizewinner whose universal catalysts transformed chemistry.

- [Parisa Mehrkhodavandi](#) 0



Credit: Caltech

In multiple branches of chemistry, Robert Grubbs combined a delight in discovery with a keen focus on applications. His organometallic catalysts transformed synthetic chemistry, polymer science, advanced materials science and pharmaceuticals. Grubbs shared the 2005 Nobel Prize in Chemistry with Richard Schrock and Yves Chauvin. He has died aged 79.

Grubbs's best-known work was on a reaction that breaks and reforms the connections between carbon atoms in hydrocarbons: olefin metathesis. It is like a dance. A metal atom holding both hands with a carbon atom approaches two carbon atoms holding both hands. They form a ring and then change partners, with each atom now bound to a new one. The reaction of a metal–carbon double bond with a carbon–carbon double bond breaks two bonds and forms two new bonds in one step.

Creation of new bonds is fundamental to the synthesis of molecules, whether small molecules used in pharmaceuticals or very large ones used in advanced materials such as television screens. The carbon–carbon double bond is often an important component of the chemical functionality that allows small molecules or polymers to be transformed into more complex ones. Metathesis, in its ability to generate new carbon–carbon double bonds, has become a powerful technique in many fields.

Grubbs made major contributions to polymer science. Using olefin metathesis, he was able to build complex polymers — chains of identical subunits that form the basis of plastics and other synthetic materials. Controlling the molecular weights and shapes of polymers, he could induce them to self-assemble into higher-order structures, or engineer them for drug delivery. Others have used some of his strategies to develop self-healing materials, among myriad other polymers.

Grubbs was born near Possum Trot, a rural community in western Kentucky. His mother taught in schools and his father was a mechanic. He began his career at the University of Florida in Gainesville, where organic chemist Merle Battiste persuaded him to switch from agricultural science. He studied thermal rearrangements of cyclopropenes, rings of three carbon atoms that contain a lot of energy because their bonds are under strain. His

fascination with strained rings extended to his PhD work at Columbia University in New York City with Ronald Breslow, on the properties of cyclobutadiene, a four-membered ring.

After postdoctoral work in organometallic chemistry at Stanford University in California, Grubbs began his independent career in 1969 at Michigan State University in East Lansing. He worked on strained rings again, this time studying their fundamental properties as supports for iron complexes. His early interest in the relationships between chemical structures and reactivity — a topic that came up repeatedly in his career — explains his fascination with the mechanism of metathesis, which involves the formation of a strained four-membered ring containing a metal.

From 1978, Grubbs continued to study metathesis at the California Institute of Technology (Caltech) in Pasadena. He recognized that for the reaction to progress from a scientific curiosity to a powerful tool, he needed to focus on alkylidenes, the metal–carbon double-bonded catalysts used in the reaction. Early metathesis catalysts were based on molybdenum or tungsten. Although these provided high reaction rates, they were sensitive to air and moisture, and so required special handling. They also had limited compatibility with functional groups prevalent in most synthetic targets, such as pharmaceuticals.

In a major breakthrough, Grubbs used strategies developed for the synthesis of tungsten complexes to generate related alkylidenes based on the metal ruthenium. These first-generation ruthenium catalysts were commercialized and made available to the wider scientific community. More soon followed. Each generation had much greater activity, stability and functional-group tolerance than the one before.

Grubbs catalysts, once esoteric, are now so ubiquitous that discussions about the synthesis of carbon–carbon double bonds are often couched only in terms of generations, as in: “I used gen-2 Grubbs” or “Gen 3 worked better for me”. The widespread use of metathesis catalysts has helped to maximize the atom economy — the amount of starting material that ends up as useful product — of synthetic routes to complex molecules. This means less waste and more sustainable processes — what the Nobel committee called “a great step forward for green chemistry”.

Grubbs had a profound effect on the scientists he trained, worked with and collaborated with. He was a champion of his students, and the many who became faculty members working in diverse fields of chemistry are an important part of his legacy. A scientific discussion with him was by turns intense, rigorous and joyful. I used to leave with a smile and a desire to run to the lab to try an experiment. He treated his team like family members, and the Grubbs group camping trips involving deep-fried turkey are legendary. At Christmas, he opened his home to members of the Caltech chemistry department.

Grubbs had a folksy wisdom hailing from his upbringing. One of my favourite pieces of unsolicited advice was: “When you reach a fork in the road ... take it!” He did. He was widely loved by the many who followed behind and mourn his loss.

*Nature* **602**, 573 (2022)

*doi:* <https://doi.org/10.1038/d41586-022-00429-4>

---

This article was downloaded by **calibre** from <https://www.nature.com/articles/d41586-022-00429-4>

| [Section menu](#) | [Main menu](#) |

- COMMENT
- 22 February 2022

# COVID-19: talk of ‘vaccine hesitancy’ lets governments off the hook

Go beyond the attitudes of individuals and focus more on what governments must do to build people’s trust and ensure easy access to vaccines for all.

- [Katie Attwell](#) <sup>0</sup>,
- [Adam Hannah](#) <sup>1</sup> &
- [Julie Leask](#) <sup>2</sup>



People wait to receive a COVID-19 vaccine at a mobile clinic in Valparaiso, Chile. Credit: Rodrigo Garrido/Reuters

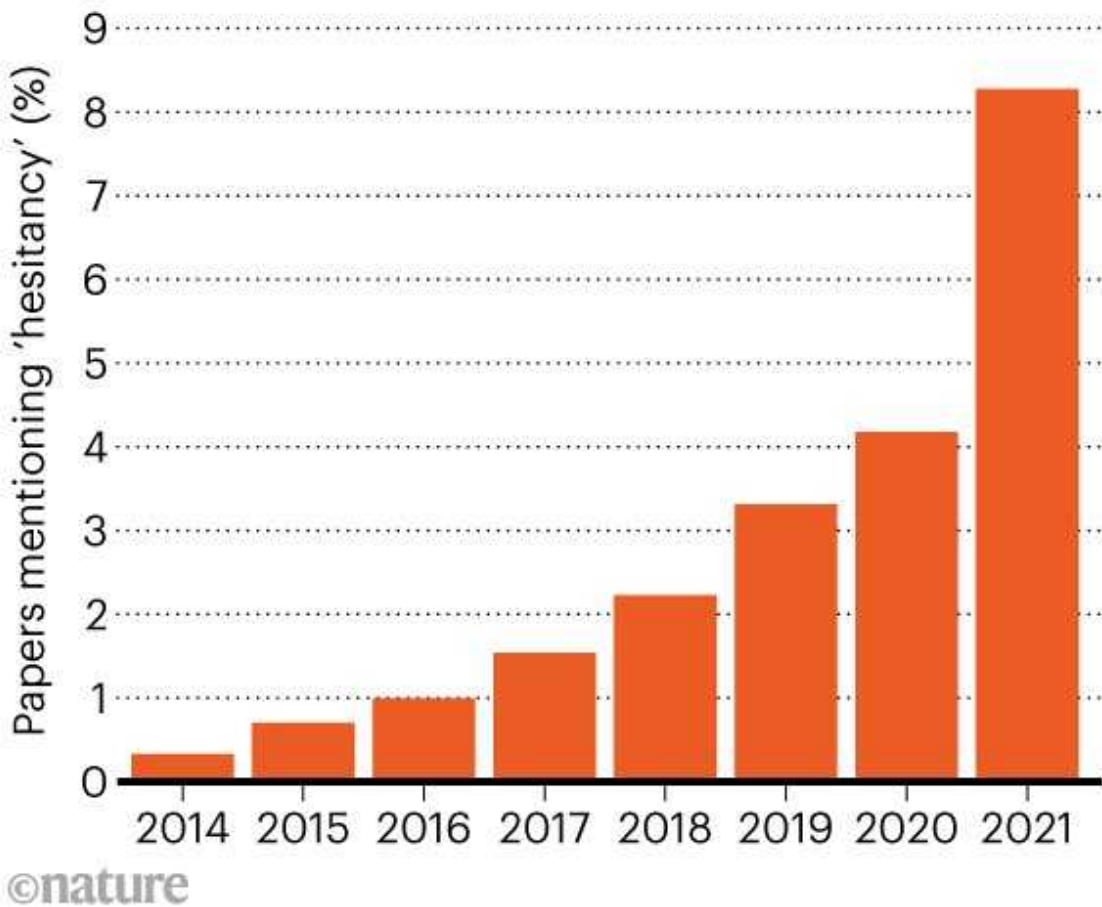
With every twist and turn of the COVID-19 pandemic, journalists, governments, policymakers and researchers have increasingly used the term ‘vaccine hesitancy’ to account for why so many people remain unvaccinated even in nations where supplies are plentiful. The share of papers with ‘vaccine’ or ‘vaccination’ in the title that also mention ‘hesitancy’ rose from 3.3% in 2019 to 8.3% in 2021 (see ‘The power of words’), according to a Web of Science search.

The most striking lesson from the pandemic is that preoccupation with vaccine hesitancy — whatever that term might mean to different people — centres too much of the responsibility for the success (or not) of a vaccination programme on individuals.

It is mainly governments that have the power to make vaccines both accessible and acceptable. Before the COVID-19 vaccine roll-out, a survey indicated that people living in Chile were more reluctant to get vaccinated than were those in other Latin American countries<sup>1</sup>. Yet more than 89% of Chile’s population has been fully vaccinated, as defined by that nation. And an early analysis indicates that this is largely thanks to vaccination being prioritized politically<sup>2</sup>. In a pre-pandemic example, Australia’s federal government started to introduce various improvements to childhood immunization programmes in 1997, including financial incentives for parents and doctors. Childhood vaccination rates rose from around 84% to 94% within three years<sup>3</sup>.

# THE POWER OF WORDS

The share of papers about vaccines or vaccination that mention 'hesitancy' has risen exponentially in recent years.



©nature

Source: Web of Science

Governments can and should be doing much more to ensure that COVID-19 vaccination becomes normal — even banal. That means fully funding the provision of vaccines and making them easily available, for instance through home visits or pop-up clinics. It also means researching and developing messaging that is appropriate for all groups. Meanwhile, more social scientists and other researchers should be trying to understand the relationship between governments (including their past and present actions) and people's acceptance of vaccines.

In short, the pandemic is producing a wealth of data on the effectiveness (or not) of vaccination programmes. Researchers, policymakers and other stakeholders must make the most of these data to scrutinize what governments (not just individuals) do — and how they can do it better.

## The coinage

According to the World Health Organization's (WHO's) 3Cs model<sup>4</sup> — which, in our view, has always been problematic<sup>5</sup> — a person's propensity to be vaccine-hesitant is a function of three things: confidence, complacency and convenience. Confidence is defined as trust in the effectiveness and safety of vaccines, the system that delivers them and the policymakers who decide that they are warranted. Complacency is when people perceive the risks of diseases as too low for vaccination to be worth the trouble. And convenience is the ease with which people can access vaccines, depending on geographical proximity, affordability and so on.

But in the more than 2,600 articles on hesitancy published since 2014, scholars have tended to focus too narrowly on the attitudes and behaviours of individuals. Most of the work on vaccine hesitancy has involved: population surveys and polls that track people's attitudes; correlation studies to assess how levels of education, income, socioeconomic background, political ideology, use of social media and so on relate to people's vaccination status; or experiments that investigate how a particular intervention (promotional messages, say) affects uptake. Such work tends to emphasize the importance of behavioural interventions for individual choices.

To be fair, there is widespread recognition among social scientists that the issues affecting vaccine uptake are many and complex<sup>6</sup>. And various behavioural interventions have improved coverage in some contexts<sup>7</sup>. But more investigations are needed into how party politics and political ideology shape the policies that governments end up pursuing, and what factors make a specific policy, such as a vaccine mandate for travel, succeed or fail in a given setting.

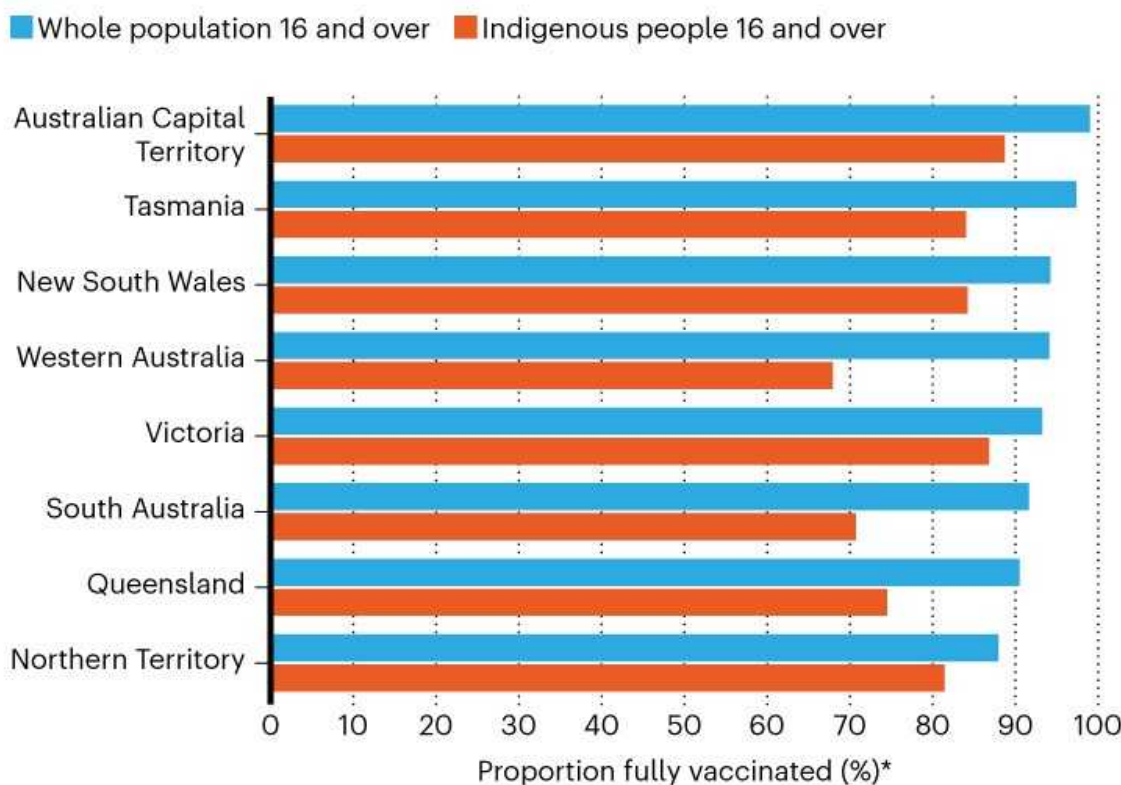
## **Access depends on governments**

Often, what has actually been slowing the uptake of vaccines in countries where supplies are plentiful is problems with access — problems that governments could take steps to address.

In Australia, coverage rates for COVID-19 vaccines are 7–26% lower in Aboriginal and Torres Strait Islander communities than in the overall population (see ‘COVID-19 vaccinations by Australian state’). When discussing drivers of low vaccine uptake in Aboriginal communities last August, the minister for Indigenous Australians, Ken Wyatt, argued that “some people have made choices because they’ve become fearful of adverse effects”. This framing as a ‘choice’ overlooked the supply problems and slow roll-out plaguing the country, as well as the lack of schemes (such as allowing people to get vaccinated without booking an appointment) for ensuring that vaccine services were reaching disadvantaged populations, including those living in remote regions.

## COVID-19 VACCINATIONS BY AUSTRALIAN STATE

Aboriginal and Torres Strait Islander communities in Australia are less likely than the overall population to get vaccinated against COVID-19, in part because it is harder for them to access vaccines.



\* Data as of 15 February 2022.

©nature

Source: Australian Government Department of Health

Similarly, in the United States, uptake of COVID-19 vaccines in Black communities was 14 percentage points lower than in white communities in the first five months of the country's vaccine roll-out. (This gap has now reduced to 6 percentage points for those receiving at least one dose.)

Various media reports homed in on vaccine hesitancy as the explanation. But Black scholars, community leaders and investigative journalists have pointed to important systemic issues. Among them is that an age-based roll-out does not take into account the disparate effects of race and social determinants of health. This means that some at-risk Black and Hispanic citizens — who have higher death rates from COVID-19 across all age

groups — had to wait longer than did their white counterparts. Black Americans are less likely to own computers, which are easier to book vaccine appointments on than smartphones. Furthermore, many people in these communities don't have easy access to the pharmacies that distribute the vaccines.

## Attitudes, too, can depend on governments

For the past decade — but especially during the COVID-19 pandemic — politicians and medical professionals, the media, even some scientists, have often attributed people's resistance to vaccination to a vulnerability to misinformation, a lack of education or simply selfishness. The implied solution is more education and persuasion, for instance through messaging campaigns, and if these strategies fail — mandates.

But a closer look at why some people are not getting vaccinated indicates that the problems are more complicated and, invariably, they start further up the chain. Also, issues around access feed into issues around acceptance. If governments fail to reach people promptly with easy-to-get vaccines and clear encouragement, other messages fill the void and people are likely to grow more worried about getting vaccinated.

Take some of the women we spoke to last August as part of a large interdisciplinary research project called Coronavax, which was designed to establish what people in Western Australia think and feel about COVID-19 vaccines, and why<sup>8</sup>. Larmina, a refugee from Afghanistan, now lives in Perth, which until recently had no community transmission of COVID-19. Even if she'd wanted to, Larmina would have struggled to book a vaccine appointment, because all the information about how to do so was in English, not Persian. If the government had provided trustworthy vaccine information in Persian, Larmina hadn't seen it. Instead, she'd been reading alarming stories about COVID-19 vaccines on social media and in WhatsApp group chats with her family.

Investigations in other countries into communities that were apparently resisting childhood vaccines have indicated the importance of governments taking swift action to address specific local concerns. In 2013, Sweden's

Public Health Agency collaborated with WHO experts, a social scientist with specific cultural expertise, and local community leaders to address the low uptake of measles vaccines in Somali migrant communities. Through in-depth interviews and multiple consultations, the team established that parents were worried about perceived dangers of the measles–mumps–rubella (MMR) vaccine, and that health workers were not equipped to deal with their concerns. Those findings led to a suite of interventions, thought to be at least partly responsible for increasing MMR coverage — such as training members of the community to become advocates of vaccination for their friends and family, educational videos for local community members, educational opportunities for health workers, and so on<sup>9</sup>.

In short, easily available services and targeted messaging at the outset help to establish people's confidence in the nation's ability to deliver a safe and effective vaccination programme. Equally, diffidence and inconsistent messaging can have enduring disastrous effects. Before Italy and France rebooted their mandates in 2017–18, uptake of some childhood vaccines had dropped below 85%. (The target is 95%.) In both countries, political leaders had resisted stepping into the fray or funding communication campaigns to address local scandals about vaccines that had arisen in previous decades<sup>10,11</sup>.

## How to do it better

Nobody is born wanting to get vaccinated. Every generation and social group across the world must be socialized into the practice. To achieve this, governments must make more investments on at least three fronts.

**Know the weaknesses.** As well as funding free and convenient vaccine services, governments should be funding, designing and constructing more analytical approaches to identify and understand the weaknesses of their systems. These should be quantitative as well as qualitative.

Countries with well-built childhood vaccination registers are ahead of the game when it comes to assessing COVID-19 vaccine coverage. Between 2012 and 2014, Denmark revamped its childhood vaccination tracking system so that it now captures a larger number of variables, such as type of

vaccine and dose. It also mandated the reporting of such data by vaccine providers<sup>[12](#)</sup>.

But information for both routine and COVID-19 vaccinations is often patchy. In Italy, for example, electronic registers documenting children's vaccination status are better in some regions than in others. In some countries, such registers don't exist, and governments instead use either less reliable or less informative data to estimate coverage rates. France, for example, uses the number of vaccine doses purchased; the United States relies on the vaccination data collected by schools when children enrol.



Actor Ernie Dingo (left) discusses COVID-19 vaccine certificates with fellow Aboriginal Australians. Credit: Tamati Smith/Getty

Countries should augment their national registers with comprehensive analyses of the behavioural and social drivers of vaccination, using validated tools. European countries, for example, conduct surveys to assess people's attitudes to vaccination. But because of sensitivities around ethnicity (among other issues), some surveys do not collect demographic data that could reliably identify minority groups who need further support, such as Roma

people<sup>13</sup>. Also, attitudinal surveys with closed answers that don't allow responders to elaborate won't reveal the complex perspectives people have and the barriers they face.

This year, the WHO is expected to release a set of survey questions and guidance for in-depth interviews that are designed to help reveal a broad range of factors affecting the uptake of childhood as well as COVID-19 vaccines. One of us (J.L.) has been involved in this effort. Questions cover how people think and feel about vaccines, but also practical issues, such as how easy it is for them to cover the cost of getting to the clinic. In our view, all countries should be using these.

**Know the needs of marginalized groups.** Governments should be investing more resources in qualitative research to better understand the unique needs of culturally and linguistically diverse groups. Some groups are likely to require extra support or interventions owing to language barriers or mistrust that stems from decades of poor treatment, racism and other forms of discrimination.

Investigators must go out to the communities and engage with people in person. Since 2014, UK public-health authorities have been working with a Charedi Jewish community in London, in which MMR (first dose) vaccination coverage was just 78% in 2015. Interviews of mothers and health professionals revealed that long waits in uncomfortable waiting rooms were more of an issue than were concerns about the safety of the vaccine, and led to a much more locally tailored approach to improving coverage<sup>14</sup>.

It is not enough to just build a resource, such as vaccine information or instructions on how to get vaccinated, in the right language. Resources must also be developed and disseminated in ways that are culturally sensitive and appropriate. In Bangladesh, the WHO helped the government to administer COVID-19 vaccines to around 900,000 Rohingya refugees who fled genocide in Myanmar in 2017. Rohingya volunteers engaged as community health workers had a key role in communicating health messages, working with community leaders and accompanying older people to vaccination centres. And by September 2021 (just two months into the vaccination

programme), more than 86% of the targeted population (those 55 or older) had received at least one dose.

**Invest in health systems.** Finally, how governments design and implement health-care policies, vaccination programmes and vaccine delivery procedures over the long term will influence how populations respond to future pandemics, as well as the likely ongoing need for boosters against new COVID-19 variants. Equity in access to health care creates myriad opportunities to normalize and socialize vaccination in child health programmes, for instance, or in maternity care programmes.

Take the example from Chile. Chile forged contracts with a wide range of potential vaccine providers early in the pandemic to ensure that it would have adequate supplies of vaccines early in the global roll-out. This might have been, in part, because the government was under pressure to succeed following the political protests (beginning in 2019) against the neoliberal economic policies that have dominated the country since the 1970s — and after it experienced one of the worst COVID-19 outbreaks in the world in mid-2020.

Chile was also able to leverage existing health systems and infrastructure. Its experience with a national programme for influenza vaccines since 1982, as well as more recent reforms aimed at strengthening its primary health system<sup>15</sup>, meant that the government was already well-equipped to work collaboratively with local communities to deliver COVID-19 vaccines. Chile used public spaces such as schools and parks as temporary vaccination hubs, partly on the basis of data drawn from existing systems for the collection and management of geospatial information. Also, an innovative country-wide vaccination calendar meant that people could turn up on their allotted day without having to book an appointment.

## Evidence base

The evidence base that governments can draw on needs building.

A survey conducted in 19 countries in 2020 before the roll-out of COVID-19 vaccines found a strong link between people's reported trust in government

and their willingness to be vaccinated<sup>16</sup>. And this has been supported by various observations in the pandemic. In the United States, for example, some Republican legislators are striving to nullify COVID-19 vaccine mandates<sup>17</sup>. And unvaccinated adults are at least three times as likely to identify as Republicans than as Democrats (see [go.nature.com/34y3snp](https://go.nature.com/34y3snp)). Meanwhile, in Russia, various surveys indicate low levels of trust in the government<sup>18</sup>. And only around 54% of the population have had at least one dose of a COVID-19 vaccine, despite the Sputnik V vaccine being free, home-grown and moderately effective, at least against the Delta variant.

But many questions remain about how populism, geopolitics and so on shape vaccination uptake. In fact, there is evidence to suggest that trust in leaders could be eroded even as trust in specific public systems, such as health care or vaccination, remains high<sup>19,20</sup>.

More studies also need to be done on the impacts of different regulatory approaches on public confidence. For example, the United Kingdom has only just announced plans to offer COVID-19 vaccines to healthy children under 11 years of age, and the delay might have increased the reluctance of some parents to get their children vaccinated. Parents outside the United Kingdom often cite differing vaccine recommendations between countries as a basis for their hesitancy.

Research programmes (including those using tools and approaches from political science) are crucial to resolving such issues, and to revealing where governments can invest most effectively. And, of course, existing interventions must be rigorously evaluated across multiple contexts.

Evidence is emerging in the Coronavax Project<sup>8</sup>, for instance, that COVID-19 vaccine mandates are undermining acceptance of other vaccines in Western Australia.

WHO-guided reviews of a country's performance during the pandemic, including in procuring and delivering vaccines, will help governments to make sense of their successes and failures<sup>21</sup>. Ultimately, it is governments that must step up and continually invest in the expensive, difficult work required to increase uptake and protect populations.

## References

1. Argote, P. *et al.* *npj Vaccines* **6**, 118 (2021).
2. Castillo, C., Villalobos Dintrans, P. & Maddaleno, M. *Vaccine X* **9**, 100114 (2021).
3. Bond, L., Davie, G., Carlin, J. B., Lester, R. & Nolan, T. *Aus. NZ J. Public Health* **26**, 58–64 (2007).
4. SAGE Working Group on Vaccine Hesitancy. *Report of the SAGE Working Group on Vaccine Hesitancy* (World Health Organization, 2014).
5. Bedford, H. *et al.* *Vaccine* **36**, 6556–6558 (2018).
6. Kata, A. *Vaccine* **28**, 1709–1716 (2010).
7. Navin, M. C., Largent, M. A. & McCright, A. M. *Prev. Med. Rep.* **17**, 101049 (2020).
8. Attwell, K. *et al.* *BMJ Open* **11**, e049356 (2021).
9. Dubé, E. *et al.* *Vaccine* **36**, 1509–1515 (2018).
10. Attwell, K. *et al.* *Pol. Sci.* **54**, 457–445 (2021).
11. Attwell, K., Ward, J. K. & Tomkinson, S. *Front. Commun.* **6**, 598602 (2020).
12. Grove Krause, T., Jakobsen, S., Haarh, M. & Mølbak, K. *Eurosurveillance* **17**, 20155 (2012).
13. Habersaat, K. B. *et al.* *Eur. J. Public Health* **30**, 986–992 (2020).
14. Letley, L. *et al.* *Vaccine* **36**, 4687–4692 (2018).

15. García-Huidobro, D. *et al.* *Rev. Panam. Salud Publica.* **42**, e160 (2018; in Spanish).
16. Lazarus, J. V. *et al.* *Nature Med.* **27**, 225–228 (2021).
17. Fernandes, B., Navin, M. C., Reiss, D. R., Omer, S. B. & Attwell, K. *JAMA* **327**, 178–179 (2022).
18. King, E. J. & Dudina, V. I. *Glob. Public Health* **16**, 1237–1250 (2021).
19. skarsson, Y. *et al.* *Vaccine* **33**, 7211–7216 (2015).
20. Erlingsson, G. Ó., Linde, J. & Öhrvall, R. *Gov. Opposition* **51**, 553–579 (2016).
21. World Health Organization. *Guidance for Conducting a Country COVID-19 Intra-Action Review (IAR)* (WHO, 2020).

---

This article was downloaded by **calibre** from <https://www.nature.com/articles/d41586-022-00495-8>

| [Section menu](#) | [Main menu](#) |

- CORRESPONDENCE
- 22 February 2022

# Apply Singapore Index on Cities' Biodiversity at scale

- [Lena Chan](#) ORCID: <http://orcid.org/0000-0001-7930-7678><sup>0</sup>,
- [Kenneth Er](#) ORCID: <http://orcid.org/0000-0003-4485-7260><sup>1</sup> &
- [Elizabeth Maruma Mrema](#)<sup>2</sup>

In the run-up to the 15th meeting of the Conference of the Parties to the Convention on Biological Diversity, the Singapore Index on Cities' Biodiversity has been updated to align with the post-2020 global biodiversity framework to halt biodiversity loss (see [Nature 601, 298; 2022](#)) and for application at scale (see [go.nature.com/3cqrknw](http://go.nature.com/3cqrknw)).

## Access options

Subscribe to Nature+

Get immediate online access to the entire Nature family of 50+ journals

\$29.99

monthly

[Subscribe](#)

Subscribe to Journal

Get full journal access for 1 year

\$199.00

only \$3.90 per issue

## Subscribe

All prices are NET prices.

VAT will be added later in the checkout.

Tax calculation will be finalised during checkout.

Buy article

Get time limited or full article access on ReadCube.

\$32.00

## Buy

All prices are NET prices.

## **Additional access options:**

- [Log in](#)
- [Learn about institutional subscriptions](#)

*Nature* **602**, 578 (2022)

*doi:* <https://doi.org/10.1038/d41586-022-00476-x>

---

This article was downloaded by **calibre** from <https://www.nature.com/articles/d41586-022-00476-x>

- CORRESPONDENCE
- 22 February 2022

# Europe reforms its research evaluation and management

- [Pier Francesco Moretti](#) <sup>0</sup>,
- [Luca Moretti](#) <sup>1</sup> &
- [Michele Guerrini](#) <sup>2</sup>

The European Commission is making its research and research-evaluation systems more efficient and more effective at responding to future crises, after learning from the COVID-19 pandemic (see [go.nature.com/34x2bub](https://go.nature.com/34x2bub)). A core group of experts will deliver a draft proposal in June to help participating research organizations to rethink their assessments of research (see [go.nature.com/3bojug3](https://go.nature.com/3bojug3)).

## Access options

Subscribe to Nature+

Get immediate online access to the entire Nature family of 50+ journals

\$29.99

monthly

[Subscribe](#)

Subscribe to Journal

Get full journal access for 1 year

\$199.00

only \$3.90 per issue

[Subscribe](#)

All prices are NET prices.

VAT will be added later in the checkout.

Tax calculation will be finalised during checkout.

Buy article

Get time limited or full article access on ReadCube.

\$32.00

[Buy](#)

All prices are NET prices.

**Additional access options:**

- [Log in](#)
- [Learn about institutional subscriptions](#)

*Nature* **602**, 578 (2022)

*doi: <https://doi.org/10.1038/d41586-022-00477-w>*

---

This article was downloaded by **calibre** from <https://www.nature.com/articles/d41586-022-00477-w>

- CORRESPONDENCE
- 22 February 2022

# Don't just mandate open data, fund it

- [Suhas Eswarappa Prameela](#) ✉

Funding agencies worldwide are moving rapidly to ensure that data from publicly funded research are shared widely and freely (see, for instance, [go.nature.com/3rsujk3](https://go.nature.com/3rsujk3)). For example, from 25 January 2023, researchers supported by the US National Institutes of Health (NIH) must submit [plans on how their raw data will be managed](#) and shared (see [go.nature.com/34hvtfh](https://go.nature.com/34hvtfh)). However, it is not always clear how such efforts will be paid for in practice.

It takes time and effort for researchers to comply with new data mandates — in reformatting, depositing and so on. Other funding agencies should follow the NIH's lead and require grant applications to set out how this work is to be done, and explicitly underwrite it with earmarked monies. Universities will need to invest in data-science centres and academic data managers.

Data mandates benefit research collaborations by ensuring that findings are reproducible and that data are safely stored in standard formats. They also enable secondary or meta-analyses that can lead to more discoveries. The potential for unrestricted data sharing has been evident during the COVID-19 pandemic (see, for instance, [E. Dong \*et al. Lancet Infect. Dis.\* \*\*20\*\*, 533–534; 2020](https://doi.org/10.1038/d41586-022-00478-9)).

*Nature* **602**, 578 (2022)

doi: <https://doi.org/10.1038/d41586-022-00478-9>

---

This article was downloaded by **calibre** from <https://www.nature.com/articles/d41586-022-00478-9>

| [Section menu](#) | [Main menu](#) |

- CORRESPONDENCE
- 17 February 2022

# Global Disability Summit demands health equity

- [Nana Addo Dankwa Akufo Addo](#) <sup>0</sup>,
- [Jonas Gahr Støre](#) <sup>1</sup>,
- [Tedros Adhanom Ghebreyesus](#) <sup>2</sup> &
- [Yannis Vardakastanis](#) <sup>3</sup>

Health-care facilities, social services and financial protection can be inaccessible for persons with disabilities — particularly for the 80% of more than one billion worldwide who live in low- and middle-income countries. This week's Global Disability Summit — organized by the governments of Norway and Ghana and the International Disability Alliance, with the support of the World Health Organization (WHO) — aims to persuade governments, civil society, United Nations organizations, the private sector and other actors to commit to concrete action, including ensuring equitable access to health services for all.

Achieving health and well-being for all will be possible only when disability is included in health-sector priorities. All stakeholders will need to collaborate in designing equitable programmes (see also [go.nature.com/3bc9m9g](https://go.nature.com/3bc9m9g)), including in health-emergency responses.

The WHO is taking steps to support countries in achieving a disability-inclusive health sector. A global report on the highest attainable standard of health for people with disability, as requested by WHO member states, will be launched in December, together with a Guide for Action. The implementation of the UN Disability Inclusion Strategy across the WHO through a three-year action plan is an example of good practice worth scaling-up.

*Nature* **602**, 578 (2022)

*doi:* <https://doi.org/10.1038/d41586-022-00405-y>

---

This article was downloaded by **calibre** from <https://www.nature.com/articles/d41586-022-00405-y>.

| [Section menu](#) | [Main menu](#) |

# Work

- **[Realizing a passion for public health in Cameroon](#)** [ 03 February 2022]  
Career Feature • A clear vision and good delegation skills can help women to advance in their careers.
- **[The superhero skills needed to juggle science and motherhood](#)** [ 01 February 2022]  
Career Feature • It might demand 12-hour days, but the chance to help shape African science makes it all worth it.
- **[Female scientists can advance by saying: ‘Yes, I’ll do it’](#)** [ 08 February 2022]  
Career Feature • A whole-hearted commitment to the demands of a job can help women to thrive in male-dominated spheres in Africa.
- **[Promoting mathematics to girls in Ghana](#)** [ 07 February 2022]  
Career Feature • Female mathematicians are inspiring young people in Africa to pursue careers in unconventional fields.
- **[Revealing chromosome contours, one dot at a time](#)** [ 21 February 2022]  
Technology Feature • Methods that meld imaging with sequencing are uncovering the organizational principles of the genome — and how it influences cell fates.
- **[Gut feeling: building a picture of Latin American microbiomes](#)** [ 21 February 2022]  
Where I Work • Computational microbiologist Gregorio Iraola leads a consortium focused on tailoring public-health interventions for local needs.

- CAREER FEATURE
- 03 February 2022

# Realizing a passion for public health in Cameroon

A clear vision and good delegation skills can help women to advance in their careers.

- [Kendall Powell](#) 0

[Find a new job](#)



Adidja Amani looked up to Cameroon's minister of women's empowerment as a youngster.Credit: Younoussa Abbosouka

## Voices from Africa

African women face all the same challenges that women in science, technology, engineering and mathematics (STEM) fields face around the world — but with a substantial number of extra barriers to success as researchers stacked in front of them.

With limited resources for research — be they human, financial or infrastructure — across the continent, researchers face an uphill battle to advance projects and publish.

*Nature* asked eight women scientists based in sub-Saharan Africa about their careers and the scientific landscape in their countries. In this second article, we hear from Adidja Amani, deputy director for vaccination at Cameroon's Ministry of Public Health in Yaoundé, and a lecturer in medicine at the University of Yaoundé.

It was not easy growing up in an environment where men are more valued than women. And the religious and cultural factors in my region mean that fewer women than men go to university. I had several marriage proposals while I was at secondary school. I did not get married, despite the pressures.

My mother was chronically ill when I was young, which motivated me to go to medical school at the University of Yaoundé I. In 2007, my last year, I won a US Fulbright scholarship to pursue a master's degree in public health at Georgia State University in Atlanta. That experience provided many opportunities to meet people from around the world, establish relationships and strengthen my bilingualism.

It also convinced me of the value of public health and the importance of investing in prevention. When I returned to Cameroon in 2010, my skills were in demand. Two directors at the Ministry of Public Health wanted to hire me: it was clear that the country needed the kind of human resource that I represented. I worked on a project to strengthen the public-health workforce. Next, I worked as a programme manager for an international non-governmental organization called Sightsavers. Then, the ministry recruited me back to become its head of child and newborn health.

Hard work and keeping good relationships with people in my networks have been key to my success. Just recently, I reached out to one of my US mentors for advice that I incorporated into a grant proposal on vaccination in Cameroon.

When I was younger, I had a role model, Yaou Aïssatou, who was then the minister of women's empowerment for Cameroon. She was from my region and she was also Muslim. During the school holidays, I would learn sewing and hairdressing because this was expected of women. I did it out of respect for my parents, but internally, I thought: "This is not for me." I would see Aïssatou, who is now the director of national investment, commanding so much respect, and I would think, "Why should I do hairdressing when I can be like her?"

Young women have to know their destination: what is their goal and what do they want people to say about them? When you are clear about where you want to go, then you can put the mechanisms in place to reach your goal.

I have a vision board in my bedroom that I renew every six months. It has my life goals — the house and car I want to have — and my physical goals to keep fit. But it also has my academic goals on it, such as "Write 25 publications by the end of February 2022" and my priorities for what I want to publish. I see that when I wake up, and I know I have to work on a particular article.

Finding a good work-life balance is hard and, honestly, I'm not sure I'm doing it right. I have made sacrifices. I have cut off everything that is leisure and I work seven days per week. My first child, who is 14, stayed with my mother when I went to the United States, and my second child, who is 3, stays with my mother in my home town of Guider, a 1,200-kilometre drive from Yaoundé.

My keyword is delegation. If I don't have to do something myself, I will delegate it to staff, or to medical graduates, students or research assistants. I also delegate housework, such as chores and cooking.

As a woman in this environment, it's not easy to evolve. I'm part of the Higher Institute for Growth in Health Research for Women, also known as

the HIGHER Women Consortium, a network of senior women researchers in Cameroon. Before the COVID-19 pandemic, we held retreats in which we talked about the challenges of marriage, family life and academic research. They were an opportunity for me to learn from other women's mistakes, and so avoid making the same ones myself.

Because these women want to see other women rise, it has been a tremendous motivation. Now, I mentor three younger researchers. When I have a research proposal or paper to write, I call them so that they can learn, and we publish together. One of the people I'm mentoring is Solange Ngo Bama, a primary-care physician at the Ministry of Public Health who is working for a master's degree in epidemiology. Together, we have three publications about mass vaccination in peer review. My wealth comes from the people around me.

*Nature* **602**, 709-710 (2022)

*doi:* <https://doi.org/10.1038/d41586-022-00320-2>

This interview has been edited for length and clarity.

---

This article was downloaded by **calibre** from <https://www.nature.com/articles/d41586-022-00320-2>

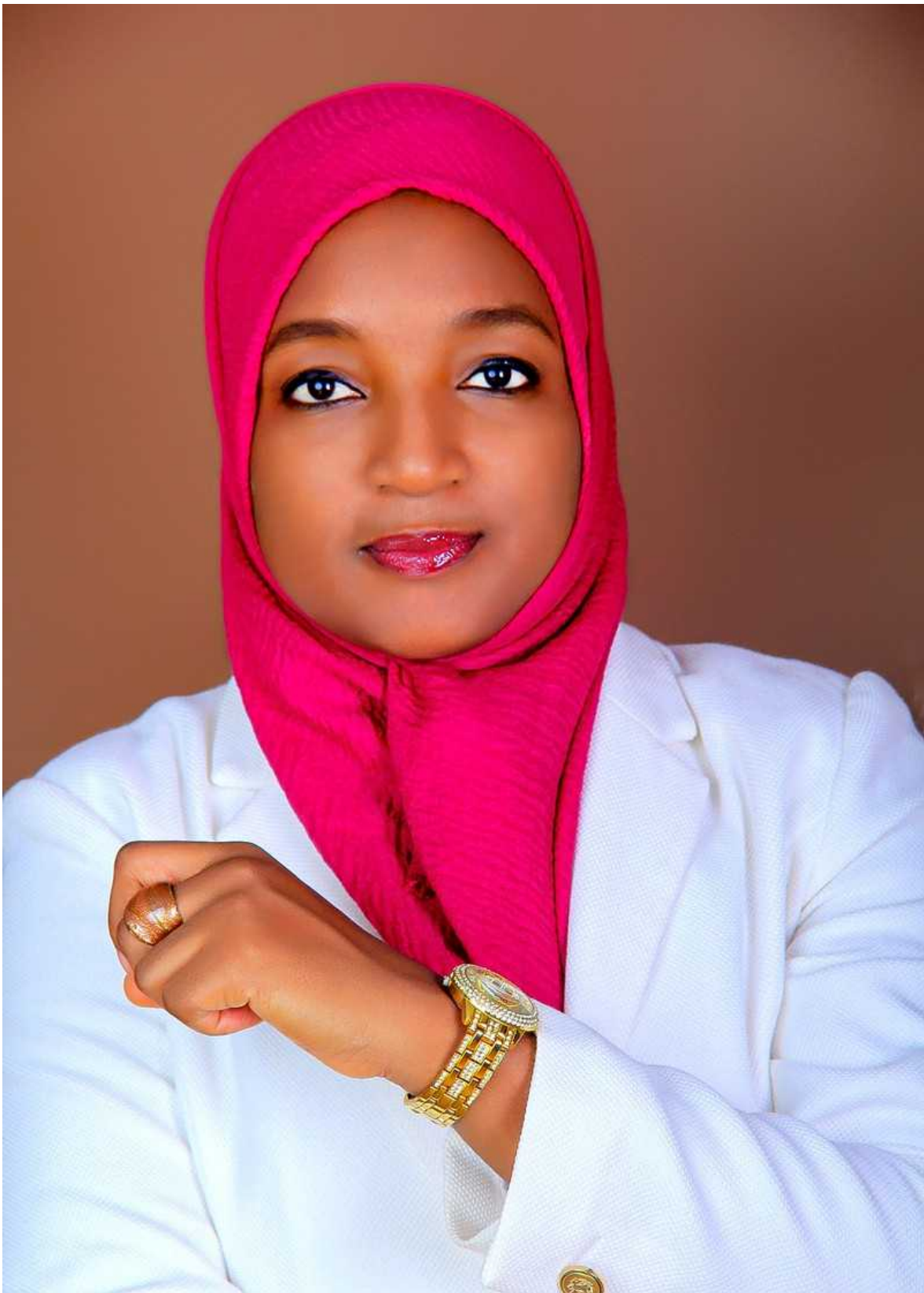
- CAREER FEATURE
- 01 February 2022

# The superhero skills needed to juggle science and motherhood

It might demand 12-hour days, but the chance to help shape African science makes it all worth it.

- [Kendall Powell](#) 0

[Find a new job](#)



Microbiologist Amina Ahmed El-Imam's personal sacrifices support her biofuel research.Credit: Carnation Consults

## Voices from Africa

Women in Africa take on a higher share of family and domestic responsibilities than many of their counterparts in the rest of the world. In 2019, the Organisation for Economic Co-operation and Development declared Africa to have the highest levels of gender discrimination towards women in the world. And in 2020, the World Economic Forum reported that [women in sub-Saharan Africa earnt 68% of what their male counterparts earnt.](#)

In the first of eight profiles in which African women share their science-career stories, Ahmed El-Iman, a microbiologist at the University of Ilorin, Nigeria, and a Fulbright scholar at North Carolina State University in Raleigh, describes the “superhero” skills needed to juggle work life and family life.

By the time I was finishing my master’s degree in microbiology at Ahmadu Bello University in Zaria, Nigeria, in 2007, I was married and had had my first child. That’s when it hit me that it was going to be difficult to be a researcher and a wife and a mother.

In my experience as an African woman, your first responsibility is to be a mother. Anything else beyond that? Well, good luck to you, even if you have an understanding partner. The domestic and childcare chores rest 100% on the mothers’ shoulders — that is just the norm in our society. As a researcher, your career path is already more difficult and resource-limited than a man’s. You need some basic level of superhero skills.

When I went to the University of Nottingham, UK, to do my PhD in 2013, I brought my three children under the age of seven with me. It was hectic — there’s no other word for it — but they also brought me joy. My husband visited as much as he could and he supported us financially, which allowed me to pay for childcare. That was the only way it was doable.

When I returned to Nigeria, I became a lecturer, teaching courses and advising students. I'm also expected to conduct research that has value to our immediate community. My research is focused on producing industrial chemicals and fuels using microorganisms. I do have a research group of students, but there's no research funding allocated by the university. If you are extremely lucky, you might get a government research grant through the university of about US\$2,000. There are not that many grants and there is a lot of competition.

What matters most for promotion is your research, even though you don't have the resources or time for it. This is not peculiar to academia. Much of Africa is poor and battling for resources — such as health care, infrastructure and education.

We just have to make it work. We apply for grants but we also pool from our own funds. The average professor's salary at federal universities in Nigeria is around \$800 per month, and everyone of a lower rank gets less. But each person sets aside a huge chunk to fund research out of their own pocket. I might set aside \$2,000 for the year, a master's student might set aside \$200–300 and an undergraduate \$100–150. This money is pooled to buy shared consumables and small equipment.

We collaborate extensively, partnering with colleagues in the engineering department to share equipment. We cannot afford basic microbiology equipment such as a large shaking incubator, which costs more than two years of my salary, so we fabricate what we can locally. And then we standardize that equipment so that quality controls are in place.

The research is not as in-depth or impactful as we'd like it to be — as we know we could make it. We do all this because we want to publish in Scopus-indexed journals. The cost of publication is another barrier. So we submit to free or open-access journals that don't charge fees, but which take a long time to publish our research. It's hectic and demoralizing, but we push on. Not happily, but willingly, we make these sacrifices to do the research.

I have published studies on food spoilage, the microbes that cause it and how to prevent it, as well as profiling the microbial community of a mining

site using metagenomics tools. I am particularly proud of that last one. It's the kind of research we can do, but we can't do much of it.

The university sits on land where there's no shortage of biomass material, which we could use to make biofuels. But the initial set-up to produce biofuels costs a lot. We applied for one government grant and were unsuccessful, but we'll keep trying.

Many people in Nigeria are afraid for their own safety amid continuing violent crimes and kidnappings. The universities do whatever they can to increase security by investing in security guards and installing cameras in strategic areas on campus. We don't leave work late, we avoid isolated places and mostly we pray a lot.

Nigeria has a severe unemployment problem among young people. I tell students in STEM to learn digital-technology skills to increase their chances. If they want to continue to an advanced degree in STEM, I suggest they do as many internships as possible in related areas to improve their chances of getting a scholarship to study abroad or here.

Being a woman in STEM in my part of Africa is daunting. I sometimes work 12-hour days for weeks at a time. When I come home at 6 p.m. or 7 p.m., I still have to cook dinner, help my children with their homework and prepare them for bed. I'm lucky to have a supportive husband who partakes in caring for our kids. Still, I rarely have the 20 extra hours or more that is needed to devote to a grant application. Who has time for attending conferences or writing papers? It's a zero-sum game: the more time you spend on domestic chores, the less time you spend on your career. All of this perpetuates the perception that women are incapable or incompetent, and that's just not true.

The burden is uniquely higher for mothers in more traditional societies. We literally spend our whole lives working hard, but I can't put raising four kids on my CV and get credit for it.

The academic job is still wonderful. In my opinion, there is nothing else that has such a direct role in shaping tomorrow. It's extra rewarding to have those eureka moments in the laboratory. My children have this love for science —

my daughter has just won a primary-school award for the ‘scientists of the future’. So yes, it’s worth it.

*Nature* **602**, 710-711 (2022)

*doi:* <https://doi.org/10.1038/d41586-022-00302-4>

This interview has been edited for length and clarity.

---

This article was downloaded by **calibre** from <https://www.nature.com/articles/d41586-022-00302-4>

| [Section menu](#) | [Main menu](#) |

- CAREER FEATURE
- 08 February 2022

## Female scientists can advance by saying: ‘Yes, I’ll do it’

A whole-hearted commitment to the demands of a job can help women to thrive in male-dominated spheres in Africa.

- [Kendall Powell](#) 0

[Find a new job](#)



Pontsho Maruping found support by creating a network of professional women with whom she could talk things through.Credit: Mintek

## **Voices from Africa**

Pontsho Maruping, deputy managing director of operations and business processes at the South African Radio Astronomy Observatory (SARAO) in Cape Town, describes a career transition from mining to space, and how she juggles the expectations of male and female colleagues. Maruping's career story is the fourth of eight in a series that profiles female scientists in sub-Saharan Africa.

I call myself a career nomad. I started out in South Africa's mining sector, but when the country transitioned to a democratic government in 1994, I wanted to help rebuild our science system. I got involved in developing our space programme and did a master's degree in space-systems engineering at the Delft University of Technology in the Netherlands, followed by a master's in business administration at the International Institute for Management Development (IMD) in Lausanne, Switzerland.

I began working with South Africa's Technology Innovation Agency to support innovators and technology start-ups with early-stage funding. I then joined SARAO about five years ago as head of commercialization, finding other applications for the technologies that were used to build the institution's radio telescope. Now, as a deputy managing director, I'm also responsible for functions such as human resources, finances, computing infrastructure and telescope operations.

I have worked in some of the most male-dominated sectors you can work in. Several things are necessary for overcoming racial or gender bias. One is to do the work you are given, commit wholeheartedly and deliver. When you are providing what is needed, that can erase people's biases.

## The power of mentoring

Having good mentors helps, too. My first boss was a woman who recognized my abilities to lead and gave me a team to manage early in my career.

When asking advice from mentors in more senior positions, I would be very specific — I would turn to them only for things they would have insights on, and not use them as a general sounding board. It's important to have more

than one person in your network and to think about how to engage them strategically.

Later in my career, as the only woman in a leadership role, I found that it was important to manage colleagues' expectations. The women expect me to be always on their side, and the men expect me to fit in with them. So, I need the courage to speak up on things that matter, but I also need to be able to let things go sometimes.

For example, I speak up a lot more about diversity and inclusion than I do about the less-than-ideal office space. I also have team members who are really passionate about community development and I advocate hard on their behalf because I understand their motivation.

## Setting an example

There was a time when I travelled a lot for work, and it was a challenge to make sure that my young daughter was taken care of. But it's also important for my daughter to see her mum doing jobs that women typically don't do. My working helps her to see that she can go after anything. Because of the policies I've worked on, future generations of women will have opportunities in science, technology, engineering and mathematics that weren't open to previous generations.

For most of my career, I've had some level of flexibility around parenting. I could take a later lunch break to pick my daughter up from school and then go back to work. I would combine work trips to visit stakeholders in other parts of the country with my daughter's field-hockey games. This let me create bonding moments with my daughter and be a hands-on parent. I never had a boss who micromanaged me, because I was professional and got my work done.

Working mothers cannot chase perfection — you cannot do everything exactly right. I used to joke with my male counterparts and say: "I need a wife, too!" They don't realize that there are some things their wives cannot do, because they are taking on the bulk of family responsibilities. There's

definitely more to be done to create work environments that enable women to integrate their work with their home life.

Simple things can be done to help women stay in science careers. One is to make grants specific to researchers rather than institutions. If a grant is attached to a researcher, they have more flexibility to take time off or move to another institution without losing their funding.

## Support networks

It's sometimes lonely without other senior women around. To help, I've created a network of professional women in other organizations. I can talk things through with them, such as the time when a male colleague agreed to a particular project in person and then objected to it in front of the full committee meeting — something I don't think he would have done if I'd been a man. I ask these other women: "Is this really happening or am I imagining it?" It helps build your morale to have those conversations. We generally experience the same kinds of issue, whether in the boardroom or when handling a conflict.

I generally consider myself a strong person, but I'm OK with losing a bit of control and not caring about what my male colleagues will say. During the pandemic, I suggested that SARAQ should make counselling available to all staff members and their families. Some colleagues suggested that people could go to their own physicians, but I pushed back, saying that not everyone has access to such services. They also suggested that people would not ask for help because it would be a sign of weakness, but I think it is actually a show of strength to acknowledge when you are not coping well.

When offered a chance to lead a new project, I tell young professionals to say 'yes'. Women tend to want to be perfect first, but it's the times when I've said yes to challenges that have provided the biggest opportunities to grow career-wise. Sometimes I've failed, but I've learnt in the process. So say to yourself, "I'll do it, I'll manage the team." In general, unless it is completely out of your reach or education level, you can learn and there's help around.

*Nature* **602**, 711-712 (2022)

*doi:* <https://doi.org/10.1038/d41586-022-00377-z>

This interview has been edited for length and clarity.

---

This article was downloaded by **calibre** from <https://www.nature.com/articles/d41586-022-00377-z>

| [Section menu](#) | [Main menu](#) |

- CAREER FEATURE
- 07 February 2022

# Promoting mathematics to girls in Ghana

Female mathematicians are inspiring young people in Africa to pursue careers in unconventional fields.

- [Kendall Powell](#) 0

[Find a new job](#)



Angela Tabiri uses social media to encourage young girls to pursue a career in mathematics. Credit: Angela Tabiri

## Voices from Africa

Angela Tabiri, who researches quantum algebra at the African Institute for Mathematical Sciences (AIMS) in Accra, was a PhD student at the University of Glasgow, UK, when she launched Femafricmaths in 2018. The network shares the stories of African female mathematicians through video interviews posted on social media. The vision is to help young girls become confident in pursuing careers in mathematics and related fields. Tabiri's profile is the third of eight in which African women share their science-career stories with *Nature*.

I graduated from the University of Ghana in Accra with a combined degree in economics and mathematics. One of my mentors told me about the opportunity to study for a master's degree at AIMS, a network of centres of excellence across Africa, which had just opened a site in Accra.

That was a turning point for me. It was like being immersed in a 24-hour learning environment. They bring in renowned lecturers from around the world to live there and teach three-week intensive courses. It was tough, with assignments due every Saturday at midnight. But I liked doing the challenging bits. That training also helped me to acquire digital and presentation skills.

I decided to apply to the University of Glasgow for a PhD. But that meant that I needed funding. I applied for and won a Faculty for the Future fellowship from the Schlumberger Foundation, which provides funding for women in science, technology, engineering and mathematics (STEM) from low-income countries to study at leading universities around the world. The foundation is looking for female leaders — you have to have academic excellence, but also show a commitment to promoting women in STEM in your home country.

In Glasgow, I really grew in terms of my skills and abilities. I also realized the power of social media to showcase and promote my research online. There is an audience out there looking for something beyond the ‘maths is difficult’ narrative.

I started the Femafricmaths initiative because I didn't see many mathematicians that were people of colour, and particularly women — it's not a narrative for most girls in Africa. Femafricmaths is a network of

African female mathematicians who highlight their different career paths through social media and promote the study of maths at schools.

I returned to Ghana in 2019 and started a postdoctoral position at AIMS. Often, in the field of maths, you might be the only female in a workplace team and that means that you have to be a bit tough. When I was teaching, instead of ‘Doctor’ the students called me ‘Madame’. Colleagues made comments about me starting a family and said that I might never get married. There’s a cultural pressure of ‘What are you doing competing in the space of men? You should be in the kitchen.’

Women should find their voice. People will always find ways to bully you or look down on you. Whatever environment I’m in, I need to find my voice and speak up.

Once you know what you want to do, carve your own niche. I’m good at algebra, but I’m also good at science communication and helping girls to follow STEM studies. So I developed myself in those areas — there are so many things I bring to the table. Find your voice, develop your skills and then when people downplay your abilities on the basis of gender, let all your success speak for you.

One challenge in abstract maths research is staying motivated. I tell myself that my research will enable technology to be built 100 years from now. So I had better make sure my work is true and accurate, so that it can be picked up when needed. I also teach pure maths to people who want to become engineers and computer scientists. They need to be taught well.

Maths research is hard — you have to be patient and determined to keep coming back to the same problem and trying it in different ways. The answer might not come to you for years. But, when you finally have a discovery and something eventually works — I don’t even know how to describe that feeling.

*Nature* **602**, 712 (2022)

*doi:* <https://doi.org/10.1038/d41586-022-00347-5>

This interview has been edited for length and clarity.

---

This article was downloaded by **calibre** from <https://www.nature.com/articles/d41586-022-00347-5>

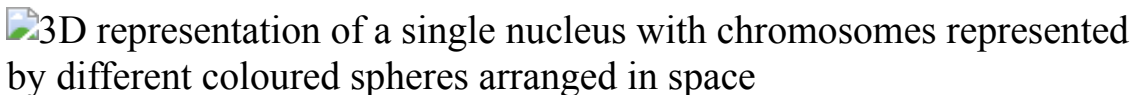
| [Section menu](#) | [Main menu](#) |

- TECHNOLOGY FEATURE
- 21 February 2022

# Revealing chromosome contours, one dot at a time

Methods that meld imaging with sequencing are uncovering the organizational principles of the genome — and how it influences cell fates.

- [Amber Dance](#) <sup>0</sup>



3D reconstruction of a nucleus. Each colour represents a different chromosome, and each dot is a gene location. Credit: Y. Takei *et al./Science*

Someone has drawn a mascot on the whiteboard in Mitchell Guttman's molecular-biology laboratory at the California Institute of Technology (Caltech) in Pasadena. It looks like a tangled ball of blue yarn a cat would chase, complete with eyes, jaunty grin, arms and legs.

Named SHARP-Y, after the gene-silencing protein SHARP the Guttman group studies, it could be the mascot for any of a handful of labs that are analysing similar tangled features — not balls of yarn, but the web of DNA in the nucleus. As these researchers are discovering, those tangles are anything but random. Chromosomes are precisely organized, as are the RNAs they make and the proteins that interact with them, and this organization seems to be crucial for gene expression to work as it should.

Efforts to trace chromatin — the complex of DNA and protein that makes up a chromosome — drive a small but growing field that is concerned with the 3D spatial positioning and dynamics of the molecular components that comprise the 'nucleome'.

These researchers are tackling a seemingly straightforward question: how does the genetic material arrange itself, physically, inside the nucleus? Biologists typically think of DNA as a string, a linear sequence of the nucleotide letters A, T, G and C that make up the DNA double helix. But cells can't treat their genetic material in that way, says Guttman. For example, when a cell has to adjust to an environmental change, a protein called a transcription factor enters the nucleus, seeking specific genes to activate for the appropriate response. But a linear search would take hours, too long for a timely response. Organization solves the problem: each chromosome has its own 'territory', where it is further subdivided into sections that are open for transcription or closed off. Those are then split into smaller domains, which unite sequences that tend to interact with each other. That way, genes and proteins can find their partners efficiently.

Thinking of DNA in 3D also solves a problem that genome sequencing has not, says Ana Pombo, a genome biologist at the Max Delbrück Center for Molecular Medicine in Berlin. Only 1–2% of the human genome encodes proteins directly. Much of the rest — where many disease-linked mutations can reside — performs regulatory roles, often influencing the expression of far-flung genes. But it isn't always easy to link these regulatory sequences to the genes they control. Chromosome structure can help to resolve those connections.

Disease links are already apparent. The gene-imprinting conditions Prader–Willi syndrome and Angelman syndrome, which cause developmental delays and intellectual disabilities, have been associated with structural differences between sister chromosomes in a person's cells, says Guttman. And scientists reported in 2016 that a genetic mutation involved in brain cancer produces an abnormal metabolite that interferes with the normal boundaries between DNA domains in chromatin<sup>1</sup>. Last year, in work that has not been peer reviewed, a team led by researchers at Columbia University in New York City suggested<sup>2</sup> that the coronavirus SARS-CoV-2 alters the architecture of chromosomes in olfactory cells, causing some people to lose their sense of smell.

Scientists have long had a well-stocked toolkit for studying these associations biochemically, for instance using the technique Hi-C to crosslink DNA regions that are found in close proximity to each other. But

those tools offer only an average view of chromosome arrangement; things can look different at the single-cell level. Imaging offers a richer picture. Some approaches build on fluorescence *in situ* hybridization (FISH), a long-standing method used to ‘paint’ chromosomes or identify individual genes using fluorescent tags. Others use *in situ* sequencing to find the location of specific genetic targets or a random subset of the genome in chemically fixed cells or tissues. Researchers are also combining methods to gain a holistic view of the nucleus, creating ‘multi-omic’ data sets.

“You don’t have to choose between imaging and sequencing,” says Xiao Wang, a genomics researcher at the Broad Institute of MIT and Harvard in Cambridge, Massachusetts. “You can do both in the same sample.”

## FISHing for loci

Caltech bioengineer Long Cai’s approach to spatial genomics stemmed from a simple realization: “Fundamentally, a DNA sequencer is a microscope.” Many modern sequencing machines decode DNA by incorporating fluorescently tagged nucleotide bases into the DNA as it is copied, reading those additions letter by letter. Cai figured: “Why take everything out of the cell, prepare it, and put it in the sequencer?” He wondered whether he could instead analyse nucleic acids right where they lie.

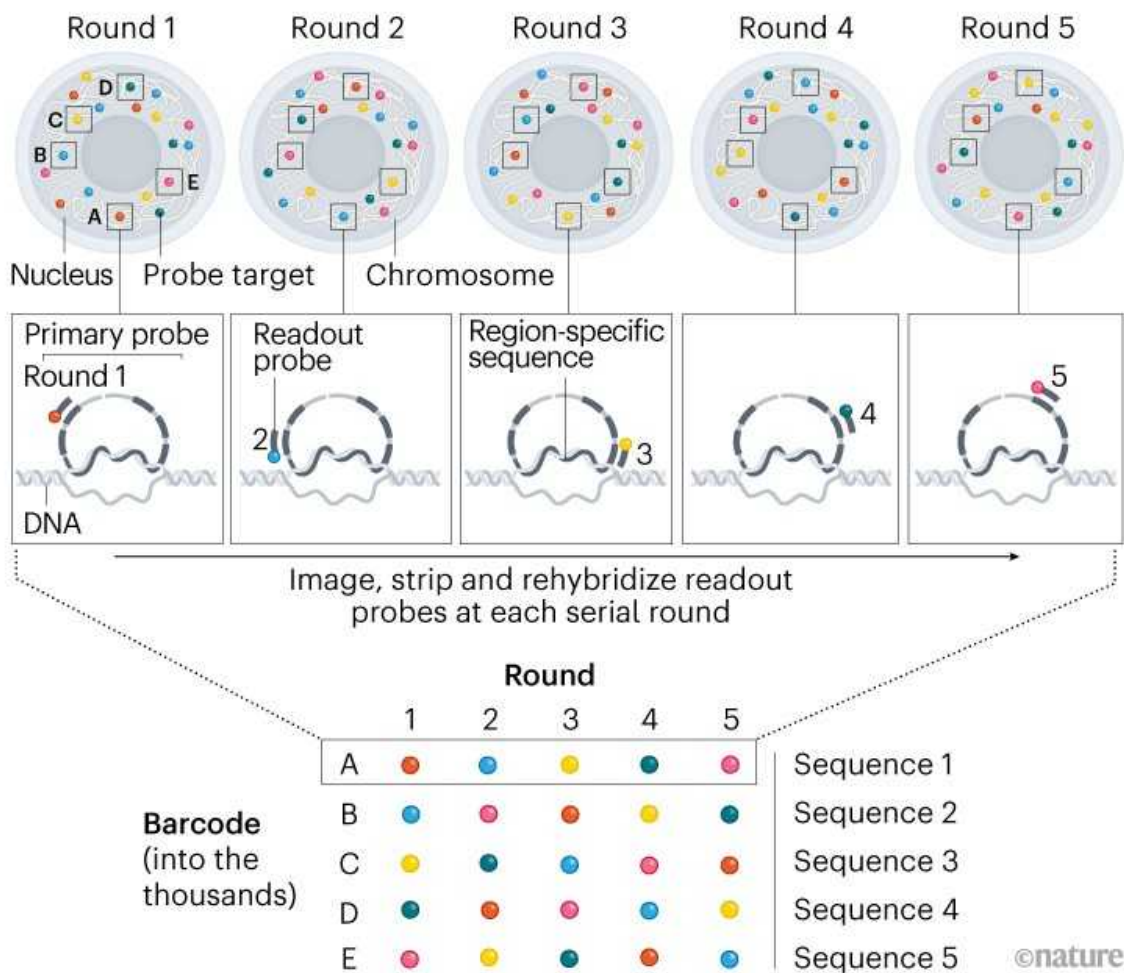
FISH provided the starting point. With this method, scientists design fluorescent nucleic-acid probes that are specific to the sequences they want to light up, and use microscopy to pinpoint the probes’ location in the cell. However, the method can look at only a handful of sites in the same sample, because microscopes can distinguish between only a few colours.

The Cai group’s innovation was to label a single sample repeatedly with different-coloured probes for several genetic loci, then decode the images later. They call the technique seqFISH, or sequential fluorescence *in situ* hybridization (see ‘Mapping a chromosome’). In their first demonstration, the researchers assigned each of 12 RNAs a unique, sequential barcode such as blue–yellow, green–purple, yellow–blue or purple–green, using four colours in total. Then they designed FISH probes using those colours for each RNA, and performed two rounds of labelling and imaging of yeast

cells. Each spot on the image indicated an RNA, and the colours it flashed in the two rounds indicated its identity<sup>3</sup>.

## MAPPING A CHROMOSOME

Researchers can trace chromosome shape using a technique called seqFISH (sequential fluorescence *in situ* hybridization). Repeated rounds of probe binding, imaging and removal creates a ‘sequential barcode’ that maps a sequence of colours onto a physical position in the genome. Thousands of gene locations can be barcoded.



Source: Adapted from Fig. 1 of Y. Takei *et al.* *Nature* **590**, 344–350 (2021).

The maximum number of targets this approach can label is 16 (or  $4^2$ : 4 dyes and 2 rounds of labelling). But when graduate student Yodai Takei joined the Cai lab in 2015, he wanted to see thousands of target sequences — and not

just RNA, but nuclear DNA as well. Last year, he and his colleagues reported doing just that<sup>4</sup>.

Takei labelled 3,660 DNA loci in slices of mouse cerebral cortex, imaging them over 125 rounds of data collection. By spacing those sites one million bases apart, Takei obtained a pattern of dots that, when joined up as in a connect-the-dots puzzle, provided a low-resolution approximation of the chromosome's conformation. The data revealed that chromosomes in the same types of cell were arranged and interacted in similar patterns. The approach could be used to explore how the nucleus is organized in many other cell types.

But 125 rounds of imaging? Working manually, each round of probe binding, imaging and stripping takes at least 50 minutes, Takei says; 125 rounds would have required, at a minimum, 7 consecutive 15-hour days. Fortunately for Takei, an automated microscope did the work for him. A typical experiment still takes about a week, but Takei — now a postdoc at Caltech — can do other things while it runs.

Cai employs two mechanical engineers to build automated microscopes such as these. In the lab's microscopy room sits a handful of machines, each occupying its own small space shrouded in black curtains to block out ambient light. Takei's set-up is built on a Leica microscope, but decking it out with an automated sampler, custom fluidics and a computer script to control it took two years. But the finishing touch is decidedly low-tech: the sample is protected from light by an upside-down cardboard box.

That's not the kind of microscope you can buy off the shelf — at least, not yet. Cai co-founded the California-based firm [Spatial Genomics](#) to commercialize seqFISH technology, and a product is expected later this year, according to Brian Fritz, vice-president of marketing for the company.

Another firm, [Acuity Spatial Genomics](#), which has offices in Newton, Massachusetts, and San Jose, California, is commercializing a different spatial-imaging technology. Called OligoFISSEQ, it was developed in the laboratory of Ting Wu, a chromosome biologist at Harvard Medical School in Boston, Massachusetts.

OligoFISSEQ combines fluorescence *in situ* sequencing (FISSEQ) — a technique that sequences nucleic acids in their tissue context — with barcoded versions of Oligopaints, which are FISH probes invented by the Wu group. The team engineered the probes so they can reveal chromosome topology in three ways: sequencing by hybridization (as for FISH); sequencing by synthesis; and sequencing by ligation. Sequencing by synthesis is the technology that many next-generation sequencers use, except in this case, the sequences are read in the tissue rather than being extracted first. Sequencing by ligation uses short, fluorescently labelled strands of DNA called oligonucleotides that are repeatedly attached to the Oligopaints barcode, imaged and then removed<sup>5</sup>.

Wu's team used that technology to trace the shape of the X chromosome through 46 loci spaced about 3 million bases apart. Using the specific barcodes and four rounds of imaging in the study<sup>5</sup>, the hybridization approach could, in theory, detect up to 1,296 loci. The other two sequencing strategies could yield as many as 65,536 loci after 8 rounds of sequencing. Wu co-founded Acuity to commercialize the approach, and the company is currently working on a product.

## Scattered sequencing

FISH's strength is its signal: researchers can tile multiple probes next to one another at each genomic locus, creating a strong, bright, fluorescent output. But researchers usually design probes only for the genes they care about. “It’s not a very good discovery tool,” says Guttman.

His team uses a biochemical technique called SPRITE to crosslink sequences in chromosomes, then barcode them at random to label any loci, without bias, that tend to be found near each other<sup>6</sup>. Sequencing of the barcodes and what they’re attached to reveals the physical associations. With collaborators, Guttman’s team has applied SPRITE in tissues from mouse brains and beetles to the plant *Arabidopsis*.

Image-based techniques also support untargeted searches through *in situ* sequencing of genomic DNA on a microscope slide. But because a single

sequence wouldn't be very bright, researchers first amplify the signal by repeatedly copying the sequences.

If that sounds simple, trust genomic scientist Fei Chen when he says it wasn't. His team at the Broad Institute spent several years developing *in situ* genome sequencing<sup>7</sup>, which they reported in 2020.

The process unfolds in three steps. First, the scientists take fixed cells or embryos and sprinkle sequencing adapters into the genome at random, creating an unbiased sample that preserves the fragments' spatial positions. Each adapter contains a unique, 20-base barcode to help the scientists read out the sequence later. Then they use a technique called rolling circle amplification to produce a 'DNA nanoball', measuring 400–500 nanometres across, which contains multiple copies of the barcoded DNA.

Next, the researchers decode those nanoballs using sequencing by ligation. But that method can read only about 20 bases: too few to conclusively identify a genetic region. This is where the barcodes come in. On the slide, the researchers sequence only the barcodes. Then they break up the cells and extract their DNA to sequence them again using standard sequencing by synthesis. Most next-generation sequencers can easily read the unique barcode together with 100 or more bases from the genomic locus where that barcode landed, allowing the scientists to match barcodes to loci on the linear sequence.

Finally, researchers use the barcodes to match up the thousands of dots seen in the microscope image, like nuclear confetti, with the linear sequence. Doing so allowed Chen and his colleagues to observe how cells with shared lineages have more similar chromosome architecture than do cells without common ancestry.

## Multi-omics

Chromosome models in papers look like highly articulated puzzles, with coloured balls and rods approximating the shape of a chromosome in the cell. But DNA by itself provides an incomplete picture of genetic activity, Guttman says. RNAs present near a DNA locus indicate that transcription is

under way. And DNA can interact with or be anchored by nuclear structures, such as the nucleolus that generates ribosome components and the nuclear speckles that contain RNA splicing factors. To get a more comprehensive view of nuclear architecture, researchers need to image the whole set of DNAs, RNAs and proteins in the same sample.

During his 125 imaging rounds, Takei included labels for 76 cellular RNAs and 8 nuclear structures and epigenetic markers. As a result, he could see that chromatin architecture, as well as a gene's proximity to nuclear speckles and chromatin modifications, correlated with gene expression. Yet at the single-cell level, cells of the same type showed differences in nucleome structure. The significance of this variation is still uncertain; one possibility Takei suggests is that the organization could reflect different external stimuli.

Xiaowei Zhuang, a biophysicist at Harvard University in Cambridge, Massachusetts, has also collected images of DNA, RNA and proteins together using a technique called multiplexed error-robust FISH (MERFISH), which her group developed for imaging RNA. In the team's latest work<sup>8</sup>, MERFISH allowed imaging of around 2,200 DNA loci and RNA species in single cells. Antibody stains for nuclear structures completed the picture, helping her team to visualize not just chromatin interactions and other nuclear structures, but also how that arrangement influenced the production of RNAs.

With Zhuang's and Cai's approaches, "you're really looking at spatial organization of the nucleus", says Bing Ren, a molecular biologist at the University of California, San Diego, who wasn't involved in either project. "This is really the future of genomics and epigenomics."

And that future is becoming more widely accessible. [Vizgen](#), a genomics company in Cambridge, Massachusetts, now sells a custom system for MERFISH studies, called MERSCOPE. (Zhuang is a co-founder of and consultant for the company.) [10x Genomics](#), based in Pleasanton, California, is also commercializing multiplex and other spatial technologies.

Meanwhile, researchers continue to innovate, for instance by combining imaging techniques with enhanced resolution methods, such as STORM,

which maps chromosome domains in fine detail, and expansion microscopy, which physically expands the volume of specimens to make *in situ* RNA sequencing more visible. They are also devising ways to make chromosome structure data easily available, for example through the [4D Nucleome Data Portal](#), where scientists can search and visualize data on nuclear components. “It’s almost like having a genome browser,” says Ren, “but now, in the 3D form.”

Wang says she sees two main applications for such data. One is to study subcellular biology, including genome organization and cellular distribution of RNAs. The other is to delineate different cell types in a complex tissue on the basis of their nucleome arrangements. With her own imaging-sequencing technique, called StarMAP, Wang is mapping chromatin, RNAs and proteins in the nuclei of several organs from mice and humans. Those data form the early stages of a new kind of cell atlas, which she hopes to share in the next couple of years.

The pace of innovation is frenetic, but invigorating, says Wu. “Inventions are happening left and right. I think everyone’s extremely excited to see what the next year’s going to bring.”

*Nature* **602**, 713–715 (2022)

doi: <https://doi.org/10.1038/d41586-022-00496-7>

## References

1. Flavahan, W. A. *et al.* *Nature* **529**, 110–114 (2016).
2. Zazhytska, M. *et al.* Preprint at bioRxiv  
<https://doi.org/10.1101/2021.02.09.430314> (2021).
3. Lubeck, E., Coskun, A. F., Zhiyentayev, T., Ahmad, M. & Cai, L. *Nature Methods* **11**, 360–361 (2014).
4. Takei, Y. *et al.* *Science* **374**, 586–594 (2021).
5. Nguyen, H. Q. *et al.* *Nature Methods* **17**, 822–832 (2020).

6. Quinodoz, S. A. *et al.* *Cell* **174**, 744–757 (2018).
  7. Payne, A. C. *et al.* *Science* **371**, eaay3446 (2020).
  8. Su, J.-H., Zheng, P., Kinrot, S. S., Bintu, B. & Zhuang, X. *Cell* **182**, 1641–1659 (2020).
- 

This article was downloaded by **calibre** from <https://www.nature.com/articles/d41586-022-00496-7>

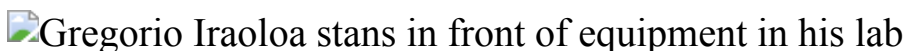
| [Section menu](#) | [Main menu](#) |

- WHERE I WORK
- 21 February 2022

# Gut feeling: building a picture of Latin American microbiomes

Computational microbiologist Gregorio Iraola leads a consortium focused on tailoring public-health interventions for local needs.

- [Jack Leeming](#)



Gregorio Iraola is head of the Microbial Genomics Laboratory at the Pasteur Institute of Montevideo in Uruguay, and a Wellcome Sanger Institute International Fellow. Credit: Pablo Albarenga for *Nature*

I'm in my wet lab at the Microbial Genomics Laboratory of the Pasteur Institute of Montevideo in Uruguay, which I set up in 2019. Most of my group's projects start here, but many move into bioinformatics research on the other side of the corridor, or through remote connections to computing systems elsewhere in the world — often at the Wellcome Sanger Institute in Hinxton, UK, where I'm also affiliated.

One long-term research goal is to better understand the gut microbiome — the composition and balance of bacteria in the gut — and how it varies across populations, to help treat many conditions. It's especially important for Latin American countries, because existing human-microbiome databases come from wealthier countries — in North America, Europe and China, especially — where much of the sampling has been done. This leads to bias. You can't make reliable medical decisions on gut health for a Latin American person with European data. Latin America has some of the

highest obesity rates in the world, so a better understanding might help policymakers.

I lead a consortium of scientists in Uruguay, Argentina, Chile, Bolivia, Brazil, Colombia, Ecuador, Mexico, Paraguay, Costa Rica, Peru and French Guiana. We gather data on microbiomes in these incredibly heterogeneous countries. I see it as a puzzle; we need to find pieces from across the region before we can put the picture together.

My long-term dream is to help other scientific communities (in Eastern Europe, southeast Asia or Africa, for example) to collect and analyse microbiome data, so that medical interventions make sense for local populations, diets and cultures.

Once I've done that, perhaps I can go back to cooking — one of my hobbies — or growing vegetables. My father is a farmer in Cardona in the southwest of Uruguay, and I visit often. It's satisfying doing worthwhile research that's specific to this continent.

*Nature* **602**, 718 (2022)

*doi:* <https://doi.org/10.1038/d41586-022-00497-6>

---

This article was downloaded by **calibre** from <https://www.nature.com/articles/d41586-022-00497-6>

# Research

- **[Atomic changes can map subterranean structures](#)** [ 23 February 2022]

News & Views Forum • A quantum device uses ultracold atoms to sense gravitational changes that can detect a tunnel under a city street. Here, scientists discuss the advance from the viewpoints of quantum sensing and geophysics.

- **[Unwinding the mutational signatures of a DNA topoisomerase enzyme](#)** [ 09 February 2022]

News & Views • Certain patterns of mutations occur frequently in cancer. The culprit behind one mutational signature is now shown to be a cellular enzyme with the mundane role of relieving stress in supercoiled DNA.

- **[Fragile nanosheets stripped from crystals](#)** [ 23 February 2022]

News & Views • Two-dimensional materials have been restricted to systems in which strong chemical bonds hold atoms together in sheets. Now, 2D materials consisting of molecules linked by weak non-covalent bonds have been peeled from crystals.

- **[Radio bursts from among the oldest stars](#)** [ 23 February 2022]

News & Views • Luminous bursts of radio emission are linked to highly magnetized neutron stars known as magnetars. Now, bursts have been detected from a globular star cluster, an environment thought to be devoid of magnetars.

- **[A repeating fast radio burst source in a globular cluster](#)** [ 23 February 2022]

Article • The fast radio burst FRB 20200120E is shown to originate from a globular cluster in the galaxy M81, and may be a collapsed white dwarf or a merged compact binary star system.

- **[Quantum sensing for gravity cartography](#)** [ 23 February 2022]

Article • A study reports a quantum gravity gradient sensor with a design that eliminates the need for long measurement times, and demonstrates the detection of an underground tunnel in an urban environment.

- **[Hyperbolic shear polaritons in low-symmetry crystals](#)** [ 23 February 2022]

Article • Shear phenomena in the infrared dielectric response of a monoclinic crystal are shown to unveil a new polariton class termed hyperbolic shear polariton that can emerge in any low-symmetry monoclinic or triclinic system.

- [\*\*Evidence for a single-layer van der Waals multiferroic\*\*](#) [ 23 February 2022]  
Article • Multiple complementary optical signatures confirm the persistence of ferroelectricity and inversion-symmetry-breaking magnetic order down to monolayer NiI<sub>2</sub>, introducing the physics of type-II multiferroics into the area of van der Waals materials.
- [\*\*Free-standing homochiral 2D monolayers by exfoliation of molecular crystals\*\*](#) [ 23 February 2022]  
Article • Sonication of layered metallacycle crystals gives free-standing nanosheets held together by weak non-covalent interactions, with chiral surfaces that show improved binding and enantiodiscrimination compared with individual metallacycle molecules.
- [\*\*Emergent constraints on future precipitation changes\*\*](#) [ 23 February 2022]  
Article • Model simulations show that the historical relationship between global temperature and precipitation under a medium greenhouse gas concentration scenario lowers the projected high end of future precipitation change.
- [\*\*Observed poleward freshwater transport since 1970\*\*](#) [ 23 February 2022]  
Article • A study uses a temperature-percentile water mass framework to analyse warm-to-cold poleward transport of freshwater in the Earth system, and establishes a constraint to help address biases in climate models.
- [\*\*Signatures of TOP1 transcription-associated mutagenesis in cancer and germline\*\*](#) [ 09 February 2022]  
Article • Defective ribonucleotide excision repair causes ID4, an indel cancer signature characterized by deletions of 2–5 base pairs.
- [\*\*A nutrient-specific gut hormone arbitrates between courtship and feeding\*\*](#) [ 09 February 2022]  
Article • Diuretic hormone 31 secreted by the gut in response to feeding on protein-rich food excites brain neurons that promote switching from feeding to mating behaviour in Drosophila.
- [\*\*A discrete neuronal population coordinates brain-wide developmental activity\*\*](#) [ 09 February 2022]  
Article • Developmental activity in transient receptor potential gamma-expressing neurons controls global brain activity and synapse structure in the developing Drosophila brain.
- [\*\*A gut-derived metabolite alters brain activity and anxiety behaviour in mice\*\*](#) [ 14 February 2022]  
Article • The gut-derived molecule 4-ethylphenol influences complex behaviours in mice through effects on oligodendrocyte function and myelin patterning in the brain.

- **Omicron extensively but incompletely escapes Pfizer BNT162b2 neutralization** [ 23 December 2021]
 

Article • Plasma from individuals vaccinated with BNT162b2 exhibits 22-fold less neutralization capacity against Omicron (B.1.1.529) than against an ancestral SARS-CoV-2 strain but residual neutralization is maintained in those with high levels of neutralization of ancestral virus.
- **Omicron escapes the majority of existing SARS-CoV-2 neutralizing antibodies** [ 23 December 2021]
 

Article • A high-throughput yeast display platform is used to analyse the profiles of mutations in the SARS-CoV-2 receptor-binding domain (RBD) that enable escape from antibodies, and suggests that most anti-RBD antibodies can be escaped by the Omicron variant.
- **Broadly neutralizing antibodies overcome SARS-CoV-2 Omicron antigenic shift** [ 23 December 2021]
 

Article • Pseudovirus assays and surface plasmon resonance show that the Omicron receptor-binding domain binds to human ACE2 with increased affinity relative to the ancestral virus, and that most neutralizing antibodies are considerably less potent against Omicron.
- **Considerable escape of SARS-CoV-2 Omicron to antibody neutralization** [ 23 December 2021]
 

Article • An isolate of the Omicron variant of SARS-CoV-2 was completely or partially resistant to neutralization by all nine clinically approved monoclonal antibodies tested.
- **Striking antibody evasion manifested by the Omicron variant of SARS-CoV-2** [ 23 December 2021]
 

Article • The B.1.1.529/Omicron variant of SARS-CoV-2 is resistant to neutralization by serum not only from patients who recovered from COVID-19, but also from individuals vaccinated with one of the four widely used COVID-19 vaccines.
- **Activity of convalescent and vaccine serum against SARS-CoV-2 Omicron** [ 31 December 2021]
 

Article • Sera from unvaccinated, vaccinated, and previously infected and vaccinated individuals show reduced neutralizing and spike protein-binding activity towards the Omicron (B.1.1.529) variant of SARS-CoV-2 compared to other variants.
- **Early prediction of preeclampsia in pregnancy with cell-free RNA** [ 09 February 2022]
 

Article • Analyses of circulating cell-free RNA (cfRNA) in blood samples from pregnant mothers identify changes in gene expression that could be used in liquid biopsy tests to identify and monitor individuals who are at risk of preeclampsia.
- **Visualizing protein breathing motions associated with aromatic ring flipping** [ 16 February 2022]

Article • Nuclear magnetic resonance spectroscopy and X-ray crystallography capture how aromatic side chains can flip within the core of a protein via the generation of a local void volume.

- **Mechanism-based traps enable protease and hydrolase substrate discovery** [ 16 February 2022]

Article • Light-activated trapping is used in a mechanism-based assay to capture and identify substrates of protein hydrolases.

- NEWS & VIEWS FORUM
- 23 February 2022

# Atomic changes can map subterranean structures

A quantum device uses ultracold atoms to sense gravitational changes that can detect a tunnel under a city street. Here, scientists discuss the advance from the viewpoints of quantum sensing and geophysics.

- [Nicola Poli](#) <sup>0</sup>,
- [Roman Pašteka](#) <sup>1</sup> &
- [Pavol Zahorec](#) <sup>2</sup>

## THE PAPER IN BRIEF

- Precise measurements of vertical gradients in gravity can be used to detect inhomogeneities in density under Earth's surface.
- In [a paper in \*Nature\*](#), Stray *et al.*<sup>1</sup> report a practical quantum sensor that uses atom interferometry to measure gravity gradients rapidly, and with high sensitivity.
- The sensor is shown to be capable of detecting a tunnel of two-metre-square cross-sectional area under a road surface between two multi-storey buildings, located in an urban environment.

## NICOLA POLI: A quantum sense for what lies beneath

Astronomical observations offer us extensive knowledge of what lies above us through both electromagnetic and now gravitational<sup>2</sup> signals — even

those from sources one billion kilometres away. But, in many ways, we lack the same detailed knowledge of what lies beneath our feet, even a few metres below Earth's surface. Although several geophysical monitoring techniques exist, most of the time, digging is still the best way to learn about small features under the soil. However, quantum sensors are gaining traction as a viable alternative to classical geophysical sensors.

Atomic gravimeters are quantum sensors that use a technique called atom interferometry to measure local gravitational acceleration on the basis of how the gravitational field affects a freely falling cloud of atoms. In a typical configuration, light pulses are used to generate, separate and recombine matter waves (every particle can be described as a wave of matter), allowing them to interfere with each other. The interference pattern detected in a gravimeter is then related to the local gravitational field. Measurements based on this principle can be amazingly precise, but they are still subject to the effects of noise. Atomic gradiometers overcome this problem to some degree by measuring gradients in such gravitational fields, instead of absolute values.

Since their first demonstration as gravimeters and gradiometers more than 20 years ago<sup>3</sup>, atom interferometers have continued to improve in performance. At the same time, research has focused on how to make such instruments compact and reliable enough to be used outdoors for real-world applications<sup>4,5</sup>. Stray and colleagues' instrument is a notable advance in this line of research.

The team developed an hourglass configuration for their gradiometer, with which they performed differential measurements on two clouds of ultracold rubidium atoms, separated vertically by one metre. This configuration provides robust and compact optics that remain properly aligned over a period of several months.

The instrument was capable of non-destructively sensing a large cavity buried beneath Earth's surface, by measuring the cavity's tiny gravitational signal alone (Fig. 1a). The sensitivity shown by the device is around  $20E$  ( $1E$  is  $10^{-9}$  per square second) for a measurement taken over 10 minutes, which makes it around 30 times less sensitive than the most sensitive interferometer reported<sup>6</sup>. However, the authors' sensor is a step forward in

terms of making atom gradiometers practically useful in real-world situations.

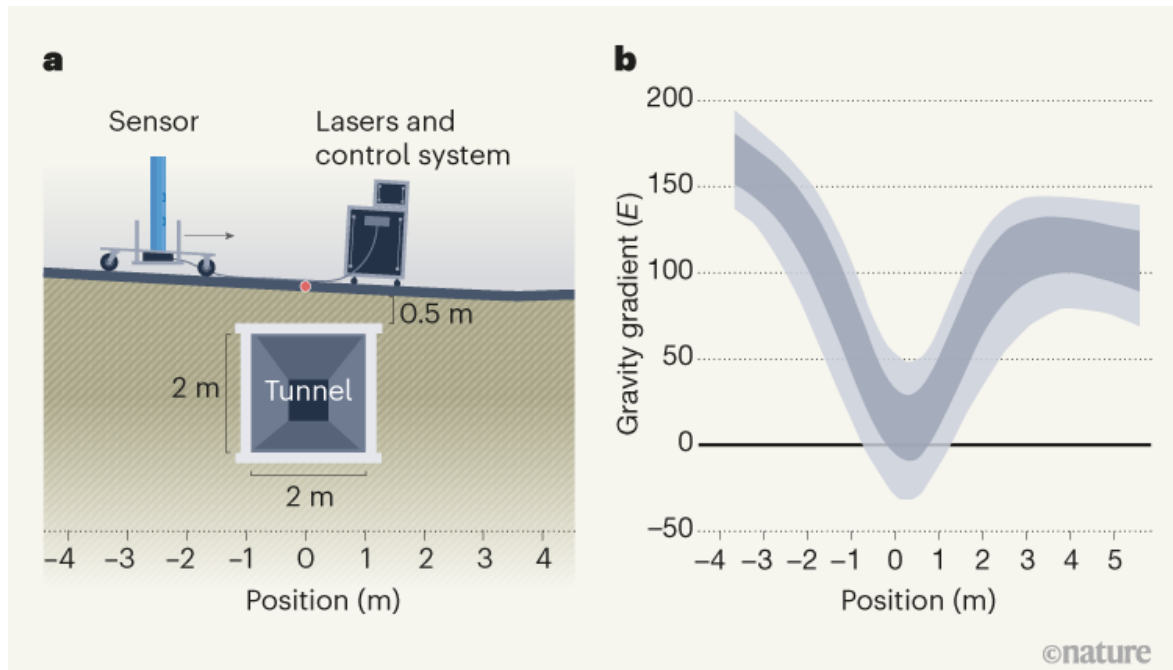


**Figure 1 | Gravity cartography in the real world. a,** Stray *et al.*<sup>1</sup> developed a quantum sensor that measures vertical gradients of gravity, which can be used to identify variations in density. The device detected an underground tunnel located beneath a road surface between two multi-storey buildings (not shown), which can affect the gradient signal and lead to its attenuation. The expected location of the tunnel on the horizontal axis is marked in red. **b,** The sensor measured gradients in gravity (in units of  $E$ , where  $1E$  is  $10^{-9}$  per square second) as a function of the sensor's position relative to the expected location of the tunnel. As well as being at least as accurate as existing commercial tools, the device can acquire data more rapidly and is more portable than other quantum sensors of its kind. (Adapted from Fig. 3 of ref. 1.)

With natural long-term stability and very low sensitivity to environmental effects such as tilt and ground vibrations, together with a lack of mechanical parts, atom gravimeters and gradiometers possess a clear advantage over their classical counterparts. Stray and colleagues' advance shows that they might soon be more portable and user-friendly, too.

# ROMAN PAŠTEKA & PAVOL ZAHOREC: Practical solutions for surface gravity mapping

Our fascination with gravity dates back to the ancient Greeks, and measuring gravitational acceleration was among the first pursuits in modern science. Geophysicists in the eighteenth century used pendula to make such measurements<sup>7</sup>. But, since then, tools for gravimetry have been the subject of intensive development — from simple spring-based devices, all the way to present-day instruments based on quantum technology. In physical geodesy and applied geophysics, gravimetry measurements are now used to determine the size and shape of Earth, and to identify inhomogeneities in the density of Earth's interior. Such measurements can reveal near-surface objects or aid the study of the lithosphere, the rocky outer edge of Earth's structure.

Gradients of gravitational acceleration are more useful than direct measurements in this respect: they are sensitive to shallow density distributions and can detect objects more precisely (Fig. 1b). In terrestrial gravimetric surveys, vertical gradients in gravity can be approximated using measurements from classical spring gravimeters, taken at different heights. But this procedure is time consuming, needing tens of minutes for each data point, and its uncertainty depends on the accuracy of the gravimeter.

Stray *et al.* estimated that the uncertainty in the measurements taken with their instrument is better than that of commercial gravimeters. Perhaps more importantly, they note that 10 data points can be collected in just 15 minutes. From this point of view, the team's results, together with those of other research groups<sup>8,9</sup>, could drastically change applied gravimetry research — lending weight to the authors' claim that the work constitutes a kind of 'gravity cartography'.

In general, gravity values (and especially gradients) reflect the distribution of density inhomogeneities below Earth's surface, but they are also influenced by the effects of terrain and nearby buildings<sup>10</sup>. The key factor in determining the magnitude of this effect is the nearby topography, which is underestimated in some geophysical studies, and should be taken into account. Gravitational attraction to nearby buildings contributes a smaller,

but measurable, addition to the gravity field (and its gradients), and must therefore be estimated and removed from the data using numerical methods, which are well developed.

Although the gravity-gradient method is extremely useful for detecting subsurface objects through density inhomogeneities, its limitations should be recognized. The probability of detecting a subsurface structure depends on the structure's size and depth, as well as on the degree to which its density differs from that of the surrounding soil or rock environment. From our experience in the detection of subsurface cavities in archaeological prospection<sup>11</sup>, we can infer the probability of identifying such cavities in common natural conditions when using an instrument with the uncertainty reported by Stray and colleagues.

We estimate that the maximum amplitude of the vertical gravity gradient arising from a tunnel of one metre cross-sectional diameter, lying one metre below Earth's surface, is more than six times this uncertainty threshold. For a tunnel with a diameter four times wider than this, we calculate that the same maximum amplitude would be measured even if the tunnel were up to four metres below the surface. Such detection ability looks very promising for many engineering and environmental applications.

*Nature* **602**, 579–580 (2022)

doi: <https://doi.org/10.1038/d41586-022-00464-1>

## References

1. Stray, B. *et al.* *Nature* **602**, 590–594 (2022).
2. Abbott, B. P. *et al.* *Phys. Rev. Lett.* **116**, 061102 (2016).
3. Kasevich, M. & Chu, S. *Phys. Rev. Lett.* **67**, 181–184 (1991).
4. Bongs, K. *et al.* *Nature Rev. Phys.* **1**, 731–739 (2019).
5. Wu, X. *et al.* *Sci. Adv.* **5**, eaax0800 (2019).

6. Asenbaum, P. *et al.* *Phys. Rev. Lett.* **118**, 183602 (2017).
7. Howarth, R. *Earth Sci. Hist.* **26**, 201–228 (2007).
8. Tino, G. M. *et al.* *Eur. Phys. J. D* **73**, 228 (2019).
9. Boddice, D., Metje, N. & Tuckwell, G. *J. Appl. Geophys.* **146**, 149–159 (2017).
10. Zahorec, P., Papčo, J., Mikolaj, M., Pašteka, R. & Szalaiová, R. *First Break* **32**, 65–71 (2014).
11. Pašteka, R. *et al.* *Archaeol. Prospect.* **27**, 415–431 (2020).

---

This article was downloaded by **calibre** from <https://www.nature.com/articles/d41586-022-00464-1>

| [Section menu](#) | [Main menu](#) |

- NEWS AND VIEWS
- 09 February 2022

# Unwinding the mutational signatures of a DNA topoisomerase enzyme

Certain patterns of mutations occur frequently in cancer. The culprit behind one mutational signature is now shown to be a cellular enzyme with the mundane role of relieving stress in supercoiled DNA.

- [Ammal Abbasi](#)<sup>0</sup> &
- [Ludmil B. Alexandrov](#)<sup>1</sup>

Cancers are fuelled by changes in DNA, known as driver mutations, that tip cells towards uncontrolled multiplication. The mutations vary from tumour to tumour and from person to person, but some common patterns are emerging from analyses of thousands of genomes from cancerous and normal human tissues<sup>1</sup>. These analyses are providing reference sets of mutational ‘signatures’ that can be used to unpick the molecular processes underlying the mutations<sup>2</sup>. Much progress has been made in understanding the events that underpin signatures involving the mutation of single DNA ‘letters’, or bases. But less is known about the causes of mutational footprints characterized by small insertions and deletions (indels) of DNA. [Writing in Nature](#), Reijns *et al.*<sup>3</sup> describe their comprehensive computational and experimental investigation of the foundations of one such signature.

## Access options

Subscribe to Nature+

Get immediate online access to the entire Nature family of 50+ journals

\$29.99

monthly

[Subscribe](#)

Subscribe to Journal

Get full journal access for 1 year

\$199.00

only \$3.90 per issue

[Subscribe](#)

All prices are NET prices.

VAT will be added later in the checkout.

Tax calculation will be finalised during checkout.

Buy article

Get time limited or full article access on ReadCube.

\$32.00

[Buy](#)

All prices are NET prices.

### **Additional access options:**

- [Log in](#)
- [Learn about institutional subscriptions](#)

*Nature* **602**, 580-581 (2022)

*doi: <https://doi.org/10.1038/d41586-022-00301-5>*

## References

1. The ICGC/TCGA Pan-Cancer Analysis of Whole Genomes Consortium. *Nature* **578**, 82–93 (2020).
2. Alexandrov, L. B. *et al.* *Nature* **578**, 94–101 (2020).
3. Reijns, M. A. M. *et al.* *Nature* **602**, 623–631 (2022).
4. Ashour, M. E., Atteya, R. & El-Khamisy, S. F. *Nature Rev. Cancer* **15**, 137–151 (2015).
5. Lippert, M. J. *et al.* *Proc. Natl Acad. Sci. USA* **108**, 698–703 (2011).
6. Takahashi, D. T., Burguiere-Slezak, G., Van der Kemp, P. A. & Boiteux, S. *Proc. Natl Acad. Sci. USA* **108**, 692–697 (2011).
7. Hevener, K. E., Verstak, T. A., Lutat, K. E., Riggsbee, D. L. & Mooney, J. W. *Acta Pharm. Sin. B* **8**, 844–861 (2018).
8. Haffner, M. C. *et al.* *Nature Genet.* **42**, 668–675 (2010).
9. Cowell, I. G. *et al.* *Proc. Natl Acad. Sci. USA* **109**, 8989–8994 (2012).
10. Federico, S. M. *et al.* *Eur. J. Cancer* **137**, 204–213 (2020).
11. Thomas, A. *et al.* *J. Clin. Oncol.* **36**, 1594–1602 (2018).

---

This article was downloaded by **calibre** from <https://www.nature.com/articles/d41586-022-00301-5>

- NEWS AND VIEWS
- 23 February 2022

# Fragile nanosheets stripped from crystals

Two-dimensional materials have been restricted to systems in which strong chemical bonds hold atoms together in sheets. Now, 2D materials consisting of molecules linked by weak non-covalent bonds have been peeled from crystals.

- [Claudia Backes](#)   [ORCID: http://orcid.org/0000-0002-4154-0439](#) 9

Much research is currently focused on the fabrication and characterization of two-dimensional nanomaterials, which are often produced by peeling ultrathin sheets of atoms from crystals. It is widely thought that this method requires the crystals to contain layers of atoms held together by strong covalent bonds, with only weak binding between the layers. [Writing in Nature](#), Dong *et al.*<sup>1</sup> show that this is not always the case. The authors demonstrate that 2D nanosheets with high aspect ratios (ratios of length to thickness) can be obtained from crystals, suspended in liquids, when the molecules in the layers are held together only by weak non-covalent bonds.

## Access options

Subscribe to Nature+

Get immediate online access to the entire Nature family of 50+ journals

\$29.99

monthly

## Subscribe

Subscribe to Journal

Get full journal access for 1 year

\$199.00

only \$3.90 per issue

## Subscribe

All prices are NET prices.

VAT will be added later in the checkout.

Tax calculation will be finalised during checkout.

Buy article

Get time limited or full article access on ReadCube.

\$32.00

## Buy

All prices are NET prices.

## **Additional access options:**

- [Log in](#)
- [Learn about institutional subscriptions](#)

*Nature* **602**, 582-583 (2022)

*doi:* <https://doi.org/10.1038/d41586-022-00466-z>

## **References**

1. Dong, J. *et al.* *Nature* **602**, 606–611 (2022).

2. Khan, K. *et al.* *J. Mater. Chem. C* **8**, 387–440 (2020).
3. Tao, H. *et al.* *Prog. Mater. Sci.* **111**, 100637 (2020).
4. Hernandez, Y. *et al.* *Nature Nanotechnol.* **3**, 563–568 (2008).
5. Nicolosi, V., Chhowalla, M., Kanatzidis, M. G., Strano, M. S. & Coleman, J. N. *Science* **340**, 1226419 (2013).
6. Yi, M. & Shen, Z. *J. Mater. Chem. A* **3**, 11700–11715 (2015).
7. Dong, J. *et al.* *J. Am. Chem. Soc.* **139**, 1554–1564 (2017).
8. Ji, L.-J. *et al.* *Chem. Mater.* **30**, 8732–8738 (2018).
9. Backes, C. *et al.* *ACS Nano* **13**, 7050–7061 (2019).
10. Rao, V. J. *et al.* *ACS Nano* **15**, 20466–20477 (2021).
11. Kang, J., Sangwan, V. K., Wood, J. D. & Hersam, M. C. *Acc. Chem. Res.* **50**, 943–951 (2017).

---

This article was downloaded by **calibre** from <https://www.nature.com/articles/d41586-022-00466-z>

- NEWS AND VIEWS
- 23 February 2022

# Radio bursts from among the oldest stars

Luminous bursts of radio emission are linked to highly magnetized neutron stars known as magnetars. Now, bursts have been detected from a globular star cluster, an environment thought to be devoid of magnetars.

- [Vikram Ravi](#) ✉

If you were to look up at the sky with radio goggles, you would notice bright flashes at random locations roughly once every minute. Over the past 15 years, astronomers have detected more than 600 sources of such bursts, which have a range of luminosities, durations and rates of repetition. More than 20 sources have now been traced to specific galaxies, the diversity of which is similarly astounding. But such varied observations have not yet produced incisive insights into the burst mechanism. Now, in [a paper in \*Nature\*](#), Kirsten *et al.*<sup>1</sup> report a surprising source of extragalactic radio bursts among some of the Universe's oldest stars, and, [in \*Nature Astronomy\*](#), Nimmo *et al.*<sup>2</sup> provide a detailed analysis of these bursts. The discovery differs from previous findings of sources among young stars, and challenges ideas on the formation of magnetars — the most magnetized objects in the Universe.

## Access options

Subscribe to Nature+

Get immediate online access to the entire Nature family of 50+ journals

\$29.99

monthly

[Subscribe](#)

Subscribe to Journal

Get full journal access for 1 year

\$199.00

only \$3.90 per issue

[Subscribe](#)

All prices are NET prices.

VAT will be added later in the checkout.

Tax calculation will be finalised during checkout.

Buy article

Get time limited or full article access on ReadCube.

\$32.00

[Buy](#)

All prices are NET prices.

### **Additional access options:**

- [Log in](#)
- [Learn about institutional subscriptions](#)

*Nature* **602**, 583-584 (2022)

*doi:* <https://doi.org/10.1038/d41586-022-00465-0>

# References

1. Kirsten, F. *et al.* *Nature* **602**, 585–589 (2022).
2. Nimmo, K. *et al.* *Nature Astron.* <https://doi.org/10.1038/s41550-021-01569-9> (2022).
3. CHIME/FRB Collaboration. *Nature* **587**, 54–58 (2020).
4. Bochenek, C. D. *et al.* *Nature* **587**, 59–62 (2020).
5. Ridnaia, A. *et al.* *Nature Astron.* **5**, 372–377 (2021).
6. Kaspi, V. M. & Beloborodov, A. M. *Annu. Rev. Astron. Astrophys.* **55**, 261–301 (2017).
7. Bhandari, S. *et al.* *Astron. J.* **163**, 69 (2022).
8. Majid, W. A. *et al.* *Astrophys. J.* **919**, L6 (2021).
9. Connor, L. *et al.* *Publ. Astron. Soc. Pacif.* **133**, 075001 (2021).
10. Macquart, J.-P. *et al.* *Nature* **581**, 391–395 (2020).
11. Connor, L. & Ravi, V. Preprint at <https://arxiv.org/abs/2107.13692> (2021).

---

This article was downloaded by **calibre** from <https://www.nature.com/articles/d41586-022-00465-0>

- Article
- [Published: 23 February 2022](#)

# A repeating fast radio burst source in a globular cluster

- [F. Kirsten](#) [ORCID: orcid.org/0000-0001-6664-8668](#)<sup>1,2</sup>,
- [B. Marcote](#) [ORCID: orcid.org/0000-0001-9814-2354](#)<sup>3</sup>,
- [K. Nimmo](#) [ORCID: orcid.org/0000-0003-0510-0740](#)<sup>2,4</sup>,
- [J. W. T. Hessels](#) [ORCID: orcid.org/0000-0003-2317-1446](#)<sup>2,4</sup>,
- [M. Bhardwaj](#)<sup>5,6</sup>,
- [S. P. Tendulkar](#)<sup>7,8</sup>,
- [A. Keimpema](#) [ORCID: orcid.org/0000-0002-5575-2774](#)<sup>3</sup>,
- [J. Yang](#) [ORCID: orcid.org/0000-0002-2322-5232](#)<sup>1</sup>,
- [M. P. Snelders](#) [ORCID: orcid.org/0000-0001-6170-2282](#)<sup>4</sup>,
- [P. Scholz](#) [ORCID: orcid.org/0000-0002-7374-7119](#)<sup>9</sup>,
- [A. B. Pearlman](#) [ORCID: orcid.org/0000-0002-8912-0732](#)<sup>5,6,10</sup>,
- [C. J. Law](#)<sup>11,12</sup>,
- [W. M. Peters](#) [ORCID: orcid.org/0000-0002-5187-7107](#)<sup>13</sup>,
- [M. Giroletti](#) [ORCID: orcid.org/0000-0002-8657-8852](#)<sup>14</sup>,
- [Z. Paragi](#) [ORCID: orcid.org/0000-0002-5195-335X](#)<sup>3</sup>,
- [C. Bassa](#) [ORCID: orcid.org/0000-0002-1429-9010](#)<sup>2</sup>,
- [D. M. Hewitt](#) [ORCID: orcid.org/0000-0002-5794-2360](#)<sup>4</sup>,
- [U. Bach](#)<sup>15</sup>,
- [V. Bezrukova](#) [ORCID: orcid.org/0000-0003-3655-2280](#)<sup>16</sup>,
- [M. Burgay](#) [ORCID: orcid.org/0000-0002-8265-4344](#)<sup>17</sup>,
- [S. T. Buttaccio](#) [ORCID: orcid.org/0000-0002-3341-466X](#)<sup>18</sup>,
- [J. E. Conway](#)<sup>1</sup>,
- [A. Corongiu](#)<sup>17</sup>,
- [R. Feiler](#)<sup>19</sup>,

- [O. Forssén<sup>1</sup>](#),
- [M. P. Gawroński<sup>19</sup>](#),
- [R. Karuppusamy](#) [ORCID: orcid.org/0000-0002-5307-2919<sup>15</sup>](#),
- [M. A. Kharinov<sup>20</sup>](#),
- [M. Lindqvist<sup>1</sup>](#),
- [G. Maccaferri](#) [ORCID: orcid.org/0000-0002-1482-708X<sup>14</sup>](#),
- [A. Melnikov](#) [ORCID: orcid.org/0000-0002-8466-7026<sup>20</sup>](#),
- [O. S. Ould-Boukattine](#) [ORCID: orcid.org/0000-0001-9381-8466<sup>4</sup>](#),
- [A. Possenti](#) [ORCID: orcid.org/0000-0001-5902-3731<sup>17,21</sup>](#),
- [G. Surcis](#) [ORCID: orcid.org/0000-0003-2775-442X<sup>17</sup>](#),
- [N. Wang](#) [ORCID: orcid.org/0000-0002-9786-8548<sup>22</sup>](#),
- [J. Yuan<sup>22</sup>](#),
- [K. Aggarwal](#) [ORCID: orcid.org/0000-0002-2059-0525<sup>23,24</sup>](#),
- [R. Anna-Thomas<sup>23,24</sup>](#),
- [G. C. Bower](#) [ORCID: orcid.org/0000-0003-4056-9982<sup>25</sup>](#),
- [R. Blaauw<sup>2</sup>](#),
- [S. Burke-Spolaoor<sup>23,24,26</sup>](#),
- [T. Cassanelli](#) [ORCID: orcid.org/0000-0003-2047-5276<sup>9,27</sup>](#),
- [T. E. Clarke<sup>13</sup>](#),
- [E. Fonseca](#) [ORCID: orcid.org/0000-0001-8384-5049<sup>5,6,23,24</sup>](#),
- [B. M. Gaensler](#) [ORCID: orcid.org/0000-0002-3382-9558<sup>9,27</sup>](#),
- [A. Gopinath<sup>4</sup>](#),
- [V. M. Kaspi](#) [ORCID: orcid.org/0000-0001-9345-0307<sup>5,6</sup>](#),
- [N. Kassim](#) [ORCID: orcid.org/0000-0001-8035-4906<sup>13</sup>](#),
- [T. J. W. Lazio<sup>28</sup>](#),
- [C. Leung](#) [ORCID: orcid.org/0000-0002-4209-7408<sup>29,30</sup>](#),
- [D. Z. Li](#) [ORCID: orcid.org/0000-0001-7931-0607<sup>11</sup>](#),
- [H. H. Lin](#) [ORCID: orcid.org/0000-0001-7453-4273<sup>31,36</sup>](#),
- [K. W. Masui](#) [ORCID: orcid.org/0000-0002-4279-6946<sup>29,30</sup>](#),
- [R. Mckinven<sup>9</sup>](#),
- [D. Michilli](#) [ORCID: orcid.org/0000-0002-2551-7554<sup>5,6,29,30</sup>](#),
- [A. G. Mikhailov](#) [ORCID: orcid.org/0000-0002-3355-2261<sup>20</sup>](#),
- [C. Ng<sup>9</sup>](#),
- [A. Orbidans<sup>16</sup>](#),

- [U. L. Pen](#) [ORCID: orcid.org/0000-0003-2155-9578](#)<sup>9,26,31,32 nAff36</sup>,
- [E. Petroff](#) [ORCID: orcid.org/0000-0002-9822-8008](#)<sup>4,5,6</sup>,
- [M. Rahman](#)<sup>33</sup>,
- [S. M. Ransom](#) [ORCID: orcid.org/0000-0001-5799-9714](#)<sup>34</sup>,
- [K. Shin](#) [ORCID: orcid.org/0000-0002-6823-2073](#)<sup>29,30</sup>,
- [K. M. Smith](#)<sup>32</sup>,
- [I. H. Stairs](#)<sup>35</sup> &
- [W. Vlemmings](#) [ORCID: orcid.org/0000-0002-2700-9916](#)<sup>1</sup>

*Nature* volume **602**, pages 585–589 (2022)

- 1049 Accesses
- 430 Altmetric
- [Metrics details](#)

## Subjects

- [Compact astrophysical objects](#)
- [Time-domain astronomy](#)
- [Transient astrophysical phenomena](#)

## Abstract

Fast radio bursts (FRBs) are flashes of unknown physical origin<sup>1</sup>. The majority of FRBs have been seen only once, although some are known to generate multiple flashes<sup>2,3</sup>. Many models invoke magnetically powered neutron stars (magnetars) as the source of the emission<sup>4,5</sup>. Recently, the discovery<sup>6</sup> of another repeater (FRB 20200120E) was announced, in the direction of the nearby galaxy M81, with four potential counterparts at other wavelengths<sup>6</sup>. Here we report observations that localized the FRB to a globular cluster associated with M81, where it is 2 parsecs away from the optical centre of the cluster. Globular clusters host old stellar populations, challenging FRB models that invoke young magnetars formed in a core-collapse supernova. We propose instead that FRB 20200120E originates

from a highly magnetized neutron star formed either through the accretion-induced collapse of a white dwarf, or the merger of compact stars in a binary system<sup>[7](#)</sup>. Compact binaries are efficiently formed inside globular clusters, so a model invoking them could also be responsible for the observed bursts.

This is a preview of subscription content

## Access options

Subscribe to Nature+

Get immediate online access to the entire Nature family of 50+ journals

\$29.99

monthly

[Subscribe](#)

Subscribe to Journal

Get full journal access for 1 year

\$199.00

only \$3.90 per issue

[Subscribe](#)

All prices are NET prices.

VAT will be added later in the checkout.

Tax calculation will be finalised during checkout.

Buy article

Get time limited or full article access on ReadCube.

\$32.00

[Buy](#)

All prices are NET prices.

### **Additional access options:**

- [Log in](#)
- [Learn about institutional subscriptions](#)

**Fig. 1: Dispersion-corrected time series and dynamic spectra of the five FRB 20200120E bursts.**

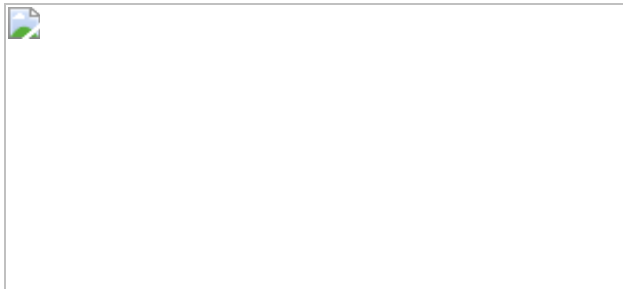


**Fig. 2: Localization plots for FRB 20200120E.**

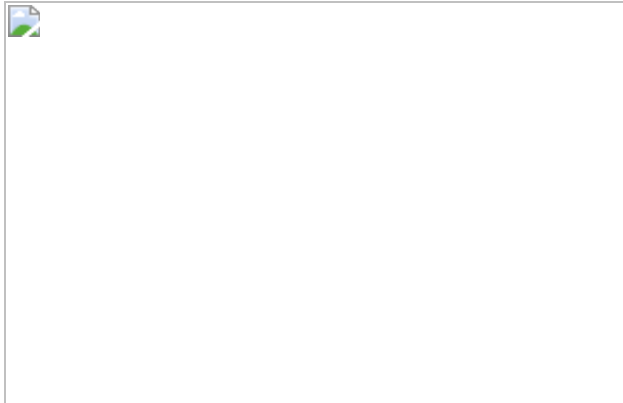


**Fig. 3: Optical images of the FRB 20200120E host and surrounding field.**

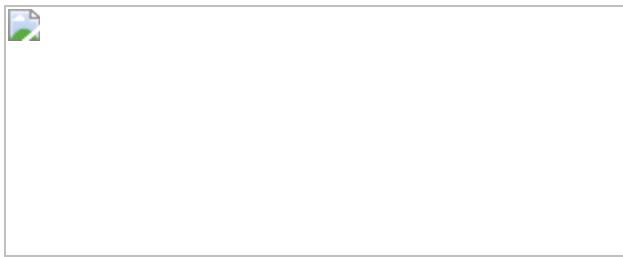
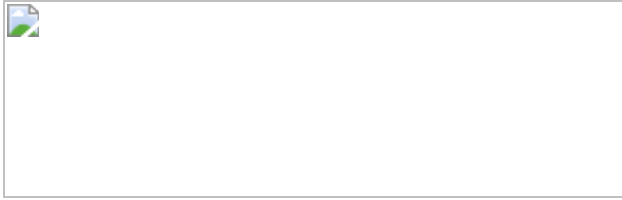


**Fig. 4: Continuum maps of the field around FRB 20200120E.**



## Data availability

The datasets generated from the EVN observations and analysed in this study are available at the Public EVN Data Archive under the experiment codes EK048B, EK048C and EK048F. The calibrated maps, plotting scripts and further data used in this manuscript are available at  
<https://doi.org/10.5281/zenodo.5708237>.

## Code availability

The codes used to analyse the data are available at the following sites: AIPS (<http://www.aips.nrao.edu/index.shtml>), CASA (<https://casa.nrao.edu>), Difmap (<https://science.nrao.edu/facilities/vlba/docs/manuals/oss2013a/post-processing-software/difmap>), DSPSR (<http://dpsr.sourceforge.net>), FETCH (<https://github.com/devanshkv/fetch>), Heimdall (<https://sourceforge.net/projects/heimdall-astro>), IRAF (<https://iraf-community.github.io/>), PRESTO (<https://github.com/scottransom/presto>), PSRCHIVE (<http://psrchive.sourceforge.net>), and SpS (<https://github.com/danielemichilli/SpS>).

## References

1. Petroff, E., Hessels, J. W. T. & Lorimer, D. R. Fast radio bursts. *Astron. Astrophys. Rev.* **27**, 4 (2019).
2. Spitler, L. G. et al. A repeating fast radio burst. *Nature* **531**, 202–205 (2016).
3. The CHIME/FRB Collaboration. The first CHIME/FRB fast radio burst catalog. *Astrophys. J. Suppl. Ser.* **257**, 59 (2021).

4. Margalit, B. & Metzger, B. D. A concordance picture of FRB 121102 as a flaring magnetar embedded in a magnetized ion–electron wind nebula. *Astrophys. J. Lett.* **868**, 4 (2018).
5. The CHIME/FRB Collaboration. A bright millisecond-duration radio burst from a Galactic magnetar. *Nature* **587**, 54–58 (2020).
6. Bhardwaj, M. et al. A nearby repeating fast radio burst in the direction of M81. *Astrophys. J. Lett.* **910**, 18 (2021).
7. Margalit, B., Berger, E. & Metzger, B. D. Fast radio bursts from magnetars born in binary neutron star mergers and accretion induced collapse. *Astrophys. J.* **886**, 110 (2019).
8. Freedman, W. L. et al. The Hubble Space Telescope Extragalactic Distance Scale Key Project. I. The discovery of cepheids and a new distance to M81. *Astrophys. J.* **427**, 628–655 (1994).
9. Lazarus, P. et al. Prospects for high-precision pulsar timing with the new Effelsberg PSRIX backend. *Mon. Not. R. Astron. Soc.* **458**, 868–880 (2016).
10. Nimmo, K. et al. Burst timescales and luminosities link young pulsars and fast radio bursts. *Nat. Astron.*, in the press (2022).
11. Keimpema, A. et al. The SFXC software correlator for very long baseline interferometry: algorithms and implementation. *Exp. Astron.* **39**, 259–279 (2015).
12. Charlot, P. et al. The third realization of the International Celestial Reference Frame by very long baseline interferometry. *Astron. Astrophys.* **644**, A159 (2020).
13. Perelmutter, J.-M., Brodie, J. P. & Huchra, J. P. Kinematics and metallicity of 25 globular clusters in M81. *Astron. J.* **110**, 620–627 (1995).

14. Perelmutter, J.-M. & Racine, R. The globular cluster system of M81. *Astron. J.* **109**, 1055–1070 (1995).
15. Moffat, A. F. J. A theoretical investigation of focal stellar images in the photographic emulsion and application to photographic photometry. *Astron. Astrophys.* **3**, 455–461 (1969).
16. Gaia Collaboration. The Gaia mission. *Astron. Astrophys.* **595**, A1 (2016).
17. Gaia Collaboration. Gaia Early Data Release 3: summary of the contents and survey properties. *Astron. Astrophys.* **649**, A1 (2021).
18. Harris, W. E., Harris, G. L. H. & Alessi, M. A catalog of globular cluster systems: what determines the size of a galaxy’s globular cluster population? *Astrophys. J.* **772**, 82 (2013).
19. Marcote, B. et al. A repeating fast radio burst source localized to a nearby spiral galaxy. *Nature* **577**, 190–194 (2020).
20. Marcote, B. et al. The repeating fast radio burst FRB 121102 as seen on milliarcsecond angular scales. *Astrophys. J. Lett.* **834**, L8 (2017).
21. Ajello, M. et al. The fourth catalog of active galactic nuclei detected by the Fermi Large Area Telescope. *Astrophys. J.* **892**, 105 (2020).
22. Abdo, A. A. et al. Detection of gamma-ray emission from the starburst galaxies M82 and NGC 253 with the Large Area Telescope on Fermi. *Astrophys. J. Lett.* **709**, L152–L157 (2010).
23. Hut, P. et al. Binaries in globular clusters. *Publ. Astron. Soc. Pac.* **104**, 981 (1992).
24. Pooley, D. et al. Dynamical formation of close binary systems in globular clusters. *Astrophys. J. Lett.* **591**, L131–L134 (2003).
25. Verbunt, F. Binary evolution and neutron stars in globular clusters. In *New Horizons in Globular Cluster Astronomy: Proceedings of a Conference Held at Università di Padova, Padova, Italy 24–28 June*,

2002 (eds Piotto, G. et al.) 245–254 (Astronomical Society of the Pacific, 2003).

26. Wang, B. & Liu, D. The formation of neutron star systems through accretion-induced collapse in white-dwarf binaries. *Res. Astron. Astrophys.* **20**, 135 (2020).
27. Giacomazzo, B. & Perna, R. Formation of stable magnetars from binary neutron star mergers. *Astrophys. J. Lett.* **771**, L26 (2013).
28. Schwab, J., Quataert, E. & Kasen, D. The evolution and fate of super-Chandrasekhar mass white dwarf merger remnants. *Mon. Not. R. Astron. Soc.* **463**, 3461–3475 (2016).
29. Zhong, S.-Q. & Dai, Z.-G. Magnetars from neutron star–white dwarf mergers: application to fast radio bursts. *Astrophys. J.* **893**, 9 (2020).
30. Prager, B. J. et al. Using long-term millisecond pulsar timing to obtain physical characteristics of the bulge globular cluster Terzan 5. *Astrophys. J.* **845**, 148 (2017).
31. Mottez, F. & Zarka, P. Radio emissions from pulsar companions: a refutable explanation for galactic transients and fast radio bursts. *Astron. Astrophys.* **569**, A86 (2014).
32. Mottez, F., Zarka, P. & Voisin, G. Repeating fast radio bursts caused by small bodies orbiting a pulsar or a magnetar. *Astron. Astrophys.* **644**, A145 (2020).
33. Ablimit, I. & Li, X.-D. Formation of binary millisecond pulsars by accretion-induced collapse of white dwarfs under wind-driven evolution. *Astrophys. J.* **800**, 98 (2015).
34. Ye, C. S., Kremer, K., Chatterjee, S., Rodriguez, C. L. & Rasio, F. A. Millisecond pulsars and black holes in globular clusters. *Astrophys. J.* **877**, 122 (2019).

35. Heinke, C. O. et al. Analysis of the quiescent low-mass X-ray binary population in Galactic globular clusters. *Astrophys. J.* **598**, 501–515 (2003).
36. Sridhar, N. et al. Periodic fast radio bursts from luminous X-ray binaries. *Astrophys. J.* **917**, 13 (2021).
37. Kaaret, P., Feng, H. & Roberts, T. P. Ultraluminous X-ray sources. *Annu. Rev. Astron. Astrophys.* **55**, 303–341 (2017).
38. Bachetti, M. et al. An ultraluminous X-ray source powered by an accreting neutron star. *Nature* **514**, 202–204 (2014).
39. Webb, N. et al. Radio detections during two state transitions of the intermediate-mass black hole HLX-1. *Science* **337**, 554–556 (2012).
40. Dage, K. C. et al. X-ray spectroscopy of newly identified ULXs associated with M87’s globular cluster population. *Mon. Not. R. Astron. Soc.* **497**, 596–608 (2020).
41. Chatterjee, S. et al. A direct localization of a fast radio burst and its host. *Nature* **541**, 58–61 (2017).
42. Ravi, V. et al. The host galaxy and persistent radio counterpart of FRB 20201124A. Preprint at <https://arxiv.org/abs/2106.09710> (2021).
43. Bassa, C. G. et al. FRB 121102 is coincident with a star-forming region in its host galaxy. *Astrophys. J. Lett.* **843**, L8 (2017).
44. Tendulkar, S. P. et al. The 60 pc environment of FRB 20180916B. *Astrophys. J. Lett.* **908**, L12 (2021).
45. Piro, L. et al. The fast radio burst FRB 20201124A in a star-forming region: constraints to the progenitor and multiwavelength counterparts. *Astron. Astrophys.* **656**, L15 (2021).
46. Fong, W.-f et al. Chronicling the host galaxy properties of the remarkable repeating FRB 20201124A. *Astrophys. J. Lett.* **919**, L23 (2021).

47. Remazeilles, M., Dickinson, C., Banday, A. J., Bigot-Sazy, M. A. & Ghosh, T. An improved source-subtracted and destriped 408-MHz all-sky map. *Mon. Not. R. Astron. Soc.* **451**, 4311–4327 (2015).
48. Reich, P. & Reich, W. Spectral index variations of the galactic radio continuum emission : evidence for a galactic wind. *Astron. Astrophys.* **196**, 211–226 (1988).
49. Mather, J. C. et al. Measurement of the cosmic microwave background spectrum by the COBE FIRAS instrument. *Astrophys. J.* **420**, 439–444 (1994).
50. Whitney, A. et al. VLBI data interchange format (VDIF). In *Sixth International VLBI Service for Geodesy and Astronomy. Proceedings from the 2010 General Meeting* (eds Navarro, R. et al.) 192–196 (NASA, 2010).
51. Whitney, A. The Mark 5B VLBI data system. In *Proc. 7th European VLBI Network Symp. on VLBI Scientific Research and Technology* (eds Bachiller, R et al.) 251–252 (EVN, 2004).
52. Kirsten, F. et al. Detection of two bright radio bursts from magnetar SGR 1935 + 2154. *Nat. Astron.* **5**, 414–422 (2021).
53. Agarwal, D., Aggarwal, K., Burke-Spolaor, S., Lorimer, D. R. & Garver-Daniels, N. FETCH: a deep-learning based classifier for fast transient classification. *Mon. Not. R. Astron. Soc.* **497**, 1661–1674 (2020).
54. Ransom, S. M. New Search Techniques for Binary Pulsars. PhD thesis, Harvard Univ. 2001).
55. Ransom, S. PRESTO: PulsaR Exploration and Search Toolkit. Astrophysics Source Code Library <http://ascl.net/1107.017> (2011).
56. Michilli, D. et al. Single-pulse classifier for the LOFAR Tied-Array All-sky Survey. *Mon. Not. R. Astron. Soc.* **480**, 3457–3467 (2018).

57. Greisen, E. W. AIPS, the VLA, and the VLBA. In *Information Handling in Astronomy – Historical Vistas* (ed. Heck, A.) 109–125 (Kluwer Academic, 2003).
58. Shepherd, M. C., Pearson, T. J. & Taylor, G. B. DIFMAP: an interactive program for synthesis imaging. *Bull. Am. Astron. Soc.* **26**, 987–989 (1994).
59. Law, C. J. et al. realfast: real-time, commensal fast transient surveys with the Very Large Array. *Astrophys. J. Suppl. Ser.* **236**, 8 (2018).
60. Polisensky, E. et al. Exploring the transient radio sky with VLITE: early results. *Astrophys. J.* **832**, 60 (2016).
61. Clarke, T. E. et al. Commensal low frequency observing on the NRAO VLA: VLITE status and future plans. In *Proc. SPIE 9906: Ground-based and Airborne Telescopes VI* (eds Hall, H. J. et al.) 99065B (SPIE, 2016).
62. Bethapudi, S. et al. The first fast radio burst detected with VLITE-Fast. *Res. Not. Am. Astron. Soc.* **5**, 46 (2021).
63. Cotton, W. D. Obit: a development environment for astronomical algorithms. *Publ. Astron. Soc. Pac.* **120**, 439–448 (2008).
64. Offringa, A. R. et al. WSCLEAN: an implementation of a fast, generic wide-field imager for radio astronomy. *Mon. Not. R. Astron. Soc.* **444**, 606–619 (2014).
65. Miyazaki, S. et al. Hyper Suprime-Cam. In *Proc. SPIE 8446: Ground-based and Airborne Instrumentation for Astronomy IV* (eds McLean, I. S. et al.) 84460Z (SPIE, 2012).
66. Bosch, J. et al. The Hyper Suprime-Cam software pipeline. *Publ. Astron. Soc. Pac.* **70**, S5 (2018).
67. Flewelling, H. A. et al. The Pan-STARRS1 database and data products. *Astrophys. J. Suppl. Ser.* **251**, 7 (2020).

68. Garmire, G. P. et al. Advanced CCD imaging spectrometer (ACIS) instrument on the Chandra X-ray Observatory. In *Proc. SPIE 4851: X-ray and Gamma-ray Telescopes and Instruments for Astronomy* (eds Truemper, J. E. & Tananbaum, H. D.) 28–44 (SPIE, 2003).
69. Fruscione, A. et al. CIAO: Chandra’s data analysis system. In *Proc. SPIE 6270: Observatory Operations: Strategies, Processes, and Systems* (eds Silva, D. R. & Doxsey, R. E.) 62701V (2006).
70. Kraft, R. P., Burrows, D. N. & Nousek, J. A. Determination of confidence limits for experiments with low numbers of counts. *Astrophys. J.* **374**, 344–355 (1991).
71. Ballet, J., Burnett, T. H., Digel, S. W. & Lott, B. Fermi Large Area Telescope Fourth Source Catalog. Preprint at <https://arxiv.org/abs/2005.11208> (2020).
72. Abdo, A. A. et al. A population of gamma-ray emitting globular clusters seen with the Fermi Large Area Telescope. *Astron. Astrophys.* **524**, A75 (2010).
73. Hessels, J. W. T. et al. FRB 121102 bursts show complex time-frequency structure. *Astrophys. J. Lett.* **876**, L23 (2019).
74. Kirsten, F., Vlemmings, W., Campbell, R. M., Kramer, M. & Chatterjee, S. Revisiting the birth locations of pulsars B1929+10, B2020+28, and B2021+51. *Astron. Astrophys.* **577**, A111 (2015).
75. Condon, J. J. et al. Resolving the radio source background: deeper understanding through confusion. *Astrophys. J.* **758**, 23 (2012).
76. Beck, R. et al. PS1-STRM: neural network source classification and photometric redshift catalogue for PS1  $3\pi$  DR1. *Mon. Not. R. Astron. Soc.* **500**, 1633–1644 (2021).
77. Bloom, J. S., Kulkarni, S. R. & Djorgovski, S. G. The observed offset distribution of gamma-ray bursts from their host galaxies: a robust clue to the nature of the progenitors. *Astrophys. J.* **123**, 1111–1148 (2002).

78. Leja, J., Johnson, B. D., Conroy, C., van Dokkum, P. G. & Byler, N. Deriving physical properties from broadband photometry with Prospector: description of the model and a demonstration of its accuracy using 129 galaxies in the local Universe. *Astrophys. J.* **837**, 170 (2017).
79. Johnson, B. D., Leja, J. L., Conroy, C. & Speagle, J. S. Prospector: stellar population inference from spectra and SEDs. Astrophysics Source Code Library <http://ascl.net/1905.025> (2019).
80. Alam, S. et al. The eleventh and twelfth data releases of the Sloan Digital Sky Survey: final data from SDSS-III. *Astrophys. J. Suppl. Ser.* **219**, 12 (2015).
81. Simha, V. et al. Parametrising star formation histories. Preprint at <https://arxiv.org/abs/1404.0402> (2014).
82. Carnall, A. C. et al. How to measure galaxy star formation histories. I. Parametric models. *Astrophys. J.* **873**, 44 (2019).
83. Draine, B. T. & Li, A. Infrared emission from interstellar dust. IV. The silicate–graphite–PAH model in the post-Spitzer era. *Astrophys. J.* **657**, 810–837 (2007).
84. Bertelli, G., Bressan, A., Chiosi, C., Fagotto, F. & Nasi, E. Theoretical isochrones from models with new radiative opacities. *Astron. Astrophys. Suppl. Ser.* **106**, 275–302 (1994).
85. Ma, J. et al. Metal abundance properties of M81 globular cluster system. *Publ. Astron. Soc. Pac.* **119**, 1085–1092 (2007).
86. Kremer, K. et al. White dwarf subsystems in core-collapsed globular clusters. *Astrophys. J.* **917**, 28 (2021).
87. Ye, C. S. et al. On the rate of neutron star binary mergers from globular clusters. *Astrophys. J. Lett.* **888**, L10 (2020).

88. Boyles, J. et al. Young radio pulsars in Galactic globular clusters. *Astrophys. J.* **742**, 51 (2011).
89. Hessels, J. et al. Pulsars in globular clusters with the SKA. In *Advancing Astrophysics with the Square Kilometre Array* (AASKA14) 47 (2015).
90. Lyne, A. G., Manchester, R. N. & D'Amico, N. PSR B1745-20 and young pulsars in globular clusters. *Astrophys. J. Lett.* **460**, L41 (1996).
91. Macquart, J. P. et al. A census of baryons in the Universe from localized fast radio bursts. *Nature* **581**, 391–395 (2020).
92. Cordes, J. M. & Lazio, T. J. W. NE2001.I. A new model for the Galactic distribution of free electrons and its fluctuations. Preprint at <https://arxiv.org/abs/astro-ph/0207156> (2002).
93. Yao, J. M., Manchester, R. N. & Wang, N. A new electron-density model for estimation of pulsar and FRB distances. *Astrophys. J.* **835**, 29 (2017).
94. Keating, L. C. & Pen, U.-L. Exploring the dispersion measure of the Milky Way halo. *Mon. Not. R. Astron. Soc.* **496**, L106–L110 (2020).
95. Yamasaki, S. & Totani, T. The Galactic halo contribution to the dispersion measure of extragalactic fast radio bursts. *Astrophys. J.* **888**, 105 (2020).
96. Prochaska, J. X. & Zheng, Y. Probing Galactic haloes with fast radio bursts. *Mon. Not. R. Astron. Soc.* **485**, 648–665 (2019).
97. Hutschenreuter, S. et al. The Galactic Faraday rotation sky 2020. *Astron. Astrophys.* **657**, A43 (2022).
98. The CHIME/FRB Collaboration. CHIME/FRB discovery of eight new repeating fast radio burst sources. *Astrophys. J. Lett.* **885**, L24 (2019).
99. Michilli, D. et al. An extreme magneto-ionic environment associated with the fast radio burst source FRB 121102. *Nature* **553**, 182–185

(2018).

100. Hobbs, G., Manchester, R., Teoh, A. & Hobbs, M. The ATNF Pulsar Catalog. In *IAU Symp. No. 218: Young Neutron Stars and Their Environments* (eds Camilo, F. & Gaensler, B. M.) 139–140 (Astronomical Society of the Pacific, 2004).
101. Karachentsev, I. D. The local group and other neighboring galaxy groups. *Astron. J.* **129**, 178–188 (2005).
102. Schlegel, D. J., Finkbeiner, D. P. & Davis, M. Maps of dust infrared emission for use in estimation of reddening and cosmic microwave background radiation foregrounds. *Astrophys. J.* **500**, 525–553 (1998).

## Acknowledgements

We thank the directors and staff at the various participating stations for allowing us to use their facilities and running the observations. The European VLBI Network is a joint facility of independent European, African, Asian and North American radio astronomy institutes. Scientific results from data presented in this publication are derived from the following EVN project code: EK048. This work was also based on simultaneous EVN and PSRIX data recording observations with the 100-m telescope of the MPIfR (Max-Planck-Institut für Radioastronomie) at Effelsberg, and we thank the local staff for this arrangement. We would like to express our gratitude to W. van Straten for modifying the DSPSR software package to fit our needs. We appreciate discussions about magnetar formation scenarios in a globular cluster environment with E. P. J. van den Heuvel. Research by the AstroFlash group at University of Amsterdam, ASTRON and JIVE is supported in part by an NWO Vici grant (principal investigator (PI) J.W.T.H.; VI.C.192.045). This project has received funding from the European Union’s Horizon 2020 research and innovation programme under grant agreements 730562 (RadioNet) and 101004719 (OPTICON-RadioNet Pilot). A.B.P. is a McGill Space Institute (MSI) Fellow and a Fonds de Recherche du Quebec – Nature et Technologies (FRQNT) postdoctoral fellow. B.M. acknowledges support from the Spanish Ministerio de Economía y Competitividad (MINECO)

under grant AYA2016-76012-C3-1-P and from the Spanish Ministerio de Ciencia e Innovación under grants PID2019-105510GB-C31 and CEX2019-000918-M of ICCUB (Unidad de Excelencia “María de Maeztu” 2020–2023). Basic research in radio astronomy at NRL is funded by 6.1 Base funding. Construction and installation of VLITE was supported by the NRL Sustainment Restoration and Maintenance fund. C.J.L. acknowledges support from the National Science Foundation grant 2022546. C.L. was supported by the US Department of Defense (DoD) through the National Defense Science & Engineering Graduate Fellowship (NDSEG) programme. D.M. is a Banting Fellow. E.P. acknowledges funding from an NWO Veni Fellowship. F.K. acknowledges support from the Swedish Research Council via grant no. 2014-05713. FRB research at UBC is supported by an NSERC Discovery Grant and by the Canadian Institute for Advanced Research. J.Yuan is supported by the National Program on Key Research and Development Project (2017YFA0402602). K.S. is supported by the NSF Graduate Research Fellowship Program. K.W.M. is supported by an NSF Grant (2008031). M.Bhardwaj is supported by an FRQNT Doctoral Research Award. N.W. acknowledges support from the National Natural Science Foundation of China (grants 12041304 and 11873080) P.S. is a Dunlap Fellow and an NSERC Postdoctoral Fellow. The Dunlap Institute is funded through an endowment established by the David Dunlap family and the University of Toronto. Part of this research was carried out at the Jet Propulsion Laboratory, California Institute of Technology, under a contract with the National Aeronautics and Space Administration. The NANOGrav project receives support from National Science Foundation (NSF) Physics Frontiers Center award number 1430284. B.M.G. acknowledges the support of the Natural Sciences and Engineering Research Council of Canada (NSERC) through grant RGPIN-2015-05948, and of the Canada Research Chairs programme. The National Radio Astronomy Observatory is a facility of the National Science Foundation operated under cooperative agreement by Associated Universities, Inc. S.M.R. is a CIFAR Fellow and is supported by the NSF Physics Frontiers Center award 1430284. This work is based in part on observations carried out using the 32-m radio telescope operated by the Institute of Astronomy of the Nicolaus Copernicus University in Toruń (Poland) and supported by a Polish Ministry of Science and Higher Education SpUB grant. This work is based in part on observations carried out using the 32-m Badary, Svetloe

and Zelenchukskaya radio telescopes operated by the Scientific Equipment Sharing Center of the Quasar VLBI Network (Russia). The Sardinia Radio Telescope (SRT) is funded by the Department of University and Research (MIUR), the Italian Space Agency (ASI), and the Autonomous Region of Sardinia (RAS) and is operated as National Facility by the National Institute for Astrophysics (INAF). V.B. acknowledges support from the Engineering Research Institute Ventspils International Radio Astronomy Centre (VIRAC). V.M.K. holds the Lorne Trottier Chair in Astrophysics & Cosmology and a Distinguished James McGill Professorship and receives support from an NSERC Discovery Grant and Herzberg Award, from an R. Howard Webster Foundation Fellowship from the Canadian Institute for Advanced Research (CIFAR), and from the FRQNT Centre de Recherche en Astrophysique du Quebec. We received support from Ontario Research Fund – Research Excellence (ORF-RE) programme, Natural Sciences and Engineering Research Council of Canada (NSERC; funding reference number RGPIN-2019-067, CRD 523638-201, 555585-20), Canadian Institute for Advanced Research (CIFAR), Canadian Foundation for Innovation (CFI), the National Science Foundation of China (grant no. 11929301), Simons Foundation, Thoth Technology Inc, and Alexander von Humboldt Foundation. Computations were performed on the SOSCIP Consortium's (Blue Gene/Q, Cloud Data Analytics, Agile and/or Large Memory System) computing platform(s). SOSCIP is funded by the Federal Economic Development Agency of Southern Ontario, the Province of Ontario, IBM Canada Ltd., Ontario Centres of Excellence, Mitacs and 15 Ontario academic member institutions. Based (in part) on data collected at Subaru Telescope, which is operated by the National Astronomical Observatory of Japan. The National Radio Astronomy Observatory (NRAO) is a facility of the National Science Foundation operated under cooperative agreement by Associated Universities, Inc. AIPS is a software package produced and maintained by the National Radio Astronomy Observatory (NRAO).

## Author information

### Author notes

1. U. L. Pen

Present address: Institute of Astronomy and Astrophysics, Academia Sinica, Taipei, Taiwan

## Affiliations

1. Department of Space, Earth and Environment, Chalmers University of Technology, Onsala Space Observatory, Onsala, Sweden

F. Kirsten, J. Yang, J. E. Conway, O. Forssén, M. Lindqvist & W. Vlemmings

2. ASTRON, Netherlands Institute for Radio Astronomy, Dwingeloo, The Netherlands

F. Kirsten, K. Nimmo, J. W. T. Hessels, C. Bassa & R. Blaauw

3. Joint Institute for VLBI ERIC, Dwingeloo, The Netherlands

B. Marcote, A. Keimpema & Z. Paragi

4. Anton Pannekoek Institute for Astronomy, University of Amsterdam, Amsterdam, The Netherlands

K. Nimmo, J. W. T. Hessels, M. P. Snelders, D. M. Hewitt, O. S. Ould-Boukattine, A. Gopinath & E. Petroff

5. Department of Physics, McGill University, Montreal, Quebec, Canada

M. Bhardwaj, A. B. Pearlman, E. Fonseca, V. M. Kaspi, D. Michilli & E. Petroff

6. McGill Space Institute, McGill University, Montreal, Quebec, Canada

M. Bhardwaj, A. B. Pearlman, E. Fonseca, V. M. Kaspi, D. Michilli & E. Petroff

7. Department of Astronomy and Astrophysics, Tata Institute of Fundamental Research, Mumbai, India

S. P. Tendulkar

8. National Centre for Radio Astrophysics, Pune, India

S. P. Tendulkar

9. Dunlap Institute for Astronomy & Astrophysics, University of Toronto, Toronto, Ontario, Canada

P. Scholz, T. Cassanelli, B. M. Gaensler, R. Mckinven, C. Ng & U. L. Pen

10. Division of Physics, Mathematics, and Astronomy, California Institute of Technology, Pasadena, CA, USA

A. B. Pearlman

11. Cahill Center for Astronomy and Astrophysics, California Institute of Technology, Pasadena, CA, USA

C. J. Law & D. Z. Li

12. Owens Valley Radio Observatory, California Institute of Technology, Pasadena, CA, USA

C. J. Law

13. Remote Sensing Division, US Naval Research Laboratory, Washington, DC, USA

W. M. Peters, T. E. Clarke & N. Kassim

14. Istituto Nazionale di Astrofisica, Istituto di Radioastronomia, Bologna, Italy

M. Giroletti & G. Maccaferri

15. Max Planck Institute for Radio Astronomy, Bonn, Germany

U. Bach & R. Karuppusamy

16. Engineering Research Institute Ventspils International Radio Astronomy Centre (ERI VIRAC), Ventspils University of Applied Sciences (VUAS), Ventspils, Latvia

V. Bezrukova & A. Orbidan

17. Istituto Nazionale di Astrofisica, Osservatorio Astronomico di Cagliari, Selargius, Italy

M. Burgay, A. Corongiu, A. Possenti & G. Surcis

18. Istituto Nazionale di Astrofisica, Istituto di Radioastronomia Radiotelescopio di Noto, Noto, Italy

S. T. Buttaccio

19. Institute of Astronomy, Faculty of Physics, Astronomy and Informatics, Nicolaus Copernicus University, Toruń, Poland

R. Feiler & M. P. Gawroński

20. Institute of Applied Astronomy of the Russian Academy of Sciences, St. Petersburg, Russia

M. A. Kharinov, A. Melnikov & A. G. Mikhailov

21. Dipartimento di Fisica, Università di Cagliari, Monserrato, Italy

A. Possenti

22. Xinjiang Astronomical Observatory, Urumqi, China

N. Wang & J. Yuan

23. Department of Physics and Astronomy, West Virginia University, Morgantown, WV, USA

K. Aggarwal, R. Anna-Thomas, S. Burke-Spoloar & E. Fonseca

24. Center for Gravitational Waves and Cosmology, West Virginia University, Morgantown, WV, USA

K. Aggarwal, R. Anna-Thomas, S. Burke-Spoloar & E. Fonseca

25. Academia Sinica Institute of Astronomy and Astrophysics, Hilo, HI, USA

G. C. Bower

26. Canadian Institute for Advanced Research, CIFAR Azrieli Global Scholar, Toronto, Ontario, Canada

S. Burke-Spoloar & U. L. Pen

27. David A. Dunlap Department of Astronomy & Astrophysics, University of Toronto, Toronto, Ontario, Canada

T. Cassanelli & B. M. Gaensler

28. Jet Propulsion Laboratory, California Institute of Technology, Pasadena, CA, USA

T. J. W. Lazio

29. MIT Kavli Institute for Astrophysics and Space Research, Massachusetts Institute of Technology, Cambridge, MA, USA

C. Leung, K. W. Masui, D. Michilli & K. Shin

30. Department of Physics, Massachusetts Institute of Technology, Cambridge, MA, USA

C. Leung, K. W. Masui, D. Michilli & K. Shin

31. Canadian Institute for Theoretical Astrophysics, University of Toronto, Toronto, Ontario, Canada

H. H. Lin & U. L. Pen

32. Perimeter Institute for Theoretical Physics, Waterloo, Ontario, Canada

U. L. Pen & K. M. Smith

33. Sidrat Research, Toronto, Ontario, Canada

M. Rahman

34. National Radio Astronomy Observatory, Charlottesville, VA, USA

S. M. Ransom

35. Department of Physics and Astronomy, University of British Columbia, Vancouver, British Columbia, Canada

I. H. Stairs

36. Institute of Astronomy and Astrophysics, Academia Sinica, Taipei, Taiwan

H. H. Lin

## Contributions

F.K. is the Principal Investigator of the PRECISE team; he organized the observations, found the five bursts in the raw voltages and coordinated writing of the manuscript. B.M. led the analysis of the correlated data, performed the localization and wrote parts of the manuscript. K.N. led the time-domain analysis of the bursts. J.W.T.H. led the interpretation of the results and wrote parts of the manuscript. M.Bhardwaj led and performed the modelling of [PR95] 30244. S.P.T. performed the data reduction and analysis of the Subaru data. A.K. wrote and modified the software correlator SFXC to allow for the highest time resolution data. J.Yang assisted with the data reduction, analysis and interpretation of the correlated data. M.P.S. helped with the manuscript and created Extended Data Fig. 1. P.S. and A.B.P. reduced and analysed the archival Chandra data. C.J.L.

reduced and analysed the Realfast data. W.M.P. reduced and analysed the VLITE data. M.G. and A.B.P. searched the Fermi catalogues. Z.P. assisted with the reduction and analysis of the correlated data. C.B. assessed the optical registration errors of the Subaru and Gaia images. D.M.H. searched the PSRIX and DFB data for bursts. U.B. coordinated and performed the observations at Effelsberg. V.B. coordinated and performed the observations at Irbene. M.Burgay helped commission the dual recording mode at SRT. S.T.B. coordinated and performed the observations at Noto. J.E.C. supported the observations at Onsala. A.C. implemented the dual recording mode at SRT and performed some of the observations. R.F. supports the observations at Toruń. O.F. wrote observing schedules. M.P.G. coordinated and performed the observations at Toruń. R.K. assisted with the dual recording at Effelsberg. M.A.K. supports the observations at Badary, Svetloe and Zelenchukskaya. M.L. supported the observations at Onsala and assisted with the manuscript. G.M. coordinated and performed the observations at Medicina. A.M. coordinated and performed the observations at Badary, Svetloe and Zelenchukskaya. A.G.M. supports the data transfer of the observations at Badary, Svetloe and Zelenchukskaya. O.S.O.-B. wrote observing schedules. A.P. supported the observations at SRT. G.S. ran most of the observations at SRT. N.W. and J.Yuan coordinated and performed the observations at Urumqi. V.M.K. played a significant coordination role that enabled these results. All other co-authors contributed to the CHIME/FRB discovery of the source or the interpretation of the analysis results and the final version of the manuscript.

## Corresponding author

Correspondence to [F. Kirsten](#).

## Ethics declarations

### Competing interests

The authors declare no competing interests.

## Peer review

## Peer review information

*Nature* thanks Anthony Walters and the other, anonymous, reviewer(s) for their contribution to the peer review of this work. Peer reviewer reports are available.

## Additional information

**Publisher's note** Springer Nature remains neutral with regard to jurisdictional claims in published maps and institutional affiliations.

## Extended data figures and tables

### [Extended Data Fig. 1 DM and rotation measure \(RM\) maps around FRB 20200120E.](#)

**a**, Expected Galactic DM contribution (background) according to the YMW16 model disk contribution only<sup>93</sup>, the DM of FRB 20200120E (pentagon) and the DMs of known pulsars from the ATNF Pulsar Catalogue in this field (circles)<sup>100</sup>. **b**, Physical Galactic Faraday depth  $\phi_g$  (background)<sup>97</sup>, the RM of FRB 20200120E (pentagon) and Galactic pulsars with a known RM (circles). We assume that the RM<sup>6</sup> of FRB 20200120E is  $-36.9 \text{ rad m}^{-2}$ .

### [Extended Data Fig. 2 Modelling the SED of \[PR95\] 30244.](#)

The Milky Way extinction corrected flux densities of [PR95] 30244 in different wavelength bands are plotted, along with the best-fit Prospector model spectrum. To assess the quality of the Prospector model, the modelled and actual photometric data are also shown. The best-fit model profile is used to estimate the physical properties of [PR95] 30244 stated in Extended Data Table 3. Finally, the shaded region around the best-fit profile is the  $1\sigma$  uncertainty region.

### [Extended Data Fig. 3 MCMC simulation corner plot.](#)

The posterior probability distributions are shown for each of the five model parameters along the diagonal panels, and the correlations between model parameter posteriors are shown along the columns. Above each probability distribution, the median of the parameter posterior is printed, along with the  $1\sigma$  error bars.

**Extended Data Table 1 Time ranges of PRECISE runs targeting FRB 20200120E between February and May 2021**

**Extended Data Table 2 Set-ups at the different stations during observations used in the analysis**

**Extended Data Table 3 Notable properties of [PR95] 30244**

**Extended Data Table 4 Broadband SDSS filters used to model the SED of [PR95] 30244**

**Extended Data Table 5 Free parameters and their associated priors for the Prospector ‘delayed tau’ model**

## Supplementary information

[\*\*Peer Review File\*\*](#)

## Rights and permissions

[Reprints and Permissions](#)

## About this article

### Cite this article

Kirsten, F., Marcote, B., Nimmo, K. *et al.* A repeating fast radio burst source in a globular cluster. *Nature* **602**, 585–589 (2022).

<https://doi.org/10.1038/s41586-021-04354-w>

- Received: 20 May 2021
- Accepted: 15 December 2021

- Published: 23 February 2022
- Issue Date: 24 February 2022
- DOI: <https://doi.org/10.1038/s41586-021-04354-w>

## Share this article

Anyone you share the following link with will be able to read this content:

[Get shareable link](#)

Sorry, a shareable link is not currently available for this article.

[Copy to clipboard](#)

Provided by the Springer Nature SharedIt content-sharing initiative

## [\*\*Burst timescales and luminosities as links between young pulsars and fast radio bursts\*\*](#)

- K. Nimmo
- J. W. T. Hessels
- J. P. Yuan

Article 23 Feb 2022

## [\*\*Radio bursts from among the oldest stars\*\*](#)

- Vikram Ravi

News & Views 23 Feb 2022

---

This article was downloaded by **calibre** from <https://www.nature.com/articles/s41586-021-04354-w>

- Article
- Open Access
- [Published: 23 February 2022](#)

# Quantum sensing for gravity cartography

- [Ben Stray](#) [ORCID: orcid.org/0000-0003-1264-552X](#)<sup>1</sup> ✉nal,
- [Andrew Lamb](#) [ORCID: orcid.org/0000-0001-8873-6415](#)<sup>1</sup> ✉nal,
- [Aisha Kaushik](#) [ORCID: orcid.org/0000-0002-6046-9930](#)<sup>1</sup>,
- [Jamie Vovrosh](#) [ORCID: orcid.org/0000-0002-4097-872X](#)<sup>1</sup>,
- [Anthony Rodgers](#) [ORCID: orcid.org/0000-0001-5554-2147](#)<sup>1</sup>,
- [Jonathan Winch](#)<sup>1</sup>,
- [Farzad Hayati](#) [ORCID: orcid.org/0000-0003-4386-2770](#)<sup>1</sup>,
- [Daniel Boddice](#) [ORCID: orcid.org/0000-0002-3738-2327](#)<sup>2</sup>,
- [Artur Stabrawa](#)<sup>1</sup>,
- [Alexander Niggebaum](#)<sup>1</sup>,
- [Mehdi Langlois](#) [ORCID: orcid.org/0000-0002-9064-9270](#)<sup>1</sup>,
- [Yu-Hung Lien](#) [ORCID: orcid.org/0000-0001-6303-1523](#)<sup>1</sup>,
- [Samuel Lellouch](#)<sup>1</sup>,
- [Sanaz Roshanmanesh](#) [ORCID: orcid.org/0000-0001-5855-7096](#)<sup>2</sup>,
- [Kevin Ridley](#) [ORCID: orcid.org/0000-0002-7099-4923](#)<sup>1</sup>,
- [Geoffrey de Villiers](#)<sup>1</sup>,
- [Gareth Brown](#)<sup>3</sup>,
- [Trevor Cross](#)<sup>4</sup>,
- [George Tuckwell](#)<sup>2,5</sup>,
- [Asaad Faramarzi](#)<sup>2</sup>,
- [Nicole Metje](#) [ORCID: orcid.org/0000-0002-6741-8183](#)<sup>2</sup>,
- [Kai Bongs](#) [ORCID: orcid.org/0000-0002-7334-1848](#)<sup>1</sup> &
- [Michael Holynski](#) [ORCID: orcid.org/0000-0003-0163-5799](#)<sup>1</sup>

[Nature](#) volume 602, pages 590–594 (2022)

- 5104 Accesses
- 253 Altmetric

- [Metrics details](#)

## Subjects

- [Atomic and molecular interactions with photons](#)
- [Civil engineering](#)
- [Hydrology](#)
- [Matter waves and particle beams](#)

## Abstract

The sensing of gravity has emerged as a tool in geophysics applications such as engineering and climate research<sup>1,2,3</sup>, including the monitoring of temporal variations in aquifers<sup>4</sup> and geodesy<sup>5</sup>. However, it is impractical to use gravity cartography to resolve metre-scale underground features because of the long measurement times needed for the removal of vibrational noise<sup>6</sup>. Here we overcome this limitation by realizing a practical quantum gravity gradient sensor. Our design suppresses the effects of micro-seismic and laser noise, thermal and magnetic field variations, and instrument tilt. The instrument achieves a statistical uncertainty of  $20 \text{ E}$  ( $1 \text{ E} = 10^{-9} \text{ s}^{-2}$ ) and is used to perform a 0.5-metre-spatial-resolution survey across an 8.5-metre-long line, detecting a 2-metre tunnel with a signal-to-noise ratio of 8. Using a Bayesian inference method, we determine the centre to  $\pm 0.19$  metres horizontally and the centre depth as  $(1.89 - 0.59 \pm 2.3)$  metres. The removal of vibrational noise enables improvements in instrument performance to directly translate into reduced measurement time in mapping. The sensor parameters are compatible with applications in mapping aquifers and evaluating impacts on the water table<sup>7</sup>, archaeology<sup>8,9,10,11</sup>, determination of soil properties<sup>12</sup> and water content<sup>13</sup>, and reducing the risk of unforeseen ground conditions in the construction of critical energy, transport and utilities infrastructure<sup>14</sup>, providing a new window into the underground.

[Download PDF](#)

## Main

The quantum gravity gradient sensor uses atom interferometry<sup>15</sup>, which has been used in laboratory-based experiments to provide sensitive measurements of gravity<sup>16</sup>, to investigate the equivalence principle<sup>17</sup>, the fine-structure constant<sup>18</sup> and Newton's gravitational constant<sup>19</sup>, prompting the desire to transition these sensors into practical devices for use in real-world environments<sup>20</sup>. For example, gravity sensors have been

created that can be used on volcanoes and mountain environments<sup>21,22</sup>, and for measurements by air<sup>23</sup>, by sea<sup>24</sup> and on rockets<sup>25</sup>. A typical approach in these devices is to use light pulses to drive two-photon stimulated Raman transitions in atoms and use these to create a superposition of matter waves in different momentum and energy states. The resulting atomic wavepackets move along two spatially separated trajectories, before being recombined and interfered. This creates the matter-wave analogue of a Mach–Zehnder interferometer. The phase difference in the resulting interference pattern is proportional to the local gravitational field. However, such devices, as with any gravimeter, are fundamentally limited in their measurement time owing to the need to average out micro-seismic vibration<sup>26</sup>. This presents a major barrier to realizing gravity maps with high spatial resolution.

To enable gravity cartography, and operation in application-relevant conditions, we implement an ‘hourglass’ configuration cold atom gravity gradiometer<sup>27</sup>. This enables robust coupled differential measurements on two clouds of atoms, separated by a vertical baseline<sup>28</sup>. Two counter-oriented single-beam magneto-optical traps (MOTs) allow passage of common Raman beams to perform interferometry (Fig. 1a). The measurement axis is aligned to measure the vertical component,  $G_{zz}$ , of the  $(3 \times 3)$  gravity gradient tensor, which is the largest and most relevant component for gravity cartography. Differential operation suppresses primary noise sources (vibration and micro-seismic), systematic shifts (such as tilt) and changes in the optical path length between the beams used to drive the Raman transitions<sup>29</sup>. The commonality of laser intensity noise for the cooling beams of the single-beam MOTs<sup>6</sup> enables cloud temperature fluctuations to be stable to within a few hundred nanokelvins (Fig. 1b, top panel), limiting the impact of a.c. Stark shifts, and reduces cloud centre-of-mass motion by an order of magnitude when compared to conventional six-beam approaches (see [Methods](#)). The resulting changes in baseline are below 75 ppm (Fig. 1b, bottom panel), which corresponds to a systematic error of less than 0.1 E.

**Fig. 1: Hourglass gradiometer.**

---

 **figure 1**

---

**a**, Hourglass gradiometer using two counter-oriented single-beam MOTs, realized using mirror assemblies (blue). The initial atom clouds (green) fall under local gravitational acceleration,  $g$ , before being subjected to light pulses separated by time  $T$  to realize the atom interferometers (purple). The beam delivery is indicated with arrows (see [Methods](#) for details). The cooling beams (red) are deflected by the in-vacuum mirrors (blue) to provide cooling in all directions, with the central portion of each input beam passing through the aperture between the mirrors to provide the final cooling beam for the opposite MOT. The atom interferometry beams (yellow arrows) have a smaller beam waist, such that they pass through the mirror aperture without significant clipping. Each interferometer is operated simultaneously, with a vertical baseline separation of 1 m. **b**, Temporal variation of atom cloud temperatures from each trapping region (top panel), measured using time of flight<sup>41</sup>, and the relative change of the 1 m cloud separation baseline over time (bottom panel) (solid lines: averaged data at a bin size of 50 measurements at 4 s per measurement; shaded regions:  $\sigma$  range of the averaged data), determined from time of arrival. **c**, Measurement of the gravity gradient variation caused by movement of a test mass between two positions—either close to the sensor (open points) or displaced from the sensor (filled points). Each measurement number represents a specific position of the test mass, with the odd measurement numbers having the mass close to the sensor. Each data point is formed from the average of eight gravity gradient measurements, with each of those containing 25 shots from the atom interferometer each taking 1.5 s. The error bar for each data point is the standard error of the eight gravity gradient readings. The test mass was moved approximately every 20 min, with a variation of  $\pm 3.5$  min, and its position was repeatable to approximately 1 cm. The modelled projection of the change in gravity gradient signal,  $\Delta G_{zz}$ , is shown in red.

[Source data](#)

The hourglass configuration provides several practical benefits (see [Methods](#)). Avoiding the need for off-axis beams creates a robust and compact optical delivery arrangement, allowing months of operation in the field with no need to correct alignment. The configuration also provides a radially compact form factor, enabling compact magnetic shielding with 25 dB attenuation that suppresses effects due to external magnetic fields, preventing these from affecting the atom cloud generation. The beam configuration, in combination with a robust all-fibre laser system, enables independent control of the counter-propagating Raman beams, facilitating reversal of the light-pulse directions<sup>30</sup>. Interleaving measurements in each direction suppresses several systematic effects, including reducing those due to residual magnetic fields to below measurement precision. Furthermore, phase shifts and contrast loss from parasitic Raman transitions<sup>31</sup> are prevented through independent delivery of the Raman beams for each direction, without the need for a phase lock.

To measure the gravity gradient (see [Methods](#)), each MOT is loaded for 1 to 1.5 s with <sup>87</sup>Rb atoms before sub-Doppler cooling is used to reduce the cloud temperatures to the microkelvin regime. The clouds are then dropped and simultaneously subjected to an atom interferometry sequence. The output of each interferometer is measured using fluorescence to detect the ratio of the populations of the two relevant atomic ground states, with approximately  $10^5$  atoms participating in each atom interferometer, for a typical measurement rate of 0.7 Hz. A Lissajous plot of the upper versus lower atom interferometer outputs is then used to extract the differential phase, from which the gravity gradient is determined (Fig. 2, inset)<sup>32</sup>. The sensor was verified under laboratory conditions by modulating the position of known test masses near the sensor to vary  $G_{zz}$  (Fig. 1c). This resulted in a measured change of  $(205 \pm 13.1)$  E, compared to a modelled signal of 202 E.

**Fig. 2: Gradiometer performance.**

---

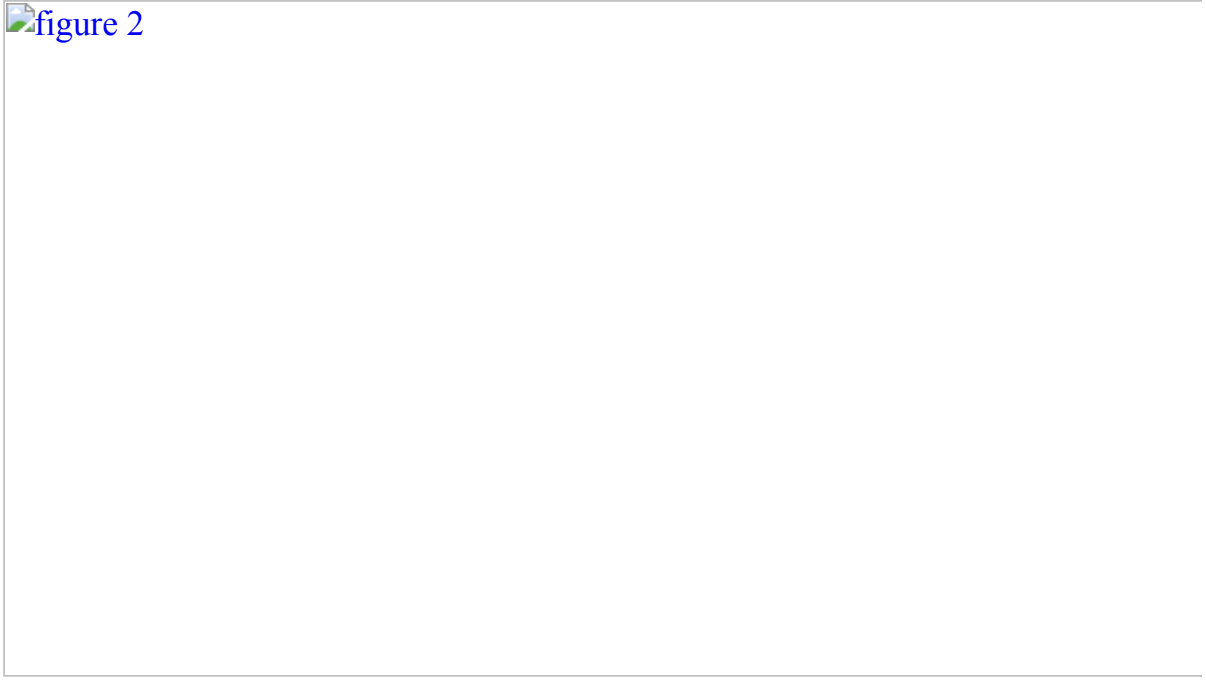


 **figure 2**

Allan deviation, with overlapping averages, of the instrument output during outdoor operation over approximately 8.6 h, shown with percentage error. Inset: a typical subset of the ellipse data (300 points) used for the Allan deviation, showing a Lissajous figure of the output signal of the upper and lower interferometers, which is used to extract the gradiometric phase. The deviation of the ellipse from a circle gives rise to a clustering of points around the extremal points of the ellipse.

#### Source data

Similarly, the sensitivity and stability of the instrument were evaluated in an outdoor environment. The Allan deviation<sup>33</sup> of the phase data (Fig. 2) showed an average short-term sensitivity of  $(466 \pm 8)$  E/ $\sqrt{\text{Hz}}$  and a statistical uncertainty of 20 E within 10 min of measurement.

To demonstrate the potential for gravity cartography, a 0.5-m-spatial-resolution survey was performed along an 8.5-m survey line above a pre-existing multi-utility tunnel. This is a tunnel with a 2-m by 2-m internal cross-section and a reinforced concrete wall of approximately 0.2-m thickness. It is situated underneath a road surface that is located between two multistorey buildings. Nearby buildings and terrain around the survey site provide further signals<sup>34</sup> that can mask targets of interest. To estimate the expected signal from the tunnel, a model of the site was constructed using an air/soil contrast infinite cuboid void, taking into account local buildings and terrain. The parameters for the model were informed using building plans (CAD files), with these being cross-checked using ground-penetrating radar, and auxiliary data from on-site measurements such as topography scanning. This provided an estimated peak signal

from the tunnel of 150 E, which corresponds to a phase change of 17.5 mrad for the atom interferometer. Fig. 3a shows a comparison between the site model and the atom interferometer data, showing that the measurement data are consistent with what is expected for a gravity gradient anomaly with the expected location and size of the tunnel. A scale representation of the site and tunnel, including local buildings and site topology, is shown in Fig. 3b.

**Fig. 3: Field survey.**



**a**, Gravity gradient data with standard error (black scatter) and total inferred uncertainty when including model uncertainty (blue scatter),  $1\sigma$  (dark blue shading) and  $2\sigma$  (light blue shading) credible interval bands, and a site model (dashed) (see [Methods](#)). **b**, Scale schematic of the site showing the dimensions and position of the tunnel and leading contributions to the gravity signal. The origin for coordinates (red dot) is defined in the vertical direction by the lowest point on the survey line, and in the horizontal direction by the expected location of the centre of the tunnel. **c**, POE (blue contours) inferred from the gravity gradiometer data, and expected tunnel position (dashed). **d**, Estimation of soil density obtained by shifting the focus of the inference process to use assumed knowledge of the tunnel geometry and inference of the gradiometer data, showing the 68% highest density interval (HDI).

## Source data

For use in practical applications, it will be important to interpret the data in an accessible way that produces information on which a user can make decisions or act. For this purpose, we have developed a Bayesian inference method and applied this to the gradiometer data with a data-generated model of a buried cuboid<sup>35</sup> assumed a priori. This uses the gradiometer data in conjunction with estimates of the site and geophysical parameters (as detailed in Extended Data Table 2) to make quantitative predictions of the depth and spatial extent of the anomaly. For instance, we assume that the soil density is within the expected range for the type of soil at the survey site by using a Gaussian distribution, with a mean of  $-1.80 \text{ g cm}^{-3}$ , to represent a void in surrounding soil, and standard deviation of  $0.10 \text{ g cm}^{-3}$ . The inference process produces distributions for the position, depth and cross-sectional area of the tunnel using the probability of excavation (POE) metric<sup>36</sup> (Fig. 3c). The observed spread of the POE is expected, due to measurement uncertainty and the ambiguity that exists between model parameters specifying depth, area and density, typical of inference from potential field data<sup>37</sup>. A signal-to-noise ratio of 8 for the detection is estimated from the data, finding the deduced horizontal position of the tunnel centre at  $(0.19 \pm 0.19) \text{ m}$  along the survey line and a depth to the centre of  $(1.89 - 0.59/+2.3) \text{ m}$  (see [Methods](#)).

Furthermore, by assuming a priori knowledge of the tunnel geometry and including topographical information of the survey site, the focus of the inference was switched to infer the soil density (Fig. 3d). This results in a near-Gaussian posterior distribution for the density parameter, with a mean of  $-1.80 \text{ g cm}^{-3}$  and standard deviation of  $0.15 \text{ g cm}^{-3}$ .

The statistical uncertainty demonstrated by the prototype instrument during static operation (which, for the 20 E gradiometer uncertainty, is equivalent to a  $1.4 \text{ ng}$  uncertainty for each of its two gravimeters) surpasses the reported performance of commercial gravimeters for survey applications by a factor of 1.5–4 (ref. <sup>38</sup>). In this first demonstration of submetre-resolution mapping with quantum gravity sensors, the repeatability of the prototype during the survey was similar to that of commercial gravimeters and limited by systematic effects (see [Methods](#)), such as due to the Coriolis effect, which can be addressed through further engineering. Furthermore, the sensor could be moved from one spatial position to another within 75 s, including alignment to the vertical to within 1 millidegree. If addressing these aspects, such as through operation on a rail or vehicle, the current instrument performance would in principle allow detection of the tunnel, or similar anomaly, with a 10-point line scan and a signal-to-noise ratio of 3 within 15 min of total measurement time.

The detection of the tunnel allows the assessment of the instrument performance for a range of potential applications. Fig. 4a shows a range of typical signal sizes for a variety of application areas in comparison to the statistical uncertainty of the sensor, with features in the range above this being detectable with the current instrument. In civil engineering applications, this performance could provide a reduction in the uncertainty of ground conditions and be used to inspect brownfield sites, to search for tunnels and large or near-surface utilities, and to detect erosion features before they become sinkholes. This performance is also relevant to archaeological applications (for example, enabling the detection of tombs or hidden chambers and investigating how previous civilizations used underground infrastructure). Furthermore, the sensor could be of particular use in the mapping of aquifers, to better understand and optimize the use of water and its impact on the environment. It could also be used to measure density distributions within the ground. On the basis of the inferred standard deviation, the soil density extraction method is currently sensitive to 10% level changes in the mean, meaning that in principle this could distinguish between soil that is either dry or saturated, or used to investigate localized soil compaction (for example, in precision agriculture). Typical anticipated signals for these applications, with the 20 E statistical uncertainty that our sensor achieves within a 10 min measurement time, are illustrated in Fig. 4b.

**Fig. 4: Application relevance.**

---

 figure 4

**a**, Contour plot for typical gravity gradient signal sizes in various applications, contours in eötvös for density contrasts of  $1.8 \text{ g cm}^{-3}$ . The parameters of the detected feature (red dot) and the statistical uncertainty of the sensor (solid line) are shown. Features in the region above the solid line are detectable with current uncertainty. **b**, A

perspective of future gravity cartography being used with 0.5 m spatial resolution over a region, at an uncertainty level of 20 E. Expected signal sizes for a range of applications are shown.

### Source data

The removal of vibration noise means, in contrast to the case in gravimeters, that future improvements in instrument sensitivity can be directly translated into reductions in measurement time or improved uncertainty. Implementation of further scientific enhancements to the sensor, including, for example, the use of large-momentum beamsplitters<sup>39,40</sup>, has the potential to provide a further 10- to 100-fold improvement in instrument sensitivity, allowing faster mapping or detection of smaller and deeper features. It is expected that such performance will be achieved in practical instruments within the next 5–10 years.

## Methods

### Experimental overview

A light-pulse atom interferometer is conceptually similar to an optical interferometer, with the roles of light and matter interchanged. Atoms, acting as matter waves, are subjected to a sequence of light pulses that impart momentum to them, acting analogously to mirrors and beamsplitters. Applying a light pulse for an appropriate length of time will cause a transition between the ground and excited states of an atom, accompanied by the absorption and stimulated emission of a photon. Such a pulse, commonly referred to as a  $\pi$  pulse, acts as an atom optic mirror owing to the momentum that is transferred. Similarly, tuning the light pulse such that it has only a 50% transition probability, commonly referred to as a  $\pi/2$  pulse, acts as a beamsplitter through providing a momentum kick to only half of the atomic probability distribution. A matter-wave equivalent of the optical Mach–Zehnder interferometer can then be created through applying a  $\pi/2$ – $\pi$ – $\pi/2$  pulse sequence with an evolution time,  $T$ , between the pulses. The resulting space-time area enclosed by the atomic trajectories (Extended Data Fig. 1b) is proportional to the local gravitational acceleration, which can then be measured from the relative population of the two atomic states after the final pulse.

A gravity gradiometer utilizes two such interferometers offset vertically and probed simultaneously with the same pulse sequence. This suppresses common-mode effects, such as noise from vibration or phase changes due to variations in tilt with respect to the gravity of the Earth, which are indistinguishable from the gravity anomalies of interest according to Einstein’s equivalence principle. Our device consists of two subunits (Extended Data Fig. 1a), a sensor head and a control system, with light and

electrical signals transferred through a 5-m umbilical. The gradiometer is shown in Extended Data Fig. 2, with an overview of its size, weight and power characteristics.

The sensor head features a vacuum system with dual MOT preparation and interrogation regions in an hourglass configuration, with all light delivered to the atoms through on-axis counter-oriented telescopes. The light is delivered in each direction, with portions of the beam being redirected towards the atom-trapping region using in-vacuum mirrors, to form the radial cooling beams in each MOT. The central portion passes through, such that each input provides the vertical laser cooling beam in a given direction for both MOTs. This makes all fluctuations in intensity common for the radial cooling beams (preventing lateral offsets), and, through use of a Gaussian beam shape, provides a higher intensity for the vertical beams to better saturate the radiation pressure force in this direction. This results in a greatly improved stability and robustness of the laser cooling process, reducing fluctuations in temperature or atom cloud position (Fig. 1b) without the need for excessive laser powers that would inhibit field operation. In a comparable test system, this provided a reduction in average cloud centre-of-mass motion to  $(0.14 \pm 0.09)$  mm as compared to  $(1.19 \pm 0.86)$  mm over an hour in similar conditions with a six-beam MOT. Both MOT regions have two coils, each formed of 92 turns of 1-mm-Kapton-coated copper wire wound around an aluminium former (fixed using epoxy), with a slit to prevent eddy currents. The coils have a radius of 43 mm and separation of 56 mm, to produce a linear field gradient of  $12.5 \text{ G cm}^{-1}$  at a driving current of 2.5 A. These are located around the vacuum system, such that the strong magnetic field axis of their quadrupole field is along the direction of travel of the cooling beam axis. In addition, two sets of rectangular coil pairs, each having 20 turns, are located around the MOT regions. These have a separation of 100 mm, and dimensions of 320 mm in the vertical and 90 mm in the horizontal, and can be used to compensate residual magnetic fields, or apply offsets. In practice, no compensation fields are used for the molasses phase. In the lower chamber, one coil pair is used to apply a 0.63 G field to adjust the atom cloud horizontal position by approximately 0.5 mm in the MOT phase, improving the interferometer contrast. A bias coil<sup>42</sup> is positioned around the system to define a quantization axis and remove degeneracy between magnetic sublevels, with other coils being switched off after the magneto-optical trapping phase. This has a variable pitch shape to account for edge effects and improve field uniformity over the atom interferometry region. The system is enclosed in a magnetic shield that provides 25 dB attenuation of the external field. The in situ magnetic field profile is measured (through spectroscopy of the Raman transition) as being homogeneous to below 5% across the atom interferometry region, limited by internal magnetic field sources from vacuum pumps.

The laser system consists of telecom lasers that are frequency doubled to 780 nm, to be near the D2 line of rubidium-87 (refs. [43,44](#)). The light for laser cooling is generated by

passing the laser output through an electro-optic modulator (EOM) and generating a sideband at a frequency of approximately 1.2 GHz output from the carrier. This is used to provide a locking signal using the  $|F=3\rangle \rightarrow |F'\rangle$  transition in rubidium-85, placing the carrier frequency such that it is tuneable around resonance with the  $|F=2\rangle \rightarrow |F'\rangle$  transition of rubidium-87 to provide the cooling light. A separate EOM is used to provide repumping light resonant with the  $|F=1\rangle \rightarrow |F'\rangle$  transition. Atom interferometry is realized through two-photon stimulated Raman transitions. The Raman laser used to drive these has a linewidth of 73 kHz and is locked with an offset of 1.9 GHz to the  $|F=2\rangle \rightarrow |F'\rangle$  transition. The second Raman frequency is generated using a pair of EOMs operating at 6.835 GHz. Performing the differential measurement suppresses phase noise that may arise owing to optical path-length changes between the two Raman beams (such as those due to vibration and thermally induced changes in the refractive index of fibres). This allows the two beams to be delivered independently without the need for a phase lock between them, facilitating an implementation in which the modulated spectrum is applied to only one of the input beams. This avoids parasitic Raman transitions that give rise to systematic offsets and dephasing when using conventional modulation-based schemes, such as those including a retro-reflected beam<sup>31</sup>. To realize a practical implementation of space-time area reversal<sup>30</sup>, also known as wavevector reversal, the system has an EOM in each input direction of the Raman beams, and the modulation signal is applied to one arm in each measurement. This allows the direction of the momentum kick imparted to the atoms to be changed between measurements, by changing which arm the modulation signal is applied to using a radiofrequency switch (see Extended Data Fig. 1). The contributions to the interferometer phases due to acceleration under gravity are sensitive to the direction of the recoil imparted by the light, whereas those arising from many other effects, such as those due to magnetic fields, are not. This allows these effects to be removed when interleaved measurements are performed in the two recoil directions.

The light is delivered to the sensor head using polarization-maintaining optical fibres, with separate fibres for the cooling and Raman beams. These fibres deliver the light to optical telescopes that collimate the light at the desired beam size. The cooling beams have a waist of 24 mm, and contain a typical maximum power of 130 mW. These impinge on the in-vacuum mirrors, which are 15-mm right-angle prisms (Thorlabs, MRA15-E03), to deliver the horizontal cooling beams. The mirrors are mounted to a titanium structure (attached using Epo-Tek H21D adhesive) in a cross configuration such that there is a 15-mm aperture in their centre. The central portion of the cooling beams passes through these apertures to provide the sixth beam required for the opposite MOT. The Raman beams are overlapped with the cooling beams using a polarizing beamsplitter cube, such that they are then delivered along the same beam axis as the cooling light. The Raman beams, each containing a typical maximum

power of 300 mW, have their waist set to 6.2 mm to limit aperturing and diffraction on the central aperture of the in-vacuum mirrors, allowing the Raman beams to pass through the system without being redirected by the prisms. Although aperturing is limited on the mirrors in the current instrument, it may be desirable to use a larger Raman beam than the aperture in more compact systems or those aiming to further reduce dephasing induced by laser beam inhomogeneity. Diffraction from the aperture would need to be given due consideration if pursuing this, as would the potential for further light shifts due to, in this case, one interferometer seeing extra light fields from mirror reflections. The polarization of the light is set to the appropriate configuration for cooling or driving Raman transitions through use of voltage-controlled variable retarder plates in the upper and lower telescopes used to deliver the light. The intensity of the Raman beams is actively stabilized using feedback from a photodiode to control acousto-optic modulators, which are also used to produce the laser pulses.

The experimental sequence starts by collecting approximately  $10^8$  rubidium-87 atoms in each MOT from a background vapour over 1–1.5 s. Molasses cooling is then used to reduce the upper- and lower-cloud temperatures to  $(2.86 \pm 0.09)$   $\mu\text{K}$  and  $(3.70 \pm 0.20)$   $\mu\text{K}$ , respectively (see Fig. 1b). The differences in temperature arise from differences in local residual magnetic fields, arising primarily from the magnetic shield geometry, and small differences in optical alignment. Optical state and velocity selection is performed to select only atoms in the  $\langle\{|F\rangle=1, \{m\}_z \{\{rm\{F\}\}\}=0\} \rangle$  magnetic sublevel and desired velocity class. This is achieved through application of  $\pi$  pulses and a series of blow-away pulses to remove atoms in undesired states and velocity classes. Atom interferometry is then performed with a pulse separation of  $T = 85$  ms and  $\pi$ -pulse length of 4  $\mu\text{s}$ . The interferometers are read out using bistate fluorescence detection to determine the atomic state population ratios of the  $|F=2\rangle$  and  $|F=1\rangle$  ground states, for which  $(2.7 \pm 0.1) \times 10^5$  and  $(1.7 \pm 0.1) \times 10^5$  atoms participate in the upper and lower interferometers, respectively, with a typical measurement rate of 0.7 Hz. The differential phase, from which the gravity gradient is derived, is extracted by plotting the upper interferometer outputs against the lower interferometer outputs, to form a Lissajous plot as shown in the inset of Fig. 2. In addition to random noise arising from vibration, we add a deliberate random phase value, from between 0 and  $2\pi$ , to the final pulse of the interferometer. At ellipse phases that do not correspond to a circle, a clustering of points around the extremal points of the ellipse is visible even for uniform noise.

The quantum projection noise of the system based on the participating atom number is approximately  $44 \text{ E}/\sqrt{\text{Hz}}$ . The total noise budget includes contributions from further terms, and is shown in Extended Data Table 1, alongside relevant systematics observed during the survey. The noise budget was investigated through computer simulation of noise processes, compared to experimental data, and ellipse fitting.

## Survey practice and processing of the measurement data

For each measurement on the survey, 600 runs of the atom interferometer were typically taken with the sensor head in one location (with the horizontal position being measured using a total station, Leica TS15, and the vertical position from the road surface being approximately 0.5 m for the lower sensor and 1.5 m for the upper sensor), giving twelve 25-point ellipses in each of the interferometer directions and therefore 12 separate estimates of the gravity gradient. Repeat measurements were taken on each measurement position, with typically three points on each position. A measurement was taken at a base station between each measurement point, with the final base-station measurement for one location used as the first for the next. The quality of fitting to each ellipse was identified using the error metric,  $\langle \langle \text{varepsilon} \rangle \rangle$ , defined as

$$\text{varepsilon} = \frac{\left| \frac{1}{N} \sum_{i=1}^N L_i - \frac{1}{2} \right|}{\frac{1}{2}}$$

in which  $N$  is the number of data points,  $L$  is the minimum distance between each data point and a point on the ellipse, and  $a$  and  $c$  correspond to an ellipse defined parametrically by equations  $(x=a \sin \theta)$  and  $(y=c \sin(\theta + \varphi))$ , respectively. Errors in the ellipse fitting are sensitive to changes in the ellipse opening angle<sup>47</sup>. On the basis of numerical simulations, we estimate this effect to be less than a few parts in one thousand; therefore, a 100 E change would be subject to an error of less than 0.5 E. Such errors are therefore small compared to other errors. Such a 100 E change in gradient would correspond to an 11.6 mrad change in the ellipse shape. This phase shift can be compared to a  $2\pi$  measurement range, meaning that measurement range of the instrument in this configuration is relevant to the majority of practical features of interest (these being typically below 400 E).

Ellipse fits found to have  $\langle \langle \text{varepsilon} \rangle \rangle > 0.05$  were automatically discarded. This resulted in 98.4% of all data being usable in normal operation, representing a favourable data up time compared to that of similar conventional geophysical devices.

To process the data, a straight line was fitted to the base-station points, with this line then being subtracted from all data points. This is standard practice to remove drift in geophysical surveys. The leading source of drift is believed to be due to the a.c. Stark shift, with this also being relevant owing to the difference in the temperature of the two clouds. The gravity gradient value is then taken as the average of the measurement points, resulting in an estimate of the difference in gradient between the measurement location and the base station. Furthermore, the variations in the data points are used to make an estimate of the error in the difference value. When multiple measurements from the same location were combined, a weighted average was used, giving less

weight to measurements with greater errors. The weighting factor is proportional to the reciprocal of the variance of each measurement<sup>48</sup>. The data, as shown in Fig. 3a, are not corrected for terrain or effects such as tides. Tidal effects are not corrected, being negligible through the differential measurement of the gravity gradient.

The average of the gravity gradient error found across the measurement positions of the survey is 17.9 E. Comparing this to an approximate signal size of 150 E gives an approximate signal-to-noise ratio of 8.

## Inference from gravity gradiometer data

Bayesian inference is a framework within which prior beliefs can be updated with information contained in data. For a model parameter vector ( $\theta$ ) and a data vector ( $d$ )

$$\Pr(\theta | d) = \frac{\Pr(d | \theta) \Pr(\theta)}{\Pr(d)}$$

in which  $\Pr(d | \theta)$  is the likelihood,  $\Pr(\theta)$  is the prior,  $\Pr(d)$  is a normalization constant and  $\Pr(\theta | d)$  is the posterior distribution.

The likelihood function provides the misfit between the measured data,  $(d)$ , and the modelled data values calculated from the model parameter vector,  $(\theta)$ . The model used here is that of a three-dimensional cuboid<sup>35</sup>; the free model parameters are shown in Extended Data Fig. 3, along with the functional form of the respective prior distributions. The rationale behind the chosen prior distributions is detailed in Extended Data Table 2. The total uncertainty for each measurement point is calculated using the Pythagorean sum of the standard error and the model uncertainty random variable multiplied by the average of the standard error across all of the measurement positions.

The probabilistic Python package pymc3 (ref. <sup>49</sup>) is used to implement the cuboid model, define the model parameter prior distributions and sample the posterior distribution, using a no U-turn sampler<sup>50</sup>. Extended Data Fig. 4 shows the Bayesian posterior distribution for select model parameters.

The parameter posterior distributions represent the updated beliefs about the model parameters, given the measurement data. To aid interpretation of the posterior distribution, the POE<sup>36</sup> is calculated, which represents the spatial probability of the anomaly underground, given the model and prior distributions (as shown in Fig. 3c). The horizontal position of the tunnel centre is determined as  $(0.19 \pm 0.19)$  m along the

survey line, with the distribution being approximately Gaussian. The depth from the origin, defined in the vertical using the lowest point on the survey line, to the centre is  $(1.7 - 0.59/+2.3)$  m. At the horizontal position of the tunnel, the distance to the surface from the origin is approximately 0.19 m, meaning that the total distance from the surface to the tunnel centre is  $(1.89 - 0.59/+2.3)$  m. From the tunnel geometry, this places the top of the tunnel at approximately 0.89 m depth from the surface.

The signals arising from local features are used to create a distinct site model. This is used to provide an estimate of the expected shape of the gravity gradient signal over the site, for comparison with the inference output. These features include the tunnel of interest, basements from nearby buildings, walls and a drain. They are shown in the scale drawing of Fig. 3b.

## Data availability

The datasets generated and/or analysed during the current study are available on an open data repository. This is located at <https://doi.org/10.25500/edata.bham.00000740>. Source data are provided with this paper.

## Code availability

The code that supports the findings of this study is available on an open repository. This is located at <https://doi.org/10.25500/edata.bham.00000740>.

## References

1. Taylor, R. et al. Ground water and climate change. *Nat. Clim. Change* **3**, 322–329 (2013).
2. Tapley, B. D., Bettadpur, S., Ries, J. C., Thompson, P. F. & Watkins, M. M. GRACE measurements of mass variability in the Earth system. *Science* **305**, 503–505 (2004).
3. Van Camp, M. et al. Geophysics from terrestrial time-variable gravity measurements. *Rev. Geophys.* **55**, 938–992 (2017).
4. Chen, K.-H., Cheinway, H., Liang-Cheng, C. & Chien-Chung, K. Short-time geodetic determination of aquifer storage coefficient in Taiwan. *J. Geophys. Res. Solid Earth* **123**, 10,987–11,015 (2018).

5. Torge, W. & Müller, J. *Geodesy* (de Gruyter, 2012).
6. Hinton, A. et al. A portable magneto-optical trap with prospects for atom interferometry in civil engineering. *Philos. Trans. R. Soc. A* **375**, 20160238 (2017).
7. Abbot, B. W. et al. Human domination of the global water cycle absent from depictions and perceptions. *Nat. Geosci.* **12**, 533–540 (2019).
8. Morishima, K. et al. Discovery of a big void in Khufu’s Pyramid by observation of cosmic-ray muons. *Nature* **552**, 386–390 (2017).
9. Panisova, J., Fraštia, M., Wunderlich, T., Pašteka, R. & Kušnírák, D. Microgravity and ground-penetrating radar investigations of subsurface features at the St Catherine’s Monastery, Slovakia. *Archaeol. Prospect.* **20**, 163–174 (2013).
10. Padín, J., Martín A. & Belén Anquela, A. Archaeological microgravimetric prospection inside don church (Valencia, Spain). *J. Archaeol. Sci.* **39**, 547–554.
11. Fais, S., Radogna, P. V., Romoli, E., Matta, P. & Klingele, E. E. Microgravity for detecting cavities in an archaeological site in Sardinia (Italy). *Near Surf. Geophys.* **13**, 495–502 (2015).
12. Soane, B. D. & van Ouwerkerk, C. Implications of soil compaction in crop production for the quality of the environment. *Soil Tillage Res.* **35**, 5–22 (1995).
13. Bishop, I., Styles, P., Emsley, S. J. & Ferguson, N. S. The detection of cavities using the microgravity technique: case histories from mining and karstic environments. *Geol. Soc. Spec. Publ.* **12**, 153–166 (1997).
14. Tuckwell, G. in *Encyclopedia of Engineering Geology* [https://doi.org/10.1007/978-3-319-12127-7\\_137-1](https://doi.org/10.1007/978-3-319-12127-7_137-1) (2017).
15. Kasevich, M. & Chu, S. Atomic interferometry using stimulated Raman transitions. *Phys. Rev. Lett.* **67**, 181–184 (1991).
16. Peters, A., Chung, K. & Chu, S. Measurement of gravitational acceleration by dropping atoms. *Nature* **400**, 849–852 (1999).
17. Asenbaum, P., Overstreet, C., Kim, M., Curti, J. & Kasevich, M. A. Atom-interferometric test of the equivalence principle at the  $10^{-12}$  level. *Phys. Rev. Lett.* **125**, 191101 (2020).

18. Parker, R. H., Yu, C., Zhong, W., Estey, B. & Müller, H. Measurement of the fine-structure constant as a test of the Standard Model. *Science* **360**, 191–195 (2018).
19. Rosi, G., Sorrentino, F., Cacciapuoti, L., Prevedelli, M. & Tino, G. M. Precision measurement of the Newtonian gravitational constant using cold atoms. *Nature* **510**, 518–521 (2014).
20. Bongs, K. et al. Taking atom interferometric quantum sensors from the laboratory to real-world applications. *Nat. Rev. Phys.* **1**, 731–739 (2019).
21. Ménoret, V. et al. Gravity measurements below  $10^{-9} g$  with a transportable absolute quantum gravimeter. *Sci. Rep.* **8**, 12300 (2018).
22. Wu, X. et al. Gravity surveys using a mobile atom interferometer. *Sci. Adv.* **5**, eaax0800 (2019).
23. Geiger, R. et al. Detecting inertial effects with airborne matter-wave interferometry. *Nat. Commun.* **2**, 474 (2011).
24. Bidel, Y. et al. Absolute marine gravimetry with matter-wave interferometry. *Nat. Commun.* **9**, 627 (2018).
25. Becker, D. et al. Space-borne Bose–Einstein condensation for precision interferometry. *Nature* **562**, 391–395 (2018).
26. Boddice, D., Metje, N. & Tuckwell, G. Capability assessment and challenges for quantum technology gravity sensors for near surface terrestrial geophysical surveying. *J. Appl. Geophys.* **146**, 149–159 (2017).
27. US patent 20200386906 16/772517 (2020).
28. Snadden, M. J., McGuirk, J. M., Bouyer, P., Haritos, K. G. & Kasevich, M. A. Measurement of the Earth’s gravity gradient with an atom interferometer-based gravity gradiometer. *Phys. Rev. Lett.* **81**, 971 (1998).
29. McGuirk, J. M., Foster, G. T., Fixler, J. B., Snadden, M. J. & Kasevich, M. A. Sensitive absolute-gravity gradiometry using atom interferometry. *Phys. Rev. A* **65**, 033608 (2002).
30. Louchet-Chauvet, A. et al. The influence of transverse motion within an atomic gravimeter. *New J. Phys.* **13**, 065025 (2011).

31. Carraz, O. et al. Phase shift in an atom interferometer induced by the additional laser lines of a Raman laser generated by modulation. *Phys. Rev. A* **86**, 033605 (2012).
32. Foster, G. T., Fixler, J. B., McGuirk, J. M., & Kasevich, M. A. Method of phase extraction between coupled atom interferometers using ellipse-specific fitting. *Opt. Lett.* **27**, 951–953 (2002).
33. Howe, D. A., Allan, D. W. & Barnes, J. A. Properties of signal sources and measurement methods. In *Proc. 35th Annual IEEE Symposium on Frequency Control* 1–47 (1981).
34. Zahorec, P., Papčo, J., Mikolaj, M., Paštka, R. & Szalaiová, V. The role of near topography and building effects in vertical gravity gradients approximation. *First Break* <https://doi.org/10.3997/1365-2397.2013033> (2014).
35. Okabe, M. Analytical expressions for gravity anomalies due to homogeneous polyhedral bodies and translations into magnetic anomalies. *Geophysics* **44**, 730–741 (1979).
36. Brown, G., Ridley, K., Rodgers, A. & de Villiers, G. Bayesian signal processing techniques for the detection of highly localised gravity anomalies using quantum interferometry technology. *Proc. SPIE* (eds Lewis, K. L. & Hollins, R. C.) **9992**, 99920M (SPIE, 2016).
37. de Villiers, G. D., Ridley, K. D., Rodgers, A. D. & Boddice, D. On the use of the profiled singular-function expansion in gravity gradiometry. *J. Appl. Geophys.* **170**, 103830 (2019).
38. Boddice, D. et al. A novel approach to reduce environmental noise in microgravity measurements using a Scintrex CG5. *J. Appl. Geophys.* **152**, 221–235 (2018).
39. Kovachy, T. et al. Quantum superposition at the half-metre scale. *Nature* **528**, 530–533 (2015).
40. McDonald, G. D. et al.  $80\hbar k$  momentum separation with Bloch oscillations in an optically guided atom interferometer. *Phys. Rev. A* **88**, 053620 (2013).
41. Brzozowski, T. M., Maczynska, M., Zawada, M., Zachorowski, J. & Brzozowski, W. G. Time-of-flight measurement of the temperature of cold atoms for short trap-probe beam distances. *J. Opt. B* **4**, 62–66 (2002).

42. Stray, B. *A Cold Atom Gravity Gradiometer with Field Application Performance*. Thesis, Univ. Birmingham (2021).
43. Lévèque, T., Antoni-Micollier, L., Faure, B. & Berthon, J. A laser setup for rubidium cooling dedicated to space applications. *Appl. Phys. B* **116**, 997–1004 (2014).
44. Theron, F. et al. Narrow linewidth single laser source system for onboard atom interferometry. *Appl. Phys. B* **118**, 1–5 (2015).
45. Rammeloo, C., Zhu, L., Lien, Y., Bongs, K. & Holynski, M. Performance of an optical single-sideband laser system for atom interferometry. *J. Opt. Soc. Am. B* **37**, 1485–1493 (2020).
46. Zhu, L. et al. Application of optical single-sideband laser in Raman atom interferometry. *Opt. Express* **26**, 6542–6553 (2018).
47. Barrett, B. et al. Correlative methods for dual-species quantum tests of the weak equivalence principle. *New J. Phys.* **17**, 085010 (2015).
48. Brennan, D. G. Linear diversity combining techniques. *Proc. IRE* **47**, 1075–1102 (1959).
49. Salvatier, J., Wiecki, T. V. & Fonnesbeck, C. Probabilistic programming in Python using PyMC3. *PeerJ Comput. Sci.* **2**, e55 (2016).
50. Hoffman, M. D. & Gelman, A. The No-U-Turn Sampler: adaptively setting path lengths in Hamiltonian Monte Carlo. *J. Mach. Learn. Res.* **15**, 1351–1381 (2014).

## Acknowledgements

This work was supported by the EPSRC (EP/M013294/1 and EP/T001046/1) and Innovate UK (104613), and the gradiometer was built under a contract with the Ministry of Defence, as part of the UK National Quantum Technologies Programme. We acknowledge S. Bennett for input on the manuscript and activity, and technical support from the UoB EPS workshop.

## Author information

### Author notes

1. These authors contributed equally: Ben Stray, Andrew Lamb

## Affiliations

1. Midlands Ultracold Atom Research Centre, School of Physics and Astronomy, University of Birmingham, Birmingham, UK

Ben Stray, Andrew Lamb, Aisha Kaushik, Jamie Vovrosh, Anthony Rodgers, Jonathan Winch, Farzad Hayati, Artur Stabrawa, Alexander Niggebaum, Mehdi Langlois, Yu-Hung Lien, Samuel Lellouch, Kevin Ridley, Geoffrey de Villiers, Kai Bongs & Michael Holynski

2. School of Engineering, University of Birmingham, Birmingham, UK

Daniel Boddice, Sanaz Roshanmanesh, George Tuckwell, Asaad Faramarzi & Nicole Metje

3. Dstl, Porton Down, Salisbury, UK

Gareth Brown

4. Teledyne e2v, Chelmsford, UK

Trevor Cross

5. RSK, Hemel Hempstead, UK

George Tuckwell

## Contributions

The design and development of the sensor was performed by B.S., A.L., A.K., J.V., A.R., J.W., F.H., K.B. and M.H. with inputs from A.S., A.N., K.R., G.d.V., M.L., Y.-H.L. and S.L., and inputs on design for field use from D.B., N.M., T.C., G.T. and G.B. The characterization and calibration measurements were provided by B.S., J.V., J.W., F.H., K.R. and M.H. The survey site modelling was performed by D.B., A.L., A.R., K.R. and F.H. with inputs from N.M. and G.T. The survey design and measurements were contributed by J.V., D.B., J.W., F.H., K.R., S.R., B.S., A.L. and M.H. with input on the survey design and process from N.M., K.B., G.T. and A.F. Data processing was carried out by J.W., K.R., J.V. and A.R., with A.R. providing the Bayesian inference. M.H. and K.B. conceived and coordinated the experiment. M.H., B.S., A.L., K.B., J.V. and A.R. wrote the manuscript. All authors contributed to the review and improvement of the manuscript.

## Corresponding author

Correspondence to [Michael Holynski](#).

## Ethics declarations

### Competing interests

The University of Birmingham has filed a patent application based on the gradiometer design, with M.H., A.L., G.d.V. and K.B. listed as inventors (number 20200386906 16/772517). G.T. is employed by a company that make commercial use of gravity sensing. T.C. is employed by a company involved in the development of quantum technology and is a member of the UK Quantum Technology Strategic Advisory Board. G.B. is employed by DSTL, which is connected to the Ministry of Defence, who are a funder of the work. The authors declare no other competing interests.

### Peer review information

*Nature* thanks Roman Pasteka, Nicola Poli and Xuejian Wu for their contribution to the peer review of this work. Peer reviewer reports are available.

### Additional information

**Publisher's note** Springer Nature remains neutral with regard to jurisdictional claims in published maps and institutional affiliations.

### Extended data figures and tables

#### [Extended Data Fig. 1 Overview of the experimental system and sequence.](#)

The system is formed of the main sensor head and an enclosure for the laser and control systems, with the laser system showing the two modes of Raman beam delivery that are used, with arrows representing the beams input to the chamber. The sensor head is formed using the hourglass configuration. This keeps all beam delivery along the central axis, improving stability and allowing the use of a radially compact magnetic shield. The laser system is formed of telecom lasers which are frequency doubled to 780 nm, to be near to the D2 transition line of rubidium-87. The laser light and electronic signals pass through an umbilical to reach the sensor head, with the laser light being delivered from the top and bottom of the sensor. The experimental sequence begins with atoms being loaded into two 3D MOTs, and then being dropped by turning off the laser light. While in free-fall, a sequence of velocity selective

Raman pulses and blow-away pulses are used to select only the desired magnetic sub-level state and velocity class, with other atoms being removed from the sequence. This is followed by a  $\pi/2$ -  $\pi$ -  $\pi/2$  interferometry sequence. The Raman transitions are realized using EOMs to create sidebands at a frequency difference equal to the hyperfine ground state splitting. In contrast to previous approaches<sup>[31,45,46](#)</sup>, each input direction contains a separate EOM with the driving frequency being applied to only one input direction, such that the laser frequencies for the upward and downward Raman beams are in either mode 1 or mode 2 of the spectral configurations shown in the figure. This removes the effect of parasitic Raman transitions that create offsets and contrast loss in conventional modulation based approaches. The use of this laser scheme is enabled through the hourglass configuration allowing independent delivery of the Raman beams, while suppressing phase noise through differential operation. Switching between these two modes changes the input direction of the modulated beam spectrum, changing the direction of the first momentum kick in the interferometer and causing it to open in the opposite direction (dashed lines in the interferometer sequence). This allows a practical implementation of the wavevector reversal procedure<sup>[30](#)</sup>, where the contributions to the phase due to the gravitational acceleration are sensitive to the direction of the recoil imparted by the light, while many other effects such as those due to magnetic fields are not. Interleaving measurements with interferometers running in each of these modes removes these sources of error while doubling the contribution due to gravity. Finally, the interferometer outputs are read out by measuring the atomic state populations of the two hyperfine ground states, using a fluorescence pulse delivered along the central axis, with the light that is scattered by the atoms being captured on a photodiode.

## **Extended Data Fig. 2 Gravity gradiometer on the survey line, above the tunnel.**

The main sensor head (blue cylinder) stands at 1.87 m high, varying by 5 cm depending on the setting of the adjustable feet. This places the measurement positions of the sensor at approximately 0.5 m from the road surface for the lower sensor, and 1.5 m for the upper sensor. The floor footprint of the sensor head is 0.64 m by 0.6 m, and the upright cylinder has a diameter of 0.27 m. The total weight of the sensor head is approximately 75 kg. This is connected to a flight case, which contains the lasers and control system. This has an internal height of 24 U standard rack units (1 U = 4.4 cm), an external footprint of 1.10 m by 0.46 m and height of 1.34 m. A secondary case is placed on top of this, with dimensions of 0.50 m by 0.59 m by 0.46 m. The combined weight of these cases is approximately 250 kg. The system operates on a single mains wall socket, drawing approximately 800 W and having a short-term battery holder over. It can also operate on a generator supply without any observed additional noise. Also shown is a frame used to move the sensor head, and prism used to reference position with a total station.

**Extended Data Fig. 3 Relationship between model parameters (white ovals), with their respective prior distribution form, to the normal likelihood distribution (grey oval).**

Deterministic parameters are shown in rectangular boxes. Parameters contained inside the rounded edge rectangle are all one dimensional arrays of length 17, the length of the gradiometer data set.

**Extended Data Fig. 4 Bayesian posterior distributions for selected model parameters.**

The horizontal and vertical directions are represented by x and z respectively. The median and 68% highest density interval (HDI, represented by the black lines and numerical extents) are shown for each distribution. The shape of the z length and z centroid distributions is non-Gaussian due to the known depth ambiguity for gravity sensing and asymmetries in the boundary condition, i.e. the parameters being limited by the ground surface above the tunnel.

**Extended Data Table 1 Sensor noise budget and survey systematics**

**Extended Data Table 2 Prior distributions defined for inference model random variables**

## Supplementary information

[\*\*Peer Review File\*\*](#)

## Source data

[\*\*Source Data Fig. 1\*\*](#)

[\*\*Source Data Fig. 2\*\*](#)

[\*\*Source Data Fig. 3\*\*](#)

[\*\*Source Data Fig. 4\*\*](#)

## Rights and permissions

**Open Access** This article is licensed under a Creative Commons Attribution 4.0 International License, which permits use, sharing, adaptation, distribution and reproduction in any medium or format, as long as you give appropriate credit to the original author(s) and the source, provide a link to the Creative Commons license, and indicate if changes were made. The images or other third party material in this article are included in the article's Creative Commons license, unless indicated otherwise in a credit line to the material. If material is not included in the article's Creative Commons license and your intended use is not permitted by statutory regulation or exceeds the permitted use, you will need to obtain permission directly from the copyright holder. To view a copy of this license, visit <http://creativecommons.org/licenses/by/4.0/>.

### Reprints and Permissions

## About this article

### Cite this article

Stray, B., Lamb, A., Kaushik, A. *et al.* Quantum sensing for gravity cartography. *Nature* **602**, 590–594 (2022). <https://doi.org/10.1038/s41586-021-04315-3>

- Received: 07 September 2021
- Accepted: 07 December 2021
- Published: 23 February 2022
- Issue Date: 24 February 2022
- DOI: <https://doi.org/10.1038/s41586-021-04315-3>

### Share this article

Anyone you share the following link with will be able to read this content:

[Get shareable link](#)

Sorry, a shareable link is not currently available for this article.

[Copy to clipboard](#)

Provided by the Springer Nature SharedIt content-sharing initiative

### Atomic changes can map subterranean structures

- Nicola Poli
- Roman Pašteka
- Pavol Zahorec

## News & Views Forum 23 Feb 2022

---

This article was downloaded by **calibre** from <https://www.nature.com/articles/s41586-021-04315-3>

| [Section menu](#) | [Main menu](#) |

- Article
- Open Access
- [Published: 23 February 2022](#)

# Hyperbolic shear polaritons in low-symmetry crystals

- [Nikolai C. Passler](#)<sup>1</sup>,
- [Xiang Ni](#)<sup>2</sup>,
- [Guangwei Hu](#) [ORCID: orcid.org/0000-0002-3023-9632](#)<sup>2,4</sup>,
- [Joseph R. Matson](#)<sup>5</sup>,
- [Giulia Carini](#)<sup>1</sup>,
- [Martin Wolf](#)<sup>1</sup>,
- [Mathias Schubert](#)<sup>6</sup>,
- [Andrea Alù](#) [ORCID: orcid.org/0000-0002-4297-5274](#)<sup>2,3</sup>,
- [Joshua D. Caldwell](#) [ORCID: orcid.org/0000-0003-0374-2168](#)<sup>5</sup>,
- [Thomas G. Folland](#) [ORCID: orcid.org/0000-0002-4665-235X](#)<sup>7</sup> &
- [Alexander Paarmann](#) [ORCID: orcid.org/0000-0002-8271-2284](#)<sup>1</sup>

[Nature](#) volume 602, pages 595–600 (2022)

- 2527 Accesses
- 41 Altmetric
- [Metrics details](#)

## Subjects

- [Infrared spectroscopy](#)
- [Nanophotonics and plasmonics](#)
- [Polaritons](#)

## Abstract

The lattice symmetry of a crystal is one of the most important factors in determining its physical properties. Particularly, low-symmetry crystals offer powerful

opportunities to control light propagation, polarization and phase<sup>1,2,3,4</sup>. Materials featuring extreme optical anisotropy can support a hyperbolic response, enabling coupled light–matter interactions, also known as polaritons, with highly directional propagation and compression of light to deeply sub-wavelength scales<sup>5</sup>. Here we show that monoclinic crystals can support hyperbolic shear polaritons, a new polariton class arising in the mid-infrared to far-infrared due to shear phenomena in the dielectric response. This feature emerges in materials in which the dielectric tensor cannot be diagonalized, that is, in low-symmetry monoclinic and triclinic crystals in which several oscillators with non-orthogonal relative orientations contribute to the optical response<sup>6,7</sup>. Hyperbolic shear polaritons complement previous observations of hyperbolic phonon polaritons in orthorhombic<sup>1,3,4</sup> and hexagonal<sup>8,9</sup> crystal systems, unveiling new features, such as the continuous evolution of their propagation direction with frequency, tilted wavefronts and asymmetric responses. The interplay between diagonal loss and off-diagonal shear phenomena in the dielectric response of these materials has implications for new forms of non-Hermitian and topological photonic states. We anticipate that our results will motivate new directions for polariton physics in low-symmetry materials, which include geological minerals<sup>10</sup>, many common oxides<sup>11</sup> and organic crystals<sup>12</sup>, greatly expanding the material base and extending design opportunities for compact photonic devices.

[Download PDF](#)

## Main

Crystal symmetry plays a critical role in dictating the optical, electronic, mechanical and thermal properties of a material. Reduced symmetry is at the heart of numerous emergent phenomena, including structural phase transitions<sup>11</sup>, charge-density waves<sup>13</sup> and topological physics<sup>14</sup>. The interaction of light with low-symmetry materials is particularly important, as it allows fine control over the phase, propagation direction and polarization<sup>1,2,3,4</sup>. This control can be especially pronounced for sub-diffractive surface waves, for instance, surface phonon polaritons (SPhPs)<sup>15</sup> and surface plasmon polaritons (SPPs), supported at the surface of polar crystals and conductors, respectively. Both SPhPs and SPPs are quasiparticles comprising photons and coherently oscillating charges, that is, polar lattice vibrations or free-carrier plasmas, respectively, and they are strongly influenced by crystal symmetry. As a relevant example, low-symmetry polaritonic materials can support hyperbolic light propagation<sup>16</sup>, constituting an exotic class of light waves that are highly directional with very large momenta. Hyperbolic polaritons occur in materials in which the real part of the permittivity along at least one crystal direction is negative and positive along at least one other. This extreme anisotropy is associated with free carriers and optic phonons in anisotropic lattices. In turn, hyperbolic polaritons enable deeply sub-

wavelength light confinement over broad bandwidths<sup>8,9</sup>. In polar crystals with symmetries that support a single optical axis (uniaxial), such as hexagonal boron nitride (hBN), hyperbolic polaritons (HPs) of type I or type II can arise<sup>5,8,9</sup>, for which the hyperbolic isofrequency surfaces do or do not intersect the optical axis, respectively. Materials or metamaterials exhibiting lower symmetry, in which all three major polarizability axes are different (biaxial) but orthogonal, such as alpha-phase molybdenum trioxide ( $\alpha$ -MoO<sub>3</sub>)<sup>1,3</sup>, Li-intercalated vanadium pentoxide (V<sub>2</sub>O<sub>5</sub>)<sup>4</sup> or nanostructured metasurfaces<sup>17</sup>, exhibit several distinct spectral regimes of hyperbolic modes propagating along different crystal axes. Notably, in-plane hyperbolicity within  $\alpha$ -MoO<sub>3</sub> films has been shown to be low loss<sup>1,3</sup>, with reconfigurable features<sup>2</sup> and capable of supporting topological transitions<sup>2</sup>. More exotic polaritonic responses may be expected in crystals with further reduced symmetry, such as monoclinic and triclinic lattices.

Monoclinic crystals make up the largest crystal system, with around one-third of the minerals of Earth belonging to one of its three classes<sup>18</sup>. These low-symmetry Bravais lattices exhibit non-orthogonal principal crystal axes (Fig. 1a), in contrast to orthorhombic (for example, biaxial  $\alpha$ -MoO<sub>3</sub> (ref. 1)), tetragonal, hexagonal, trigonal (for example, uniaxial  $\alpha$ -quartz, aQ, Fig. 1b) or cubic crystal systems. As a consequence, their dielectric permittivity tensor has major polarizability directions that strongly depend on the frequency, with off-diagonal terms that cannot be completely removed through coordinate rotation<sup>6,7</sup>, and exhibits shear terms analogous to viscous flow<sup>19</sup>. These features arise due to the non-trivial relative orientation (neither parallel nor orthogonal) of several optical transitions that, at a given frequency, contribute to a net polarization that cannot be aligned with the crystal axes. In turn, this property results in exotic light propagation not supported by higher-symmetry crystals<sup>6,7,20</sup>. Here we show exemplary consequences of these material features for nanophotonics, in particular, the emergence of a new form of waves — hyperbolic shear polaritons (HShPs) — which have not been previously observed.

**Fig. 1: Hyperbolic shear polaritons in monoclinic bGO compared with hyperbolic polaritons in uniaxial aQ.**

---

 **figure 1**

**a**, Monoclinic crystal structure of bGO (monoclinic angle  $\beta = 103.7^\circ$ ). The sample surface of the investigated bGO crystal is the monoclinic (010) plane ( $x$ - $y$  plane). **b**, Rhombic unit cell of aQ with the  $c$  axis oriented along the  $x$  direction, lying in the sample surface plane. The Cartesian coordinate system used in this work is shown. **c**, **d**, Isofrequency surfaces for bGO and aQ, respectively, at two frequencies (red and green) in which the material supports hyperbolic polaritons. The contour lines at  $k_z = 0$  are plotted as solid lines at the bottom and their mirror axes are shown as dash-dotted lines. **e**, **f** Real-space electric fields at the bGO and aQ surfaces, respectively. **g**, **h** The respective two-dimensional Fourier transformation. Lines indicate the frequency-dependent optical axes for bGO and the crystal axes for aQ. FFT, fast Fourier transform.

[Source data](#)

In this work, we theoretically and experimentally demonstrate the emergence of HShPs in monoclinic crystals. As an exemplary material to demonstrate this phenomenon, we study beta-phase  $\text{Ga}_2\text{O}_3$  (bGO), which has gained a large amount of research and industrial attention for its high breakdown field<sup>21</sup> and applications in photovoltaics<sup>22</sup>, optical displays<sup>23</sup> and gas sensors<sup>24</sup>. In the low-energy range, bGO features several strong infrared-active, non-orthogonal phonon resonances<sup>6</sup>, making the permittivity tensor of bGO naturally non-diagonalizable. Its low symmetry has two

consequences on the polariton propagation when compared with more conventional hyperbolic materials with a diagonal permittivity tensor, such as hBN, aQ and  $\alpha$ -MoO<sub>3</sub>. First, both the bGO polariton wavelength and the propagation direction strongly disperse with frequency. Second, we demonstrate that the asymmetric nature of optical loss in such crystals gives rise to shear, resulting in polariton propagation with tilted wavefronts. Such tilted wavefronts are a direct consequence of the low symmetry of the material and are one of the most notable and unique features of HShPs. New opportunities for polaritonics arise for HShPs stemming directly from their non-Hermitian and topological nature. Yet, surprisingly, they can be observed in low-loss, naturally occurring materials, without the need for artificial structuring of a material surface<sup>17</sup>.

To highlight the role of the asymmetry of monoclinic crystals in their polariton response, we compare HShPs with HPs supported by higher-symmetry anisotropic crystals, such as aQ<sup>25</sup>. In this vein, we compare the crystal structure of monoclinic bGO in Fig. 1a with the trigonal crystal of aQ in Fig. 1b, illustrating the low crystal symmetry present in bGO. In general, the description of the dielectric response of monoclinic crystals requires inclusion of identical off-diagonal elements in the monoclinic plane within the frequency-dependent, complex-valued dielectric tensor.

$$\overline{\overline{\varepsilon}}(\omega) = \begin{bmatrix} \varepsilon_{xx}(\omega) & \varepsilon_{xy}(\omega) & 0 \\ \varepsilon_{yx}(\omega) & \varepsilon_{yy}(\omega) & 0 \\ 0 & 0 & \varepsilon_{zz}(\omega) \end{bmatrix}$$

(1)

The coordinate systems used to define the response of bGO and aQ are sketched in Fig. 1a,b, respectively. To analyse the properties of HShPs in monoclinic materials, we first rigorously solve Maxwell's equations (see [Methods](#)) to calculate the dispersion relation of the polaritonic modes supported by bGO and — for comparison — aQ, each at two distinct frequencies. Initially, we consider the lossless case, in which the imaginary part of each term in the dielectric tensor is neglected for both bGO and aQ. The solutions for the polariton wavevectors in both materials at two different frequencies are provided in Fig. 1c,d. For aQ, we observe two open hyperboloid surfaces — as expected for uniaxial hyperbolic materials — in which a change in frequency results in a corresponding change in wavevector, while preserving the hyperboloid orientation, that is, the direction of polariton propagation (Fig. 1d). By contrast, as we change the frequency, not only does the bGO polariton wavevector magnitude change but the direction of the hyperboloid also rotates within the monoclinic plane, as can be appreciated by examining the  $k_z=0$  projections (Fig. 1c). This is a direct consequence of the non-trivial relative orientation of the phonon resonances supporting the hyperbolic response<sup>6</sup>, which results in polariton bands that

disperse in azimuth angle as a function of frequency. This feature represents a signature of the reduced symmetry associated with HShPs supported in monoclinic crystals (and is also anticipated in triclinic crystals), in contrast to HPs observed in higher-symmetry lattices.

When we also account for natural material losses resulting from inherent phonon-scattering processes, the polariton propagation in bGO shows a reduced symmetry in comparison with hyperbolic polaritons in aQ, even at individual frequencies, as illustrated in Fig. 1e,f. In these panels, we show the results of full-wave calculations of dipole-launched surface polaritons propagating across the surface of a semi-infinite slab of bGO and y-cut aQ, in which — in both cases — natural material losses were explicitly taken into account. For in-plane hyperbolic materials, these surface waves show a hyperbolic dispersion within the surface plane and are referred to as hyperbolic surface or hyperbolic Dyakonov polaritons<sup>26,27</sup>, constituting a subset of HPs supported in these materials similar to volume-confined HPs in thin films. For aQ, HPs spread out along one crystal axis of the surface and are symmetric with respect to the crystal axes, as can be confirmed by a Fourier transform of the real-space electric field profile (Fig. 1h). However, for bGO (Fig. 1e), we observe that HPs are rotated with respect to the coordinate system of the monoclinic plane, as anticipated by the isofrequency contours (Fig. 1c). In addition, the wavefronts are tilted with respect to the major propagation direction, with no apparent mirror symmetry. This feature can also be clearly seen by examining the Fourier transform of the real-space profile (Fig. 1g), exhibiting a stronger intensity along one side of the hyperbola. These observations constitute the discovery of HShPs in low-symmetry crystals.

To experimentally demonstrate the effects of reduced symmetry in polariton propagation in bGO in contrast to higher-symmetry materials, we compare the azimuthal dispersion of HShPs in bGO to the one of HPs in aQ using an Otto-type prism-coupling geometry<sup>28,29</sup> (sketched in Fig. 2a; for details, see [Methods](#)). The experimental azimuthal dispersion of HPs on the surface of aQ is shown in Fig. 2b (see also Extended Data Fig. 3), in excellent agreement with the corresponding simulations (Fig. 2c). The dips in the reflectance spectra show the polariton resonances, which are only observable along specific azimuth angles and are symmetric about the crystal axes,  $\phi = 0^\circ$  ( $180^\circ$ ) and  $90^\circ$ . By contrast, the experimental azimuthal dispersion of HShPs on monoclinic bGO (Fig. 2d) exhibits no mirror symmetry, again in excellent agreement with the simulated dispersion (Fig. 2e).

**Fig. 2: Experimental observation of HPs on aQ and HShPs on bGO.**

---

 **figure 2**

**a**, Otto-type prism-coupling configuration for the experimental observation of surface waves. The p-polarized free-electron laser (FEL) excitation beam is reflected at the prism back side at an incident angle of  $\theta = 28^\circ$ . The reflectance detection is unpolarized. The gap size was fixed to  $d_{\text{gap}} \approx 10.4 \mu\text{m}$  for aQ and  $d_{\text{gap}} \approx 8.3 \mu\text{m}$  for bGO. Datasets at other gap sizes are shown in Extended Data Fig. 3. **b**, Experimental azimuth dependence of HPs on aQ. **c**, Corresponding simulated reflectance map calculated by means of a transfer matrix method. **d**, Experimental azimuth dependence of HShPs on bGO. **e**, Corresponding simulated reflectance map. The white lines in e correspond to the directions of the frequency-dependent major polarizability axes  $n$  and  $m$ ; see text. **f**, Experimental polariton resonance frequency map for bGO in the  $680\text{--}720 \text{ cm}^{-1}$  frequency range, extracted from Otto reflectance measurements at various incidence angles  $\theta$  and azimuth angles  $\phi$ . Experiments were performed at constant gap size  $d_{\text{gap}} \approx 4.0 \mu\text{m}$ . **g**, Simulated polariton resonance frequency map. Experimental (**h**) and simulated (**i**) in-plane hyperbolic dispersion for bGO at selected frequencies interpolated from **f** and **g**, respectively. Dashed lines mark extrapolated values outside the accessed momentum range. **j**, Radial component of the group velocity extracted from **g**. Dash-dotted lines in **i** and **j** mark the symmetry axis for each dispersion curve, which shift with frequency. The asymmetric distribution of the radial group velocity shows the asymmetry of energy flow for HShPs.

[Source data](#)

To experimentally access the in-plane hyperbolic dispersion of the HShP in bGO observed in Fig. 1e, we mapped out the frequency–momentum dispersion in close spectral proximity of that mode ( $680\text{--}720\text{ cm}^{-1}$ ) at many azimuth angles (see Extended Data Fig. 4). The resulting map of polariton resonance frequencies is shown in Fig. 2f, in excellent agreement with the simulated resonance frequencies shown in Fig. 2g. These data allow extraction of single-frequency in-plane dispersion curves shown in Fig. 2h,i from experiment and simulations, respectively, for several selected frequencies, clearly demonstrating a hyperbolic dispersion, in excellent agreement with Fig. 1e. Notably, the base of the hyperbola shifts continuously with frequency, as marked by the symmetry axes for each curve in Fig. 2i, which directly leads to an asymmetric distribution of the group velocity along the hyperbolic dispersion curve, as shown in Fig. 2j (see also Extended Data Fig. 7).

The reduced symmetry observed in the polaritonic dispersion of bGO (Fig. 2d) is a direct consequence of the lack of symmetry in its vibrational structure<sup>6</sup>. Therefore, the HShPs are not propagating along fixed axes but show a continuous rotation of the HShP propagation direction as the frequency is varied. To describe the nature of this rotation, we diagonalize the real part of the permittivity tensor of bGO  $\langle \langle \rm{Re} \rangle \rangle$  individually at each frequency, by rotating the monoclinic plane by the frequency-dependent angle.

$$\gamma(\omega) = \frac{1}{2} \arctan \left( \frac{2 \langle \langle \rm{Re} \rangle \rangle (\langle \langle \varepsilon_{xy} \rangle \rangle(\omega) - \langle \langle \rm{Re} \rangle \rangle (\langle \langle \varepsilon_{yy} \rangle \rangle(\omega)))}{\langle \langle \rm{Re} \rangle \rangle (\langle \langle \varepsilon_{xx} \rangle \rangle(\omega))} \right) \quad (2)$$

The dispersion of  $\gamma(\omega)$  is shown in Fig. 2e (white lines), illustrating that the major polarizability directions within the monoclinic plane, denoted as  $m$  and  $n$ , vary widely across the range. This frequency-dependent coordinate system enables an easier understanding and classification of the polaritonic response (see [Methods](#) and Extended Data Fig. 1 for details). The rotated coordinate axes are shown in Fig. 1e,g (see also Extended Data Fig. 2 for further modes), illustrating their alignment with the hyperbolic dispersion.

Although equation (2) describes the frequency variation of the polariton propagation direction, it does not capture the tilted wavefronts observed in Fig. 1e. This is because, as we choose the rotated coordinate system [mnz], we still retain a purely imaginary off-diagonal permittivity component (see Extended Data Fig. 1). These terms are associated with the non-orthogonal relative orientation of the material resonances, coupling the two crystal axes in the monoclinic plane. As a result, even in the rotated coordinate system [mnz], the dielectric tensor has off-diagonal terms associated with shear phenomena.

To selectively analyse the role of these shear terms, we simulate the polariton propagation in the rotated coordinate system  $[mnz]$  at  $718\text{ cm}^{-1}$ . In particular, we include a scaling factor for the magnitude of the off-diagonal imaginary component, indicated as  $i \times f \text{Im}(\epsilon_{mn})$ , with  $f = 0, 0.5$  and  $1$  (shown in Fig. 3a–c), while retaining the diagonal loss terms. When we remove the off-diagonal component ( $f = 0$ ), bGO essentially becomes a shear-free biaxial material, akin to  $\alpha\text{-MoO}_3$  and similar to uniaxial aQ, with polaritons propagating along the optical axes (Fig. 3a). Therefore, whereas polariton propagation in such a fictional form of bGO is anisotropic in specific spectral ranges (similar to polaritons in  $\text{MoO}_3$  (refs. 1,3)), mode propagation without shear phenomena is symmetric about the (frequency-dependent) major polarizability axes (Fig. 3a). As we gradually increase the magnitude of the off-diagonal imaginary terms back to its natural value ( $f = 1$ ), the wavefronts become increasingly skewed from the major polarizability axis (Fig. 3b,c). The respective reciprocal space maps in Fig. 3d–f show a strong symmetry breaking in the intensity distribution within the hyperbolic isofrequency curves. This observation provides further evidence that the propagation of polaritons is non-trivial within low-symmetry monoclinic — and, by extension, triclinic — systems, and it cannot be expected in higher-symmetry materials in which polariton propagation patterns are symmetric about the principal crystal axes<sup>1,3,4</sup>.

**Fig. 3: Symmetry breaking by shear phenomena for hyperbolic polaritons in monoclinic bGO.**

---

 **figure 3**

**a–c**, Real-space electric fields at the bGO surface for three different magnitudes of the off-diagonal permittivity element  $i \times \text{Im}(\varepsilon_{mn})$  calculated in the frequency-dispersive rotated coordinate system at  $718 \text{ cm}^{-1}$ . **d–f**, Respective Fourier transformation  $k$ -space maps in arbitrary units. The thin crosshairs indicate the principal axes in the frequency-dispersive rotated coordinate system, aligned horizontally and vertically because the maps were calculated within the rotated coordinate system [ $m_nz$ ]. **g**, Isofrequency surface of bulk eigenmodes in bGO with complex frequency  $\tilde{\omega} = \omega / k_0 = 1 + \{i\} \{ \omega / \{i\} \} / \{k_0\}$  calculated in the rotated frame for  $f = 0$  and  $1$  (red and blue, respectively). See [Methods](#) for details on the approach. **h**, Imaginary part  $\omega_i$  for  $f = 0$  and  $1$  (red and blue, respectively). **i**, Contour lines of the isofrequency surface at  $k_z = 0$  for  $f = 0, 0.5$  and  $1$ . The imaginary part  $\omega_i$  at the corresponding point in  $k$ -space is colour-coded.

FFT, fast Fourier transform.

## [Source data](#)

To connect the reduced symmetry of the surface subset of HShPs observed here experimentally (Fig. 2) and through our simulations (Fig. 3a–c) to the more general HShPs in the bulk, we now calculate isofrequency surfaces for polariton modes in bGO explicitly including loss, to account for the effect of shear phenomena. To this end, we solve Maxwell's equations for real momentum values, yielding complex frequency eigenvalues, whose imaginary part accounts for the finite lifetime of the supported modes (see [Methods](#) for details). The results of these calculations are shown in Fig. 3g–i. Here the real part of the eigenfrequency is fixed and we find its imaginary part  $\omega_i$  (Fig. 3h), which is proportional to the modal lifetime, and the corresponding value of  $k_z$  (Fig. 3g) for each pair of  $k_m$  and  $k_n$ . The calculations are performed in the rotated coordinate system for both  $f=0$  and  $f=1$ , showing that both the shape of the isofrequency surfaces as well as their lifetimes change greatly with the inclusion of the off-diagonal imaginary components. Notably, these calculations prove that, at individual frequencies and in the major polarizability frame, mirror symmetry of polariton propagation is lost in monoclinic materials as a direct consequence of shear.

To relate the isofrequency contours of HShPs to the surface mode dispersions in Fig. 3d–f, we plot the  $k_z=0$  solution in Fig. 3i, with the colour scale indicating the relative loss  $\omega_i$  of the mode. Two important observations can be made: first, the mirror symmetry of the isofrequency curves is broken for  $f>0$  and it requires higher-order terms to account for the asymmetric shape; second, the mode losses are redistributed asymmetrically, with losses decreasing in one arm of the hyperbolae but increasing on the other arm. We note that, also in the experimental data (Extended Data Fig. 4), we observe an indication of asymmetric distribution of polariton quality factors along the hyperbolic dispersion curves (see Extended Data Fig. 5).

These observations naturally link HShPs in monoclinic crystals to the rich, emerging area of non-Hermitian and topological photonics. Although loss in orthogonal systems alone can already have interesting consequences for polariton propagation<sup>30</sup>, the off-diagonal shear terms highlighted here can provide new opportunities for non-Hermitian photonics and for manipulation of topological polaritons in low-symmetry materials. For instance, we foresee asymmetric topological transitions experienced by HShPs, generalizing previous results in orthorhombic systems<sup>2</sup> by exploiting the unique non-Hermitian features emerging in low-symmetry materials. In addition, recent studies suggest the connection between Dyakonov surface waves and surface states emerging from one-dimensional band degeneracy (nodal lines) of topological nature of high-symmetry metacrystals<sup>31</sup>. We anticipate that HShPs may generalize these opportunities to asymmetric topological bands in which non-Hermiticity in the natural materials plays a dominant role.

Here we have demonstrated that low-symmetry crystals can support a new class of hyperbolic polariton modes with broken symmetry due to shear phenomena, which we refer to as HShPs. We introduce bGO as an exemplary material to enable the observation of these phenomena and experimentally demonstrate the symmetry-broken dispersion of the supported surface waves. The non-diagonalizable dielectric permittivity plays a key role in the unique properties of low-symmetry crystals, including monoclinic and triclinic lattices. Our findings are generalizable to engineered photonic systems with at least two non-orthogonal oscillators, including new metasurface designs capturing these physics. Beyond the results provided here for intrinsic, compensation-doped bGO, the presence of free charge carriers in bGO<sup>32</sup> may allow for methods for direct steering of the HShP propagation direction (see Extended Data Fig. 6). Finally, exfoliation of thin flakes of single-crystal bGO has also been recently reported<sup>33</sup>, which will allow to make use of volume-confined HShPs in such bGO thin films or — potentially — even in monolayers<sup>34</sup>. We anticipate that HShPs may have important implications in the manipulation of phase and directional energy transfer, including radiative heat transport<sup>35</sup>, ultra-fast asymmetric thermal dissipation in the near field<sup>35</sup> and gate-tunability for on-chip all-optical circuitry<sup>36</sup>. Beyond advances in nanophotonics, infrared polariton propagation has been demonstrated as a means for quantifying crystal strain<sup>37</sup>, polytypes<sup>38</sup>, variations in free-carrier density, as well as phononic and electronic properties around defects<sup>39</sup>, thereby also promising a new metrology tool for characterizing low-symmetry ultra-wide-bandgap semiconductors. We highlight that our results are applicable to any material with non-orthogonal optically active transitions and may therefore be extended to other optical phenomena, such as excitons in triclinic ReSe<sub>2</sub> (ref. 40).

## Methods

### Experimental

The insulating (010)-oriented,  $5 \times 5 \times 0.5\text{-mm}^3$  bGO substrate was produced by means of Fe compensation doping and was purchased from Novel Crystal Technology, Inc., Japan. The aQ sample was purchased from MaTeck GmbH, Germany. The absolute azimuth orientation of the samples was extracted from a global fit for each of the datasets of aQ and bGO (plotted in Fig. 2b,d, respectively), resulting in a rotation with respect to the principal  $x$  axis of the laboratory coordinate system of  $\Delta\phi_{\text{bGO}} = 27.95^\circ$  and  $\Delta\phi_{\text{aQ}} = 26.96^\circ$ . The aQ data have been rotated accordingly to shift the crystal axes (mirror planes) onto multiples of  $90^\circ$ . On the other hand, the bGO data are plotted as measured, as there is no principal azimuth angle for alignment because of the broken mirror symmetry. Here the simulation was rotated accordingly to match the data.

The Otto-type prism-coupling experiment measures the spectral dependence of surface waves through sharp absorption peaks observed as dips in the reflectance spectra, by using a prism placed near the material surface<sup>28,41</sup>. The crystals are oriented such that the monoclinic plane (bGO) and the optical axis (aQ) are parallel to the sample surface. By following the spectral position of the polariton resonances as a function of azimuth angle, we investigate the dispersion of hyperbolic waves at the surface for both bGO and aQ. The Otto geometry effectively selects a specific in-plane momentum component of those surface waves induced by the dipole excitation in Fig. 1e,f, as set by the incidence angle  $\theta$  and azimuth angle  $\phi$  that define the magnitude<sup>28,29</sup> and direction of the selected momentum, respectively.

As an excitation source for the Otto-type prism-coupled experiments, we use a mildly focused mid-infrared free-electron laser (FEL) (spot size  $\sim 1\text{ mm}^2$ ) with small bandwidth ( $\sim 0.3\%$ ) and wide tunability of  $3\text{--}50\text{ }\mu\text{m}$ , covering the spectral range  $350\text{--}800\text{ cm}^{-1}$ , in which aQ and bGO support polaritonic modes (details on the FEL have been reported elsewhere<sup>42</sup>). Although the frequency is scanned by tuning the FEL, different in-plane momenta can be accessed by means of changes in the incidence angle  $\theta$  by rotating the entire Otto geometry (details on the setup have been reported elsewhere<sup>28,43</sup>). For the experiments shown in Fig. 2b,d, the incident angle was fixed to  $28^\circ$ , resulting in an in-plane momentum of  $\langle k \rangle_{\parallel}/k_0 \approx 1.10$  (at  $500\text{ cm}^{-1}$ ). In contrast to alternative approaches, the Otto geometry features experimental control over the excitation efficiency through tunability of the air gap width  $d_{\text{gap}}$ . Here the gap was adjusted to a separation in which all excited modes could be observed in the spectra simultaneously, that is,  $d_{\text{gap}} \approx 8.3\text{ }\mu\text{m}$  for bGO and  $d_{\text{gap}} \approx 14.4\text{ }\mu\text{m}$  for aQ. Direct readout of  $d_{\text{gap}}$  with a range of  $1\text{--}50\text{ }\mu\text{m}$  is realized through white-light interferometry, whereas the contrast of the interference range grants parallel alignment of prism and sample<sup>43</sup>.

Mapping of the in-plane hyperbolic dispersion (Fig. 2f,h) was performed analogously to the Otto reflectance measurements shown in Fig. 2b,d. However, here we additionally varied the incidence angle  $\theta$  to map out the frequency–momentum dispersion at each azimuth angle. Reflectance spectra were taken in a narrow frequency range of  $670\text{--}730\text{ cm}^{-1}$ , at  $\theta = 26^\circ, 28^\circ, 30^\circ, 32^\circ$  and  $34^\circ$ , corresponding to in-plane momenta of  $\langle k \rangle_{\parallel}/k_0 \approx 1.03, 1.11, 1.18, 1.25, \{ \text{rm and } \}, 1.32$  (at  $700\text{ cm}^{-1}$ ), at nine azimuth angles. To allow prism coupling to the polaritons also for larger momenta, these data were taken at a constant air gap  $d_{\text{gap}} \approx 4.0\text{ }\mu\text{m}$ . The reflectance minima marking the polariton resonance were extracted from these data and are shown in Fig. 2f. The theoretical polariton resonance map, Fig. 2g, was calculated using a transfer matrix formalism<sup>44</sup>, by extracting the peak positions of  $\text{Im}(r_{\text{pp}})$  of the air–bGO interface. To extract the single-frequency in-plane hyperbolic dispersion curves (Fig. 2h,i), we interpolated the momentum for a given

frequency in the frequency–momentum dispersion for each measured/calculated azimuth angle.

## Theoretical

### Transfer matrix

The calculations of the optical response shown in Fig. 2c,e and the polariton resonance map in Fig. 2g, as well as the dispersion maps in Extended Data Fig. 2c,d, were performed using a generalized  $4 \times 4$  transfer matrix formalism<sup>44</sup>. In short, the formalism enables the calculation of reflection and transmission coefficients in any number of stratified media with arbitrary dielectric tensor, which enables to account for the anisotropy of our samples.

### COMSOL simulations

COMSOL<sup>45</sup> version 5.6 was used for simulating point dipole excitation of HShPs on bGO. A point dipole was placed 100 nm above the surface of an infinite slab of bGO, with a dielectric permittivity matching that of ref. 6. The dielectric function of aQ was taken from ref. 46. Perfectly matched impedance boundary conditions were used on the sides of the simulation, which — in principle — absorb all radiation. However, to account for the imperfect behaviour of the boundaries, we ensured that the bGO slab was sufficiently large ( $250 \times 250 \times 8 \mu\text{m}$ ), such that the wave is sufficiently damped when it reaches the boundary so as not to influence the results. Reciprocal space maps were generated by 2D Fourier transformation of the real-space electric field profiles.

### Isofrequency surface with complex frequency

To obtain the isofrequency contour surface of the bulk wave when losses are considered in the materials, we turn to the complex-frequency method and solve the source-free Maxwell equations as follows:

$$\begin{aligned}
 & \$(\begin{array}{ccc} \tilde{\omega}^2 \varepsilon_{xx} - \\ (\tilde{k}_z^2 + \tilde{k}_y^2) & \& \tilde{\omega}^2 \varepsilon_{yy} - \\ \tilde{k}_x \tilde{k}_y & \& \tilde{\omega}^2 \varepsilon_{xy} + \tilde{k}_x \tilde{k}_y & \& \tilde{k}_x \tilde{k}_z \\ \tilde{\omega}^2 \varepsilon_{xy} + \tilde{k}_x \tilde{k}_y & \& \tilde{\omega}^2 \varepsilon_{yy} - (\tilde{k}_z^2 + \tilde{k}_x^2) & \& \tilde{k}_x \tilde{k}_y \\ \tilde{\omega}^2 \varepsilon_{yy} - (\tilde{k}_z^2 + \tilde{k}_x^2) & \& \tilde{k}_x \tilde{k}_y & \& \tilde{k}_x \tilde{k}_z \\ \tilde{k}_x \tilde{k}_y & \& \tilde{k}_x \tilde{k}_z & \& \tilde{\omega}^2 \varepsilon_{zz} - (\tilde{k}_z^2 + \tilde{k}_y^2) \end{array}) = 0, \\
 & \$(\begin{array}{c} E_x \\ E_y \\ E_z \end{array}) = 0
 \end{aligned}$$

in which  $\langle \{varepsilon\}_{nn} \rangle = \langle \{varepsilon\}_{nn}^r \rangle + i \langle \{varepsilon\}_{nn}^i \rangle$  and  $\langle \{varepsilon\}_{xy} \rangle = \langle \{varepsilon\}_{xy}^r \rangle + i \langle \{varepsilon\}_{xy}^i \rangle$ . We fix the real component  $k_0$  of the complex frequency  $\omega$  and normalize it as  $\langle \tilde{\omega} \rangle = \frac{\omega}{k_0} = 1 + \langle \{varepsilon\}_i \rangle / \langle \{varepsilon\}_r \rangle$ ,  $\langle \tilde{\omega}^2 \rangle = 1 - \langle \{varepsilon\}_i^2 \rangle / \langle \{varepsilon\}_r^2 \rangle + 2 \langle \{varepsilon\}_i \rangle \langle \tilde{\omega} \rangle$ , in which  $\omega_i$  is an effective inverse mode lifetime, calculated neglecting the effect of the complex frequency on the material dispersion, and normalize the wavevector as  $\langle \{\tilde{k}\}_{xyz} \rangle = \frac{\{k\}_{xyz}}{\{k\}_0}$ . Note that we choose a negative sign for the time-dependent term  $e^{-i\omega t}$ , so  $\langle \{\tilde{\omega}\}_i \rangle$  must be real and negative to reflect the decaying nature of the wave. The analytic expression  $\langle F(\{\tilde{\omega}\}_i) \rangle = \langle \{\tilde{k}\}_x \rangle, \langle \{\tilde{k}\}_y \rangle, \langle \{\tilde{k}\}_z \rangle = 0$  is found by means of the secular equation of the above matrix, and two equations are obtained by separating the real and imaginary components of  $F$ , namely,

```
 $$\begin{array}{c} F_{\{\rm r\}}(\tilde{\omega}_i), \tilde{k}_x, \\ \tilde{k}_y, \tilde{k}_z=0, \\ F_{\{\rm i\}}(\tilde{\omega}_i), \tilde{k}_x, \tilde{k}_y, \tilde{k}_z=0.\end{array}$$
```

The isofrequency contour of the bulk wave and the imaginary component \(\langle \tilde{\omega} \rangle\_{\rm i}\) are evaluated from those two equations. The numerical examples at  $718 \text{ cm}^{-1}$  are given in Fig. 3g,h on the basis of the above method ( $k_{x,y} \rightarrow k_{m,n}$ ). Notice that, in this procedure, we use the permittivity tensor elements calculated at  $\text{Re}(\omega)$ . When \(\langle \tilde{k} \rangle\_z = 0\), the analytic expression for the isofrequency contour of the bulk wave can be written as

```
$$[\{\tilde{\omega}\}^2(\{\varepsilon_{xx}\}\{\varepsilon_{yy}\}-\{\varepsilon_{xy}\}^2)-(\{\varepsilon_{xx}\}\{\tilde{k}_x\}^2+\{\varepsilon_{yy}\}\{\tilde{k}_y\}^2+2\{\varepsilon_{xy}\}\{\tilde{k}_x\}\{\tilde{k}_y\})]=0,$$
```

which turns into two equations by separating the real and imaginary parts,

```

$ $$\begin{array}{c}(1-\{\tilde{\omega}\})_{-}\{{\rm i}\}^2)\\
\{F\}_{-}\{{\rm r}\}-2\{\tilde{\omega}\}_{-}\{{\rm i}\}\{F\}_{-}k-(\varepsilon_{xx}^r\\
\{\tilde{k}\}_x^2+\varepsilon_{yy}^r\{\tilde{k}\}_y^2+2\varepsilon_{xy}^r\{\tilde{k}\}_x\{\tilde{k}\}_y)=0,\backslash 2\{\tilde{\omega}\}_{-}\{{\rm i}\}\\
\{F\}_{-}\{{\rm r}\}+(1-\{\tilde{\omega}\})_{-}\{{\rm i}\}^2)\{F\}_{-}k-(\varepsilon_{xx}^k\\
\{\tilde{k}\}_x^2+\varepsilon_{yy}^k\{\tilde{k}\}_y^2+2\varepsilon_{xy}^k\{\tilde{k}\}_x\\
\{\tilde{k}\}_y)=0;\end{array}$$

```

$$\begin{aligned}
\$ \$ \begin{array}{c} \{F\}_{\{r\}} = \{\varepsilon_{xx}\}_{\{r\}} \{\varepsilon_{yy}\}_{\{r\}} - \\
\{\varepsilon_{xx}\}_{\{k\}} \{\varepsilon_{yy}\}_{\{k\}} - (\{\varepsilon_{xy}\}_{\{r\}})^2 - \\
(\{\varepsilon_{xy}\}_{\{k\}})^2) \\ \{F\}_{\{k\}} = \{\varepsilon_{xx}\}_{\{r\}} \{\varepsilon_{yy}\}_{\{k\}} + \{\varepsilon_{xx}\}_{\{k\}} \{\varepsilon_{yy}\}_{\{r\}} - 2 \{\varepsilon_{xy}\}_{\{r\}} \{\varepsilon_{xy}\}_{\{k\}}. \end{array} \end{aligned}$$

and they can be further simplified into the following equation

$$\begin{aligned}
\$ \$ \begin{array}{l} [(\{\varepsilon_{xx}\}_{\{r\}} \{F\}_{\{k\}} - \{\varepsilon_{xx}\}_{\{k\}} \{F\}_{\{r\}}) \{\tilde{k}\}_{\{x\}}^2 + 2(\{\varepsilon_{xy}\}_{\{r\}} \{F\}_{\{k\}} - \{\varepsilon_{xy}\}_{\{k\}} \{F\}_{\{r\}}) \{\tilde{k}\}_{\{x\}} \{\tilde{k}\}_{\{y\}} + (\{\varepsilon_{yy}\}_{\{r\}} \{F\}_{\{k\}} - \{\varepsilon_{yy}\}_{\{k\}} \{F\}_{\{r\}}) \{\tilde{k}\}_{\{y\}}^2] \\
+ 4(\{F\}_{\{\rm r\}})^2 + \{F\}_{\{k\}}^2] [(\{\varepsilon_{xx}\}_{\{r\}} \{F\}_{\{\rm r\}} + \{\varepsilon_{xx}\}_{\{k\}} \{F\}_{\{k\}}) \{\tilde{k}\}_{\{x\}}^2 + 2(\{\varepsilon_{xy}\}_{\{r\}} \{F\}_{\{\rm r\}} + \{\varepsilon_{xy}\}_{\{k\}} \{F\}_{\{k\}}) \{\tilde{k}\}_{\{x\}} \{\tilde{k}\}_{\{y\}} + (\{\varepsilon_{yy}\}_{\{r\}} \{F\}_{\{\rm r\}} + \{\varepsilon_{yy}\}_{\{k\}} \{F\}_{\{k\}}) \{\tilde{k}\}_{\{y\}}^2 - \\
\{F\}_{\{\rm r\}}^2 - \{F\}_{\{k\}}^2] = 0. \end{array} \end{aligned}$$

Therefore, the isofrequency curves in the  $\{\tilde{k}\}_{\{z\}}=0$  plane as well as the imaginary component of the bulk complex frequency are obtained from the above expression.

## Characterization of the polariton modes in bGO

### Assignment of the polariton mode nature

First, we briefly outline how conventional polariton materials are classified. A material supports surface polaritons at frequencies for which the real part of the crystal permittivity fulfills  $\text{Re}(\varepsilon) < -1$  (ref. 47). In uniaxial crystals, the diagonal permittivity elements can be of different sign, leading to hyperbolic behaviour in which either the real part of one element is negative and the other two are positive (type I) or two are negative and one is positive (type II)<sup>9</sup>. However, this classification of anisotropic materials relies on the off-diagonal permittivity tensor elements being zero at all frequencies for an appropriate choice of coordinate system. The lower symmetry of bGO requires the emergence of  $\varepsilon_{xy} \neq 0$ . The dielectric permittivity elements using coordinates as indicated in Fig. 1a are shown in Extended Data Fig. 1a–e, but no coordinate system exists in which  $\text{Re}(\varepsilon_{x,y}) \neq 0$  at all frequencies. This, as we have demonstrated in the Otto-geometry experiments (Fig. 2d), results in a non-trivial polaritonic response with highly directional modes that propagate along frequency-dictated propagation angles in the  $a-c$  plane. Furthermore, because  $\varepsilon_{xy} \neq 0$ , it is not

straightforward to determine whether the modes are elliptical ( $\varepsilon_{xx}, \varepsilon_{yy}, \varepsilon_{zz} < -1$ ) or hyperbolic in nature (type I or type II), as the propagation angle is typically not aligned with one of the principal axes.

To unambiguously describe the nature of the polariton modes, we switch to a frequency-dispersive coordinate system [ $m nz$ ], in which the real part of the permittivity tensor is diagonal. This is achieved by rotating the monoclinic plane by the frequency-dependent angle  $\gamma(\omega)$  (equation (2)). The dispersion of  $\gamma(\omega)$  and the resulting diagonal elements of  $\varepsilon^{[m nz]}$  are plotted in Extended Data Fig. 1f–j. This new frequency-dispersive coordinate system enables the unique assignment of the supported polariton mode nature, which we have colour-coded in Extended Data Fig. 1g–j. For bGO, we observe the full range of possible combinations of positive and negative real parts of  $\varepsilon_{mm}$ ,  $\varepsilon_{nn}$  and  $\varepsilon_{zz}$ , leading to dielectric (white), elliptical (grey) and hyperbolic spectral regimes of type I (in-plane in blue, out-of-plane in red) and type II (in-plane in green, out-of-plane in yellow). By performing such a frequency-dependent rotation of the permittivity tensor, we have simplified the system into a pseudo-biaxial crystal at each frequency. However, as the dielectric tensor of a monoclinic crystal is not diagonalizable<sup>20,48,49</sup>, the in-plane, off-diagonal element of  $\varepsilon^{[m nz]}$  retains a non-vanishing imaginary part at all frequencies, that is,  $\text{Im}(\varepsilon_{mn}) \neq 0$  (plotted in Extended Data Fig. 1i), giving rise to the reduced symmetry of hyperbolic shear polaritons in monoclinic crystals, as discussed in Fig. 3.

The frequency-dependent rotation of the dielectric permittivity tensor is performed in three subsequent steps. First, the in-plane permittivity tensor as shown in Extended Data Fig. 1a–c is rotated about the angle  $\gamma(\omega)$  (equation (2)). However,  $\gamma(\omega)$  has jumps of  $90^\circ$  at arbitrary frequencies, resulting in abrupt discontinuities in the real parts of  $\varepsilon_{mm}$  and  $\varepsilon_{nn}$ , for which the two curves switch values. By analysing the derivative of  $\varepsilon_{mm}$ , we extract the frequency values  $\omega_{\text{jump}}$ , in which the jumps occur and reassign the permittivity curves, respectively. At the eight in-plane TO frequencies  $\omega_{\text{TO}}$  of bGO, the permittivity curves feature a pole, which is also captured in the analysis of the derivative. Therefore, at this step, the resulting curves are smooth between the TO frequencies, but switch assignment at every  $\omega_{\text{TO}}$ . The switching of the curves at every  $\omega_{\text{TO}}$  is performed in the last step. However, near  $\omega_{\text{TO}}$ , the permittivity features a large imaginary part, which is not accounted for in the rotation angle  $\gamma(\omega)$ . This leads to poles in  $\gamma(\omega)$  at  $\omega_{\text{TO}}$  (see Extended Data Fig. 1f), which — in turn — results in a small avoided crossing of  $\varepsilon_{mm}$  and  $\varepsilon_{nn}$  at the TO frequencies. Therefore, the reassignment of the last step results in discontinuous solutions near  $\omega_{\text{TO}}$ , which is clearly not physical. To resolve this issue, we cut out  $\pm 1 \text{ cm}^{-1}$  in both  $\varepsilon_{mm}$  and  $\varepsilon_{nn}$  at all eight  $\omega_{\text{TO}}$  and smooth the curves by interpolation, resulting in the pseudo-biaxial permittivity curves as shown in Extended Data Fig. 1g–h. The rotation about  $\gamma(\omega)$  also leads to

discontinuities in the off-diagonal imaginary part  $\text{Im}(\varepsilon_{mn})$  at the frequencies  $\omega_{\text{jump}}$ . However, because  $\varepsilon_{mn} = \varepsilon_{nm}$ , the abrupt rotation about  $90^\circ$  only leads to sign changes at every  $\omega_{\text{jump}}$ . The curve of  $\text{Im}(\varepsilon_{mn})$  shown in Extended Data Fig. 1*i* is corrected for these sign changes.

## Polariton behaviour in bGO in the rotated frame

To verify the polaritonic behaviour of bGO in the rotated frame, that is, the pseudo-biaxial crystal, we subsequently analyse the surface polariton dispersion in the rotated coordinate system [ $m$ - $z$ ] in Extended Data Fig. 2. For electric fields in the  $m$ - $z$  or  $n$ - $z$  planes, the analytical expression describing extraordinary surface polaritons in uniaxial crystals can be used<sup>50</sup>:

$$\frac{k}{\{\varepsilon_{\text{in-plane}} - \varepsilon_{mm}\}} = \frac{\omega}{c} \sqrt{\frac{\varepsilon_{zz}}{\varepsilon_{zz} - \varepsilon_{in-plane}} - \frac{\varepsilon_{zz}}{\varepsilon_{zz} - \varepsilon_{in-plane}}} \quad , \quad \text{where } \varepsilon_{in-plane} = \varepsilon_{mm}, \varepsilon_{nn}$$

in which  $\varepsilon_{\text{in-plane}} = \varepsilon_{mm}, \varepsilon_{nn}$ . In bGO, the solutions yield four polariton branches for each direction,  $m$  and  $n$ , respectively, plotted as red dotted lines in Extended Data Fig. 2*c,d*. These analytical results are in perfect agreement with the numerically obtained surface polariton dispersion using a transfer matrix formalism<sup>44</sup>. To obtain the polariton propagation properties of the system, we calculate the full electric field patterns by placing a point dipole source above the bGO surface at  $x=y=0$  and simulating the optical response along the bGO–air interface ( $z=0$ ) with COMSOL Multiphysics<sup>45</sup>. The real-space field profiles clearly show the rotation of the major polarizability direction as a function of frequency, demonstrated for six different modes M1–M3 and N1–N3 (See Extended Data Fig. 2*e–g,k–m*). Frequencies are indicated as black dash-dotted lines in Extended Data Fig. 2*a–d*. Mode N4 is shown in Fig. 1*e,g*. The field profiles align with the rotated coordinate system, with basis vectors indicated by the ‘ $m$ ’ and ‘ $n$ ’ crosshair in each figure.

To relate the calculated dispersion of the polariton branches to the field profiles, we calculate the momentum– $k$  maps of these modes, as obtained by a 2D Fourier transformation of the respective electric field patterns of Extended Data Fig. 2*e–g,k–m* in Extended Data Fig. 2*h–j,n–p*, respectively. At all selected frequency positions, the electric field patterns contain a directional wave of large amplitude with low spatial frequency, as well as a wave with high spatial frequency. The observed in-plane momenta of the low- $k$  modes follow the modal dispersion predicted in Extended Data Fig. 2*c,d*, along the  $m$  and  $n$  axes for modes M1–M3 and N1–N3, respectively, as indicated by the black circles in Extended Data Fig. 2*h–j,n–p*. According to the mode characterization provided in Extended Data Fig. 1, these modes are hyperbolic, either

of type I in-plane (M1–M3 and N1) or of type II in-plane (N2, N3). For all HShP modes, field patterns and  $k$ -space maps are characterized by twofold rotational symmetry only, in agreement with the 2D plane group 2 (no mirror plane symmetries). Further, the distinct peaks in the  $k$ -space maps verify the principal polariton propagation direction, whereas the corresponding radial and azimuthal spreads are representative of their decay length and degree of directionality, respectively.

Analogous to the model at  $718\text{ cm}^{-1}$  discussed in the main text, the maxima of the  $k$ -space maps shown in Extended Data Fig. 2 do not lie on the major polarizability axes (most prominently for the cases in Extended Data Fig. 2n,o), owing to shear phenomena in monoclinic bGO. This is discussed further in the main text and in Fig. 3.

## Data availability

The data and data analysis scripts that support the findings of this study are available from <https://doi.org/10.5281/zenodo.5613335>. Additionally, the [Source data](#) are provided with this paper.

## Code availability

The code generating Fig. 1c,d and Fig. 2g,i,j can be downloaded from <https://doi.org/10.5281/zenodo.5613335>. The code used for Fig. 3g-i is available from Andrea Alù (aalu@gc.cuny.edu) on reasonable request.

## References

1. Ma, W. et al. In-plane anisotropic and ultra-low-loss polaritons in a natural van der Waals crystal. *Nature* **562**, 557–562 (2018).
2. Hu, G. et al. Topological polaritons and photonic magic angles in twisted  $\alpha$ - $\text{MoO}_3$  bilayers. *Nature* **582**, 209–213 (2020).
3. Zheng, Z. et al. A mid-infrared biaxial hyperbolic van der Waals crystal. *Sci. Adv.* **5**, eaav8690 (2019).
4. Taboada-Gutiérrez, J. et al. Broad spectral tuning of ultra-low-loss polaritons in a van der Waals crystal by intercalation. *Nat. Mater.* **19**, 964–968 (2020).
5. Low, T. et al. Polaritons in layered two-dimensional materials. *Nat. Mater.* **16**, 182–194 (2016).

6. Schubert, M. et al. Anisotropy, phonon modes, and free charge carrier parameters in monoclinic  $\beta$ -gallium oxide single crystals. *Phys. Rev. B* **93**, 125209 (2016).
7. Claus, R. Polariton dispersion and crystal optics in monoclinic materials. *Phys. Status Solidi* **88**, 683–688 (1978).
8. Dai, S. et al. Tunable phonon polaritons in atomically thin van der Waals crystals of boron nitride. *Science* **343**, 1125–1129 (2014).
9. Caldwell, J. D. et al. Sub-diffractive volume-confined polaritons in the natural hyperbolic material hexagonal boron nitride. *Nat. Commun.* **5**, 5221 (2014).
10. Armbruster, T. et al. Recommended nomenclature of epidote-group minerals. *Eur. J. Mineral.* **18**, 551–567 (2006).
11. Liu, M. et al. Symmetry breaking and geometric confinement in  $\text{VO}_2$ : results from a three-dimensional infrared nano-imaging. *Appl. Phys. Lett.* **104**, 121905 (2014).
12. Koch, E. E., Otto, A. & Kliewer, K. L. Reflection spectroscopy on monoclinic crystals. *Chem. Phys.* **3**, 362–369 (1974).
13. Basov, D. N., Averitt, R. D. & Hsieh, D. Towards properties on demand in quantum materials. *Nat. Mater.* **16**, 1077–1088 (2017).
14. Shiozaki, K. & Sato, M. Topology of crystalline insulators and superconductors. *Phys. Rev. B* **90**, 165114 (2014).
15. Caldwell, J. D. et al. Low-loss, infrared and terahertz nanophotonics using surface phonon polaritons. *Nanophotonics* **4**, 44–68 (2015).
16. Poddubny, A., Iorsh, I., Belov, P. & Kivshar, Y. Hyperbolic metamaterials. *Nat. Photon.* **7**, 948–957 (2013).
17. Li, P. et al. Infrared hyperbolic metasurface based on nanostructured van der Waals materials. *Science* **359**, 892–896 (2018).
18. Peck, D. & Ostrander, A. Crystallography: the monoclinic system. *Mindat.org* <https://www.mindat.org/article.php?2787/Crystallography%3A+The+Monoclinic+System> (2020).
19. Wu, Y., Zhang, W., Wang, Y., Zou, Z. & Chen, J. Energy dissipation analysis based on velocity gradient tensor decomposition. *Phys. Fluids* **32**, 035114 (2020).

20. Sturm, C. et al. Dipole analysis of the dielectric function of color dispersive materials: application to monoclinic  $\text{Ga}_2\text{O}_3$ . *Phys. Rev. B* **94**, 035148 (2016).
21. Higashiwaki, M. & Jessen, G. H. Guest Editorial: The dawn of gallium oxide microelectronics. *Appl. Phys. Lett.* **112**, 60401 (2018).
22. Granqvist, C. G. *Handbook of Inorganic Electrochromic Materials* (Elsevier, 1995).
23. Miyata, T., Nakatani, T. & Minami, T. Gallium oxide as host material for multicolor emitting phosphors. *J. Lumin.* **87–89**, 1183–1185 (2000).
24. Réti, F., Fleischer, M., Meixner, H. & Giber, J. Effect of coadsorption of reducing gases on the conductivity of  $\beta\text{-Ga}_2\text{O}_3$  thin films in the presence of  $\text{O}_2$ . *Sens. Actuators B Chem.* **19**, 573–577 (1994).
25. Winta, C. J., Wolf, M. & Paarmann, A. Low-temperature infrared dielectric function of hyperbolic  $\alpha$ -quartz. *Phys. Rev. B* **99**, 144308 (2019).
26. Jacob, Z. & Narimanov, E. E. Optical hyperspace for plasmons: Dyakonov states in metamaterials. *Appl. Phys. Lett.* **93**, 221109 (2008).
27. Álvarez-Pérez, G., Voronin, K. V., Volkov, V. S., Alonso-González, P. & Nikitin, A. Y. Analytical approximations for the dispersion of electromagnetic modes in slabs of biaxial crystals. *Phys. Rev. B* **100**, 235408 (2019).
28. Passler, N. C. et al. Second-harmonic generation from critically coupled surface phonon polaritons. *ACS Photonics* **4**, 1048–1053 (2017).
29. Folland, T. G., Nordin, L., Wasserman, D. & Caldwell, J. D. Probing polaritons in the mid- to far-infrared. *J. Appl. Phys.* **125**, 191102 (2019).
30. Antoniou, P., Suchanek, F., Varner, J. F. & Foley, J. J. Role of cavity losses on nonadiabatic couplings and dynamics in polaritonic chemistry. *J. Phys. Chem. Lett.* **11**, 9063–9069 (2020).
31. Gao, W. et al. Experimental observation of photonic nodal line degeneracies in metacrystals. *Nat. Commun.* **9**, 950 (2018).
32. Schubert, M. et al. Longitudinal phonon plasmon mode coupling in  $\beta\text{-Ga}_2\text{O}_3$ . *Appl. Phys. Lett.* **114**, 102102 (2019).

33. Hwang, W. S. et al. High-voltage field effect transistors with wide-bandgap  $\beta$ - $\text{Ga}_2\text{O}_3$  nanomembranes. *Appl. Phys. Lett.* **104**, 203111 (2014).
34. Rivera, N., Christensen, T. & Narang, P. Phonon polaritronics in two-dimensional materials. *Nano Lett.* **19**, 2653–2660 (2019).
35. Salihoglu, H. et al. Energy transport by radiation in hyperbolic material comparable to conduction. *Adv. Funct. Mater.* **30**, 1905830 (2020).
36. Maia, F. C. B. et al. Anisotropic flow control and gate modulation of hybrid phonon-polaritons. *Nano Lett.* **19**, 708–715 (2019).
37. Gigler, A. M. et al. Nanoscale residual stress-field mapping around nanoindents in SiC by IR s-SNOM and confocal Raman microscopy. *Opt. Express* **17**, 22351 (2009).
38. Huber, A., Ocelic, N., Taubner, T. & Hillenbrand, R. Nanoscale resolved infrared probing of crystal structure and of plasmon–phonon coupling. *Nano Lett.* **6**, 774–778 (2006).
39. Hauer, B. et al. Exploiting phonon-resonant near-field interaction for the nanoscale investigation of extended defects. *Adv. Funct. Mater.* **30**, 1907357 (2020).
40. Arora, A. et al. Highly anisotropic in-plane excitons in atomically thin and bulklike 1T-ReSe<sub>2</sub>. *Nano Lett.* **17**, 3202–3207 (2017).
41. Passler, N. C. et al. Strong coupling of epsilon-near-zero phonon polaritons in polar dielectric heterostructures. *Nano Lett.* **18**, 4285–4292 (2018).
42. Schöllkopf, W. et al. The new IR and THz FEL facility at the Fritz Haber Institute in Berlin. *Proc. SPIE* **9512**, 95121L (2015).
43. Pufahl, K. et al. Controlling nanoscale air-gaps for critically coupled surface polaritons by means of non-invasive white-light interferometry. *Appl. Phys. Lett.* **113**, 161103 (2018).
44. Passler, N. C. & Paarmann, A. Generalized  $4 \times 4$  matrix formalism for light propagation in anisotropic stratified media: study of surface phonon polaritons in polar dielectric heterostructures. *J. Opt. Soc. Am. B* **34**, 2128–2139 (2017).
45. COMSOL Multiphysics (COMSOL, 2020).

46. Spitzer, W. G. & Kleinman, D. A. Infrared lattice bands of quartz. *Phys. Rev.* **121**, 1324–1335 (1961).
47. Raether, H. *Surface Plasmons on Smooth and Rough Surfaces and on Gratings* (Springer, 1988).
48. Jellison, G. E. et al. Spectroscopic dielectric tensor of monoclinic crystals: CdWO<sub>4</sub>. *Phys. Rev. B* **84**, 195439 (2011).
49. Mock, A. et al. Band-to-band transitions, selection rules, effective mass, and excitonic contributions in monoclinic  $\beta$ -Ga<sub>2</sub>O<sub>3</sub>. *Phys. Rev. B* **96**, 245205 (2017).
50. Falge, H. J. & Otto, A. Dispersion of phonon-like surface polaritons on  $\alpha$ -quartz observed by attenuated total reflection. *Phys. Status Solidi* **56**, 523–534 (1973).
51. Schubert, M. et al. in *Gallium Oxide: Materials Properties, Crystal Growth, and Devices* (eds. Higashiwaki, M. & Fujita, S.) 501–534 (Springer, 2020).

## Acknowledgements

We thank W. Schöllkopf and S. Gewinner (FHI Berlin) for operating the infrared free-electron laser. N.C.P., G.C., M.W. and A.P. thank R. Ernstorfer (TU Berlin) and S. Mährlein (FHI Berlin) for careful reading of the manuscript. N.C.P. acknowledges support by the International Max Planck Research School for Functional Interfaces in Physics and Chemistry. G.H. acknowledges the support from A\*STAR AME Young Individual Research Grants (YIRG, no. A2084c0172). X.N., G.H. and A.A. acknowledge the Office of Naval Research with grant no. N00014-19-1-2011 and the Vannevar Bush Faculty Fellowship. M.S. acknowledges National Science Foundation awards DMR 1808715, DMR 1420645 and OIA-2044049, and Air Force Office of Scientific Research awards FA9550-18-1-0360, FA9550-19-S-0003 and FA9550-21-1-0259, and the Knut and Alice Wallenberg Foundation. J.D.C. was supported by the Office of Naval Research grant no. N00014-18-12107 and J.R.M. by the National Science Foundation, Division of Materials Research grant no. 1904793. T.G.F. was supported by University of Iowa Startup Funding.

## Funding

Open access funding provided by Max Planck Society.

## Author information

## Affiliations

1. Fritz Haber Institute of the Max Planck Society, Berlin, Germany

Nikolai C. Passler, Giulia Carini, Martin Wolf & Alexander Paarmann

2. Photonics Initiative, Advanced Science Research Center, City University of New York, New York, NY, USA

Xiang Ni, Guangwei Hu & Andrea Alù

3. Physics Program, Graduate Center, City University of New York, New York, NY, USA

Andrea Alù

4. Department of Electrical and Computer Engineering, National University of Singapore, Singapore, Singapore

Guangwei Hu

5. Vanderbilt University, Nashville, TN, USA

Joseph R. Matson & Joshua D. Caldwell

6. University of Nebraska, Lincoln, NE, USA

Mathias Schubert

7. The University of Iowa, Iowa City, IA, USA

Thomas G. Folland

## Contributions

N.C.P. and G.C. performed the experiments. N.C.P. and A.P. performed the transfer matrix simulations. N.C.P., T.G.F. and A.P. performed COMSOL simulations. X.N., G.H. and A.A. performed the analytical derivations and the calculation of isofrequency surfaces. All authors contributed to writing the manuscript. A.A., J.D.C., T.G.F. and A.P. oversaw the project. M.S. and J.D.C. initiated the research.

## Corresponding authors

Correspondence to [Andrea Alù](#), [Joshua D. Caldwell](#), [Thomas G. Folland](#) or [Alexander Paarmann](#).

## Ethics declarations

### Competing interests

The authors declare no competing interests.

### Peer review

### Peer review information

*Nature* thanks Raul Freitas, Prineha Narang and the other, anonymous, reviewer for their contribution to the peer review of this work. Peer reviewer reports are available.

### Additional information

**Publisher's note** Springer Nature remains neutral with regard to jurisdictional claims in published maps and institutional affiliations.

### Extended data figures and tables

#### [Extended Data Fig. 1 Frequency-dispersive dielectric permittivity of bGO and surface polariton mode assignment.](#)

**a–e**, Dielectric permittivity tensor elements  $\varepsilon_{xx}$ ,  $\varepsilon_{yy}$ ,  $\varepsilon_{xy}$  ( $=\varepsilon_{yx}$ ) and  $\varepsilon_{zz}$ , respectively, of charge carrier-free bGO at infrared frequencies<sup>6</sup>. **f**, Rotation angle  $\gamma$  (equation (2)) as a function of frequency. **g**, **h**, Diagonal elements  $\varepsilon_{mm}$  and  $\varepsilon_{nn}$  of the frequency-dispersive in-plane permittivity, featuring four distinct reststrahlen bands each. **i**, Non-zero imaginary part of the off-diagonal element  $\text{Im}(\varepsilon_{mn})$ . **j**, Unchanged out-of-plane permittivity  $\varepsilon_{zz}$ . Depending on the combination of positive or negative real parts of  $\varepsilon_{mn}$ ,  $\varepsilon_{nn}$  and  $\varepsilon_{zz}$ , different types of phonon polariton are supported (colour-shaded), such as elliptical SPhPs and type I and type II, in-plane (\parallel) and out-of-plane (\perp) hyperbolic polariton modes, respectively.

#### [Source data](#)

#### [Extended Data Fig. 2 Rotating HShPs on bGO.](#)

**a, b**, Rotation angle  $\gamma$  as a function of frequency. **c, d**, Dispersion of HShPs on the surface of a bulk bGO crystal calculated with the frequency-dispersive permittivity tensor along the (rotating)  $m$  axis (**c**) and the  $n$  axis (**d**), obtained using a transfer matrix method<sup>44</sup>. The four supported polaritons along each axis  $m$  and  $n$  are clearly distinguishable, in perfect agreement with the theoretically calculated polariton dispersion (red dotted lines)<sup>50</sup>. Black horizontal dash-dotted lines mark the frequencies M1–M3 and N1–N4 at which the electric field distribution is plotted. N4 is shown in Fig. 1e,g. **e–g**, Real-space electric fields at the bGO surface at frequencies M1–M3, respectively. **h–j**, The respective two-dimensional Fourier transformation. The fields were calculated using COMSOL Multiphysics<sup>45</sup> (see [Methods](#) for details). **k–m**, Real-space electric fields at frequencies N1–N3, respectively. **n–p**, The respective Fourier transforms. All maps (**e–p**) were calculated using the non-dispersive permittivity tensor (Extended Data Fig. 1a–e), thus showing rotated field patterns with different orientations, depending on the frequency. The thin black and white crosshairs indicate the principal axes of the respective frequency-dispersive coordinate system, its rotation given by  $\gamma$  at the corresponding frequency. Small black circles in **h–j** and **n–p** mark the momentum value of the analytical dispersion in **c** and **d**, respectively.

### [Extended Data Fig. 3 Experimental datasets for bGO and aQ at different gap sizes.](#)

The gap size  $d_{\text{gap}}$  in our Otto geometry setup can be tuned and monitored<sup>43</sup>, enabling control over the excitation efficiency of the polariton modes<sup>44</sup>. Datasets measured for bGO (**a–c**) and for aQ (**d–f**) at three different gap sizes each. For smaller gaps, some modes are overcoupled and their resonance features broadened (such as the mode at  $500 \text{ cm}^{-1}$  in bGO), whereas for larger gaps, some modes are undercoupled and their resonance features too weak to be clearly distinguishable (in particular, the mode at  $725 \text{ cm}^{-1}$  in bGO). The centre gap sizes compromise between these effects. Note that the gap sizes indicated here are the values monitored with a white-light interferometry setup<sup>43</sup>. The fits performed for the datasets shown in Fig. 2, that is, the datasets shown in Extended Data Fig. 3b for bGO and Extended Data Fig. 3e for aQ, however, yielded larger gap sizes of  $8.3 \mu\text{m}$  (bGO) and  $10.4 \mu\text{m}$  (aQ). The offset can be attributed to non-perfect parallel alignment between prism and sample and a lateral offset between the polariton excitation site with the FEL and the white-light spot for the gap measurement.

### [Extended Data Fig. 4 Mapping of the in-plane hyperbolic dispersion in bGO.](#)

Experimental Otto reflectance spectra for various azimuthal angles (**a–i**), each at five different incidence angles  $\theta = 26^\circ, 28^\circ, 30^\circ, 32^\circ$  and  $34^\circ$ . All data were acquired at

constant Otto air gap of  $d_{\text{gap}} \approx 4.0 \mu\text{m}$ . Further data were taken also for  $d_{\text{gap}} \approx 6.0 \mu\text{m}$  but showed the same behaviour at generally reduced polariton resonance amplitudes.

### Extended Data Fig. 5 Q-factor asymmetry along the in-plane hyperbolic dispersion of bGO.

The full width at half maximum (FWHM) of the polariton resonance dips in Extended Data Fig. 4 was extracted, indicative of the (inverse) quality factor (Q-factor) of the polariton. We used the MATLAB function ‘findpeaks’ to extract the FWHM of the resonance dips, which works robustly independent of the specific peak shapes. To account for the effect of different optical coupling efficiencies for different momenta in the Otto geometry at constant air gap<sup>28</sup>, the FWHM should only be compared at the same momentum values. Therefore, we first interpolated the azimuth angle at which the polariton crosses the experimental momenta from Fig. 2f and then interpolated the resonance width extracted for these momenta from Extended Data Fig. 4 to that same azimuth angle. This procedure was performed for each frequency at both sides of the hyperbolic curves (Fig. 2h). Finally, the Q-factor asymmetry is given as the ratio of the FWHM on the left side (smaller azimuth angles) and the right side (larger azimuth angles) of the hyperbolic dispersion for each momentum and frequency. Please note that not all hyperbolic dispersions in Fig. 2h cross all experimental momentum values, which is why the Q-factor asymmetry can only be evaluated at selected momentum values as shown for each frequency. Owing to the larger experimental uncertainty of the FWHM analysis (as compared with the peak position), we refrained from extrapolation during this procedure. Also note that the polariton dip shapes for  $k/k_0 = 1.03$  (incidence angle  $\theta = 26^\circ$ ) are strongly asymmetric (see Extended Data Fig. 4), such that the quality factor analysis is not very reliable there, explaining the outlier for which the Q-factor asymmetry is  $<1$ . For all other cases, we find values clearly  $>1$ , that is, we find consistently that the Q-factor is smaller on the left side than on the right side of the hyperbolic dispersion. Also, the data show a trend of increasing asymmetry with increasing momenta, that is, further out in the dispersion. Both effects are in very good agreement with the theoretical predictions (Fig. 3).

### Extended Data Fig. 6 Active tuning of the propagation direction of HShPs in bGO.

Rotation angle  $\gamma$  (equation (2)) calculated as a function of doping concentration  $N$  (in  $\text{cm}^{-3}$ ), assuming a Drude contribution with anisotropic charge carrier mobility,  $\mu_x = 296 \text{ cm}^2 \text{ V}^{-1} \text{ s}^{-1}$ ,  $\mu_y = \mu_z = 37 \text{ cm}^2 \text{ V}^{-1} \text{ s}^{-1}$ . (Literature values of  $\mu$  in bGO feature a large variance<sup>51</sup>. We assume here strong anisotropy of the charge carrier mobility to emphasize the rotation mechanism.) Clearly, between the TO frequencies at which the HShPs disperse, the rotation angle  $\gamma$  is strongly dependent on the doping

concentration, enabling active tuning of the propagation direction of the supported polariton modes. Note that, for an isotropic Drude contribution, on the other hand, equation (2) predicts no rotation of the propagation direction as a function of doping concentration.

## **Extended Data Fig. 7 Group velocity analysis for hyperbolic shear polaritons.**

Analytical solutions of isofrequency contours of lossless bGO for  $k_z = 0$  (see Fig. 1c) are used to numerically evaluate gradients with respect to frequency along the curves. The resulting group velocity ( $v_g$ ) distribution is shown as arrows along the isofrequency curves. The maximum value near the base of the hyperbola for  $\omega = 718$  cm<sup>-1</sup> is  $|v_g| \approx 0.038c_0$ , in which  $c_0$  is the speed of light in vacuum. The continuous rotation of the hyperbola axis with frequency (see main text) results in a pronounced asymmetry of the group velocity distribution: the peak of  $|v_g|$  is shifted off the base of the hyperbola (a) and  $|v_g|$  is notably different along the two arms of the hyperbola (b). This asymmetric distribution of  $|v_g|$  certainly contributes greatly to the tilted wavefronts of HShPs observed in the main text. The asymmetric distribution of  $|v_g|$  around the base of the hyperbola is in excellent agreement with the results shown in Fig. 2j.

## **Supplementary information**

### **Peer Review File**

### **Source data**

#### **Source Data Fig. 1**

#### **Source Data Fig. 2**

#### **Source Data Fig. 3**

### **Rights and permissions**

**Open Access** This article is licensed under a Creative Commons Attribution 4.0 International License, which permits use, sharing, adaptation, distribution and reproduction in any medium or format, as long as you give appropriate credit to the original author(s) and the source, provide a link to the Creative Commons license, and

indicate if changes were made. The images or other third party material in this article are included in the article's Creative Commons license, unless indicated otherwise in a credit line to the material. If material is not included in the article's Creative Commons license and your intended use is not permitted by statutory regulation or exceeds the permitted use, you will need to obtain permission directly from the copyright holder. To view a copy of this license, visit <http://creativecommons.org/licenses/by/4.0/>.

## Reprints and Permissions

## About this article

### Cite this article

Passler, N.C., Ni, X., Hu, G. *et al.* Hyperbolic shear polaritons in low-symmetry crystals. *Nature* **602**, 595–600 (2022). <https://doi.org/10.1038/s41586-021-04328-y>

- Received: 25 May 2021
- Accepted: 07 December 2021
- Published: 23 February 2022
- Issue Date: 24 February 2022
- DOI: <https://doi.org/10.1038/s41586-021-04328-y>

### Share this article

Anyone you share the following link with will be able to read this content:

[Get shareable link](#)

Sorry, a shareable link is not currently available for this article.

[Copy to clipboard](#)

Provided by the Springer Nature SharedIt content-sharing initiative

---

This article was downloaded by **calibre** from <https://www.nature.com/articles/s41586-021-04328-y>

- Article
- [Published: 23 February 2022](#)

# Evidence for a single-layer van der Waals multiferroic

- [Qian Song<sup>1,2</sup>](#) na1,
- [Connor A. Occhialini](#) [ORCID: orcid.org/0000-0002-2133-5155](#)<sup>1</sup> na1,
- [Emre Ergeçen](#)<sup>1</sup> na1,
- [Batyry Ilyas](#) [ORCID: orcid.org/0000-0002-5135-2378](#)<sup>1</sup> na1,
- [Danila Amoroso<sup>3,4</sup>](#),
- [Paolo Barone](#) [ORCID: orcid.org/0000-0001-7222-8627](#)<sup>5</sup>,
- [Jesse Kapeghian](#)<sup>6</sup>,
- [Kenji Watanabe](#) [ORCID: orcid.org/0000-0003-3701-8119](#)<sup>7</sup>,
- [Takashi Taniguchi](#) [ORCID: orcid.org/0000-0002-1467-3105](#)<sup>8</sup>,
- [Antia S. Botana](#) [ORCID: orcid.org/0000-0001-5973-3039](#)<sup>6</sup>,
- [Silvia Picozzi](#)<sup>3</sup>,
- [Nuh Gedik](#) [ORCID: orcid.org/0000-0002-6394-4987](#)<sup>1</sup> &
- [Riccardo Comin](#) [ORCID: orcid.org/0000-0002-1069-9973](#)<sup>1</sup>

[Nature](#) volume 602, pages 601–605 (2022)

- 2419 Accesses
- 92 Altmetric
- [Metrics details](#)

## Subjects

- [Ferroelectrics and multiferroics](#)
- [Magnetic properties and materials](#)

# Abstract

Multiferroic materials have attracted wide interest because of their exceptional static<sup>1,2,3</sup> and dynamical<sup>4,5,6</sup> magnetoelectric properties. In particular, type-II multiferroics exhibit an inversion-symmetry-breaking magnetic order that directly induces ferroelectric polarization through various mechanisms, such as the spin-current or the inverse Dzyaloshinskii–Moriya effect<sup>3,7</sup>. This intrinsic coupling between the magnetic and dipolar order parameters results in high-strength magnetoelectric effects<sup>3,8</sup>. Two-dimensional materials possessing such intrinsic multiferroic properties have been long sought for to enable the harnessing of magnetoelectric coupling in nanoelectronic devices<sup>1,9,10</sup>. Here we report the discovery of type-II multiferroic order in a single atomic layer of the transition-metal-based van der Waals material NiI<sub>2</sub>. The multiferroic state of NiI<sub>2</sub> is characterized by a proper-screw spin helix with given handedness, which couples to the charge degrees of freedom to produce a chirality-controlled electrical polarization. We use circular dichroic Raman measurements to directly probe the magneto-chiral ground state and its electromagnon modes originating from dynamic magnetoelectric coupling. Combining birefringence and second-harmonic-generation measurements with theoretical modelling and simulations, we detect a highly anisotropic electronic state that simultaneously breaks three-fold rotational and inversion symmetry, and supports polar order. The evolution of the optical signatures as a function of temperature and layer number surprisingly reveals an ordered magnetic polar state that persists down to the ultrathin limit of monolayer NiI<sub>2</sub>. These observations establish NiI<sub>2</sub> and transition metal dihalides as a new platform for studying emergent multiferroic phenomena, chiral magnetic textures and ferroelectricity in the two-dimensional limit.

This is a preview of subscription content

## Access options

Subscribe to Nature+

Get immediate online access to the entire Nature family of 50+ journals

\$29.99

monthly

[Subscribe](#)

Subscribe to Journal

Get full journal access for 1 year

\$199.00

only \$3.90 per issue

[Subscribe](#)

All prices are NET prices.

VAT will be added later in the checkout.

Tax calculation will be finalised during checkout.

Buy article

Get time limited or full article access on ReadCube.

\$32.00

[Buy](#)

All prices are NET prices.

### **Additional access options:**

- [Log in](#)
- [Learn about institutional subscriptions](#)

**Fig. 1: Crystal structure, magnetic order and optical characterization of bulk NiI<sub>2</sub>.**

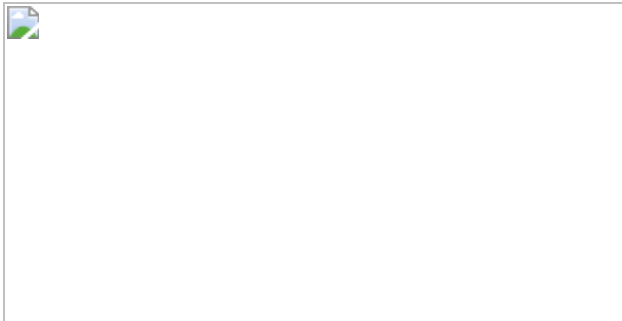


**Fig. 2: Birefringence and SHG in few- and single-layer NiI<sub>2</sub>.**

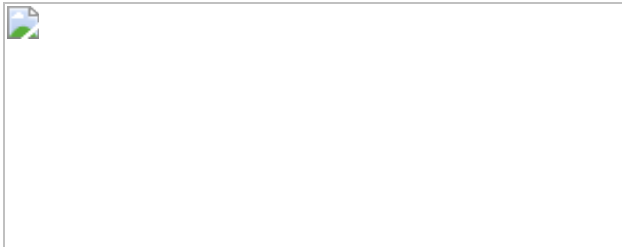


**Fig. 3: Layer-dependent magnetic transition temperatures and the ground state of single-layer NiI<sub>2</sub>.**



## Data availability

The datasets generated during and/or analysed during the current study are available from the corresponding author on reasonable request.

## References

1. Matsukura, F., Tokura, Y. & Ohno, H. Control of magnetism by electric fields. *Nat. Nanotechnol.* **10**, 209–220 (2015).
2. Kurumaji, T. et al. Magnetoelectric responses induced by domain rearrangement and spin structural change in triangular-lattice helimagnets  $\text{NiI}_2$  and  $\text{CoI}_2$ . *Phys. Rev. B* **87**, 014429 (2013).
3. Tokura, Y., Seki, S. & Nagaosa, N. Multiferroics of spin origin. *Rep. Prog. Phys.* **77**, 076501 (2014).
4. Pimenov, A. et al. Possible evidence for electromagnons in multiferroic manganites. *Nat. Phys.* **2**, 97–100 (2006).
5. Rovillain, P. et al. Magnetoelectric excitations in multiferroic  $\text{TbMnO}_3$  by Raman scattering. *Phys. Rev. B* **81**, 054428 (2010).
6. Kibayashi, S., Takahashi, Y., Seki, S. & Tokura, Y. Magnetochiral dichroism resonant with electromagnons in a helimagnet. *Nat. Commun.* **5**, 4583 (2014).
7. Khomskii, D. Classifying multiferroics: mechanisms and effects. *Physics* **2**, 20 (2009).
8. Spaldin, N. A. & Ramesh, R. Advances in magnetoelectric multiferroics. *Nat. Mater.* **18**, 203–212 (2019).
9. Huang, B. et al. Electrical control of 2D magnetism in bilayer  $\text{CrI}_3$ . *Nat. Nanotechnol.* **13**, 544–548 (2018).
10. Jiang, S., Li, L., Wang, Z., Mak, K. F. & Shan, J. Controlling magnetism in 2D  $\text{CrI}_3$  by electrostatic doping. *Nat. Nanotechnol.* **13**, 549–553 (2018).
11. Gong, C. et al. Discovery of intrinsic ferromagnetism in two-dimensional van der Waals crystals. *Nature* **546**, 265–269 (2017).
12. Huang, B. et al. Layer-dependent ferromagnetism in a van der Waals crystal down to the monolayer limit. *Nature* **546**, 270–273 (2017).

13. Burch, K. S., Mandrus, D. & Park, J. G. Magnetism in two-dimensional van der Waals materials. *Nature* **563**, 47–52 (2018).
14. Mak, K. F., Shan, J. & Ralph, D. C. Probing and controlling magnetic states in 2D layered magnetic materials. *Nat. Rev. Phys.* **1**, 646–661 (2019).
15. Astrov, D. N. The magnetoelectric effect in antiferromagnetics. *Sov. Phys. – JETP* **11**, 708 (1960).
16. Rado, G. T. & Folen, V. J. Observation of the magnetically induced magnetoelectric effect and evidence for antiferromagnetic domains. *Phys. Rev. Lett.* **7**, 310–311 (1961).
17. Newnham, R. E., Kramer, J. J., Schulze, W. A. & Cross, L. E. Magnetoferroelectricity in  $\text{Cr}_2\text{BeO}_4$ . *J. Appl. Phys.* **49**, 6088–6091 (1978).
18. Kimura, T. et al. Magnetic control of ferroelectric polarization. *Nature* **426**, 55–58 (2003).
19. McGuire, M. A. Crystal and magnetic structures in layered, transition metal dihalides and trihalides. *Crystals* **7**, 121 (2017).
20. Lai, Y. et al. Two-dimensional ferromagnetism and driven ferroelectricity in van der Waals  $\text{CuCrP}_2\text{S}_6$ . *Nanoscale* **11**, 5163–5170 (2019).
21. Botana, A. S. & Norman, M. R. Electronic structure and magnetism of transition metal dihalides: bulk to monolayer. *Phys. Rev. Mater.* **3**, 44001 (2019).
22. Amoroso, D., Barone, P. & Picozzi, S. Spontaneous skyrmionic lattice from anisotropic symmetric exchange in a Ni-halide monolayer. *Nat. Commun.* **11**, 5784 (2020).
23. Pollini, I., Thomas, J. & Lenselink, A. Optical properties of layered transition-metal iodides. *Phys. Rev. B* **30**, 2140–2148 (1984).

24. Ju, H. et al. Possible persistence of multiferroic order down to bilayer limit of van der Waals material NiI<sub>2</sub>. *Nano Lett.* **21**, 5126–5132 (2021).
25. Kurumaji, T. Spiral spin structures and skyrmions in multiferroics. *Phys. Sci. Rev.* <https://doi.org/10.1515/psr-2019-0016> (2020).
26. Amoroso, D., Barone, P. & Picozzi, S. Interplay between single-ion and two-ion anisotropies in frustrated 2D semiconductors and tuning of magnetic structures topology. *Nanomaterials* **11**, 1873 (2021).
27. Friedt, J. M., Sanchez, J. P. & Shenoy, G. K. Electronic and magnetic properties of metal diiodides MI<sub>2</sub> (M = V, Cr, Mn, Fe, Co, Ni, and Cd) from <sup>129</sup>I Mössbauer spectroscopy. *J. Chem. Phys.* **65**, 5093–5102 (1976).
28. Kuindersma, S., Sanchez, J. & Haas, C. Magnetic and structural investigations on NiI<sub>2</sub> and CoI<sub>2</sub>. *Phys. B+C* **111**, 231–248 (1981).
29. Liu, H. et al. Vapor deposition of magnetic van der Waals NiI<sub>2</sub> crystals. *ACS Nano* **14**, 10544–10551 (2020).
30. Kumdersma, S. R., Boudeijn, P. R. & Haas, C. Near infrared d-d transitions of NiI<sub>2</sub>, CdI<sub>2</sub>:Ni<sup>2+</sup>, and CoI<sub>2</sub>. *Phys. Stat. Sol. (b)* **108**, 187–194 (1981).
31. Xiao, J. et al. Intrinsic two-dimensional ferroelectricity with dipole locking. *Phys. Rev. Lett.* **120**, 227601 (2018).
32. Cenker, J. et al. Direct observation of two-dimensional magnons in atomically thin CrI<sub>3</sub>. *Nat. Phys.* **17**, 20–25 (2021).
33. Jin, W. et al. Raman fingerprint of two terahertz spin wave branches in a two-dimensional honeycomb Ising ferromagnet. *Nat. Commun.* **9**, 5122 (2018).
34. Deng, Y. et al. Gate-tunable room-temperature ferromagnetism in two-dimensional Fe<sub>3</sub>GeTe<sub>2</sub>. *Nature* **563**, 94–99 (2018).

35. Sivadas, N., Okamoto, S., Xu, X., Fennie, C. J. & Xiao, D. Stacking-dependent magnetism in bilayer CrI<sub>3</sub>. *Nano Lett.* **18**, 7658–7664 (2018).
36. Akram, M. et al. Moiré skyrmions and chiral magnetic phases in twisted CrX<sub>3</sub> (X = I, Br, and Cl) bilayers. *Nano Lett.* **21**, 6633–6639 (2021).
37. Nguyen, T. P. T., Yamauchi, K., Oguchi, T., Amoroso, D. & Picozzi, S. Electric-field tuning of the magnetic properties of bilayer VI<sub>3</sub>: a first-principles study. *Phys. Rev. B* **104**, 014414 (2021).
38. Xiang, H. J., Kan, E. J., Zhang, Y., Whangbo, M.-H. & Gong, X. G. General theory for the ferroelectric polarization induced by spin-spiral order. *Phys. Rev. Lett.* **107**, 157202 (2011).
39. Prayitno, T. B. Controlling phase transition in monolayer metal diiodides XI<sub>2</sub> (X: Fe, Co, and Ni) by carrier doping. *J. Phys. Condens. Matter* **33**, 335803 (2021).
40. Narayan, A., Cano, A., Balatsky, A. V. & Spaldin, N. A. Multiferroic quantum criticality. *Nat. Mater.* **18**, 223–228 (2019).
41. Zomer, P., Guimarães, M., Brant, J., Tombros, N. & Van Wees, B. Fast pick up technique for high quality heterostructures of bilayer graphene and hexagonal boron nitride. *Appl. Phys. Lett.* **105**, 013101 (2014).
42. Kresse, G. & Furthmüller, J. Efficient iterative schemes for ab initio total-energy calculations using a plane-wave basis set. *Phys. Rev. B* **54**, 11169–11186 (1996).
43. Kresse, G. & Joubert, D. From ultrasoft pseudopotentials to the projector augmented-wave method. *Phys. Rev. B* **59**, 1758–1775 (1999).
44. Blaha, P. et al. WIEN2k: an APW+lo program for calculating the properties of solids. *J. Chem. Phys.* **152**, 074101 (2020).

45. Perdew, J. P., Burke, K. & Ernzerhof, M. Generalized gradient approximation made simple. *Phys. Rev. Lett.* **77**, 3865–3868 (1996).
46. Rohrbach, A., Hafner, J. & Kresse, G. Electronic correlation effects in transition-metal sulfides. *J. Phys. Condens. Matter* **15**, 979–996 (2003).
47. Liechtenstein, A. I., Anisimov, V. I. & Zaanen, J. Density-functional theory and strong interactions: Orbital ordering in Mott-Hubbard insulators. *Phys. Rev. B* **52**, R5467–R5470 (1995).
48. Perdew, J. P. et al. Restoring the density-gradient expansion for exchange in solids and surfaces. *Phys. Rev. Lett.* **100**, 136406 (2008).
49. Becke, A. D. On the large-gradient behavior of the density functional exchange energy. *J. Chem. Phys.* **85**, 7184–7187 (1986).

## Acknowledgements

Q.S., C.A.O. and R.C. acknowledge support from the US Department of Energy, BES under Award No. DE-SC0019126 (materials synthesis and characterization), the National Science Foundation under grant No. DMR-1751739 (optical measurements) and the STC Center for Integrated Quantum Materials, NSF grant No. DMR-1231319 (device fabrication). E.E., B.I. and N.G. acknowledge support from the US Department of Energy, BES DMSE (data taking and analysis) and Gordon and Betty Moore Foundation’s EPiQS Initiative grant no. GBMF9459 (instrumentation). J.K. and A.S.B. acknowledge NSF grant No. DMR-1904716 and the ASU Research Computing Center for high-performance computing resources. D.A. and S.P. acknowledge support by the Nanoscience Foundries and Fine Analysis (NFFA-MIUR Italy) project. P.B. and S.P. acknowledge financial support from the Italian Ministry for Research and Education through PRIN-2017 projects ‘Tuning and understanding Quantum phases in 2D materials—Quantum 2D’ (IT-MIUR grant No. 2017Z8TS5B) and ‘TWEET: Towards ferroelectricity in two dimensions’ (IT-MIUR grant No. 2017YCTB59), respectively. D.A., P.B. and S.P. also acknowledge high-performance computing systems operated

by CINECA (IsC722DFmF, IsC80-Em2DvdWd, IsC88-FeCoSMO and IsB21-IRVISH projects) and computing resources at the Pharmacy Department, University of Chieti-Pescara, and thank L. Storchi for his technical support.

## Author information

### Author notes

1. These authors contributed equally: Qian Song, Connor A. Occhialini, Emre Ergeçen, Batyr Ilyas

### Affiliations

1. Department of Physics, Massachusetts Institute of Technology, Cambridge, MA, USA

Qian Song, Connor A. Occhialini, Emre Ergeçen, Batyr Ilyas, Nuh Gedik & Riccardo Comin

2. Department of Material Science and Engineering, Massachusetts Institute of Technology, Cambridge, MA, USA

Qian Song

3. Consiglio Nazionale delle Ricerche CNR-SPIN, c/o Università degli Studi ‘G. D’Annunzio’, Chieti, Italy

Danila Amoroso & Silvia Picozzi

4. NanoMat/Q-mat/CESAM, Université de Liège, Liège, Belgium

Danila Amoroso

5. Consiglio Nazionale delle Ricerche CNR-SPIN, Area della Ricerca di Tor Vergata, Rome, Italy

Paolo Barone

6. Department of Physics, Arizona State University, Tempe, AZ, USA

Jesse Kapeghian & Antia S. Botana

7. Research Center for Functional Materials, National Institute for Materials Science, Tsukuba, Japan

Kenji Watanabe

8. International Center for Materials Nanoarchitectonics, National Institute for Materials Science, Tsukuba, Japan

Takashi Taniguchi

## Contributions

Q.S. and R.C. conceived the project. Q.S. synthesized the NiI<sub>2</sub> samples. Q.S. and C.A.O. performed the Raman and birefringence measurements supervised by R.C. E.E. and B.I. performed the SHG measurements supervised by N.G. T.T. and K.W. provided and characterized the bulk hBN crystals. D.A., A.S.B. and J.K. performed the first-principles calculations. P.B. and D.A. performed the MC simulations, and discussed the results with S.P. All authors contributed to the writing of the manuscript.

## Corresponding author

Correspondence to [Riccardo Comin](#).

## Ethics declarations

## Competing interests

The authors declare no competing interests.

## Peer review

## Peer review information

*Nature* thanks Masakazu Matsubara and the other, anonymous, reviewers for the peer review of this work. Peer reviewer reports are available.

## Additional information

**Publisher's note** Springer Nature remains neutral with regard to jurisdictional claims in published maps and institutional affiliations.

## Extended data figures and tables

### [Extended Data Fig. 1 X-ray and electron diffraction of NiI<sub>2</sub> crystals.](#)

**a**, X-ray diffraction of a CVT-grown NiI<sub>2</sub> single crystal along the *c*-axis. **b**, X-ray powder diffraction of CVT-grown NiI<sub>2</sub>. **c**, An optical image of a 7 nm PVD grown NiI<sub>2</sub> flake transferred onto a SiN<sub>x</sub> membrane. **d**, The electron diffraction pattern of the PVD grown NiI<sub>2</sub> flake shown in **c**, using a transmission electron microscope.

### [Extended Data Fig. 2 Linear dichroism and birefringence-induced polarization rotation measurements in bulk NiI<sub>2</sub>.](#)

**a**, Polarized microscopy image of bulk NiI<sub>2</sub>. The positions where the optical measurements were performed are labelled as Domain I-III. **b**, Comparison of the temperature-dependent birefringence-induced polarization rotation (top) and linear dichroism (bottom) on Domain I. **c**, Angular-dependent linear dichroism measurements from the three distinct domains identified in **a**. Radial lines indicate the crystallographic **a**-axes determined from the edges of the as-grown PVD sample. **d**, Schematics of the domains as identified from AD-LD measurements in **c**, denoting the local *C*<sub>2</sub> axis orientation, the polar vector **P** and the in-plane component of the helimagnetic ordering vector **Q**.

## Extended Data Fig. 3 Wavelength-dependent Second Harmonic Generation of NiI<sub>2</sub>.

Rotational anisotropy SHG (RA-SHG), fits to nonlinear tensor elements and their temperature dependence on a single domain CVT grown bulk NiI<sub>2</sub> using **a–c**, 826 nm laser, and **d–f**, 991 nm laser. The RA-SHG traces obtained with 826 nm can only be fit with a combination of electric dipole (ED) and magnetic dipole (MD) radiation, whereas the RA-SHG traces obtained with 991 nm only exhibit ED component. **g, h**, RA-SHG on PVD grown bulk NiI<sub>2</sub> samples shows the same signatures as the CVT grown samples. **i**, SHG imaging of the PVD sample at 15 K. The red circle shows the single domain region where the RA-SHG was taken.

## Extended Data Fig. 4 Temperature-dependent polarized Raman spectra of bulk NiI<sub>2</sub>.

**a**, Raman data in the cross-polarized XY channel from 30 K to 300 K. **b**, Comparison of the cross-polarized (XY) and parallel-polarized (XX) channels at high and low temperature. **c**, Circularly polarized Raman spectra at 30 K on domain I and domain II regions for  $\sigma^+/\sigma^-$  incident polarization (top) and the net ROA ( $\sigma^+-\sigma^-$ ) (bottom).

## Extended Data Fig. 5 Angular Resolved Polarized Raman Spectroscopy (ARPRS) in cross-polarized (XY) configuration.

**a, b**, The ARPRS polar plots of the 31 cm<sup>-1</sup> and 37 cm<sup>-1</sup> modes appearing in the multiferroic phase. Neither agrees with a pure phonon or magnon mode, suggesting they may be consistent with electromagnons. **c, d**, The 80 cm<sup>-1</sup> peak is composed of two phonons below  $T_{N,2}$ , one at 79.9 cm<sup>-1</sup> and the other at 80.2 cm<sup>-1</sup>. These closely-spaced phonon modes display out-of-phase modulation with respect to the incident linear polarization and both display an  $E_g$  symmetry with respect to the high-temperature  $\bar{R}\bar{3}m$  phase. **e, f**, The 120.8 cm<sup>-1</sup> and 168.8 cm<sup>-1</sup> are magnon modes. Red lines: ARPRS fits to the Raman tensors for different mode symmetries.

## Extended Data Fig. 6 Bulk photovoltaic effect (BPE) in bulk NiI<sub>2</sub>.

**a**, Optical image of the BPE device. A PVD grown bulk-like NiI<sub>2</sub> flake was transferred across a sapphire gap, bridging two gold pads as electrodes. The electric field was applied between the electrodes and in a direction nearly parallel to the *a*-axis, while the magnetic field was applied perpendicular to the electric field in plane. **b**, The electric field dependence of the photocurrent at 30 K, in the multiferroic phase and at 100 K, in the paramagnetic phase, reveals the presence of a polarization-induced internal electric field the multiferroic phase. **c**, The position dependence of the photocurrent along the dashed line in **a**, under zero bias shows a major contribution of the photocurrent from the NiI<sub>2</sub> between the electrodes. **d**, The temperature dependence of the zero-bias photocurrent shows a strong enhancement in the multiferroic phase. **e**, The external magnetic field increased the zero-bias photocurrent by 10–15%, which we ascribe to an increase of the electric polarization from magnetoelectric coupling. Linearly polarized 532 nm light (0.3 mW power) was used in the BPE measurement.

## Extended Data Fig. 7 Cross-polarization images of the bulk, 1- and 2-layer NiI<sub>2</sub>.

Temperature-dependent histogram plots of the polarization contrast images for **a**, bulk, **c**, 1-layer region and **e**, 2-layer region. The upper-left images in **b**, **d**, **f** show optical images of bulk, 1- and 2-layer NiI<sub>2</sub> flakes, respectively. Subsequent images depict the temperature-dependent polarization contrast images for key temperatures. The raw cross-polarization images at various temperatures across the multiferroic transition provide signatures of the domain dynamics, explaining the spatial inhomogeneity of the transition temperature identified through polarization rotation measurements. The domain texture vanishes in **d**, 1-layer near 20 K, and in **f**, 2-layer near 35 K, consistent with polarization rotation measurements (Fig. 2d).

## Extended Data Fig. 8 Temperature dependent Second Harmonic Generation imaging of the single-layer NiI<sub>2</sub> crystals.

**a, b**, Optical images of the region where the SHG imaging was performed. **c**, Integrated SHG counts on three single-layer NiI<sub>2</sub> crystals show a transition around 20 K, which is consistent with the polarization rotation measurement. **d**, Temperature dependent SHG imaging of the rectangular region in **a** using 780 nm excitation. **e**, Temperature dependent SHG imaging of the region in **b** using 991 nm laser. Colorbar: SHG counts.

**Extended Data Fig. 9 Temperature dependent Raman Spectroscopy of two- and three-layer NiI<sub>2</sub> in cross-polarized (XY) configuration.**

The soft modes at around 38 cm<sup>-1</sup> in **a**, 2-layer and **b**, 3-layer built up below 25 K and 35 K respectively, which are consistent with the transition temperature measured from polarization rotation and SHG.

**Extended Data Fig. 10 Atomic Force Microscopy and additional polarization rotation measurements on few-layer NiI<sub>2</sub> crystals.**

**a–c**, Wide-field optical images of one- to four-layer NiI<sub>2</sub> samples used in the optical measurements. **d–h**, Corresponding AFM maps of the region shown in the optical images. **i–k**, Temperature dependent polarization rotation measurements on one- to four-layer samples in different domain regions.

## Supplementary information

**This file contains Supplementary Text; Supplementary equations and Supplementary References**

**Peer Review Information**

## Rights and permissions

## [Reprints and Permissions](#)

## About this article

### Cite this article

Song, Q., Occhialini, C.A., Ergeçen, E. *et al.* Evidence for a single-layer van der Waals multiferroic. *Nature* **602**, 601–605 (2022).  
<https://doi.org/10.1038/s41586-021-04337-x>

- Received: 24 May 2021
- Accepted: 10 December 2021
- Published: 23 February 2022
- Issue Date: 24 February 2022
- DOI: <https://doi.org/10.1038/s41586-021-04337-x>

### Share this article

Anyone you share the following link with will be able to read this content:

[Get shareable link](#)

Sorry, a shareable link is not currently available for this article.

[Copy to clipboard](#)

Provided by the Springer Nature SharedIt content-sharing initiative

---

This article was downloaded by **calibre** from <https://www.nature.com/articles/s41586-021-04337-x>

- Article
- [Published: 23 February 2022](#)

# Free-standing homochiral 2D monolayers by exfoliation of molecular crystals

- [Jinqiao Dong](#)<sup>1,2</sup> na1,
- [Lingmei Liu](#)<sup>3</sup> na1,
- [Chunxia Tan](#)<sup>1</sup>,
- [Qisong Xu](#) ORCID: [orcid.org/0000-0002-1337-543X](https://orcid.org/0000-0002-1337-543X)<sup>4</sup>,
- [Jiachen Zhang](#)<sup>5</sup>,
- [Zhiwei Qiao](#)<sup>4</sup>,
- [Dandan Chu](#) ORCID: [orcid.org/0000-0002-2912-6390](https://orcid.org/0000-0002-2912-6390)<sup>1</sup>,
- [Yan Liu](#) ORCID: [orcid.org/0000-0002-7560-519X](https://orcid.org/0000-0002-7560-519X)<sup>1</sup>,
- [Qun Zhang](#) ORCID: [orcid.org/0000-0002-5777-9276](https://orcid.org/0000-0002-5777-9276)<sup>5</sup>,
- [Jianwen Jiang](#) ORCID: [orcid.org/0000-0003-1310-9024](https://orcid.org/0000-0003-1310-9024)<sup>4</sup>,
- [Yu Han](#) ORCID: [orcid.org/0000-0003-1462-1118](https://orcid.org/0000-0003-1462-1118)<sup>6</sup>,
- [Anthony P. Davis](#) ORCID: [orcid.org/0000-0001-5213-624X](https://orcid.org/0000-0001-5213-624X)<sup>2</sup> &
- [Yong Cui](#) ORCID: [orcid.org/0000-0002-7921-8197](https://orcid.org/0000-0002-7921-8197)<sup>1</sup>

*Nature* volume **602**, pages 606–611 (2022)

- 3625 Accesses
- 44 Altmetric
- [Metrics details](#)

## Subjects

- [Supramolecular chemistry](#)
- [Two-dimensional materials](#)

## Abstract

Two-dimensional materials with monolayer thickness and extreme aspect ratios are sought for their high surface areas and unusual physicochemical properties<sup>1</sup>. Liquid exfoliation is a straightforward and scalable means of accessing such materials<sup>2</sup>, but has been restricted to sheets maintained by strong covalent, coordination or ionic interactions<sup>3,4,5,6,7,8,9,10</sup>. The exfoliation of molecular crystals, in which repeat units are held together by weak non-covalent bonding, could generate a greatly expanded range of two-dimensional crystalline materials with diverse surfaces and structural features. However, at first sight, these weak forces would seem incapable of supporting such intrinsically fragile morphologies. Against this expectation, we show here that crystals composed of discrete supramolecular coordination complexes can be exfoliated by sonication to give free-standing monolayers approximately 2.3 nanometres thick with aspect ratios up to approximately 2,500:1, sustained purely by apolar intermolecular interactions. These nanosheets are characterized by atomic force microscopy and high-resolution transmission electron microscopy, confirming their crystallinity. The monolayers possess complex chiral surfaces derived partly from individual supramolecular coordination complex components but also from interactions with neighbours. In this respect, they represent a distinct type of material in which molecular components are all equally exposed to their environment, as if in solution, yet with properties arising from cooperation between molecules, because of crystallinity. This unusual nature is reflected in the molecular recognition properties of the materials, which bind carbohydrates with strongly enhanced enantiodiscrimination relative to individual molecules or bulk three-dimensional crystals.

This is a preview of subscription content

## Access options

Subscribe to Nature+

Get immediate online access to the entire Nature family of 50+ journals

\$29.99

monthly

[Subscribe](#)

Subscribe to Journal

Get full journal access for 1 year

\$199.00

only \$3.90 per issue

[Subscribe](#)

All prices are NET prices.

VAT will be added later in the checkout.

Tax calculation will be finalised during checkout.

Buy article

Get time limited or full article access on ReadCube.

\$32.00

[Buy](#)

All prices are NET prices.

### **Additional access options:**

- [Log in](#)
- [Learn about institutional subscriptions](#)

**Fig. 1: Top-down fabrication of chiral 2D monolayer nanosheets of supramolecular metallacycles.**



**Fig. 2: HR-TEM of chiral 2D nanosheets of 1–3.**

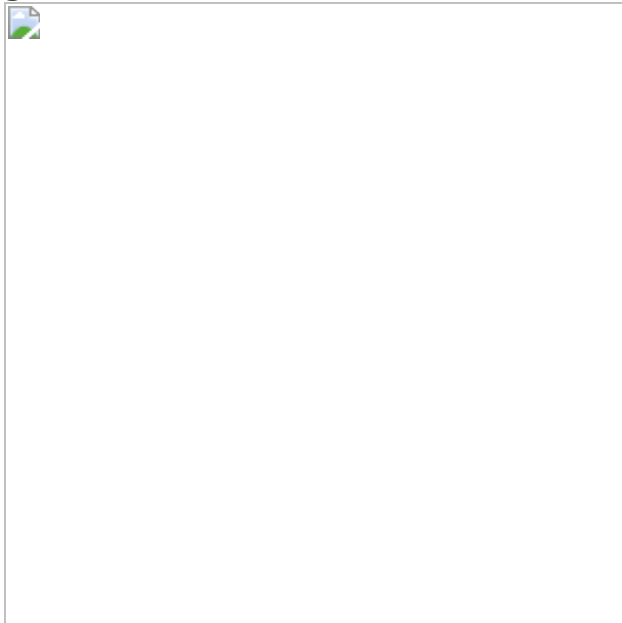


**Fig. 3: CTF-corrected HR-TEM imaging.**



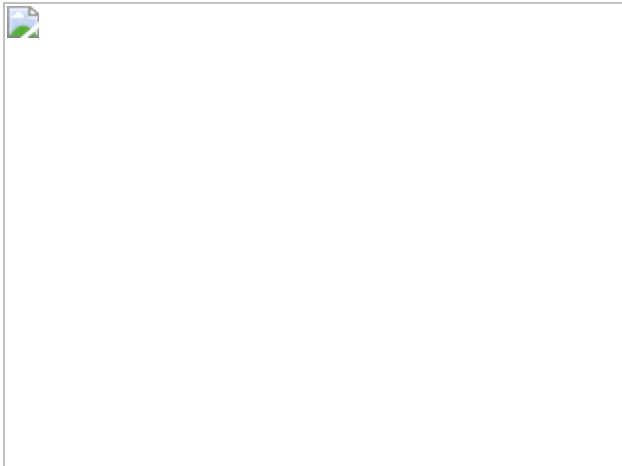
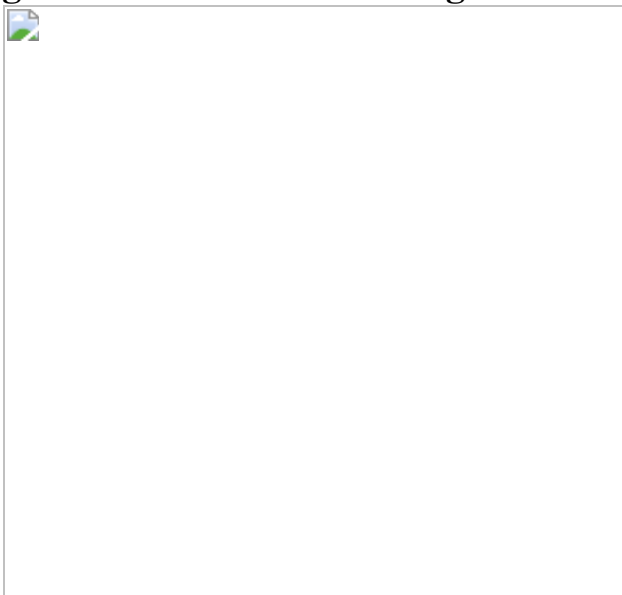


**Fig. 4: Enantioselective recognition of chiral 2D monolayer nanosheets.**



## Data availability

The data that support the findings of this study are available from the corresponding authors.

## References

1. Tan, C. et al. Recent advances in ultrathin two-dimensional nanomaterials. *Chem. Rev.* **117**, 6225–6331 (2017).

2. Nicolosi, V., Chhowalla, M., Kanatzidis, M. G., Strano, M. S. & Coleman, J. N. Liquid exfoliation of layered materials. *Science* **340**, 1226419 (2013).
3. Hernandez, Y. et al. High-yield production of graphene by liquid-phase exfoliation of graphite. *Nat. Nanotechnol.* **3**, 563–568 (2008).
4. Kory, M. J. et al. Gram-scale synthesis of two-dimensional polymer crystals and their structure analysis by X-ray diffraction. *Nat. Chem.* **6**, 779–784 (2014).
5. Coleman, J. N. et al. Two-dimensional nanosheets produced by liquid exfoliation of layered materials. *Science* **331**, 568–571 (2011).
6. Li, J. et al. Printable two-dimensional superconducting monolayers. *Nat. Mater.* **20**, 181–187 (2021).
7. Puthirath Balan, A. et al. Exfoliation of a non-van der Waals material from iron ore hematite. *Nat. Nanotechnol.* **13**, 602–609 (2018).
8. Varoon, K. et al. Dispersible exfoliated zeolite nanosheets and their application as a selective membrane. *Science* **334**, 72–75 (2011).
9. Peng, Y. et al. Metal-organic framework nanosheets as building blocks for molecular sieving membranes. *Science* **346**, 1356–1359 (2014).
10. Nicks, J., Boer, S. A., White, N. G. & Foster, J. A. Monolayer nanosheets formed by liquid exfoliation of charge-assisted hydrogen-bonded frameworks. *Chem. Sci.* **12**, 3322–3327 (2021).
11. Novoselov, K. S. et al. Electric field effect in atomically thin carbon films. *Science* **306**, 666–669 (2004).
12. Huang, P. Y. et al. Imaging atomic rearrangements in two-dimensional silica glass: watching silica's dance. *Science* **342**, 224–227 (2013).
13. Wasio, N. A. et al. Self-assembly of hydrogen-bonded two-dimensional quasicrystals. *Nature* **507**, 86–89 (2014).

14. Suzuki, Y. et al. Self-assembly of coherently dynamic, auxetic, two-dimensional protein crystals. *Nature* **533**, 369–373 (2016).
15. Xing, L. B., Peng, Z. T., Li, W. T. & Wu, K. On controllability and applicability of surface molecular self-assemblies. *Acc. Chem. Res.* **52**, 1048–1058 (2019).
16. Cook, T. R., Zheng, Y.-R. & Stang, P. J. Metal–organic frameworks and self-assembled supramolecular coordination complexes: comparing and contrasting the design, synthesis, and functionality of metal–organic materials. *Chem. Rev.* **113**, 734–777 (2013).
17. Olenyuk, B., Whiteford, J. A., Fechtenkötter, A. & Stang, P. J. Self-assembly of nanoscale cuboctahedra by coordination chemistry. *Nature* **398**, 796–799 (1999).
18. Fujita, M., Yazaki, J. & Ogura, K. Preparation of a macrocyclic polynuclear complex,  $[(\text{en})\text{Pd}(4,4'\text{-bpy})]_4(\text{NO}_3)_8$  ( $\text{en} =$  ethylenediamine, bpy = bipyridine), which recognizes an organic molecule in aqueous media. *J. Am. Chem. Soc.* **112**, 5645–5647 (1990).
19. Fujita, M. et al. Self-assembly of ten molecules into nanometre-sized organic host frameworks. *Nature* **378**, 469–471 (1995).
20. Mal, P., Breiner, B., Rissanen, K. & Nitschke, J. R. White phosphorus is air-stable within a self-assembled tetrahedral capsule. *Science* **324**, 1697–1699 (2009).
21. Rizzuto, F. J. & Nitschke, J. R. Stereochemical plasticity modulates cooperative binding in a CoII12L6 cuboctahedron. *Nat. Chem.* **9**, 903–908 (2017).
22. Yamashina, M. et al. An antiaromatic-walled nanospace. *Nature* **574**, 511–515 (2019).
23. Chen, B., Holstein, J. J., Horiuchi, S., Hiller, W. G. & Clever, G. H. Pd(II) coordination sphere engineering: pyridine cages, quinoline

- bowls, and heteroleptic pills binding one or two fullerenes. *J. Am. Chem. Soc.* **141**, 8907–8913 (2019).
24. Yoshizawa, M., Tamura, M. & Fujita, M. Diels-Alder in aqueous molecular hosts: unusual regioselectivity and efficient catalysis. *Science* **312**, 251–254 (2006).
  25. Kaphan, D. M., Levin, M. D., Bergman, R. G., Raymond, K. N. & Toste, F. D. A supramolecular microenvironment strategy for transition metal catalysis. *Science* **350**, 1235–1238 (2015).
  26. Cullen, W., Misuraca, M. C., Hunter, C. A., Williams, N. H. & Ward, M. D. Highly efficient catalysis of the Kemp elimination in the cavity of a cubic coordination cage. *Nat. Chem.* **8**, 231–236 (2016).
  27. Xuan, W., Zhang, M., Liu, Y., Chen, Z. & Cui, Y. A chiral quadruple-stranded helicate cage for enantioselective recognition and separation. *J. Am. Chem. Soc.* **134**, 6904–6907 (2012).
  28. Li, G., Yu, W. & Cui, Y. A homochiral nanotubular crystalline framework of metallomacrocycles for enantioselective recognition and separation. *J. Am. Chem. Soc.* **130**, 4582–4583 (2008).
  29. Liu, T., Liu, Y., Xuan, W. & Cui, Y. Chiral nanoscale metal–organic tetrahedral cages: diastereoselective self-assembly and enantioselective separation. *Angew. Chem. Int. Ed.* **49**, 4121–4124 (2010).
  30. Dong, J. et al. Self-Assembly of highly stable zirconium(IV) coordination cages with aggregation induced emission molecular rotors for live-cell imaging. *Angew. Chem. Int. Ed.* **59**, 10151–10159 (2020).
  31. Sun, Y. et al. Rhomboidal Pt(II) metallacycle-based NIR-II theranostic nanoprobe for tumor diagnosis and image-guided therapy. *Proc. Natl Acad. Sci. USA* **116**, 1968–1973 (2019).
  32. August, D. P. et al. Self-assembly of a layered two-dimensional molecularly woven fabric. *Nature* **588**, 429–435 (2020).

33. Dong, J. et al. Chiral NH-controlled supramolecular metallacycles. *J. Am. Chem. Soc.* **139**, 1554–1564 (2017).
34. Backes, C. et al. Equipartition of energy defines the size–thickness relationship in liquid-exfoliated nanosheets. *ACS Nano* **13**, 7050–7061 (2019).
35. Dou, L. et al. Atomically thin two-dimensional organic-inorganic hybrid perovskites. *Science* **349**, 1518–1521 (2015).
36. Dazzi, A. & Prater, C. B. AFM-IR: technology and applications in nanoscale infrared spectroscopy and chemical imaging. *Chem. Rev.* **117**, 5146–5173 (2017).
37. Zhang, D. et al. Atomic-resolution transmission electron microscopy of electron beam–sensitive crystalline materials. *Science* **359**, 675–679 (2018).
38. Liu, L. et al. Imaging defects and their evolution in a metal–organic framework at sub-unit-cell resolution. *Nat. Chem.* **11**, 622–628 (2019).
39. Ferrand, Y., Crump, M. P. & Davis, A. P. A synthetic lectin analog for biomimetic disaccharide recognition. *Science* **318**, 619–622 (2007).
40. Ke, C., Destecroix, H., Crump, M. P. & Davis, A. P. A simple and accessible synthetic lectin for glucose recognition and sensing. *Nat. Chem.* **4**, 718–723 (2012).
41. Tromans, R. A. et al. A biomimetic receptor for glucose. *Nat. Chem.* **11**, 52–56 (2019).
42. Dong, J. et al. Ultrathin two-dimensional porous organic nanosheets with molecular rotors for chemical sensing. *Nat. Commun.* **8**, 1142 (2017).
43. Tan, C. et al. High-yield exfoliation of ultrathin two-dimensional ternary chalcogenide nanosheets for highly sensitive and selective

fluorescence DNA sensors. *J. Am. Chem. Soc.* **137**, 10430–10436 (2015).

44. QSTEM v.2.51 (2018); <http://www.qstem.org>

45. Mei, X. & Wolf, C. Enantioselective sensing of chiral carboxylic acids. *J. Am. Chem. Soc.* **126**, 14736–14737 (2004).

## Acknowledgements

This work was financially supported by the National Science Foundation of China (grant nos 21875136, 91856204 and 91956124), the National Key Basic Research Program of China (grant nos 2021YFA1200402, 2021YFA1501501 and 2021YFA1200300), the Shanghai Rising-Star Program (grant no. 19QA1404300), the National Research Foundation Singapore (grant no. NRF-CRP14-2014-01), the National University of Singapore and the Ministry of Education of Singapore (grant no. C-261-000-207-532/C-261-000-777-532), and the University of Bristol. Y.H. acknowledges the support of the CCF grant (no. FCC/1/1972-19) from King Abdullah University of Science and Technology.

## Author information

### Author notes

1. These authors contributed equally: Jinqiao Dong, Lingmei Liu

## Affiliations

1. School of Chemistry and Chemical Engineering, Frontiers Science Center for Transformative Molecules and State Key Laboratory of Metal Matrix Composites, Shanghai Jiao Tong University, Shanghai, P. R. China

Jinqiao Dong, Chunxia Tan, Dandan Chu, Yan Liu & Yong Cui

2. School of Chemistry, University of Bristol, Bristol, UK

Jinqiao Dong & Anthony P. Davis

3. Multi-scale Porous Materials Center, Institute of Advanced Interdisciplinary Studies & School of Chemistry and Chemical Engineering, Chongqing University, Chongqing, P. R. China

Lingmei Liu

4. Department of Chemical and Biomolecular Engineering, National University of Singapore, Singapore, Singapore

Qisong Xu, Zhiwei Qiao & Jianwen Jiang

5. Hefei National Laboratory for Physical Sciences at the Microscale, Synergetic Innovation Center of Quantum Information and Quantum Physics, Department of Chemical Physics, University of Science and Technology of China, Hefei, P. R. China

Jiachen Zhang & Qun Zhang

6. Advanced Membranes and Porous Materials Center, Physical Sciences and Engineering Division, King Abdullah University of Science and Technology (KAUST), Thuwal, Saudi Arabia

Yu Han

## Contributions

Y.C. formulated and supervised the project. J.D., C.T. and D.C. performed the synthesis and purification of the chiral ultrathin 2D nanosheets of **1–3**; performed the AFM, field-emission scanning electron microscopy, powder X-ray diffraction, ultraviolet–visible spectrometry, electrospray ionization mass spectrometry, FT-IR, TGA, dynamic light scattering, XPS, optical band gaps and Brunauer–Emmett–Teller analyses, and the fluorescence titration and electrospinning membrane sensing experiments. L.L. and Y.H. performed the HR-TEM imaging and analyses. J.Z. and Q.Z. performed the ultrafast TA experiments and analyses. Q.X., Z.Q. and J.J. performed the theoretical calculations and simulations. Y.L. and A.P.D. advised on the

interpretation of results. J.D., A.P.D. and Y.C. wrote the manuscript. All authors contributed to the data analysis, discussion and manuscript revision.

## Corresponding authors

Correspondence to [Yu Han](#), [Anthony P. Davis](#) or [Yong Cui](#).

## Ethics declarations

### Competing interests

The authors declare no competing interests.

### Peer review information

*Nature* thanks Jonathan Foster and the other, anonymous, reviewer(s) for their contribution to the peer review of this work.

## Additional information

**Publisher's note** Springer Nature remains neutral with regard to jurisdictional claims in published maps and institutional affiliations.

## Supplementary information

[Supplementary Information](#)  
Supplementary Information, including Figs. 1–77, Tables 1–4 and References.

## [Supplementary Video 1](#)

Molecular dynamics simulation of l-glucose (orange colour) and d-glucose (green colour) binding to zero-dimensional discrete metallacycles of (*R*)-1 in acetonitrile solution.

## Supplementary Video 2

Molecular dynamics simulation of l-glucose (orange colour) and d-glucose (green colour) binding to 3D bulk crystals of (*R*)-**1** in acetonitrile solution.

## Supplementary Video 3

Molecular dynamics simulation of l-glucose (orange colour) and d-glucose (green colour) binding to 2D monolayer nanosheets of (*R*)-**1** in acetonitrile solution.

## Rights and permissions

### Reprints and Permissions

## About this article

### Cite this article

Dong, J., Liu, L., Tan, C. *et al.* Free-standing homochiral 2D monolayers by exfoliation of molecular crystals. *Nature* **602**, 606–611 (2022).  
<https://doi.org/10.1038/s41586-022-04407-8>

- Received: 22 April 2021
- Accepted: 04 January 2022
- Published: 23 February 2022
- Issue Date: 24 February 2022
- DOI: <https://doi.org/10.1038/s41586-022-04407-8>

## Share this article

Anyone you share the following link with will be able to read this content:

[Get shareable link](#)

Sorry, a shareable link is not currently available for this article.

[Copy to clipboard](#)

Provided by the Springer Nature SharedIt content-sharing initiative

## [Fragile nanosheets stripped from crystals](#)

- Claudia Backes

News & Views 23 Feb 2022

---

This article was downloaded by **calibre** from <https://www.nature.com/articles/s41586-022-04407-8>

| [Section menu](#) | [Main menu](#) |

- Article
- [Published: 23 February 2022](#)

# Emergent constraints on future precipitation changes

- [Hideo Shiogama](#) ORCID: [orcid.org/0000-0001-5476-2148](https://orcid.org/0000-0001-5476-2148)<sup>1</sup>,
- [Masahiro Watanabe](#) ORCID: [orcid.org/0000-0001-6500-2101](https://orcid.org/0000-0001-6500-2101)<sup>2</sup>,
- [Hyungjun Kim](#) ORCID: [orcid.org/0000-0003-1083-8416](https://orcid.org/0000-0003-1083-8416)<sup>3,4,5</sup> &
- [Nagio Hirota](#)<sup>1</sup>

[Nature](#) volume 602, pages 612–616 (2022)

- 832 Accesses
- 17 Altmetric
- [Metrics details](#)

## Subjects

- [Climate and Earth system modelling](#)
- [Projection and prediction](#)

## Abstract

Future projections of global mean precipitation change ( $\Delta P$ ) based on Earth-system models have larger uncertainties than projections of global mean temperature changes ( $\Delta T$ )<sup>1</sup>. Although many observational constraints on  $\Delta T$  have been proposed, constraints on  $\Delta P$  have not been well studied<sup>2,3,4,5</sup> and are often complicated by the large influence of aerosols on precipitation<sup>4</sup>. Here we show that the upper bound (95th percentile) of  $\Delta P$

(2051–2100 minus 1851–1900, percentage of the 1980–2014 mean) is lowered from 6.2 per cent to 5.2–5.7 per cent (minimum–maximum range of sensitivity analyses) under a medium greenhouse gas concentration scenario. Our results come from the Coupled Model Intercomparison Project phase 5 and phase 6 ensembles<sup>6,7,8</sup>, in which  $\Delta P$  for 2051–2100 is well correlated with the global mean temperature trends during recent decades after 1980 when global anthropogenic aerosol emissions were nearly constant.  $\Delta P$  is also significantly correlated with the recent past trends in precipitation when we exclude the tropical land areas with few rain-gauge observations. On the basis of these significant correlations and observed trends, the variance of  $\Delta P$  is reduced by 8–30 per cent. The observationally constrained ranges of  $\Delta P$  should provide further reliable information for impact assessments.

This is a preview of subscription content

## Access options

Subscribe to Nature+

Get immediate online access to the entire Nature family of 50+ journals

\$29.99

monthly

[Subscribe](#)

Subscribe to Journal

Get full journal access for 1 year

\$199.00

only \$3.90 per issue

[Subscribe](#)

All prices are NET prices.  
VAT will be added later in the checkout.  
Tax calculation will be finalised during checkout.

Buy article

Get time limited or full article access on ReadCube.

\$32.00

[Buy](#)

All prices are NET prices.

### **Additional access options:**

- [Log in](#)
- [Learn about institutional subscriptions](#)

**Fig. 1: Observational constraints on the future  $\Delta P$ .**

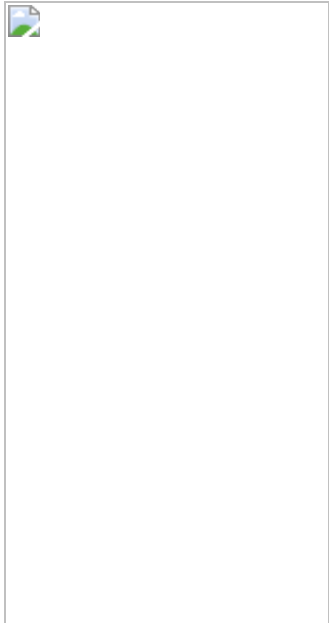


**Fig. 2: Discrepancies between observed precipitation datasets.**

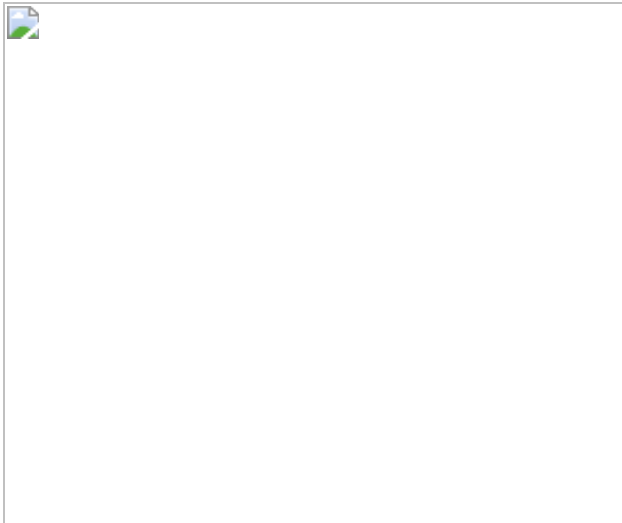
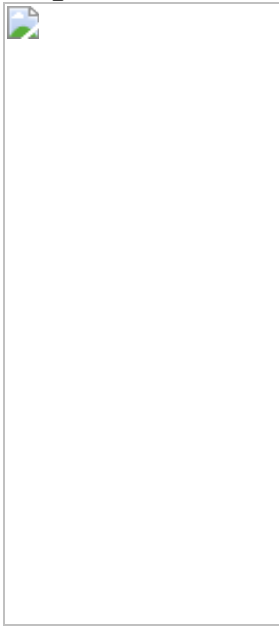


**Fig. 3: Spatial patterns of differences in future temperature and precipitation changes.**



## Data availability

All data that support the findings of this study are available from the following: CMIP5, <https://esgf-node.llnl.gov/search/cmip5/> (last access, 9 February 2021); CMIP6, <https://esgf-node.llnl.gov/search/cmip6/> (last access, 9 February 2021); HadCRUT4, <https://www.metoffice.gov.uk/hadobs/hadcrut4/> (last access, 7 October 2020); GISTEMP4, <https://data.giss.nasa.gov/gistemp/> (last access, 9 March 2020); MSWEP2 (v2.2), <http://www.gloh2o.org/> (last access, 30 September 2020).

2020); GSWP3, [http://search.diasjp.net/en/dataset/GSWP3\\_EXP1\\_Force](http://search.diasjp.net/en/dataset/GSWP3_EXP1_Force) (last access, 13 October 2020); GPCC, <https://www.dwd.de/EN/ourservices/gpcc/gpcc.html> (last access, 26 February 2021).

## Code availability

The codes are available from <https://doi.org/10.6084/m9.figshare.16816714>.

## References

1. Collins, M. et al. in Climate Change 2013: The Physical Science Basis (eds Stocker, T. F. et al.) Ch. 12 (Cambridge Univ. Press, 2013).
2. Hall, A. et al. Progressing emergent constraints on future climate change. *Nat. Clim. Change* **9**, 269–278 (2019).
3. Brient, F. Reducing uncertainties in climate projections with emergent constraints: concepts, examples and prospects. *Adv. Atmos. Sci.* **37**, 1–15 (2020).
4. Allen, M. & Ingram, W. Constraints on future changes in climate and the hydrologic cycle. *Nature* **419**, 228–232 (2002).
5. Schlund, M. et al. Emergent constraints on equilibrium climate sensitivity in CMIP5: do they hold for CMIP6? *Earth Syst. Dyn.* **11**, 1233–1258 (2020).
6. Taylor, K. E., Stouffer, R. J. & Meehl, G. A. An overview of CMIP5 and the experiment design. *Bull. Am. Meteorol. Soc.* **93**, 485–498 (2012).
7. Eyring, V. et al. Overview of the Coupled Model Intercomparison Project phase 6 (CMIP6) experimental design and organization. *Geosci. Model Dev.* **9**, 1937–1958 (2016).

8. O'Neill, B. C. et al. A new scenario framework for climate change research: the concept of shared socioeconomic pathways. *Climatic Change* **122**, 387–400 (2014).
9. Knutti, R. The end of model democracy? *Climatic Change* **102**, 395–404 (2010).
10. Shiogama, H. et al. Observational constraints indicate risk of drying in the Amazon Basin. *Nat. Commun.* **2**, 253 (2011).
11. Caldwell, P. M. et al. Statistical significance of climate sensitivity predictors obtained by data mining. *Geophys. Res. Lett.* **41**, 1803–1808 (2014).
12. Samset, B. H. et al. Fast and slow precipitation responses to individual climate forcers: a PDRMIP multimodel study. *Geophys. Res. Lett.* **43**, 2782–2791 (2016).
13. Thorpe, L. & Andrews, T. The physical drivers of historical and 21st century global precipitation changes. *Environ. Res. Lett.* **9**, 064024 (2014).
14. Salzmann, M. Global warming without global mean precipitation increase? *Sci. Adv.* **2**, e1501572 (2016).
15. Wu, P., Christidis, N. & Stott, P. Anthropogenic impact on Earth's hydrological cycle. *Nat. Clim. Change* **3**, 807–810 (2013).
16. Rao, S. et al. Future air pollution in the shared socio-economic pathways. *Glob. Environ. Change* **42**, 346–358 (2017).
17. Lund, M. T., Myhre, G. & Samset, B. H. Anthropogenic aerosol forcing under the shared socioeconomic pathways. *Atmos. Chem. Phys.* **19**, 13827–13839 (2019).
18. Fläschner, D., Mauritsen, T. & Stevens, B. Understanding the intermodel spread in global-mean hydrological sensitivity. *J. Clim.* **29**, 801–817 (2016).

19. DeAngelis, A. M., Qu, X., Zelinka, M. D. & Hall, A. An observational radiative constraint on hydrologic cycle intensification. *Nature* **528**, 249–253 (2015).
20. Watanabe, M. et al. Low clouds link equilibrium climate sensitivity to hydrological sensitivity. *Nat. Clim. Change* **8**, 901–906 (2018).
21. Pendergrass, A. G. The global-mean precipitation response to CO<sub>2</sub>-induced warming in CMIP6 models. *Geophys. Res. Lett.* **47**, e2020GL089964 (2020).
22. Jiménez-de-la-Cuesta, D. & Mauritsen, T. Emergent constraints on Earth’s transient and equilibrium response to doubled CO<sub>2</sub> from post-1970s global warming. *Nat. Geosci.* **12**, 902–905 (2019).
23. Tokarska, K. B. et al. Past warming trend constrains future warming in CMIP6 models. *Sci. Adv.* **6**, eaaz9549 (2020).
24. Nijssse, F. J. M. M., Cox, P. M. & Williamson, M. S. Emergent constraints on transient climate response (TCR) and equilibrium climate sensitivity (ECS) from historical warming in CMIP5 and CMIP6 models. *Earth Syst. Dyn.* **11**, 737–750 (2020).
25. Liang, Y., Gillett, N. P. & Monahan, A. H. Climate model projections of 21st century global warming constrained using the observed warming trend. *Geophys. Res. Lett.* **47**, e2019GL086757 (2020).
26. Hegerl, G. C. et al. Challenges in quantifying changes in the global water cycle. *Bull. Am. Meteorol. Soc.* **96**, 1097–1115 (2015).
27. Bowman, K. W., Cressie, N., Qu, X. & Hall, A. A hierarchical statistical framework for emergent constraints: application to snow-albedo feedback. *Geophys. Res. Lett.* **45**, 13050–13059 (2018).
28. Morice, C. P., Kennedy, J. J., Rayner, N. A. & Jones, P. D. Quantifying uncertainties in global and regional temperature change using an ensemble of observational estimates: the HadCRUT4 dataset. *J. Geophys. Res.* **117**, D08101 (2012).

29. Lenssen, N. et al. Improvements in the GISTEMP uncertainty model. *J. Geophys. Res. Atmos.* **124**, 6307–6326 (2019).
30. Gillett, N. P. et al. The Detection and Attribution Model Intercomparison Project (DAMIP v1.0) contribution to CMIP6. *Geosci. Model Dev.* **9**, 3685–3697 (2016).
31. Gillett, N. P. et al. Constraining human contributions to observed warming since preindustrial. *Nat. Clim. Change* **11**, 207–212 (2021).
32. Sun, Q. et al. A review of global precipitation data sets: data sources, estimation, and intercomparisons. *Rev. Geophys.* **56**, 79–107 (2018).
33. Kobayashi, S. et al. The JRA-55 reanalysis: general specifications and basic characteristics. *J. Meteorol. Soc. Jpn* **93**, 5–48 (2015).
34. Adler, R. et al. The Global Precipitation Climatology Project (GPCP) monthly analysis (new version 2.3) and a review of 2017 global precipitation. *Atmosphere* **9**, 138 (2018).
35. Beck, H. E. et al. MSWEP V2 global 3-hourly 0.1° precipitation: methodology and quantitative assessment. *Bull. Am. Meteorol. Soc.* **100**, 473–500 (2019).
36. van den Hurk, B. et al. LS3MIP (v1.0) contribution to CMIP6: the Land Surface, Snow and Soil moisture Model Intercomparison Project —aims, setup and expected outcome. *Geosci. Model Dev.* **9**, 2809–2832 (2016).
37. Becker, A. et al. A description of the global land-surface precipitation data products of the Global Precipitation Climatology Centre with sample applications including centennial (trend) analysis from 1901–present. *Earth Syst. Sci. Data* **5**, 71–99 (2013).
38. Emori, S. & Brown, S. J. Dynamic and thermodynamic changes in mean and extreme precipitation under changed climate. *Geophys. Res. Lett.* **32**, L17706 (2005).

39. Xie, P. & Arkin, P. A. Global precipitation: a 17-year monthly analysis based on gauge observations, satellite estimates, and numerical model outputs. *Bull. Am. Meteorol. Soc.* **78**, 2539–2558 (1997).
40. Yin, X. A. & Gruber Arkin, P. Comparison of the GPCP and CMAP merged gauge–satellite monthly precipitation products for the period 1979–2001. *J. Hydrometeorol.* **5**, 1207–1222 (2004).
41. Compo, G. P. et al. The Twentieth Century Reanalysis Project. *Q. J. R. Meteorol. Soc. A* **137**, 1–28 (2011).
42. Kim, H. *Global Soil Wetness Project Phase 3 atmospheric boundary conditions (experiment I)* (DIAS, 2017);  
<https://doi.org/10.20783/DIAS.501>
43. Schneider, U. et al. *GPCC Full Data Monthly Product Version 2020 at 1.0°: Monthly Land-Surface Precipitation from Rain-Gauges Built on GTS-Based and Historical Data* (2020);  
[https://doi.org/10.5676/DWD\\_GPCC/FD\\_M\\_V2020\\_100](https://doi.org/10.5676/DWD_GPCC/FD_M_V2020_100)

## Acknowledgements

This work was supported by the Integrated Research Program for Advancing Climate Models (JPMXD0717935457), Grants-in-Aid for Scientific Research (JP21H01161) of the Ministry of Education, Culture, Sports, Science and Technology of Japan, the Environment Research and Technology Development Fund (JPMEERF20202002) and the National Research Foundation of Korea grant (MSIT) (2021H1D3A2A03097768).

## Author information

### Affiliations

1. Earth System Division, National Institute for Environmental Studies, Tsukuba, Japan

Hideo Shiogama & Nagio Hirota

2. Atmosphere and Ocean Research Institute, University of Tokyo,  
Kashiwa, Japan

Masahiro Watanabe

3. Moon Soul Graduate School of Future Strategy, Korea Advanced  
Institute of Science and Technology, Daejeon, Korea

Hyungjun Kim

4. Dept. of Civil and Environmental Engineering, Korea Advanced  
Institute of Science and Technology, Daejeon, Korea

Hyungjun Kim

5. Institute of Industrial Science, University of Tokyo, Tokyo, Japan

Hyungjun Kim

## Contributions

H.S. mainly performed the analyses and wrote the paper. M.W. provided insights about the physics of precipitation changes and emergent constraints. H.K. provided the GSWP3 data and the information about the uncertainty sources of the observed precipitation datasets. N.H. contributed to the data collection, the selection of the observed datasets and the interpretation of the results. All authors discussed the results and commented on the manuscript.

## Corresponding author

Correspondence to [Hideo Shiogama](#).

## Ethics declarations

## Competing interests

The authors declare no competing interests.

## Peer review

### Peer review information

*Nature* thanks Chad Thackeray, Sabine Undorf and the other, anonymous, reviewer(s) for their contribution to the peer review of this work.

## Additional information

**Publisher's note** Springer Nature remains neutral with regard to jurisdictional claims in published maps and institutional affiliations.

## Extended data figures and tables

### Extended Data Fig. 1 Relationships between future $\Delta T$ and $\Delta P$ .

Horizontal and vertical axes indicate the future (2051–2100 minus 1851–1900)  $\Delta T$  ( $^{\circ}$ C) and  $\Delta P$  (% of the 1980–2014 mean), respectively. Crosses and diamonds are CMIP5 and CMIP6 ESMs (ensemble mean for each ESM), respectively. Pearson's correlations of the CMIP5 and CMIP6 ESMs are denoted in the panel. Those correlations are significant at the 5% level.

### Extended Data Fig. 2 Definition of $P^*$ .

White shaded areas in the top panels indicate tropical ( $30^{\circ}$  S– $30^{\circ}$  N) land regions where 1980–2014 mean numbers of rain gauge observations<sup>37</sup> (Methods) are less than (a) 1, (b) 2 and (c) 3. Panels (d), (e) and (f) show  $P^*$  anomalies relative to the 1980–2014 mean (%). Here  $P^*$  represents the precipitation averaged over the pink shading areas of panels (a), (b) and (c), respectively. Solid lines are GPCP<sup>34</sup> (red), MSWEP2<sup>35</sup> (green) and GSWP3<sup>36</sup> (blue). Dashed lines show their linear trends. Panel (e) is the same as Fig. 2b. We mainly focus on the case of panels (b) and (e) in this paper. (g) Relationships between the 1980–2014 trends of  $P$  and  $P^*$  ( $P^*$  in

the case of (e)). Vertical and horizontal axes indicate the 1980–2014 trends of  $P$  and  $P^*$  (% per 35 yr), respectively. Crosses and diamonds are CMIP5<sup>6</sup> and CMIP6<sup>7,8</sup> ESMs (ensemble mean for each ESM), respectively. Dashed line indicates the linear regression. Pearson’s correlation of the CMIP5 and CMIP6 ESMs is denoted in the panel. This correlation is significant at the 5% level. Grads was used to draw the maps.

### Extended Data Fig. 3 Observational constraints on the future $\Delta P$ using only CMIP5 or CMIP6.

Horizontal axes show the recent past (1980–2014) trends of (top)  $T$  ( $^{\circ}\text{C}$  per 35 yr) and (bottom)  $P^*$  (% per 35 yr) for (left) CMIP5 and (right) CMIP6. Vertical axes indicate the future  $\Delta P$  (2051–2100 minus 1851–1900 of hist+4.5, % of the 1980–2014 mean values).  $P^*$  indicates precipitation averaged over the world except for some tropical land regions with few rain gauge observations (Extended Data Fig. 2b). Crosses and diamonds are CMIP5 and CMIP6 ESMs (ensemble mean for each ESM), respectively. Purple crosses/diamonds denote the ESMs whose recent past  $T$  trends are higher than the upper bound of HadCRUT4. Pearson’s correlations of the ESMs are denoted in the panels. Those correlations are significant at the 5% level. Dashed lines show the linear regressions. Horizontal bars indicate the 5–95% ranges of HadCRUT4 (light blue), GISTEMP4 (light green), GPCP (red), MSWEP2 (green) and GSWP3 (blue) (Methods). Box plots show the average (white line), 17–83% range (box), and 5–95% range (vertical bar) for the raw ESMs (black) and the constrained ranges using the observations (colours; navy and yellow for Had+GIS and GP+MS+GS, respectively).

### Extended Data Fig. 4 Past trends of $P$ due to individual and all forcing factors.

(a) Long-term (left, 1851–2014, % per 164 yr) and recent (right, 1980–2014, % per 35 yr) past trends of  $P$  in the ensembles of hist-GHG (red), hist-aer (blue) and hist-nat (green). (b) Horizontal and vertical axes are the long-term past trends of  $P$  (% per 164 yr) in hist+4.5 and hist-GHG, respectively. (c) Horizontal and vertical axes are the recent past trends of  $P$  (% per 35 yr) in hist+4.5 and hist-GHG, respectively.

## Extended Data Fig. 5 Observational constraints on the future $\Delta P$ using historical $P$ trend.

Vertical axis indicates the future  $\Delta P$  (2051–2100 minus 1851–1900 of hist+4.5, % of the 1980–2014 mean values). Horizontal axis shows the recent past (1980–2014) trends of  $P$  (% per 35 yr). Crosses and diamonds are CMIP5 and CMIP6 ESMs (ensemble mean for each ESM), respectively. Purple crosses/diamonds denote the ESMs whose recent past  $T$  trends are higher than the upper bound of HadCRUT4. Dashed line shows the linear regression. Horizontal bars indicate the 5–95% ranges of GPCP (red), MSWEP2 (green) and GSWP3 (blue) (see Methods). Box plots show the average (white line), 17–83% range (box), and 5–95% range (vertical bar) for the raw CMIP5 and CMIP6 ESMs (black) and the constrained ranges using the observations (colours; yellow for GP+MS+GS). Triangle and asterisk symbols denote the 5–95% ranges using only the CMIP5 or CMIP6 ESMs, respectively. Pearson’s correlations of the CMIP5 and CMIP 6 ESMs are denoted in the panel. Those correlations are significant at the 5% level.

## Extended Data Fig. 6 Discrepancies between observed precipitation datasets over the ocean and land.

Solid lines indicate the time series of precipitation anomalies relative to the 1980–2014 mean (%) averaged over (a) the ocean area plus Antarctica and (b) the land area except for Antarctica. Dashed lines show the linear trends. Red, green, blue and black (only for (b)) lines are GPCP, MSWEP2, GSWP3 and GPCC, respectively.

## Extended Data Fig. 7 Effects of difference in the $P^*$ definition on the constraints.

Vertical axes indicate the future  $\Delta P$  (2051–2100 minus 1851–1900 of hist+4.5, % of the 1980–2014 mean values) of the CMIP5 and CMIP6 ESMs. Box plots show the average (white line), 17–83% range (box), and 5–95% range (vertical bar) for the raw CMIP5/6 ESMs (black) and the constrained ranges using the  $P^*$  trends of GP+MS+GS (yellow). The

horizontal axis indicates the thresholds of rain gauge numbers used for the calculation of  $P^*$ .

### **Extended Data Fig. 8 Relationships between past and future $dP/dT$ (% per °C).**

Vertical axes indicate the future  $dP/dT$  (calculated by dividing  $\Delta P$  by  $\Delta T$  of ‘2051–2100 minus 1851–1900’). Horizontal axes show the recent past (a)  $dP/dT$  and (b)  $dP^*/dT$  (calculated by dividing the 1980–2014 trends of  $P$  and  $P^*$  by the 1980–2014  $T$  trends). Pearson’s correlations of the CMIP5 and CMIP6 ESMs are denoted in the panels. Those correlations are significant at the 5% level except for the CMIP5 of (b). Horizontal bars indicate the 5–95% ranges of GPCP (red), MSWEP2 (green) and GSWP3 (blue). Box plots show the average (white line), 17–83% range (box), and 5–95% range (vertical bar) for the raw CMIP5 and CMIP6 ESMs (black) and the constrained ranges using observations (colours). Because all the CMIP5 and CMIP6 ESMs are out of the range of MSWEP2/GISTEMP4 in (a), the corresponding constrained range is not available. Triangle and asterisk symbols denote the 5–95% ranges using only the CMIP5 or CMIP6 ESMs, respectively.

**Extended Data Table 1 The analysed CMIP6 (left) and CMIP5 (right) ESMs and their ensemble sizes**

**Extended Data Table 2 The mean values and the constrained 5–95% ranges of the future  $\Delta P$  (2051–2100 minus 1851–1900, % of 1980–2014)**

## Rights and permissions

[Reprints and Permissions](#)

## About this article

### Cite this article

Shiogama, H., Watanabe, M., Kim, H. *et al.* Emergent constraints on future precipitation changes. *Nature* **602**, 612–616 (2022).

<https://doi.org/10.1038/s41586-021-04310-8>

- Received: 17 December 2020
- Accepted: 06 December 2021
- Published: 23 February 2022
- Issue Date: 24 February 2022
- DOI: <https://doi.org/10.1038/s41586-021-04310-8>

## Share this article

Anyone you share the following link with will be able to read this content:

[Get shareable link](#)

Sorry, a shareable link is not currently available for this article.

[Copy to clipboard](#)

Provided by the Springer Nature SharedIt content-sharing initiative

---

This article was downloaded by **calibre** from <https://www.nature.com/articles/s41586-021-04310-8>

| [Section menu](#) | [Main menu](#) |

- Article
- [Published: 23 February 2022](#)

# Observed poleward freshwater transport since 1970

- [Taimoor Sohail](#) [ORCID: orcid.org/0000-0002-4162-3269<sup>1</sup>](#),
- [Jan D. Zika](#) [ORCID: orcid.org/0000-0003-3462-3559<sup>1,2,3</sup>](#),
- [Damien B. Irving](#) [ORCID: orcid.org/0000-0003-1258-5002<sup>4,5</sup>](#) &
- [John A. Church](#) [ORCID: orcid.org/0000-0002-7037-8194<sup>3,5</sup>](#)

[Nature](#) volume **602**, pages 617–622 (2022)

- 1143 Accesses
- 319 Altmetric
- [Metrics details](#)

## Subjects

- [Climate and Earth system modelling](#)
- [Ocean sciences](#)
- [Physical oceanography](#)

## Abstract

Warming-induced global water cycle changes pose a significant challenge to global ecosystems and human society. However, quantifying historical water cycle change is difficult owing to a dearth of direct observations, particularly over the ocean, where 77% and 85% of global precipitation and evaporation occur, respectively<sup>1,2,3</sup>. Air–sea fluxes of freshwater imprint on

ocean salinity such that mean salinity is lowest in the warmest and coldest parts of the ocean, and is highest at intermediate temperatures<sup>4</sup>. Here we track salinity trends in the warm, salty fraction of the ocean, and quantify the observed net poleward transport of freshwater in the Earth system from 1970 to 2014. Over this period, poleward freshwater transport from warm to cold ocean regions has occurred at a rate of 34–62 milli-sverdrups ( $\text{mSv} = 10^3 \text{ m}^3 \text{ s}^{-1}$ ), a rate that is not replicated in the current generation of climate models (the Climate Model Intercomparison Project Phase 6 (CMIP6)). In CMIP6 models, surface freshwater flux intensification in warm ocean regions leads to an approximately equivalent change in ocean freshwater content, with little impact from ocean mixing and circulation. Should this partition of processes hold for the real world, the implication is that the historical surface flux amplification is weaker (0.3–4.6%) in CMIP6 compared with observations (3.0–7.4%). These results establish a historical constraint on poleward freshwater transport that will assist in addressing biases in climate models.

This is a preview of subscription content

## Access options

Subscribe to Nature+

Get immediate online access to the entire Nature family of 50+ journals

\$29.99

monthly

[Subscribe](#)

Subscribe to Journal

Get full journal access for 1 year

\$199.00

only \$3.90 per issue

[Subscribe](#)

All prices are NET prices.

VAT will be added later in the checkout.

Tax calculation will be finalised during checkout.

Buy article

Get time limited or full article access on ReadCube.

\$32.00

[Buy](#)

All prices are NET prices.

### **Additional access options:**

- [Log in](#)
- [Learn about institutional subscriptions](#)

**Fig. 1: Coherent patterns of historical salinity change in observed and modelled zonally averaged salinity.**

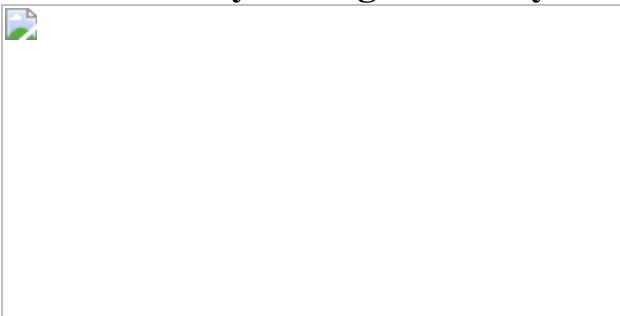


**Fig. 2: Enhanced salinity contrasts in observed and modelled global T–S curves.**

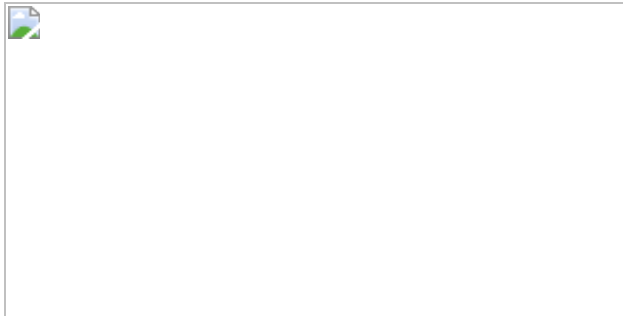


**Fig. 3: Historical freshwater content change in observations and climate models, quantified from 1970 to 2014.**

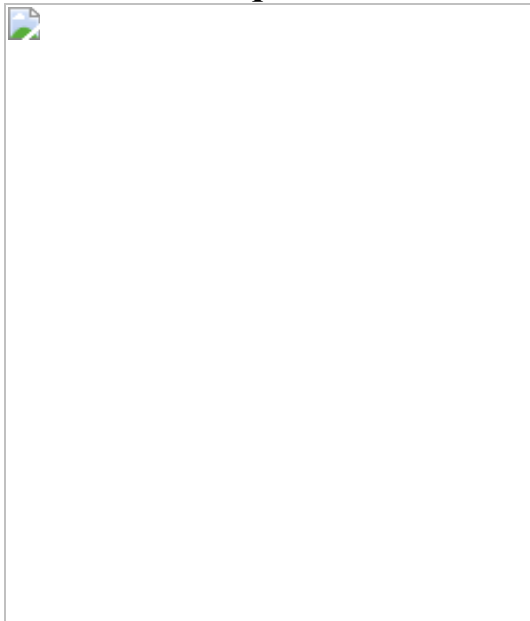
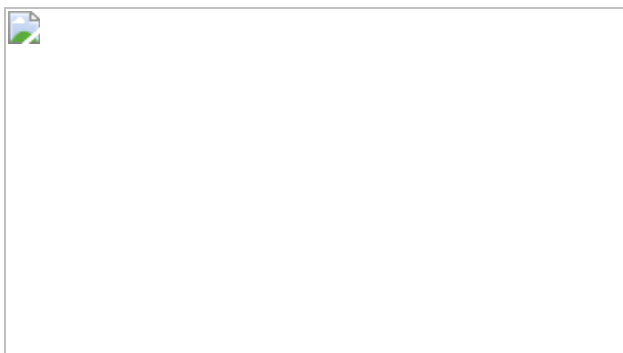


**Fig. 4: Impact of changing surface freshwater fluxes on freshwater content in climate models.**



## Data availability

All datasets used in this study are publicly available. EN4 data are available from the Met Office Hadley Centre

(<https://www.metoffice.gov.uk/hadobs/en4/download.html>), IAP data are available from the Chinese Academy of Sciences (temperature: <https://climatedataguide.ucar.edu/climate-data/ocean-temperature-analysis-and-heat-content-estimate-institute-atmospheric-physics>; salinity: <http://159.226.119.60/cheng/>), Ishii data are available from the National Center for Atmospheric Research (<https://rda.ucar.edu/datasets/ds285.3/>) and ERA5 data are available from ECMWF (<https://www.ecmwf.int/en/forecasts/datasets/reanalysis-datasets/era5>). CMIP6 and DAMIP model outputs are available from the Earth System Grid Federation [34,35,36,37,38,39,40,41,42,43,44,45,46,47,48,49,50,51,52,53,54,55,56,57,58,59](#) (ESGF; <https://sgf-node.llnl.gov/search/cmip6>).

## References

1. Trenberth, K. E., Smith, L., Qian, T., Dai, A. & Fasullo, J. Estimates of the global water budget and its annual cycle using observational and model data. *J. Hydrometeorol.* **8**, 758–769 (2007).
2. Schanze, J. J., Schmitt, R. W. & Yu, L. L. The global oceanic freshwater cycle: a state-of-the-art quantification. *J. Mar. Res.* **68**, 569–595 (2010).
3. Hegerl, G. C. et al. Challenges in quantifying changes in the global water cycle. *Bull. Am. Meteorol. Soc.* **96**, 1097–1115 (2015).
4. Grist, J. P., Josey, S. A., Zika, J. D., Evans, D. G. & Skliris, N. Assessing recent air-sea freshwater flux changes using a surface temperature-salinity space framework. *J. Geophys. Res. Oceans* **121**, 8787–8806 (2016).
5. Durack, P. J., Wijffels, S. E. & Boyer, T. P. In Ocean Circulation and Climate: a 21st Century Perspective Vol. 103 (eds Siedler, G. et al.) Ch. 28, 727–757 (2013).
6. Yu, L., Josey, S. A., Bingham, F. M. & Lee, T. Intensification of the global water cycle and evidence from ocean salinity: a synthesis

- review. *Ann. N. Y. Acad. Sci.* **1472**, 76–94 (2020).
7. Durack, P. J., Wijffels, S. E. & Matear, R. J. Ocean salinities reveal strong global water cycle intensification during 1950 to 2000. *Science* **336**, 455–458 (2012).
  8. Zika, J. D. et al. Improved estimates of water cycle change from ocean salinity: the key role of ocean warming. *Environ. Res. Lett.* **13**, 074036 (2018).
  9. Helm, K. P., Bindoff, N. L. & Church, J. A. Changes in the global hydrological-cycle inferred from ocean salinity. *Geophys. Res. Lett.* **37**, L18701, (2010).
  10. Skliris, N., Zika, J. D., Nurser, G., Josey, S. A. & Marsh, R. Global water cycle amplifying at less than the Clausius-Clapeyron rate. *Sci. Rep.* **6**, 38752 (2016).
  11. Held, I. M. & Soden, B. J. Robust responses of the hydrological cycle to global warming. *J. Clim.* **19**, 5686–5699 (2006).
  12. Skliris, N. et al. Salinity changes in the world ocean since 1950 in relation to changing surface freshwater fluxes. *Clim. Dyn.* **43**, 709–736 (2014).
  13. Allan, R. P. et al. Advances in understanding large-scale responses of the water cycle to climate change. *Ann. N. Y. Acad. Sci.* **1472**, 49–75 (2020).
  14. Cheng, L. et al. Improved estimates of changes in upper ocean salinity and the hydrological cycle. *J. Clim.* **33**, 10357–10381 (2020).
  15. Boyer, T. P., Levitus, S., Antonov, J. I., Locarnini, R. A. & Garcia, H. E. Linear trends in salinity for the world ocean, 1955–1998. *Geophys. Res. Lett.* <https://doi.org/10.1029/2004gl021791> (2005).
  16. Silvy, Y., Guilyardi, E., Sallée, J.-B. & Durack, P. J. Human-induced changes to the global ocean water masses and their time of emergence.

*Nat. Clim. Change* <https://doi.org/10.1038/s41558-020-0878-x> (2020).

17. Worthington, L. V. In Evolution of Physical Oceanography: Scientific Surveys in Honor of Henry Stommel Vol. 1 (eds Warren, B. A. & Wunsch, C.) Ch. 2, 42–57 (MIT Press, 1981).
18. Zika, J. D. et al. Maintenance and broadening of the ocean's salinity distribution by the water cycle. *J. Clim.* **28**, 9550–9560 (2015).
19. Bindoff, N. L. & McDougall, T. J. Diagnosing climate change and ocean ventilation using hydrographic data. *J. Phys. Oceanogr.* **24**, 1137–1152 (1994).
20. Sohail, T., Irving, D. B., Zika, J. D., Holmes, R. M. & Church, J. A. Fifty year trends in global ocean heat content traced to surface heat fluxes in the sub-polar ocean. *Geophys. Res. Lett.* **48**, e2020GL091439 (2021).
21. Cheng, L. & Zhu, J. Benefits of CMIP5 multimodel ensemble in reconstructing historical ocean subsurface temperature variations. *J. Clim.* **29**, 5393–5416 (2016).
22. Ishii, M., Shouji, A., Sugimoto, S. & Matsumoto, T. Objective analyses of sea-surface temperature and marine meteorological variables for the 20th century using ICOADS and the Kobe Collection. *Int. J. Climatol.* **25**, 865–879 (2005).
23. Good, S. A., Martin, M. J. & Rayner, N. A. EN4: quality controlled ocean temperature and salinity profiles and monthly objective analyses with uncertainty estimates. *J. Geophys. Res. Oceans* **118**, 6704–6716 (2013).
24. Eyring, V. et al. Overview of the Coupled Model Intercomparison Project Phase 6 (CMIP6) experimental design and organization. *Geosci. Model Dev.* **9**, 1937–1958 (2016).
25. Gillett, N. P. et al. The Detection and Attribution Model Intercomparison Project (DAMIP v1.0) contribution to CMIP6.

*Geosci. Model Dev.* **9**, 3685–3697 (2016).

26. Hersbach, H. et al. The ERA5 global reanalysis. *Q. J. R. Meteorolog. Soc.* **146**, 1999–2049 (2020).
27. Irving, D., Hobbs, W., Church, J. & Zika, J. A mass and energy conservation analysis of drift in the CMIP6 ensemble. *J. Clim.* **34**, 3157–3170 (2020).
28. Cai, W., Cowan, T., Arblaster, J. M. & Wijffels, S. On potential causes for an under-estimated global ocean heat content trend in CMIP3 models. *Geophys. Res. Lett.* **37**, L17709 (2010).
29. Gouretski, V. & Reseghetti, F. On depth and temperature biases in bathythermograph data: development of a new correction scheme based on analysis of a global ocean database. *Deep Sea Res. I* **57**, 812–833 (2010).
30. Graham, F. S. & McDougall, T. J. Quantifying the nonconservative production of conservative temperature, potential temperature, and entropy. *J. Phys. Oceanogr.* **43**, 838–862 (2013).
31. McDougall, T. J. Potential enthalpy: a conservative oceanic variable for evaluating heat content and heat fluxes. *J. Phys. Oceanogr.* **33**, 945–963 (2003).
32. McDougall, T. J. & Barker, P. M. *Getting Started with TEOS-10 and the Gibbs Seawater (GSW) Oceanographic Toolbox* (SCOR/IAPSO WG127, 2011); [https://www.teos-10.org/pubs/Getting\\_Started.pdf](https://www.teos-10.org/pubs/Getting_Started.pdf)
33. McDougall, T. J. et al. The interpretation of temperature and salinity variables in numerical ocean model output, and the calculation of heat fluxes and heat content. *Geosci. Model Dev.* **14**, 6445–6466 (2021).
34. Dix, M. et al. *CSIRO-ARCCSS ACCESS-CM2 Model Output Prepared for CMIP6 CMIP* (Earth System Grid Federation, 2019); <https://doi.org/10.22033/esgf/cmip6.2281>

35. Ziehn, T. et al. *CSIRO ACCESS-ESM1.5 Model Output Prepared for CMIP6 CMIP* (Earth System Grid Federation, 2019);  
<https://doi.org/10.22033/esgf/cmip6.2288>
36. Swart, N. C. et al. *CCCma CanESM5 Model Output Prepared for CMIP6 CMIP* (Earth System Grid Federation, 2019);  
<https://doi.org/10.22033/esgf/cmip6.1303>
37. Swart, N. C. et al. *CCCma CanESM5-CanOE Model Output Prepared for CMIP6 CMIP* (Earth System Grid Federation, 2019),  
<https://doi.org/10.22033/esgf/cmip6.10205>
38. Lovato, T. & Peano, D. *CMCC CMCC-CM2-SR5 Model Output Prepared for CMIP6 CMIP* (Earth System Grid Federation, 2020);  
<https://doi.org/10.22033/esgf/cmip6.1362>
39. Voldoire, A. *CNRM-CERFACS CNRM-CM6-1 Model Output Prepared for CMIP6 CMIP* (Earth System Grid Federation, 2018);  
<https://doi.org/10.22033/esgf/cmip6.1375>
40. Seferian, R. *CNRM-CERFACS CNRM-ESM2-1 Model Output Prepared for CMIP6 CMIP* (Earth System Grid Federation, 2018);  
<https://doi.org/10.22033/esgf/cmip6.1391>
41. EC-Earth Consortium. *EC-Earth-Consortium EC-Earth3 model Output Prepared for CMIP6 CMIP* (Earth System Grid Federation, 2019); <https://doi.org/10.22033/esgf/cmip6.181>
42. EC-Earth Consortium. *EC-Earth-Consortium EC-Earth3-Veg Model Output Prepared for CMIP6 CMIP* (Earth System Grid Federation, 2019); <https://doi.org/10.22033/esgf/cmip6.642>
43. EC-Earth Consortium. *EC-Earth-Consortium EC-Earth3-Veg-LR Model Output Prepared for CMIP6 CMIP* (Earth System Grid Federation, 2020); <https://doi.org/10.22033/esgf/cmip6.643>
44. Yu, Y. *CAS FGOALS-f3-L Model Output Prepared for CMIP6 CMIP* (Earth System Grid Federation, 2018);

<https://doi.org/10.22033/esgf/cmip6.1782>

45. Ridley, J., Menary, M., Kuhlbrodt, T., Andrews, M. & Andrews, T. *MOHC HadGEM3-GC31-LL Model Output Prepared for CMIP6 CMIP* (Earth System Grid Federation, 2018);  
<https://doi.org/10.22033/esgf/cmip6.419>
46. Boucher, O. et al. *IPSL IPSL-CM6A-LR Model Output Prepared for CMIP6 CMIP* (Earth System Grid Federation, 2018);  
<https://doi.org/10.22033/esgf/cmip6.1534>
47. Hajima, T. et al. *MIROC MIROC-ES2L Model Output Prepared for CMIP6 CMIP* (Earth System Grid Federation, 2019);  
<https://doi.org/10.22033/esgf/cmip6.902>
48. Neubauer, D. et al. *HAMMOZ-Consortium MPI-ESM1.2-HAM Model Output Prepared for CMIP6 CMIP* (Earth System Grid Federation, 2019); <https://doi.org/10.22033/esgf/cmip6.1622>
49. Jungclaus, J. et al. *MPI-M MPIESM1.2-HR model Output Prepared for CMIP6 CMIP* (Earth System Grid Federation, 2019);  
<https://doi.org/10.22033/esgf/cmip6.741>
50. Wieners, K.-H. et al. *MPI-M MPIESM1.2-LR Model Output Prepared for CMIP6 CMIP* (Earth System Grid Federation, 2019);  
<https://doi.org/10.22033/esgf/cmip6.742>
51. Selander, O. et al. *NCC NorESM2-LM Model Output Prepared for CMIP6 CMIP* (Earth System Grid Federation, 2019);  
<https://doi.org/10.22033/esgf/cmip6.502>
52. Bentsen, M. et al. *NCC NorESM2-MM Model Output Prepared for CMIP6 CMIP* (Earth System Grid Federation, 2019);  
<https://doi.org/10.22033/esgf/cmip6.506>
53. Tang, Y. et al. *OHC UKESM1.0-LL Model Output Prepared for CMIP6 CMIP* (Earth System Grid Federation, 2019);  
<https://doi.org/10.22033/esgf/cmip6.1569>

54. Dix, M. et al. *ACCESS-CM2 Model Output Prepared for CMIP6 under 'DAMIP'*. v1. CSIRO (Service Collection, 2020);  
<http://hdl.handle.net/102.100.100/422726?index=1>
55. Ziehn, T. et al. *CSIRO ACCESS-ESM1.5 Model Output Prepared for CMIP6 DAMIP* (Earth System Grid Federation, 2019);  
<https://doi.org/10.22033/esgf/cmip6.14362>
56. Swart, N. C. et al. *CCCma CanESM5 Model Output Prepared for CMIP6 DAMIP* (Earth System Grid Federation, 2019);  
<https://doi.org/10.22033/esgf/cmip6.1305>
57. Volodire, A. *CNRM-CERFACS CNRM-CM6-1 Model Output Prepared for CMIP6 DAMIP* (Earth System Grid Federation, 2019);  
<https://doi.org/10.22033/esgf/cmip6.1376>
58. Jones, G. *MOHC HadGEM3-GC31-LL Model Output Prepared for CMIP6 DAMIP* (Earth System Grid Federation, 2019);  
<https://doi.org/10.22033/esgf/cmip6.471>
59. Boucher, O. et al. *IPSL IPSL-CM6A-LR Model Output Prepared for CMIP6 DAMIP* (Earth System Grid Federation, 2018);  
<https://doi.org/10.22033/esgf/cmip6.13801>

## Acknowledgements

We acknowledge the World Climate Research Programme, the CMIP6 and DAMIP climate modelling groups, the ESGF and the funding agencies supporting CMIP6, DAMIP and ESGF. Modelling and analysis were undertaken with National Computational Infrastructure facilities, supported by the Australian Government. This work is supported by the Australian Research Council Centre of Excellence for Climate Extremes, the Centre for Southern Hemisphere Oceans Research (a joint research centre between the Qingdao National Laboratory for Marine Science and Technology and CSIRO) and the Australian Research Council Discovery Project scheme (DP190101173). We appreciate feedback from L. Zhang, which served to greatly sharpen the focus and direction of this work.

# **Author information**

## **Affiliations**

1. School of Mathematics and Statistics, University of New South Wales, Sydney, New South Wales, Australia

Taimoor Sohail & Jan D. Zika

2. UNSW Data Science Hub, University of New South Wales, Sydney, New South Wales, Australia

Jan D. Zika

3. Australian Centre for Excellence in Antarctic Science (ACEAS), University of New South Wales, Sydney, New South Wales, Australia

Jan D. Zika & John A. Church

4. Climate Science Centre, Commonwealth Scientific and Industrial Research Organisation (CSIRO), Hobart, Tasmania, Australia

Damien B. Irving

5. Climate Change Research Centre, University of New South Wales, Sydney, New South Wales, Australia

Damien B. Irving & John A. Church

## **Contributions**

This study was conceived by T.S. and J.D.Z. T.S. wrote the manuscript, with editing and feedback from all co-authors. D.B.I. analysed the raw CMIP6 and DAMIP files, binning into fixed-temperature space, and zonally averaging the CMIP6 data. T.S. analysed all observational datasets, as well as the binned and zonally averaged CMIP6 and DAMIP files. All authors contributed to the research direction of the study by providing scientific

advice and help with interpretation of results through all stages of the research process.

## Corresponding author

Correspondence to [Taimoor Sohail](#).

## Ethics declarations

### Competing interests

The authors declare no competing interests.

## Peer review

### Peer review information

*Nature* thanks Lei Zhang and the other, anonymous, reviewer(s) for their contribution to the peer review of this work. Peer reviewer reports are available.

## Additional information

**Publisher's note** Springer Nature remains neutral with regard to jurisdictional claims in published maps and institutional affiliations.

## Extended data figures and tables

### [Extended Data Fig. 1 Time-averaged T—S curve and surface freshwater fluxes in observations and models.](#)

a) Global T – S curve averaged from 1970 to 2014 in the observations<sup>14,21,23</sup> and over the pre-industrial control period in the CMIP6 models<sup>24</sup>, and b) global surface freshwater fluxes  $\langle \{ \{ \mathbf{F} \} \} \rangle_s$ ,

averaged over the pre-industrial control period in the CMIP6 models, and integrated from hot to cold. Thin grey lines represent each of the 20 CMIP6 models analysed, from Table S1, and thick grey line represents the CMIP6 multi-model mean (MMM). The right-hand y-axis shows the corresponding accumulated temperature-percentile in observations, and horizontal dotted lines indicate the warmest 2% and warmest 6% of the ocean by volume.

### **Extended Data Fig. 2 Comparing mean salinity changes in fixed-temperature and temperature-percentile frameworks.**

Mean salinity change from 1970 to 2014, in g/kg/year, in temperature-percentiles (black lines) and absolute temperature coordinates (red lines), in a) composite observations<sup>14,21,23</sup> and b) the CMIP6 MMM<sup>24</sup>.

### **Extended Data Fig. 3 Tracking northward outcrop migration of fixed-temperature and temperature-percentile surfaces.**

Sea surface salinity tendency, in g/kg/year, in a) composite observations<sup>14,21,23</sup>, and b) the CMIP6 MMM<sup>24</sup>. Dashed red lines show the time-mean outcrop of the 2% and 6% warmest ocean by volume from 1970–1980, and solid red lines show the time-mean outcrop of the 2% and 6% warmest ocean by volume from 2004–2014. Solid blue lines show the time-mean outcrop location of the 1970–1980 isotherm (corresponding to the dashed red line) in 2004–2014. Maps sources are a) composite observations<sup>14,21,23</sup> and b) the CMIP6 suite of models<sup>24</sup>.

### **Extended Data Fig. 4 Enhanced salinity contrasts in observed and modelled global T—S curves.**

The global time-mean T–S curve from 1970–2014 (dashed black line), and the 1970–2014 time-mean T–S curve after 100 years of the 1970–2014 linear trend in temperature and salinity (solid black line), in a) observations<sup>14,21,23</sup>, and b) the subset of CMIP6 models which correspond to the DAMIP models analysed, c) the GHG-only DAMIP runs, and d) the AA-only DAMIP runs<sup>25</sup>. The y-component of the arrow vectors is the change in temperature at constant temperature-percentile [°C/century] and

the x-component is the change in salinity [g/kg/century], as shown in the key in d). The colour of the arrows indicates salinification (red) or freshening (blue). The right-hand y-axis shows the corresponding accumulated temperature percentile in observations.

### **Extended Data Fig. 5 Impact of internal variability on freshwater content change in climate models.**

The change in freshwater content in a) and b) the warmest 2% of the ocean, c) and d) the warmest 6% of the ocean, and e) and f) the layer of 2–6% warmest ocean volume, relative to a 1970–1980 baseline, in all observational data sets<sup>14,21,22,23</sup>, CMIP6 model historical model runs<sup>24</sup>, a), c) and e) 30 ACCESS-ESM1-5 historical ensemble members (thin blue lines) and b), d) and f) 28 CNRM-CM6-1 historical ensemble members (thin orange lines). Thick blue (orange) lines show the ensemble mean freshwater content change in the ACCESS-ESM1-5 (CNRM-CM6-1) model. Dotted blue (orange) lines show the specific ACCESS-ESM1-5 (CNRM-CM6-1) ensemble member used in the CMIP6 multi-model analysis. Thin grey lines represent each of the 20 CMIP6 model members analysed (from Table S1). Histograms show the rate of freshwater change, calculated as the slope of a linear regression (in mSv), of each model, ensemble member and observational product.

### **Extended Data Fig. 6 Impact of changing surface freshwater fluxes on freshwater content in historical climate models.**

The relationship between surface freshwater flux amplification (relative to pre-industrial surface freshwater fluxes) and the rate of freshwater content change (based on the 1970–2014 linear trend; in mSv) in the DAMIP<sup>25</sup> GHG-only, AA-only and corresponding six CMIP6 historical runs<sup>24</sup> (red, blue and purple dots, respectively), in a) the warmest 2% of the ocean and b) the warmest 6% of the ocean. Small black dots show the broader suite of fourteen other CMIP6 historical simulations. The dotted line represents the linear regression across the DAMIP runs and their corresponding CMIP6 historical runs. The grey shaded region shows the envelope of maximum error associated with the linear regression. The green shaded region is an

estimate of surface flux intensification based on the (known) observed freshwater content change and the linear regression (considering the regression error in shaded in grey). The vertical black line in the green shaded area is an estimate of surface flux intensification based on the mean rate of freshwater content change across all observations.

### **Extended Data Fig. 7 Relationship between surface freshwater fluxes and global freshwater content across all temperature-percentiles.**

a) The global freshwater accumulation rate, integrated from hot to cold, inferred from the salinity tendency in observations<sup>14,21,22,23</sup> and the CMIP6 models<sup>24</sup>. b) The surface freshwater flux ( $(P-E+R)$ ) change, integrated from hot to cold, in the CMIP6 models. Thin grey lines represent each of the 20 CMIP6 model members analysed (from Table S1). c) The global freshwater accumulation rate, integrated from hot to cold, inferred from the salinity tendency in the DAMIP models<sup>25</sup> and corresponding CMIP6 historical runs. d) The surface freshwater flux change, integrated from hot to cold, in the DAMIP model and corresponding CMIP6 historical runs. Orange shading in a) shows the standard error of the slope of the linear regression over time. The right-hand y-axis shows the corresponding temperature-percentile in the observational dataset. Horizontal dotted lines indicate the warmest 2% and warmest 6% of the ocean.

**Extended Data Table 1 Suite of CMIP6 models analysed in this study**  
**Extended Data Table 2 Suite of DAMIP models analysed in this study**

## **Supplementary information**

### **Peer Review File**

## **Rights and permissions**

### **Reprints and Permissions**

## About this article

### Cite this article

Sohail, T., Zika, J.D., Irving, D.B. *et al.* Observed poleward freshwater transport since 1970. *Nature* **602**, 617–622 (2022).  
<https://doi.org/10.1038/s41586-021-04370-w>

- Received: 15 July 2021
- Accepted: 17 December 2021
- Published: 23 February 2022
- Issue Date: 24 February 2022
- DOI: <https://doi.org/10.1038/s41586-021-04370-w>

### Share this article

Anyone you share the following link with will be able to read this content:

[Get shareable link](#)

Sorry, a shareable link is not currently available for this article.

[Copy to clipboard](#)

Provided by the Springer Nature SharedIt content-sharing initiative

---

This article was downloaded by **calibre** from <https://www.nature.com/articles/s41586-021-04370-w>

- Article
- Open Access
- [Published: 09 February 2022](#)

# Signatures of TOP1 transcription-associated mutagenesis in cancer and germline

- [Martin A. M. Reijns](#) [ORCID: orcid.org/0000-0002-5048-2752](#)<sup>1</sup> na1,
- [David A. Parry](#) [ORCID: orcid.org/0000-0003-0376-7736](#)<sup>1</sup> na1,
- [Thomas C. Williams](#) [ORCID: orcid.org/0000-0002-3866-1344](#)<sup>1,2</sup> na1,
- [Ferran Nadeu](#) [ORCID: orcid.org/0000-0003-2910-9440](#)<sup>3,4</sup>,
- [Rebecca L. Hindshaw](#)<sup>5</sup>,
- [Diana O. Rios Szwed](#) [ORCID: orcid.org/0000-0003-0893-6324](#)<sup>1</sup>,
- [Michael D. Nicholson](#) [ORCID: orcid.org/0000-0003-2813-8979](#)<sup>6</sup>,
- [Paula Carroll](#)<sup>1</sup>,
- [Shelagh Boyle](#)<sup>7</sup>,
- [Romina Royo](#)<sup>8</sup>,
- [Alex J. Cornish](#) [ORCID: orcid.org/0000-0002-3966-3501](#)<sup>9</sup>,
- [Hang Xiang](#)<sup>10</sup>,
- [Kate Ridout](#)<sup>11</sup>,
- [The Genomics England Research Consortium](#),
- [Colorectal Cancer Domain UK 100,000 Genomes Project](#),
- [Anna Schuh](#) [ORCID: orcid.org/0000-0002-3938-8490](#)<sup>11</sup>,
- [Konrad Aden](#)<sup>10</sup>,
- [Claire Palles](#) [ORCID: orcid.org/0000-0002-9670-2263](#)<sup>5</sup>,
- [Elias Campo](#) [ORCID: orcid.org/0000-0001-9850-9793](#)<sup>3,4,12,13</sup>,
- [Tatjana Stankovic](#) [ORCID: orcid.org/0000-0002-3780-274X](#)<sup>5</sup>,
- [Martin S. Taylor](#) [ORCID: orcid.org/0001-7656-330X](#)<sup>2</sup> &
- [Andrew P. Jackson](#) [ORCID: orcid.org/0000-0002-8739-2646](#)<sup>1</sup>

[Nature](#) volume 602, pages 623–631 (2022)

- 11k Accesses

- 1 Citations
- 198 Altmetric
- [Metrics details](#)

## Subjects

- [Cancer genomics](#)
- [Genomic instability](#)
- [Nucleotide excision repair](#)

## Abstract

The mutational landscape is shaped by many processes. Genic regions are vulnerable to mutation but are preferentially protected by transcription-coupled repair<sup>1</sup>. In microorganisms, transcription has been demonstrated to be mutagenic<sup>2,3</sup>; however, the impact of transcription-associated mutagenesis remains to be established in higher eukaryotes<sup>4</sup>. Here we show that ID4—a cancer insertion–deletion (indel) mutation signature of unknown aetiology<sup>5</sup> characterized by short (2 to 5 base pair) deletions—is due to a transcription-associated mutagenesis process. We demonstrate that defective ribonucleotide excision repair in mammals is associated with the ID4 signature, with mutations occurring at a TNT sequence motif, implicating topoisomerase 1 (TOP1) activity at sites of genome-embedded ribonucleotides as a mechanistic basis. Such TOP1-mediated deletions occur somatically in cancer, and the ID-TOP1 signature is also found in physiological settings, contributing to genic de novo indel mutations in the germline. Thus, although topoisomerases protect against genome instability by relieving topological stress<sup>6</sup>, their activity may also be an important source of mutations in the human genome.

[Download PDF](#)

## Main

Eukaryotic cells have many strategies to ensure the integrity of their genomes, with high-fidelity DNA replication<sup>7</sup> and DNA-repair processes countering exogenous and endogenous DNA lesions<sup>8</sup>. The process of transcription targets DNA repair machinery to expressed genes, preferentially reducing their mutation rate after DNA damage<sup>1</sup>. Despite this targeted repair, in microorganisms, the process of transcription itself is mutagenic—a phenomenon that is referred to as transcription-associated mutagenesis (TAM)<sup>2,3</sup>. In yeast, topoisomerase 1 (Top1) activity is a major source of TAM and

results in a distinctive transcription-dependent signature of 2–5 bp deletions at tandem repeat sequences<sup>9,10,11</sup>. Genome-embedded ribonucleotides have been established as a cause of Top1-TAM deletions in yeast<sup>12</sup>. Such ribonucleotides are frequently incorporated by DNA polymerases during replication, and represent the most prevalent aberrant nucleotides in the eukaryotic genome<sup>13,14</sup>. These genome-embedded ribonucleotides are normally removed by ribonucleotide excision repair (RER), a process initiated by the heterotrimeric ribonuclease H2 enzyme<sup>15</sup>. However, when Top1 cleaves at embedded ribonucleotides instead of RNase H2, this can result in small deletions<sup>16,17</sup>.

In the last decade, the widespread use of genome sequencing has enabled unbiased sampling of human mutations, substantially advancing understanding of mutagenesis in the germline<sup>18</sup> and in neoplasia<sup>19</sup>. Multiple mutational processes act during cancer evolution, and mathematical methods decomposing tumour mutational profiles have been developed to define signatures that may correspond to individual mutagenic mechanisms<sup>19</sup>. This has successfully defined cell-intrinsic, environmental and treatment-related origins for many base-substitution signatures in cancer<sup>20,21,22</sup>. However, the origin of a substantial number of signatures remains unknown, and some may be artefactual. Recently, cancer signature analysis has been extended to indels<sup>5</sup>, small (1–49 bp) insertions and deletions. Such indels are an important class of mutations that contribute substantially to disease-causing germline variants (>20%) and human variation<sup>23</sup>.

Here we investigate an indel signature of unknown cause—ID4. We show experimentally that ID4 deletions are increased in RNase-H2-deficient cell lines and cancers and delineate a human TOP1-mediated TAM signature (ID-TOP1) that is relevant to both somatic and germline mutagenesis.

## ID4, a distinct cancer indel signature

The ID4 cancer signature, as categorized by COSMIC<sup>24</sup>, comprises 2–5 bp deletions, often with the loss of a single repeat unit in short repeat sequences<sup>5</sup>. These most commonly occur in regions in which the deleted sequence is repeated one, two or three times in tandem (Fig. 1a). Hereafter we use the term short-short tandem repeats (SSTRs) to distinguish between such short tandem repeats (STRs) with less than 5 repeats (that is, less than 6 repeat units) and microsatellite STRs with many repeats. In addition to these SSTR deletions, ID4 is characterized by small deletions at sequences with microhomology (MH), in particular, 2 bp deletions with single-nucleotide MH (SNMH). Both features are distinct from cancer deletion signatures resulting from other well-recognized mechanisms such as replication slippage and non-homologous/MH-mediated end joining (NHEJ/MMEJ) (Extended Data Fig. 1a,b). In

support of a distinct aetiology, SSTR and SNMH deletions are not apparent in cancer associated with homologous recombination or mismatch repair deficiency, which are expected to have higher levels of MMEJ and replication slippage mutagenesis, respectively (Extended Data Fig. [1c](#),[d](#)).

**Fig. 1: Top1-dependent deletions in *S. cerevisiae* resemble ID4, a cancer mutational signature of unknown aetiology.**

 figure 1



**a**, The ID4 signature comprises small deletions (typically 2, 3 or 4 bp in size) of one repeat unit at SSTR and MH sites. Repeated sequences (i–vi) are shown in bold and colour. Deletions are shown in red. **b**, Indel mutations similar to those detected in ID4 accumulate genome-wide in yeast with high levels of genome-embedded ribonucleotides. Reanalysis of WGS data for *rnh201Δ pol2-M644G* yeast<sup>[25](#)</sup>. **c**, Schematic of a frameshift mutation reporter containing many 2 bp SSTRs. Frameshift mutations in HygroR result in neomycin-resistant yeast colonies. P<sub>TEF</sub>, TEF promoter; P2A, self-cleaving peptide. **d**, **e**, Fluctuation assays demonstrated that Top1-mediated 2 bp SSTR mutations occur in wild-type and RNase-H2-deficient (*rnh201Δ*) backgrounds. **d**, Mutation rates for  $n = 16$  independent cultures per strain. Data are median  $\pm$  95% confidence intervals. **e**, WT and *rnh201Δ* have similar indel mutation spectra, and differ from *top1Δ* strains. Spectra of neomycin-resistant colonies.  $n$  indicates the number of independent indels detected. Cosine similarity  $P$  values were empirically determined (Extended Data Fig. [2e](#),[f](#)). Del, deletion; ins, insertion.

## ID4 resembles a yeast mutation signature

Noting similarities to a Top1-induced TAM (Top1-TAM) in *Saccharomyces cerevisiae*, we reanalysed published genome-wide mutation-accumulation experiments performed with *rnh201Δpol2-M644G* yeast<sup>25</sup>. This strain is particularly susceptible to Top1-TAM as it accumulates genome-embedded ribonucleotides at high levels due to RNase H2/RER deficiency and enhanced ribonucleotide incorporation by a steric-gate mutation at the catalytic site of the replicative polymerase Pol ε<sup>26</sup>. Similarities to the ID4 signature were apparent with a comparable pattern of small deletions at SSTRs, although mutational events at sites of SNMH were not evident in the yeast data (Fig. 1b). As more than 1 million ribonucleotides are incorporated by DNA polymerases per replicating mouse cell<sup>14</sup>, we reasoned that genome-embedded ribonucleotides might cause similar mutational events in mammalian cells. To experimentally assess whether TAM contributes to indel formation in human RER-deficient cells, we developed a reporter to enable sensitive and specific detection of mutational events arising from TOP1 activity in both yeast and mammals.

## Top1-dependent deletions in yeast

Mutation rates are routinely measured in *S. cerevisiae* using well-characterized but species-specific selectable markers (LYS2, URA3, CAN1). Thus, to establish a system that could be transferred between yeast and mammalian cells, we used an approach inspired by the Traffic Light reporter assay<sup>27</sup>, incorporating both positive and negative selection cassettes in a single transcriptional unit (Fig. 1c). The hygromycin-resistance gene (HygroR) was used both as the mutational target and negative selection marker. Indels causing a 2 bp frameshift within HygroR, including 2 bp deletions, result in translation of an otherwise out-of-frame P2A self-cleaving peptide and the neomycin-resistance (NeoR) gene, permitting positive selection of mutated colonies with neomycin (Extended Data Fig. 2a). To enrich the target for 2 bp tandem repeats, *in silico* redesign incorporated synonymous substitutions such that SSTRs accounted for >50% of the HygroR open reading frame.

For validation, the reporter was inserted into the *S. cerevisiae* genome and fluctuation assays were performed to assess the mutation rates in strains deficient for RER and/or Top1. A 37-fold increase in mutation rate was observed for the *rnh201Δ* (RNase H2 null) strain compared with the wild type (Fig. 1d), with a mutation rate of  $6.1 \times 10^{-9}$  per bp per generation (95% confidence interval =  $5.4 \times 10^{-9}$ – $6.9 \times 10^{-9}$ ), whereas the increased mutation rate was abolished in the *rnh201Δtop1Δ* double-mutant strain, consistent with Top1-dependent mutagenesis at genome-embedded ribonucleotides<sup>12,28</sup>. Notably, there was a 10-fold decrease in the mutation rate for *top1Δ* compared with the wild-type strain, and a 35-fold decrease in 2 bp SSTR

deletions (Extended Data Fig. 2b), consistent with previous reports<sup>10,11</sup>. Furthermore, the observed mutational spectrum was most similar for wild-type and *rnh201Δ* strains, but substantially different compared with the *top1Δ* and *rnh201Δ top1Δ* strains (Fig. 1e and Extended Data Fig. 2c–f). Taken together, we conclude that the same Top1-mediated mutations occur, albeit at different frequencies, in wild-type cells when RER is functional and in RNase-H2-deficient strains when elevated levels of ribonucleotides are present in the genome.

## TOP1-mediated mutations in human cells

Having validated the reporter in yeast, the same 2 bp repeat-enriched HygroR sequence was used to determine whether TOP1-mediated mutagenesis at embedded ribonucleotides is conserved in human cells (Fig. 2 and Extended Data Fig. 2g). NeoR was replaced by the puromycin-resistance (PuroR) gene, with reporter expression driven from the mammalian ubiquitous CAG promoter, permitting rapid antibiotic selection in mammalian cells. This modified reporter was inserted at the *AAVS1* safe harbour locus in HeLa cells (Fig. 2a and Extended Data Fig. 3a–e). CRISPR–Cas9-mediated genome editing targeting the catalytic site of *RNASEH2A* was then used to generate two independent knockout (KO) reporter clones, alongside a control clone that had also been processed through the editing and clonal selection steps (Fig 2b,c and Extended Data Fig. 3). The control clone retained RNase H2 activity, whereas there was complete loss of cellular RNase H2 activity in the KO clones, accompanied by high levels of ribonucleotides in genomic DNA (Fig. 2b,c and Extended Data Fig. 3f,g).

**Fig. 2: SSTR deletions of 2 bp are increased in RNase-H2-null HeLa cells.**



**a**, Schematic of the reporter targeting the *AAVS1* safe harbour locus to generate reporter cells (Extended Data Fig. 3). HA, homology arm; L, left; R, right. **b, c**, Validation of *RNASEH2A*-KO reporter clones. **b**, Immunoblot analysis of cell lysates detecting the three RNase H2 subunits. GAPDH was used as the loading control. Gel source data are provided in Supplementary Fig. 1. **c**, Cellular RNase H2 enzyme activity. Data are mean  $\pm$  s.d.  $n = 3$  technical replicates. HeLa, no modification; parental, HeLa with reporter (grey); KO1 and KO2, CRISPR-mediated *RNASEH2A*-KO clones (red); *RNASEH2A*<sup>+</sup>, CRISPR-edited reporter clone retaining RNase H2 activity (green). **d**, Fluctuation assays establish a significantly increased mutation rate in RNase-H2-null (KO) cells ( $P = 2 \times 10^{-6}$ ). Statistical analysis was performed using a two-sided Mann–Whitney test. Data are median  $\pm$  95% confidence intervals. The data points show the rates for independent cultures.  $n = 9$  (RNase H2 proficient, *RNASEH2A*<sup>+</sup>);  $n = 10$  (KO1, open circles) and  $n = 6$  (KO2, open squares). **e**, 2 bp SSTR and SNMH deletions are frequent in both *RNASEH2A*<sup>+</sup> and *RNASEH2A*-KO cells. Indel mutation spectra.  $n$  shows the number of indels identified by sequencing colonies from independent cultures.

In fluctuation assays, RNase-H2-null clones demonstrated a significant 3.1-fold increase in mutation rate (Fig. 2d) and 5.2-fold more 2 bp SSTR deletions (Extended Data Fig. 3h) compared with RNase-H2-proficient cells (*RNASEH2A*<sup>+</sup>), consistent with conservation of TOP1-directed mutagenesis in human cells. As in yeast (Fig. 1e), the overall mutational profile of reporter mutations was similar between RNase-H2-proficient and null HeLa cells (cosine similarity = 0.89,  $P < 10^{-4}$ ), predominantly comprising 2 bp SSTR deletions (Fig. 2e).

The mutation rate for RNase-H2-null HeLa cells ( $8.0 \times 10^{-9}$  per bp per generation; 95% confidence interval =  $6.7\text{--}9.5 \times 10^{-9}$ ) was similar to that observed for *rnh201Δ* yeast (Fig. 1d), whereas the rate was substantially higher for *RNASEH2A*<sup>+</sup> control cells compared with wild-type yeast. However, the increased mutation rate in RNase-H2-null HeLa cells probably underestimates the true impact of RER deficiency in human cells as, despite the fact that the control *RNASEH2A*<sup>+</sup> HeLa reporter cells retained protein expression (Fig. 2b), the clone had also acquired mutations at the CRISPR editing site that reduced enzymatic activity (Fig. 2c), causing a moderate increase in genomic ribonucleotide content (Extended Data Fig. 3f,g).

To confirm these findings, we used a complementary approach to establish the relevance of such mutational events genome-wide, performing mutation-accumulation experiments using human hTERT RPE-1 (*TP53*<sup>-/-</sup>) diploid cell lines. Ancestral populations for RNase-H2-wild-type and RNase-H2-null cells (*RNASEH2A*-KO or *RNASEH2B*-KO; Extended Data Fig. 4a-d) were established after initial single-cell sorting, and the clones were then grown for approximately 100 generations. Single-cell sorting was performed every 25 generations, creating bottlenecks to capture

accumulating mutations (Fig. 3a). Combined variant calling on whole-genome sequencing (WGS) from paired ancestral and end-point cultures identified a total of 1,698 acquired high-confidence indel mutations, captured by at least 3 out of 4 variant callers. Consistent with TOP1-mediated mutagenesis, among all indel categories, only 2–5 bp deletions were found to be substantially (7.4-fold) and significantly enriched in RNase-H2-null RPE-1 cells compared with the wild type (Fig. 3b and Extended Data Fig. 4e,f), with an estimated rate of  $1.1 \times 10^{-10}$  2–5 bp deletions per generation per bp for KO and  $1.4 \times 10^{-11}$  for the wild type. Of these deletions in RNase-H2-null cells, 82% were 2 bp deletions, of which 48% were at SSTRs (Extended Data Fig. 4g). Furthermore, signature decomposition using SigProfilerExtractor<sup>5</sup> reported a 21% ID4 contribution in RNase-H2-null cells that increased to 61% after background mutation patterns were subtracted to identify RER-deficiency-specific mutation signatures (Fig. 3c,d and Extended Data Fig. 5). The ID4 signature was substantially enriched in transcribed genomic regions (Extended Data Fig. 5e). ID5, a clock-like signature<sup>5</sup>, was also enriched in KO cells, probably due to slower growth and the longer culture time needed to achieve the same number of doublings for RNase-H2-null cells<sup>14</sup>.

**Fig. 3: ID4 SSTR and MH mutations are increased genome-wide in RNase-H2-deficient RPE-1 cells.**



**a**, Schematic of the mutation-accumulation experiment. Long-term culture of hTERT RPE-1 *TP53*<sup>-/-</sup> RNase-H2-wildtype (WT) and RNase-H2-null cell lines (*RNASEH2A*-KO (AKO), *RNASEH2B*-KO (BKO)) bottlenecked every 25 doublings by single-cell sorting. **b**, Mutations acquired during long-term culture were significantly enriched for 2–5 bp deletions in RNase-H2-null cells, but the other mutation categories were not

(Extended Data Fig. 4e). Data are mean  $\pm$  s.d. Statistical analysis was performed using two-sided Fisher's exact tests with Bonferroni correction, comparing wild type (counts pooled from  $n = 3$  independent clones) versus KO ( $n = 2$  independent clones) for 2–5 bp deletions versus all of the other indel types. c, d, ID4 occurs in RNase-H2-null cells (c) and is the major signature after subtracting background mutations that are observed in wild-type cells (d).

## MH deletions specific to mammals

Small deletions at sequences with MH are an additional feature of ID4 (Fig. 1a) that is not observed in *rnh201Δpol2-M644G* yeast (Fig. 1b). However, consistent with a ribonucleotide-induced mutational origin in mammalian cells, MH deletions are observed frequently in RNase-H2-deficient RPE-1 cells, in which SNMH sites account for 31% of 2 bp deletions, indicating that, in humans, deletions at SNMH sites share the same aetiology as deletions occurring at SSTRs. Taken together, our reporter and mutation-accumulation experiments demonstrate that genome-embedded ribonucleotides cause a similar mutational signature in yeast and mammalian cells. Thus, topoisomerase-1-mediated mutagenesis probably also occurs in humans and is associated with 2–5 bp deletions at SSTR and SNMH sequences.

## ID4 mutations in a mouse cancer model

To determine whether TOP1-induced mutations resulting in the ID4 signature can be detected *in vivo*, we next studied an RER-deficient mouse cancer model in which *Villin-cre* conditional deletion of *Rnaseh2b* and *Tp53* results in intestinal malignancy<sup>29</sup>. WGS analysis of paired tumour–normal tissue samples from 6 mice identified a total of 989 high-confidence tumour-specific somatic indels. An analysis of the resulting mutational signature established that ID4 substantially contributed in all tumours (Fig. 4a, b and Extended Data Fig. 6a), accounting for 32% of acquired indels. Consistent with a transcription-associated process, the ID4 signature was again most evident in transcribed genomic regions (Fig. 4b). The commonly occurring cancer signatures<sup>5</sup> ID1, ID2 and ID5 were also observed, consistent with expectations of multiple mutational processes active in neoplasia.

**Fig. 4: RER-deficient tumours have an ID4 signature associated with transcription and a TNT sequence motif.**

---

 **figure 4**

**a**, ID4 contributes substantially to the mutational spectrum of *Rnaseh2b*-KO mouse intestinal tumours (WGS, paired tumour–normal samples from  $n = 6$  mice). **b**, ID4 contribution is greater in transcribed regions of the genome. Statistical analysis was performed using a two-sided Fisher's exact test, comparing ID4 versus other indels.  $n = 969$  indels from 6 biologically independent tumours. **c**, 2 bp STR/SNMH deletions have biased sequence composition. Genome, frequency of dinucleotides in STR/SNMH sequences in the mappable genome. Deletions are right aligned and indicated by bold red font. **d**, **e**, A TNT sequence motif is present at all 2 bp STR and SNMH deletions. **d**, Sequence logo: two-bit representation of the sequence context of 2 bp deletions at STR and SNMH sequences. **e**, Deletion sites are significantly enriched for the TNT sequence motif compared with genome-wide occurrence, for all genome sequences, as well as STR and SNMH sites. Statistical analysis was performed using two-sided Fisher's exact tests, comparing observed versus expected.  $n = 228$  (all,  $P = 1.7 \times 10^{-28}$ ),  $n = 124$  (STR,  $P = 0.0008$ ),  $n = 77$  (SNMH,  $P = 1.4 \times 10^{-8}$ ) deletions in 6 biologically independent tumours. **f**, Model for TOP1-mediated mutations at TNT sequences containing embedded ribonucleotides, in which strand realignment results in a two-nucleotide deletion (see main text). nt, nucleotide.

The observed ID4 mutation spectrum corresponded closely to that observed in the RPE-1 mutation-accumulation experiment: 28% of indels were at 2–5 bp deletions, of which the majority were again 2 bp deletions (82%) predominantly at SSTRs (51%)

and sites of SNMH (34%) (Extended Data Fig. 6b, c). This is consistent with the occurrence of TOP1-induced somatic mutations at genome-embedded ribonucleotides in vivo, conserved across different tissue and cellular contexts, and shows that this process can be detected in a cancer setting.

## A sequence motif for ID4 mutations

Although COSMIC defines the ID4 signature on the basis of indel size and repeat/MH context (Fig. 1a), the number of indels in the mouse RER-deficient tumour model enabled us to further investigate the characteristics of mammalian topoisomerase-1-induced mutations. We focussed our analysis on 2 bp deletions, as such events represented 81% of >1 bp deletions in the context of tandem repeats and 85% of deletions in sequences with MH.

First, we classified all 2 bp deletions at STR/SNMH sequences into six non-redundant dinucleotide classes, grouping together complementary sequences (Fig. 4c). We noted that the deleted sequences substantially deviated from genome-wide frequencies, with a complete absence of CC/GG and CG/GC deletions, as well as an overrepresentation of the CT category (containing CT, TC, GA and AG deletions). All of the observed deletions therefore included at least one thymidine (T), which functionally could be accounted for by the very strong preference of mammalian topoisomerase 1 to cleave at a phosphodiester bond with a T immediately upstream<sup>30</sup>.

Next, to investigate the wider sequence context, we aligned sequences containing all 228 two-bp deletions (Extended Data Fig. 6d), which indicated that deletions preferentially occur when T nucleotides are spaced at a two-base interval. Indeed, this TNT motif was present in 100% of SNMH ( $n = 77$ ) and STR sites ( $n = 124$ ), providing a common unifying sequence context for both deletion types (Fig. 4d), a finding that was replicated in both our RPE-1 (Extended Data Fig. 6e) and yeast datasets (Extended Data Fig. 7). We found that TNT is substantially over-represented at deletion sites compared with the genome-wide null expectation. Furthermore, although the TNT motif is common at tandem repeat sequences, 2 bp deletions at this motif are still significantly enriched when considering the occurrence of 2 bp STR and SNMH sequences in mouse and human genomes (Fig. 4e and Extended Data Fig. 6f), and STR sequences in the yeast genome (Extended Data Fig. 7).

## A model for TOP1-mediated deletions

To account for thymidines spaced at a two-base interval and the occurrence of mammalian SNMH deletions, we developed a revised model based on the established strand realignment model for yeast Top1-mediated mutagenesis<sup>12,16,17</sup>. In this ‘TNT

model', TOP1 cleaves preferentially 3' of an embedded ribouridine, with nucleophilic attack by the 2'-OH of the ribose ring resulting in TOP1 release and formation of a non-ligatable nick with a terminal 2',3'-cyclic phosphate (Fig. 4f (i–iii)). This then provides a substrate for TOP1 cleavage 2 bp or more upstream<sup>17</sup>, preferentially at a thymidine<sup>30</sup>. When this second cleavage event happens at a base that is identical to that of the first cleaved nucleotide—an event that is more likely at STR and MH sequences—strand realignment can then occur, resulting in a nick that is permissive to religation and TOP1 cleavage complex (TOP1cc) reversal (Fig. 4f (iv–vi)). An alternative mechanism of sequential Top1 cleavage, in which double-strand breaks occur due to nicking of opposite strands<sup>31</sup> could not be reconciled with our TNT model, but may account for deletions occurring at non-STR/SNHM sites. Within the TNT motif, deletions were most common at CT and GT dinucleotides in both mammals and yeast (Fig. 4c and Extended Data Figs. 6 and 7b,e), which may be explained, at least in part, by preferential incorporation of ribouridine at CT and GT dinucleotides<sup>32</sup> (Extended Data Fig. 7f).

Implicating TOP1-TAM as the cause of the ID4 signature enables us to include additional features in the definition of this COSMIC signature, namely preference for a TNT sequence motif at 2 bp deletion sites and enrichment in transcribed genes. Hereafter, we refer to this extended definition as ID-TOP1. To establish the relevance of the ID-TOP1 signature for human disease and genetic variation, we next examined publicly available datasets.

## ID-TOP1 in human cancer

*RNASEH2B* is frequently deleted in human cancer, in particular, in chronic lymphocytic leukaemia (CLL), given its proximity to a tumour suppressor locus, the *DLEU2-miR-15a/miR-16-1* microRNA cluster<sup>33</sup>. Such RNase-H2-deficient human cancers should therefore be enriched for the ID4/ID-TOP1 signature. We analysed WGS data for 348 patients with CLL from two independent cohorts<sup>34,35</sup>, stratified on the basis of *RNASEH2B*-deletion status. Somatic variant calling identified a significant increase in 2–5 bp deletions in RNase-H2-null tumours (Fig. 5a), whereas other indels were equally represented across wild-type, heterozygous and null categories (Extended Data Fig. 8a). Of the 2–5 bp deletions in tumours with biallelic *RNASEH2B* loss, more than half (57%) were 2 bp deletions, which were predominantly at STR and SNMH sequences and substantially enriched for the TNT motif (Extended Data Fig. 8b,c), consistent with the ID-TOP1 mutational signature. Furthermore, mutational signature decomposition for RNase-H2-null CLL cases confirmed the presence of the ID4 signature, most apparent in genic regions (Extended Data Fig. 8d). We therefore conclude that the ID-TOP1 signature is present in human cancer and enriched in tumours that are RNase H2 deficient.

**Fig. 5: TOP1-mediated deletions in human cancer and germline.**

 figure 5

**a**, Deletions of 2–5 bp are significantly increased in CLL with biallelic *RNASEH2B* deletions (null). For the box plots, the box limits show from 25% to 75%, the centre line shows the median, the whiskers show from 5% to 95% and the data points show values outside the range. For GEL and ICGC, respectively,  $n = 116$  and  $n = 85$  (wild type);  $n = 72$  and  $n = 59$  (heterozygous (het)); and  $n = 10$  and  $n = 6$  (null) tumours. Multiple-testing-corrected  $q$  values were determined using two-sided Mann–Whitney  $U$ -tests. **b–d**, ID-TOP1 deletions are frequent somatic mutations in cancer. **b**, Indels per expression stratum of ubiquitously expressed genes (defined in Extended Data Fig. 8e). The dotted line shows the genome-wide rate. **c**, Deletions of 2 bp preferentially occur at TNT motifs. Statistical analysis was performed using two-sided Fisher’s exact tests, comparing observed versus expected.  $n = 11,853$  (all;  $P < 10^{-200}$ ),  $n = 6,699$  (STR;  $P = 1.9 \times 10^{-60}$ ),  $n = 2,872$  (SNMH;  $P = 1.5 \times 10^{-51}$ ) deletions. **d**, Deletions of 2–5 bp increase with TOP1 cleavage activity in ID4-positive PCAWG tumours. The solid lines show the relative deletion rate. The shading shows the 95% confidence intervals from 100 (**b**) or 1,000 (**d**) bootstrap replicates. For **b–d**,  $n = 11,853$  biologically independent tumours<sup>50</sup>. **e**, Deletions of 2–5 bp are enriched at tissue-

specific highly transcribed genes in associated cancers. Heat map of significant odds ratio scores (2–5 bp deletions in top 10% tissue-restricted genes versus 2–5 bp deletions in other genes, relative to expected frequency from all other tissues) for normal-tissue–tumour pairs. Statistical analysis was performed using two-sided Fisher’s exact tests. Adeno, adenocarcinoma; HCC, hepatocellular carcinoma; RCC, renal cell carcinoma. **f–h**, ID-TOP1 deletions are frequent human de novo mutations that are enriched in highly transcribed germ cell genes. **f**, Deletions of 2–5 bp are the most common indels in the human germline. Gene4Denovo WGS data<sup>39</sup> ( $n = 40,936$  indels). **g**, TNT sequence motif is significantly enriched in de novo 2 bp deletions. Statistical analysis was performed using two-sided Fisher’s exact tests, comparing observed versus expected.  $n = 5,569$  2 bp deletions ( $P < 10^{-200}$ ), at STR ( $n = 3,294$ ;  $P = 5.2 \times 10^{-47}$ ) and SNMH sequences ( $n = 1,093$ ;  $P = 2.9 \times 10^{-26}$ ). **h**, The 2–5 bp deletion frequency is correlated with gene transcription level in germ cells. Solid lines, Gene4Denovo indel mutations per individual per Mb. The shading shows the 95% confidence intervals from 100 bootstrap replicates.

Topoisomerase 1 also causes mutations in RER-proficient cells<sup>10,11</sup> (Fig. [1d–f](#)) and is therefore likely to cause mutations in other cancers, with deletions expected to occur most frequently in highly transcribed genes<sup>4</sup>. Accordingly, analysis of WGS data across cancer types (International Cancer Genome Consortium (ICGC)/Pan-Cancer Analysis of Whole Genomes (PCAWG)) demonstrated that the 2–5 bp deletion rate correlates with expression levels of ubiquitously expressed genes (Pearson’s  $r = 0.86$ ,  $P = 0.0014$ ), with deletions markedly elevated in the most highly expressed genes (Fig. [5b](#)), consistent with previous reports of such deletions in certain cancer genes<sup>36,37</sup>. Examination of 2 bp deletions (42% of 2–5 bp deletions) across cancer types also demonstrated them to be predominantly in STR and SNMH contexts (Extended Data Fig. [8f](#)) and enriched for the TNT sequence motif (Fig. [5c](#)). Furthermore, using a dataset of TOP1 cleavage events captured by TOP1-seq<sup>38</sup>, we found that 2–5 bp deletions increase in frequency with TOP1 enzymatic activity, with such deletions more prevalent in regions of high TOP1 activity (Fig. [5d](#)). Similarly, TOP1-ID deletion rates also corresponded to TOP1 activity and transcription level, in contrast to all other deletions (Extended Data Fig. [8g,h](#)). Taken together, this establishes a substantial role for TOP1-mediated mutagenesis in the generation of somatic deletions.

To further examine the role of transcription in deletion mutagenesis of cancer genomes, we identified genes that are highly expressed, but only in certain tissues. For prostate adenocarcinoma, highly expressed prostate-restricted genes were significantly enriched for 2–5 bp deletion mutations compared with other genes in this cancer type, as well as the same genes in other cancers (two-tailed Fisher’s exact test, odds ratio = 3.5,  $P = 2.5 \times 10^{-8}$  after Bonferroni correction; Extended Data Fig. [8i](#)). Importantly, this analysis considers the same sets of genes between cancer types and therefore rules out sequence composition biases as a confounding effect for elevated ID-TOP1

mutagenesis in highly expressed genes. Extending this approach in an all-versus-all comparison between 8 cancer types and 17 tissues demonstrated specificity between high expression in a tissue of origin and enrichment for 2–5 bp deletions (Fig. 5e). These results extend the relevance of TOP1-mediated mutagenesis to other cancers, confirm the ID-TOP1 mutational signature to be transcription-associated and support the occurrence of TAM in humans.

## TOP1-mediated deletions in the germline

TOP1 is ubiquitously expressed, so we reasoned that it could cause germline as well as somatic mutations. To investigate this possibility, we examined mutations from parent–child trio WGS studies in the Gene4Denovo database<sup>39</sup>. De novo mutations identified in such datasets represent germline events, as they occur in germ cells or during early embryonic cell divisions. Strikingly, 2–5 bp deletions were the largest category identified, accounting for 33% of the 40,936 de novo indels (Fig. 5f), and the majority of these were compatible with the ID-TOP1 signature. Analysis of 2 bp deletions (41% of 2–5 bp deletions) demonstrated that most occur at SSTR or MH sites (Extended Data Fig. 9a, b), with enrichment of the TNT sequence motif both genome wide and in the context of STR/SNMH sites (Fig. 5g and Extended Data Fig. 9c). Similarly, for 3 and 4 bp deletions, respectively, TNNT and TNNNT motifs were significantly over-represented compared with genome-wide expectation (Extended Data Fig. 9d), supporting sequential TOP1 cleavage and strand realignment as the underlying cause. Consistent with TOP1-TAM aetiology, 2–5 bp deletion and ID-TOP1 deletion frequency correlated with transcript expression in male germ cells (Fig. 5h and Extended Data Fig. 9e). We therefore conclude that the ID-TOP1 mutational signature also occurs in the human germline, implicating TOP1-induced strand realignment mutagenesis as an important mutational process in mammalian cells.

## Discussion

Here we establish a biological basis for the ID4 cancer signature<sup>5</sup>, experimentally demonstrating that it occurs in RNase-H2-deficient cells both in vitro and in vivo. This implicates TOP1-mediated cleavage at genome-embedded ribonucleotides as its cause. TOP1 is cell-essential in mammals and it is therefore not possible to similarly confirm a genetic dependency on TOP1 in human cells, as has been done in yeast<sup>12</sup>. However, conservation of this mechanism across eukaryotes is supported by us finding a topoisomerase-1-dependent TNT deletion motif that is present in both yeast and humans, and demonstrating that deletion frequency is dependent on human TOP1 activity levels. Previously published research also provides evidence for TOP1 mutagenesis at ribonucleotide sites in humans. The reversible transesterification reaction of type 1 topoisomerases is conserved from yeast to humans<sup>6</sup>, and human

TOP1 has site-specific activity for ribonucleotides<sup>40</sup>, causing DNA breaks in mammalian RNase-H2-deficient cells<sup>33</sup>. Furthermore, the generation of 2 bp deletions through sequential TOP1 cleavage at embedded ribonucleotides has been biochemically reconstituted with both human and yeast enzymes<sup>17,31</sup>.

We define additional features of this ID-TOP1 mutational signature, with deletions strongly enriched at TNT motifs in both yeast and mammals, a sequence context that is specific to topoisomerase 1 (Extended Data Fig. 7g,h) and deletions that are most frequent in highly transcribed regions. As a consequence, we show that a TAM process that was first identified in yeast<sup>10,12,41</sup> is relevant to higher eukaryotes, establishing TOP1-induced mutagenesis as an important process for human variation and disease. Additional signatures associated with topoisomerases or indeed RNase H2 may be identified in the future, particularly given that ID17 has recently been linked to TOP2A<sup>K743N</sup> cancers<sup>42</sup>.

The substantial contribution of ID-TOP1 deletions to germline mutagenesis has particular importance given that such deletions will be disproportionately disruptive, particularly in transcribed regions. Notably, such deletions occur in the context of normal RER function, consistent with the mutagenic potential of topoisomerase 1 in physiological wild-type settings<sup>10,11</sup> (Fig. 1d). Given that genome-embedded ribonucleotides are the most common endogenous lesion in replicating mammalian cells<sup>14</sup>, they are the most likely sites of TOP1-TAM mutagenesis, where TOP1 could cleave before their removal by RNase H2-dependent RER. Processing of TOP1cc may be an alternative, less frequent source of 2–5 bp deletions<sup>41</sup>, but we did not detect ID4 in cancers treated with topoisomerase 1 inhibitor (Extended Data Fig. 8j). The canonical function of TOP1 is to relieve DNA topological stress, arising during both transcription and replication<sup>6</sup> (Extended Data Fig. 10). Thus, TOP1-mediated deletions are not restricted to transcribed regions of the genome, with deletions also evident in non-genic regions with high TOP1 activity (Extended Data Fig. 8k). However, overall, enhanced TOP1 activity associated with transcription accounts for more frequent mutagenesis within genes.

Given the essential nature of topoisomerase activity across tissues and cell states, TOP1-mediated mutagenesis probably occurs in many contexts. The frequent TOP1-mediated human germline mutations (Fig. 5i–k) and the identification of ID4 at early embryonic stages<sup>43</sup> suggest developmental vulnerability to TOP1-TAM. Moreover, 2–5 bp somatic deletions at SSTRs are also observed at high frequency in non-dividing neurons<sup>36</sup>, and ID4 has been identified in multiple tumour types<sup>5</sup>. As such, this mutational process is likely to be important not only in cancers with RER deficiency, but also those with high TOP1 activity and tumours with defects in relevant repair mechanisms, such as enzymes that process TOP1cc<sup>6</sup> or non-ligatable TOP1-induced nicks<sup>44,45,46</sup>. Furthermore, alternative RER pathways may exist<sup>47</sup> that could reduce

TOP1 mutagenesis. The ID-TOP1 signature may provide a useful biomarker with potential future diagnostic and therapeutic use<sup>48</sup>, for example, as an indicator of TOP1-induced genome instability targetable by PARP or ATR inhibitors<sup>33,49</sup>.

In conclusion, alongside its essential role in relieving DNA torsional stress, TOP1 also drives mutagenesis in somatic and germline contexts, relevant to neoplasia, inherited disease and human variation.

## Methods

### Plasmids

A description of all plasmids used in this work is provided in Supplementary Table 1. The *S. cerevisiae* reporter was generated by DNA synthesis (GeneArt Gene Synthesis, Thermo Fisher Scientific; gBlocks Gene Fragments, IDT) and conventional cloning (restriction, ligation and Quikchange site-directed mutagenesis). The final construct (pTCW12) was used for *S. cerevisiae* reporter strain construction and fluctuation assays. A Gateway compatible reporter construct for mammalian cells (pTCW14) was generated in a similar manner using a combination of DNA synthesis and conventional cloning strategies. Gateway cloning was then used to move the reporter cassette into pAAVS-Nst-CAG-Dest (a gift from K. Woltjen; Addgene plasmid, 80489)<sup>51</sup> to generate pTCW15 for targeting it to the human *AAVS1* locus.

### In silico redesign of the hygromycin-resistance gene

To increase the frequency of 2 bp tandem repeats, synonymous substitutions were introduced in the 1 kb *hph* coding sequence, the *Klebsiella pneumoniae* hygromycin-resistance gene (HygroR)<sup>52</sup>. Using Python, a 5-codon (15-base) sliding window was moved one codon at a time, to identify all possible synonymous permutations. Permutations were ranked on the basis of tandem dinucleotide repeat sequence length, with the highest ranking sequences used to replace whole codons, prioritising dinucleotide repeats over mononucleotide repeats. Edited codons were then censored from subsequent permutation. Subsequently, to eliminate stop codons that would arise after a 2 bp deletion or equivalent frameshift mutations, further synonymous changes were made, where possible preserving tandem repeat sequences.

### Yeast strains and growth conditions

All *S. cerevisiae* strains used in this research (Supplementary Table 2) are isogenic with BY4741 (ref. <sup>53</sup>) and were grown at 30 °C. *TOP1* and *RNH201* open reading frames were deleted using one-step allele replacement using PCR products generated

from plasmid templates with selection cassettes (Supplementary Table 2) and primers containing 60-nucleotide homology directly upstream and downstream of the open reading frame. Gene deletions were confirmed by PCR. The 2 bp deletion reporter was inserted at the *AGP1* locus using a PCR product amplified from pTCW12 using primers AGP1-MX6-F and AGP1-MX6-R (Supplementary Table 3). The correct reporter insertion was confirmed by PCR and Sanger sequencing. Growth under selection was on YPD medium ( $10\text{ g l}^{-1}$  yeast extract,  $20\text{ g l}^{-1}$  bactopeptone,  $20\text{ g l}^{-1}$  dextrose,  $20\text{ g l}^{-1}$  agar) supplemented with hygromycin B ( $300\text{ mg l}^{-1}$ ), nourseothricin ( $100\text{ mg l}^{-1}$ ) and/or G418 ( $1\text{ g l}^{-1}$ ), or on synthetic defined medium ( $6.7\text{ g l}^{-1}$  yeast nitrogen base without amino acids, complete supplement single dropout mixture (Formedium),  $20\text{ g l}^{-1}$  dextrose,  $20\text{ g l}^{-1}$  agar).

## Fluctuation assays in yeast

Fluctuation assays were performed as previously described<sup>54</sup>. Yeast was grown overnight in YPD medium with hygromycin B ( $300\text{ mg l}^{-1}$ ), plated on YPD and grown at  $30\text{ }^{\circ}\text{C}$  to obtain individual colonies derived from a single cell without HygroR mutations. For each strain, 16 independent colonies were then used to inoculate 5 ml YPD, and grown for 3 days at  $30\text{ }^{\circ}\text{C}$  with shaking at 250 rpm. Cells were pelleted by centrifugation and resuspended in 1 ml of  $\text{H}_2\text{O}$ . Undiluted suspensions for each culture were plated ( $100\text{ }\mu\text{l}$  per plate) on 2 YPD plates supplemented with  $1\text{ g l}^{-1}$  G418, with the exception of *rnh201Δ* for which a  $10^{-2}$  dilution was used. Furthermore, each suspension was serially diluted to  $10^{-6}$  of which  $100\text{ }\mu\text{l}$  per plate was spread on 2 YPD plates to estimate the total number of viable cells per culture. Plates were incubated at  $30\text{ }^{\circ}\text{C}$  for 2–3 days, and colonies counted. Mutation rates were determined in Microsoft Excel 2016 for each individual culture, and an overall rate for each strain calculated using the Lea Coulson method of the median<sup>55</sup>. The number of mutants for each culture was ranked, and those ranked 4th and 13th were used to calculate the rates that define the lower and upper limits of the 95% CI<sup>56</sup>. A single G418-resistant colony for each independent culture was used to determine the spectrum of frame-shift mutations. A 1.3 kb region including HygroR was amplified in two overlapping amplicons (primers S297F and S1113R; S752 and S1658R) using FastStart PCR Master Mix (Roche) and direct colony PCR (5 min at  $95\text{ }^{\circ}\text{C}$ ; then 35 cycles of 30 s at  $95\text{ }^{\circ}\text{C}$ , 30 s at  $58\text{ }^{\circ}\text{C}$  and 45 s at  $72\text{ }^{\circ}\text{C}$ ; and then 45 s at  $72\text{ }^{\circ}\text{C}$ ). Each amplicon was Sanger sequenced using the primers described in Supplementary Table 3, and analysed using Sequencher v.5.4.6 (Gene Codes Corporation) and/or Mutation Surveyor v.3.30 (SoftGenetics). Mutation rates (per bp) were calculated for 1,032 bp of sequence in which productive frameshift mutations can occur.

## Cell lines

A summary of the human cell lines used in this research is provided in Supplementary Table 4. All cells were grown at 37 °C and 5% CO<sub>2</sub>, authenticated using STR DNA profiling in the laboratories of origin and shown to be mycoplasma negative through routine testing. HeLa cells (a gift from G. Stewart, University of Birmingham, UK; originally purchased from ATCC) were grown in Dulbecco's Modified Eagle Medium (DMEM; Gibco/Thermo Fisher Scientific) supplemented with 10% fetal bovine serum (FBS), 50 U ml<sup>-1</sup> penicillin and 50 µg ml<sup>-1</sup> streptomycin. hTERT RPE-1 cells (a gift from D. Durocher, University of Toronto, Canada; originally purchased from ATCC) were grown in DMEM/F12 medium mixture (Gibco/Thermo Fisher Scientific) supplemented with 10% FBS, 50 U ml<sup>-1</sup> penicillin and 50 µg ml<sup>-1</sup> streptomycin. The 2 bp deletion reporter was integrated at the *AAVS1* safe harbour locus in HeLa cells using a published CRISPR–Cas9 targeting protocol<sup>51</sup>. HeLa cells were transfected with pXAT2 and pTCW15 in Opti-MEM reduced-serum medium using Invitrogen Lipofectamine 2000 (Thermo Fisher Scientific). After 48 h cells were replated in medium containing 500 µg ml<sup>-1</sup> G418 and, after another 48 h and a second round of replating in selective medium, single cells were sorted into 96-well plates using a BD FACSJazz instrument (BD Biosciences). The resulting G418-resistant clones were screened by PCR for reporter integration at the correct locus, retention of integration-free *AAVS1* and Sanger sequencing of resulting PCR products. Single-locus integration was confirmed by fluorescence in situ hybridization (FISH) as previously described<sup>57</sup>, using pTCW16 to generate a fluorescently labelled probe. The full reporter sequence of selected clones was checked, with amplification of a 1.9 kb fragment using Prime Star Max PCR Master Mix (Takara Bio) with the primers HygroR\_up and PuroR\_rev (40 cycles of 10 s at 98 °C, 15 s at 70 °C and 2 min at 72 °C), followed by Sanger sequencing with additional primers (Supplementary Table 3). To generate *RNASEH2A*-KO reporter cells, the selected parental HeLa reporter clone was transfected with pMAR526 and pMAR527 (Supplementary Table 1), using Lipofectamine 2000. Then, 48 h after transfection, single EGFP-expressing cells were sorted into 96-well plates and grown until colonies formed. Initial screening was based on PCR amplification (primers RNASEH2A-ex1F and RNASEH2A-ex1R) of the CRISPR–Cas9-targeted region of *RNASEH2A* with mutations present in selected clones determined by Sanger sequencing. The cellular RNase H2 status was then confirmed by immunoblotting, RNase H2 enzymatic activity assay and alkaline gel electrophoresis to determine ribonucleotide content of genomic DNA (detailed methods are provided below).

## Fluctuation assays in human

Hygromycin resistant HeLa reporter cells (400 µg ml<sup>-1</sup> hygromycin B) were recovered from frozen stocks in the absence of selection. The next day, 10 wells of a 96-well plate were seeded with 2,000 cells per well for each line. The experiment was

performed with the operator blinded to the identity of the cell lines. Cells were cultured under non-selective conditions and replated subsequently in 24-well, 6-well plates and ultimately T75 flasks, in which they were grown to confluence. Cells were then dissociated using Gibco TrypLE (Thermo Fisher Scientific) and the cells were counted using a Moxi Z automated cell counter. After serial dilution, 1,000 cells were plated into two 10 cm plates for each culture and grown for 14 days to determine plating efficiency. All other cells were plated into two 10 cm plates, and  $0.5 \mu\text{g ml}^{-1}$  puromycin was added after 4 h, with the medium subsequently changed every 2–3 days for 14 days to remove dead cells and maintain a puromycin concentration of  $0.5 \mu\text{g ml}^{-1}$ .

To establish mutation spectra, colonies were removed by scraping and then cultured in a 96-well plate. When confluent, cells were lysed with 75  $\mu\text{l}$  DirectPCR Lysis Reagent (Viagen Biotech) and  $0.4 \text{ mg ml}^{-1}$  PCR-grade Proteinase K (Roche), heating overnight at 55 °C followed by 45 min at 85 °C. Only one sample per independent culture was used for PCR amplification and Sanger sequencing to determine the nature of mutations in the HygroR coding sequence. A 1.24 kb region including HygroR was amplified with Prime Star Max PCR Master Mix (Takara Bio), HygroR\_up and H1327R primers (40 cycles of 10 s at 98 °C, 15 s at 70 °C, 2 min at 72 °C). Sanger sequencing was then performed with additional primers (Supplementary Table 3) and mutations identified using Mutation Surveyor v.3.30 (SoftGenetics). All mutants showed double traces of equal height from the point of indel mutations, consistent with the presence of two copies of the reporter in all reporter lines. As FISH indicated the presence of the reporter at a single *AAVS1* locus, we inferred that two copies of the reporter were inserted in tandem at this locus. As a 2 bp deletion or equivalent frameshift mutation in either HygroR copy would bring the associated PuroR coding sequence into the translated reading frame, we corrected mutation rate calculations (per bp) for the presence of two copies.

To determine colony numbers, plates were washed with PBS, fixed with 2% formaldehyde in PBS for 10 min, rinsed with water and colonies were stained with 0.1% crystal violet solution for 10 min. Plates were then washed with water and left to dry before counting colonies. After counting, the experiment was performed in an unblinded manner. Mutation rates were determined for each individual culture in Microsoft Excel 2016, and an overall rate for wild-type and KO strains was calculated using the Lea Coulson method of the median. The number of mutants for each culture was ranked, and appropriate ranks<sup>56</sup> were used to calculate the rates that define the lower and upper limits of the 95% CI.

## Immunoblotting

Whole-cell extracts (WCE) to determine protein levels of RNase H2 subunits by immunoblotting and for RNase H2 activity assays were prepared as previously described<sup>58</sup>. Equal amounts of protein from WCE were separated by SDS-PAGE on 4–12% NuPAGE gels and transferred to PVDF. Membranes were probed in 5% milk (w/v; Marvel Original Dried Skimmed), TBS + 0.2% Tween-20 (v/v) with the following antibodies: sheep anti-RNase H2 (raised against human recombinant RNase H2, 1:1,000)<sup>14</sup>; mouse anti-RNASEH2A G-10 (Santa Cruz Biotechnologies, sc-515475, A1416, 1:1,000); rabbit anti-GAPDH (Abcam, ab9485, 1:2,000, GR3380498-1). For detection, we used rabbit anti-sheep immunoglobulins/HRP (Dako, P04163, 00047199, 1:2,000); goat anti-mouse immunoglobulins/HRP (Dako, P0447, 20039214, 1:10,000); anti-rabbit IgG, HRP-linked antibodies (Cell Signaling Technologies, 7074S, 29, 1:10,000); Amersham ECL Prime Western Blotting Detection Reagent (GE Healthcare Life Sciences) and an ImageQuantLAS4000 device, or IRDye secondary antibodies and an Odyssey CLx Imaging System (LI-COR Biosciences). The uncropped immunoblots are presented in Supplementary Fig. 1.

## RNase H2 activity assays

To assess cellular RNase H2 activity, a FRET-based fluorescence substrate release assay was performed as previously described<sup>14</sup>. In brief, RNase-H2-specific activity was determined by measuring the cleavage of double-stranded DNA substrate containing a single embedded ribonucleotide. Activity against a DNA-only substrate of the same sequence was used to correct for background activity. Substrates were formed by annealing a 3'-fluorescein-labelled oligonucleotide (GATCTGAGCCTGGGaGCT or GATCTGAGCCTGGGAGCT; uppercase DNA, lowercase RNA) to a complementary 5'-DABCYL-labelled DNA oligonucleotide (Eurogentec). The reactions were performed in 100 µl reaction buffer (60 mM KCl, 50 mM Tris-HCl pH 8.0, 10 mM MgCl<sub>2</sub>, 0.01% BSA, 0.01% Triton X-100) with 250 nM substrate in black 96-well flat-bottomed plates (Costar) at 24 °C. WCE was prepared as described above, protein concentrations determined using the Bio-Rad Bradford Protein Assay and the final protein concentration per reaction was 50 ng µl<sup>-1</sup>. Fluorescence was read (100 ms) every 5 min for up to 90 min using the VICTOR2 1420 multilabel counter (Perkin Elmer), with a 480 nm excitation filter and a 535 nm emission filter. Initial substrate conversion after background subtraction was used to calculate RNase H2 enzyme activity.

## Alkaline gel electrophoresis

To determine the presence of excess genome-embedded ribonucleotides in nuclear DNA, alkaline gel electrophoresis of RNase-H2-treated genomic DNA was performed as previously described<sup>58</sup>. In brief, total nucleic acids were isolated from pellets from

around 1 million cells by incubation in ice-cold buffer (20 mM Tris-HCl pH 7.5, 75 mM NaCl, 50 mM EDTA) with 200 µg ml<sup>-1</sup> proteinase K (Roche) for 10 min on ice, followed by addition of *N*-lauroylsarcosine sodium salt (Sigma-Aldrich) to a final concentration of 1%. Nucleic acids were extracted using phenol–chloroform, then isopropanol-precipitated and dissolved in nuclease-free water. For alkaline gel electrophoresis, 500 ng of total nucleic acids was incubated with 1 pmol of purified recombinant human RNase H2 (isolated as previously described<sup>59</sup>) and 0.25 µg of DNase-free RNase (Roche) for 30 min at 37 °C in 100 µl reaction buffer (60 mM KCl, 50 mM Tris-HCl pH 8.0, 10 mM MgCl<sub>2</sub>, 0.01% Triton X-100). Nucleic acids were ethanol-precipitated, dissolved in nuclease-free water and 250 ng was separated on 0.7% agarose gels in 50 mM NaOH, 1 mM EDTA. After overnight electrophoresis, the gel was neutralised in 0.7 M Tris-HCl pH 8.0, 1.5 M NaCl and stained with SYBR Gold (Invitrogen). Imaging was performed on a FLA-5100 imaging system (Fujifilm), and densitometry plots were generated using AIDA Image Analyzer v.3.44.035 (Raytest).

## Mutation-accumulation experiment

*TP53*-KO hTERT RPE-1 cells without and with loss-of-function mutations in *RNASEH2A* or *RNASEH2B*, introduced by CRISPR–Cas9 genome editing, a gift from D. Durocher, have previously been described<sup>33</sup>. RNase-H2-proficient (wild type), *RNASEH2A*-KO and *RNASEH2B*-KO cells were single-cell sorted into 96-well plates using the BD FACSJazz instrument (BD Biosciences). Multiple individual clones for each were expanded to confluent T75 flasks for cryopreservation and genomic DNA isolation of these ancestral populations. Moreover, lines were again single-cell sorted into 96-well plates to start the mutation-accumulation experiment. Cultures were expanded by subsequent growth in 24-well, 6-well plates and T75 flasks until confluent (approximately 25 population doublings), and this process of single-cell sorting and expansion was repeated four more times, providing bottlenecks to capture mutations that occurred since the previous sort. From the first to the last single-cell sort, a total of approximately 100 population doublings occurred and the final culture was expanded for cryopreservation and genomic DNA isolation of these end-point populations.

Genomic DNA was isolated using phenol extraction as previously described<sup>58</sup>, for alkaline gel electrophoresis and WGS. Library preparations and sequencing were performed by Edinburgh Genomics. Libraries were prepared using Illumina SeqLab specific TruSeq PCRFree High Throughput library preparation kits according to the manufacturer's instructions, with DNA samples sheared to a mean insert size of 450 bp. Libraries were sequenced using paired-end reads on the Illumina HiSeqX instrument using v2.5 chemistry to achieve minimum mean genome-wide sequencing depth of 30× per sample.

## Mouse WGS analysis

*Villin-cre<sup>+</sup> Trp53<sup>f/f</sup> Rnaseh2b<sup>f/f</sup>* mice with epithelial-specific deletion of *Trp53* and *Rnaseh2b* on a C57Bl/6J background have been described previously<sup>29</sup>. Animal experiments were conducted with appropriate permission, in accordance with guidelines for animal care of the Christian-Albrechts-University, in agreement with national and international laws and policies. No randomization or blinding was performed. Paired tumour–normal DNA was isolated from small intestinal tumours (*Trp53<sup>-/-</sup> Rnaseh2b<sup>-/-</sup>*) and liver tissue (*Trp53<sup>+/+</sup> Rnaseh2b<sup>+/+</sup>*) from female mice (aged 52 weeks), using the Qiagen DNeasy Blood & Tissue Kit. Library preparations and sequencing were performed by Edinburgh Genomics using Illumina DNA PCR-Free Library Prep according to the manufacturer’s instructions. Paired-end sequencing was performed by Edinburgh Genomics on a NovaSeq 6000 using v1.5 chemistry. Mean genome-wide sequencing depth of at least 30× for liver samples and 60× for tumour samples was obtained.

## *S. cerevisiae* WGS analysis

WGS SRA files for *rnh201Δpol2-M644G* *S. cerevisiae*<sup>25</sup> from the NCBI Sequence Read Archive (SRA) were converted to FASTQ files using SRA Toolkit v.2.5.4-1 (SRA Toolkit Development Team; <http://ncbi.github.io/sra-tools/>). FASTQ reads were aligned to the GSE56939\_L03\_ref\_v2 reference genome<sup>60</sup> (Supplementary Table 5) and sorted BAM files were created using BWA-MEM (v.0.7.12)<sup>61</sup>, and deduplicated with SAMBLASTER (v.0.1.22)<sup>62</sup>. To select high-quality indel variants, GATK (v.3.6-0) Haplotype Caller (without base quality score recalibration)<sup>63</sup> variant calling was performed with ‘Hard Filters’ (--filterExpression “QD < 2.0 || FS > 200.0 || ReadPosRankSum < -20.0”). Filtering for strain-specific variants was performed as previously described<sup>60</sup>, with minor modifications. The filters were as follows: (1) eliminate variants shared with an ancestral clone; (2) required ≥20 reads for variant allele in descendent; (3) exclusion of repetitive sequences as defined in ref. <sup>60</sup>; and (4) reference/variant depth ratio 0.4–0.6, <0.4 if homozygous variant allele.

## RPE-1 WGS analysis

FASTQ files were converted to unaligned BAM format and Illumina adaptors were marked using GATK (v.4.1.9.0) FastqToSam and MarkIlluminaAdapters tools<sup>64</sup>. Reads were aligned to the human genome (hg38, including alt, decoy and HLA sequences) using BWA-MEM (v.0.7.16)<sup>61</sup> and read metadata were merged using GATK’s MergeBamAlignment tool. PCR and optical duplicate marking and base quality score recalibration were performed using GATK. Variants from NCBI dbSNP build 151 were used as known sites for base quality score recalibration. Post-processed

alignments were genotyped using Mutect2, Strelka2, Platypus and SvABA using somatic calling models for each pair of ancestral and end-point cultures, as described below.

## Mouse WGS analysis

FASTQ processing and alignment were performed as for RPE-1 WGS analysis, using the GRCm38 mouse genome reference and known variant sites from the Mouse Genomes Project<sup>65</sup> (REL-1807-SNPs\_Indels) for base quality score recalibration. Somatic variant calling of post-processed alignments was performed using Mutect2, Strelka2, Platypus and SvABA for each tumour-liver pair, as described below. Somalier v.0.2.12 (<https://github.com/brentp/somalier>) was used to confirm each paired tumour and liver sample originated from the same animal.

## Human ethics approval

Data generated from Genomics England 100,000 genomes and ICGC-CLL studies were analysed. In these respective studies, informed consent for participation was obtained. Ethical approval for Genomics England 100,000 genomes project: East of England and South Cambridge Research Ethics Committee; CLL-ICGC: International Cancer Genome Consortium (ICGC) guidelines from the ICGC Ethics and Policy committee were followed and the study was approved by the Research Ethics Committee of the Hospital Clínic of Barcelona.

## CLL WGS analysis

### Genomics England

CLL tumour–normal pairs ( $n = 198$ ) were processed as part of the 100,000 Genomes Project (pilot and main programme v8). Samples were sequenced using the Illumina HiSeq X System with 150 bp paired-end reads at a minimum of 75 $\times$  coverage for tumours and 30 $\times$  coverage for germline samples. Reads were mapped to GRCh38 using ISAAC aligner (v.03.16.02.19)<sup>66</sup>. Single-nucleotide variants (SNVs) and indels were called using Strelka v.2.4.7 using somatic calling mode. Structural and copy number variants were called using Manta (v.0.28.0) and Canvas (v.1.3.1)<sup>67</sup>, respectively. Samples with a tumour purity estimate from Canvas of less than 50% were excluded from analysis. *RNASEH2B* copy number was determined using a combination of Canvas, Manta, read depth counts with samtools (v.1.9) and confirmed by manual inspection using IGV (v.2.5.0)<sup>68</sup>.

### ICGC

WGS from the ICGC-CLL cohort<sup>35</sup> ( $n = 150$ ) was reanalysed. Raw reads were mapped to the human reference genome (GRCh37) using BWA-MEM (v.0.7.15)<sup>61</sup>. BAM files were generated, sorted and indexed, and optical or PCR duplicates were flagged using biobambam2 (<https://gitlab.com/german.tischler/biobambam2>, v.2.0.65). Copy-number alterations were called from WGS data using Battenberg (cgpBattenberg, v.3.2.2)<sup>69</sup>, ASCAT (ascatNgs, v.4.1.0)<sup>70</sup>, and Genome-wide Human SNP Array 6.0 (Thermo Fisher Scientific) data<sup>35</sup> reanalysed using Nexus 9.0 Biodiscovery software (Biodiscovery). *RNASEH2B* copy number was established by combining the three analyses and manual review with IGV.

## Colorectal cancer WGS analysis

Irinotecan-treated ( $n = 39$ ) and irinotecan-untreated ( $n = 78$ ) colorectal cancers from the 100,000 Genomes Project Colorectal Cancer Domain were 1:2 matched using a multivariate greedy matching algorithm without replacement, implemented in the Matching R-package<sup>71</sup>. Matching was conducted considering sex, age at sampling, whether a primary tumour or metastasis had been sequenced, microsatellite instability status, and whether the individual had previously received radiotherapy, oxaliplatin, capecitabine or fluorouracil treatment.

## Somatic variant calling

Somatic variant calling was performed in parallel using four distinct methods: Mutect2 (as part of GATK v.4.1.9.0)<sup>72,73</sup>, Strelka2 (v.2.1.9.10)<sup>74</sup>, SvABA (v.1.1.3)<sup>75</sup> and Platypus (v.0.8.1)<sup>76</sup>. High-confidence indel calls were defined as the intersected output of these four tools, where variants passed all filters for  $\geq 3$  of 4 callers. The intersection was performed using the bcftools (v.1.10.2)<sup>77</sup> isec function after normalizing variant calls and left-aligning ambiguous alignment gaps using the bcftools norm function. For Platypus (v.0.8.1)<sup>76</sup>, joint calling all samples in each cohort was performed before filtering for somatic variants; the other variant callers were run in paired tumour–normal mode. For the RPE-1 mutation-accumulation experiment the end-point and ancestral cultures were defined as ‘tumour’ and ‘normal’ samples, respectively. Variant filtering strategies were optimized to both available information on segregating genetic variation for humans and mice, and the functionality of each calling method as detailed below.

### Mutect2

Unfiltered genotypes for all normal samples were combined to filter germline variants. Somatic calls were obtained using GATK’s FilterMutectCalls command. Human

polymorphism data and allele frequencies from gnomAD<sup>78</sup> were provided to Mutect2 for the filtering of germline variants.

## SvABA

Germline indel and structural variants were filtered using the --dbsnp-vcf and --germline-sv-database options. Mouse indels were obtained from Mouse Genomes Project version 5 SNP ([ftp://ftp-mouse.sanger.ac.uk/REL-1505-SNPs\\_Indels/mgp.v5.merged.indels.dbSNP142.normed.vcf.gz](ftp://ftp-mouse.sanger.ac.uk/REL-1505-SNPs_Indels/mgp.v5.merged.indels.dbSNP142.normed.vcf.gz)); structural variants from SV release version 5 ([ftp://ftp-mouse.sanger.ac.uk/REL-1606-SV/mgpv5.SV\\_insertions.bed.gz](ftp://ftp-mouse.sanger.ac.uk/REL-1606-SV/mgpv5.SV_insertions.bed.gz) and [ftp://ftp-mouse.sanger.ac.uk/REL-1606-SV/mgpv5.SV\\_deletions.bed.gz](ftp://ftp-mouse.sanger.ac.uk/REL-1606-SV/mgpv5.SV_deletions.bed.gz)). Human indels were extracted from NCBI dbSNP build 151 and common structural variants from dbVAR (<https://hgdownload.soe.ucsc.edu/gbdb/hg38/bbi/dbVar/>).

## Strelka2

Candidate small indels for each pair were first generated by Manta (v.1.6.0)<sup>79</sup> in somatic calling mode. Strelka2 was then executed in somatic calling mode for each pair with Manta's candidate small indels output provided to the --indelCandidates option.

## Platypus

Germline variants were filtered on the basis of any normal sample with  $\geq 2$  variant allele reads. Somatic variant calls for each sample pair were retained if tumour/end-point sample  $> 2$  variant reads; site depth  $> 9$ ; and normal sample read depth  $\geq 20$ ,  $< 2$  variant reads. Moreover, a  $> 10\times$  ratio of tumour to normal for variant/total depth was required.

For Genomics England CLL tumour–normal pairs, pre-existing Strelka2 calls from the 100,000 Genomes Project pipeline were used, while variant calling with Mutect2, Platypus and SvABA was performed as above. Colorectal cancer tumour–normal pairs from Genomics England were processed as for Genomics England CLL but without Mutect2 analysis. For ICGC CLL, somatic indels were called using Mutect2 (GATK v.4.0.2.0)<sup>72,73</sup>, Strelka2 (v.2.8.2)<sup>74</sup>, SvABA (v.1.1.0)<sup>75</sup> and Platypus (v.0.8.1)<sup>76</sup>. Candidate small indels generated by Manta (v.1.2)<sup>79</sup> were used as input for Strelka2. Mutect2, Strelka2 and SvABA were run in paired tumour–normal mode. `somaticMutationDetector.py` (<https://github.com/andyrimmer/Platypus/tree/master/extensions/Cancer>) was used to identify somatic indels called by Platypus with a minimum posterior of 1. SNVs called

by Platypus were considered to be somatic if they had at least 2 alternative reads in the tumour, fewer than 2 alternative reads in the normal, a minimum tumour VAF of 10 $\times$  the control VAF, and a minimum depth of 10.

## Germline mutation analysis

De novo WGS variants were downloaded from the Gene4Denovo database (Supplementary Table 5). Reference assembly conversion errors were removed by discarding variants for which the reference allele did not match the genome reference at the given position or for which the variant position was greater than the length of the reference chromosome. Furthermore, individuals with total de novo variants below the 10th ( $n = 33$ ) or above the 90th ( $n = 140$ ) percentile were excluded. For germline gene expression we used predefined expression groups<sup>80</sup> based on Ensembl release 90 annotation ([ftp://ftp.ensembl.org/pub/release-90/gtf/homo\\_sapiens/Homo\\_sapiens.GRCh38.90.gtf.gz](ftp://ftp.ensembl.org/pub/release-90/gtf/homo_sapiens/Homo_sapiens.GRCh38.90.gtf.gz)). Initially stratified as nine expression groups from 1 (unexpressed) to 9 (high), we collapsed them into a smaller set of unexpressed (1), low (2, 3, 4), mid (5, 6, 7) and high (8, 9). The annotations were converted to GRCh37 coordinates using liftover (kent source v.417). Genomic segments overlapping multiple distinct expression groups, due to overlapping genes, were assigned to the higher of those expression groups. For each expression group, we summed the count ( $c$ ) of de novo indels contained within the genomic span of those genes. This was converted to rate estimates by dividing by the union genomic span ( $g$  nucleotides) of genes in that expression group, and adjusting for the number of mutated genomes considered ( $n$ ); rate =  $c/(gn)$ . To obtain 95% CIs, gene selection was bootstrapped (sampled to an identical number with replacement) 100 times and the 0.025 and 0.975 quantiles of the bootstrapped rate calculation taken as the 95% CI.

## ICGC pan-cancer expression analysis

The ICGC PCAWG somatic mutations<sup>50</sup> ([https://dcc.icgc.org/api/v1/download?fn=PCAWG/consensus\\_snv\\_indel/final\\_consensus\\_passonly.snv\\_mnv\\_indel.icgc.public.maf.gz](https://dcc.icgc.org/api/v1/download?fn=PCAWG/consensus_snv_indel/final_consensus_passonly.snv_mnv_indel.icgc.public.maf.gz)) and ICGC PCAWG ‘baseline’ gene expression data<sup>50</sup> were obtained (ArrayExpress, <https://www.ebi.ac.uk/arrayexpress/experiments/E-MTAB-5200/>). Genomic annotation of gene extents on the GRCh37 reference genome match the Ensembl version 75 annotation ([http://ftp.ensembl.org/pub/release-75/gtf/homo\\_sapiens/Homo\\_sapiens.GRCh37.75.gtf.gz](http://ftp.ensembl.org/pub/release-75/gtf/homo_sapiens/Homo_sapiens.GRCh37.75.gtf.gz)) of the ICGC gene expression calls. Mean, median and maximal gene expression (transcripts per million (TPM)) were calculated for each gene across the 76 ICGC baseline gene expression tissues/samples. Only genes annotated on the main autosomal chromosomes, 1 to 22, and the X chromosome were considered. Overlapping genes were removed, retaining only the most abundantly (highest median, then mean in the case of ties) expressed genes from overlapping pairs. This filtering was applied hierarchically, starting with

the most abundant. Following ref. 81, genes with housekeeping-like expression were defined as those with maximal expression of less than ten times median expression. Housekeeping-like genes were decile-binned into expression groups on the basis of median expression. Mutations were stratified by type (1 bp deletion, 2–5 bp deletion) or by the ‘TN\*T’ motif defined below and counted by intersection with the annotated genomic extents of genes in each expression group.

For the analysis of tissue-biased gene expression, the 76 ICGC baseline samples were grouped by annotated tissue (such as breast, prostate, kidneys, liver) and matched where possible to the tissue of origin for ICGC cancer types. For each tissue, the median expression (in TPM) of each gene was calculated for (1) within-tissue samples and (2) for all other samples. The 90th quantile of gene expression (q90, top 10%) within a tissue was set as a threshold for high level expression. Genes with high expression in a tissue (1) but a median expression of less than q90\*0.1 in the other tissues (2) were considered to be highly expressed but tissue restricted (HETR). For the set of HETR genes from a tissue, we counted the number of 2–5 bp deletions within the annotated genomic extent of the HETR genes in a cancer type of interest. We similarly counted 2–5 bp deletions in all other genes for that cancer type, and counted both the HETR and non-HETR 2–5 bp deletions from all other cancer types within the ICGC cohort. For each cancer–tissue pair, this provided four sets of counts, analysed using two-tailed Fisher’s exact tests using the R function `fisher.test`. A positive odds ratio indicated enrichment of 2–5 bp deletions in the HETR genes, compared with a background of the remainder of the ICGC cohort in which HETR genes are not highly expressed. For each cancer type considered, this test was repeated for each tissue type ( $n = 17$ ). Analyses were carried out for eight of the ICGC cohort cancer types that met the combined criteria of having a well-matched and known tissue of origin among the ICGC baseline samples, and requiring the cancer type cohort to have at least  $n = 2,500$  2–5 bp deletions in aggregate. This represents  $n = 17 \times 8 = 136$  statistical tests, adjusted by Bonferroni correction. Odds ratios ( $r$ ) for mutation depletion were transformed to their reciprocal ( $1/r$ ) for display purposes.

## ICGC pan-cancer TOP1-seq analysis

Data corresponding to two replicates of TOP1-seq, a modified ChIP–seq technique to immunoprecipitate only catalytically engaged TOP1 (ref. 38), were downloaded from the NCBI Gene Expression Omnibus database (accession code [GSE57628](#), samples [GSM1385717](#) and [GSM1385718](#)). Autosomal chromosomes 1 to 22 and the X chromosome were divided into 1 kb bins and, for each bin, the amount of mappable sequence was determined using Umap’s regions mappable using 36-mers<sup>82</sup> to approximate the read length of the TOP1-seq data. For each 1 kb window, the TOP1-seq signal within mappable regions was summed for each replicate and the mean signal was calculated. This mean was divided by the amount of mappable sequence to

calculate the TOP1-seq signal per bp and each 1 kb window was then assigned to decile bins using this value.

Somatic deletion calls from ID4-positive PCAWG samples (as defined in [https://dcc.icgc.org/api/v1/download?  
fn=/PCAWG/mutational\\_signatures/Signatures\\_in\\_Samples/SP\\_Signatures\\_in\\_Samples/PCAWG\\_SigProfiler\\_ID\\_signatures\\_in\\_samples.csv](https://dcc.icgc.org/api/v1/download?fn=/PCAWG/mutational_signatures/Signatures_in_Samples/SP_Signatures_in_Samples/PCAWG_SigProfiler_ID_signatures_in_samples.csv)) were counted within the same

36-mer mappable regions for each 1 kb window and either stratified by type (1 bp deletion, 2–5 bp deletion) or by the TN\*T motif defined below. Relative rates of deletions in each category were calculated relative to the first TOP1-seq signal decile.

## Mutational signatures

De novo extraction and decomposition of mutational signatures was performed in Python v.3.8.5 using SigProfilerExtractor (v.1.1.0)<sup>5</sup>, along with SigprofilerMatrixGenerator (v.1.1.14/1.1.15)<sup>83</sup> and SigprofilerPlotting (v.1.1.27). The recommended default settings (including 500 NMF replicates) were applied

(<https://github.com/AlexandrovLab/SigProfilerExtractor>). Subtraction of mutations in RPE-1 wild-type cells from those detected in RNase H2 null cells was performed as follows. The average number of indels per line for each of the 83 categories was determined for the three wild-type lines. Counts per category for AKO and BKO lines were subtracted using these averages, with negative values set to 0. SigProfilerExtractor was then performed on the resulting WT-subtracted AKO and BKO ID-83 matrices for both de novo signature detection and decomposition analysis.

## Indel sequence context analysis

WGS indels were categorized on the basis of repeat sequence context. Genome-wide occurrence of short repeats and regions of MH were identified and filtered to include only the mappable genome, defined by Umap's regions mappable using 100-mers<sup>82</sup>. For both WGS-identified indel variants and genome-wide occurrence, scoring of 2 bp deletions compliant with the TNT motif at MH/SSTR sites required the deleted bases to match the sequence NT with a T immediately 5' of the deleted dinucleotides. More generally, for varying sized deletions these were considered to fit a TN\*T motif if the deletion lay within an SSTR or region of MH containing the motif TN<sub>(d-1)</sub>T where  $d$  is the length of the deletion. Genome-wide occurrences were estimated from 100,000 randomly generated deletions of given lengths within the mappable genome. For SSTRs and MH regions, all regions containing the respective motifs (TN<sub>(r-1)</sub>)<sub>n</sub> or TN<sub>(r-1)</sub>T were identified (where  $r$  is the length of the repeat unit and  $n > 1$ ), and the fraction of SSTR/MH sequence containing TNT motifs was determined against total SSTR/MH sequence in the mappable genome.

To derive a null expectation for de novo deletions matching the TNT, TNNT and TNNNT motif for 2, 3 and 4 bp deletions, respectively, deletions at repeats from the Gene4Denovo database were first classified by deletion length, repeat type (STR or MH) and repeat length. Bootstrap samples of corresponding repeats from the genome were generated with 1,000 replicates. That is, for each deletion category an equal number of repeats of matching repeat type, repeat unit length and total repeat length were randomly drawn from the genome for each bootstrap sample.

## Sequence logos

Genomic sequences containing 2 bp deletions were reversed and complemented when the deleted dinucleotide contained an adenosine (A), except when the dinucleotide was AT or TA. For SNMH and STR deletions, the position of the deleted dinucleotide cannot be unequivocally assigned and, therefore, the deleted sequence was right-aligned in the repeat/MH region, either to the most 3' T, where present, or otherwise to the limit of the repeat/MH region. Sequences were converted to bit score matrices and logos were drawn using Logomaker (v.0.8)<sup>84</sup>.

## Embedded ribonucleotide sequence context analysis

EmRiboSeq data from *rnh201Δ* yeast prepared during mid-log phase growth<sup>85</sup> were obtained (Supplementary Table 5) and aligned to the sacCer3 reference genome as previously described to identify the genomic coordinates of genome-embedded ribonucleotides<sup>86</sup>. The Bedtools (v.2.30.0)<sup>87</sup> utilities groupby, slop and getfasta were used to extract and count the sequence context of genome-embedded ribonucleotides with downstream analysis and plotting implemented in R (v.4.0.5). Genome sequence composition-adjusted relative rates were calculated as previously described<sup>32</sup> such that, under the null expectation of no sequence bias in ribonucleotide incorporation, all sequence contexts have an expected relative rate of  $1/n$  where  $n$  is the number of contexts considered.

## Statistical methods

Statistical testing was performed using GraphPad Prism v.9.1.1, Python v.3.8.5 or R v.3.3.1. Two-sided non-parametric Mann–Whitney  $U$ -tests were performed for quantitative measurements; multiple testing correction, FDR set at 0.05; and, for categorical data, Fisher’s exact tests were performed in Python using stats.fisher\_exact from scipy v.1.6.3. Calculation of cosine similarities was performed as follows. Mutations for each strain were converted into a vector, with ordered values representing different mutation categories as a proportion of total mutations. These were then compared in a pairwise manner. Given two vectors  $\mathbf{A}$  and  $\mathbf{B}$ , the cosine similarity ( $\cos(\theta)$ ) was calculated as:

$$\cos(\theta) = \frac{\sum_{i=1}^n (\text{bf}\{\mathbf{A}\})_i (\text{bf}\{\mathbf{B}\})_i}{\sqrt{\sum_{i=1}^n ((\text{bf}\{\mathbf{A}\})_i)^2} \sqrt{\sum_{i=1}^n ((\text{bf}\{\mathbf{B}\})_i)^2}}$$

Hierachical clustering used the hclust function of R (v.4.1.0) with complete linkage clustering of pairwise cosine distances (1 – cosine similarity) between ID-83 mutation spectra, with 41 categories of productive reporter frameshift mutations. For bootstrap support,  $n = 1,000$  bootstrap datasets were generated by sampling with replacement the mutations observed with a strain, for each strain, and then calculating the cosine distance and hierarchical clustering for each bootstrap dataset. Reported bootstrap scores are the percentage of bootstrap replicates hierarchical clustering of which supports the clustering to the right of the indicated position.

To test the significance of cosine similarities, we used a null model based on the Dirichlet-multinomial distribution. In brief, when comparing two mutation count vectors, with total mutations  $m_1$  and  $m_2$ , over  $n$  mutation classes, we constructed a distribution of cosine values by comparing 10,000 simulated pairs of random vectors generated as follows. For each simulated pair, we sampled from a Dirichlet-multinomial distribution with the concentration parameters as a vector of ones of dimension  $n$ , and number of trials as  $m_1$  for the first vector in the pair, and  $m_2$  for the second vector. The null distribution was obtained by computing the cosine similarity of the 10,000 pairs of mutation count vectors.

## Reporting summary

Further information on research design is available in the [Nature Research Reporting Summary](#) linked to this paper.

## Data availability

RPE-1 mutation-accumulation experiment and mouse tumour WGS data are available from the European Nucleotide Archive under accession number [PRJEB48753](#). All other data were previously published and the sources are cited in Supplementary Table 5.

## Code availability

Code documented in the Methods is available online (<https://git.ecdf.ed.ac.uk/ID-TOP1>).

## References

1. Hanawalt, P. C. & Spivak, G. Transcription-coupled DNA repair: two decades of progress and surprises. *Nat. Rev. Mol. Cell Biol.* **9**, 958–970 (2008).
2. Datta, A. & Jinks-Robertson, S. Association of increased spontaneous mutation rates with high levels of transcription in yeast. *Science* **268**, 1616–1619 (1995).
3. Herman, R. K. & Dworkin, N. B. Effect of gene induction on the rate of mutagenesis by ICR-191 in *Escherichia coli*. *J. Bacteriol.* **106**, 543–550 (1971).
4. Jinks-Robertson, S. & Bhagwat, A. S. Transcription-associated mutagenesis. *Annu. Rev. Genet.* **48**, 341–359 (2014).
5. Alexandrov, L. B. et al. The repertoire of mutational signatures in human cancer. *Nature* **578**, 94–101 (2020).

6. Pommier, Y., Sun, Y., Huang, S. N. & Nitiss, J. L. Roles of eukaryotic topoisomerases in transcription, replication and genomic stability. *Nat. Rev. Mol. Cell Biol.* **17**, 703–721 (2016).
7. Kunkel, T. A. Evolving views of DNA replication (in)fidelity. *Cold Spring Harb. Symp. Quant. Biol.* **74**, 91–101 (2009).
8. Ciccia, A. & Elledge, S. J. The DNA damage response: making it safe to play with knives. *Mol. Cell* **40**, 179–204 (2010).
9. Lippert, M. J., Freedman, J. A., Barber, M. A. & Jinks-Robertson, S. Identification of a distinctive mutation spectrum associated with high levels of transcription in yeast. *Mol. Cell. Biol.* **24**, 4801–4809 (2004).
10. Lippert, M. J. et al. Role for topoisomerase 1 in transcription-associated mutagenesis in yeast. *Proc. Natl Acad. Sci. USA* **108**, 698–703 (2011).
11. Takahashi, T., Burguiere-Slezak, G., Auffret Van Der Kemp, P. & Boiteux, S. Topoisomerase 1 provokes the formation of short deletions in repeated sequences upon high transcription in *Saccharomyces cerevisiae*. *Proc. Natl Acad. Sci. USA* **108**, 692–697 (2011).
12. Kim, N. et al. Mutagenic processing of ribonucleotides in DNA by yeast topoisomerase I. *Science* **332**, 1561–1564 (2011).
13. Nick McElhinny, S. A. et al. Abundant ribonucleotide incorporation into DNA by yeast replicative polymerases. *Proc. Natl Acad. Sci. USA* **107**, 4949–4954 (2010).
14. Reijns, M. A. M. et al. Enzymatic removal of ribonucleotides from DNA is essential for mammalian genome integrity and development. *Cell* **149**, 1008–1022 (2012).
15. Sparks, J. L. et al. RNase H2-initiated ribonucleotide excision repair. *Mol. Cell* **47**, 980–986 (2012).

16. Huang, S. Y., Ghosh, S. & Pommier, Y. Topoisomerase I alone is sufficient to produce short DNA deletions and can also reverse nicks at ribonucleotide sites. *J. Biol. Chem.* **290**, 14068–14076 (2015).
17. Sparks, J. L. & Burgers, P. M. Error-free and mutagenic processing of topoisomerase 1-provoked damage at genomic ribonucleotides. *EMBO J.* **34**, 1259–1269 (2015).
18. Rahbari, R. et al. Timing, rates and spectra of human germline mutation. *Nat. Genet.* **48**, 126–133 (2016).
19. Alexandrov, L. B. & Stratton, M. R. Mutational signatures: the patterns of somatic mutations hidden in cancer genomes. *Curr. Opin. Genet. Dev.* **24**, 52–60 (2014).
20. Alexandrov, L. B. et al. Signatures of mutational processes in human cancer. *Nature* **500**, 415–421 (2013).
21. Nik-Zainal, S. et al. The genome as a record of environmental exposure. *Mutagenesis* **30**, 763–770 (2015).
22. Pich, O. et al. The mutational footprints of cancer therapies. *Nat. Genet.* **51**, 1732–1740 (2019).
23. Eichler, E. E. Genetic variation, comparative genomics, and the diagnosis of disease. *New Engl. J. Med.* **381**, 64–74 (2019).
24. Tate, J. G. et al. COSMIC: the catalogue of somatic mutations in cancer. *Nucleic Acids Res.* **47**, D941–D947 (2019).
25. Conover, H. N. et al. Stimulation of chromosomal rearrangements by ribonucleotides. *Genetics* **201**, 951–961 (2015).
26. Nick McElhinny, S. A. et al. Genome instability due to ribonucleotide incorporation into DNA. *Nat. Chem. Biol.* **6**, 774–781 (2010).
27. Certo, M. T. et al. Tracking genome engineering outcome at individual DNA breakpoints. *Nat. Methods* **8**, 671–676 (2011).

28. Williams, J. S. et al. Topoisomerase 1-mediated removal of ribonucleotides from nascent leading-strand DNA. *Mol. Cell* **49**, 1010–1015 (2013).
29. Aden, K. et al. Epithelial RNase H2 maintains genome integrity and prevents intestinal tumorigenesis in mice. *Gastroenterology* **156**, 145–159 (2019).
30. Tanizawa, A., Kohn, K. W. & Pommier, Y. Induction of cleavage in topoisomerase I c-DNA by topoisomerase I enzymes from calf thymus and wheat germ in the presence and absence of camptothecin. *Nucleic Acids Res.* **21**, 5157–5166 (1993).
31. Huang, S. N., Williams, J. S., Arana, M. E., Kunkel, T. A. & Pommier, Y. Topoisomerase I-mediated cleavage at unrepaired ribonucleotides generates DNA double-strand breaks. *EMBO J.* **36**, 361–373 (2017).
32. Balachander, S. et al. Ribonucleotide incorporation in yeast genomic DNA shows preference for cytosine and guanosine preceded by deoxyadenosine. *Nat. Commun.* **11**, 2447 (2020).
33. Zimmermann, M. et al. CRISPR screens identify genomic ribonucleotides as a source of PARP-trapping lesions. *Nature* **559**, 285–289 (2018).
34. The National Genomics Research and Healthcare Knowledgebase v5. *Genomics England* <https://doi.org/10.6084/m9.figshare.4530893.v5> (2019).
35. Puente, X. S. et al. Non-coding recurrent mutations in chronic lymphocytic leukaemia. *Nature* **526**, 519–524 (2015).
36. Abascal, F. et al. Somatic mutation landscapes at single-molecule resolution. *Nature* **593**, 405–410 (2021).
37. Rheinbay, E. et al. Analyses of non-coding somatic drivers in 2,658 cancer whole genomes. *Nature* **578**, 102–111 (2020).

38. Baranello, L. et al. RNA polymerase II regulates topoisomerase 1 activity to favor efficient transcription. *Cell* **165**, 357–371 (2016).
39. Zhao, G. et al. Gene4Denovo: an integrated database and analytic platform for de novo mutations in humans. *Nucleic Acids Res.* **48**, D913–D926 (2020).
40. Sekiguchi, J. & Shuman, S. Site-specific ribonuclease activity of eukaryotic DNA topoisomerase I. *Mol. Cell* **1**, 89–97 (1997).
41. Cho, J. E., Kim, N., Li, Y. C. & Jinks-Robertson, S. Two distinct mechanisms of topoisomerase 1-dependent mutagenesis in yeast. *DNA Repair* **12**, 205–211 (2013).
42. Boot, A. et al. Recurrent mutations in topoisomerase II $\alpha$  cause a previously undescribed mutator phenotype in human cancers. *Proc. Natl Acad. Sci. USA* **119**, e2114024119 (2022).
43. Park, S. et al. Clonal dynamics in early human embryogenesis inferred from somatic mutation. *Nature* **597**, 393–397 (2021).
44. Alvarez-Quilon, A. et al. Endogenous DNA 3' blocks are vulnerabilities for BRCA1 and BRCA2 deficiency and are reversed by the APE2 nuclease. *Mol. Cell* **78**, 1152–1165 (2020).
45. Li, F. et al. Apn2 resolves blocked 3' ends and suppresses Top1-induced mutagenesis at genomic rNMP sites. *Nat. Struct. Mol. Biol.* **26**, 155–163 (2019).
46. Potenski, C. J., Niu, H., Sung, P. & Klein, H. L. Avoidance of ribonucleotide-induced mutations by RNase H2 and Srs2-Exo1 mechanisms. *Nature* **511**, 251–254 (2014).
47. Riva, V. et al. Novel alternative ribonucleotide excision repair pathways in human cells by DDX3X and specialized DNA polymerases. *Nucleic Acids Res.* **48**, 11551–11565 (2020).

48. Davies, H. et al. HRDetect is a predictor of BRCA1 and BRCA2 deficiency based on mutational signatures. *Nat. Med.* **23**, 517–525 (2017).
49. Wang, C. et al. Genome-wide CRISPR screens reveal synthetic lethality of RNASEH2 deficiency and ATR inhibition. *Oncogene* **38**, 2451–2463 (2019).
50. The ICGC/TCGA Pan-Cancer Analysis of Whole Genomes Consortium. Pan-cancer analysis of whole genomes. *Nature* **578**, 82–93 (2020).
51. Oceguera-Yanez, F. et al. Engineering the AAVS1 locus for consistent and scalable transgene expression in human iPSCs and their differentiated derivatives. *Methods* **101**, 43–55 (2016).
52. Gritz, L. & Davies, J. Plasmid-encoded hygromycin B resistance: the sequence of hygromycin B phosphotransferase gene and its expression in *Escherichia coli* and *Saccharomyces cerevisiae*. *Gene* **25**, 179–188 (1983).
53. Brachmann, C. B. et al. Designer deletion strains derived from *Saccharomyces cerevisiae* S288C: a useful set of strains and plasmids for PCR-mediated gene disruption and other applications. *Yeast* **14**, 115–132 (1998).
54. Spell, R.M. & Jinks-Robertson, S. in *Genetic Recombination* (ed. Waldman, A.S.) 3–12 (Humana Press, 2004)
55. Lea, D. E. & Coulson, C. A. The distribution of the numbers of mutants in bacterial populations. *J. Genet.* **49**, 264–285 (1949).
56. Altman, D. G. Practical Statistics for Medical Research (Chapman and Hall, 1991).
57. Vallot, C., Herault, A., Boyle, S., Bickmore, W. A. & Radvanyi, F. PRC2-independent chromatin compaction and transcriptional repression in cancer. *Oncogene* **34**, 741–751 (2015).

58. Benitez-Guijarro, M. et al. RNase H2, mutated in Aicardi-Goutières syndrome, promotes LINE-1 retrotransposition. *EMBO J.* **37**, e98506 (2018).
59. Reijns, M. A. M. et al. The structure of the human RNase H2 complex defines key interaction interfaces relevant to enzyme function and human disease. *J. Biol. Chem.* **286**, 10530–10539 (2011).
60. Lujan, S. A. et al. Heterogeneous polymerase fidelity and mismatch repair bias genome variation and composition. *Genome Res.* **24**, 1751–1764 (2014).
61. Li, H. Aligning sequence reads, clone sequences and assembly contigs with BWA-MEM. Preprint at <https://arxiv.org/abs/1303.3997> (2013).
62. Faust, G. G. & Hall, I. M. SAMBLASTER: fast duplicate marking and structural variant read extraction. *Bioinformatics* **30**, 2503–2505 (2014).
63. Van der Auwera, G. A. et al. From fastQ data to high-confidence variant calls: the genome analysis toolkit best practices pipeline. *Curr. Protoc. Bioinform.* **43**, 11.10.1–11.10.33 (2013).
64. Van der Auwera, G. A. & O'Connor, B. D. Genomics in the Cloud: Using Docker, GATK, and WDL in Terra (O'Reilly Media, 2020).
65. Keane, T. M. et al. Mouse genomic variation and its effect on phenotypes and gene regulation. *Nature* **477**, 289–294 (2011).
66. Raczy, C. et al. Isaac: ultra-fast whole-genome secondary analysis on Illumina sequencing platforms. *Bioinformatics* **29**, 2041–2043 (2013).
67. Roller, E., Ivakhno, S., Lee, S., Royce, T. & Tanner, S. Canvas: versatile and scalable detection of copy number variants. *Bioinformatics* **32**, 2375–2377 (2016).
68. Robinson, J. T. et al. Integrative genomics viewer. *Nat. Biotechnol.* **29**, 24–26 (2011).

69. Nik-Zainal, S. et al. The life history of 21 breast cancers. *Cell* **149**, 994–1007 (2012).
70. Raine, K. M. et al. ascatNgs: identifying somatically acquired copy-number alterations from whole-genome sequencing data. *Curr. Protoc. Bioinform.* **56**, 15.19.11–15.19.17 (2016).
71. Sekhon, J. S. Multivariate and propensity score matching software with automated balance optimization: the Matching package for R. *J. Stat. Softw.* **42**, 1–52 (2011).
72. Benjamin, D. et al. Calling somatic SNVs and indels with Mutect2. Preprint at <https://doi.org/10.1101/861054> (2019).
73. McKenna, A. et al. The Genome Analysis Toolkit: a MapReduce framework for analyzing next-generation DNA sequencing data. *Genome Res.* **20**, 1297–1303 (2010).
74. Kim, S. et al. Strelka2: fast and accurate calling of germline and somatic variants. *Nat. Methods* **15**, 591–594 (2018).
75. Wala, J. A. et al. SvABA: genome-wide detection of structural variants and indels by local assembly. *Genome Res.* **28**, 581–591 (2018).
76. Rimmer, A. et al. Integrating mapping-, assembly- and haplotype-based approaches for calling variants in clinical sequencing applications. *Nat. Genet.* **46**, 912–918 (2014).
77. Danecek, P. et al. Twelve years of SAMtools and BCFtools. *Gigascience* **10**, giab008 (2021).
78. Karczewski, K. J. et al. The mutational constraint spectrum quantified from variation in 141,456 humans. *Nature* **581**, 434–443 (2020).
79. Chen, X. et al. Manta: rapid detection of structural variants and indels for germline and cancer sequencing applications. *Bioinformatics* **32**, 1220–1222 (2016).

80. Xia, B. et al. Widespread transcriptional scanning in the testis modulates gene evolution rates. *Cell* **180**, 248–262 (2020).
81. The FANTOM Consortium and the RIKEN PMI and CLST (DGT). A promoter-level mammalian expression atlas. *Nature* **507**, 462–470 (2014).
82. Karimzadeh, M., Ernst, C., Kundaje, A. & Hoffman, M. M. Umap and Bismap: quantifying genome and methylome mappability. *Nucleic Acids Res.* **46**, e120 (2018).
83. Bergstrom, E. N. et al. SigProfilerMatrixGenerator: a tool for visualizing and exploring patterns of small mutational events. *BMC Genom.* **20**, 685–685 (2019).
84. Tareen, A. & Kinney, J. B. Logomaker: beautiful sequence logos in Python. *Bioinformatics* **36**, 2272–2274 (2020).
85. Reijns, M. A. M. et al. Lagging-strand replication shapes the mutational landscape of the genome. *Nature* **518**, 502–506 (2015).
86. Ding, J., Taylor, M. S., Jackson, A. P. & Reijns, M. A. M. Genome-wide mapping of embedded ribonucleotides and other noncanonical nucleotides using emRiboSeq and EndoSeq. *Nat. Protoc.* **10**, 1433–1444 (2015).
87. Quinlan, A. R. & Hall, I. M. BEDTools: a flexible suite of utilities for comparing genomic features. *Bioinformatics* **26**, 841–842 (2010).
88. Kornberg, A., Bertsch, L. L., Jackson, J. F. & Khorana, H. G. Enzymatic synthesis of deoxyribonucleic acid, XVI. Oligonucleotides as templates and the mechanism of their replication. *Proc. Natl Acad. Sci. USA* **51**, 315–323 (1964).
89. Fan, H. & Chu, J. Y. A brief review of short tandem repeat mutation. *Genom. Proteom. Bioinform.* **5**, 7–14 (2007).

90. Stok, C., Kok, Y. P., van den Tempel, N. & van Vugt, M. Shaping the BRCAness mutational landscape by alternative double-strand break repair, replication stress and mitotic aberrancies. *Nucleic Acids Res.* **49**, 4239–4257 (2021).
91. Drost, J. et al. Use of CRISPR-modified human stem cell organoids to study the origin of mutational signatures in cancer. *Science* **358**, 234–238 (2017).
92. Hiller, B. et al. Mammalian RNase H2 removes ribonucleotides from DNA to maintain genome integrity. *J. Exp. Med.* **209**, 1419–1426 (2012).

## Acknowledgements

We thank S. Jinks-Robertson for suggesting the traffic light reporter approach; H. Klein for guidance on fluctuation assays; R. van Boxtel for sharing sequencing data for MLH1-KO organoids; A. Bretherick, O. B. Reina and G. Kudla for advice on HygroR re-coding; staff at the IGC core services (L. Murphy, C. Nicol, C. Warnock, E. Freyer, S. Brown and J. Joseph), C. Logan, A. Fluteau, A. Robertson and the staff at Edinburgh Genomics for technical assistance; staff at Liverpool CLL Biobank (funded by Blood Cancer UK) for samples used to generate GEL WGS data; A. Ewing, C.-A. Martin, N. Hastie and W. Bickmore for discussions. Funding for this work: UK Medical Research Council Human Genetics Unit core grants (MC\_UU\_00007/5 to A.P.J., MC\_UU\_00007/11 to M.S.T.); Edinburgh Clinical Academic Track PhD programme (Wellcome Trust 204802/Z/16/Z) to T.C.W.; 2021 AACR-Amgen Fellowship in Clinical/Translational Cancer Research (grant number 21-40-11-NADE) to F.N.; a CRUK Brain Tumour Centre of Excellence Award (C157/A27589) to M.D.N.; EKFS research grant (2019\_A09), Wilhelm Sander-Stiftung (2019.046.1) to K.A., CRUK programme grant (C20807/A2864) to T.S.; La Caixa Foundation (CLLEvolution-LCF/PR/HR17/52150017, Health Research 2017 Program HR17-00221) to E.C.; E.C. is an Academia Researcher of the Institució Catalana de Recerca i Estudis Avançats of the Generalitat de Catalunya. Edinburgh Genomics is partly supported by NERC (R8/H10/56), MRC (MR/K001744/1) and BBSRC (BB/J004243/1).

This research was made possible through access to the data and findings generated by the 100,000 Genomes Project. The 100,000 Genomes Project is managed by Genomics England Limited (a wholly owned company of the Department of Health and Social Care). The 100,000 Genomes Project is funded by the National Institute for Health Research and NHS England. The Wellcome Trust, Cancer Research UK and the Medical Research Council have also funded research infrastructure. The 100,000 Genomes Project uses data provided by patients and collected by the National Health Service as part of their care and support.

## Author information

### Author notes

1. These authors contributed equally: Martin A. M. Reijns, David A. Parry, Thomas C. Williams

### Affiliations

1. Disease Mechanisms, MRC Human Genetics Unit, Institute of Genetics and Cancer, The University of Edinburgh, Edinburgh, UK

Martin A. M. Reijns, David A. Parry, Thomas C. Williams, Diana O. Rios Szwed, Paula Carroll & Andrew P. Jackson

2. Biomedical Genomics, MRC Human Genetics Unit, Institute of Genetics and Cancer, The University of Edinburgh, Edinburgh, UK

Thomas C. Williams & Martin S. Taylor

3. Institut d'Investigacions Biomèdiques August Pi i Sunyer (IDIBAPS), Barcelona, Spain

Ferran Nadeu & Elias Campo

4. Centro de Investigación Biomédica en Red de Cáncer (CIBERONC), Madrid, Spain

Ferran Nadeu & Elias Campo

5. Institute of Cancer and Genomic Sciences, University of Birmingham, Birmingham, UK

Rebecca L. Hindshaw, Boris Noyvert, Claire Palles & Tatjana Stankovic

6. Cancer Research UK Edinburgh Centre, Institute of Genetics and Cancer, The University of Edinburgh, Edinburgh, UK

Michael D. Nicholson, Henry Wood & Ian Tomlinson

7. Genome Regulation, MRC Human Genetics Unit, Institute of Genetics and Cancer, The University of Edinburgh, Edinburgh, UK

Shelagh Boyle

8. Barcelona Supercomputing Center (BSC), Barcelona, Spain

Romina Royo

9. The Institute of Cancer Research, London, UK

Alex J. Cornish, Daniel Chubb, Alex Cornish, Ben Kinnersley, Richard Houlston, Andrea Sottoriva, Giulio Caravagna & Richard Culliford

10. Institute of Clinical Molecular Biology, Christian-Albrechts-University and University Hospital Schleswig-Holstein, Kiel, Germany

Hang Xiang & Konrad Aden

11. Department of Oncology, University of Oxford, Oxford, UK

Kate Ridout & Anna Schuh

12. Hospital Clínic of Barcelona, Barcelona, Spain

Elias Campo

13. Departament de Fonaments Clínics, Universitat de Barcelona,  
Barcelona, Spain

Elias Campo

14. Genomics England, London, UK

John C. Ambrose, Prabhu Arumugam, Roel Bevers, Marta Bleda, Freya Boardman-Pretty, Christopher R. Bousted, Helen Brittain, Mark J. Caulfield, Georgia C. Chan, Greg Elgar, Tom Fowler, Adam Giess, Angela Hamblin, Shirley Henderson, Tim J. P. Hubbard, Rob Jackson, Louise J. Jones, Dalia Kasperaviciute, Melis Kayikci, Athanasios Kousathanas, Lea Lahnstein, Sarah E. A. Leigh, Ivonne U. S. Leong, Javier F. Lopez, Fiona Maleady-Crowe, Meriel McEntagart, Federico Minneci, Loukas Moutsianas, Michael Mueller, Nirupa Murugaesu, Anna C. Need, Peter O'Donovan, Chris A. Odhams, Christine Patch, Mariana Buongermino Pereira, Daniel Perez-Gil, John Pullinger, Tahrima Rahim, Augusto Rendon, Tim Rogers, Kevin Savage, Kushmita Sawant, Richard H. Scott, Afshan Siddiq, Alexander Sieghart, Samuel C. Smith, Alona Sosinsky, Alexander Stuckey, Mélanie Tanguy, Ana Lisa Taylor Tavares, Ellen R. A. Thomas, Simon R. Thompson, Arianna Tucci, Matthew J. Welland, Eleanor Williams, Katarzyna Witkowska & Suzanne M. Wood

15. William Harvey Research Institute, Queen Mary University of London, London, UK

Freya Boardman-Pretty, Mark J. Caulfield, Greg Elgar, Shirley Henderson, Louise J. Jones, Dalia Kasperaviciute, Loukas Moutsianas, Michael Mueller, Anna C. Need, Christine Patch, Alona Sosinsky, Ellen R. A. Thomas, Arianna Tucci, Katarzyna Witkowska & Suzanne M. Wood

16. Manchester Interdisciplinary Biocentre, University of Manchester, Manchester, UK

David Wedge & Andreas Gruber

17. Wellcome Centre for Human Genetics, Oxford, UK

Anna Frangou & David Church

18. Cancer Institute, University College London, London, UK

William Cross

19. Barts Cancer Institute, Barts and The London School of Medicine and Dentistry, Queen Mary University of London, London, UK

Trevor Graham

20. Institute for Research in Biomedicine (IRB Barcelona), The Barcelona Institute of Science and Technology (BIST), Barcelona, Spain

Nuria Lopez-Bigas & Claudia Arnedo-Pac

21. Pathology and Data Analytics, Leeds Institute of Medical Research, St James's University Hospital, University of Leeds, Leeds, UK

Steve Thorn & Phil Quirke

## **Consortia**

### **The Genomics England Research Consortium**

- John C. Ambrose
- , Prabhu Arumugam
- , Roel Bevers
- , Marta Bleda
- , Freya Boardman-Pretty
- , Christopher R. Bousted
- , Helen Brittain
- , Mark J. Caulfield
- , Georgia C. Chan
- , Greg Elgar
- , Tom Fowler

- , Adam Giess
- , Angela Hamblin
- , Shirley Henderson
- , Tim J. P. Hubbard
- , Rob Jackson
- , Louise J. Jones
- , Dalia Kasperaviciute
- , Melis Kayikci
- , Athanasios Kousathanas
- , Lea Lahnstein
- , Sarah E. A. Leigh
- , Ivonne U. S. Leong
- , Javier F. Lopez
- , Fiona Maleady-Crowe
- , Meriel McEntagart
- , Federico Minneci
- , Loukas Moutsianas
- , Michael Mueller
- , Nirupa Murugaesu
- , Anna C. Need
- , Peter O'Donovan
- , Chris A. Odhams
- , Christine Patch
- , Mariana Buongermino Pereira
- , Daniel Perez-Gil
- , John Pullinger
- , Tahrima Rahim
- , Augusto Rendon
- , Tim Rogers
- , Kevin Savage
- , Kushmita Sawant
- , Richard H. Scott
- , Afshan Siddiq
- , Alexander Sieghart
- , Samuel C. Smith
- , Alona Sosinsky
- , Alexander Stuckey

- , Mélanie Tanguy
- , Ana Lisa Taylor Tavares
- , Ellen R. A. Thomas
- , Simon R. Thompson
- , Arianna Tucci
- , Matthew J. Welland
- , Eleanor Williams
- , Katarzyna Witkowska
- & Suzanne M. Wood

## **Colorectal Cancer Domain UK 100,000 Genomes Project**

- Daniel Chubb
- , Alex Cornish
- , Ben Kinnersley
- , Richard Houlston
- , David Wedge
- , Andreas Gruber
- , Anna Frangou
- , William Cross
- , Trevor Graham
- , Andrea Sottoriva
- , Giulio Caravagna
- , Nuria Lopez-Bigas
- , Claudia Arnedo-Pac
- , David Church
- , Richard Culliford
- , Steve Thorn
- , Phil Quirke
- , Henry Wood
- , Ian Tomlinson
- & Boris Noyvert

## **Contributions**

M.A.M.R., T.C.W., M.S.T. and A.P.J. conceived the project and designed the experiments. T.C.W. and M.A.M.R., with help from P.C., performed

fluctuation assays and sequencing experiments. M.A.M.R., with help from P.C., performed the RPE-1 mutation-accumulation experiment. S.B. performed FISH experiments. M.A.M.R., T.C.W. and D.O.R.S. performed all of the other molecular biology experiments. H.X. and K.A. provided mouse tumour and control tissue samples. D.A.P., T.C.W., M.D.N. and M.S.T. designed and implemented computational analyses. D.A.P., T.C.W. and M.S.T. analysed yeast, mouse, RPE-1 and Gene4Denovo WGS data. D.A.P. and M.S.T. performed pan-cancer analyses. The Genomics England Research Consortium, K.R. and A.S. provided CLL WGS data. A.J.C. provided CRC data. D.A.P., F.N., R.L.H., R.R. and C.P. analysed CLL data. D.A.P. analysed CRC data. M.A.M.R., C.P., T.S., E.C., M.S.T. and A.P.J. supervised the work. T.C.W., F.N., E.C., T.S., M.S.T. and A.P.J. funded the work. M.A.M.R. and A.P.J. wrote the manuscript. All of the authors had the opportunity to edit the manuscript. All of the authors approved the final manuscript.

## Corresponding authors

Correspondence to [Martin A. M. Reijns](#), [Martin S. Taylor](#) or [Andrew P. Jackson](#).

## Ethics declarations

### Competing interests

The authors declare no competing interests.

## Peer review

### Peer review information

*Nature* thanks Francesca Storici and the other, anonymous reviewer(s) for their contribution to the peer review of this work. Peer reviewer reports are available.

## Additional information

**Publisher's note** Springer Nature remains neutral with regard to jurisdictional claims in published maps and institutional affiliations.

## Extended data figures and tables

### Extended Data Fig. 1 ID4 is distinct from small deletion signatures of known aetiology.

**a, b**, The mechanistic basis for many COSMIC indel signatures is unknown, with only 9 out of 18 having a proposed aetiology. ID2 (**a**) is attributed to DNA polymerase slippage<sup>88,89</sup> and ID6 (**b**) to microhomology mediated end-joining (MMEJ) activity, associated with HR deficiency<sup>5,90</sup>. **c, d**, Mechanism for these signatures supported by: impaired MMR promoting replication slippage mutagenesis in  $MLH1^{-/-}$  colonic organoids resulting in ID2 (and ID1) signatures (**c**); ID6 contributing substantially (along with ID8) to the indel signature in ovarian cancer, in which HR deficiency is common (**d**). Analysis of data from<sup>91</sup> in **c**; data for 73 ovarian adenocarcinomas with ID6 contribution from ICGC<sup>5,50</sup> in **d**.

### Extended Data Fig. 2 Yeast and human frameshift mutation reporters detect indels at tandem repeats.

**a**, Yeast reporter. Synonymous substitutions were made in the hygromycin resistance gene (HygroR), such that it contained many short 2 bp tandem repeats (SSTRs). Expression from the TEF promoter ( $P_{TEF}$ ) ensures a constitutive high level of transcription. Mutations within HygroR that result in a frameshift simultaneously put the HygroR coding sequence out of frame and the downstream neomycin resistance (NeoR) sequence in frame, allowing antibiotic selection of cells with such mutations. **b**, Top1-dependent 2 bp SSTR deletions occur in both WT and  $rnh201\Delta$  (RNase H2 null) yeast, with the highest mutation rate for  $rnh201\Delta$  (related to Fig. 1d). **c–e**, WT and  $rnh201\Delta$  have similar spectra, and differ from  $top1\Delta$  strains. Mutation spectra of neomycin resistant colonies. n, number of independent

colonies sequenced. Other: complex indels, missense mutations or mutation not characterised (**c**). Tree for pairwise clustering with percent bootstrap support to the right of the indicated position, based on cosine scores calculated for mutation spectra (Fig. 1e) of the 41 mutation categories that give productive reporter frameshift mutations (**d**). Matrix of pairwise cosine similarities and P-values between reporter mutation spectra in different yeast strains. Darker blue indicates greater similarity; darker grey greater significance. Test statistic is the cosine similarity value for 41 mutation categories and the null hypothesis is that the cosine value will be distributed according to the Dirichlet-multinomial model, as described in Methods. The test is one-sided and no adjustments were made for multiple comparisons (**e**). **f**, Null distribution for cosine pairwise vector comparisons for 41 and 83 mutation categories. Plots, cosine values for 10,000 randomly generated pairs of vectors of mutation spectra. Each vector contained 100 randomly assigned mutations (see [Methods](#) for further details). Cosine value thresholds indicated for  $P < 0.05$  and  $P < 0.01$ . **g**, The human reporter is expressed from the ubiquitous CAG promoter ( $P_{CAG}$ ), and NeoR is replaced with the puromycin resistance gene (PuroR) to allow more rapid antibiotic selection in mammalian cell culture.

### **Extended Data Fig. 3 Validation and characterisation of RNASEH2A+ and KO HeLa reporter cells.**

**a–c**, Reporter integration at the *AAVS1* locus and retention of a reporter-free locus with a 200 bp deletion at the target site was confirmed by PCR and Sanger sequencing. Green arrow head, specific PCR product. Representative of at least 2 independent experiments. **d, e**, FISH shows integration of the reporter (**d**) at a single *AAVS1* locus (**e**). Representative image of approximately one hundred mitotic chromosome spreads in 3 independent experiments. SA, splice acceptor; T2A, self-cleaving peptide; pA, polyadenylation site; also see Fig. 2a. **f, g**, Alkaline gel electrophoresis of RNase H2 treated genomic DNA (**f**) shows a small increase in fragmentation for the *RNASEH2A*+ control clone and a more substantial increase in two independent *RNASEH2A*-KO clones (representative of 4 independent experiments), indicating the presence of more genome-embedded ribonucleotides compared to HeLa and parental reporter cells (**g**). “Control KO” cells were reported previously [33,58](#). RFU, relative

fluorescence units. **h**, 2 bp SSTR deletions are frequent in both *RNASEH2A*+ and KO cells. Mutation spectra, quantitation of indel type. Relative area of pie charts scaled to mutation rate. n, number of colonies sequenced from independent cultures. Other: complex indels or missense mutations.

**Extended Data Fig. 4 RPE1 RNase H2 null cells accumulate embedded ribonucleotides and 2–5 bp deletions across the genome.**

**a, b**, *RNASEH2A* and *RNASEH2B* KO cells (AKO, BKO, respectively) have substantially reduced cellular levels of RNase H2 subunits (**a**) and are deficient for RNase H2 enzyme activity (**b**) at the outset (ancestral) and at the end of the mutation accumulation experiment (end point). Individual data points, n = 3 technical replicates; mean ± s.d. For gel source data, see Supplementary Fig. 1. **c, d**, Alkaline gel electrophoresis of RNase H2 treated genomic DNA (**c**) shows a substantial increase in fragmentation for *RNASEH2A* and *RNASEH2B* KO clones (representative of 3 independent experiments), indicating the presence of more genome-embedded ribonucleotides compared to two WT control clones (**d**). Densitometry plots of **c**. RFU, relative fluorescence units. As RNase H2 deficiency activates the p53 pathway<sup>14,92</sup>, experiments were performed in a *TP53* knockout background. **e**, Only 2–5 bp deletions are significantly increased in RNase H2 null cells. Data points for acquired indel mutations in individual cell lines after 100 population doublings. Individual data points, indel counts per cell line; mean ± s.d.; P-values for two-sided Fisher's exact test between WT (pooled counts from n = 3 independent clones) and KO (n = 2 independent clones) for one indel type vs all other indel types, after Bonferroni correction. **f**, Proportions of acquired indels in WT and KO RPE cells. After correction for indels occurring in WT, 69% of indels in RNase H2 null cells are 2–5 bp deletions. n, total indel counts. **g**, Quantification of 2 bp deletions by context. n, total number of 2 bp deletions. For **f, g**, chart areas scaled to mutation counts per line.

**Extended Data Fig. 5 ID4 occurs in RNase H2 null RPE1 cells, particularly in transcribed regions.**

**a–d**, Mutational spectra detected by WGS after 100 population doublings in RPE1 cells demonstrates that SSTR and SNMH/MH deletions are enriched in RNase H2 null cells. Spectra for combined RNase H2 null and wildtype cell lines (**a**), and individual cell lines (**b**). Mutational signature analysis confirms ID4 contribution in RNase H2 null (**c**), but not WT cells (**d**). **e**, In RNase H2 null cells, ID4 contributes significantly more to indel mutations in transcribed genomic regions ( $P = 1.3 \times 10^{-29}$ ). Two-sided Fisher's exact test, ID4 indels vs other indels.

**Extended Data Fig. 6 ID4 mutations in RNase H2 null mouse tumours and RPE1 cells occur at a TNT motif, defining ID-TOP1.**

**a**, Mutation spectra for individual *Rnaseh2b*-KO mouse intestinal tumours (WGS, paired tumour–normal samples from 6 mice). **b**, Indel classes, detected in mouse *Rnaseh2b*-KO tumours. n, total indel count for 6 tumours. **c**, Most 2 bp deletions in these tumours occur at SSTRs and sites of single nucleotide microhomology (SNMH). n, number of 2 bp deletions. **d, e**, A TNT sequence motif is present at all 2 bp STR and SNMH deletions in RNase H2 null mouse tumours (**d**) and RPE1 cells (**e**). Related to Fig. 4d and Fig. 3, respectively. Sequence logo: 2-bit representation of the sequence context of 2 bp deletions. Top, all deletions, with those sequences containing a deleted adenine (except AT/TA) reverse complemented, and deletions right-aligned. Middle, re-aligned on right-hand T. Bottom, aligned on T (STR and SNMH context only). n, number of deletions. **f**, Deletion sites in RNase H2 null RPE1 cells are significantly enriched for the TNT sequence motif compared to genome-wide occurrence, for all genome sequence, as well as SNMH sites. P-values, two-sided Fisher's exact, observed vs expected. n = 98 (all;  $P = 8.3 \times 10^{-14}$ ), 54 (STR;  $P = 0.057$ ), 30 (SNMH;  $P = 0.0008$ ) deletions.

**Extended Data Fig. 7 ID4 deletions in RNase H2 null *S. cerevisiae* occur at a TNT motif in a Top1-dependent manner.**

**a**, 2 bp deletion sites in *rnh201Δ pol2-M644G* yeast are significantly enriched for the TNT sequence motif compared to genome-wide

occurrence, for all genome sequence, as well as STR sites. P-values, two-sided Fisher's exact, observed vs expected.  $n = 94$  (all;  $P = 1.0 \times 10^{-9}$ ), 91 (STR;  $P = 0.029$ ), 3 (SNMH;  $P = 1$ ) deletions. **b**, A TNT sequence motif is present at all 2 bp STR and SNMH deletions in *rnh201Δ pol2-M644G* yeast. Sequence logo: 2-bit representation of the sequence context of 2 bp deletions. Top, all deletions, with those sequences containing a deleted adenosine (except AT/TA) reverse complemented, and deletions aligned on right-hand T. Bottom, aligned on T (STR and SNMH context only). n, number of deletions. **c**, **d**, TN\*T motifs extend beyond 2 bp deletions, with enrichment above expectation for 2 bp deletions at TNT, 3 bp deletions at TNNT and 4 bp deletions at TNNNT motifs in *rnh201Δ pol2-M644G* yeast WGS. Null expectations were generated by randomly simulating deletions of 2, 3 and 4 bp (**c**) or 2 bp STR sequences (**d**) genome-wide and scoring those simulated events for TN\*T compliance. Each simulated dataset matched the count of observed mutations for the corresponding deletion class and  $n = 1,000$  replicate simulated datasets were produced. The frequency distribution of TN\*T compliance in simulations is plotted as histograms, and comparison to the observed frequency of TN\*T compliance (dotted red lines) used to derive a two-tailed empirical P-value. **e**, 2 bp STR deletions have biased sequence composition. Deletions observed in *rnh201Δ pol2-M644G* yeast WGS. Genome, frequency of dinucleotides in STR sequences in mappable genome. **f**, Ribouridine (rU) is more common in a CrU/GrU than in an ArU/TrU dinucleotide context. Genome-embedded ribonucleotide frequency determined by emRiboSeq<sup>86</sup>. Dotted line indicates relative rate in absence of bias (=0.25). Horizontal lines, mean; individual data points, values for  $n = 4$  independent experiments<sup>85</sup>. **g**, **h**, 2 bp TNT deletions in wildtype and RNase H2 null cells are dependent on Topoisomerase 1. Mutation rates for 2 bp deletions at TNT-compliant SSTRs (**g**). Deletions at TNT motifs are significantly increased above expectation in WT and *rnh201Δ*, but not in *top1Δ* and *rnh201Δ top1Δ* yeast. Horizontal bars, 95% confidence intervals for odds ratio estimates (diamonds). P-values, two-sided Fisher's exact after Bonferroni correction;  $n = 86, 28, 103, 19$  2-bp deletions, with each deletion from an independent culture, for WT, *top1Δ*, *rnh201Δ*, *rnh201Δ top1Δ*, respectively. Null expectation, random occurrence of mutations in reporter target sequence (**h**).

## Extended Data Fig. 8 TOP1-mediated mutagenesis causes increased 2–5 bp deletions in cancer.

**a**, Of all indels, only 2–5 bp deletions are significantly increased in CLL with biallelic *RNASEH2B* loss. Box, 25–75%; line, median; whiskers 5–95% with data points for values outside this range. WT (2 copies),  $n = 201$ ; monallelic loss (1 copy),  $n = 131$ ; biallelic loss (0 copies),  $n = 16$  independent tumours. Indels as percentage of all variants per sample (GEL and ICGC data combined). q-values, 2-sided Mann-Whitney test with 5% FDR. **b, c**, In RNase H2 null CLL, 2 bp deletions predominantly occur at STR and SNMH sequences (**b**), and at the TNT sequence motif (**c**), consistent with TOP-mediated mutagenesis. Mean  $\pm$  s.e.m., percentage of all variants per sample. GEL and ICGC data combined.  $n = 1,711$ ; 1,244; 443 2-bp indels identified in 201, 131, 16 biologically independent tumours, respectively. **d**, ID4 contribution in RNase H2 null CLL is greater in transcribed regions. Two-sided Fisher's exact test, ID4 indels vs other indels ( $P = 9.2 \times 10^{-16}$ ). **e**, Pan-cancer transcript expression data divided into ten expression strata for ubiquitously expressed genes (used in panel **h** and Fig. 5b analysis). Data points, median/maximum expression across cancer types for individual genes. Genes with similar median and maximum TPMs were considered to be ubiquitously expressed and divided into expression groups from low (1) to high (10) expression. **f**, Two bp deletions in cancer preferentially occur at STRs. **g**, ID-TOP1 deletions increase in frequency with TOP1 cleavage activity (measured by TOP1-Seq;<sup>38</sup>). Dotted line, relative rate in lowest TOP1-seq category set to 1. Solid lines, relative deletion rate. ID-TOP1, 2–5 bp MH and SSTR deletions containing the TN\*T sequence motif. **h**, ID-TOP1, but not deletions in other sequence contexts, correlate with transcription. **i**, 2–5 bp deletions from prostate adenocarcinoma are most enriched amongst the top 10% of highly expressed prostate 'tissue-restricted' genes. Odds ratio (OR): number of 2–5 bp deletions in top 10% tissue restricted genes vs 2–5 bp deletions in other genes, relative to expected frequency from all other tissues. **j**, ID4 is not detected in the indel signature of irinotecan-treated colorectal cancers. Untreated ( $n = 78$ ), treated ( $n = 39$ ). **k**, 2–5 bp deletion frequency in cancer corresponds to TOP1 cleavage activity, in both genic and non-genic regions. Data analysed from PCAWG<sup>50</sup>, all tumours in **e, h**; ID4 positive tumours in

**g, k**; Genomics England in **j**. In **g, h** and **k**, solid line, relative deletion rate; shading indicates 95% confidence intervals from 1,000 (**g, k**) or 100 (**h**) bootstrap replicates.

### Extended Data Fig. 9 Human germline de novo indels are enriched for ID-TOP1 deletions.

**a**, Most de novo 2 bp deletions occur at SSTR, STR and SNMH sequences. **b, c**, A TNT sequence motif is present at the majority of 2 bp STR and SNMH deletions (**b**). Sequence logos: 2-bit representation of the sequence context of 2 bp deletions. Top, all deletions, with those containing A (except AT/TA) reverse complemented, and deletions right-aligned on T (where present). Bottom, STR/SNMH deletions only (**c**). **d**, TN\*T motifs extend beyond 2 bp deletions, with enrichment above expectation for 2 bp deletions at TNT, 3 bp deletions at TNNT and 4 bp deletions at TNNNT motifs ( $P < 0.001$ ; two-tailed empirical P-value determined for each category). Bootstrap sampling ( $n = 1,000$ ) of 2, 3 and 4 bp STR/MH sequences genome-wide to derive expected frequencies of those matching TN\*T motifs. Sampling was performed to match the numbers of deletions at repeats observed in the Gene4Denovo database for each category defined by repeat type, repeat unit length and total repeat length. Histograms, distribution of the number of repeats matching TN\*T motifs over these samplings. Solid blue lines, kernel density estimates for these distributions. Dotted red lines, number of deletions observed in Gene4Denovo matching TN\*T motifs for each category. **e**, ID-TOP1 correlates with germline expression level. ID-TOP1, defined as 2–5 bp MH and SSTR deletions containing the TN\*T sequence motif. Shading, 95% confidence intervals from 100 bootstrap replicates.

### Extended Data Fig. 10 Topoisomerase 1 causes small deletions while protecting against topological stress.

**a**, The canonical role of Topoisomerase 1 (TOP1) is to relieve torsional stress (sc, supercoiling) during replication and transcription. **b**, TOP1 acts by forming ssDNA nicks to release supercoils and then religates the relaxed DNA. However, TOP1 cleavage at genome-embedded ribonucleotides

(frequently incorporated by replicative polymerases such as Pol ε), can lead to short deletions that will be most frequent at sites of torsional stress in the genome, such as occurs at highly transcribed genes. Adapted with permission from ref. <sup>6</sup>, SpringerNature.

## Supplementary information

### Supplementary Information

Supplementary Fig. 1, Tables 1–5 and references.

### Reporting Summary

### Peer Review File

## Rights and permissions

**Open Access** This article is licensed under a Creative Commons Attribution 4.0 International License, which permits use, sharing, adaptation, distribution and reproduction in any medium or format, as long as you give appropriate credit to the original author(s) and the source, provide a link to the Creative Commons license, and indicate if changes were made. The images or other third party material in this article are included in the article's Creative Commons license, unless indicated otherwise in a credit line to the material. If material is not included in the article's Creative Commons license and your intended use is not permitted by statutory regulation or exceeds the permitted use, you will need to obtain permission directly from the copyright holder. To view a copy of this license, visit <http://creativecommons.org/licenses/by/4.0/>.

### Reprints and Permissions

## About this article

### Cite this article

Reijns, M.A.M., Parry, D.A., Williams, T.C. *et al.* Signatures of TOP1 transcription-associated mutagenesis in cancer and germline. *Nature* **602**, 623–631 (2022). <https://doi.org/10.1038/s41586-022-04403-y>

- Received: 03 August 2021
- Accepted: 04 January 2022
- Published: 09 February 2022
- Issue Date: 24 February 2022
- DOI: <https://doi.org/10.1038/s41586-022-04403-y>

## Share this article

Anyone you share the following link with will be able to read this content:

[Get shareable link](#)

Sorry, a shareable link is not currently available for this article.

[Copy to clipboard](#)

Provided by the Springer Nature SharedIt content-sharing initiative

## Further reading

- [Unwinding the mutational signatures of a DNA topoisomerase enzyme](#)

- Ammal Abbasi
- Ludmil B. Alexandrov

*Nature* (2022)

## Unwinding the mutational signatures of a DNA topoisomerase enzyme

- Ammal Abbasi
- Ludmil B. Alexandrov

News & Views 09 Feb 2022

---

This article was downloaded by **calibre** from <https://www.nature.com/articles/s41586-022-04403-y>.

| [Section menu](#) | [Main menu](#) |

- Article
- [Published: 09 February 2022](#)

# A nutrient-specific gut hormone arbitrates between courtship and feeding

- [Hui-Hao Lin<sup>1</sup>](#),
- [Meihua Christina Kuang<sup>1</sup>](#),
- [Imran Hossain<sup>1,2</sup>](#),
- [Yinan Xuan<sup>1</sup>](#),
- [Laura Beebe<sup>1</sup>](#),
- [Andrew K. Shepherd<sup>1</sup>](#),
- [Marco Rolandi<sup>2</sup>](#) &
- [Jing W. Wang](#)    [ORCID: orcid.org/0000-0001-6291-5802<sup>1</sup>](#)

[Nature](#) volume 602, pages 632–638 (2022)

- 6756 Accesses
- 318 Altmetric
- [Metrics details](#)

## Subjects

- [Feeding behaviour](#)
- [Neural circuits](#)
- [Sensory processing](#)
- [Sexual behaviour](#)

## Abstract

Animals must set behavioural priority in a context-dependent manner and switch from one behaviour to another at the appropriate moment<sup>1,2,3</sup>. Here we probe the molecular and neuronal mechanisms that orchestrate the transition from feeding to courtship in *Drosophila melanogaster*. We find that feeding is prioritized over courtship in starved males, and the consumption of protein-rich food rapidly reverses this order within a few minutes. At the molecular level, a gut-derived, nutrient-specific neuropeptide hormone—Diuretic hormone 31 (Dh31)—propels a switch from feeding to courtship. We further address the underlying kinetics with calcium imaging experiments. Amino acids from food acutely activate Dh31<sup>+</sup> enteroendocrine cells in the gut, increasing Dh31 levels in the circulation. In addition, three-photon functional imaging of intact flies shows that optogenetic stimulation of Dh31<sup>+</sup> enteroendocrine cells rapidly excites a subset of brain neurons that express Dh31 receptor (Dh31R). Gut-derived Dh31 excites the brain neurons through the circulatory system within a few minutes, in line with the speed of the feeding–courtship behavioural switch. At the circuit level, there are two distinct populations of Dh31R<sup>+</sup> neurons in the brain, with one population inhibiting feeding through allatostatin-C and the other promoting courtship through corazonin. Together, our findings illustrate a mechanism by which the consumption of protein-rich food triggers the release of a gut hormone, which in turn prioritizes courtship over feeding through two parallel pathways.

This is a preview of subscription content

## Access options

Subscribe to Nature+

Get immediate online access to the entire Nature family of 50+ journals

\$29.99

monthly

## Subscribe

Subscribe to Journal

Get full journal access for 1 year

\$199.00

only \$3.90 per issue

## Subscribe

All prices are NET prices.

VAT will be added later in the checkout.

Tax calculation will be finalised during checkout.

Buy article

Get time limited or full article access on ReadCube.

\$32.00

## Buy

All prices are NET prices.

## **Additional access options:**

- [Log in](#)
- [Learn about institutional subscriptions](#)

**Fig. 1: Consumption of amino acids suppresses feeding and promotes male courtship.**

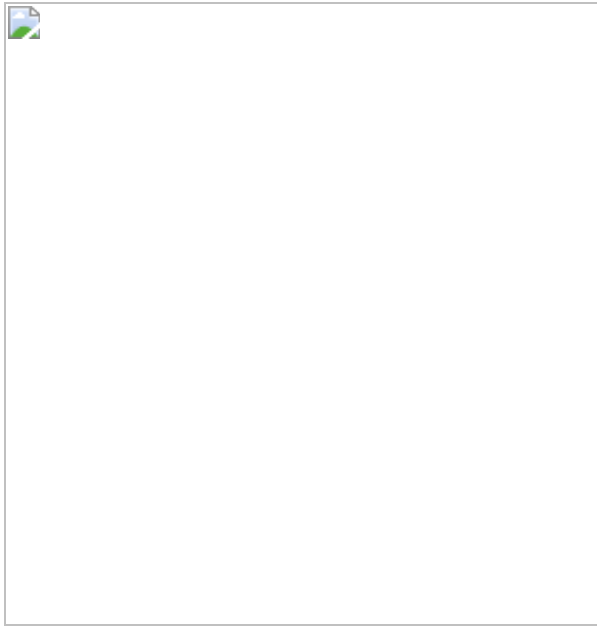


**Fig. 2: Gut Dh31 and brain Dh31R are required for the switch from feeding to courtship.**

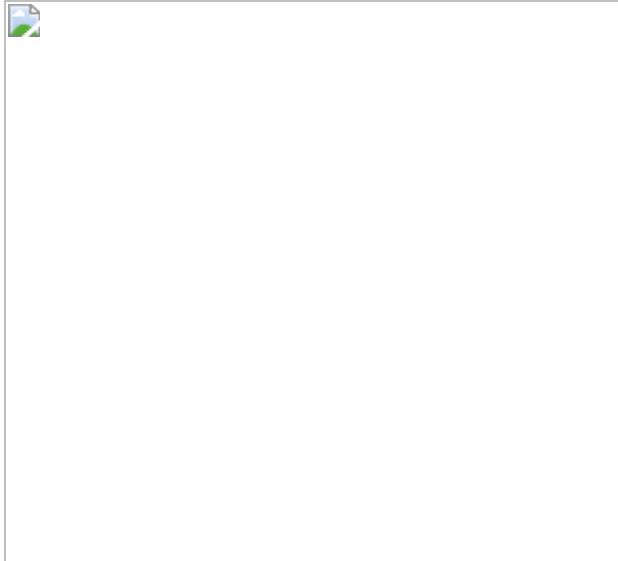


**Fig. 3: Dh31 released from the gut by amino acids activates Dh31R<sup>+</sup> neurons in the brain through circulation.**

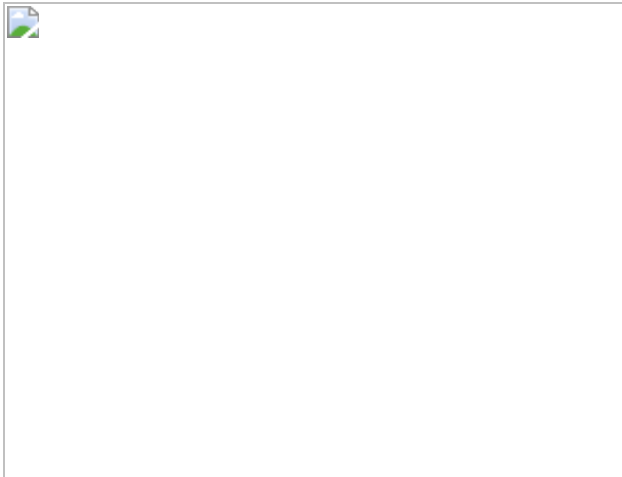
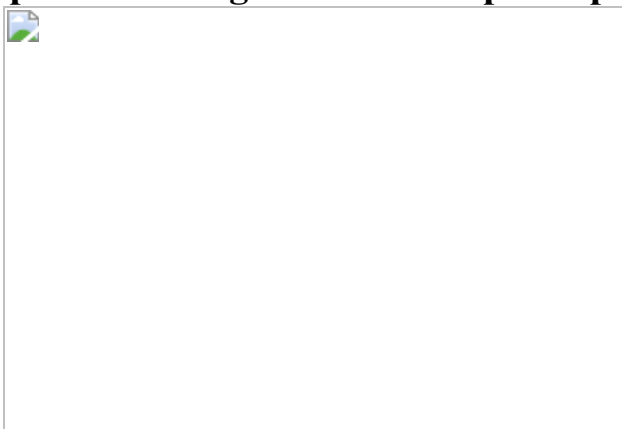


**Fig. 4: Dh31R-expressing Crz<sup>+</sup> and AstC<sup>+</sup> neurons in the brain operate in parallel to regulate courtship and protein feeding, respectively.**



## Data availability

[Source data](#) are provided with this paper.

## References

1. Tinbergen, N. *The Study of Instinct* (Clarendon Press, 1951).
2. McFarland, D. J. Decision making in animals. *Nature* **269**, 15–21 (1977).
3. Stearns, S. C. *The Evolution of Life Histories* (Oxford Univ. Press, 1992).

4. Sutton, A. K. & Krashes, M. J. Integrating hunger with rival motivations. *Trends Endocrinol. Metab.* **31**, 495–507 (2020).
5. Marella, S., Mann, K. & Scott, K. Dopaminergic modulation of sucrose acceptance behavior in *Drosophila*. *Neuron* **73**, 941–950 (2012).
6. Morton, G. J., Meek, T. H. & Schwartz, M. W. Neurobiology of food intake in health and disease. *Nat. Rev. Neurosci.* **15**, 367–378 (2014).
7. Inagaki, H. K. et al. Visualizing neuromodulation in vivo: TANGO-mapping of dopamine signaling reveals appetite control of sugar sensing. *Cell* **148**, 583–595 (2012).
8. Hadjieconomou, D. et al. Enteric neurons increase maternal food intake during reproduction. *Nature* **587**, 455–459 (2020).
9. Karigo, T. et al. Distinct hypothalamic control of same- and opposite-sex mounting behaviour in mice. *Nature* **589**, 258–263 (2021).
10. Bayless, D. W. et al. Limbic neurons shape sex recognition and social behavior in sexually naive males. *Cell* **176**, 1190–1205.e20 (2019).
11. Yang, C. F. et al. Sexually dimorphic neurons in the ventromedial hypothalamus govern mating in both sexes and aggression in males. *Cell* **153**, 896–909 (2013).
12. Dickson, B. J. Wired for sex: the neurobiology of *Drosophila* mating decisions. *Science* **322**, 904–909 (2008).
13. Yamamoto, D., Sato, K. & Koganezawa, M. Neuroethology of male courtship in *Drosophila*: from the gene to behavior. *J. Comp. Physiol. A* **200**, 251–264 (2014).
14. Zhang, S. X., Rogulja, D. & Crickmore, M. A. Dopaminergic circuitry underlying mating drive. *Neuron* **91**, 168–181 (2016).
15. Piper, M. D. W. et al. A holidic medium for *Drosophila melanogaster*. *Nat. Methods* **11**, 100–105 (2014).

16. Cheriyamkunnel, S. J. et al. A neuronal mechanism controlling the choice between feeding and sexual behaviors in *Drosophila*. *Curr. Biol.* **31**, 4231–4245.e4 (2021).
17. Lin, H.-H. et al. Hormonal modulation of pheromone detection enhances male courtship success. *Neuron* **90**, 1272–1285 (2016).
18. Schneider, J. E., Wise, J. D., Benton, N. A., Brozek, J. M. & Keen-Rhinehart, E. When do we eat? Ingestive behavior, survival, and reproductive success. *Horm. Behav.* **64**, 702–728 (2013).
19. Guo, X. et al. The cellular diversity and transcription factor code of *Drosophila* enteroendocrine cells. *Cell Rep.* **29**, 4172–4185.e5 (2019).
20. Hung, R.-J. et al. A cell atlas of the adult *Drosophila* midgut. *Proc. Natl Acad. Sci. USA* **117**, 1514–1523 (2020).
21. Veenstra, J. A. & Ida, T. More *Drosophila* enteroendocrine peptides: Orcokinin B and the CCHamides 1 and 2. *Cell Tissue Res.* **357**, 607–621 (2014).
22. Park, J.-H. et al. A subset of enteroendocrine cells is activated by amino acids in the *Drosophila* midgut. *FEBS Lett.* **590**, 493–500 (2016).
23. Bellen, H. J. et al. The BDGP Gene Disruption Project. *Genetics* **167**, 761–781 (2004).
24. Asahina, K. et al. Tachykinin-expressing neurons control male-specific aggressive arousal in *Drosophila*. *Cell* **156**, 221–235 (2014).
25. Hergarden, A. C., Tayler, T. D. & Anderson, D. J. Allatostatin-A neurons inhibit feeding behavior in adult *Drosophila*. *Proc. Natl Acad. Sci. USA* **109**, 3967–3972 (2012).
26. Clyne, J. D. & Miesenböck, G. Sex-specific control and tuning of the pattern generator for courtship song in *Drosophila*. *Cell* **133**, 354–363 (2008).

27. Marella, S. et al. Imaging taste responses in the fly brain reveals a functional map of taste category and behavior. *Neuron* **49**, 285–295 (2006).
28. Jordt, S.-E. & Julius, D. Molecular basis for species-specific sensitivity to ‘hot’ chili peppers. *Cell* **108**, 421–430 (2002).
29. Klapoetke, N. C. et al. Independent optical excitation of distinct neural populations. *Nat. Methods* **11**, 338–346 (2014).
30. Johnson, E. C. et al. A novel diuretic hormone receptor in *Drosophila*: evidence for conservation of CGRP signaling. *J. Exp. Biol.* **208**, 1239–1246 (2005).
31. Dana, H. et al. High-performance calcium sensors for imaging activity in neuronal populations and microcompartments. *Nat. Methods* **16**, 649–657 (2019).
32. Tao, X. et al. Transcutical imaging with cellular and subcellular resolution. *Biomed. Opt. Express* **8**, 1277–1289 (2017).
33. Badre, N. H., Martin, M. E. & Cooper, R. L. The physiological and behavioral effects of carbon dioxide on *Drosophila melanogaster* larvae. *Comp. Biochem. Physiol. A* **140**, 363–376 (2005).
34. Masuyama, K., Zhang, Y., Rao, Y. & Wang, J. W. Mapping neural circuits with activity-dependent nuclear import of a transcription factor. *J. Neurogenet.* **26**, 89–102 (2012).
35. Wu, Q. et al. Excreta quantification (EX-Q) for longitudinal measurements of food intake in *Drosophila*. *iScience* **23**, 100776 (2020).
36. Al-Anzi, B. et al. The leucokinin pathway and its neurons regulate meal size in *Drosophila*. *Curr. Biol.* **20**, 969–978 (2010).
37. Clark, L., Zhang, J. R., Tobe, S. & Lange, A. B. Proctolin: a possible releasing factor in the corpus cardiacum/corpus allatum of the locust.

*Peptides* **27**, 559–566 (2006).

38. Down, R. E., Matthews, H. J. & Audsley, N. Effects of *Manduca sexta* allatostatin and an analog on the pea aphid *Acyrthosiphon pisum* (Hemiptera: Aphididae) and degradation by enzymes from the aphid gut. *Peptides* **31**, 489–497 (2010).
39. Gáliková, M., Dircksen, H. & Nässel, D. R. The thirsty fly: Ion transport peptide (ITP) is a novel endocrine regulator of water homeostasis in *Drosophila*. *PLoS Genet.* **14**, e1007618 (2018).
40. Min, S. et al. Identification of a peptidergic pathway critical to satiety responses in *Drosophila*. *Curr. Biol.* **26**, 814–820 (2016).
41. Scopelliti, A. et al. A neuronal relay mediates a nutrient responsive gut/fat body axis regulating energy homeostasis in adult *Drosophila*. *Cell Metab.* **29**, 269–284.e10 (2019).
42. Söderberg, J. A. E., Carlsson, M. A. & Nässel, D. R. Insulin-producing cells in the *Drosophila* brain also express satiety-inducing cholecystokinin-like peptide, drosulfakinin. *Front. Endocrinol.* **3**, 109 (2012).
43. Wu, Q. et al. Developmental control of foraging and social behavior by the *Drosophila* neuropeptide Y-like system. *Neuron* **39**, 147–161 (2003).
44. Pfeiffer, B. D. et al. Refinement of tools for targeted gene expression in *Drosophila*. *Genetics* **186**, 735–755 (2010).
45. Ng, R. et al. Amplification of *Drosophila* olfactory responses by a DEG/ENaC channel. *Neuron* **104**, 947–959.e5 (2019).
46. Maslow, A. H. A theory of human motivation. *Psychol. Rev.* **50**, 370–396 (1943).
47. Alhadeff, A. L. et al. A neural circuit for the suppression of pain by a competing need state. *Cell* **173**, 140–152.e15 (2018).

48. Saper, C. B., Fuller, P. M., Pedersen, N. P., Lu, J. & Scammell, T. E. Sleep state switching. *Neuron* **68**, 1023–1042 (2010).
49. Jourjine, N., Mullaney, B. C., Mann, K. & Scott, K. Coupled sensing of hunger and thirst signals balances sugar and water consumption. *Cell* **166**, 855–866 (2016).
50. Kondo, S. & Ueda, R. Highly improved gene targeting by germline-specific Cas9 expression in *Drosophila*. *Genetics* **195**, 715–721 (2013).
51. Sakai, T., Isono, K., Tomaru, M. & Oguma, Y. Light-affected male following behavior is involved in light-dependent mating in *Drosophila melanogaster*. *Genes Genet. Syst.* **72**, 275–281 (1997).
52. Itskov, P. M. et al. Automated monitoring and quantitative analysis of feeding behaviour in *Drosophila*. *Nat. Commun.* **5**, 4560 (2014).
53. Veenstra, J. A., Agricola, H.-J. & Sellami, A. Regulatory peptides in fruit fly midgut. *Cell Tissue Res.* **334**, 499–516 (2008).
54. Peabody, N. C. et al. Bursicon functions within the *Drosophila* CNS to modulate wing expansion behavior, hormone secretion, and cell death. *J. Neurosci.* **28**, 14379–14391 (2008).
55. Goda, T. et al. Calcitonin receptors are ancient modulators for rhythms of preferential temperature in insects and body temperature in mammals. *Genes Dev.* **32**, 140–155 (2018).
56. Kunst, M. et al. Calcitonin gene-related peptide neurons mediate sleep-specific circadian output in *Drosophila*. *Curr. Biol.* **24**, 2652–2664 (2014).
57. Wang, J. W., Wong, A. M., Flores, J., Vosshall, L. B. & Axel, R. Two-photon calcium imaging reveals an odor-evoked map of activity in the fly brain. *Cell* **112**, 271–282 (2003).

58. Pnevmatikakis, E. A. & Giovannucci, A. NoRMCorre: An online algorithm for piecewise rigid motion correction of calcium imaging data. *J. Neurosci. Methods* **291**, 83–94 (2017).
59. Dorostkar, M. M., Dreosti, E., Odermatt, B. & Lagnado, L. Computational processing of optical measurements of neuronal and synaptic activity in networks. *J. Neurosci. Methods* **188**, 141–150 (2010).
60. Lindsay, S. A., Lin, S. J. H. & Wasserman, S. A. Short-form bomanins mediate humoral immunity in *Drosophila*. *J. Innate Immun.* **10**, 306–314 (2018).
61. Lee, J., Iyengar, A. & Wu, C.-F. Distinctions among electroconvulsion- and proconvulsant-induced seizure discharges and native motor patterns during flight and grooming: quantitative spike pattern analysis in *Drosophila* flight muscles. *J. Neurogenet.* **33**, 125–142 (2019).
62. Klassen, M. P. et al. Age-dependent diastolic heart failure in an in vivo *Drosophila* model. *eLife* **6**, e20851 (2017).
63. Dus, M. et al. Nutrient sensor in the brain directs the action of the brain–gut axis in *Drosophila*. *Neuron* **87**, 139–151 (2015).
64. Branon, K., Robie, A. A., Bender, J., Perona, P. & Dickinson, M. H. High-throughput ethomics in large groups of *Drosophila*. *Nat. Methods* **6**, 451–457 (2009).

## Acknowledgements

We thank D. Kleinfeld, C.-Y. Su and K. Asahina for comments on the manuscript; Y. Jin for sharing the spectrophotometer; D. Kleinfeld and C. Xu for continuous advice on three-photon microscopy; the following individuals for reagents: J. Veenstra (Dh31, AstB and AstC antiserum), B. White (Bursicon antiserum), F. Hamada (Dh31R antiserum) and R. Bodmer (R94C02::tdTomato transgenic line); and members of the Wang laboratory and the Su laboratory for stimulating discussions. Confocal imaging was

supported by NINDS P30 NS047101 (UC San Diego Neuroscience Microscopy Imaging Core). I.H. and M.R. acknowledge funding from the National Science Foundation (1429810). This work was supported by NIH grants to J.W.W. (R01DK127516, R01DK092640 and R01DC009597) and to H.-H.L. (K99DC016338).

## Author information

### Affiliations

1. Neurobiology Section, Division of Biological Sciences, University of California San Diego, La Jolla, CA, USA

Hui-Hao Lin, Meihua Christina Kuang, Imran Hossain, Yinan Xuan, Laura Beebe, Andrew K. Shepherd & Jing W. Wang

2. Department of Electrical and Computer Engineering, University of California Santa Cruz, Santa Cruz, CA, USA

Imran Hossain & Marco Rolandi

### Contributions

H.-H.L. conceived the project, designed experiments, analysed data, prepared figures and wrote the manuscript. M.C.K. designed experiments, wrote the manuscript, performed gut imaging experiments and analysed the data. I.H. designed experiments, wrote the manuscript, built the three-photon scope and used it to carry out experiments. Y.X. analysed gut imaging data. L.B. analysed behavioural data. A.K.S. performed genetic experiments and reagents validation. M.R. secured partial funding for three-photon microscopy. J.W.W. supervised the project and wrote the manuscript. All authors discussed the project, results and contributed to the manuscript.

### Corresponding author

Correspondence to [Jing W. Wang](#).

# Ethics declarations

## Competing interests

The authors declare no competing interests.

## Peer review

### Peer review information

*Nature* thanks the anonymous reviewers for their contribution to the peer review of this work. Peer review reports are available.

## Additional information

**Publisher's note** Springer Nature remains neutral with regard to jurisdictional claims in published maps and institutional affiliations.

## Extended data figures and tables

### [Extended Data Fig. 1 Amino acid refeeding promotes the transition from feeding to courtship in starved males.](#)

**(a–b)** Starvation reduces courtship activity. Arena size, Ø35mm. Raster plots show second-by-second behaviors of individual males **(a)**. Left, males starved for 24 h. Right, males *ad libitum* fed with standard fly food containing protein and carbohydrates. Fraction of time each male spent on courtship **(b)**. Two-tailed t-test, n = 10 males per condition. **(c–d)** Consumption of amino acids promotes male courtship. Arena size, Ø20mm. The raster plots show second-by-second behaviors (top panel in **c**). Four conditions (from left to right): 1) males starved for 24 h before test, in an arena without food; 2) males *ad libitum* fed with standard fly food containing protein and carbohydrates before test, in an arena without food; 3) males starved for 24 h before test, in an arena with sucrose-containing food; 4) males starved for 24 h before test, in an arena with amino acids-

containing food. Each arena also contained one virgin female. Average fraction of time on feeding, courtship and grooming is plotted against time in solid lines in 2-min time bin with SEM as shaded areas (bottom panel in **c**). (**d**) Fraction of time (during the period of 10–30 min) each male spent on feeding, courtship and grooming. Time after the start of copulation was excluded from calculation. Two-tailed t-test (left panel in d). Significant differences ( $p < 0.05$ ) are indicated by different letters, One-way ANOVA followed by Tukey's test (**d**).  $n = 10$  flies for each condition. Detailed statistical analysis is available in Supplementary Tables [7](#). All box and whisker plots show min, max, lower quartile, upper quartile and median.

[Source data](#)

[Extended Data Fig. 2 Locomotion of male flies.](#)

(**a–c**) Male flies exhibit similar locomotion activity after consuming food containing isocaloric sucrose or amino acids. After deprived of food for 24 h, individual flies were given access to food for 10 min. Male flies were then placed in a circular arena (60 mm in diameter, 3.5 mm depth) for video recordings. Food: sucrose (50 mM) or amino acids (200 mM). (**a**) Walking trajectories of individual flies during the 5-min observation period. (**b**) Average walking velocity of individual flies.  $n = 10$  flies for each food. Two-tailed t-test. (**c**) Average path length traveled by flies.  $n = 10$  flies for each condition. (**d–f**) Gut *Dh31* knockdown does not affect locomotion activity. Ctrl1: *Dh31-GAL4*, *Tsh-GAL80*. Ctrl2: *UAS-Dh31-RNAi*. Gut *Dh31* KD flies contain all three transgenes. (**d**) Walking trajectories of individual flies. (**e**) Average walking velocity of individual flies during the 5-min observation period.  $n = 10$  flies for each genotype. One-way ANOVA test. (**f**) Average path length traveled by flies.  $n = 10$  flies for each genotype.

[Source data](#)

[Extended Data Fig. 3 Schematic illustration of gene structures and knock-in constructs.](#)

(**a**) A *T2A-GAL4.2* cassette was inserted at the C-terminus of *Dh31* by Cas9-mediated knock-in strategy. 3XP3-RFP was used as a positive

selection marker. (b) An *nls-LexA::p65* cassette was inserted after the start codon of *Dh31R* by Cas9-mediated knock-in strategy. (c) An *nls-LexA::p65* cassette was inserted after the start codon of *Crz* by Cas9-mediated knock-in strategy.

### **Extended Data Fig. 4 Dh31 expression outside the brain is required for the effect of ingested amino acids on courtship.**

(a). Validation of the *Dh31<sup>T2A-GAL4</sup>* driver line by a Dh31 antiserum. Representative confocal images show the expression pattern of *Dh31<sup>T2A-GAL4</sup>* (Blue) and Dh31 (magenta) in the brain, ventral nerve cord (VNC) and midgut of male flies carrying *Dh31<sup>T2A-GAL4</sup>* and *UAS-Redstinger*. Schematic indicates the distribution of Dh31 cells in the brain, VNC, and GI tract, drawn from the confocal stacks of the sample shown in the left panel. Magenta dots show cell positive for Dh31 antibody and Redstinger; black dots show cells positive for Dh31 antibody and negative for Redstinger. The average number ( $\pm$  SEM) of cells in each region is from 5 different male flies. Scale bar, 50  $\mu$ m. (b-d) The courtship effect of region-specific *Dh31* knockdown. *Dh31* knockdown in all *Dh31<sup>T2A-GAL4</sup>* cells (b); *Dh31* knockdown in brain *Dh31<sup>T2A-GAL4</sup>* cells (c); *Dh31* knockdown in *Dh31<sup>T2A-GAL4</sup>* cells outside the brain (d). Representative images from 3 samples. For each condition, the total number of matches (n) from 5 independent experiments is indicated in the figure. *p*-value was determined by Chi-square test to indicate whether males of a given genetic manipulation respond to amino acids. Blue bar indicates the average copulation percentage, and the dashed line indicates chance level. AAs, amino acids (200 mM). S, sucrose (50 mM).

[Source data](#)

### **Extended Data Fig. 5 Dh31 expression in enteroendocrine cells is required for the effect of ingested amino acids.**

(a) Expression of Redstinger (blue) and Dh31 (anti-Dh31, magenta) in the brain, VNC and midgut of a male containing *Dh31-GAL4* and *UAS-Redstinger*. Scale bar, 50  $\mu$ m. Schematic: cell distribution in the brain, VNC

and GI tract, drawn from the confocal stacks of the sample shown in the left panel. Magenta dots: Dh31 antibody<sup>+</sup> and GAL4<sup>+</sup> cells; black dots: Dh31 antibody<sup>+</sup> and GAL4<sup>-</sup> cells. The average number ( $\pm$  SEM) of cells in each region is from 5 different male flies. (b) Validation of *Dh31* knockdown. Knockdown of *Dh31* in the gut is achieved by using *Dh31-GAL4* and *Tsh-GAL80* to drive *UAS-Dh31-RNAi*. Immunostaining with an antiserum to Dh31 (magenta) shows that knockdown is effective (3 different experiments). Scale bar, 50  $\mu$ m. (c). The courtship effect of gut-specific *Dh31* knockdown (left) or chemo-activation of gut Dh31<sup>+</sup> cells (right). Chemo-activation is achieved by using *Dh31-GAL4* and *Tsh-GAL80* to drive *UAS-VR1*. Each data point represents one experiment. For each condition, the total number of matches (n) is indicated in the figure. Chi-square test was used to determine whether males of a given genetic manipulation respond to amino acids (left) or capsaicin (right). Blue bar indicates average copulation percentage, and the dashed line indicates chance level. AAs, amino acids (200 mM). S, sucrose (50 mM).

[Source data](#)

[Extended Data Fig. 6 The role of Dh31 signaling in feeding to courtship transition.](#)

(a–b) Optogenetic activation of gut Dh31<sup>+</sup> enteroendocrine cells promotes courtship and suppresses protein feeding. After a brief optogenetic stimulation of gut Dh31<sup>+</sup> cells, 24-h starved males directly engage in courtship, unlike control flies that typically consumed amino acids (200 mM) before proceeding to courtship. Male flies were exposed to 660-nm LED light for 5 min and then transferred to the behavioral chamber for video recording for 30 min. Flies: Gut *Dh31-GAL4*: *Dh31-GAL4*, *Tsh-GAL80*. UAS: *UAS-CsChrimson*. Gut *Dh31 CsChrimson* flies contain all three transgenes. (a) Raster plots showing second-by-second behaviors of 5 representative males of each genotype. Behaviors: feeding (blue), courtship (orange) and copulation (black). (b) Fraction of time spent by each male on feeding and courtship. One-way ANOVA followed by Tukey's test. n = 7 flies for each condition and genotype. (c–f) Dh31 in the gut and Dh31R in brain Crz<sup>+</sup> neurons are required for males to transition from feeding to

courtship. The Raster Plots show the second-by-second behaviors of 5 representative males. Gut *Dh31-GAL4*: *Dh31-GAL4*, *Tsh-GAL80*. Starved, 24 h. (c) Gut *Dh31* knockdown reduced courtship activity and increased feeding in males *ad libitum* fed with standard fly food containing protein and carbohydrates. The fraction of time individual males spent on feeding and courtship is shown. Gut *Dh31* KD flies had *UAS-Dh31-RNAi* and Gut *Dh31-GAL4*. One-way ANOVA followed by Tukey's test. n = 7 flies for each condition. (d) Gut *Dh31* knockdown increased feeding duration and eliminated courtship when food contained amino acids, but had no effect when food contained only sucrose. (e) Chemogenetic activation of gut *Dh31-GAL4* cells. The ingestion of capsaicin-containing food induced courtship but food containing only sucrose had no effect. Gut *Dh31* VR1 flies contained *UAS-VR1* and Gut *Dh31-GAL4*. (f) *Dh31R* knockdown in brain Crz<sup>+</sup> neurons eliminated the effect of amino acids on courtship, but not feeding. GAL4: *Crz-GAL4*, *tub>GAL80>stop*. UAS: *otd-nls::flp*, *UAS-Dh31R-RNAi*. Brain *Dh31R* KD flies had all four transgenes.

### Source data

## Extended Data Fig. 7 Expression of Dh31R and Crz in brain Crz<sup>+</sup> neurons is required for the aphrodisiac effect of amino acids.

(a) Validation of *Dh31R* knockdown. qRT-PCR results show that *Dh31R* expression level is reduced in flies containing the *Actin-GAL4* and *UAS-Dh31R-RNAi* transgenes. RNA was extracted from 5 male flies per experiment, with 6 experiments for each genotype. One-way ANOVA followed by Tukey's test. (b-d) Schematic indicates genetic strategies to perturb Crz<sup>+</sup> neurons in the brain and VNC (b), only in the brain (c), and only in the VNC (d). Representative confocal images from 3 samples show the different intersections between *Crz-GAL4* and *otd-nls::flp* (corresponding genotypes are shown below the images). Samples were immuostained with anti-GFP (green), nc82 (blue). Scale bar, 50 μm. The courtship effect of *Dh31R* knockdown in both brain and VNC, in brain only or in VNC only. Each data point represents one experiment. For each condition, the total number of matches (n) is indicated in the figure. p-value

was determined by Chi-square test to indicate whether males of a given genetic manipulation respond to amino acids. Blue bar indicates average copulation percentage, and the dashed line indicates chance level. AAs, amino acids (200 mM). S, sucrose (50 mM). (e) Validation of *Crz* knockdown. Immunostaining of anti-*Crz* (red) showed *Crz* is undetectable in brain *Crz*<sup>+</sup> neurons in *Crz-Gal4, UAS-Crz-RNAi* flies, based on 3 independent experiments. Scale bar, 50 μm. (f–g) The courtship effect of *Crz* knockdown in brain *Crz*<sup>+</sup> neurons (f) or in VNC *Crz*<sup>+</sup> neurons (g). For each condition, the total number of matches (n) from 5 independent experiments is shown in the figure. *p*-value was determined by Chi-square test to indicate whether males of a given genetic manipulation respond to amino acids. Blue bar indicates average copulation percentage, and the dashed line indicates chance level. AAs, amino acids (200 mM). S, sucrose (50 mM).

[Source data](#)

**Extended Data Fig. 8 Dh31 enteroendocrine cells respond to amino acids.**

(a) Response of Dh31<sup>+</sup> cells to different nutrients at the indicated concentrations. Suc: sucrose, Fru+Glu: mixture of fructose and glucose, EAA: essential amino acids, NEAA: nonessential amino acids. The average calcium response ( $\Delta F/F$ ) is shown in black with SEM as gray shaded areas (n = 6 male flies). (b) The response of individual Dh31<sup>+</sup> cells to a mixture of amino acids at different concentrations (amino acid composition is detailed in Supplementary Tables 4). Gray lines below the traces indicate the stimulation period of amino acids or saline control.

[Source data](#)

**Extended Data Fig. 9 Ex vivo brain Crz<sup>±</sup> neurons respond to bath application of Dh31 peptide.**

Brain *Crz*<sup>+</sup> neurons exhibited increased calcium activity in response to synthetic Dh31 peptide. The evoked response latency decreased with

increasing concentration of Dh31, while the peak  $\Delta F/F$  did not change. *Ex vivo* brain preparations of flies carrying *Crz-GAL4* and *UAS-GCaMP7s* were imaged with two-photon microscopy. **(a)** Representative calcium responses ( $\Delta F/F$ ) of brain  $Crz^+$  neurons in response to different concentrations of Dh31 peptide. The time of Dh31 application is marked by an arrowhead below the calcium response ( $\Delta F/F$ ) trace. **(b)** Response latency (left) and peak  $\Delta F/F$  (right) of brain  $Crz^+$  neurons in response to different concentrations of Dh31 peptide. Error bars, SEM. n = 7 samples. Significant differences ( $p < 0.05$ ) are indicated by different letters, One-way ANOVA followed by Tukey's test. Detailed statistical analysis is available in Supplementary Tables [7](#).

### Source data

### Extended Data Fig. 10 Imaging brain $Crz^+$ neurons with three-photon microscopy.

**(a–b)** Effect of  $CO_2$  exposure on heartbeat and the response of brain  $Crz^+$  neurons to the activation of gut  $Dh31^+$  cells. **(a)** Images show the changing diameter of the heart-tube before, during and after  $CO_2$  exposure. Heartbeat frequency was extracted from the changing diameter in male flies expressing tdTomato in cardiomyocytes. The light and dark blue lines show the heartbeat frequency of individual flies and the average, respectively (n = 6 flies). **(b)** The effect of  $CO_2$ -exposure on the peak  $\Delta F/F$  of  $Crz^+$  neurons in response to optogenetic activation of  $Dh31^+$  enteroendocrine cells. Average  $\Delta F/F$  traces are shown as solid lines with SEM as shaded areas. Stimulation intensity: 1.75 mW/mm<sup>2</sup>. Error bars, SEM. Two-tailed t-test (n = 5 samples). **(c)** Schematic of a three-photon microscope, custom built with a MOM scope (Sutter). Pump laser emission of 1,035 nm is converted to 1,320 nm or 1,650 nm with OPA. Average laser power was controlled by a half-wave plate ( $\lambda/2$ ) and a polarizing beamsplitter (BS). The pulse width of 1,320 nm emission was compressed through the light path containing P1, P2, RM, Mpu, KT1 and the pulse width of 1,650 nm emission was compressed by the light path containing M1, Si, M2. Beam size at the scan mirror (SM) was matched by KT2. Green and Red emission was collected

from the sample with two photomultiplier tubes (PMTs). LP: 1200 nm long pass filter; MM: movable mirror; Mpu: pick up mirror; P1, P2: prism; RM: roof mirror; KT1, KT2: keplerian telescope; Si: silicon crystal; M1, M2: mirror; SL: scan lens; TL: tube lens.

### Source data

### Extended Data Fig. 11 Identification of brain Dh31R<sup>+</sup> neurons that regulate the intake of protein-containing food.

**(a)** Expression pattern of neuropeptides, neuropeptidergic driver lines and Dh31R in the brain. Top row: arrowheads indicate neurons that co-express Dh31R with *AstA-GAL4*, *Lk-GAL4*, or *Dsk-GAL4*. Bottom row: arrowheads indicate neurons that co-express AstC with Dh31R or *R67F03-GAL4*. Scale bar, 50 µm. **(b)** Food intake of flies with *Dh31R* knockdown in different neurons. Gal4 lines (*Itp*, *AstA*, *LK*, *R67F03*) were crossed to *UAS-Dh31R-RNAi* and tested for amino acid food consumption. Male flies with *Dh31R* knockdown in *R67F03-GAL4* cells consumed more amino acids than controls. The number of independent experiments is indicated in each panel. One-way ANOVA followed by Tukey's test. **(c and d)** Genetic strategies to label *R67F03-GAL4* neurons in the brain **(c)** and outside the brain **(d)**. Representative confocal images from 3 independent experiments show the different intersections between *R67F03-GAL4* and *otd-nls::flp* (corresponding genotypes are shown). Samples were immunostained with anti-GFP (green), nc82 (blue). Scale bar, 50 µm. **(e)** Knockdown of *Dh31R* (left panel) or *AstC* (right panel) in *R67F03-GAL4* cells outside the brain. Knockdown male flies consumed the same amount of amino acids and sucrose food compared with control flies. GAL4: *R67F03-GAL4*, *otd-nls::flp*; UAS: *UAS-Dh31R-RNAi*, *tub>stop>GAL80*; *Dh31R* KD flies have all four transgenes (left panel). GAL4: *R67F03-GAL4*, *otd-nls::flp*; UAS: *UAS-AstC-RNAi*, *tub>stop>GAL80*; *AstC* KD flies have all four transgenes (right panel). n = 10 independent experiments for each condition/genotype. One-way ANOVA test. **(f–g)** The elevated calcium levels in brain *AstC<sup>+</sup>* neurons in response to dietary amino acids require Dh31R expression. Calcium levels in brain *AstC<sup>+</sup>* neurons were higher in male flies fed with amino acids compared to those fed with sucrose, as measured by the

calcium level reporter, CaLexA. Expression of Dh31R in brain AstC<sup>+</sup> neurons was required for the increased calcium levels. Foods: sucrose (50 mM); AAs, amino acids (200 mM). Flies: Control (*R67F03-GAL4, UAS-CaLexA*), *Dh31R* KD (*R67F03-GAL4, UAS-CaLexA, UAS-Dh31R RNAi*). Confocal images show representative samples. Scale bar, 20 µm. Box plots show quantification of fluorescence intensity from AstC<sup>+</sup> neurons. 2 neurons per sample. The number of samples for each condition is indicated. Two-tailed Mann-Whitney U test.

#### [Source data](#)

#### [Extended Data Fig. 12 Roles of brain Crz<sup>±</sup> or AstC<sup>±</sup> neurons in courtship and feeding.](#)

**(a–d)** Courtship and protein feeding behavior of flies expressing TrpA1 in brain Crz<sup>+</sup> or AstC<sup>+</sup> neurons at 21 °C. **(a, b)** The copulation percentages and total protein consumption (200 mM AAs) of male flies expressing TrpA1 in brain Crz<sup>+</sup> neurons and controls. Flies: Bain *Crz-GAL4, otd-nls::flp; UAS:UAS>stop>TrpA1*; Brain *Crz TrpA1* flies have all three transgenes. **(c, d)** The copulation percentages and total protein consumption (200 mM AAs) of male flies expressing TrpA1 in brain AstC<sup>+</sup> neurons and controls. Flies: Brain *Astc-GAL4: R67F03-GAL4, otd-nls::flp; UAS:UAS>stop>TrpA1*; Brain *AstC TrpA1* flies contains all three transgenes. **(e)** *AstC* knockdown in brain AstC<sup>+</sup> neurons does not affect male courtship. Male flies with *AstC* knockdown in brain AstC<sup>+</sup> neurons exhibited similar copulation percentage as their genetic controls. Three males of different genotypes were given access to one virgin female in three-male courtship assay. Copulation percentages of the different genotypes in the three-male courtship assay are shown, with the average value of each genotype indicated by a horizontal bar. Lines connect results from the same experiment **(a, c, e)**. The number of independent experiments is indicated in each panel. One-way ANOVA test.

#### [Source data](#)

## Supplementary information

## **Supplementary Information**

This file contains Supplementary Fig. 1 (uncropped images of western blots shown in this study), Tables 1–7, discussion relevant to the main text and additional references.

## **Reporting Summary**

### **Peer Review File**

## **Source data**

**Source Data Fig. 1**

**Source Data Fig. 2**

**Source Data Fig. 3**

**Source Data Fig. 4**

**Source Data Extended Data Fig. 1**

**Source Data Extended Data Fig. 2**

**Source Data Extended Data Fig. 4**

**Source Data Extended Data Fig. 5**

**Source Data Extended Data Fig. 6**

**Source Data Extended Data Fig. 7**

**Source Data Extended Data Fig. 8**

[\*\*Source Data Extended Data Fig. 9\*\*](#)

[\*\*Source Data Extended Data Fig. 10\*\*](#)

[\*\*Source Data Extended Data Fig. 11\*\*](#)

[\*\*Source Data Extended Data Fig. 12\*\*](#)

## Rights and permissions

[Reprints and Permissions](#)

## About this article

### Cite this article

Lin, HH., Kuang, M.C., Hossain, I. *et al.* A nutrient-specific gut hormone arbitrates between courtship and feeding. *Nature* **602**, 632–638 (2022).  
<https://doi.org/10.1038/s41586-022-04408-7>

- Received: 10 March 2021
- Accepted: 22 December 2021
- Published: 09 February 2022
- Issue Date: 24 February 2022
- DOI: <https://doi.org/10.1038/s41586-022-04408-7>

## Share this article

Anyone you share the following link with will be able to read this content:

[Get shareable link](#)

Sorry, a shareable link is not currently available for this article.

[Copy to clipboard](#)

Provided by the Springer Nature SharedIt content-sharing initiative

---

This article was downloaded by **calibre** from <https://www.nature.com/articles/s41586-022-04408-7>

| [Section menu](#) | [Main menu](#) |

- Article
- [Published: 09 February 2022](#)

# A discrete neuronal population coordinates brain-wide developmental activity

- [Bryce T. Bajar<sup>1</sup>](#),
- [Nguyen T. Phi](#) ORCID: [orcid.org/0000-0002-2215-1884<sup>2</sup>](https://orcid.org/0000-0002-2215-1884),
- [Jesse Isaacman-Beck<sup>3</sup>](#),
- [Jun Reichl<sup>4</sup>](#),
- [Harpreet Randhawa<sup>4</sup>](#) &
- [Orkun Akin](#) ORCID: [orcid.org/0000-0003-1719-4887<sup>4</sup>](https://orcid.org/0000-0003-1719-4887)

[Nature](#) volume **602**, pages 639–646 (2022)

- 2967 Accesses
- 38 Altmetric
- [Metrics details](#)

## Subjects

- [Developmental neurogenesis](#)
- [Ion channels in the nervous system](#)
- [Synaptic development](#)

## Abstract

In vertebrates, stimulus-independent activity accompanies neural circuit maturation throughout the developing brain<sup>1,2</sup>. The recent discovery of similar activity in the developing *Drosophila* central nervous system suggests that developmental activity is fundamental to the assembly of complex brains<sup>3</sup>. How such activity is coordinated across disparate brain regions to influence synaptic development at the level of defined cell types is not well understood. Here we show that neurons expressing the cation channel transient receptor potential gamma (Trpy) relay and pattern developmental activity throughout the *Drosophila* brain. In *trpy* mutants, activity is attenuated globally, and both patterns of activity and synapse structure are altered in a cell-type-specific manner. Less than 2% of the neurons in the brain express Trpy. These neurons arborize throughout the brain, and silencing or activating them leads to loss or gain of brain-wide activity. Together, these results indicate that this small population of neurons coordinates brain-wide developmental activity. We propose that stereotyped patterns of developmental activity are driven by a discrete, genetically specified network to instruct neural circuit assembly at the level of individual cells and synapses. This work establishes the fly brain as an experimentally tractable system for studying how activity contributes to synapse and circuit formation.

This is a preview of subscription content

## Access options

Subscribe to Nature+

Get immediate online access to the entire Nature family of 50+ journals

\$29.99

monthly

[Subscribe](#)

Subscribe to Journal

Get full journal access for 1 year

\$199.00

only \$3.90 per issue

[Subscribe](#)

All prices are NET prices.

VAT will be added later in the checkout.

Tax calculation will be finalised during checkout.

Buy article

Get time limited or full article access on ReadCube.

\$32.00

[Buy](#)

All prices are NET prices.

### **Additional access options:**

- [Log in](#)
- [Learn about institutional subscriptions](#)

**Fig. 1: *Trpγ* is necessary for wild-type PSINA.**

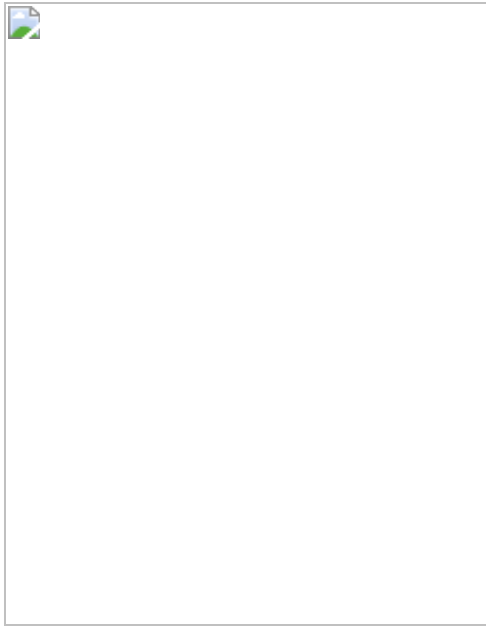


**Fig. 2: Activity patterns in visual processing neurons are altered in *trpy* mutants.**

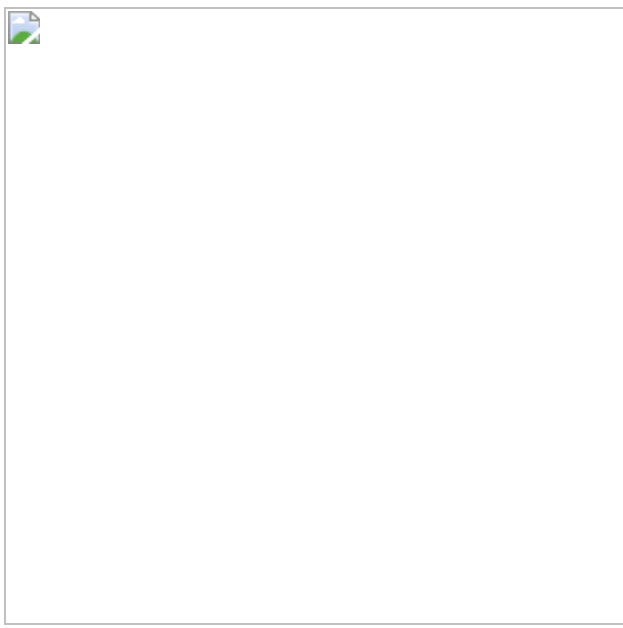


**Fig. 3: Synapse formation in the visual system depends on PSINA.**

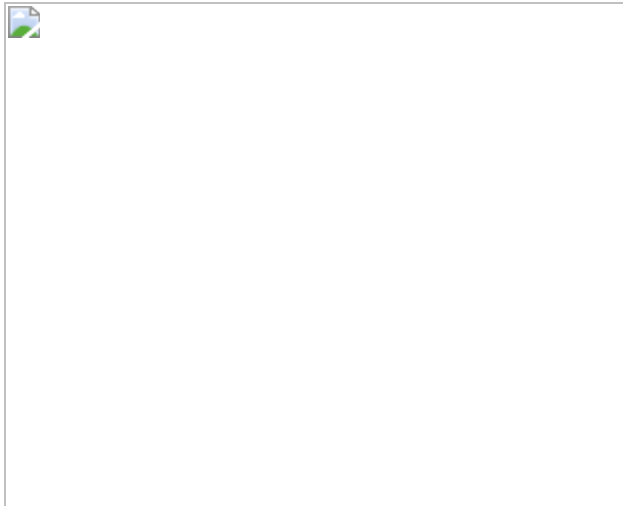


**Fig. 4: Trpy<sup>+</sup> neurons are the template for brain-wide PSINA.**

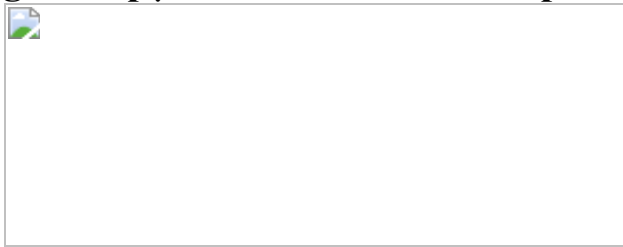
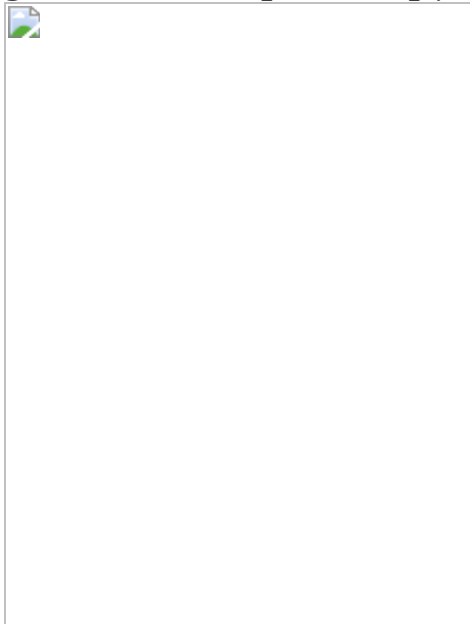


**Fig. 5: PSINA requires Trpy<sup>+</sup> neuron activity.**



## Data availability

The authors declare that all data supporting the findings of this study are available within the paper and its supplementary information files.

## References

1. Blankenship, A. G. & Feller, M. B. Mechanisms underlying spontaneous patterned activity in developing neural circuits. *Nat. Rev. Neurosci.* **11**, 18–29 (2010).
2. Ackman, J. B. & Crair, M. C. Role of emergent neural activity in visual map development. *Curr. Opin. Neurobiol.* **24**, 166–175 (2014).
3. Akin, O., Bajar, B. T., Keles, M. F., Frye, M. A. & Zipursky, S. L. Cell-type-specific patterned stimulus-independent neuronal activity in the *Drosophila* visual system during synapse formation. *Neuron* **101**, 894–904.e5 (2019).
4. Galli, L. & Maffei, L. Spontaneous impulse activity of rat retinal ganglion cells in prenatal life. *Science* **242**, 90–91 (1988).
5. Meister, M., Wong, R. O., Baylor, D. A. & Shatz, C. J. Synchronous bursts of action potentials in ganglion cells of the developing mammalian retina. *Science* **252**, 939–943 (1991).
6. Ackman, J. B., Burbridge, T. J. & Crair, M. C. Retinal waves coordinate patterned activity throughout the developing visual system. *Nature* **490**, 219–225 (2012).
7. Bansal, A. et al. Mice lacking specific nicotinic acetylcholine receptor subunits exhibit dramatically altered spontaneous activity patterns and reveal a limited role for retinal waves in forming ON and OFF circuits in the inner retina. *J. Neurosci.* **20**, 7672–7681 (2000).
8. Burbridge, T. J. et al. Visual circuit development requires patterned activity mediated by retinal acetylcholine receptors. *Neuron* **84**, 1049–1064 (2014).
9. McLaughlin, T., Hindges, R. & O’Leary, D. D. Regulation of axial patterning of the retina and its topographic mapping in the brain. *Curr. Opin. Neurobiol.* **13**, 57–69 (2003).

10. Sugie, A., Marchetti, G. & Tavosanis, G. Structural aspects of plasticity in the nervous system of *Drosophila*. *Neural Dev.* **13**, 14 (2018).
11. Hiesinger, P. R. et al. Activity-independent prespecification of synaptic partners in the visual map of *Drosophila*. *Curr. Biol.* **16**, 1835–1843 (2006).
12. Chen, Y. et al. Cell-type-specific labeling of synapses in vivo through synaptic tagging with recombination. *Neuron* **81**, 280–293 (2014).
13. Muthukumar, A. K., Stork, T. & Freeman, M. R. Activity-dependent regulation of astrocyte GAT levels during synaptogenesis. *Nat. Neurosci.* **17**, 1340–1350 (2014).
14. Takemura, S. Y. et al. A visual motion detection circuit suggested by *Drosophila* connectomics. *Nature* **500**, 175–181 (2013).
15. Venkatachalam, K. & Montell, C. TRP channels. *Annu. Rev. Biochem.* **76**, 387–417 (2007).
16. Chen, T. W. et al. Ultrasensitive fluorescent proteins for imaging neuronal activity. *Nature* **499**, 295–300 (2013).
17. Akitake, B. et al. Coordination and fine motor control depend on *Drosophila* TRP $\gamma$ . *Nat. Commun.* **6**, 7288 (2015).
18. Kanca, O. et al. An efficient CRISPR-based strategy to insert small and large fragments of DNA using short homology arms. *eLife* **8**, e51539 (2019).
19. Xu, X. Z., Chien, F., Butler, A., Salkoff, L. & Montell, C. TRP $\gamma$ , a drosophila TRP-related subunit, forms a regulated cation channel with TRPL. *Neuron* **26**, 647–657 (2000).
20. Batut, P. & Gingeras, T. R. RAMPAGE: promoter activity profiling by paired-end sequencing of 5'-complete cDNAs. *Curr. Protoc. Mol. Biol.* **104**, Unit 25B.11 (2013).

21. McGuire, S. E., Le, P. T., Osborn, A. J., Matsumoto, K. & Davis, R. L. Spatiotemporal rescue of memory dysfunction in *Drosophila*. *Science* **302**, 1765–1768 (2003).
22. Akin, O. & Zipursky, S. L. Frazzled promotes growth cone attachment at the source of a Netrin gradient in the. *eLife* **5**, e20762 (2016).
23. Takemura, S. Y., Lu, Z. & Meinertzhagen, I. A. Synaptic circuits of the *Drosophila* optic lobe: the input terminals to the medulla. *J. Comp. Neurol.* **509**, 493–513 (2008).
24. Lee, T. & Luo, L. Mosaic analysis with a repressible cell marker for studies of gene function in neuronal morphogenesis. *Neuron* **22**, 451–461 (1999).
25. Kurmangaliyev, Y. Z., Yoo, J., Valdes-Aleman, J., Sanfilippo, P. & Zipursky, S. L. Transcriptional programs of circuit assembly in the *Drosophila* visual system. *Neuron* **108**, 1045–1057.e6 (2020).
26. Baines, R. A., Uhler, J. P., Thompson, A., Sweeney, S. T. & Bate, M. Altered electrical properties in *Drosophila* neurons developing without synaptic transmission. *J. Neurosci.* **21**, 1523–1531 (2001).
27. Peng, J. et al. *Drosophila* Fezf coordinates laminar-specific connectivity through cell-intrinsic and cell-extrinsic mechanisms. *eLife* **7**, e33962 (2018).
28. Isaacman-Beck, J. et al. SPARC enables genetic manipulation of precise proportions of cells. *Nat. Neurosci.* **23**, 1168–1175 (2020).
29. Chiang, A. S. et al. Three-dimensional reconstruction of brain-wide wiring networks in *Drosophila* at single-cell resolution. *Curr. Biol.* **21**, 1–11 (2011).
30. Dana, H. et al. Sensitive red protein calcium indicators for imaging neural activity. *eLife* **5**, e12727 (2016).

31. Pulver, S. R., Pashkovski, S. L., Hornstein, N. J., Garrity, P. A. & Griffith, L. C. Temporal dynamics of neuronal activation by channelrhodopsin-2 and TRPA1 determine behavioral output in *Drosophila* larvae. *J. Neurophysiol.* **101**, 3075–3088 (2009).
32. Crair, M. C. Neuronal activity during development: permissive or instructive. *Curr. Opin. Neurobiol.* **9**, 88–93 (1999).
33. Valdes-Aleman, J. et al. Comparative connectomics reveals how partner identity, location, and activity specify synaptic connectivity in *Drosophila*. *Neuron* **109**, 105–122.e7 (2021).
34. Mulloney, B. & Smarandache, C. Fifty years of CPGs: two neuroethological papers that shaped the course of neuroscience. *Front. Behav. Neurosci.* **4**, 45 (2010).
35. Tritsch, N. X., Yi, E., Gale, J. E., Glowatzki, E. & Bergles, D. E. The origin of spontaneous activity in the developing auditory system. *Nature* **450**, 50–55 (2007).
36. Wang, H. C. et al. Spontaneous activity of cochlear hair cells triggered by fluid secretion mechanism in adjacent support cells. *Cell* **163**, 1348–1359 (2015).
37. Luhmann, H. J. et al. Spontaneous neuronal activity in developing neocortical networks: from single cells to large-scale interactions. *Front. Neural Circuits* **10**, 40 (2016).
38. Özal, M. N. et al. Neuronal diversity and convergence in a visual system developmental atlas. *Nature* **589**, 88–95 (2021).
39. Helfrich-Förster, C. Development of pigment-dispersing hormone-immunoreactive neurons in the nervous system of *Drosophila melanogaster*. *J. Comp. Neurol.* **380**, 335–354 (1997).
40. Leong, A. T. et al. Long-range projections coordinate distributed brain-wide neural activity with a specific spatiotemporal profile. *Proc. Natl Acad. Sci. USA* **113**, E8306–E8315 (2016).

41. Fischbach, K. F. & Dittrich, A. P. M. The optic lobe of *Drosophila melanogaster*. 1. A Golgi analysis of wild-type structure. *Cell Tissue Res.* **258**, 441–475 (1989).
42. Bainbridge, S. P. & Bownes, M. Staging the metamorphosis of *Drosophila melanogaster*. *J. Embryol. Exp. Morphol.* **66**, 57–80 (1981).
43. Brand, A. H. & Perrimon, N. Targeted gene expression as a means of altering cell fates and generating dominant phenotypes. *Development* **118**, 401–415 (1993).
44. Lai, S. L. & Lee, T. Genetic mosaic with dual binary transcriptional systems in *Drosophila*. *Nat. Neurosci.* **9**, 703–709 (2006).
45. Piper, M. D. & Partridge, L. Protocols to study aging in *Drosophila*. *Methods Mol. Biol.* **1478**, 291–302 (2016).
46. Schindelin, J. et al. Fiji: an open-source platform for biological-image analysis. *Nat. Methods* **9**, 676–682 (2012).
47. Daniels, R. W. et al. Increased expression of the *Drosophila* vesicular glutamate transporter leads to excess glutamate release and a compensatory decrease in quantal content. *J. Neurosci.* **24**, 10466–10474 (2004).
48. Fei, H. et al. Mutation of the *Drosophila* vesicular GABA transporter disrupts visual figure detection. *J. Exp. Biol.* **213**, 1717–1730 (2010).
49. Park, D., Veenstra, J. A., Park, J. H. & Taghert, P. H. Mapping peptidergic cells in *Drosophila*: where DIMM fits in. *PLoS ONE* **3**, e1896 (2008).
50. Cabrero, P. et al. The *Dh* gene of *Drosophila melanogaster* encodes a diuretic peptide that acts through cyclic AMP. *J. Exp. Biol.* **205**, 3799–3807 (2002).

51. Terhzaz, S., Rosay, P., Goodwin, S. F. & Veenstra, J. A. The neuropeptide SIFamide modulates sexual behavior in *Drosophila*. *Biochem. Biophys. Res. Commun.* **352**, 305–310 (2007).
52. Preibisch, S., Saalfeld, S. & Tomancak, P. Globally optimal stitching of tiled 3D microscopic image acquisitions. *Bioinformatics* **25**, 1463–1465 (2009).
53. Peng, H., Ruan, Z., Long, F., Simpson, J. H. & Myers, E. W. V3D enables real-time 3D visualization and quantitative analysis of large-scale biological image data sets. *Nat. Biotechnol.* **28**, 348–353 (2010).

## Acknowledgements

We thank S. L. Zipursky for discussions, support and feedback on the manuscript; C. Montell for sharing fly lines and other reagents; T. R. Clandinin for support in generating the SPARC3-Out-GAL80 flies; J. M. Donlea, V. Hartenstein, D. E. Krantz and Y. Lin for sharing antibodies; J. A. Veenstra for sharing neuropeptide antibodies; D. Hattori for the Kir2.1 flies; A. Nern and G. M. Rubin for the 29C07-FLP flies; the Banerjee Laboratory at UCLA for the UAS-rpr,-hid flies; O. Kanca and H. J. Bellen for the *Trpy*<sup>DropIn-TG4</sup> flies; S. Yamamoto and T. Takano-Shimizu for the UAS-TRPC4 and TRPC5 flies; and members of the Zipursky laboratory for feedback and discussion. B.T.B. is supported by NIH grants F30EY029952 and T32GM008042; OA is supported by NIH grant R01NS123376.

## Author information

### Affiliations

1. Department of Biological Chemistry, Medical Scientist Training Program, David Geffen School of Medicine at UCLA, University of California, Los Angeles, Los Angeles, CA, USA

Bryce T. Bajar

2. Molecular, Cellular, and Integrative Physiology Interdepartmental Graduate Program, University of California, Los Angeles, Los Angeles, CA, USA

Nguyen T. Phi

3. Department of Neurobiology, Stanford University School of Medicine, Stanford University, Stanford, CA, USA

Jesse Isaacman-Beck

4. Department of Neurobiology, David Geffen School of Medicine at UCLA, University of California, Los Angeles, Los Angeles, CA, USA

Jun Reichl, Harpreet Randhawa & Orkun Akin

## Contributions

B.T.B.: conceptualization, methodology, analysis, investigation and writing.  
N.T.P.: methodology, investigation (confocal microscopy) and writing (review and editing). J.I.-B.: methodology (SPARC), investigation and writing (review and editing). J.R.: methodology (assistance with TARGET system experiments, lifespan and eclosion analysis) and writing (review and editing). H.R.: investigation (dissections and assistance with image analysis) and writing (review and editing). O.A.: conceptualization, methodology, analysis, investigation, writing, project administration and funding acquisition.

## Corresponding author

Correspondence to [Orkun Akin](#).

## Ethics declarations

## Competing interests

The authors declare no competing interests.

# Peer review

## Peer review information

*Nature* thanks Gerald Rubin and the other, anonymous reviewers for their contribution to the peer review of this work.

## Additional information

**Publisher's note** Springer Nature remains neutral with regard to jurisdictional claims in published maps and institutional affiliations.

## Extended data figures and tables

### Extended Data Fig. 1 *Trpγ* is necessary for PSINA.

- a.** Raw values binned by hour for active phase signal amplitude, sweeps/cycle, cycles/hour, and cycle duration for control (black, n=19) and *trpγ* null (orange, n=31) pupae. Shaded areas, SD. **b.** Active phase average amplitude (left) and sweeps/cycle (right) binned by hour and normalized to control activity during the turbulent stage, between 65 and 80 hAPF, for control (black, n=19), *trpγ* null (orange, n=31), and *trpγ* null with Trpγ-D expressed in Trpγ+ cells (cyan, n=4) pupae. Shaded areas, SD. **c.** Cycle duration (left) and cycles/hour (right) binned by hour and normalized to control activity between 55 and 65 hAPF. Shaded areas, SD. Genotypes color-matched to B. **d.** Representative traces of activity in control (black, n=19), *trpγ/Trpγ<sup>G4</sup>* (orange, n=5), *trpγ/Trpγ<sup>DropIn-TG4</sup>* (gray, n=5), *trpγ/Df(2L)1102* (magenta, n=7), and *trpγ/Df(2L)1109* pupae (green, n=7). **e.** Average amplitude (left) and sweeps/cycle (right) binned by hour and normalized to control activity between 55 and 65 hAPF. Shaded areas, SD. Genotypes color-matched to D. **f.** Active phase average amplitude (left) and sweeps/cycle (right) binned by hour and normalized to control activity during the periodic stage, between 55 and 65 hAPF, for control (black, n=10), *trpγ* null (orange, n=9), *trp* null (blue, n=10), and *trp* null + *trpγ* null (green, n=10). Shaded areas, SD. **g.** Active phase average amplitude (left)

and sweeps/cycle (right) binned by hour and normalized to control activity during the periodic stage, between 55 and 65 hAPF, for control (black, n=10), *trpy* null (orange, n=10), *trpL* null (blue, n=10), and *trpL* null+ *trpy* null (green, n=10). Shaded areas, SD.

### Extended Data Fig. 2 PSINA rescue in *trpy* null background.

- a.** Schematic of *Trpy* locus indicating locations of exons (orange rectangles), untranslated regions (gray rectangles), and introns (black lines between exons or untranslated regions) for each isoform. Scale bar, 500 bp.
- b.** Representative traces of activity in: Trpy-D expression with *Trpy*<sup>G4</sup> (blue, n=8), Trpy-D expression with *Trpy*<sup>DropIn-TG4</sup> (magenta, n=7), Trpy-AB expression with *Trpy*<sup>G4</sup> (green, n=9), Trpy-AB and Trpy-D expression with *Trpy*<sup>G4</sup> (red, n=10), double Trpy-D expression with *Trpy*<sup>G4</sup> (cyan, n=4), control (black, n=19), and *trpy* mutant (orange, n=31) pupae.
- c.** Active phase average amplitude (left) and sweeps/cycle (right) binned by hour and normalized to control activity between 55 and 65 hAPF. All plots contain data for control (black) and *trpy* (orange). Shaded areas, SD. Genotypes color-matched to B.
- d.** Expression control of UAS-Trpy-D with TARGET (i.e. GAL80ts). In the ‘all-on’ condition, flies are reared at 29°C. In the ‘all-off’ condition, flies are reared at 18°C.
- e, g.** Representative traces of activity in control pupae (black, n=3), *trpy* null pupae (orange, n=3), and (E) all-off pupae (blue, n=3) or (G) all-on pupae (red, n=3).
- f, h.** Active phase average amplitude (left) and sweeps/cycle (right) binned by hour and normalized to control activity between 55 and 65 hAPF. Shaded areas, SD. Genotypes color-matched to E and G.

### Extended Data Fig. 3 Synapse formation in the visual system depends on PSINA.

- a.** Table comparing control synapse counts in cells with sparse synaptic density across EM and light microscopy studies. Values are mean synapse count ± SD, with sample size in parentheses.
- b–g.** *Left:* representative micrographs of R8 (B), L1 (C), L4 (D), L5 (E), Dm9 (F), and Tm9 (G) neurons in control (left set) and *trpy* (right set) animals with cell membranes (myr::tdTOM, magenta in merged) and presynaptic sites (BRP-V5, cyan in

merged) labeled. *Right*: Brp puncta counts by layer in heterozygous control (black, n=18-61 per cell type) and *trpy* (orange, n=26-65 per cell type) animals. Points indicate individual cells. Box-and-whiskers mark 5<sup>th</sup>, 25<sup>th</sup>, 50<sup>th</sup>, 75<sup>th</sup>, and 95<sup>th</sup> percentiles. \*, p<0.05; \*\*, p<0.01; \*\*\*, p<0.001 by Welch's t-test following Shapiro-Wilk test. **h**. Brp puncta counts in *Trpy* heterozygotes (black, n=18 for Dm9, n=30 for Tm9), *trpy* nulls (orange, n=24 for Dm9, n=30 for Tm9), or *trpy* nulls with Trpy-D expressed in Trpy+ cells (cyan, n=24 for Dm9, n=30 for Tm9). Boxplots as in B-G. \*, p<0.05; \*\*, p<0.01; \*\*\*, p<0.001 by Tukey's post-hoc test following ANOVA for multiple groups. **i**. Brp puncta counts in control (black, n = 24) or *trpy* null (orange, n = 30) L5 clones generated by MARCM. Boxplots as in B-G. \*, p<0.05; \*\*, p<0.01; \*\*\*, p<0.001 by Welch's t-test following Shapiro-Wilk test. **j**. Average Brp puncta through development in control (black, n=64-88 per timepoint) or animals with PSINA blocked with pan-neuronally expressed TNT (magenta, n=35-68 per timepoint). Presynaptic sites assessed at 60, 72, and 84 hAPF. Error bars, SD.

## Extended Data Fig. 4 *TrpyG4* drives expression in a dynamic neuronal population during development.

**a.** MIPs of half-brain confocal stacks from different times during pupal development and early adult life. Nuclei of mCherry-NLS expressing Trpy+ neurons shown (cyan); reference marker is Ncad (magenta). Average, SD, and number of samples for each time point are printed top-right of panels; these values are plotted in Fig. 4a. Dashed yellow lines mark the median plane. CB, central brain. OL, optic lobe. Scale bar, 100μm. **b.** *Top*: 13μm-thick MIP of a 72 hAPF brain stained for neuronal nuclei (anti-Elav, yellow), Trpy+ nuclei (mCherry-NLS, cyan), and a reference marker (Ncad, magenta). Image derived from three stitched confocal stacks. Scale bar, 100μm. *Bottom*: Expanded views of two regions-of-interest (ROIs) boxed in top panel. Columns are neuronal, Trpy+, and merged channels, left to right. All Trpy+ nuclei fully captured in the MIP (red asterisks) co-localize with the neuronal stain. Scale bar, 20μm. **c.** *Top*: 13μm-thick MIP of a 72 hAPF brain stained for glial nuclei (anti-Repo, yellow), Trpy+ nuclei (mCherry-NLS, cyan), and a reference marker (Ncad, magenta). Image derived from three stitched confocal stacks. Scale bar, 100μm. *Bottom-left*:

Histogram of average voxel intensities of segmented Repo+ and Trp $\gamma$ + nuclei measured in the anti-Repo channel of the top image. n=5055 (Repo+), 1464 (Trp $\gamma$ +); half-brain complements analyzed. Inset shows where 9/1464 Trp $\gamma$ + cell intensities overlap with the dimmest Repo+ glia. *Bottom-right:* Histogram of minimum pairwise distance between centroids of 1464 segmented Trp $\gamma$ + and Repo+ nuclei. Inset shows all pairs of Trp $\gamma$ + and Repo+ nuclei are at least 1 $\mu$ m apart. **d.** Representative traces of activity in control pupae (black), pan-neuronal control knockdown pupae (gray, n=2), pan-neuronal *Trp $\gamma$*  knockdown (magenta, n=3; green, n=3), pan-glial *Trp $\gamma$*  knockdown (red, n=2; blue, n=2) in heterozygous *Trp $\gamma$*  background. **e.** Active phase average amplitude (left) and sweeps/cycle (right) binned by hour and normalized to control activity between 55 and 65 hAPF. Shaded areas, SD. Genotypes color-matched to D.

### Extended Data Fig. 5 Trp $\gamma$ + neurons are a diverse population.

**a–i.** *Top:* 13 $\mu$ m-thick (A-C) or full (D-I) MIPs of 72 hAPF brains stained for neuronal class marker (yellow), Trp $\gamma$ + nuclei (mCherry-NLS or GFP-NLS, cyan), and a reference marker (Ncad, magenta). Images (A-C, E-H) derived from three stitched confocal stacks. Scale bar, 100 $\mu$ m. *Bottom:* Expanded view(s) of ROI(s) boxed in top panel. Columns (D, rows) are class marker, Trp $\gamma$ +, and merged channels, left to right (D, top to bottom). Marked Trp $\gamma$ + nuclei (red asterisks) co-localize with the neuronal class marker. ROI 2 in (G) shows transient PDF-TRI cells (38). Scale bar, 20 $\mu$ m.

### Extended Data Fig. 6 SPARC3-Out-GAL80 reveals morphologies of individual Trp $\gamma$ + neurons.

**a.** Schematic of the SPARC3-Out-GAL80 cassette. PhiC31 recombines one of two competing *attP* target sequences with one *attB* target sequence. Rxn 1 leads to loss of the GAL80 ORF, disinhibiting GAL4-driven effector expression. Rxn 2 preserves Tubulin promoter driven GAL80 expression, maintaining GAL4 inhibition. Three progressively truncated variants for the first *attP* sequence were designed (25) to bias the recombination in favor of Rxn 2, resulting in frequent (Dense), sporadic (Intermediate), or rare (Sparse) loss of GAL80 and disinhibition of GAL4>UAS expression. **b.** Map of pHD-3xP3-DsRed- $\Delta$ *attP* (a CRISPR-HDR-donor precursor)

showing multiple cloning sites for homology arm insertion (right). **c**. Map of pHD-3xP3-DsRed- $\Delta attP$ -CRISPR-donor (example includes homology arms targeting the *Su(Hw)AttP5* region of the *Drosophila* genome). **d**. Assembled SPARC3-Out-GAL80 cassette; see Materials and Methods for details. MCS, multiple cloning site. gRNA, guide RNA. HDVR, hepatitis delta virus ribozyme sequence. **e, g**. Single Trp $\gamma^+$  neuron (orange, manually segmented) in the context of others (cyan) labeled using SPARC. Neurons expressing myr::SM-V5. Reference marker (magenta), Ncad. Image MIP of stitched confocal stacks of 72 hAPF brain. Scale bar, 100 $\mu$ m. **f**. Trp $\gamma^+$  visual processing neurons identified in 72 hAPF brains using SPARC. We observed a given neuron up to three times in 30 sparsely labeled brains.

### Extended Data Fig. 7 Additional characterization of Trp $\gamma^+$ neuron activity.

**a**. Representative autocorrelograms from pan-neuronal GCaMP6s in control (empty-GAL4, black), panN-GAL4>Kir2.1 (blue), and *Trp $\gamma^{G4}$* >Kir2.1 (orange) pupae. **b, c**. Representative micrographs (B) and traces (C) from 2PM imaging of pan-neuronal GCaMP6s in control (empty-GAL4, black), panN-GAL4>Kir2.1 (blue), and *Trp $\gamma^{G4}$* >Kir2.1 (orange) pupae. Scale bar, 40 $\mu$ m. **d**. *Inset*: expanded view showing fewer sweeps in panN-GAL4 and *Trp $\gamma^{G4}$*  conditions. **e**. Representative traces for Trp $\gamma^+$  neurons expressing GCaMP6s (cyan, n=10) and pan-neuronal expression of GCaMP6s (black, n=10) by wide-field imaging with a ROI encompassing the head. **f**. Active phase average amplitude for Trp $\gamma^+$  neurons expressing GCaMP6s (cyan) binned by hour and normalized to pan-neuronal expression of GCaMP6s (black). Shaded areas, SD. **g, h**. AIP of pupae expressing pan-neuronal GCaMP6s (g). ROIs indicate regions used to calculate traces (h) from optic lobes. Scale bar, 200 $\mu$ m. **i**. 0-lag correlation between traces in each optic lobe in control (empty-GAL4, black, n=4), and *Trp $\gamma^{G4}$* >Kir2.1 (orange, n=4) pupae. Round markers are values from individual time series, bars are averages for each genotype. **j**. Correlogram between traces in each optic lobe in *Trp $\gamma^{G4}$* >Kir2.1 pupa. **k**. Cell-type-specific Brp puncta counts in control (empty-GAL4>Kir2.1 pupae, black, n=35 per cell type), PanN-GAL4>Kir2.1 pupae (cyan, n=40 for Dm9, n=25 for Tm9) and in *Trp $\gamma^{G4}$* >Kir2.1 pupae (orange, n=40 cells for Dm9, n=35 cells for Tm9).

## Extended Data Fig. 8 Silencing Trpy<sup>+</sup> neurons in the central brain, but not the optic lobes, attenuates PSINA.

**a.** Schematic of spatially-targeted Kir2.1 expression. Both experimental genotypes carry two variants of tubP-GAL80: GAL80ts and one of two FLP-responsive conditional alleles. In the optic lobes, ey-FLP either turns on GAL80 expression by removing the interruption cassette ('-STOP-', top) or turns it off by locally excising the FRT-flanked ORF (bottom). Animals are reared at 18°C and shifted 29°C at 40 hAPF to unmask these differential GAL80 expression domains (blue) just prior to PSINA onset; GAL4-driven Kir2.1 expression is disinhibited in the complementary domains (yellow). CB, central brain. OL, optic lobe. **b, c.** MIPs of half-brains (top) or optic lobes (bottom) at 60 hAPF in which *Trpy*<sup>G4</sup> is driving Kir2.1 expression in the CB (B) or the OL (C). The OL condition also includes expression in the antennal lobes and a small number of CB neurons. Kir2.1 expression domain detected by staining against 3xHA tagged co-cistronic tdTOM. Scale bar, 100μm. **d, g.** AIP of ~60 hAPF pupa expressing GCaMP6s pan-neuronally. CB (D) and OL (G) ROIs used for measuring PSINA outlined (cyan). Scale bar, 200μm. **e, h.** PSINA traces from CB (E) and OL (H) for control (no Kir2.1, black, n=5), *Trpy*<sup>G4</sup>(CB)>Kir2.1 (red, n=3), and *Trpy*<sup>G4</sup>(OL)>Kir2.1 (blue, n=3) genotypes. **f, i.** Average amplitude measured in CB (F) and OL (G) normalized to corresponding control activity. Shaded areas, SD. Genotypes color-matched to E.

## Extended Data Fig. 9 Trpy<sup>+</sup> neurons are necessary for PSINA.

**a.** Temporal expression control with TARGET; animals shifted from 18°C to 29°C at 40 hAPF. **b.** PSINA traces from pan-neuronal GCaMP6s in control (empty-GAL4, black, n=3), panN-GAL4>hid, rpr (blue, n=3), and *Trpy*<sup>G4</sup>>hid, rpr (orange, n=3) pupae. **c.** Average amplitude normalized to control activity between 55 and 75 hAPF. Shaded areas, SD. Genotypes color-matched to B. **d.** PSINA traces from pan-neuronal GCaMP6s in control (empty-GAL4, black, n=7), panN-GAL4>TNT (blue, n=7), and *Trpy*<sup>G4</sup>>TNT (orange, n=8) pupae. **e.** Average amplitude normalized to control activity between 55 and 75 hAPF. Shaded areas, SD. Genotypes color-matched to D. **f.** Representative traces of pupae expressing pan-

neuronal GCaMP6s, with TNT expressed in expression domains of the indicated neuronal class. n=4 tested for each genotype.

### Extended Data Fig. 10 Activation of Trp $\gamma$ + neurons increases brain-wide activity frequency.

**a, b.** *Left:* PSINA traces from pan-neuronal GCaMP6s in control (empty-GAL4, black, n=3), panN-GAL4>TrpA1 (blue, n=3), and *Trp $\gamma$ <sup>G4</sup>*>TrpA1 (orange, n=3) pupae at 18°C (A) or 29°C (B). *Right:* representative autocorrelograms calculated from the first trace shown for each genotype. *Inset (B):* expanded view of boxed region. Scale bar, 2min. **c.** Activity from pan-neuronal GCaMP6s in control (empty-GAL4, black, n=6), panN-GAL4>TRpA1 (blue, n=6), VGlut-GAL4>TrpA1 (red, n=6), Gad1-GAL4 (green, n=5), *Trp $\gamma$ <sup>G4</sup>*>TrpA1 (orange, n=6) pupae at 60 hAPF. Pupae reared at 18°C and shifted to 29°C. **d.** MIPs of 60 hAPF brains stained for a nuclear marker (Cherry-NLS, cyan) driven by *Gad1*- or *Vglut-GAL4*, and a reference marker (Ncad, magenta). Images derived from three stitched confocal stacks. Scale bar, 100 $\mu$ m. **e.** Conceptual circuit organizations for coordinating and propagating PSINA. Metronomes indicate CPGs. Colored arrows indicate Trp $\gamma$ + and other relay neurons.

## Supplementary information

### Supplementary Materials

This file contains additional references; supplementary discussion and captions for Supplementary Videos 1–4

### Reporting Summary

### Supplementary Table 1

Experimental genotypes

### Supplementary Table 2

Primers used to amplify the Trp $\gamma$  coding sequence

### **Supplementary Table 3**

Plasmids used in the generation of SPARC3-Out-GAL80 flies

### **Supplementary Table 4**

gRNA sequences used in pCFD5-U6-3-t-Su(Hw)attP5

### **Supplementary Video 1**

See Supplementary Materials for video caption

### **Supplementary Video 2**

See Supplementary Materials for video caption

### **Supplementary Video 3**

See Supplementary Materials for video caption

### **Supplementary Video 4**

See Supplementary Materials for video caption

## **Rights and permissions**

### **Reprints and Permissions**

## **About this article**

### **Cite this article**

Bajar, B.T., Phi, N.T., Isaacman-Beck, J. *et al.* A discrete neuronal population coordinates brain-wide developmental activity. *Nature* **602**, 639–646 (2022). <https://doi.org/10.1038/s41586-022-04406-9>

- Received: 27 February 2021
- Accepted: 05 January 2022
- Published: 09 February 2022
- Issue Date: 24 February 2022
- DOI: <https://doi.org/10.1038/s41586-022-04406-9>

## Share this article

Anyone you share the following link with will be able to read this content:

[Get shareable link](#)

Sorry, a shareable link is not currently available for this article.

[Copy to clipboard](#)

Provided by the Springer Nature SharedIt content-sharing initiative

## Further reading

- [Coordinating early activity](#)

- Katherine Whalley

*Nature Reviews Neuroscience* (2022)

## [Coordinating early activity](#)

- Katherine Whalley

# Research Highlight 23 Feb 2022

---

This article was downloaded by **calibre** from <https://www.nature.com/articles/s41586-022-04406-9>

| [Section menu](#) | [Main menu](#) |

- Article
- [Published: 14 February 2022](#)

# A gut-derived metabolite alters brain activity and anxiety behaviour in mice

- [Brittany D. Needham](#) [ORCID: orcid.org/0000-0002-0280-1886](#)<sup>1</sup>,
- [Masanori Funabashi](#)<sup>2,3</sup>,
- [Mark D. Adame](#)<sup>1</sup>,
- [Zhuo Wang](#)<sup>4</sup>,
- [Joseph C. Boktor](#)<sup>1</sup>,
- [Jillian Haney](#)<sup>5</sup>,
- [Wei-Li Wu](#)<sup>1,6,7</sup>,
- [Claire Rabut](#)<sup>8</sup>,
- [Mark S. Ladinsky](#) [ORCID: orcid.org/0000-0002-1036-3513](#)<sup>1</sup>,
- [Son-Jong Hwang](#) [ORCID: orcid.org/0000-0002-3210-466X](#)<sup>8</sup>,
- [Yumei Guo](#)<sup>4</sup>,
- [Qiyun Zhu](#)<sup>9,10</sup>,
- [Jessica A. Griffiths](#)<sup>1</sup>,
- [Rob Knight](#) [ORCID: orcid.org/0000-0002-0975-9019](#)<sup>9,11,12</sup>,
- [Pamela J. Bjorkman](#) [ORCID: orcid.org/0000-0002-2277-3990](#)<sup>1</sup>,
- [Mikhail G. Shapiro](#) [ORCID: orcid.org/0000-0002-0291-4215](#)<sup>8</sup>,
- [Daniel H. Geschwind](#) [ORCID: orcid.org/0000-0003-2896-3450](#)<sup>5</sup>,
- [Daniel P. Holschneider](#)<sup>4,13,14</sup>,
- [Michael A. Fischbach](#) [ORCID: orcid.org/0000-0003-3079-8247](#)<sup>2</sup> &
- [Sarkis K. Mazmanian](#) [ORCID: orcid.org/0000-0003-2713-1513](#)<sup>1</sup>

[Nature](#) volume 602, pages 647–653 (2022)

- 16k Accesses
- 1 Citations
- 291 Altmetric
- [Metrics details](#)

## Subjects

- [Bacterial genes](#)
- [Bacterial host response](#)
- [Myelin biology and repair](#)

## Abstract

Integration of sensory and molecular inputs from the environment shapes animal behaviour. A major site of exposure to environmental molecules is the gastrointestinal tract, in which dietary components are chemically transformed by the microbiota<sup>1</sup> and gut-derived metabolites are disseminated to all organs, including the brain<sup>2</sup>. In mice, the gut microbiota impacts behaviour<sup>3</sup>, modulates neurotransmitter production in the gut and brain<sup>4,5</sup>, and influences brain development and myelination patterns<sup>6,7</sup>. The mechanisms that mediate the gut–brain interactions remain poorly defined, although they broadly involve humoral or neuronal connections. We previously reported that the levels of the microbial metabolite 4-ethylphenyl sulfate (4EPS) were increased in a mouse model of atypical neurodevelopment<sup>8</sup>. Here we identified biosynthetic genes from the gut microbiome that mediate the conversion of dietary tyrosine to 4-ethylphenol (4EP), and bioengineered gut bacteria to selectively produce 4EPS in mice. 4EPS entered the brain and was associated with changes in region-specific activity and functional connectivity. Gene expression signatures revealed altered oligodendrocyte function in the brain, and 4EPS impaired oligodendrocyte maturation in mice and decreased oligodendrocyte–neuron interactions in ex vivo brain cultures. Mice colonized with 4EP-producing bacteria exhibited reduced myelination of neuronal axons. Altered

myelination dynamics in the brain have been associated with behavioural outcomes<sup>7,9,10,11,12,13,14</sup>. Accordingly, we observed that mice exposed to 4EPS displayed anxiety-like behaviours, and pharmacological treatments that promote oligodendrocyte differentiation prevented the behavioural effects of 4EPS. These findings reveal that a gut-derived molecule influences complex behaviours in mice through effects on oligodendrocyte function and myelin patterning in the brain.

This is a preview of subscription content

## Access options

Subscribe to Nature+

Get immediate online access to the entire Nature family of 50+ journals

\$29.99

monthly

[Subscribe](#)

Subscribe to Journal

Get full journal access for 1 year

\$199.00

only \$3.90 per issue

[Subscribe](#)

All prices are NET prices.

VAT will be added later in the checkout.

Tax calculation will be finalised during checkout.

Buy article

Get time limited or full article access on ReadCube.

\$32.00

[Buy](#)

All prices are NET prices.

### **Additional access options:**

- [Log in](#)
- [Learn about institutional subscriptions](#)

**Fig. 1: Discovery of a 4EP biosynthetic pathway, strain engineering of gut bacteria and colonization of mice to produce 4EPS.**

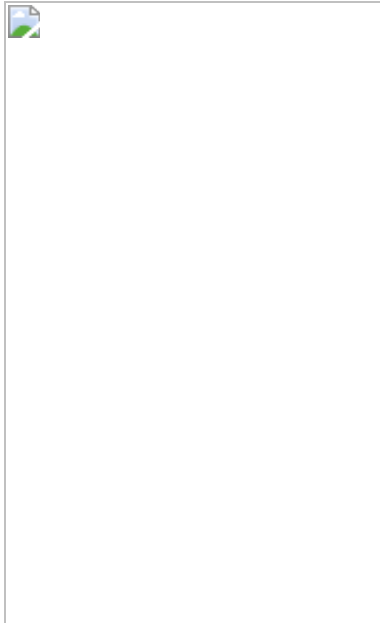


**Fig. 2: Functional brain connectivity and regional activation is altered in response to colonization by 4EP-producing bacteria.**

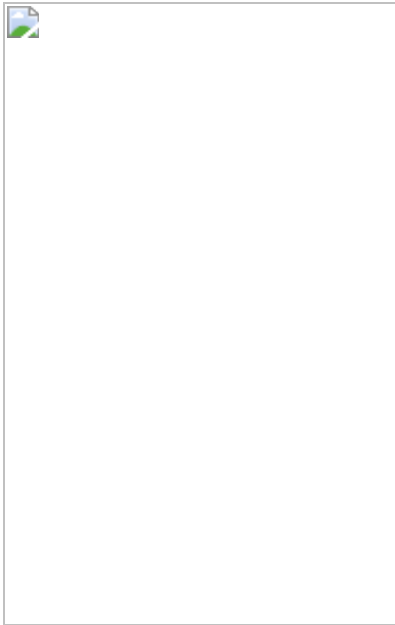


**Fig. 3: Reduced oligodendrocyte maturation in 4EP<sup>+</sup> mice.**

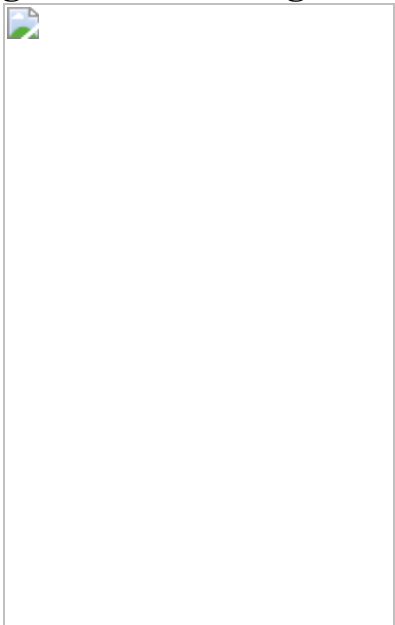
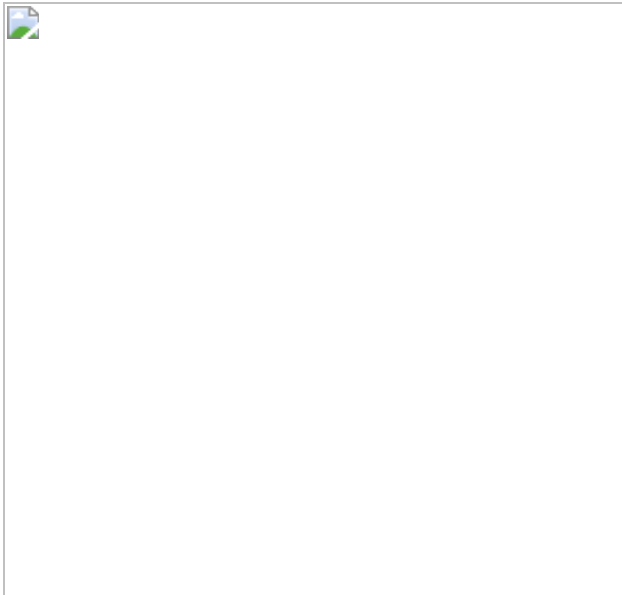


**Fig. 4: 4EP(S) alters myelination and anxiety-like behaviour.**



## Data availability

All data analysed for this study are included in this published Article and its [Supplementary Information](#). Additional 2DG data are available online ([https://gin.g-node.org/bneedham/Needham\\_Nature\\_2022](https://gin.g-node.org/bneedham/Needham_Nature_2022)). The WoL database annotation files are publicly available at GitHub (<https://biocore.github.io/wol/download>). The Greengenes database is publicly available online (<https://greengenes.secondgenome.com/>). [Source data](#) are provided with this paper.

## Code availability

Custom scripts used in the fUSi analysis are available at GitHub ([https://github.com/brittanyneedham/Needham\\_Nature2022](https://github.com/brittanyneedham/Needham_Nature2022)).

## References

1. Sharon, G. et al. Specialized metabolites from the microbiome in health and disease. *Cell Metab.* **20**, 719–730 (2014).
2. Swann, J. R. et al. Application of  $^1\text{H}$  NMR spectroscopy to the metabolic phenotyping of rodent brain extracts: a metabonomic study

of gut microbial influence on host brain metabolism. *J. Pharm. Biomed. Anal.* **143**, 141–146 (2017).

3. Vuong, H. E., Yano, J. M., Fung, T. C. & Hsiao, E. Y. The microbiome and host behavior. *Annu. Rev. Neurosci.* **40**, 21–49 (2017).
4. Needham, B. D., Kaddurah-Daouk, R. & Mazmanian, S. K. Gut microbial molecules in behavioural and neurodegenerative conditions. *Nat. Rev. Neurosci.* **21**, 717–731 (2020).
5. Huang, F. & Wu, X. Brain neurotransmitter modulation by gut microbiota in anxiety and depression. *Front. Cell Dev. Biol.* **9**, 649103 (2021).
6. Gacias, M. et al. Microbiota-driven transcriptional changes in prefrontal cortex override genetic differences in social behavior. *eLife* **5**, e13442 (2016).
7. Hoban, A. E. et al. Regulation of prefrontal cortex myelination by the microbiota. *Transl. Psychiatry* **6**, e774 (2016).
8. Hsiao, E. Y. et al. Microbiota modulate behavioral and physiological abnormalities associated with neurodevelopmental disorders. *Cell* **155**, 1451–1463 (2013).
9. Berer, K. et al. Commensal microbiota and myelin autoantigen cooperate to trigger autoimmune demyelination. *Nature* **479**, 538–541 (2011).
10. Pan, S., Mayoral, S. R., Choi, H. S., Chan, J. R. & Kheirbek, M. A. Preservation of a remote fear memory requires new myelin formation. *Nat. Neurosci.* **23**, 487–499 (2020).
11. Maher, K. J. et al. Absence of claudin 11 in CNS myelin perturbs behavior and neurotransmitter levels in mice. *Sci. Rep.* **8**, 3798 (2018).
12. Bonnefil, V. et al. Region-specific myelin differences define behavioral consequences of chronic social defeat stress in mice. *eLife*

**8**, e40855 (2019).

13. Galvez-Contreras, A. Y., Zarate-Lopez, D., Torres-Chavez, A. L. & Gonzalez-Perez, O. Role of oligodendrocytes and myelin in the pathophysiology of autism spectrum disorder. *Brain Sci.* **10**, 951 (2020).
14. Cassoli, J. S. et al. Disturbed macro-connectivity in schizophrenia linked to oligodendrocyte dysfunction: from structural findings to molecules. *npj Schizophrenia* **1**, 15034 (2015).
15. Needham, B. D. et al. Plasma and fecal metabolite profiles in autism spectrum disorder. *Biol. Psychiatry* **89**, 451–462 (2020).
16. Gamage, N. et al. Human sulfotransferases and their role in chemical metabolism. *Toxicol. Sci.* **90**, 5–22 (2006).
17. Chamkha, M., Garcia, J. L. & Labat, M. Metabolism of cinnamic acids by some Clostridiales and emendation of the descriptions of *Clostridium aerotolerans*, *Clostridium celerecrescens* and *Clostridium xylanolyticum*. *Int. J. Syst. Evol. Microbiol.* **51**, 2105–2111 (2001).
18. Santamaría, L., Reverón, I., Felipe, F. L. D., Rivas, B. D. L. & Muñoz, R. Ethylphenol Formation by *Lactobacillus plantarum*: identification of the enzyme involved in the reduction of vinylphenols. *Appl. Environ. Microbiol.* **84**, e01064-18 (2018).
19. Agency for Toxic Substances and Disease Registry (ATSDR). Toxicological Profile for Cresols (CDC, 2008);  
<https://www.cdc.gov/TSP/ToxProfiles/ToxProfiles.aspx?id=946&tid=196>
20. Penzo, M. A. et al. The paraventricular thalamus controls a central amygdala fear circuit. *Nature* **519**, 455–459 (2015).
21. Ahrens, S. et al. A central extended amygdala circuit that modulates anxiety. *J. Neurosci.* **38**, 5567–5583 (2018).

22. Duval, E. R., Javanbakht, A. & Liberzon, I. Neural circuits in anxiety and stress disorders: a focused review. *Ther. Clin. Risk Manag.* **11**, 115–126 (2015).
23. Robinson, O. J., Pike, A. C., Cornwell, B. & Grillon, C. The translational neural circuitry of anxiety. *J. Neurol. Neurosurg. Psychiatry* **90**, 1353–1360 (2019).
24. Barson, J. R., Mack, N. R. & Gao, W.-J. The paraventricular nucleus of the thalamus is an important node in the emotional processing network. *Front. Behav. Neurosci.* **14**, 598469 (2020).
25. Kirouac, G. J. The paraventricular nucleus of the thalamus as an integrating and relay node in the brain anxiety network. *Front. Behav. Neurosci.* **15**, 627633 (2021).
26. Park, H.-C. & Appel, B. Delta-notch signaling regulates oligodendrocyte specification. *Development* **130**, 3747–3755 (2003).
27. Wang, S. et al. Notch receptor activation inhibits oligodendrocyte differentiation. *Neuron* **21**, 63–75 (1998).
28. Williamson, J. M. & Lyons, D. A. Myelin Dynamics Throughout Life: An Ever-Changing Landscape? *Front. Cell. Neurosci.* **12**, 424 (2018).
29. Holschneider, D. P., Wang, Z. & Pang, R. D. Functional connectivity-based parcellation and connectome of cortical midline structures in the mouse: a perfusion autoradiography study. *Front. Neuroinform.* **8**, 61 (2014).
30. Kaller, M. S., Lazari, A., Blanco-Duque, C., Sampaio-Baptista, C. & Johansen-Berg, H. Myelin plasticity and behaviour—connecting the dots. *Curr. Opin. Neurobiol.* **47**, 86–92 (2017).
31. Barak, B. et al. Neuronal deletion of Gtf2i, associated with Williams syndrome, causes behavioral and myelin alterations rescuable by a remyelinating drug. *Nat. Neurosci.* **22**, 700–708 (2019).

32. Xie, D. et al. Clemastine improves hypomyelination in rats with hypoxic–ischemic brain injury by reducing microglia-derived IL-1 $\beta$  via P38 signaling pathway. *J. Neuroinflammation* **17**, 57 (2020).
33. Kirouac, G. J. Placing the paraventricular nucleus of the thalamus within the brain circuits that control behavior. *Neurosci. Biobehav. Rev.* **56**, 315–329 (2015).
34. Sharon, G., Sampson, T. R., Geschwind, D. H. & Mazmanian, S. K. The central nervous system and the gut microbiome. *Cell* **167**, 915–932 (2016).
35. Tian, P., Wang, G., Zhao, J., Zhang, H. & Chen, W. Bifidobacterium with the role of 5-hydroxytryptophan synthesis regulation alleviates the symptom of depression and related microbiota dysbiosis. *J. Nutr. Biochem.* **66**, 43–51 (2019).
36. Koyama, H. et al. Effects of housing conditions on behaviors and biochemical parameters in juvenile cynomolgus monkeys (*Macaca fascicularis*). *Exp. Anim.* **68**, 195–211 (2019).
37. Tian, J.-S. et al. A GC-MS urinary quantitative metabolomics analysis in depressed patients treated with TCM formula of Xiaoyaosan. *J. Chromatogr. B Analyt. Technol. Biomed. Life Sci.* **1026**, 227–235 (2016).
38. Sankowski, B. et al. Higher cerebrospinal fluid to plasma ratio of *p*-cresol sulfate and indoxyl sulfate in patients with Parkinson’s disease. *Clin. Chim. Acta* **501**, 165–173 (2020).
39. Gabriele, S. et al. Urinary *p*-cresol is elevated in young French children with autism spectrum disorder: a replication study. *Biomarkers* **19**, 463–470 (2014).
40. Neul, J. L. et al. Metabolic signatures differentiate Rett syndrome from unaffected siblings. *Front. Integr. Neurosci.* **14**, 7 (2020).

41. Takesada, M., Miyamoto, E., Kakimoto, Y., Sano, I. & Kaneko, Z. Phenolic and indole amines in the urine of schizophrenics. *Nature* **207**, 1199–1200 (1965).
42. Sun, C.-Y. et al. *p*-Cresol sulfate caused behavior disorders and neurodegeneration in mice with unilateral nephrectomy involving oxidative stress and neuroinflammation. *Int. J. Mol. Sci.* **21**, 6687 (2020).
43. Franklin, K. & Paxinos, G. *The Mouse Brain in Stereotaxic Coordinates* (Elsevier Science, 2007).
44. Holdeman, L. V. & Moore, W. E. C. *Anaerobe Laboratory Manual* 4th edn (Virginia Polytechnic Institute and State University, 1977).
45. Martens, E. C., Chiang, H. C. & Gordon, J. I. Mucosal glycan foraging enhances fitness and transmission of a saccharolytic human gut bacterial symbiont. *Cell Host Microbe* **4**, 447–457 (2008).
46. Koropatkin, N. M., Martens, E. C., Gordon, J. I. & Smith, T. J. Starch catabolism by a prominent human gut symbiont is directed by the recognition of amylose helices. *Structure* **16**, 1105–1115 (2008).
47. Bolyen, E. et al. Reproducible, interactive, scalable and extensible microbiome data science using QIIME 2. *Nat. Biotechnol.* **37**, 852–857 (2019).
48. Callahan, B. J. et al. DADA2: high-resolution sample inference from Illumina amplicon data. *Nat. Methods* **13**, 581–583 (2016).
49. Banoglu, E. & King, R. S. Sulfation of indoxyl by human and rat aryl (phenol) sulfotransferases to form indoxyl sulfate. *Eur. J. Drug Metab. Pharmacokinet.* **27**, 135–140 (2002).
50. Teubner, W., Meinl, W., Florian, S., Kretzschmar, M. & Glatt, H. Identification and localization of soluble sulfotransferases in the human gastrointestinal tract. *Biochem. J.* **404**, 207–215 (2007).

51. Sharon, G. et al. Human gut microbiota from autism spectrum disorder promote behavioral symptoms in mice. *Cell* **177**, 1600–1618 (2019).
52. Iadecola, C. The neurovascular unit coming of age: a journey through neurovascular coupling in health and disease. *Neuron* **96**, 17–42 (2017).
53. Mace, E. et al. Functional ultrasound imaging of the brain: theory and basic principles. *IEEE Trans. Ultrason. Ferroelectr. Freq. Control* **60**, 492–506 (2013).
54. Tiran, E. et al. Transcranial functional ultrasound imaging in freely moving awake mice and anesthetized young rats without contrast agent. *Ultrasound Med. Biol.* **43**, 1679–1689 (2017).
55. Needham, B. D. et al. A gut-derived metabolite alters brain activity and anxiety behaviour in mice. GitHub  
[https://github.com/brittanyneedham/Needham\\_Nature2022](https://github.com/brittanyneedham/Needham_Nature2022) (2022).
56. Demené, C. et al. Spatiotemporal clutter filtering of ultrafast ultrasound data highly increases doppler and fultrasound sensitivity. *IEEE Trans. Med. Imaging* **34**, 2271–2285 (2015).
57. Osmanski, B.-F., Pezet, S., Ricobaraza, A., Lenkei, Z. & Tanter, M. Functional ultrasound imaging of intrinsic connectivity in the living rat brain with high spatiotemporal resolution. *Nat. Commun.* **5**, 5023 (2014).
58. Armstrong, R. A. When to use the Bonferroni correction. *Ophthalmic Physiol. Opt.* **34**, 502–508 (2014).
59. Holschneider, D. P., Guo, Y., Wang, Z., Vidal, M. & Scremin, O. U. Positive allosteric modulation of cholinergic receptors improves spatial learning after cortical contusion injury in mice. *J. Neurotrauma* **36**, 2233–2245 (2019).
60. Sokoloff, L. Localization of functional activity in the central nervous system by measurement of glucose utilization with radioactive

deoxyglucose. *J. Cereb. Blood Flow Metab.* **1**, 7–36 (1981).

61. Wang, Z., Pang, R. D., Hernandez, M., Ocampo, M. A. & Holschneider, D. P. Anxiolytic-like effect of pregabalin on unconditioned fear in the rat: an autoradiographic brain perfusion mapping and functional connectivity study. *Neuroimage* **59**, 4168–4188 (2012).
62. Dobin, A. et al. STAR: ultrafast universal RNA-seq aligner. *Bioinformatics* **29**, 15–21 (2013).
63. Patro, R., Duggal, G., Love, M. I., Irizarry, R. A. & Kingsford, C. Salmon provides fast and bias-aware quantification of transcript expression. *Nat. Methods* **14**, 417–419 (2017).
64. Xu, X., Wells, A. B., O'Brien, D. R., Nehorai, A. & Dougherty, J. D. Cell type-specific expression analysis to identify putative cellular mechanisms for neurogenetic disorders. *J. Neurosci.* **34**, 1420–1431 (2014).
65. Zhang, Y. et al. An RNA-sequencing transcriptome and splicing database of glia, neurons, and vascular cells of the cerebral cortex. *J. Neurosci.* **34**, 11929–11947 (2014).
66. Zambon, A. C. et al. GO-Elite: a flexible solution for pathway and ontology over-representation. *Bioinformatics* **28**, 2209–2210 (2012).
67. Tyszka, J. M., Readhead, C., Bearer, E. L., Pautler, R. G. & Jacobs, R. E. Statistical diffusion tensor histology reveals regional dysmyelination effects in the shiverer mouse mutant. *Neuroimage* **29**, 1058–1065 (2006).
68. Mastronarde, D. N. Automated electron microscope tomography using robust prediction of specimen movements. *J. Struct. Biol.* **152**, 36–51 (2005).
69. Yeh, F.-C. et al. Deterministic diffusion fiber tracking improved by quantitative anisotropy. *PLoS ONE* **8**, e80713 (2013).

70. Kremer, J. R., Mastronarde, D. N. & McIntosh, J. R. Computer visualization of three-dimensional image data using IMOD. *J. Struct. Biol.* **116**, 71–76 (1996).
71. Mastronarde, D. N. Correction for non-perpendicularity of beam and tilt axis in tomographic reconstructions with the IMOD package. *J. Microsc.* **230**, 212–217 (2008).
72. Carranza-Torres, I. E. et al. Organotypic culture of breast tumor explants as a multicellular system for the screening of natural compounds with antineoplastic potential. *BioMed Res. Int.* **2015**, 618021 (2015).
73. Leger, M. et al. Object recognition test in mice. *Nat. Protoc.* **8**, 2531–2537 (2013).
74. Sampson, T. R. et al. Gut microbiota regulate motor deficits and neuroinflammation in a model of Parkinson’s disease. *Cell* **167**, 1469–1480 (2016).
75. Komada, M., Takao, K. & Miyakawa, T. Elevated plus maze for mice. *J. Vis. Exp.* <https://doi.org/10.3791/1088> (2008).
76. Takao, K. & Miyakawa, T. Light/dark transition test for mice. *J. Vis. Exp.* <https://doi.org/10.3791/104> (2006).
77. Miedel, C. J., Patton, J. M., Miedel, A. N., Miedel, E. S. & Levenson, J. M. Assessment of spontaneous alternation, novel object recognition and limb clasping in transgenic mouse models of amyloid- $\beta$  and Tau neuropathology. *J. Vis. Exp.* **28**, 55523 (2017).
78. Shih, H.-T. & Mok, H.-K. ETHOM: event-recording computer software for the study of animal behavior. *Acta Zool. Taiwanica* **11**, 47–61 (2000).

## Acknowledgements

We thank the members of the Mazmanian laboratory for evaluating the manuscript; S. Reisman and L. Chapman (Caltech) for synthesizing 4EPS; the staff at the Caltech Kavli Nanoscience Institute for help with maintaining the TF30 electron microscope, and the Gordon and Betty Moore and Beckman Foundations for gifts to Caltech to support electron microscopy. Funding: this work was supported by funds from the Center for Environmental Microbial Interactions to B.D.N., National Science Foundation MRI grant 1920364 for Bruker console upgrading, the Human Frontier Science Program (grant no. LT000217/2020-C) to C.R., the National Institutes of Health (NIH) (2 P50 GM082545-08) to P.J.B., the Ministry of Science and Technology in Taiwan (MOST107-2320-B-006-072-MY3; MOST108-2321-B-006-025-MY2) to W.-L.W., and the Heritage Medical Research Institute, L. and B. Fetter, and the NIH (MH100556 and AG063744) to S.K.M.

## Author information

### Affiliations

1. Division of Biology and Biological Engineering, California Institute of Technology, Pasadena, CA, USA

Brittany D. Needham, Mark D. Adame, Joseph C. Boktor, Wei-Li Wu, Mark S. Ladinsky, Jessica A. Griffiths, Pamela J. Bjorkman & Sarkis K. Mazmanian

2. Department of Bioengineering and ChEM-H, Stanford University, Stanford, CA, USA

Masanori Funabashi & Michael A. Fischbach

3. Translational Research Department, Daiichi Sankyo RD Novare Co Ltd, Tokyo, Japan

Masanori Funabashi

4. Department of Psychiatry and the Behavioral Sciences, Keck School of Medicine, University of Southern California, Los Angeles, CA, USA

Zhuo Wang, Yumei Guo & Daniel P. Holschneider

5. Department of Neurology, University of California Los Angeles, Los Angeles, CA, USA

Jillian Haney & Daniel H. Geschwind

6. Department of Physiology, College of Medicine, National Cheng Kung University, Tainan, Taiwan

Wei-Li Wu

7. Institute of Basic Medical Sciences, College of Medicine, National Cheng Kung University, Tainan, Taiwan

Wei-Li Wu

8. Division of Chemistry and Chemical Engineering, California Institute of Technology, Pasadena, CA, USA

Claire Rabut, Son-Jong Hwang & Mikhail G. Shapiro

9. Department of Pediatrics, University of California San Diego, La Jolla, CA, USA

Qiyun Zhu & Rob Knight

10. School of Life Sciences, Arizona State University, Tempe, AZ, USA

Qiyun Zhu

11. Department of Computer Science and Engineering, University of California San Diego, La Jolla, CA, USA

Rob Knight

12. Center for Microbiome Innovation, University of California San Diego, La Jolla, CA, USA

Rob Knight

13. Department of Neurology, Keck School of Medicine, University of Southern California, Los Angeles, CA, USA

Daniel P. Holschneider

14. Viterbi School of Engineering, Department of Biomedical Engineering, University of Southern California, Los Angeles, CA, USA

Daniel P. Holschneider

## Contributions

Conceptualization: B.D.N. and S.K.M. Methodology: B.D.N., M.F., M.D.A., Z.W., W.-L.W., J.H., M.S.L., J.A.G., C.R., S.-J.H. and D.P.H. Formal analysis: B.D.N., M.D.A., Z.W. and J.H. Investigation: B.D.N., M.F., M.D.A., Z.W., W.-L.W., J.C.B., C.R., J.H., S.-J.H., Q.Z., M.S.L. and Y.G. Biochemical pathway investigation and strain engineering: M.F. and M.A.F. Gene abundance analysis: Q.Z., J.C.B. and R.K. fUSi imaging: C.R., J.C.B., B.D.N. and M.G.S. 2DG analysis: Z.W., B.D.N., Y.G. and D.P.H. QuantSeq analysis: J.H., W.-L.W., B.D.N. and D.H.G. Oligodendrocyte characterization: B.D.N., M.D.A., J.C.B., M.S.L. and J.A.G. ET: M.S.L., B.D.N. and M.D.A. MRI/diffusion tensor imaging: S.-J.H. and B.D.N. Animal behaviour: B.D.N. and M.D.A. Resources: P.J.B., D.G., D.P.H., M.A.F., R.K., M.G.S. and S.K.M. Writing original draft: B.D.N. Writing review and editing: B.D.N., M.F., M.D.A., Z.W., W.-L.W., J.H., M.S.L., J.A.G., D.P.H., M.A.F. and S.K.M. Visualization: B.D.N., M.F., M.D.A., Z.W., W.-L.W., J.H., J.C.B., C.R., S.-J.H., M.S.L. and M.A.F. Supervision: S.K.M. Project administration: B.D.N. Funding acquisition: B.D.N., W.-L.W., P.J.B. and S.K.M.

## Corresponding authors

Correspondence to [Brittany D. Needham](#) or [Sarkis K. Mazmanian](#).

## Ethics declarations

### Competing interests

S.K.M. has financial interests in Axial Biotherapeutics. The other authors declare no competing interests.

### Peer review

### Peer review information

*Nature* thanks Gabriel Corfas, Jane Foster, Robert Quinn and the other, anonymous, reviewer(s) for their contribution to the peer review of this work.

## Additional information

**Publisher's note** Springer Nature remains neutral with regard to jurisdictional claims in published maps and institutional affiliations.

## Extended data figures and tables

### [Extended Data Fig. 1 Strain engineering and 4EPS quantification.](#)

**a**, Strain legend corresponding to Fig. [1b–d](#), containing further details for strain names and cloning strategy. Additional information can be found in the [Methods](#) and Supplementary Tables [1–3](#). **b–e**, Maps for integration vectors. **b**, The BO1194 gene was cloned into the pNBU2 vector with an erythromycin resistant marker under the phage promoter. **c**, The PAD gene was cloned into pNBU2 vector with an erythromycin resistant marker under the phage promoter. **d**, The PAD gene was cloned into the pNBU2 vector with a tetracycline resistant marker under the phage promoter. **e**, BO1194

and PAD were tandemly connected, putting the phage promoter in front of both genes, then cloned into the pNBU2 vector with the erythromycin resistant marker. **f**, Creatinine corrected urinary levels of 4EPS from SPF, GF, gnotobiotic mice colonized with strains as labelled, and a mouse model of atypical behaviour including anxiety-like phenotypes. This data corresponds to abbreviated data in Fig. [1f](#). SPF, specific pathogen free mice; BO, *Bacteroides ovatus* mono-colonized mice; 4EP<sup>-</sup>, GF mice colonized with non-producing strain pair (*B. ovatus* Δ1194 and WT *L. plantarum* with endogenous VPR) used throughout; WT, GF mice colonized with wild type strain pair (WT *B. ovatus* and WT *L. plantarum* with endogenous VPR) before optimal engineering; 4EP<sup>+</sup>, colonized with strain pair engineered for higher production of 4EP<sup>+</sup> (*B. ovatus*+1194/PAD and WT *L. plantarum* with endogenous VPR), used throughout; CNTNAP2, conventionally colonized mouse model of atypical behaviour (left to right columns: n=15, 5, 5, 9, 7, 9, 11). **g**, 4EPS levels (creatinine corrected) in urine of wild type, specific pathogen free (SPF) mice fed one of two isocaloric diets matched for protein, mineral, carbohydrate, and fat levels but differing in either high tyrosine fish meal (fish diet), or a high plant protein (soy diet) (n=8 each group) $p=0.002$ . **h**, 4EPS levels (creatinine corrected) in urine of gnotobiotic mice colonized with isogenic strain pairs of *B. ovatus* and wild type *L. plantarum*, which differ only in the presence or absence of gene 1194, and thus the tyrosine lyase activity requires to convert tyrosine to p-coumaric acid (n=2 each group). **i**, Alignments of genes used to engineer the 4EP synthesis pathway to the reference genomes in the WoL database, showing that these genes are found in ~25 genomes each, most of which are common human gut lineages. **j**, 4EP and 4EPS levels (ug/ml) in serum of colonized mice (n=7 each group). **k**, 4EP<sup>+</sup> and 4EP<sup>-</sup> colonized mice were injected with the organic anion transporter to inhibit potential 4EPS transport out of the brain, then analysed by LCMS (n=6 each group). Extended Data Fig. [1g](#). **l**, Conventionally colonized (SPF) mice were injected with probenecid and then injected with high dose 4EPS (n=8) or saline vehicle (n=8), and whole brain lysate was analysed by LCMS compared to 4EPS injection alone (n=4) $p<0.0001$ . **m**, Conventionally colonized (SPF) mice were injected with probenecid and then gavaged with 4EP, then whole brains were harvested at 30-minute intervals and 4EPS levels were quantified by LCMS (n=4; vehicle group n=3) $p=0.01$ . Two independent trials on biological replicates were used for the experiments in the figure.

Abbreviations: SPF, specific pathogen-free; GF, germ-free; BO, *Bacteroides ovatus*; WT, wild type; LP, *Lactobacillus plantarum*. Data represent mean  $\pm$  SEM analysed by a two-tailed Welch's t-test or one-way ANOVA with Dunnett multiple comparisons test as appropriate. \*  $p \leq 0.05$ ; \*\*  $p \leq 0.01$ ; \*\*\*  $p \leq 0.001$ ; \*\*\*\*  $p \leq 0.0001$ .

[Source data](#)

[Extended Data Fig. 2 4EP sulfation, experimental timeline, normal weight gain, colonization and intestinal barrier of 4EP<sup>+</sup> mice.](#)

**a**, In vitro recombinant SULT1A1 sulfotransferase assay with 4EP as potential sulfate acceptor ( $n=5$ )  $p < 0.0001$ . **b**, Results of the sulfotransferase assay using various recombinant SULTs ( $n=3$ )  $p < 0.0001$ . **c**, 4EP sulfation capacity of cytosolic fractions of brain, colon, liver, and small intestinal tissue, each containing endogenous sulfotransferases ( $n=2$  datapoints of samples pooled from triplicate biological replicates, with only 1 pool for SI). Ion intensity of 4EPS measured by LCMS is plotted along the y-axis. **d**, Confirmation of expression of the *Sult1a1* gene measured by qPCR in tissue from the brain, colon, liver, and small intestine of colonized mice ( $n=8$ ; brain  $n=6$ )  $p < 0.0001$ . **e**, Schematic of mouse experimental timeline, showing ages of mice at colonization of GF mice with 4EP<sup>+/−</sup> strains, behaviour testing and tissue collection. **f**, Weights of mice (grams) after colonization of GF mice with 4EP<sup>−</sup> or 4EP<sup>+</sup> bacteria ( $n=13$ ). **g**, Ambulatory activity of 4EP<sup>−</sup> and 4EP<sup>+</sup> mice over ten minutes, measured by distance moved when mice were placed in an open arena and allowed to explore (4EP<sup>−</sup>  $n=21$ ; 4EP<sup>+</sup>  $n=24$ ). **h**, FITC-dextran levels in serum as a measure of intestinal permeability (4EP<sup>−</sup>  $n=5$ , 4EP<sup>+</sup>  $n=6$ ). **i**, Faecal output of colonized mice over 10 min ( $n=13$ ). **j**, Images of hematoxylin and eosin (H&E) stained small intestine and colon of 4EP<sup>+/−</sup> mice (representative images of  $n=4$ ). Scale bar 50μm. **k**, Colonization of ex-GF mice with engineered *Bacteroides ovatus* (BO) and *Lactobacillus plantarum* (LP), plotted as colony forming units (CFU) per gram of intestinal contents ( $n=4$ ). **l**, Quantification of bacterial distance from the intestinal epithelium imaged by electron tomography, where each data point represents a separate animal

comprised of an average of 5-10 bacterial cells per image per mouse ( $4EP^-$  n=4;  $4EP^+$  n=5). **m**, Example images of bacterial cells near the intestinal epithelial layer of  $4EP^{+/-}$  mice. Two independent trials using multiple randomized litters were used for the experiments in the figure.

Abbreviations: SULT, sulfotransferase; SI, small intestine. Data represent mean  $\pm$  SEM. Panel f was analysed by a 2-way ANOVA with a Bonferroni multiple comparison correction. Panels g-i and l were analysed using two-tailed Welch's t-tests and panels a-d, k by a one-way ANOVA with Dunnett multiple comparisons test.

### Source data

### Extended Data Fig. 3 Lack of inflammatory signals in peripheral and brain cytokine and immune profiles of $4EP^{+/-}$ mice.

**a, b**, Cytokine and chemokine levels presented in bar graph where grey (−) is  $4EP^-$  and green (+) is  $4EP^+$ , measured by bioplex in colon (n=9) **a**, and serum (n=9) **b**. No significant differences were observed. **c–d**, Flow cytometry of spleens of  $4EP^+$  and  $4EP^-$  mice. For gating strategy see Supplementary Fig. 2. **c**, Percentages of CD4<sup>+</sup> or CD8<sup>+</sup> T cells ( $4EP^-$  n=11,  $4EP^+$  n=10). **d**, Percentage of B cells ( $4EP^-$  n=11,  $4EP^+$  n=10)  $p < 0.0001$ . **e**, Cytokine and chemokine levels presented in bar graph where grey (−) is  $4EP^-$  and green (+) is  $4EP^+$ , measured by bioplex (n=9) in brain tissue (Il-3  $p = 0.046$ ; Il-5  $p = 0.01$ ; KC  $p = 0.02$ ; TNF-a  $p = 0.01$ ). **f**, Flow cytometry percentages of microglia in the brain of  $4EP^-$  and  $4EP^+$  mice. For gating strategy see Supplementary Fig. 2. **g**, Relative expression of microglial genes in microglial-enriched samples (n=8). Multiple randomized litters were used for the experiments in the figure. Each data point represents biologically independent mice from multiple randomized litters examined over one (a-b) or two (c-h) respective experiments. Data represent mean  $\pm$  SEM. Panels a, b, d, f, and h were analysed by one-way ANOVA with Dunnett multiple comparisons test comparing each  $4EP^+/4EP^-$  pair, and panels g and e by a two-tailed Welch's t-test. \*  $p \leq 0.05$ ; \*\*  $p \leq 0.01$ ; \*\*\*  $p \leq 0.001$ .

## Source data

### Extended Data Fig. 4 Extended information on functional connectivity experiments fUSi and autoradiography.

**a**, Schematic representation of the functional ultrasound (fUSi) set-up. Functional acquisitions are acquired non-invasively through intact skull and scalp in anesthetized mice during 15 min per coronal plane. Created with BioRender.com. **b**, Maps overlaid with regions of interest coloured in a gradient for easier visualization. Significant pairs are indicated, corresponding to the data in main Fig. 2b. Three coronal planes per mouse were studied: Bregma -0.9 mm, Bregma -1.6 mm, Bregma -2mm. 50, 52 and 52 ROIS are respectively delineated for each plane according the Paxinos Atlas. Coronal plane B-0.9mm: ROIs #1 to #8 are located in the left cortex, ROI#9 is the left hippocampus, ROIs#11 to #21 are located in the thalamus, ROI#22 is the right hippocampus, ROIs#23 to #30 are located in the right cortex and finally ROIs#31 to #48 are subthalamic regions. Coronal plane B-1.6mm: ROIs #1 to #20 are located in the cortex, ROIs#21 #22 are the left and right hippocampi, ROIs#23 to #38 are located in the thalamus and ROIs#39 to #42 are subthalamic regions. Coronal plane B-2mm: ROIs #1 to #9 are located in the left cortex, ROI#10 is the left hippocampus, ROIs#11 to #22 are located in the thalamus, ROI#23 is the right hippocampus, ROIs#24 to #32 are located in the right cortex and finally ROIs#33 to #50 are subthalamic regions. **c-d**, Colour-coded overlays over representative coronal (c) and sagittal (d) sections of the mouse brain template showing significant differences in regional cerebral glucose uptake following open field exposure in 4EP<sup>+</sup> mice compared to 4EP<sup>-</sup> mice (n=11) (*t*-test,  $p \leq 0.05$ , extent threshold > 200 contiguous voxels, with both conditions met to be deemed significant; red/blue: increase/decrease in glucose uptake in 4EP<sup>+</sup> compared to 4EP<sup>-</sup> mice). **e**, Quantitated 2DG-uptake by region of interest, including the amygdala, hypothalamus and PVT, confirming changes in relative 2DG uptake in the open field groups (n=11 each group) From left to right,  $p=0.01$ ; 0.03; 0.02; 0.009; 0.003). Average optical density of each ROI in each animal was normalized to whole-brain average of that animal. Abbreviations: AM, amygdala; HY, hypothalamus; PVT, paraventricular nucleus of the thalamus; BNST, bed nucleus of the stria terminalis; S1, primary

somatosensory cortex; CPu, caudate putamen; Hb, habenular nucleus; RT, reticular nucleus of the thalamus; VPL/VPM, Posterior Lateral/Ventral Posterior Medial Thalamus; R, right; L, left. Two cohorts of mice from multiple litters were used for each experiment in this figure. Panel e was analysed by one-way ANOVA with multiple comparison correction and two-stage linear step-up procedure of Benjamini, Krieger and Yekutieli. \*  $p \leq 0.05$ .

[Source data](#)

**Extended Data Fig. 5 Extended results of mRNA high throughput sequencing (QuantSeq), and oligodendrocyte analysis by immunofluorescence implicating oligodendrocyte differences in 4EP<sup>+</sup> mice.**

**a**, Principal component analysis of all samples analysed by QuantSeq, with tight clustering by brain region. Each brain region is coloured according to the legend. **b**, Differential gene analysis summary showing number of significantly different genes in 6 tested brain regions. Top pie chart refers to total number of differential genes by one-way group ANOVA with all the 4EP<sup>-</sup> and 4EP<sup>+</sup>, at baseline and post-EPM. The bottom pie chart was generated according to the specific significant ( $p < 0.05$ ) contrasts between 4EP<sup>+</sup> and 4EP<sup>-</sup> conditions of post-EPM conditions as calculated with the post-hoc Tukey HSD test. **c-d**, GO terms enriched in genes that are upregulated (c) or downregulated (d) in the PVT in 4EP<sup>+</sup> relative to 4EP<sup>-</sup> mice in the baseline, home cage condition. X-axis represents -log10(P) of enrichment analysis. **e**,  $p$ -value histogram of PVT sequencing at baseline, graphed as  $p$ -values binned by 0.05 along the x-axis and number of genes along the y-axis. **f**, Adjusted  $p$ -values for 4EP<sup>+/</sup>4EP<sup>-</sup> comparison of expression of oligodendrocyte specific genes in all 6 brain regions analysed by QuantSeq, corresponding to data presented in Main Fig. [3c](#) for the PVT.  $p < 0.05$  in bold. **g**, PVT seed analysis correlating 2DG uptake in the PVT to the rest of the brain. Images show 3D rendered, average whole brain correlation data ( $n=11$ ). The centre of the PVT is indicated at the cross section of the red lines, and the number of negatively correlated voxels is shown below in each. Significance is illustrated according to the legend. A

minimum threshold of 200 contiguous voxels with  $p < 0.05$  was used. **h**, Schematic of immature OPC and mature, myelinating oligodendrocyte markers used for immunostaining, flow cytometry, or western blots in this study. **i**, Raw counts of mature oligodendrocytes, measured by CC1<sup>+</sup> and OLIG2<sup>+</sup> staining in 4EP<sup>+</sup> and 4EP<sup>-</sup> mice in the PVT, used to calculate maturity quotient in Fig. 3f (n=8).  $p = 0.04$ . **j**, Raw counts of immature oligodendrocytes, measured by NG2<sup>+</sup> and OLIG2<sup>+</sup> staining in 4EP<sup>+</sup> and 4EP<sup>-</sup> mice in the PVT, used to calculate maturity quotient in Fig. 3f (n=8 each group).  $p = 0.055$ . **k**, Representative images (corresponding to main Fig. 3e,f) of the PVT in brain sections from 4EP<sup>-</sup> and 4EP<sup>+</sup> mice, stained for OLIG2, using total cumulative counts from 3-5 images per replicate (n=8). Scale bar 100  $\mu$ m. **l**, Raw counts of OLIG2<sup>+</sup> cells in the PVT of 4EP<sup>+-</sup> mice. Each data point represents an individual mouse, with total cumulative counts from the PVT (n=8)  $p = 0.8$ . **m**, Raw counts of NeuN<sup>+</sup> staining in the PVT (4EP<sup>-</sup> n=10, 4EP<sup>+</sup> n=9), using average counts from 3-5 images per replicate. **n**, Representative images of pan-neuronal NeuN staining in the PVT, with 3-5 images per replicate (4EP<sup>-</sup> n=10, 4EP<sup>+</sup> n=9). Scale bar 100  $\mu$ m. **o**, NG2<sup>+</sup> staining in extended regions of the brain (n=3 each group)  $p = 0.009$ . Abbreviations: PVT, the paraventricular nucleus of the thalamus; BNST, bed nucleus of the stria terminalis; BLA, basolateral amygdala; mPFC, medial prefrontal cortex; HY, hypothalamus; vHPC, ventral hippocampus; OLIG2, oligodendrocyte transcription factor 2; NG2, neural/glial antigen 2; CC1, antibody (anti-adenomatous polyposis coli (APC) clone) that binds mature oligodendrocyte marker; MOG, myelin oligodendrocyte glycoprotein; MBP, myelin basic protein; ACA, anterior commissure; CC, corpus callosum; LHB, lateral habenula; LS, lateral septum; MHB, medial habenula; MS, medial septum; ME, median eminence; PFC, prefrontal cortex; PVN, paraventricular nucleus of the hypothalamus; SM, stria medullaris of thalamus. Two cohorts of mice from multiple litters were used for experiments in panels g-o in this figure. Data represent mean  $\pm$  SEM. Analysis performed using two-tailed Welch's t-tests (i-m) or one-way ANOVA with Dunnett multiple comparison between 4EP<sup>+-</sup> pairs (o). \*  $p \leq 0.05$ .

[Source data](#)

## Extended Data Fig. 6 Extended results of oligodendrocyte analysis implicating oligodendrocyte differences in 4EP<sup>+</sup> mice in vivo and in vitro.

**a**, Extended quantitation of flow cytometry with MOG<sup>+</sup>/NG2<sup>+</sup> ratio by quadrant in the cerebellum, cortex, and hypothalamus (n=4). **b–c**, Western blot analysis of MOG ( $p=0.03$ ) and MBP ( $p=0.002$ ) markers (respectively) of mature oligodendrocytes from the PVT brain region. PVT punches from two mice were pooled per data point in quantitative data (n=6 pooled samples each group). For gel source data, see Supplementary Fig. 1. **d–g**, Organotypic brain slices were cultured in the presence of 10 uM 4EPS. **d**, Representative images of CC1, NG2 and Olig2 staining. Two cohorts of mice were used, with each data point in Fig 3i representing quantified images from samples from individual mice. Scale bar 20  $\mu$ m. **e**, Example high-magnification image of axon in organotypic brain slices, stained with antibodies specific to NF (red), and PLP (green), with DAPI (blue), taken from image set used for quantification in 3i and Extended Data Fig. 6d. Scale bar 8  $\mu$ m. **f**, qPCR results of oligodendrocyte genes, *Cspg4* ( $p=0.04$ ), *Mog* ( $p=0.03$ ), and *Mpb* from organotypic brain slices (n=7). **g**, Western blot image of mature oligodendrocyte marker MBP (quantified in main Fig. 3l). For gel source data, see Supplementary Fig. 1. Abbreviations: NG2, neural/glial antigen 2; CC1, antibody (anti-adenomatous polyposis coli (APC) clone) that binds mature oligodendrocyte marker; MOG, myelin oligodendrocyte glycoprotein; MBP, myelin basic protein. Two cohorts of mice from multiple litters were used for experiments in this figure. Data represent mean  $\pm$  SEM. Statistics were performed using two-tailed Welch's t-tests. \*  $p \leq 0.05$ ; \*\*  $p \leq 0.01$ .

[Source data](#)

## Extended Data Fig. 7 Extended results of myelin analysis by electron microscopy and DTI.

**a**, Additional ET of myelinated axons in 4EP<sup>-</sup> (top) and 4EP<sup>+</sup> (bottom) mice visualized longitudinally along an axon (n=3; 4 images each). These longitudinal images were used only for qualitative visual assessment of

myelin to accompany the other quantitative measures. **b**, Axon diameters (measured from cell membrane, not including myelin layer) from all axons used to calculate g-ratio ( $4EP^-$ , 56;  $4EP^+$ , 70 axons) ( $n=4$ ; 4 images each).  $p=0.1$ . **c**, g-ratio ( $r/R$ ), the inner axon diameter/outer diameter of the myelin sheath, of  $4EP^+$  and  $4EP^-$  mice. Each data point represents a mouse ( $n=4$ ), which is an average of the g-ratio of all axons quantified from 4 images per mouse, where a larger g-ratio indicates a thinner layer of myelin.  $p=0.046$ . **d**, Plot of g-ratio ( $r/R$ ) on the y-axis and axon diameter on the x-axis, with linear regression noted by lines ( $4EP^-$ , 56;  $4EP^+$ , 70 axons) ( $n=4$ ; 4 images each). **e**, Average g-ratio of each animal, binned by axon size, indicating that mid-sized range of axons are driving the change in overall g-ratio phenotype observed in the mice ( $n=4$ ). **f–g**, Defined regions of interest for the PVT and corpus callosum (CC) overlaid on representative sagittal MRI image. **h–i**, representative tracts observed from a bilateral coronal plane view (left) and fractional anisotropy (FA) analysis (right) for the corpus callosum (CC), and whole brain ( $p=0.009$ ), respectively ( $n=4$ ). Two independent trials using multiple litters were used for experiments in this figure. Data represent mean  $\pm$  SEM. Statistics were performed using two-tailed Welch's t-tests (b,c,h,i), simple linear regression test (d), or one-way ANOVA with Dunnett multiple comparison between  $4EP^+/-$  groups at each size group. \*  $p \leq 0.05$ ; \*\*  $p \leq 0.01$ .

### [Source data](#)

## [Extended Data Fig. 8 Additional behaviour tests in \$4EP^-\$ and \$4EP^+\$ mice.](#)

**a**, Distance traveled ( $p=0.06$ ), time in centre ( $p=0.01$ ), and thigmotaxis time ( $p=0.007$ ), during open field test over a period of 10 min (distance traveled data was also shown in Extended Data Fig. 2g) ( $4EP^- n=21$ ,  $4EP^+ n=24$ ). **b**, Time spent in the open arms of the elevated plus maze (EPM) (left) ( $p=0.02$ ) and ratio of time spent in the open/time spent in the closed arms of the EPM (right) ( $4EP^- n=21$ ,  $4EP^+ n=24$ ). **c**, Light/dark box: time mice spent in the open, lit portion of the arena. Test time, 10 min ( $4EP^- n=25$ ,  $4EP^+ n=23$ )  $p=0.02$ . **d**, Grooming: total time mice spent self-grooming over a period of 10 min ( $4EP^- n=27$ ,  $4EP^+ n=24$ ). **e**, Social interaction: with an unfamiliar,

age-matched male intruder. Total time socializing (left) and percent of total socializing that is anogenital sniffing (right) (4EP<sup>-</sup> n=25, 4EP<sup>+</sup> n=22)  $p=0.0009$ . **f**, Ultrasonic vocalization: time spent vocalizing to an unfamiliar, age-matched female for 3 min (4EP<sup>-</sup> n=23, 4EP<sup>+</sup> n=21)  $p=0.01$ . **g**, Novel object recognition (NOR): time spent investigating a novel object when presented with a novel and a familiar object (n=22). **h**, Y-maze alternations: percent of times mice repeated entry into an arm it had just visited rather than alternate to all arms in succession (4EP<sup>-</sup> n=15, 4EP<sup>+</sup> n=16). **i**, Beam traversal: time required for the mouse to cross the narrowing beam (4EP<sup>-</sup> n=19, 4EP<sup>+</sup> n=22). **j**, Pole descent: time required for the mouse to descend from the pole to the home cage (4EP<sup>-</sup> n=19, 4EP<sup>+</sup> n=22). **k**, Wire hang: time the mouse hung on and explored the underside of the wire grid before releasing into cage below (4EP<sup>-</sup> n=19, 4EP<sup>+</sup> n=22). **l**, Faecal 16s profiles of 4EP<sup>+-</sup> mice after behaviour tests, where tan is the colonization group and contamination from exposure to behaviour tests is coloured according to the legend (left panel) and a magnified view of contaminants only (right panel) (4EP<sup>-</sup> n=8, 4EP<sup>+</sup> n=10). Two independent cohorts of mice from multiple litters were used for each experiment in this figure. Data a-k represent mean  $\pm$  SEM analysed by two-tailed Welch's t-test. \*  $p \leq 0.05$ ; \*\*  $p \leq 0.01$ .

### Source data

### Extended Data Fig. 9 Behaviour results from 4EP or 4EPS administration by drinking water and anxiety behaviour tests of 4EP<sup>+-</sup> mice relative to GF and SPF mice.

**a-f**, Behaviour tests of conventionally colonized mice administered 4EP or 4EPS by drinking water. **a**, Left panel: EPM, time spent in open arms over time spent in closed arms (seconds). Right panel: time spent at terminus (outer 1/3 of open arms)(Veh. n=15; 4EPS n=17; 4EP n=16) (Open/closed: Veh. vs 4EPS  $p<0.0001$ ; Veh vs 4EP  $p=0.007$ ; 4EPS vs 4EP  $p=0.03$ ; Terminus: Veh vs 4EPS  $p=0.004$ ). **b**, Open field test, from left to right: time spent in the centre area over thigmotaxis, time spent in centre (seconds), distance moved in open field test, showing an increase in activity in 4EP-treated animals (Veh. n=16; 4EPS n=16; 4EP n=18)  $p=0.02$ . **c**, Grooming test, total percent of time spent grooming, showing an increase in grooming

in the 4EPS-treated animals (Veh. n=16; 4EPS n=18; 4EP n=17). **d**, Number of marbles buried (Veh. n=16; 4EPS n=17; 4EP n=18). **e**, Social interaction. Left panel: total socialization time (seconds). Right panel: % of total socialization time spent as anogenital sniffing (Veh. n=8; 4EPS n=7; 4EP n=7). **f**, USV test. Left panel: Vocalization events. Right panel: Total duration spent vocalizing (seconds) (Veh. n=16; 4EPS n=15; 4EP n=18). **g**, 4EPS levels in urine of mice administered 4EP or 4EPS in the drinking water (creatinine corrected)(Veh. n=12; 4EPS n=9; 4EP n=11)(Veh. vs 4EPS  $p=0.0005$ ; Veh vs 4EP  $p=0.008$ ; 4EPS vs 4EP  $p=0.03$ ). **h**, 4EPS levels in serum of mice administered 4EP or 4EPS in the drinking water (Veh. n=4; 4EPS n=4; 4EP n=3). **i**, Quantified flow cytometry data of PVT of mice administered 4EP or 4EPS in the drinking water, with ratio of MOG+ quartile percentages/NG2+ quartile percentages presented (Veh. n=5; 4EPS n=5; 4EP n=4)  $p=0.03$ . For gating strategy see Supplementary Fig. 2 and main Fig. 3h. **j**, Quantified western blot data for MOG and MBP in the PVT of mice administered 4EP or 4EPS in the drinking water, with blots shown below (n=4 each group). (MBP: H<sub>2</sub>O vs 4EPS  $p=0.04$ ; vs 4EP  $p=0.02$ ). For gel source data, see Supplementary Figure 1. **k–m**, Anxiety behaviour tests contextualizing 4EP+/- mice to GF and SPF mice. **k**, Open field test, from left to right: time spent in the centre area over time spent along walls (4EP<sup>-</sup> vs 4EP<sup>+</sup>  $p=0.04$ ; 4EP<sup>+</sup> vs GF  $p=0.02$ ; 4EP<sup>+</sup> vs SPF  $p=0.04$ ), time spent in the centre (seconds), distance moved in open field test(4EP<sup>+</sup> vs SPF  $p=0.047$ ; GF vs SPF  $p=0.01$ ) (4EP<sup>-</sup> n=8; 4EP<sup>+</sup> n=9; GF n=9; SPF n=11). **l**, Elevated plus maze, time spent in the open arms/time spent in the closed arms ration (left)(4EP<sup>-</sup> vs 4EP<sup>+</sup>  $p=0.03$ ; 4EP<sup>+</sup> vs SPF  $p=0.03$ ) and time spent at the terminus (right) (4EP<sup>-</sup> n=9; 4EP<sup>+</sup> n=9; GF n=11; SPF n=13). **m**, Marble burying (4EP<sup>-</sup> n=9; 4EP<sup>+</sup> n=9; GF n=9; SPF n=112)(4EP<sup>-</sup> vs 4EP<sup>+</sup>  $p=0.02$ ; 4EP<sup>-</sup> vs SPF  $p=0.03$ ; 4EP<sup>+</sup> vs GF  $p=0.02$ ; GF vs SPF  $p=0.03$ ). Abbreviations: Veh., vehicle control; MOG, myelin oligodendrocyte glycoprotein; MBP, myelin basic protein. Two independent cohorts of mice from multiple litters were used for the experiments in this figure. Data represent mean ± SEM analysed by one-way ANOVA with Dunnett multiple comparison between all groups. \*  $p \leq 0.05$ ; \*\*  $p \leq 0.01$ ; \*\*\*  $p \leq 0.001$ ; \*\*\*\*  $p \leq 0.0001$ .

[Source data](#)

**Extended Data Fig. 10 Fluorescence imaging and extended behaviour test results of clemastine fumarate and miconazole-treated mice, and preliminary behaviour tests performed on both sexes, used to determine continued studies on males for the study.**

**a–i**, 4EP<sup>+/−</sup> mice were administered vehicle (control), clemastine fumarate (clem.), or miconazole and then behaviour tested and imaged. **a**, Representative images of CC1 (green), NG2 (red), and OLIG2 (blue) staining in 4EP<sup>+/−</sup> mice with or without treatment. Representative of group of individual mice used for quantification: 4EP<sup>−</sup> control=7, treated=10; 4EP<sup>+</sup> control=6, treated=6, which came from two cohorts (Scale bar 100 μm). **b**, Quantification of fluorescent imaging, presented as a ratio of CC1<sup>+/−</sup>/NG2<sup>+/−</sup> cells (from left to right n=7, 10, 6, 6, 4, 4). The first four columns are also shown in Main Fig. 4i (Cont 4EP<sup>−</sup> vs 4EP<sup>+</sup> p=0.04; 4EP<sup>+</sup>Cont vs 4EP<sup>+</sup>Clem p=0.01). **c–d**, Confirmation that treatment does not reduce 4EPS levels with clemastine (c) (Control. 4EP<sup>−</sup> n=4; Control. 4EP<sup>+</sup> n=6, Clem 4EP<sup>−</sup> n=3; Clem 4EP<sup>+</sup> n=4) or miconazole (d) (Control. 4EP<sup>−</sup> n=4; Control. 4EP<sup>+</sup> n=4, Mic 4EP<sup>−</sup> n=4; Mic 4EP<sup>+</sup> n=5) treatment. **e**, Extended EPM results (Control 4EP<sup>−</sup> n=13; Control 4EP<sup>+</sup> n=13; Clem 4EP<sup>−</sup> n=12; Clem 4EP<sup>+</sup> n=14). **f**, Extended open field results (Control 4EP<sup>−</sup> n=15; Control 4EP<sup>+</sup> n=17; Clem 4EP<sup>−</sup> n=17; Clem 4EP<sup>+</sup> n=17). **g–i**, Behavioural results for mice treated with miconazole, including **g**, Open field (Control 4EP<sup>−</sup> n=24; Control 4EP<sup>+</sup> n=25; Mic. 4EP<sup>−</sup> n=18; Mic. 4EP<sup>+</sup> n=20)(left graph: 4EP<sup>−</sup> Cont vs 4EP<sup>+</sup> Cont p=0.02; 4EP<sup>+</sup>cont vs 4EP<sup>+</sup>Mic p=0.008)(middle graph: 4EP<sup>−</sup> Cont vs 4EP<sup>+</sup> Cont p=0.02; 4EP<sup>+</sup>cont vs 4EP<sup>+</sup>Mic p=0.005). **h**, EPM (Control 4EP<sup>−</sup> n=24; Control 4EP<sup>+</sup> n=25; Mic. 4EP<sup>−</sup> n=15; Mic. 4EP<sup>+</sup> n=17)(left graph: 4EP<sup>−</sup> Cont vs 4EP<sup>+</sup> Cont p=0.002; 4EP<sup>+</sup>cont vs 4EP<sup>+</sup>Mic p=0.03)(right graph: 4EP<sup>−</sup> Cont vs 4EP<sup>+</sup>Cont p=0.0009). **i**, Marble Burying (Control 4EP<sup>−</sup> n=24; Control 4EP<sup>+</sup> n=26; Mic. 4EP<sup>−</sup> n=21; Mic. 4EP<sup>+</sup> n=21)(p=0.001) **j**, Left panel: EPM, time spent in open arms over time spent in closed arms. Right panel: time spent at terminus (outer 1/3 of open arms) (Males 4EP<sup>−</sup> n=17; Males 4EP<sup>+</sup> n=17; Females 4EP<sup>−</sup> n=20; Females 4EP<sup>+</sup> n=21)p=0.02. **k**, Open field test, time

spent in the centre area over time spent in thigmotaxis left), time spent in the centre (right) (Males 4EP<sup>-</sup> n=16; Males 4EP<sup>+</sup> n=14; Females 4EP<sup>-</sup> n=18; Females 4EP<sup>+</sup> n=13)*p*-values left to right: 0.005, 0.003. **I**, Number of marbles buried in marble burying test (Males 4EP<sup>-</sup> n=24; Males 4EP<sup>+</sup> n=23; Females 4EP<sup>-</sup> n=17; Females 4EP<sup>+</sup> n=26)*p*=0.03. Abbreviations: NG2, neural/glial antigen 2; CC1, antibody (anti-adenomatous polyposis coli (APC) clone) that binds mature oligodendrocyte marker; OLIG2, oligodendrocyte transcription factor 2; clem, clemastine fumarate; mic, miconazole. Two independent cohorts of mice from multiple litters were used for each experiment in this figure. Data represent mean ± SEM analysed by two-way ANOVA with Dunnett multiple comparison to 4EP<sup>+</sup> group (panels b-i) or Sidak multiple comparison between 4EP<sup>+-</sup> groups within each sex (panels j-l). \* *p* ≤ 0.05, \*\* *p* ≤ 0.01.

### [Source data](#)

## **Supplementary information**

### [Supplementary Information](#)

Supplementary Figs. 1 and 2, Supplementary Tables 1–6 and the captions for the Supplementary Tables.

### [Reporting Summary](#)

## **Source data**

### [Source Data Fig. 1](#)

### [Source Data Fig. 2](#)

### [Source Data Fig. 3](#)

### [Source Data Fig. 4](#)

[\*\*Source Data Extended Data Fig. 1\*\*](#)

[\*\*Source Data Extended Data Fig. 2\*\*](#)

[\*\*Source Data Extended Data Fig. 3\*\*](#)

[\*\*Source Data Extended Data Fig. 4\*\*](#)

[\*\*Source Data Extended Data Fig. 5\*\*](#)

[\*\*Source Data Extended Data Fig. 6\*\*](#)

[\*\*Source Data Extended Data Fig. 7\*\*](#)

[\*\*Source Data Extended Data Fig. 8\*\*](#)

[\*\*Source Data Extended Data Fig. 9\*\*](#)

[\*\*Source Data Extended Data Fig. 10\*\*](#)

## Rights and permissions

[Reprints and Permissions](#)

## About this article

### Cite this article

Needham, B.D., Funabashi, M., Adame, M.D. *et al.* A gut-derived metabolite alters brain activity and anxiety behaviour in mice. *Nature* **602**, 647–653 (2022). <https://doi.org/10.1038/s41586-022-04396-8>

- Received: 11 June 2020
- Accepted: 02 January 2022

- Published: 14 February 2022
- Issue Date: 24 February 2022
- DOI: <https://doi.org/10.1038/s41586-022-04396-8>

## Share this article

Anyone you share the following link with will be able to read this content:

[Get shareable link](#)

Sorry, a shareable link is not currently available for this article.

[Copy to clipboard](#)

Provided by the Springer Nature SharedIt content-sharing initiative

## Further reading

- [\*\*Targeting microbial metabolites to treat autism\*\*](#)

- Rochellys Diaz Heijtz
- Pierre Gressens
- Jonathan R. Swann

*Nature Medicine* (2022)

## [\*\*Safety and target engagement of an oral small-molecule sequestrant in adolescents with autism spectrum disorder: an open-label phase 1b/2a trial\*\*](#)

- A. Stewart Campbell
- Brittany D. Needham
- Sarkis K. Mazmanian

Article 14 Feb 2022

## Targeting microbial metabolites to treat autism

- Rochellys Diaz Heijtz
- Pierre Gressens
- Jonathan R. Swann

News & Views 14 Feb 2022

---

This article was downloaded by **calibre** from <https://www.nature.com/articles/s41586-022-04396-8>

| [Section menu](#) | [Main menu](#) |

- Article
- Open Access
- [Published: 23 December 2021](#)

# Omicron extensively but incompletely escapes Pfizer BNT162b2 neutralization

- [Sandile Cele<sup>1,2</sup>,](#)
- [Laurelle Jackson<sup>1</sup>,](#)
- [David S. Khoury<sup>3</sup>,](#)
- [Khadija Khan<sup>1,2</sup>,](#)
- [Thandeka Moyo-Gwete<sup>4,5</sup>,](#)
- [Hourriyah Tegally<sup>6,7</sup>,](#)
- [James Emmanuel San<sup>6</sup>,](#)
- [Deborah Cromer<sup>3</sup>,](#)
- [Cathrine Scheepers<sup>4,5</sup>,](#)
- [Daniel G. Amoako<sup>2,4</sup>,](#)
- [Farina Karim<sup>1,2</sup>,](#)
- [Mallory Bernstein<sup>1</sup>,](#)
- [Gila Lustig<sup>8</sup>,](#)
- [Derseree Archary<sup>8,9</sup>,](#)
- [Muneerah Smith ORCID: orcid.org/0000-0002-1516-3270<sup>10</sup>,](#)
- [Yashica Ganga<sup>1</sup>,](#)
- [Zesuliwe Jule<sup>1</sup>,](#)
- [Kajal Reedoy<sup>1</sup>,](#)
- [Shi-Hsia Hwa ORCID: orcid.org/0000-0002-5648-9808<sup>1,11</sup>,](#)
- [Jennifer Giandhari<sup>6</sup>,](#)
- [Jonathan M. Blackburn ORCID: orcid.org/0000-0001-8988-9595<sup>10,12</sup>,](#)
- [Bernadett I. Gosnell ORCID: orcid.org/0000-0002-6336-7489<sup>13</sup>,](#)
- [Salim S. Abdoel Karim<sup>8,14</sup>,](#)
- [Willem Hanekom<sup>1,11</sup>,](#)
- [NGS-SA,](#)
- [COMMIT-KZN Team,](#)
- [Anne von Gottberg<sup>4,5</sup>,](#)
- [Jinal N. Bhiman ORCID: orcid.org/0000-0001-6354-4003<sup>4,5</sup>,](#)

- [Richard J. Lessells<sup>6,8</sup>](#),
- [Mahomed-Yunus S. Moosa<sup>13</sup>](#),
- [Miles P. Davenport<sup>3</sup>](#),
- [Tulio de Oliveira<sup>6,7,8,15</sup>](#),
- [Penny L. Moore ORCID: orcid.org/0000-0001-8719-4028<sup>4,5,8,12</sup>](#) &
- [Alex Sigal ORCID: orcid.org/0000-0001-8571-2004<sup>1,2,16</sup>](#)

[\*Nature\*](#) volume **602**, pages 654–656 (2022)

- 11k Accesses
- 22 Citations
- 46 Altmetric
- [Metrics details](#)

## Subjects

- [Antimicrobial responses](#)
- [SARS-CoV-2](#)

## Abstract

The emergence of the SARS-CoV-2 variant of concern Omicron (Pango lineage B.1.1.529), first identified in Botswana and South Africa, may compromise vaccine effectiveness and lead to re-infections<sup>1</sup>. Here we investigated Omicron escape from neutralization by antibodies from South African individuals vaccinated with Pfizer BNT162b2. We used blood samples taken soon after vaccination from individuals who were vaccinated and previously infected with SARS-CoV-2 or vaccinated with no evidence of previous infection. We isolated and sequence-confirmed live Omicron virus from an infected person and observed that Omicron requires the angiotensin-converting enzyme 2 (ACE2) receptor to infect cells. We compared plasma neutralization of Omicron relative to an ancestral SARS-CoV-2 strain and found that neutralization of ancestral virus was much higher in infected and vaccinated individuals compared with the vaccinated-only participants. However, both groups showed a 22-fold reduction in vaccine-elicited neutralization by the Omicron variant. Participants who were vaccinated and had previously been infected exhibited residual neutralization of Omicron similar to the level of neutralization of the ancestral virus observed in the vaccination-only group. These data support the notion that reasonable protection against Omicron may be maintained using vaccination approaches.

[Download PDF](#)

## Main

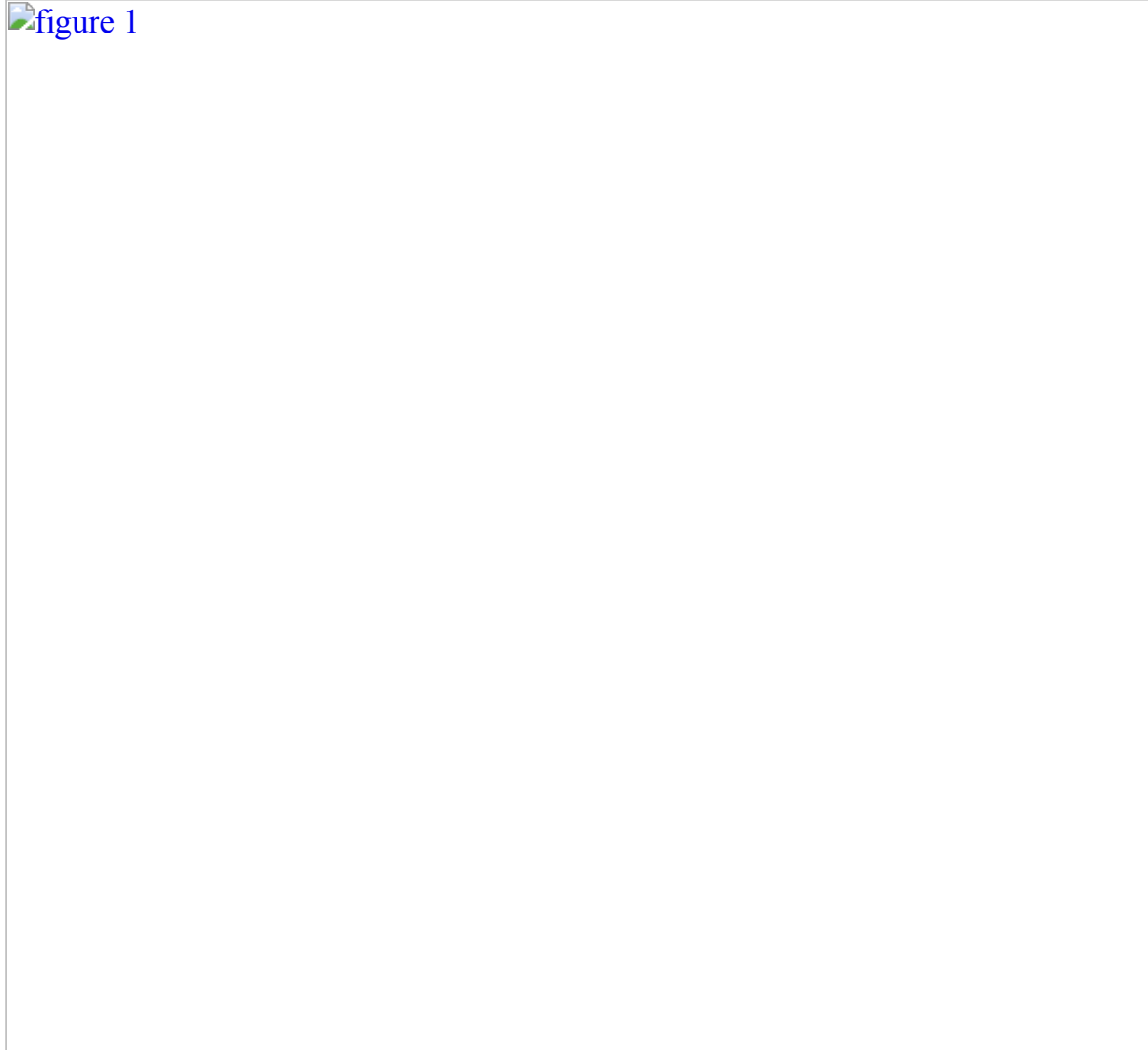
The emergence of the Omicron variant of SARS-CoV-2 in November 2021, first identified in South Africa and Botswana, was first described in South Africa<sup>2</sup>, followed shortly afterwards by confirmed transmission in Hong Kong<sup>3</sup>. Owing to the large number of mutations in the spike protein and elsewhere on the virus (<https://covdb.stanford.edu/page/mutation-viewer/#omicron>), there is concern that this variant will exhibit substantial escape from vaccine-elicited immunity<sup>4,5</sup>. Furthermore, several mutations in the spike receptor-binding domain and S2 fusion domain are predicted to increase transmission<sup>5</sup>.

Here we have used the human lung cell line H1299-ACE2 (Extended Data Fig. 1), which overexpresses the human ACE2 receptor<sup>6</sup>, to both isolate Omicron and test its neutralization by human plasma. We isolated Omicron virus using one passage on H1299-ACE2 cells and a second passage on H1299-ACE2 cells in co-culture with the Vero E6 African green monkey kidney cell line. Sequencing of the isolated virus confirmed it was the Omicron variant bearing the R346K mutation. We observed no mutations introduced in vitro as majority or minority variants (Extended Data Table 1). H1299-ACE2 cells were similar to Vero E6 cells in that they formed infection foci during infection with ancestral D614G and Beta variant viruses; however, the H1299-ACE2 cells formed more foci than unmodified Vero E6 cells (Extended Data Fig. 2a, b). Infection by cell-free Omicron of unmodified Vero E6 cells was inefficient (Extended Data Fig. 2c) and we could not use cell-free Omicron infection in Vero E6 cells to generate a useable virus stock of this isolate (Extended Data Fig. 2d).

We observed that Omicron infected the H1299-ACE2 cells in a concentration-dependent manner but did not infect the parental H1299 cells, indicating that human ACE2 is required for Omicron entry (Fig. 1a, b). We then tested the ability of plasma from individuals vaccinated with BNT162b2 to neutralize Omicron versus ancestral D614G virus in a live virus neutralization assay. We tested plasma samples taken from 19 individuals after they had received 2 doses of BNT162b2 (Extended Data Tables 2, 3), 6 of whom had no previous record of SARS-CoV-2 infection or detectable SARS-CoV-2 nucleocapsid antibodies indicative of previous infection (Methods). We also tested samples from a later time point for two of the vaccinated-only participants (Extended Data Table 3). The previously infected and vaccinated participants were infected with either ancestral SARS-CoV-2 strains or the Delta variant (Extended Data Table 3). To quantify neutralization in the live virus neutralization assay, we calculated the focus reduction neutralization test value (FRNT<sub>50</sub>, the inverse of the plasma dilution required for a 50% reduction in infection focus number).

**Fig. 1: ACE2 dependence and neutralization of the Omicron variant by Pfizer BNT162b2-elicited immunity.**

 figure 1



**a**, Representative images showing infection foci in wells of a multi-well plate with titration of live SARS-CoV-2 Omicron virus on H1299-ACE2 and H1299 parental cells. Numbers above well images denote viral stock dilution. Scale bars, 2 mm. **b**, Number of foci as a function of Omicron virus stock dilution. Data are mean  $\pm$  s.d. of six replicates from two independent experiments. **c**, Neutralization of Omicron virus compared with D614G ancestral virus by plasma from participants vaccinated with two doses of BNT162b2 and previously SARS-CoV-2 infected (blue) or uninfected (orange). Numbers in black above each virus strain are geometric mean titres (GMT) of the reciprocal plasma dilution ( $FRNT_{50}$ ) resulting in 50% reduction in infection foci. The red horizontal line denotes the most concentrated plasma used. Twenty-one samples were tested from  $n = 19$  participants in 2 independent experiments ( $n = 13$  vaccinated and previously infected;  $n = 6$  vaccinated only). Grey points denote

measurements where 50% neutralization was not achieved with the most concentrated plasma used.  $P = 4.8 \times 10^{-5}$ , Wilcoxon rank-sum test. **d**, Geometric mean and 95% confidence interval of the fold change in neutralization between ancestral D614G and Omicron neutralization in plasma. Purple denotes all participants, blue denotes vaccinated individuals with previous SARS-CoV-2 infection, orange denotes vaccinated-only individuals, and yellow denotes all participants excluding those in whom 50% neutralization was not achieved. **e**, Mean predicted vaccine efficacy and 95% confidence intervals against symptomatic infection with Omicron using data from previous randomized controlled trials and the 22-fold difference between D614G and Omicron observed in this study<sup>17,18</sup>. Predictions are for vaccinated and boosted (B, red) or vaccinated-only (V, blue) individuals.

Consistent with previous studies<sup>7,8,9</sup>, we observed that individuals who were vaccinated and had previously been infected exhibited higher neutralization capacity for ancestral virus relative to those who were vaccinated only (Fig. 1c). For all participants, the ability to neutralize Omicron was lower than for ancestral virus (Fig. 1c). The geometric mean titre (GMT) FRNT<sub>50</sub> for all participants was 1,963 for D614G and 89 for Omicron, a 22-fold difference (95% confidence interval 16–30) (Fig. 1d); the fold drop was the same for individuals who were vaccinated and had previously been infected (95% confidence interval 16–34) and in the vaccinated-only group (95% confidence interval 15–32) (Fig. 1d). Six of the samples showed fitted values for 50% Omicron neutralization that corresponded to a plasma concentration higher than the most concentrated plasma tested (a 1:25 dilution). This included the two samples collected at a later time point after vaccination, one of which showed a complete knockout of neutralization activity with Omicron (Fig. 1c, Extended Data Table 3). Excluding these 6 values from the analysis reduced the difference in GMT FRNT<sub>50</sub> between D614G and Omicron to 19-fold (95% confidence interval 14–25), well within the 95% confidence intervals of the fold differences for the raw values (Fig. 1d). Of note, Omicron virus neutralization by samples from individuals who were previously infected and vaccinated was similar to D614G neutralization by samples from participants vaccinated with two doses of BNT162b2 but not previously infected (Fig. 1c). GMT FRNT<sub>50</sub> for Omicron in the previously infected and vaccinated group was 305 (95% confidence interval 134–695), whereas GMT FRNT<sub>50</sub> for ancestral virus in the vaccinated-only group was 263 (95% confidence interval 147–472).

We compared these results with neutralization of the Beta variant<sup>6,10,11,12,13,14,15,16</sup> using Beta and D614G virus infection of H1299-ACE2 (Extended Data Fig. 3a) and Vero E6 (Extended Data Fig. 3b) cells. The fold difference relative to the ancestral D614G virus was 4.3 for H1299-ACE2 cells and 5.0 for Vero E6 cells. Thus, results

from these two cell lines indicated that Omicron exhibited approximately fourfold greater escape relative to Beta in our assays.

This study was not designed to reliably evaluate vaccine efficacy or protection from severe disease. However, a prediction of vaccine efficacy after a 22-fold drop in neutralization can be made in individuals vaccinated with BNT162b2 and individuals who were both vaccinated and boosted on the basis of data from randomized control trials using a model relating neutralization level to vaccine efficacy<sup>17,18</sup>. Using this model and the differences in neutralization between Omicron and other SARS-CoV-2 strains (Methods), we predict a vaccine efficacy for preventing symptomatic infection by Omicron of 73% (95% confidence interval 58–83%) for vaccinated and boosted individuals, and 35% (95% confidence interval 20–50%) for vaccinated-only individuals; this suggests that Omicron compromises the ability of the vaccine to protect against infection in individuals in the vaccinated-only group but not in vaccinated and boosted individuals (Fig. 1e). We note that these predictions are similar to reports of actual vaccine efficacy in the UK<sup>19</sup>.

Shortly after we released these findings, several other groups have reported similar results<sup>3,20,21,22,23</sup> including Pfizer–BioNTech (<https://www.businesswire.com/news/home/20211208005542/en/>). These results mirror ours, with large reductions in neutralization of Omicron compared with ancestral virus by vaccine-elicited immunity, neutralizing monoclonal antibodies and plasma from convalescent individuals previously infected with other variants. Notably, the Pfizer–BioNTech study reports that boosting seems to increase neutralization breadth, which reduces the escape by Omicron relative to ancestral virus; these results have been validated independently<sup>21</sup>. Unlike what was reported for boosting, we did not observe a lower fold drop in previously vaccinated and infected relative to the vaccinated-only participants in this study.

Limitations of this study include the presence of an R346K substitution in our virus stock. This putative escape mutation<sup>24</sup>, which may confer moderate antibody resistance ([https://bloomlab.github.io/SARS2\\_RBD\\_Ab\\_escape\\_maps/escape-calc/](https://bloomlab.github.io/SARS2_RBD_Ab_escape_maps/escape-calc/)), is not found in the majority of Omicron genomes. In addition, the timing of sample collection soon after vaccination (Supplementary Tables 2, 3) does not account for the waning of neutralization capacity<sup>25,26</sup>.

So far, a milder course of Omicron infection has been observed in South Africa relative to previous infection waves in terms of reported numbers of patients in intensive care units and needing ventilation<sup>27</sup>. Although there may be other unidentified contributing factors that lower pathogenicity<sup>28</sup>, pre-existing immunity would be expected to be higher in the Omicron wave because of vaccination as well as immunity elicited by previous infection during one of three preceding infection waves

in South Africa<sup>28</sup>. Therefore, the incomplete Omicron escape from previous immunity described here may be an important factor accounting for the milder course of infection. Despite the extensive neutralization escape of Omicron, residual neutralization levels may still be sufficient to protect from severe disease<sup>17,18</sup>. Other facets of the adaptive immune response elicited by vaccination and previous infection may increase protection. Furthermore, we observed that vaccination combined with previous infection elicits similar neutralization capacity against Omicron as vaccination without previous infection elicits against ancestral virus. This indicates that protection from symptomatic Omicron infection may occur when vaccination is combined with previous infection or boosting. This may explain why Pfizer BNT162b2 vaccination has been shown to substantially decrease the risk of hospital admission caused by Omicron infection in South Africa<sup>29</sup> and supports the use of further vaccination and boosting to combat Omicron.

## Methods

### Whole-genome sequencing, genome assembly and phylogenetic analysis

cDNA synthesis was performed on the extracted RNA using random primers followed by gene-specific multiplex PCR using the ARTIC V.3 protocol (<https://www.protocols.io/view/covid-19-artic-v3-illumina-library-construction-an-bibtkann>). In brief, extracted RNA was converted to cDNA using the Superscript IV First Strand synthesis system (Life Technologies) and random hexamer primers. SARS-CoV-2 whole-genome amplification was performed by multiplex PCR using primers designed using Primal Scheme (<http://primal.zibraproject.org/>) to generate 400-bp amplicons with an overlap of 70 bp that covers the 30-kb SARS-CoV-2 genome. PCR products were cleaned up using AmpureXP purification beads (Beckman Coulter) and quantified using the Qubit dsDNA High Sensitivity assay on the Qubit 4.0 instrument (Life Technologies). We then used the Illumina Nextera Flex DNA Library Prep kit according to the manufacturer's protocol to prepare indexed paired-end libraries of genomic DNA. Sequencing libraries were normalized to 4 nM, pooled and denatured with 0.2 N sodium acetate. Then, a 12-pM sample library was spiked with 1% PhiX (a PhiX Control v.3 adaptor-ligated library was used as a control). We sequenced libraries on a 500-cycle v.2 MiSeq Reagent Kit on the Illumina MiSeq instrument (Illumina). We assembled paired-end fastq reads using Genome Detective 1.126 (<https://www.genomedetective.com>) and the Coronavirus Typing Tool. We polished the initial assembly obtained from Genome Detective by aligning mapped reads to the reference sequences and filtering out low-quality mutations using the bcftools 1.7-2 mpileup method. Mutations were confirmed visually with BAM files using Geneious software (Biomatters). P2 stock was sequenced and confirmed Omicron with the following substitutions: E:T9I, M:D3G, M:Q19E, M:A63T, N:P13L,

N:R203K, N:G204R, ORF1a:K856R, ORF1a:L2084I, ORF1a:A2710T, ORF1a:T3255I, ORF1a:P3395H, ORF1a:I3758V, ORF1b:P314L, ORF1b:I1566V, ORF9b:P10S, S:A67V, S:T95I, S:Y145D, S:L212I, S:G339D, S:R346K, S:S371L, S:S373P, S:S375F, S:K417N, S:N440K, S:G446S, S:S477N, S:T478K, S:E484A, S:Q493R, S:G496S, S:Q498R, S:N501Y, S:Y505H, S:T547K, S:D614G, S:H655Y, S:N679K, S:P681H, S:N764K, S:D796Y, S:N856K, S:Q954H, S:N969K and S:L981F. Deletions: N:E31, N:R32, N:S33, ORF1a:S2083, ORF1a:L3674, ORF1a:S3675, ORF1a:G3676, ORF9b:E27, ORF9b:N28, ORF9b:A29, S:H69, S:V70, S:G142, S:V143, S:Y144 and S:N211. The sequence was deposited at GISAID under accession EPI\_ISL\_7358094.

## SARS-CoV-2 nucleocapsid enzyme-linked immunosorbent assay (ELISA)

Nucleocapsid protein ( $2 \mu\text{g ml}^{-1}$ ) (Biotech Africa; catalogue (cat.) no. BA25-P) was used to coat 96-well, high-binding plates and incubated overnight at  $4^\circ\text{C}$ . The plates were incubated in a blocking buffer consisting of 5% skimmed milk powder, 0.05% Tween 20, 1× PBS. Plasma samples were diluted to a 1:100 dilution in a blocking buffer and added to the plates. Horseradish peroxidase (HRP)-conjugated IgG secondary antibody was diluted to 1:3,000 in blocking buffer and added to the plates followed by tetramethylbenzidine (TMB) peroxidase substrate (Thermo Fisher Scientific). Upon stopping the reaction with 1 M  $\text{H}_2\text{SO}_4$ , absorbance was measured at a 450-nm wavelength.

## Cells

Vero E6 cells (ATCC CRL-1586, obtained from Cellonex) were propagated in complete growth medium consisting of Dulbecco's modified Eagle medium (DMEM) with 10% fetal bovine serum (Hyclone) containing 10 mM of HEPES, 1 mM sodium pyruvate, 2 mM l-glutamine and 0.1 mM nonessential amino acids (Sigma-Aldrich). Vero E6 cells were passaged every 3–4 days. H1299 cell lines were propagated in growth medium consisting of complete Roswell Park Memorial Institute (RPMI) 1640 medium with 10% fetal bovine serum containing 10 mM of HEPES, 1 mM sodium pyruvate, 2 mM l-glutamine and 0.1 mM nonessential amino acids. H1299 cells were passaged every second day. The H1299-E3 (H1299-ACE2, clone E3) cell line was derived from H1299 (CRL-5803) as described in previous work<sup>6</sup> and Supplementary Fig. 1. In brief, vesicular stomatitis virus G glycoprotein (VSVG) pseudotyped lentivirus containing ACE2 was used to spinfect H1299 cells. ACE-2 transduced H1299 cells (containing an endogenously yellow fluorescent protein labelled histone H2AZ gene<sup>30</sup>) were then subcloned at single-cell density in 96-well plates (Eppendorf) in conditioned medium derived from confluent cells. After 3 weeks, wells were

detached using a 0.25% trypsin-EDTA solution (Gibco) and plated in 2 replicate plates, where the first plate was used to determine infectivity and the second was stock. The first plate was screened for the fraction of mCherry-positive cells per cell clone upon infection with a SARS-CoV-2 mCherry expressing spike pseudotyped lentiviral vector. Screening was performed using a Metamorph-controlled (Molecular Devices) Nikon TiE motorized microscope (Nikon) with a 20 $\times$ , 0.75 NA phase objective, 561-nm laser line, and 607-nm emission filter (Semrock). Images were captured using an 888 EMCCD camera (Andor). The clone with the highest fraction of mCherry expression was expanded from the stock plate and denoted H1299-E3. Infectivity was confirmed with mCherry expressing lentivirus by flow cytometry using a BD Fortessa instrument and analysed using BD FACSDiva Software (BD Biosciences). This clone was used in the outgrowth and focus forming assay. Cell lines have not been authenticated. The cell lines have been tested for mycoplasma contamination and are mycoplasma negative.

## Virus expansion

All work with live virus was performed in biosafety level 3 containment using protocols for SARS-CoV-2 approved by the Africa Health Research Institute Biosafety Committee. ACE2-expressing H1299-E3 cells were seeded at  $4.5 \times 10^5$  cells in a well on a 6-well plate and incubated for 18–20 h. After one DPBS wash, the sub-confluent cell monolayer was inoculated with 500  $\mu$ l universal transport medium diluted 1:1 with growth medium filtered through a 0.45- $\mu$ m filter. Cells were incubated for 1 h. Wells were then filled with 3 ml complete growth medium. After 4 days of infection (completion of passage 1 (P1)), cells were trypsinized, centrifuged at 300g for 3 min and resuspended in 4 ml growth medium. Then, 2 ml was added to Vero E6 cells that had been seeded at  $2 \times 10^5$  cells per ml, 5 ml total, 18–20 h earlier in a T25 flask (approximately 1:8 donor-to-target cell dilution ratio) for cell-to-cell infection. The co-culture of ACE2-expressing H1299-E3 and Vero E6 cells was incubated for 1 h and 7 ml of complete growth medium was added to the flask and incubated for 4 days. The viral supernatant (passage 2 (P2) stock) was used for experiments. Further optimization of the viral outgrowth protocol used for subsequent Omicron isolates showed that addition of 4 ml instead of 2 ml of infected H1299-E3 cells to Vero E6 cells that had been seeded at  $2 \times 10^5$  cells per ml, 20 ml total, 18–20 h earlier in a T75 flask gave P2 stocks with substantially higher titres that could detectably infect Vero E6 cells. The Omicron virus isolate is available from the authors contingent on verification that it will be received and used in a biosafety level 3 facility.

## Live virus neutralization assay

H1299-E3 cells were plated in a 96-well plate (Corning) at 30,000 cells per well 1 day before infection. Plasma was separated from EDTA-anticoagulated blood by

centrifugation at 500g for 10 min and stored at  $-80^{\circ}\text{C}$ . Aliquots of plasma samples were heat-inactivated at  $56^{\circ}\text{C}$  for 30 min and clarified by centrifugation at 10,000g for 5 min. Virus stocks were used at approximately 50–100 focus-forming units per microwell and added to diluted plasma. Antibody–virus mixtures were incubated for 1 h at  $37^{\circ}\text{C}$ , 5% CO<sub>2</sub>. Cells were infected with 100  $\mu\text{l}$  of the virus–antibody mixtures for 1 h, then 100  $\mu\text{l}$  of a 1× RPMI 1640 (Sigma-Aldrich, R6504), 1.5% carboxymethylcellulose (Sigma-Aldrich, C4888) overlay was added without removing the inoculum. Cells were fixed 18 h after infection using 4% PFA (Sigma-Aldrich) for 20 min. Foci were stained with a rabbit anti-spike monoclonal antibody (BS-R2B12, GenScript A02058) at 0.5  $\mu\text{g ml}^{-1}$  in a permeabilization buffer containing 0.1% saponin (Sigma-Aldrich), 0.1% BSA (Sigma-Aldrich) and 0.05% Tween-20 (Sigma-Aldrich) in PBS. Plates were incubated with primary antibody overnight at  $4^{\circ}\text{C}$ , then washed with wash buffer containing 0.05% Tween-20 in PBS. Secondary goat anti-rabbit HRP conjugated antibody (Abcam ab205718) was added at 1  $\mu\text{g ml}^{-1}$  and incubated for 2 h at room temperature with shaking. TrueBlue peroxidase substrate (SeraCare 5510-0030) was then added at 50  $\mu\text{l}$  per well and incubated for 20 min at room temperature. Plates were imaged in an ImmunoSpot Ultra-V S6-02-6140 Analyzer ELISPOT instrument with BioSpot Professional built-in image analysis (C.T.L.).

## Statistics and fitting

All statistics and fitting were performed in MATLAB v.2019b. Neutralization data were fit to:

$$\$ \$ \{ \backslash \text{rm}\{ \text{Tx} \} \} = \backslash \text{frac}\{ 1 \} \{ 1 + (D / \{ \backslash \text{rm}\{ \text{ID} \} \}) - \{ 50 \} \} \$ \$$$

Here Tx is the number of foci normalized to the number of foci in the absence of plasma on the same plate at dilution D and ID<sub>50</sub> is the plasma dilution giving 50% neutralization. FRNT<sub>50</sub> = 1/ID<sub>50</sub>. Values of FRNT<sub>50</sub> < 1 are set to 1 (undiluted), the lowest measurable value. The most concentrated plasma dilution was 1:25 and therefore FRNT<sub>50</sub> < 25 were extrapolated. We have marked these values in Fig. 1c and calculate the fold-change FRNT<sub>50</sub> either for the raw values or for values where FRNT<sub>50</sub> > 25 in Fig. 1d.

## Estimating vaccine efficacy from neutralization titres

Previously, the fold reduction in neutralization was shown to correlate and predict vaccine efficacy against symptomatic infection with ancestral SARS-CoV-2<sup>18</sup>, and more recently with variants of concern<sup>17</sup> in data from randomized controlled trials. The model was used here to estimate the vaccine efficacy against Omicron based on

the fold drop observed in this study applied to the randomized controlled trial data. In brief, vaccine efficacy (VE) was estimated based on the ( $\log_{10}$ ) fold drop in neutralization titre to Omicron ( $f$ ), and the ( $\log_{10}$ ) mean neutralization titre as a fold of the mean convalescent titre reported for BNT162b2 in phase I/II trials ( $\mu$ ) using the equation:

$$\text{VE} = \int_{-\infty}^{\infty} N(x, \mu - f, \sigma) \frac{1}{1 + e^{-k(x - x_{50})}} dx$$

Here,  $N$  is the probability density function of a normal distribution with mean  $\mu - f$  and standard deviation  $\sigma$ , and  $k$  and  $x_{50}$  are the parameters of the logistic function relating neutralization to protection for the Pfizer BNT162b2 vaccine which were fitted from randomized controlled trial data:  $\sigma = 0.46$ ,  $k = 3$  and  $x_{50} = \log_{10} 0.2$  for symptomatic infection<sup>18</sup>. Importantly,  $\mu = \log_{10} 2.4$  for trial participants vaccinated with two doses of BNT162b2, and  $\mu = \log_{10} 12$  for vaccinated and boosted trial participants<sup>17,18</sup>.

## Informed consent and ethical statement

Blood samples were obtained after written informed consent from hospitalized adults with PCR-confirmed SARS-CoV-2 infection and/or vaccinated individuals who were enrolled in a prospective cohort study approved by the Biomedical Research Ethics Committee at the University of KwaZulu-Natal (reference BREC/00001275/2020). Use of residual swab sample was approved by the University of the Witwatersrand Human Research Ethics Committee (HREC) (ref. M210752).

## Reporting summary

Further information on research design is available in the [Nature Research Reporting Summary](#) linked to this paper.

## Data availability

Sequence of outgrown virus has been deposited in GISAID with accession EPI\_ISL\_7358094. Raw images of the data are available upon reasonable request.

## Code availability

The sequence analysis and visualization pipeline are available on GitHub (<https://github.com/nextstrain/ncov>). Image analysis and curve fitting scripts in

MATLAB v.2019b are available on GitHub (<https://github.com/sigallab/NatureMarch2021>).

## References

1. Pulliam, J. R. C. et al. Increased risk of SARS-CoV-2 reinfection associated with emergence of the Omicron variant in South Africa. Preprint at <https://doi.org/10.1101/2021.11.11.21266068> (2021).
2. Viana, R. et al. Rapid epidemic expansion of the SARS-CoV-2 Omicron variant in southern Africa. *Nature*, <https://doi.org/10.1038/s41586-022-04411-y> (2022).
3. Lu, L. et al. Neutralization of SARS-CoV-2 Omicron variant by sera from BNT162b2 or Coronavac vaccine recipients. *Clin. Infect. Dis.* <https://doi.org/10.1093/cid/ciab1041> (2021).
4. Harvey, W. T. et al. SARS-CoV-2 variants, spike mutations and immune escape. *Nat. Rev. Microbiol.* **19**, 409–424 (2021).
5. Tao, K. et al. The biological and clinical significance of emerging SARS-CoV-2 variants. *Nat. Rev. Genet.* **22**, 757–773 (2021).
6. Cele, S. et al. Escape of SARS-CoV-2 501Y.V2 from neutralization by convalescent plasma. *Nature* **593**, 142–146 (2021).
7. Keeton, R. et al. Prior infection with SARS-CoV-2 boosts and broadens Ad26.COV2.S immunogenicity in a variant-dependent manner. *Cell Host Microbe* **29**, 1611–1619.e1615 (2021).
8. Stamatatos, L. et al. mRNA vaccination boosts cross-variant neutralizing antibodies elicited by SARS-CoV-2 infection. *Science* **372**, 1413–1418 (2021).
9. Ebinger, J. E. et al. Antibody responses to the BNT162b2 mRNA vaccine in individuals previously infected with SARS-CoV-2. *Nat. Med.* **27**, 981–984 (2021).
10. Tegally, H. et al. Detection of a SARS-CoV-2 variant of concern in South Africa. *Nature* **592**, 438–443 (2021).
11. Garcia-Beltran, W. F. et al. Multiple SARS-CoV-2 variants escape neutralization by vaccine-induced humoral immunity. *Cell* **184**, 2372–2383.e2379 (2021).

12. Wibmer, C. K. et al. SARS-CoV-2 501Y.V2 escapes neutralization by South African COVID-19 donor plasma. *Nat. Med.* **27**, 622–625 (2021).
13. Zhou, D. et al. Evidence of escape of SARS-CoV-2 variant B.1.351 from natural and vaccine-induced sera. *Cell* **184**, 2348–2361.e2346 (2021).
14. Planas, D. et al. Sensitivity of infectious SARS-CoV-2 B.1.1.7 and B.1.351 variants to neutralizing antibodies. *Nat. Med.* **27**, 917–924 (2021).
15. Wang, P. et al. Antibody resistance of SARS-CoV-2 variants B.1.351 and B.1.1.7. *Nature* **593**, 130–135 (2021).
16. Wang, Z. et al. mRNA vaccine-elicited antibodies to SARS-CoV-2 and circulating variants. *Nature* **592**, 616–622 (2021).
17. Cromer, D. et al. Neutralising antibody titres as predictors of protection against SARS-CoV-2 variants and the impact of boosting: a meta-analysis. *Lancet Microbe* **3**, e52–e61 (2021).
18. Khoury, D. S. et al. Neutralizing antibody levels are highly predictive of immune protection from symptomatic SARS-CoV-2 infection. *Nat. Med.* **3**, 1205–1211 (2021).
19. Andrews, N. et al. Effectiveness of COVID-19 vaccines against the Omicron (B.1.1.529) variant of concern. Preprint at <https://doi.org/10.1101/2021.12.14.21267615> (2021).
20. Wilhelm, A. et al. Reduced neutralization of SARS-CoV-2 Omicron variant by vaccine sera and monoclonal antibodies. Preprint at <https://doi.org/10.1101/2021.12.07.21267432> (2021).
21. Garcia-Beltran, W. F. et al. mRNA-based COVID-19 vaccine boosters induce neutralizing immunity against SARS-CoV-2 Omicron variant. Preprint at <https://doi.org/10.1101/2021.12.14.21267615> (2021).
22. Rössler, A., Riepler, L., Bante, D., Laer, D. V. & Kimpel, J. SARS-CoV-2 B.1.1.529 variant (Omicron) evades neutralization by sera from vaccinated and convalescent individuals. Preprint at <https://doi.org/10.1101/2021.12.08.21267491> (2021).
23. Cao, Y. et al. Omicron escapes the majority of existing SARS-CoV-2 neutralizing antibodies. *Nature*, <https://doi.org/10.1038/s41586-021-04385-3> (2021).

24. Weisblum, Y. et al. Escape from neutralizing antibodies by SARS-CoV-2 spike protein variants. *eLife* **9**, e61312 (2020).
25. Goldberg, Y. et al. Waning immunity after the BNT162b2 vaccine in Israel. *N. Engl. J. Med.* **385**, e85 (2021).
26. Chemaitelly, H. et al. Waning of BNT162b2 vaccine protection against SARS-CoV-2 infection in Qatar. *N. Engl. J. Med.* **385**, e83 (2021).
27. Abdullah, F. et al. Decreased severity of disease during the first global Omicron variant COVID-19 outbreak in a large hospital in Tshwane, South Africa. *Int. J. Infect. Dis.* **116**, 38–42 (2022).
28. Cele, S. et al. SARS-CoV-2 evolved during advanced HIV disease immunosuppression has Beta-like escape of vaccine and Delta infection elicited immunity. Preprint at <https://doi.org/10.1101/2021.09.14.21263564> (2021).
29. Collie S., Champion J., Moultrie H., Bekker L. G. & Gray G. Effectiveness of BNT162b2 vaccine against Omicron variant in South Africa. *N. Engl. J. Med.* **386**, 494–496 (2022).
30. Sigal, A. et al. Variability and memory of protein levels in human cells. *Nature* **444**, 643–646 (2006).

## Acknowledgements

This study was supported by the Bill and Melinda Gates award INV-018944 (A.S.), National Institutes of Health award R01 AI138546 (A.S.), and South African Medical Research Council awards (A.S., T.d.O. and P.L.M.) and the UK Foreign, Commonwealth and Development Office and Wellcome Trust (grant no. 221003/Z/20/Z to P.L.M.). P.L.M. is also supported by the South African Research Chairs Initiative of the Department of Science and Innovation and the NRF (grant no. 98341). D.S.K., D.C. and M.P.D. are supported by NHMRC (Australia) Fellowship/Investigator grants. D.A. was supported by the European and Developing Countries Clinical Trials Partnership (EDCTP) Senior Fellowship (grant no. TMA2017SF-1960). The funders had no role in study design, data collection and analysis, decision to publish, or preparation of the manuscript.

## Author information

### Affiliations

1. Africa Health Research Institute, Durban, South Africa

Sandile Cele, Laurelle Jackson, Khadija Khan, Farina Karim, Mallory Bernstein, Yashica Ganga, Zesuliwe Jule, Kajal Reedoy, Shi-Hsia Hwa, Willem Hanekom, Kobus Herbst, Thandeka Khoza, Henrik Kløverpris, Alasdair Leslie, Mohlopheni Marakalala, Matilda Mazibuko, Ntombifuthi Mthabela, Zaza Ndhlovu, Thumbi Ndung'u, Nokuthula Ngcobo, Theresa Smit, Adrie Steyn, Emily Wong & Alex Sigal

2. School of Laboratory Medicine and Medical Sciences, University of KwaZulu-Natal, Durban, South Africa

Sandile Cele, Khadija Khan, Daniel G. Amoako, Farina Karim & Alex Sigal

3. Kirby Institute, University of New South Wales, Sydney, New South Wales, Australia

David S. Khoury, Deborah Cromer & Miles P. Davenport

4. National Institute for Communicable Diseases of the National Health Laboratory Service, Johannesburg, South Africa

Thandeka Moyo-Gwete, Cathrine Scheepers, Daniel G. Amoako, Constantinos Kurt Wibmer, Carolyn Williamson, Anne von Gottberg, Jinal N. Bhiman & Penny L. Moore

5. SA MRC Antibody Immunity Research Unit, School of Pathology, Faculty of Health Sciences, University of the Witwatersrand, Johannesburg, South Africa

Thandeka Moyo-Gwete, Cathrine Scheepers, Anne von Gottberg, Jinal N. Bhiman & Penny L. Moore

6. KwaZulu-Natal Research Innovation and Sequencing Platform, Durban, South Africa

Houriyyah Tegally, James Emmanuel San, Jennifer Giandhari, Richard J. Lessells & Tulio de Oliveira

7. Centre for Epidemic Response and Innovation, School of Data Science and Computational Thinking, Stellenbosch University, Stellenbosch, South Africa

Houriyyah Tegally & Tulio de Oliveira

8. Centre for the AIDS Programme of Research in South Africa, Durban, South Africa

Gila Lustig, Derseree Archary, Salim S. Abdool Karim, Kogie Naidoo, Richard J. Lessells, Tulio de Oliveira & Penny L. Moore

9. Department of Medical Microbiology, University of KwaZulu-Natal, Durban, South Africa

Derseree Archary

10. Department of Integrative Biomedical Sciences, Faculty of Health Sciences, University of Cape Town, Cape Town, South Africa

Muneerah Smith & Jonathan M. Blackburn

11. Division of Infection and Immunity, University College London, London, UK

Shi-Hsia Hwa, Willem Hanekom, Alasdair Leslie & Mohlopheni Marakalala

12. Institute of Infectious Disease and Molecular Medicine, University of Cape Town, Cape Town, South Africa

Jonathan M. Blackburn, Darren Martin, Carolyn Williamson & Penny L. Moore

13. Department of Infectious Diseases, Nelson R. Mandela School of Clinical Medicine, University of KwaZulu-Natal, Durban, South Africa

Bernadett I. Gosnell, Nithendra Manickchund & Mahomed-Yunus S. Moosa

14. Department of Epidemiology, Mailman School of Public Health, Columbia University, New York, NY, USA

Salim S. Abdool Karim

15. Department of Global Health, University of Washington, Seattle, WA, USA

Tulio de Oliveira

16. Max Planck Institute for Infection Biology, Berlin, Germany

Thumbi Ndung'u & Alex Sigal

17. Center for Infectious Disease Epidemiology and Research, School of Public Health and Family Medicine, University of Cape Town, Cape Town, South Africa

Mary-Ann Davies

18. University of Cape Town/Groote Schuur Complex of the National Health Laboratory Service (N HLS), University of Cape Town, Cape Town, South Africa

Marvin Hsiao

19. Division of Computational Biology, Department of Integrative Biomedical Sciences, University of Cape Town, Cape Town, South Africa

Darren Martin

20. Medical Microbiology Department, University of KwaZulu-Natal, Durban, South Africa

Koleka Mlisana

21. National Health Laboratory Services (N HLS), Durban, South Africa

Koleka Mlisana

22. Wellcome Centre for Infectious Diseases Research in Africa, University of Cape Town, Cape Town, South Africa

Carolyn Williamson

23. Molecular Diagnostics Services, Durban, South Africa

Denis York

24. Department of Neurosurgery, University of KwaZulu-Natal, Durban, South Africa

Rohen Harrichandparsad

25. South African Population Research Infrastructure Network, Durban, South Africa

Kobus Herbst

26. Department of Paediatrics and Child Health, University of KwaZulu-Natal, Durban, South Africa

Prakash Jeena

27. Department of Immunology and Microbiology, University of Copenhagen,  
Copenhagen, Denmark  
  
Henrik Kløverpris
28. Department of Cardiothoracic Surgery, University of KwaZulu-Natal, Durban,  
South Africa  
  
Rajhmun Madansein
29. Department of Medicine, King Edward VIII Hospital and University of KwaZulu  
Natal, Durban, South Africa  
  
Nombulelo Magula
30. College of Health Sciences, University of KwaZulu-Natal, Durban, South Africa  
  
Mosa Moshabela
31. Ragon Institute of MGH, MIT and Harvard, Boston, MA, USA  
  
Zaza Ndhlovu & Thumi Ndung'u
32. HIV Pathogenesis Programme, The Doris Duke Medical Research Institute,  
University of KwaZulu-Natal, Durban, South Africa  
  
Thumi Ndung'u
33. Department of Pulmonology and Critical Care, University of KwaZulu-Natal,  
Durban, South Africa  
  
Kennedy Nyamande
34. Department of Neurology, University of KwaZulu-Natal, Durban, South Africa  
  
Vinod Patel
35. Division of Infectious Diseases, University of Alabama at Birmingham,  
Birmingham, AL, USA  
  
Adrie Steyn & Emily Wong

## **Consortia**

## **NGS-SA**

- Mary-Ann Davies
- , Marvin Hsiao
- , Darren Martin
- , Koleka Mlisana
- , Constantinos Kurt Wibmer
- , Carolyn Williamson
- & Denis York

## **COMMIT-KZN Team**

- Rohen Harrichandparsad
- , Kobus Herbst
- , Prakash Jeena
- , Thandeka Khoza
- , Henrik Kløverpris
- , Alasdair Leslie
- , Rajhmun Madansein
- , Nombulelo Magula
- , Nithendra Manickchund
- , Mohlopheni Marakalala
- , Matilda Mazibuko
- , Mosa Moshabela
- , Ntombifuthi Mthabela
- , Kogie Naidoo
- , Zaza Ndhlovu
- , Thumbi Ndung'u
- , Nokuthula Ngcobo
- , Kennedy Nyamande
- , Vinod Patel
- , Theresa Smit
- , Adrie Steyn
- & Emily Wong

## **Contributions**

A.S., P.L.M. and T.d.O. and R.J.L. conceived the study. A.S., S.C., K.K., T.M.-G. and L.J. designed the study and experiments. A.v.G., P.L.M. and J.N.B. identified and provided the virus sample. S.-H.H. generated and provided plaque purified Beta variant virus. M.-Y.S.M., F.K., B.I.G., M.B., K.K. and Y.G. set up and managed the cohort and cohort data. S.C., L.J., K.K., T.M.-G., H.T., J.E.S., C.S., D.G.A., G.L.,

D.A., M.S., Y.G., Z.J. and K.R. performed experiments and sequence analysis with input from A.S., T.d.O., R.J.L. and J.M.B. D.S.K., D.C. and M.P.D. performed predictions of vaccine efficacy based on the data. A.S., S.C., P.L.M., T.d.O., L.J., K.K., W.H., S.S.A.K., D.S.K., M.P.D., J.N.B., R.J.L. and M.-Y.S.M. interpreted data. A.S., L.J., D.S.K., S.C., G.L., P.L.M. and M.P.D. prepared the manuscript with input from all authors.

## Corresponding author

Correspondence to [Alex Sigal](#).

## Ethics declarations

### Competing interests

Salim S. Abdool Karim is a member of the COVID advisory panel for emerging markets at Pfizer. The authors declare no other competing interests.

## Peer review

### Peer review information

*Nature* thanks the anonymous reviewer(s) for their contribution to the peer review of this work.

## Additional information

**Publisher's note** Springer Nature remains neutral with regard to jurisdictional claims in published maps and institutional affiliations.

## Extended data figures and tables

### [Extended Data Fig. 1 Generation of H1299-ACE2 clonal cell line.](#)

(A) The H1299 human non-small cell lung carcinoma cell line with YFP labelled histone H2AZ was spinfected with the pHAGE2-EF1a-Int-ACE2 lentivector. Cells were single cell cloned by limiting dilution in a 384-well plate. Clones were expanded into duplicate 96-well plates, where one plate was used to select infectable clones based on mCherry signal from infection with SARS-CoV-2 mCherry expressing spike pseudotyped lentivirus. Clones were chosen based on infectability and expanded from

the non-infected replicate 96-well plate. **(B)** Flow cytometry of SARS-CoV-2 mCherry expressing spike pseudotyped lentivirus infection in H1299-ACE2 cells versus H1299 parental cells.

### **Extended Data Fig. 2 Comparison of SARS-CoV-2 infection in H1299-ACE2 and Vero E6 cells.**

Both H1299-ACE2 and Vero E6 cells were infected with the same viral stock in the same experiment with D614G virus (**A**) or Beta virus (**B**) and a focus forming assay was performed. **(C)** Focus forming assay with stock of Omicron virus isolate on H1299-ACE2 and Vero E6 cells. **(D)** Comparison of passage 2 (P2) and passage 3 (P3) stock, where P3 stock was generated by infection of 1 mL of cell-free P2 stock in 20 mL of Vero E6 cells seeded at  $2 \times 10^5$  cells per mL and incubated over 4 days. Numbers above well images denote viral stock dilution. Scale bar is 2 mm.

### **Extended Data Fig. 3 Neutralization of the Beta variant by Pfizer BNT162b2 elicited immunity.**

Neutralization of the Beta variant virus compared to D614G ancestral virus in H1299-ACE2 (**A**) or Vero E6 cells (**B**) in participants vaccinated with BNT162b2 and infected by SARS-CoV-2 (green) or vaccinated only (orange). Numbers in black above each virus strain are geometric mean titers (GMT) of the reciprocal plasma dilution ( $\text{FRNT}_{50}$ ) resulting in 50% reduction in the number of infection foci. Numbers in red denote fold-change in GMT between virus strain on the left and the virus strain on the right of each panel. Red horizontal line denotes most concentrated plasma used. Samples were tested from the  $n = 19$  participants described in Table S2 and S3, where  $n = 6$  were vaccinated only and  $n = 13$  were vaccinated and previously infected.  $p = 0.006$  for both (A) and (B) as determined by the Wilcoxon rank sum test.

**Extended Data Table 1 Codon frequency table**

**Extended Data Table 2 Summary table of participants**

**Extended Data Table 3 Participant information per sample**

## **Supplementary information**

### **Reporting Summary**

### **Rights and permissions**

**Open Access** This article is licensed under a Creative Commons Attribution 4.0 International License, which permits use, sharing, adaptation, distribution and reproduction in any medium or format, as long as you give appropriate credit to the original author(s) and the source, provide a link to the Creative Commons license, and indicate if changes were made. The images or other third party material in this article are included in the article's Creative Commons license, unless indicated otherwise in a credit line to the material. If material is not included in the article's Creative Commons license and your intended use is not permitted by statutory regulation or exceeds the permitted use, you will need to obtain permission directly from the copyright holder. To view a copy of this license, visit <http://creativecommons.org/licenses/by/4.0/>.

### Reprints and Permissions

## About this article

### Cite this article

Cele, S., Jackson, L., Khoury, D.S. *et al.* Omicron extensively but incompletely escapes Pfizer BNT162b2 neutralization. *Nature* **602**, 654–656 (2022).  
<https://doi.org/10.1038/s41586-021-04387-1>

- Received: 14 December 2021
- Accepted: 23 December 2021
- Published: 23 December 2021
- Issue Date: 24 February 2022
- DOI: <https://doi.org/10.1038/s41586-021-04387-1>

### Share this article

Anyone you share the following link with will be able to read this content:

[Get shareable link](#)

Sorry, a shareable link is not currently available for this article.

[Copy to clipboard](#)

Provided by the Springer Nature SharedIt content-sharing initiative

## Further reading

- [Milder disease with Omicron: is it the virus or the pre-existing immunity?](#)
  - Alex Sigal

*Nature Reviews Immunology* (2022)
- [COVID reinfections surge during Omicron onslaught](#)
  - Smriti Mallapaty

*Nature* (2022)
- [Impaired detection of omicron by SARS-CoV-2 rapid antigen tests](#)
  - Andreas Osterman
  - Irina Badell
  - Oliver T. Keppler

*Medical Microbiology and Immunology* (2022)
- [Considerable escape of SARS-CoV-2 Omicron to antibody neutralization](#)
  - Delphine Planas
  - Nell Saunders
  - Olivier Schwartz

*Nature* (2022)
- [Activity of convalescent and vaccine serum against SARS-CoV-2 Omicron](#)
  - Juan Manuel Carreño
  - Hala Alshammary
  - Florian Krammer

*Nature* (2022)

This article was downloaded by **calibre** from <https://www.nature.com/articles/s41586-021-04387-1>

| [Section menu](#) | [Main menu](#) |

- Article
- Open Access
- [Published: 23 December 2021](#)

# Omicron escapes the majority of existing SARS-CoV-2 neutralizing antibodies

- [Yunlong Cao](#) [ORCID: orcid.org/0000-0001-5918-1078](#)<sup>1,2 na1</sup>,
- [Jing Wang](#) [ORCID: orcid.org/0000-0002-9084-9985](#)<sup>1,3 na1</sup>,
- [Fanchong Jian](#) [ORCID: orcid.org/0000-0001-8703-3507](#)<sup>1,4 na1</sup>,
- [Tianhe Xiao](#)<sup>1,5 na1</sup>,
- [Weiliang Song](#)<sup>1,3 na1</sup>,
- [Ayijiang Yisimayi](#)<sup>1,3 na1</sup>,
- [Weijin Huang](#) [ORCID: orcid.org/0000-0002-4246-8889](#)<sup>6 na1</sup>,
- [Qianqian Li](#)<sup>6</sup>,
- [Peng Wang](#)<sup>1</sup>,
- [Ran An](#)<sup>1</sup>,
- [Jing Wang](#)<sup>1</sup>,
- [Yao Wang](#)<sup>1</sup>,
- [Xiao Niu](#)<sup>1,4</sup>,
- [Sijie Yang](#)<sup>1,7</sup>,
- [Hui Liang](#)<sup>1</sup>,
- [Haiyan Sun](#)<sup>1</sup>,
- [Tao Li](#)<sup>6</sup>,
- [Yuanling Yu](#)<sup>6</sup>,
- [Qianqian Cui](#)<sup>6</sup>,
- [Shuo Liu](#)<sup>6</sup>,
- [Xiaodong Yang](#)<sup>8</sup>,
- [Shuo Du](#) [ORCID: orcid.org/0000-0003-0936-0785](#)<sup>3</sup>,
- [Zhiying Zhang](#) [ORCID: orcid.org/0000-0002-5690-9796](#)<sup>3</sup>,
- [Xiaohua Hao](#)<sup>9</sup>,
- [Fei Shao](#)<sup>1</sup>,
- [Ronghua Jin](#)<sup>9</sup>,
- [Xiangxi Wang](#) <sup>10</sup>,
- [Junyu Xiao](#) [ORCID: orcid.org/0000-0003-1822-1701](#)<sup>2,3</sup>,

- [Youchun Wang](#) [ORCID: orcid.org/0000-0001-9769-5141<sup>6</sup>](#) &
- [Xiaoliang Sunney Xie](#) [ORCID: orcid.org/0000-0001-9281-5239<sup>1,2</sup>](#)

*Nature* volume 602, pages 657–663 (2022)

- 13k Accesses
- 20 Citations
- 351 Altmetric
- [Metrics details](#)

## Subjects

- [High-throughput screening](#)
- [Infectious diseases](#)
- [SARS-CoV-2](#)

## Abstract

The SARS-CoV-2 B.1.1.529 (Omicron) variant contains 15 mutations of the receptor-binding domain (RBD). How Omicron evades RBD-targeted neutralizing antibodies requires immediate investigation. Here we use high-throughput yeast display screening<sup>1,2</sup> to determine the profiles of RBD escaping mutations for 247 human anti-RBD neutralizing antibodies and show that the neutralizing antibodies can be classified by unsupervised clustering into six epitope groups (A–F)—a grouping that is highly concordant with knowledge-based structural classifications<sup>3,4,5</sup>. Various single mutations of Omicron can impair neutralizing antibodies of different epitope groups. Specifically, neutralizing antibodies in groups A–D, the epitopes of which overlap with the ACE2-binding motif, are largely escaped by K417N, G446S, E484A and Q493R. Antibodies in group E (for example, S309)<sup>6</sup> and group F (for example, CR3022)<sup>7</sup>, which often exhibit broad sarbecovirus neutralizing activity, are less affected by Omicron, but a subset of neutralizing antibodies are still escaped by G339D, N440K and S371L. Furthermore, Omicron pseudovirus neutralization showed that neutralizing antibodies that sustained single mutations could also be escaped, owing to multiple synergistic mutations on their epitopes. In total, over 85% of the tested neutralizing antibodies were escaped by Omicron. With regard to neutralizing-antibody-based drugs, the neutralization potency of LY-CoV016, LY-CoV555, REGN10933, REGN10987, AZD1061, AZD8895 and BRII-196 was greatly undermined by Omicron, whereas VIR-7831 and DXP-604 still functioned at a reduced efficacy. Together, our data suggest that infection with Omicron would result

in considerable humoral immune evasion, and that neutralizing antibodies targeting the sarbecovirus conserved region will remain most effective. Our results inform the development of antibody-based drugs and vaccines against Omicron and future variants.

[Download PDF](#)

## Main

The SARS-CoV-2 variant B.1.1.529 was first reported to the World Health Organization (WHO) on 24 November 2021. It spread rapidly, and the WHO classified it as a variant of concern only two days after, designating it as Omicron<sup>8,9</sup>. An unusually large number of mutations are found in Omicron, including more than 30 in the spike protein (Extended Data Fig. 1a). The RBD, which is responsible for interacting with the angiotensin-converting enzyme 2 (ACE2) receptor, contains 15 of these mutations: G339D, S371L, S373P, S375F, K417N, N440K, G446S, S477N, T478K, E484A, Q493R, G496S, Q498R, N501Y and Y505H. Some of these mutations are very concerning because of their well-understood functional consequences. For example, K417N and N501Y contribute to immune escape and higher infectivity<sup>10,11,12,13</sup>. The functional effects of many other mutations still require investigation.

The spike protein is the target of essentially all neutralizing antibodies that are found in the sera of convalescent individuals or that are elicited by vaccines. Most of the N-terminal domain (NTD)-directed neutralizing antibodies target an antigenic ‘supersite’ in the NTD, which involves the N3 (residues 141–156) and N5 (residues 246–260) loops<sup>14,15</sup>; these antibodies are thus very susceptible to NTD mutations. Omicron carries the Δ143–145 mutation, which would alter the N3 loop and is likely to result in the immune escape of most anti-NTD neutralizing antibodies (Extended Data Fig. 1b). Compared to NTD-targeting neutralizing antibodies, RBD-targeting neutralizing antibodies are particularly abundant and potent, and display diverse epitopes. An evaluation of how Omicron affects the neutralization capability of anti-RBD neutralizing antibodies of diverse classes and epitopes is urgently needed.

RBD-directed SARS-CoV-2 neutralizing antibodies can be assigned into different classes or binding sites on the basis of structural analyses by cryo-electron microscopy or high-resolution crystallography<sup>3,4,5</sup>. However, analysis based on structural data only indicates the contacting amino acids, and does not enable the escaping mutations for a specific antibody to be identified. Advances in deep antigen mutation screening using a fluorescence-activated cell sorting (FACS)-based yeast display platform has allowed the quick mapping of all single-amino-acid mutations in the RBD that affect the binding of SARS-CoV-2 RBD neutralizing antibodies<sup>1,16</sup>. The method has proven

highly effective in predicting the efficacy of neutralizing antibody-based drugs towards mutations<sup>2</sup>. However, to study how human humoral immunity may react to highly mutated variants such as Omicron requires mutation profiling of a large collection of neutralizing antibodies that target different regions of the RBD, and mutation screening with the FACS-based yeast display method is limited by low experimental throughput. Here we developed a magnetic-activated cell sorting (MACS)-based screening method that increases the throughput by nearly 100-fold while obtaining a comparable data quality to FACS (Fig 1a, Extended Data Fig. 2). Using this method, we rapidly characterized the profile of RBD escaping mutations for a total of 247 neutralizing antibodies (Supplementary Data 1). Half of the neutralizing antibodies were part of the antibodies identified by us using single-cell V(D)J sequencing of antigen-specific memory B cells from individuals who had been infected with SARS-CoV-2 (hereafter, SARS-CoV-2 convalescent individuals); individuals who had been vaccinated against SARS-CoV-2; and individuals with a previous infection of SARS-CoV-1 (SARS-CoV-1 convalescent individuals) who had recently been vaccinated against SARS-CoV-2 (Supplementary Data 2). The other half of the neutralizing antibodies were identified by groups worldwide<sup>3,5,6,11,17,18,19,20,21,22,23,24,25,26,27,28,29,30,31,32,33,34,35,36,37,38,39,40</sup> (Supplementary Table 1).

**Fig. 1: Omicron greatly reduces the neutralization potency of neutralizing antibodies of diverse epitopes.**

---

 **figure 1**

**a**, Schematic of MACS-based high-throughput yeast display mutation screening. mAb, monoclonal antibody. **b**, Representative antibody structures of each epitope group. **c**, *t*-distributed stochastic neighbour embedding (*t*-SNE) and unsupervised clustering of SARS-CoV-2 human neutralizing antibodies on the basis of each antibody escaping mutation profile. A total of six epitope groups (groups A–F) could be defined. **d**, Neutralization of the Omicron variant (spike-pseudotyped VSV) by 247 RBD neutralizing antibodies. Shades of red show the fold change in IC<sub>50</sub> compared with D614G for each antibody. **e**, Neutralization of SARS-CoV-1 (spike-pseudotyped VSV) by 247 RBD neutralizing antibodies. Shades of red show the IC<sub>50</sub> value (μg ml<sup>-1</sup>) of each antibody. All pseudovirus neutralization assays were conducted in biological duplicates or triplicates.

The high-throughput screening capability allowed us to classify these neutralizing antibodies into six epitope groups (A–F) using unsupervised clustering without dependence on structural studies, and the grouping is highly concordant with knowledge-based structural classifications<sup>3,4,5</sup> (Fig. 1b, c). In particular, group A–D neutralizing antibodies largely correspond to the RBS A–D neutralizing antibodies described by Yuan et al.<sup>4</sup>, and overlap with the class 1–2 neutralizing antibodies described by Barnes et al.<sup>3</sup> in general. The epitopes of these neutralizing antibodies largely overlap with RBD residues that are involved in binding to ACE2. Group A and

B neutralizing antibodies, represented by LY-CoV016 and AZD8895, respectively, can usually only bind to the RBDs in the ‘up’ conformation, whereas most of the group C and D antibodies—such as LY-CoV555 and REGN-10987—bind to RBDs regardless of their ‘up’ and ‘down’ conformations. Group E and F neutralizing antibodies are very similar to the class 3 and 4 antibodies described by Barnes et al.<sup>3</sup>, and target the S309 (VIR-7831) site and CR3022 site, which could exhibit pan-sarbecovirus neutralization capacity (Fig 1e). Most of these neutralizing antibodies neutralize SARS-CoV-2 using mechanisms other than directly interfering with ACE2 binding.

Inferred from the escaping mutation profiles, various single mutations of Omicron could impair neutralizing antibodies of different epitope groups (Extended Data Fig. 3). Specifically, neutralizing antibodies in groups A–D, the epitopes of which overlap with the ACE2-binding motif, are largely escaped by the single mutations K417N, G446S, E484A, and Q493R. In addition, a subset of neutralizing antibodies of groups E and F are escaped by single mutations of G339D, N440K, S371L and S375F. However, owing to the extensive mutations accumulated on the RBD of Omicron, studying the response of neutralizing antibodies to Omicron only in the context of single mutations is insufficient. Indeed, Omicron pseudovirus neutralization and spike protein enzyme-linked immunosorbent assay (ELISA) showed that neutralizing antibodies that tolerate single mutations could also be escaped by Omicron owing to multiple synergetic mutations on their epitopes (Fig 1d, Extended Data Fig. 3). In total, over 85% of the tested human neutralizing antibodies are escaped, suggesting that Omicron could cause substantial humoral immune evasion and potential antigenic shifting.

It is crucial to analyse how each group of neutralizing antibodies reacts to Omicron to inform the development of drugs and vaccines that are based on these antibodies. Group A neutralizing antibodies mainly comprise antibodies that are encoded by the *VH3-53* and *VH3-66* (also known as *IGHV3-53* and *IGHV3-66*) germline genes; these are present at high levels in our present collection of SARS-CoV-2 neutralizing antibodies<sup>17,21,22,26,41,42,43</sup>, including several antibodies that have obtained emergency use authorization (CB6/LY-CoV016)<sup>19</sup> or that are currently being studied in clinical trials (P2C-1F11/BRII-196 and BD-604/DXP-604)<sup>18,44</sup> (Fig. 2a, Extended Data Fig. 4a). Group A neutralizing antibodies often exhibit fewer somatic mutations and have a shorter complementarity-determining region 3 (CDR3) length compared to other groups (Extended Data Fig. 5a,b). The epitopes of these antibodies extensively overlap with the binding site of ACE2 and are frequently evaded by RBD mutations at the K417, D420, F456, A475 and L455 sites (Fig 2d, Extended Data Figs. 6a, 7a). Most neutralizing antibodies in group A were already escaped by the B.1.351 (Beta) variant (Extended Data Fig. 5d); specifically, by the K417N mutation (Extended Data Fig. 8a), owing to a critical salt-bridge interaction between Lys417 and a negatively charged residue in the antibody (Fig. 2g). Neutralizing antibodies that survived the

Beta strain, such as BRII-196 and DXP-604, are insensitive to the K417N single-site change but could also be heavily affected by the combination of K417N and other RBD mutations located on their epitopes, such as S477N, Q493R, G496S, Q498R, N501Y and Y505H of Omicron, thus causing a loss or reduction of neutralization (Fig 2d, Extended Data Fig. 7a).

**Fig. 2: The neutralizing abilities of group A–C antibodies are mostly abolished by Omicron.**

 figure 2

**a–c**, Escaping mutation profiles of representative neutralizing antibodies for group A (a), B (b) and C (c). For each site, the height of a letter indicates the detected mutation escape score of its corresponding residue. Sites mutated in Omicron are highlighted.  
**d–f**, Heat maps of site escape scores for neutralizing antibodies of epitope group A (d), B (e) and C (f). ACE2 interface residues are annotated with red blocks, and mutated sites in Omicron are marked in red. Annotations on the right side of heat maps

represent the pseudovirus neutralizing IC<sub>50</sub> fold change (FC) for Omicron and Beta compared to D614G. **g–i**, Representative structures of group A (**g**), group B (**h**) and group C (**i**) antibodies in complex with the RBD. Residues that are involved in important contacts are labelled. Omicron mutations are marked in blue. Antibody escaping mutations (Omicron) inferred from yeast display are labelled with squares.

The neutralizing antibodies encoded by *VHI-58* (*IGHV1-58*) are enriched in group B (Extended Data Fig. [4b](#)). These antibodies—for example, AZD8895 (ref. [36](#)), REGN-10933 (ref. [42](#)) and BD-836 (ref. [45](#))—bind to the left shoulder of the RBD, often focusing on the far tip (Fig. [2h](#)). These neutralizing antibodies are very sensitive to the changes at the F486, N487 and G476 sites (Fig [2b](#), Extended Data Fig. [6b](#)). However, F486 and a few other major targeting sites of these neutralizing antibodies are critically involved in ACE2 binding, and therefore they are generally more difficult to escape. A subset of neutralizing antibodies in group B, such as AZD8895 and BD-836, could survive the Beta variant (Fig [2e](#)); however, Omicron significantly reduced the binding affinity of group B neutralizing antibodies to the RBD, potentially as a result of S477N/T478K/E484A on their epitope<sup>46</sup> (Extended Data Fig. [7b](#)), resulting in the loss of neutralization.

Group C neutralizing antibodies are frequently encoded by *VHI-2* and *VHI-69* (*IGHV1-2* and *IGHV1-69*) (Extended Data Fig. [4c](#)). Most antibodies in this group could bind to both ‘up’ and ‘down’ RBDs, resulting in higher neutralization potency compared to other groups (Fig. [2c](#), Extended Data Fig. [5c](#)). Several highly potent antibodies are found in group C, including BD-368-2/DXP-593 (ref. [44](#)), C002 (ref. [3](#)) and LY-CoV555 (ref. [47](#)). They bind to the right shoulder of the RBD (Fig. [2i](#)), and are mostly susceptible to changes at E484 (Extended Data Figs. [6c](#), [7c](#)), such as the E484K mutation found in Beta (Fig. [2f](#)). The E484A mutation that is seen in Omicron elicited a similar escaping effect, although the change to alanine is slightly subtler, and could be tolerated by certain antibodies in this group (Extended Data Fig. [8b](#)). All group C neutralizing antibodies tested are escaped by Omicron.

Group D neutralizing antibodies consist of diverse IGHV gene-encoded antibodies (Extended Data Fig. [4d](#)). Prominent members in this group include REGN-10987 (ref. [42](#)) and AZD1061 (ref. [36](#)) (Fig. [3a](#)). They further rotate down from the RBD right shoulder towards the S309 site when compared to group C antibodies (Fig. [3g](#)). As a loop formed by residues 440–449 in the RBD is critical for the targeting of this group of antibodies, they are sensitive to changes at N440, K444, G446 and N448 (Extended Data Figs. [6d](#), [7d](#)). Most neutralizing antibodies in group D remain active against Beta; however, G446S would substantially affect their neutralization capability against Omicron (Fig. [3d](#)). Also, for those antibodies that could tolerate a G446S single mutation, the N440K/G446S combination may considerably reduce their binding affinity, with the result that most group D antibodies are escaped by Omicron.

**Fig. 3: Most group D and E neutralizing antibodies are escaped by Omicron.**

 figure 3



**a–c**, Escaping mutation profiles of representative neutralizing antibodies for groups D (**a**), E (**b**) and F (**c**). For each site, the height of a letter indicates the detected mutation escape score of its corresponding residue. Sites mutated in Omicron are highlighted. **d–f**, Heat maps of site escape scores for neutralizing antibodies of epitope groups D (**d**), E (**e**) and F (**f**). ACE2 interface residues are annotated with red blocks, and mutated sites in Omicron are marked in red. Annotations on the right side of heat maps represent the pseudovirus neutralizing IC<sub>50</sub> fold change (FC) for Omicron and Beta compared to D614G. **g–j**, Representative structures of group D (**g**), E (**h**) and F (**i, j**) antibodies in complex with the RBD. Residues that are involved in important contacts are labelled. Omicron mutations are marked in blue. Antibody escaping mutations (Omicron) inferred from yeast display are labelled with squares.

Group E and F neutralizing antibodies are rarer when compared to the other four groups. The archetypal member of each group was originally isolated from a SARS-

CoV-1 convalescent individual, and exhibits SARS-CoV-2 cross-neutralizing activity. There is no clear V(D)J convergent effect compared to groups A, B and C (Extended Data Fig. 4e,f), and the mutation rate and CDR3 length are larger than other groups. Neutralizing antibodies in groups E and F rarely compete with ACE2; thus, their average half-maximal inhibitory concentration ( $IC_{50}$ ) is higher than that of antibodies in groups A–D (Extended Data Fig. 5c). Neutralizing antibodies in group E—such as VIR-7831/S309—may recognize a mixed protein and carbohydrate epitope that involves the *N*-linked glycan on N343 (ref. 6) (Fig. 3h). Inferred from the escaping mutation profiles (Fig. 3b), group E antibodies are often sensitive to changes at G339, T345 and R346 (Extended Data Figs. 6e, 7e). The G339D mutation would affect the neutralization performance of a subset of neutralizing antibodies (Fig. 3e). Also, part of the epitope of group E antibodies would extend to the 440–449 loop, rendering them sensitive to the N440K mutation in Omicron (Fig. 3e). Notably, the frequency of Omicron with the R346K mutation is continuously increasing, which may severely affect the neutralization capacity of group E antibodies.

Group F neutralizing antibodies (for example, S304) target a cryptic site in the RBD that is generally not exposed (Fig. 3i), and therefore their neutralizing activities are generally weaker<sup>7</sup>. Group F antibodies are often sensitive to changes at F374, T376 and K378 (Extended Data Figs. 6f, 7f). A loop involving the RBD residues 371–375 lies in the ridge between the E and F sites; thus, a subset of group F antibodies—including some group E antibodies—could be affected by the S371L/S373P/S375F mutations if their epitopes extend to this region (Fig. 3c,f). Of note, some group F antibodies are highly sensitive to V503 and G504, similar to the epitopes of S2X259 (Fig. 3f,j), suggesting that they can compete with ACE2. Indeed, several neutralizing antibodies, such as BD55-5300 and BD55-3372, exhibit higher neutralization potency than other antibodies in group F (Figs. 3c, 4b). However, the neutralization capability of these antibodies might be undermined by N501Y and Y505H in Omicron (Fig. 3j).

**Fig. 4: Omicron escapes most neutralizing-antibody-based drugs.**

---

 **figure 4**

**a**, Neutralization of SARS-CoV-2 variants of concern (pseudotyped VSV) by nine neutralizing-antibody-based drugs. The pseudovirus neutralization assays for every VOC were performed in biological triplicates. The IC<sub>50</sub> values shown are the average of three replicates shown in Extended Data Fig. 9. **b**, The sarbecovirus neutralization and binding capability (half-maximal effective concentration, EC<sub>50</sub>) of selected potent Omicron-neutralizing antibodies. The monoclonal antibody HG1K (IgG1 antibody against influenza A virus subtype H7N9) was used as the negative control.

With regard to drugs based on neutralizing antibodies, consistent with their escaping mutation profiles, the neutralization potency of LY-CoV016, LY-CoV555, REGN-10933, REGN-10987 and AZD1061 are greatly reduced by Omicron (Fig. 4a, Extended Data Fig. 9). The binding affinities of AZD8895 and BRII-196 towards the Omicron RBD are also largely reduced, probably owing to multiple mutations accumulating on the epitopes of these antibodies, such that AZD8895 and BRII-196 did not neutralize Omicron (Extended Data Fig. 10). BRII-198 was not tested as the antibody sequence was not released. VIR-7831 retains strong RBD-binding capability; although G339 is part of its epitope, the G339D mutation in Omicron does not appear to affect the binding of VIR-7831. However, the IC<sub>50</sub> of VIR-7831 is reduced to 181 ng ml<sup>-1</sup>, and may be subject to further reduction against Omicron with R346K. The binding affinity of DXP-604 against the Omicron RBD is markedly reduced compared to the wild-type RBD; nonetheless, it can still neutralize Omicron at an IC<sub>50</sub> of 287 ng ml<sup>-1</sup>—a reduction of nearly 30-fold compared to wild type (Fig. 4a). In addition, several neutralizing antibodies in groups E and F have shown high potency against Omicron and broad pan-sarbecovirus neutralization ability, suggesting that they have promise for the development of neutralizing-antibody-based drugs (Fig. 4b). Many more neutralizing antibodies identified from SARS-CoV-1 convalescent individuals who have been vaccinated are waiting to be characterized.

The high-throughput yeast screening method provides a laboratory means for quickly examining the epitope of a certain neutralizing antibody; however, the throughput that can be achieved using FACS is limited and cannot be used to evaluate a large library of antibodies. Using MACS, we were able to increase the throughput by two orders of magnitude. In doing so, we were able to gain statistical confidence for the survival proportion of anti-RBD neutralizing antibodies in each epitope group against Omicron. The experimental accuracy for predicting the neutralization reduction for single-amino-acid mutations is relatively high (Extended Data Fig. 8a, b); however, mutation screening through yeast display is not at present able to effectively examine the consequences of multiple mutations simultaneously, and this will require further technical optimization.

So far, a large number of SARS-CoV-2 anti-RBD neutralizing antibodies have been identified from SARS-CoV-2 convalescent individuals and from individuals who have been vaccinated. The most potent antibodies are frequently found in groups A–D, which tend to directly interfere with the binding of ACE2. Nevertheless, the neutralizing powers of these antibodies are often abrogated by RBD mutations in the evolutionary arms race between SARS-CoV-2 and human humoral immunity. Indeed, we showed that Omicron would escape most of the SARS-CoV-2 neutralizing antibodies in this collection (Extended Data Fig. 5e). On the other hand, group E and F antibodies are less affected by Omicron, probably because they are not abundant in the population<sup>48</sup> and hence exert less evolutionary pressure for RBD to mutate in the corresponding epitope groups. These neutralizing antibodies target conserved RBD regions in sarbecovirus and are therefore ideal targets for the future development of pan-sarbecovirus antibody-based drugs.

## Methods

### Isolation of human peripheral blood mononuclear cells

SARS-CoV-2 convalescent individuals, SARS-CoV-1 convalescent individuals and individuals who had been vaccinated against SARS-CoV-2 were recruited on the basis of previous SARS-CoV-2 infection or SARS-CoV-1 infection at Beijing Youan and Ditan hospitals. Relevant experiments regarding SARS-CoV-2 convalescent individuals and vaccinated individuals were approved by the Beijing Youan Hospital Research Ethics Committee (ethics committee archiving no. LL-2020-010-K).

Relevant experiments regarding SARS-CoV-1 convalescent individuals were approved by the Beijing Ditan Hospital Capital Medical University (ethics committee archiving no. LL-2021-024-02). All participants provided written informed consent for the collection of information, and for their clinical samples to be stored and used for research. It was agreed that data generated from the research were to be published. Detailed information on SARS-CoV-2 convalescent individuals and vaccinated

individuals has been published previously<sup>11</sup>. In brief, blood samples from short-term convalescent individuals were obtained at day 62 on average after the onset of symptoms. Blood samples from long-term convalescent individuals were obtained at day 371 on average after the onset of symptoms. No vaccination was received before blood collection. Blood samples from individuals who had been vaccinated against SARS-CoV-2 were obtained two weeks after complete vaccination of ZF2001 (RBD-subunit vaccine). For SARS-CoV-1 convalescent individuals who received SARS-CoV-2 vaccines (average age 58,  $n = 21$ ), all recruited participants were previously identified for SARS-CoV-1 infection in 2003, and received a two-dose vaccination of CoronaVac and a booster dose of ZF2001 with a 180-day interval. Blood samples (20 ml) from the SARS-CoV-1 convalescent individuals who were vaccinated against SARS-CoV-2 were obtained two weeks after the booster shot. Three healthy vaccinated donors (average age 25) were also included to serve as negative control for FACS gating. Peripheral blood mononuclear cells (PBMCs) were separated from whole-blood samples based on the detailed protocol described previously<sup>11</sup>. In brief, blood samples were first diluted with 2% fetal bovine serum (FBS) (Gibco) in phosphate buffered saline (PBS) (Invitrogen) and subjected to Ficoll (Cytiva) gradient centrifugation. After red blood cell lysis and washing steps, PBMCs were resuspended with 2% FBS in PBS for downstream B cell isolation or 10% dimethyl sulfoxide (Sigma-Aldrich) in FBS for further preservation.

## Antigen-specific B cell sorting and sequencing

Starting with freshly isolated or thawed PBMCs, B cells were enriched by positive selection using a CD19<sup>+</sup> B cell isolation kit according to the manufacturer's instructions (STEMCELL). The enriched B cells were stained in FACS buffer (1× PBS, 2% FBS, 1 mM EDTA) with the following anti-human antibodies and antigens: For every 10<sup>6</sup> cells, 3 µl FITC anti-CD19 antibody (Biolegend, 392508), 3 µl FITC anti-CD20 antibody (Biolegend, 302304), 3.5 µl Brilliant Violet 421 anti-CD27 antibody (Biolegend, 302824), 3 µl PE/Cyanine7 anti-IgM(Biolegend, 314532), and fluorophore-labelled RBD and ovalbumin (Ova) for 30 min on ice. Cells were stained with 5 µl 7-AAD (eBioscience, 00-6993-50) for 10 min before sorting. Biotinylated RBD of SARS-CoV-1 (Sino Biological, 40634-V27H-B) or SARS-CoV-2 (Sino Biological, 40592-V27H-B) were multimerized with fluorescently labelled streptavidin (SA) for 1 h at 4 °C. RBD was mixed with SA-PE (Biolegend, 405204) and SA-APC (Biolegend, 405207) at a 4:1 molar ratio. For every 10<sup>6</sup> cells, 6 ng SA was used to stain. Single CD19 or CD20<sup>+</sup> CD27<sup>+</sup>IgM<sup>-</sup>Ova<sup>-</sup>RBD-PE<sup>+</sup>RBD-APC<sup>+</sup> live B cells were sorted on an Astrios EQ (BeckMan Coulter) into PBS containing 30% FBS (Supplementary Data 2). FACS sorting was controlled by Summit 6.0 (Beckman Coulter). FACS data analyses were done by FlowJo v.10.8. Cells obtained after FACS were sent for 5'-mRNA and V(D)J library preparation as previously described<sup>11</sup>,

which were further submitted for Illumina sequencing on a Hiseq 2500 platform, with the 26×91 paired-end reading mode.

## V(D)J sequence data analysis

The raw FASTQ files were processed by Cell Ranger (v.6.1.1) pipeline using GRCh38 reference. Sequences were generated using ‘cellranger multi’ or ‘cellranger vdj’ with default parameters. Antibody sequences were processed by IMGT/DomainGapAlign (v.4.10.2) to obtain the annotations of V(D)J, regions of complementarity determining regions (CDRs), and the mutation frequency<sup>49,50</sup>. The mutation count divided by the length of the V gene peptide is defined as the amino acid mutation rate of the V gene.

## Recombinant antibody production

Paired immunoglobulin heavy and light chain genes obtained from 10X Genomics V(D)J sequencing and analysis were submitted to recombinant monoclonal antibody synthesis. In brief, heavy and light genes were cloned into expression vectors, respectively, based on Gibson assembly, and subsequently co-transfected into HEK293F cells (Thermo Fisher Scientific, R79007). The secreted monoclonal antibodies from cultured cells were purified by protein A affinity chromatography. The specificities of these antibodies were determined by ELISA.

## ELISA

ELISA plates were coated with RBD (SARS-CoV-2 wild type, SARS-CoV-2 Omicron, SARS-CoV-1 RBD, Sino Biological) at 0.03 µg ml<sup>-1</sup> and 1 µg ml<sup>-1</sup> in PBS at 4 °C overnight. After standard washing and blocking, 100 µl of 1 µg ml<sup>-1</sup> antibodies were added to each well. After a 2-h incubation at room temperature, plates were washed and incubated with 0.08 µg ml<sup>-1</sup> goat anti-human IgG (H+L)/HRP (Jackson, 109-035-003) for 1 h incubation at room temperature. Tetramethylbenzidine (TMB) (Solarbio) was then added, and the reaction was stopped by adding H<sub>2</sub>SO<sub>4</sub>. Optical density at 450 nm (OD<sub>450</sub>) was measured by an ELISA microplate reader. An antibody is defined as ELISA-positive when the OD<sub>450</sub> (1 µg ml<sup>-1</sup> RBD) is three times larger than the negative control, which uses an H7N9-specific human IgG1 antibody (HG1K, Sino Biological).

## Pseudovirus neutralization assay

A pseudovirus neutralization assay was performed to evaluate the neutralizing ability of antibodies. The detailed process has been previously described<sup>12</sup>. In brief, serially diluted antibodies were first incubated with pseudotyped virus for 1 h, and the mixture

was then incubated with Huh-7 cells. After a 24-h incubation in an incubator at 37 °C, cells were collected and lysed with luciferase substrate (PerkinElmer), then underwent luminescence intensity measurement by a microplate reader. IC<sub>50</sub> was determined by a four-parameter non-linear regression model using PRISM (v.9.0.1). Omicron pseudovirus contains the following mutations: A67V, H69del, V70del, T95I, G142D, V143del, Y144del, Y145del, N211del, L212I, ins214EPE, G339D, S371L, S373P, S375F, K417N, N440K, G446S, S477N, T478K, E484A, Q493R, G496S, Q498R, N501Y, Y505H, T547K, D614G, H655Y, N679K, P681H, N764K, D796Y, N856K, Q954H, N969K and L981F.

## Biolayer interferometry

Biolayer interferometry (BLI) assays were conducted on an Octet R8 Protein Analysis System (ForteBio) following the manufacturer's instructions. In brief, after baseline calibration, Protein A biosensors (ForteBio) were immersed with antibodies to capture the antibody, then sensors were immersed in PBS with 0.05% Tween-20 to the baseline. After association with different concentrations of RBD of SARS-CoV-2 variants (Omicron RBD: 40592-V08H85), disassociation was conducted. Data were recorded using Octet BLI Discovery (12.2) and analysed using Octet BLI Analysis (12.2).

## Construction of RBD deep mutational scanning library

The yeast display RBD mutant libraries used here were constructed as described previously<sup>12</sup>, on the basis of the spike RBD from SARS-CoV-2 (NCBI GenBank: MN908947, residues N331–T531) with the modification that instead of a 16-nucleotide barcode (N16), a unique 26-nucleotide (N26), barcode was appended to each RBD variant as an identifier, to decrease sequencing cost by eliminating the use of PhiX. In brief, three rounds of mutagenesis PCR were performed with designed and synthesized mutagenetic primer pools; to support our conclusions, we constructed two RBD mutant libraries independently. RBD mutant libraries were then cloned into the pETcon 2649 vector and the assembled products were electroporated into electrocompetent DH10B cells to enlarge the plasmid yield. Plasmid extracted form *Escherichia coli* were transformed into the EBY100 strain of *Saccharomyces cerevisiae* using the method described in a previous report<sup>51</sup>. Transformed yeast populations were screened on SD-CAA selective plate and further cultured in SD-CAA liquid medium at a large scale. The resulted yeast libraries were flash-frozen by liquid nitrogen and preserved at –80 °C.

## PacBio library preparation, sequencing and analysis

The correspondence of RBD gene sequence in mutant library and N26 barcode was obtained by PacBio sequencing. First, the bacterially extracted plasmid pools were digested by NotI restriction enzyme and purified by agarose gel electrophoresis, then SMRTbell ligation was performed. Four RBD mutant libraries were sequenced in one SMRT cell on a PacBio Sequel II platform. PacBio SMRT sequencing subreads were converted to HiFi ccs reads with pbccs, and then processed with a slightly modified version of the script previously described<sup>12</sup> to generate the barcode-variant dictionary. To reduce noise, variants that contained stop codons or that were supported by only one ccs read were removed from the dictionary and ignored during further analysis.

## MACS-based profiling of escape mutations

ACE2-binding mutants were sorted using magnetic beads to eliminate non-functional RBD variants. In brief, the biotin binder beads (Thermo Fisher Scientific) were washed and prepared as per the manufacturer's instructions and incubated with biotinylated ACE2 protein (Sino Biological) at room temperature with mild rotation. The ACE2-bound beads were washed twice and resuspended with 0.1% BSA buffer (PBS supplemented with 0.1% bovine serum albumin), ready for ACE2 positive selection. Transformed yeast libraries were inoculated into SD-CAA and grown at 30 °C with shaking for 16–18 h, then back-diluted into SG-CAA at 23 °C with shaking to induce RBD surface expression. Yeasts were collected and washed twice with 0.1% BSA buffer and incubated with the aforementioned ACE2-bound beads at room temperature for 30 min with mild rotating. Then, the bead-bound cells were washed, resuspended with SD-CAA medium and grown at 30 °C with shaking. After overnight growth, the bead-unbound yeasts were separated with a magnet and cultured on a large scale. The above ACE2-positive selected yeast libraries were preserved at –80 °C in aliquots as a seed bank for antibody escape mapping.

One aliquot of the ACE2-positive selected RBD library was thawed and inoculated into SD-CAA, then grown at 30 °C with shaking for 16–18 h. 120 OD units were back-diluted into SG-CAA medium and induced for RBD surface expression. Two rounds of sequential negative selection to sort yeast cells that escape Protein A conjugated antibody binding were performed according to the manufacturer's protocol. In brief, Protein A magnetic beads (Thermo Fisher Scientific) were washed and resuspended in PBST (PBS with 0.02% Tween-20). Then beads were incubated with neutralizing antibody and rotated at room temperature for 30 min. The antibody-conjugated beads were washed and resuspended in PBST. Induced yeast libraries were washed and incubated with antibody-conjugated beads for 30 min at room temperature with agitation. The supernatant was separated and underwent a second round of negative selection to ensure full depletion of antibody-binding yeast.

To eliminate yeast that did not express RBD, MYC-tag-based RBD positive selection was conducted according to the manufacturer's protocol. First, anti-c-Myc magnetic beads (Thermo Fisher Scientific) were washed and resuspended with 1× TBST (TBS with Tween-20), then the prepared beads were incubated for 30 min with the antibody-escaping yeasts after two rounds of negative selection. Yeasts bound by anti-c-Myc magnetic beads were washed with 1× TBST and grown overnight in SD-CAA to expand the yeast population before plasmid extraction.

Overnight cultures of MACS-sorted antibody-escaped and ACE2-preselected yeast populations were passed on to a yeast plasmid extraction kit (Zymo Research). PCRs were performed to amplify the N26 barcode sequences as previously described<sup>13</sup>. The PCR products were purified with 0.9X Ampure XP beads (Beckman Coulter) and submitted to 75-bp single-end Illumina Nextseq 500 sequencing.

## Processing of deep mutational scanning data

Raw single-end Illumina sequencing reads were trimmed and aligned to the reference barcode-variant dictionary generated as described above to get the count of each variant with the dms\_variants Python package (v.0.8.9). For libraries with N26 barcodes, we slightly modified the illuminabarcodeparser class of this package to tolerate one low sequencing quality base in the barcode region. The escape score of variant X is defined as  $F \times (n_{X,ab}/N_{ab})/(n_{X,ref}/N_{ref})$ , in which  $n_{X,ab}$  and  $n_{X,ref}$  are the number of detected barcodes for variant X, and  $N_{ab}$  and  $N_{ref}$  are the total number of barcodes in the antibody-selected (ab) library and the reference (ref) library, respectively, as described previously<sup>12</sup>. Different to FACS experiments, as we couldn't measure the number of cells retained after MACS selection precisely, here  $F$  is considered as a scaling factor to transform raw escape fraction ratios to the 0–1 range, and is calculated from the first and 99th percentiles of raw escape fraction ratios. Scores less than the first percentile or larger than the 99th percentile are considered to be outliers and set to zero or one, respectively. For each experiment, barcodes detected by fewer than 6 reads in the reference library were removed to reduce the effect of sampling noise, and variants with ACE2 binding below -2.35 or RBD expression below -1 were removed as previously described<sup>12</sup>. Finally, we built global epistasis models with the dms\_variants package for each library to estimate single mutation escape scores, using the Python scripts provided in a previous report<sup>16</sup>. To reduce experimental noise, a site was retained for further analysis only if its total escape score was at least 0.01, and at least 3 times greater than the median score of all sites. For antibodies measured by two independent experiments, only sites that passed the filter in both experiments were retained. Logo plots in Figs. 2, 3, Extended Data Fig. 2 and Supplementary Data 1 are generated by the Python package logomaker (v.0.8).

## Antibody clustering

Antibody clustering and epitope group identification were performed on the basis of the  $N \times M$  escape score matrix, in which  $N$  is the number of antibodies that pass the quality controlling filters, and  $M$  is the number of informative sites on the SARS-CoV-2 RBD. Each entry of the matrix  $A_{nm}$  refers to the total escape score of all kinds of mutations on site  $m$  of antibody  $n$ . The dissimilarity between two antibodies is defined on the basis of the Pearson's correlation coefficient of their escape score vectors; that is,  $D_{ij} = 1 - \text{Corr}(\mathbf{A}_i, \mathbf{A}_j)$ , in which  $\text{Corr}(\mathbf{A}_i, \mathbf{A}_j) = \mathbf{x}_i \cdot \mathbf{x}_j / (\|\mathbf{x}_i\| \|\mathbf{x}_j\|)$  and vector  $\mathbf{x}_i = \mathbf{A}_i - \text{Mean}(\mathbf{A}_i)$ . Sites with at least six escaped antibodies (site escape score > 1) were considered informative and selected for dimensionality reduction and clustering. We used the R function cmdscale to convert the cleaned escape matrix into an  $N \times 6$  feature matrix by multidimensional scaling (MDS) with the dissimilarity metric described above, followed by unsupervised  $k$ -medoids clustering within this 6-dimensional antibody feature space, using the pam function of the R package cluster (v.2.1.1). Finally, two-dimensional t-SNE embeddings were generated with the Rtsne package (v.0.15) for visualization. Two-dimensional t-SNE plots are generated by ggplot2 (v.3.3.3), and heat maps are generated by the ComplexHeatmap package (v.2.6.2).

## Reporting summary

Further information on research design is available in the [Nature Research Reporting Summary](#) linked to this paper.

## Data availability

Processed escape maps for neutralizing antibodies are available in Supplementary Data 1 (as figures) or at <https://github.com/sunneyxielab/SARS-CoV-2-RBD-Abs-HTDMS> (as mutation escape score data). Raw Illumina and PacBio sequencing data are available through the NCBI Sequence Read Archive BioProject (accession number [PRJNA787091](#)). We used vdj\_GRCh38\_alts\_ensembl-5.0.0 as the reference for V(D)J alignment, which can be obtained from <https://support.10xgenomics.com/single-cell-vdj/software/downloads/latest>. IMGT/DomainGapAlign is based on the built-in latest IMGT antibody database, and we left the 'Species' parameter as '*Homo sapiens*' and kept the others as default. FACS-based deep mutational scanning datasets can be downloaded from [https://media.githubusercontent.com/media/jbloomlab/SARS2\\_RBD\\_Ab\\_escape\\_maps/main/processed\\_data/escape\\_data.csv](https://media.githubusercontent.com/media/jbloomlab/SARS2_RBD_Ab_escape_maps/main/processed_data/escape_data.csv). Processed data from this study have also been added to this repository.

## Code availability

Scripts for analysing SARS-CoV-2 escaping mutation profile data and for reproducing figures in this paper are available at <https://github.com/sunneyxielab/SARS-CoV-2-RBD-Abs-HTDMS>.

## References

1. Starr, T. N. et al. Prospective mapping of viral mutations that escape antibodies used to treat COVID-19. *Science* **371**, 850–854 (2021).
2. Starr, T. N., Greaney, A. J., Dingens, A. S. & Bloom, J. D. Complete map of SARS-CoV-2 RBD mutations that escape the monoclonal antibody LY-CoV555 and its cocktail with LY-CoV016. *Cell Rep. Med.* **2**, 100255 (2021).
3. Barnes, C. O. et al. SARS-CoV-2 neutralizing antibody structures inform therapeutic strategies. *Nature* **588**, 682–687 (2020).
4. Yuan, M. et al. Structural and functional ramifications of antigenic drift in recent SARS-CoV-2 variants. *Science* **373**, 818–823 (2021).
5. Dejnirattisai, W. et al. The antigenic anatomy of SARS-CoV-2 receptor binding domain. *Cell* **184**, 2183–2200 (2021).
6. Pinto, D. et al. Cross-neutralization of SARS-CoV-2 by a human monoclonal SARS-CoV antibody. *Nature* **583**, 290–295 (2020).
7. Yuan, M. et al. A highly conserved cryptic epitope in the receptor binding domains of SARS-CoV-2 and SARS-CoV. *Science* **368**, 630–633 (2020).
8. Callaway, E. Heavily mutated Omicron variant puts scientists on alert. *Nature* **600**, 21 (2021).
9. Callaway, E. & Ledford, H. How bad is Omicron? What scientists know so far. *Nature* **600**, 97–199 (2021).
10. Li, Q. et al. SARS-CoV-2 501Y.V2 variants lack higher infectivity but do have immune escape. *Cell* **184**, 2362–2371 (2021).
11. Cao, Y. et al. Humoral immune response to circulating SARS-CoV-2 variants elicited by inactivated and RBD-subunit vaccines. *Cell Res.* **31**, 732–741 (2021).

12. Starr, T. N. et al. Deep mutational scanning of SARS-CoV-2 receptor binding domain reveals constraints on folding and ACE2 binding. *Cell* **182**, 1295–1310 (2020).
13. Gu, H. et al. Adaptation of SARS-CoV-2 in BALB/c mice for testing vaccine efficacy. *Science* **369**, 1603–1607 (2020).
14. Cerutti, G. et al. Potent SARS-CoV-2 neutralizing antibodies directed against spike N-terminal domain target a single supersite. *Cell Host Microbe* **29**, 819–833 (2021).
15. McCallum, M. et al. N-terminal domain antigenic mapping reveals a site of vulnerability for SARS-CoV-2. *Cell* **184**, 2332–2347 (2021).
16. Greaney, A. J. et al. Complete mapping of mutations to the SARS-CoV-2 spike receptor-binding domain that escape antibody recognition. *Cell Host Microbe* **29**, 44–57 (2021).
17. Cao, Y. et al. Potent neutralizing antibodies against SARS-CoV-2 identified by high-throughput single-cell sequencing of convalescent patients' B cells. *Cell* **182**, 73–84 (2020).
18. Ju, B. et al. Human neutralizing antibodies elicited by SARS-CoV-2 infection. *Nature* **584**, 115–119 (2020).
19. Shi, R. et al. A human neutralizing antibody targets the receptor-binding site of SARS-CoV-2. *Nature* **584**, 120–124 (2020).
20. Wu, Y. et al. A noncompeting pair of human neutralizing antibodies block COVID-19 virus binding to its receptor ACE2. *Science* **368**, 1274–1278 (2020).
21. Yuan, M. et al. Structural basis of a shared antibody response to SARS-CoV-2. *Science* **369**, 1119–1123 (2020).
22. Robbiani, D. F. et al. Convergent antibody responses to SARS-CoV-2 in convalescent individuals. *Nature* **584**, 437–442 (2020).
23. Liu, L. et al. Potent neutralizing antibodies against multiple epitopes on SARS-CoV-2 spike. *Nature* **584**, 450–456 (2020).
24. Baum, A. et al. Antibody cocktail to SARS-CoV-2 spike protein prevents rapid mutational escape seen with individual antibodies. *Science* **369**, 1014–1018 (2020).

25. Brouwer, P. J. M. et al. Potent neutralizing antibodies from COVID-19 patients define multiple targets of vulnerability. *Science* **369**, 643–650 (2020).
26. Rogers, T. F. et al. Isolation of potent SARS-CoV-2 neutralizing antibodies and protection from disease in a small animal model. *Science* **369**, 956–963 (2020).
27. Piccoli, L. et al. Mapping neutralizing and immunodominant sites on the SARS-CoV-2 spike receptor-binding domain by structure-guided high-resolution serology. *Cell* **183**, 1024–1042 (2020).
28. Zost, S. J. et al. Potently neutralizing and protective human antibodies against SARS-CoV-2. *Nature* **584**, 443–449 (2020).
29. Tortorici, M. A. et al. Ultrapotent human antibodies protect against SARS-CoV-2 challenge via multiple mechanisms. *Science* **370**, 950–957 (2020).
30. Lv, Z. et al. Structural basis for neutralization of SARS-CoV-2 and SARS-CoV by a potent therapeutic antibody. *Science* **369**, 1505–1509 (2020).
31. Zost, S. J. et al. Rapid isolation and profiling of a diverse panel of human monoclonal antibodies targeting the SARS-CoV-2 spike protein. *Nat. Med.* **26**, 1422–1427 (2020).
32. Seydoux, E. et al. Analysis of a SARS-CoV-2-infected individual reveals development of potent neutralizing antibodies with limited somatic mutation. *Immunity* **53**, 98–105 (2020).
33. Kreye, J. et al. A therapeutic non-self-reactive SARS-CoV-2 antibody protects from lung pathology in a COVID-19 hamster model. *Cell* **183**, 1058–1069 (2020).
34. Scheid, J. F. et al. B cell genomics behind cross-neutralization of SARS-CoV-2 variants and SARS-CoV. *Cell* **184**, 3205–3221 (2021).
35. Tortorici, M. A. et al. Broad sarbecovirus neutralization by a human monoclonal antibody. *Nature* **597**, 103–108 (2021).
36. Dong, J. et al. Genetic and structural basis for SARS-CoV-2 variant neutralization by a two-antibody cocktail. *Nat. Microbiol.* **6**, 1233–1244 (2021).
37. Starr, T. N. et al. SARS-CoV-2 RBD antibodies that maximize breadth and resistance to escape. *Nature* **597**, 97–102 (2021).

38. Martinez, D. R. et al. A broadly cross-reactive antibody neutralizes and protects against sarbecovirus challenge in mice. *Sci. Transl. Med.* **https://doi.org/10.1126/scitranslmed.abj7125** (2021).
39. Onodera, T. et al. A SARS-CoV-2 antibody broadly neutralizes SARS-related coronaviruses and variants by coordinated recognition of a virus-vulnerable site. *Immunity* **54**, 2385–2398 (2021).
40. Raybould, M. I. J., Kovaltsuk, A., Marks, C. & Deane, C. M. CoV-AbDab: the coronavirus antibody database. *Bioinformatics* **37**, 734–735 (2021).
41. Barnes, C. O. et al. Structures of human antibodies bound to SARS-CoV-2 spike reveal common epitopes and recurrent features of antibodies. *Cell* **182**, 828–842 (2020).
42. Hansen, J. et al. Studies in humanized mice and convalescent humans yield a SARS-CoV-2 antibody cocktail. *Science* **369**, 1010–1014 (2020).
43. Kim, S. I. et al. Stereotypic neutralizing VH clonotypes against SARS-CoV-2 RBD in patients with COVID-19 and healthy individuals. *Sci. Transl. Med.* **13**, eabd6990 (2021).
44. Du, S. et al. Structurally resolved SARS-CoV-2 antibody shows high efficacy in severely infected hamsters and provides a potent cocktail pairing strategy. *Cell* **183**, 1013–1023 (2020).
45. Du, S. et al. Structures of SARS-CoV-2 B.1.351 neutralizing antibodies provide insights into cocktail design against concerning variants. *Cell Res.* **31**, 1130–1133 (2021).
46. Harvey, W. T. et al. SARS-CoV-2 variants, spike mutations and immune escape. *Nat. Rev. Microbiol.* **19**, 409–424 (2021).
47. Jones, B. E. et al. The neutralizing antibody, LY-CoV555, protects against SARS-CoV-2 infection in nonhuman primates. *Sci. Transl. Med.* **13**, eabf1906 (2021).
48. Tan, C. W. et al. Pan-sarbecovirus neutralizing antibodies in BNT162b2-immunized SARS-CoV-1 survivors. *N. Engl. J. Med.* **385**, 1401–1406 (2021).
49. Ehrenmann, F., Kaas, Q. & Lefranc, M. P. IMGT/3Dstructure-DB and IMGT/DomainGapAlign: a database and a tool for immunoglobulins or antibodies, T cell receptors, MHC, IgSF and MhcSF. *Nucleic Acids Res.* **38**, D301–D307 (2010).

50. Ehrenmann, F. & Lefranc, M. P. IMGT/DomainGapAlign: IMGT standardized analysis of amino acid sequences of variable, constant, and groove domains (IG, TR, MH, IgSF, MhSF). *Cold Spring Harb. Protoc.* **2011**, 737–749 (2011).
51. Gietz, R. D. & Schiestl, R. H. High-efficiency yeast transformation using the LiAc/SS carrier DNA/PEG method. *Nat. Protoc.* **2**, 31–34 (2007).

## Acknowledgements

We thank J. Bloom for his gift of the yeast SARS-CoV-2 RBD libraries; Beijing BerryGenomics for help with DNA sequencing; Sino Biological for technical assistance with monoclonal antibodies and Omicron RBD expression; Sartorius (Shanghai) Trading Co. for providing instrumental help with BLI measurement; and J. Luo and H. Lv for help with flow cytometry. This project is financially supported by the Ministry of Science and Technology of China (CPL-1233).

## Author information

### Author notes

1. These authors contributed equally: Yunlong Cao, Jing Wang, Fanchong Jian, Tianhe Xiao, Weiliang Song, Ayijiang Yisimayi, Weijin Huang.

### Affiliations

1. Biomedical Pioneering Innovation Center (BIOPIC), Peking University, Beijing, P. R. China

Yunlong Cao, Jing Wang, Fanchong Jian, Tianhe Xiao, Weiliang Song, Ayijiang Yisimayi, Peng Wang, Ran An, Jing Wang, Yao Wang, Xiao Niu, Sijie Yang, Hui Liang, Haiyan Sun, Fei Shao & Xiaoliang Sunney Xie

2. Beijing Advanced Innovation Center for Genomics (ICG), Peking University, Beijing, P. R. China

Yunlong Cao, Junyu Xiao & Xiaoliang Sunney Xie

3. School of Life Sciences, Peking University, Beijing, P. R. China

Jing Wang, Weiliang Song, Ayijiang Yisimayi, Shuo Du, Zhiying Zhang & Junyu Xiao

4. College of Chemistry and Molecular Engineering, Peking University, Beijing, P. R. China

Fanchong Jian & Xiao Niu

5. Joint Graduate Program of Peking–Tsinghua–NIBS, Academy for Advanced Interdisciplinary Studies, Peking University, Beijing, P. R. China

Tianhe Xiao

6. Division of HIV/AIDS and Sex-transmitted Virus Vaccines, Institute for Biological Product Control, National Institutes for Food and Drug Control (NIFDC), Beijing, P. R. China

Weijin Huang, Qianqian Li, Tao Li, Yuanling Yu, Qianqian Cui, Shuo Liu & Youchun Wang

7. Tsinghua-Peking Center for Life Sciences, Beijing, P. R. China

Sijie Yang

8. Beijing YouAn Hospital, Capital Medical University, Beijing, P. R. China

Xiaodong Yang

9. Beijing Ditan Hospital, Capital Medical University, Beijing, P. R. China

Xiaohua Hao & Ronghua Jin

10. CAS Key Laboratory of Infection and Immunity, National Laboratory of Macromolecules, Institute of Biophysics, Chinese Academy of Sciences, Beijing, P. R. China

Xiangxi Wang

## Contributions

Y.C. and X.S.X. designed the study. Y.C. and F.S. coordinated the characterizations of the neutralizing antibodies. J.W. (School of Life Sciences, Peking University), F.J., H.L. and H.S. performed and analysed the yeast display mutation screening experiments. T.X., J.W. (BIOPIC, Peking University), X.Y., P.W. and H.L. performed the pseudovirus neutralization assays. W.H., Q.L., T.L., Y.Y., Q.C., S.L. and Youchun Wang prepared the VSV-based SARS-CoV-2 pseudovirus. A.Y., Yao Wang, S.Y., R.A. and W.S. performed and analysed the antigen-specific single-B-cell V(D)J

sequencing. X.N. and R.A. performed the antibody BLI studies. S.D., Z.Z., X.W. and J.X. performed the antibody structural analyses. P.W., Yao Wang, J.W. (BIOPIC, Peking University), H.S. and H.L. performed the ELISA experiments. X.H. and R.J. coordinated the blood samples of SARS-CoV-1 convalescent individuals who had been vaccinated. Y.C., X.W., J.X. and X.S.X. wrote the manuscript with inputs from all authors.

## Corresponding authors

Correspondence to [Yunlong Cao](#), [Xiangxi Wang](#), [Junyu Xiao](#), [Youchun Wang](#) or [Xiaoliang Sunney Xie](#).

## Ethics declarations

### Competing interests

X.S.X. and Y.C. are listed as inventors on a patent related to BD series antibodies and DXP-604 (PCT/CN2021/093305) under Peking University. X.S.X. and Y.C. are founders of Singlomics Biopharmaceuticals. The remaining authors declare no competing interests.

## Peer review

### Peer review information

*Nature* thanks the anonymous reviewer(s) for their contribution to the peer review of this work.

## Additional information

**Publisher's note** Springer Nature remains neutral with regard to jurisdictional claims in published maps and institutional affiliations.

## Extended data figures and tables

### [Extended Data Fig. 1 Illustration of the SARS-CoV-2 spike protein with Omicron's mutations.](#)

**a**, SARS-CoV-2 D614G spike protein structure overlayed with Omicron mutations. Omicron's (BA.1) popular mutations are marked by red (for substitutions), blue (for

insertions) and grey balls (for deletions). **b**, NTD-binding neutralizing antibodies shown together in complex with NTD. Substitutions and deletions of Omicron NTD are coloured blue and red, respectively.

### [Extended Data Fig. 2 Comparison between FACS- and MACS-based deep mutational scanning.](#)

Deep mutational scanning maps with MACS-based (left) and FACS-based assays (right) of seven therapeutic neutralizing antibodies that have received emergency use authorization. Sites mutated in the Omicron variant are highlighted. Mutation amino acids of each site are shown by single letters. The heights represent mutation escape score, and colours represent chemical properties. FACS-based data were obtained from public datasets by Jesse Bloom.

### [Extended Data Fig. 3 Omicron neutralization IC<sub>50</sub> fold-change distribution of 247 neutralizing antibodies of diverse epitopes.](#)

Fold-change of IC<sub>50</sub> (VSV pseudovirus neutralization) compared to D614G by Beta and Omicron (BA.1) are shown for all 247 neutralizing antibodies tested. The effect of each RBD mutation of Omicron on antibody binding is inferred from yeast display mutation screening. Each antibody's binding to Omicron RBD was validated through ELISA. All neutralization and ELISA assays were conducted in biological duplicates.

### [Extended Data Fig. 4 Heavy chain V/J segment recombination of neutralizing antibodies of each epitope group.](#)

**a–f**, Chord diagrams showing the heavy chain V segment and J segment recombination of epitope group A (**a**), B (**b**), C (**c**), D (**d**), E (**e**) and F (**f**). The width of the arc linking a V segment to a J segment indicates the antibody number of the corresponding recombination. The inner layer scatter plots show the V segment amino acid mutation rate, and black strips show the 25%~75% quantile of mutation rates.

### [Extended Data Fig. 5 Neutralization potency, heavy chain CDR3 length and mutation rate distribution for neutralizing antibodies of each epitope group.](#)

**a**, The length of H chain complementarity-determining region 3 (HCDR3) amino acid sequence for neutralizing antibodies in each epitope group (n = 66, 26, 57, 27, 39, 32 antibodies for epitope group A, B, C, D, E, F, respectively). HCDR3 lengths are displayed as mean ± s.d. **b**, The V segment amino acid mutation rate for neutralizing

antibodies in each epitope group ( $n = 66, 26, 57, 27, 39, 32$  antibodies for epitope group A, B, C, D, E, F, respectively). Mutation rates are calculated and displayed as mean  $\pm$  s.d. **c–e**, The  $IC_{50}$  against D614G (**c**), Beta (**d**) and Omicron (**e**) variants for neutralizing antibodies in each epitope group ( $n = 66, 26, 57, 27, 39, 32$  antibodies for epitope group A, B, C, D, E, F, respectively).  $IC_{50}$  values are displayed as mean  $\pm$  s.d. in the log<sub>10</sub> scale. Pseudovirus assays for each variant are biologically replicated twice. Dotted lines show the detection limit, which is from 0.0005 µg/mL to 10 µg/mL.  $IC_{50}$  geometric means are also labelled on the figure.

**Extended Data Fig. 6 Escape hotspots of different epitope groups on the RBD surface.**

**a–f**, Aggregated site escape scores of antibodies for epitope group A–F, respectively. Epitope groups are distinguished by distinct colours, and the shades show normalized site escape scores. Escape hotspots of each epitope group are annotated by arrows.

**Extended Data Fig. 7 Antibody-RBD interface distribution for neutralizing antibodies of each epitope group.**

**a–f**, Aggregated antibody-antigen interface of antibodies for epitope group A–F, respectively. Antibody-antigen interface was indicated from publicly available structures of neutralizing antibodies in complex with SARS-CoV-2 RBD. Different colours distinguish epitope groups, and the shade reflects group-specific site popularity to appear on the complex interface. Shared interface residues (Omicron) of each group are annotated.

**Extended Data Fig. 8 Comparison between mutation escape scores estimated from yeast display and neutralization of variants carrying corresponding mutations.**

**a**, K417N escape scores and corresponding K417N pseudovirus neutralizing  $IC_{50}$  fold change compared to D614G pseudovirus of antibodies within epitope group A. **b**, E484K/E484A escape scores and corresponding E484K pseudovirus neutralizing  $IC_{50}$  fold change compared to D614G pseudovirus of antibodies within epitope group C.

**Extended Data Fig. 9 Pseudovirus neutralization of neutralizing-antibody-based drugs against SARS-CoV-2 variants of concern.**

Pseudovirus (VSV-based) assays were performed using Huh-7 cells. Data are collected from three biological replicates and represented as mean  $\pm$  s.d.

## [Extended Data Fig. 10 BLI response between neutralizing-antibody-based drugs and the RBD of SARS-CoV-2 wild type, Beta or Omicron strains.](#)

Antibodies were captured by Protein A sensor. The concentrations of RBD are shown in different colours. Dissociation constant ( $K_D$ ), association constant ( $k_a$ ), and dissociation rate constant ( $k_d$ ) are labelled. Neutralizing antibodies without binding are marked as 'Escaped'.

## Supplementary information

### [Supplementary Table 1](#)

Summarized information of all 247 neutralizing antibodies, including their sources, epitope groups, pseudovirus neutralizing IC<sub>50</sub> for D614G, SARS-CoV, Beta and Omicron variants, and sequences of heavy and light chains.

### [Reporting Summary](#)

### [Supplementary Data 1](#)

Escaping mutation profiles of 247 SARS-CoV-2 neutralizing antibodies of 6 epitope groups. For each site, the height of each amino acid represents its mutation escape score. Sites mutated frequently in Omicron variant are highlighted.

### [Supplementary Data 2](#)

FACS strategy to isolate SARS-CoV-2 RBD and SARS-CoV-1 RBD double-positive B cell for single-cell VDJ sequencing. The target cell population of each step is labelled in the figure.

## Rights and permissions

**Open Access** This article is licensed under a Creative Commons Attribution 4.0 International License, which permits use, sharing, adaptation, distribution and reproduction in any medium or format, as long as you give appropriate credit to the original author(s) and the source, provide a link to the Creative Commons license, and indicate if changes were made. The images or other third party material in this article are included in the article's Creative Commons license, unless indicated otherwise in a credit line to the material. If material is not included in the article's Creative Commons

license and your intended use is not permitted by statutory regulation or exceeds the permitted use, you will need to obtain permission directly from the copyright holder. To view a copy of this license, visit <http://creativecommons.org/licenses/by/4.0/>.

## Reprints and Permissions

## About this article

### Cite this article

Cao, Y., Wang, J., Jian, F. *et al.* Omicron escapes the majority of existing SARS-CoV-2 neutralizing antibodies. *Nature* **602**, 657–663 (2022).  
<https://doi.org/10.1038/s41586-021-04385-3>

- Received: 07 December 2021
- Accepted: 23 December 2021
- Published: 23 December 2021
- Issue Date: 24 February 2022
- DOI: <https://doi.org/10.1038/s41586-021-04385-3>

### Share this article

Anyone you share the following link with will be able to read this content:

[Get shareable link](#)

Sorry, a shareable link is not currently available for this article.

[Copy to clipboard](#)

Provided by the Springer Nature SharedIt content-sharing initiative

## Further reading

- [\*\*ACE2-Targeting antibody suppresses SARS-CoV-2 Omicron and Delta variants\*\*](#)
  - Jianxia Ou

- Yanan Zhang
- Chunhe Wang

*Signal Transduction and Targeted Therapy* (2022)

- **Structure genomics of SARS-CoV-2 and its Omicron variant: drug design templates for COVID-19**

- Can-rong Wu
- Wan-chao Yin
- H. Eric Xu

*Acta Pharmacologica Sinica* (2022)

- **Considerable escape of SARS-CoV-2 Omicron to antibody neutralization**

- Delphine Planas
- Nell Saunders
- Olivier Schwartz

*Nature* (2022)

- **Omicron extensively but incompletely escapes Pfizer BNT162b2 neutralization**

- Sandile Cele
- Laurelle Jackson
- Alex Sigal

*Nature* (2022)

- **Broadly neutralizing antibodies overcome SARS-CoV-2 Omicron antigenic shift**

- Elisabetta Cameroni
- John E. Bowen
- Davide Corti

*Nature* (2022)

| [Section menu](#) | [Main menu](#) |

- Article
- [Published: 23 December 2021](#)

# Broadly neutralizing antibodies overcome SARS-CoV-2 Omicron antigenic shift

- [Elisabetta Cameroni](#)<sup>1</sup> na1,
- [John E. Bowen](#) [ORCID: orcid.org/0000-0003-3590-9727](#)<sup>2</sup> na1,
- [Laura E. Rosen](#) [ORCID: orcid.org/0000-0002-8030-0219](#)<sup>3</sup> na1,
- [Christian Saliba](#)<sup>1</sup> na1,
- [Samantha K. Zepeda](#) [ORCID: orcid.org/0000-0003-0005-9793](#)<sup>2</sup>,
- [Katja Culap](#) [ORCID: orcid.org/0000-0002-0956-0018](#)<sup>1</sup>,
- [Dora Pinto](#)<sup>1</sup>,
- [Laura A. VanBlargan](#) [ORCID: orcid.org/0000-0002-8922-8946](#)<sup>4</sup>,
- [Anna De Marco](#)<sup>1</sup>,
- [Julia di Julio](#)<sup>3</sup>,
- [Fabrizia Zatta](#)<sup>1</sup>,
- [Hannah Kaiser](#) [ORCID: orcid.org/0000-0002-3991-7401](#)<sup>3</sup>,
- [Julia Noack](#)<sup>3</sup>,
- [Nisar Farhat](#)<sup>3</sup>,
- [Nadine Czudnochowski](#)<sup>3</sup>,
- [Colin Havenar-Daughton](#) [ORCID: orcid.org/0000-0002-2880-3927](#)<sup>3</sup>,
- [Kaitlin R. Sprouse](#) [ORCID: orcid.org/0000-0003-0007-2226](#)<sup>2</sup>,
- [Josh R. Dillen](#)<sup>3</sup>,
- [Abigail E. Powell](#)<sup>3</sup>,
- [Alex Chen](#) [ORCID: orcid.org/0000-0003-2620-5066](#)<sup>3</sup>,
- [Cyrus Maher](#) [ORCID: orcid.org/0000-0002-6666-3574](#)<sup>3</sup>,
- [Li Yin](#) [ORCID: orcid.org/0000-0003-2634-9158](#)<sup>3</sup>,
- [David Sun](#)<sup>3</sup>,
- [Leah Soriaga](#) [ORCID: orcid.org/0000-0001-5852-741X](#)<sup>3</sup>,
- [Jessica Bassi](#)<sup>1</sup>,
- [Chiara Silacci-Fregni](#)<sup>1</sup>,
- [Claes Gustafsson](#)<sup>5</sup>,

- [Nicholas M. Franko](#) ORCID: [orcid.org/0000-0001-8165-6332<sup>6</sup>](https://orcid.org/0000-0001-8165-6332),
- [Jenni Logue](#) ORCID: [orcid.org/0000-0002-7889-8960<sup>6</sup>](https://orcid.org/0000-0002-7889-8960),
- [Najeeha Talat Iqbal<sup>7</sup>](#),
- [Ignacio Mazzitelli<sup>8</sup>](#),
- [Jorge Geffner<sup>8</sup>](#),
- [Renata Grifantini<sup>9</sup>](#),
- [Helen Chu<sup>6</sup>](#),
- [Andrea Gori<sup>10</sup>](#),
- [Agostino Riva](#) ORCID: [orcid.org/0000-0003-3171-3049<sup>11</sup>](https://orcid.org/0000-0003-3171-3049),
- [Olivier Giannini<sup>12,13</sup>](#),
- [Alessandro Ceschi](#) ORCID: [orcid.org/0000-0002-4308-0405<sup>12,14,15,16</sup>](https://orcid.org/0000-0002-4308-0405),
- [Paolo Ferrari](#) ORCID: [orcid.org/0000-0002-9619-3104<sup>12,17,18</sup>](https://orcid.org/0000-0002-9619-3104),
- [Pietro E. Cippà<sup>13,17,19</sup>](#),
- [Alessandra Franzetti-Pellanda<sup>20</sup>](#),
- [Christian Garzoni<sup>21</sup>](#),
- [Peter J. Halfmann](#) ORCID: [orcid.org/0000-0002-1648-1625<sup>22</sup>](https://orcid.org/0000-0002-1648-1625),
- [Yoshihiro Kawaoka](#) ORCID: [orcid.org/0000-0001-5061-8296<sup>22,23,24</sup>](https://orcid.org/0000-0001-5061-8296),
- [Christy Hebner<sup>3</sup>](#),
- [Lisa A. Purcell<sup>3</sup>](#),
- [Luca Piccoli](#) ORCID: [orcid.org/0000-0002-1085-6502<sup>1</sup>](https://orcid.org/0000-0002-1085-6502),
- [Matteo Samuele Pizzuto](#) ORCID: [orcid.org/0000-0001-5776-654X<sup>1</sup>](https://orcid.org/0000-0001-5776-654X),
- [Alexandra C. Walls](#) ORCID: [orcid.org/0000-0002-9636-8330<sup>2,25</sup>](https://orcid.org/0000-0002-9636-8330),
- [Michael S. Diamond](#) ORCID: [orcid.org/0000-0002-8791-3165<sup>4,26,27</sup>](https://orcid.org/0000-0002-8791-3165),
- [Amilio Telenti](#) ORCID: [orcid.org/0000-0001-6290-7677<sup>3</sup>](https://orcid.org/0000-0001-6290-7677),
- [Herbert W. Virgin](#) ORCID: [orcid.org/0000-0001-8580-7628<sup>3,26,28 na2</sup>](https://orcid.org/0000-0001-8580-7628),
- [Antonio Lanzavecchia<sup>1,9 na2</sup>](#),
- [Gyorgy Snell](#) ORCID: [orcid.org/0000-0003-1475-659X<sup>3 na2</sup>](https://orcid.org/0000-0003-1475-659X),
- [David Veesler](#) ORCID: [orcid.org/0000-0002-6019-8675<sup>2,25 na2</sup>](https://orcid.org/0000-0002-6019-8675) &
- [Davide Corti](#) ORCID: [orcid.org/0000-0002-5797-1364<sup>1 na2</sup>](https://orcid.org/0000-0002-5797-1364)

*Nature* volume 602, pages 664–670 (2022)

- 18k Accesses
- 26 Citations
- 145 Altmetric
- [Metrics details](#)

## Subjects

- [SARS-CoV-2](#)
- [Viral infection](#)

## Abstract

The recently emerged SARS-CoV-2 Omicron variant encodes 37 amino acid substitutions in the spike protein, 15 of which are in the receptor-binding domain (RBD), thereby raising concerns about the effectiveness of available vaccines and antibody-based therapeutics. Here we show that the Omicron RBD binds to human ACE2 with enhanced affinity, relative to the Wuhan-Hu-1 RBD, and binds to mouse ACE2. Marked reductions in neutralizing activity were observed against Omicron compared to the ancestral pseudovirus in plasma from convalescent individuals and from individuals who had been vaccinated against SARS-CoV-2, but this loss was less pronounced after a third dose of vaccine. Most monoclonal antibodies that are directed against the receptor-binding motif lost in vitro neutralizing activity against Omicron, with only 3 out of 29 monoclonal antibodies retaining unaltered potency, including the ACE2-mimicking S2K146 antibody<sup>1</sup>. Furthermore, a fraction of broadly neutralizing sarbecovirus monoclonal antibodies neutralized Omicron through recognition of antigenic sites outside the receptor-binding motif, including sotrovimab<sup>2</sup>, S2X259<sup>3</sup> and S2H97<sup>4</sup>. The magnitude of Omicron-mediated immune evasion marks a major antigenic shift in SARS-CoV-2. Broadly neutralizing monoclonal antibodies that recognize RBD epitopes that are conserved among SARS-CoV-2 variants and other sarbecoviruses may prove key to controlling the ongoing pandemic and future zoonotic spillovers.

[Download PDF](#)

## Main

The evolution of RNA viruses can result in immune escape and modulation of binding to host receptors through the accumulation of mutations<sup>5</sup>. Previously emerged SARS-CoV-2 variants of concern (VOCs) have developed resistance to neutralizing antibodies, including some clinical antibodies that are used as therapeutics<sup>6,7,8</sup>. The B.1.351 (Beta) VOC showed the greatest magnitude of immune evasion from serum neutralizing antibodies<sup>6,7</sup>, whereas B.1.617.2 (Delta) quickly outcompeted all other circulating isolates through the acquisition of mutations that enhanced transmission and pathogenicity<sup>9,10,11</sup> and eroded the neutralizing activity of antibody responses<sup>9</sup>.

The Omicron (B.1.1.529) variant was first detected in November 2021, was immediately declared to be a VOC by the World Health Organization (WHO) and quickly rose in frequency worldwide. The Omicron variant is substantially mutated compared to any previously described SARS-CoV-2 isolates, including 37 substitutions of residues in the spike protein in the predominant haplotype (Fig. 1a, Extended Data Figs. 1–4). Fifteen of the Omicron mutations are clustered in the RBD, which is the main target of neutralizing antibodies after infection or vaccination<sup>12,13</sup>, suggesting that Omicron might escape infection- and vaccine-elicited antibodies and therapeutic monoclonal antibodies. Nine of these mutations map to the receptor-binding motif (RBM), which is the RBD subdomain that directly interacts with the host receptor, ACE2<sup>14</sup>.

**Fig. 1: The Omicron RBD shows increased binding to human ACE2 and gains binding to mouse ACE2.**

---

 **figure 1**

**a**, Omicron mutations are shown in a primary structure of the SARS-CoV-2 spike protein, with domains and cleavage sites highlighted. BH, beta hairpin; C, C domain; CD, connector domain; CH, central helix; D, domain D; FP, fusion peptide; HR1/2, heptad repeat 1/2; SH, stem helix; SP, signal

---

peptide; TM, transmembrane domain; UH, upstream helix. **b**, Single-cycle kinetics SPR analysis of ACE2 binding to six RBD variants. ACE2 is injected successively at 11, 33, 100 and 300 nM (human) or 33, 100, 300 and 900 nM (mouse). Dashed black curves show fits to a 1:1 binding model. White and grey stripes indicate association and dissociation phases, respectively.  $K_D$ , dissociation constant; RU, response units. **c**, Quantification of human ACE2 binding data (mean  $\pm$  s.d. of three replicates). Asterisks indicate that Delta was measured in a separate experiment with a different chip surface and capture tag. Delta fold change (FC) is calculated relative to the affinity of Wuhan-Hu-1 measured in parallel ( $91 \pm 1.6$  nM). **d**, Entry of Wuhan-Hu-1, Alpha, Beta, Delta, Gamma, Kappa and Omicron spike VSV pseudoviruses into mouse ACE2-expressing HEK293T cells. RLU, luciferase relative light units. Shown are two biological replicates (technical triplicates). Lines, geometric mean.

Preliminary reports indicate that the neutralizing activity of plasma from individuals who had received the Pfizer–BioNTech BNT162b2 vaccine is reduced against the Omicron variant<sup>15,16</sup>, documenting a substantial—albeit not complete—escape from mRNA-vaccine-elicited neutralizing antibodies. Another report also shows that vaccine effectiveness against symptomatic disease induced by the Omicron variant is significantly lower than for the Delta variant<sup>17</sup>. The potential for booster doses to ameliorate this decline in neutralization is being investigated. In addition, the neutralizing activity of several therapeutic monoclonal antibodies appears to be decreased or abolished against Omicron<sup>16,18</sup>.

To understand the consequences of the high number of mutations found in the Omicron spike protein, we used a pseudovirus assay to study receptor use and neutralization mediated by monoclonal and polyclonal antibodies, as well as surface plasmon resonance (SPR) to measure binding of the RBD to human and mouse ACE2 receptors.

## Omicron RBD binds ACE2 with increased affinity

At present, 23 out of the 37 amino acid mutations in the Omicron spike protein have been individually observed previously in SARS-CoV-2 variants of interest, VOCs or other sarbecoviruses, whereas the remaining 14 substitutions have not to our knowledge been described before (Extended Data Fig. 5a). Analysis of the GISAID database indicates that there are rarely more than 10–15 Omicron spike mutations present in a given non-Omicron haplotype or Pango lineage (Extended Data Fig. 5b–d). Although we have not formally assessed the possibility of recombination events, persistent replication in immunocompromised individuals or inter-species ping-pong transmission<sup>5</sup> are possible scenarios for the rapid accumulation of mutations that could have been selected on the basis of viral fitness and immune evasion.

Several of the Omicron RBD mutations are found at positions that are key contact sites with human ACE2, such as K417N, Q493R and G496S<sup>19</sup>. Except for N501Y, which increases ACE2-binding affinity by sixfold<sup>20,21</sup>, all other substitutions were shown by deep mutational scanning either to reduce binding or to have no effect on human ACE2 affinity when present individually<sup>22</sup>, resulting in an overall predicted decrease of binding affinity (Supplementary Table 1). However, we found that the Omicron RBD has a 2.4-fold increased binding affinity to human ACE2 (Fig. 1b, c, Extended Data Fig. 6a), suggesting epistasis of the full constellation of RBD mutations. It remains to be determined whether and how the spike mutations in Omicron may influence the dynamics of RBD opening, which may also affect the engagement of the RBD with ACE2.

The presence of the N501Y mutation has previously been reported to enable some SARS-CoV-2 VOCs to infect mice<sup>23</sup>. As Omicron contains the N501Y mutation, along with 14 other RBD mutations, we investigated whether the Omicron RBD binds mouse ACE2 using SPR (Fig. 1b, Extended Data Fig. 6). The Omicron RBD binds mouse ACE2 with a 1:1 binding affinity of 470 nM (Fig. 1b), whereas weak binding of the Beta RBD and very weak binding of the Alpha RBD to mouse ACE2 was observed (Fig. 1b, Extended Data Fig. 6b), consistent with previous reports<sup>23,24</sup>. Conversely, our assay did not detect any binding of the Wuhan-Hu-1, Delta or K417N RBDs to mouse ACE2. The enhanced binding of the Omicron RBD to mouse ACE2 is likely to be explained by the Q493R substitution, which is similar to the Q493K mutation isolated in mouse-adapted SARS-CoV-2<sup>19</sup>. Our binding data correlate with our observation of Omicron spike protein-mediated but not Wuhan-Hu-1/G614 spike protein-mediated entry of VSV pseudoviruses into mouseACE2-expressing cells (Fig. 1d), as recently reported<sup>25</sup>. Collectively, these findings highlight the plasticity of the SARS-CoV-2 RBM, which in the case of the Omicron VOC acquired enhanced binding to human and mouse ACE2 orthologues, relative to other SARS-CoV-2 isolates. The influence of these findings on viral load and replication kinetics in humans and animal models remains to be evaluated, owing to the interplay of additional factors besides receptor binding. Preliminary data suggest that Omicron appears to be attenuated in some laboratory mouse strains (M.S.D., personal communication) and that it replicates less efficiently in human lung tissue as compared to Delta<sup>26</sup>.

## Extent of Omicron escape from plasma antibodies

To investigate the magnitude of immune evasion that is mediated by the 37 mutations present in the Omicron spike protein, we used Wuhan-Hu-1 and Omicron spike VSV pseudoviruses and compared plasma neutralizing activity in different cohorts of convalescent individuals (that is, individuals who had recovered from COVID-19) or

individuals who had been vaccinated with six major COVID-19 vaccines (mRNA-1273, BNT162b2, AZD1222, Ad26.COV2.S, Sputnik V and BBIBP-CorV) (Fig. 2, Supplementary Figs. 1–3, Extended Data Table 1).

**Fig. 2: Neutralization of Omicron SARS-CoV-2 VSV pseudovirus by plasma from convalescent and vaccinated individuals.**

 figure 2

Plasma neutralizing activity in convalescent or vaccinated individuals (mRNA-1273, BNT162b2, AZD1222, Ad26.COV2.S (single dose), Sputnik V and BBIBP-CorV). **a**, Pairwise neutralizing antibody titres (half-maximum inhibitory dose; ID<sub>50</sub>) against Wuhan-Hu-1 (D614G), Beta and Omicron VOCs, and SARS-CoV. Vero E6-TMPRSS2 cells were used as target cells. Data are the geometric mean of  $n = 3$  biologically independent experiments except for SARS-CoV for which  $n = 1$ . **b**,

Pairwise neutralizing antibody titres of plasma ( $ID_{50}$ ) against Wuhan-Hu-1 and Omicron. Data are the geometric mean of  $n = 2$  biologically independent experiments. **c**, Plasma neutralizing activity in individuals undergoing dialysis who received three doses of either the BNT162b2 or mRNA-1273. Pairwise neutralizing antibody titres of plasma ( $ID_{50}$ ) against Wuhan-Hu-1 and Omicron. One representative experiment out of two is shown. Vero E6 cells were used as target cells in **b**, **c**, Line, geometric mean of  $1/ID_{50}$  titres. Shown is the percentage of samples that lost detectable neutralization against Omicron or SARS-CoV, excluding samples with  $1/ID_{50}$  below the limit of detection. The demographics of enrolled donors are provided in Extended Data Table 1. Statistical significance is set as  $P < 0.05$  and  $P$  values are indicated with asterisks (\* $P = 0.033$ ; \*\* $P = 0.002$ ; \*\*\* $P < 0.001$ ), using a paired two-sided  $t$ -test (Wilcoxon rank test).

Convalescent individuals and individuals who had been vaccinated with Ad26.COV2.S (single dose), Sputnik V or BBIBP-CorV had no detectable neutralizing activity against Omicron, with only one convalescent subject and three BBIBP-CorV vaccinees exhibiting  $ID_{50}$  values above 10 (Fig. 2a). Individuals who were immunized with mRNA-1273, BNT162b2 and AZD1222 had more potent neutralizing activity against Wuhan-Hu-1 and retained detectable neutralization against Omicron, with decreases of 39-, 37- and 21-fold, respectively (Fig. 2a). The dampening of neutralizing activity against Omicron was comparable to that observed against SARS-CoV, a virus that differs from Wuhan-Hu-1 by 52 residues in the RBD. Reductions of neutralization potency were less pronounced in vaccinated individuals who had been previously infected (fivefold; Fig. 2b) and in individuals undergoing dialysis (fourfold; Fig. 2c) who were boosted with a third mRNA vaccine dose. In the same cohort of individuals undergoing dialysis, the levels of antibodies that neutralize the vaccine-matched Wuhan-Hu-1 strain were found to be low (less than 1/100) or undetectable in 44% of individuals after the second dose of mRNA vaccine<sup>27</sup>.

Collectively, these findings provide evidence of a substantial reduction in plasma neutralizing activity against Omicron as compared to the ancestral virus, with neutralizing activity probably falling below the protective threshold in several cases<sup>28</sup>. Our data further indicate that multiple exposures to the ancestral virus through infection or vaccination result in the production of antibodies that can neutralize divergent viruses, such as Omicron or even SARS-CoV, as a consequence of affinity maturation or epitope masking by immune-dominant RBM antibodies<sup>28,29,30</sup>.

## Broadly neutralizing antibodies inhibit Omicron

Neutralizing monoclonal antibodies with demonstrated in vivo efficacy in the prevention or treatment of COVID-19<sup>31,32,33,34,35,36,37</sup> can be divided into two groups

on the basis of whether they do or do not block the binding of the spike protein to ACE2. Of the eight currently authorized or approved monoclonal antibodies, seven (LY-CoV555, LY-CoV016, REGN10987, REGN10933, COV2-2130, COV2-2196 and CT-P59; all synthesized on the basis of publicly available sequences) block the binding of spike protein to ACE2 and are often used as two-antibody cocktails<sup>8</sup>. They bind to epitopes that overlap with the RBM (Fig. 3a), which is structurally and evolutionary plastic<sup>38</sup>, as shown by the accumulation of mutations throughout the pandemic and the genetic diversity of this subdomain among ACE2-using sarbecoviruses<sup>39</sup>. Combining two such ACE2-blocking monoclonal antibodies can provide greater resistance to variant viruses that carry RBM mutations<sup>31</sup>. The second class of monoclonal antibodies, represented by sotrovimab, do not block ACE2 binding but neutralize SARS-CoV-2 by targeting non-RBM epitopes that are shared across many sarbecoviruses, including SARS-CoV<sup>4,40</sup>.

**Fig. 3: Neutralization of Omicron SARS-CoV-2 VSV pseudovirus by clinical-stage monoclonal antibodies.**

 figure 3

**a**, RBD sequence of SARS-CoV-2 Wuhan-Hu-1 with highlighted footprints of ACE2 (light blue) and monoclonal antibodies (mAbs; coloured according to the RBD antigenic site recognized). The Omicron RBD is also shown, and amino acid substitutions are boxed. **b**, Neutralization of SARS-CoV-2 VSV pseudoviruses displaying Wuhan-Hu-1 (white) or Omicron (coloured as in Fig. 4b) spike proteins by clinical-stage monoclonal antibodies. Data are representative of at least two independent experiments. Shown is the mean of two technical replicates. **c**, Geometric mean half-maximum inhibitory concentration ( $IC_{50}$ ) values for Omicron (coloured as in Fig. 4b) and Wuhan-Hu-1 (white) (top), and geometric mean fold change (bottom). Vero E6 cells were used as target cells. Shown in blue (right) is neutralization of authentic virus by sotrovimab (WA1/2020 versus hCoV-19/USA/WI-WSLH-221686/2021). Non-neutralizing  $IC_{50}$  titres and fold change were set to  $10^4$  and  $10^3$ , respectively. Orange dots for sotrovimab indicate neutralization of Omicron VSV pseudovirus carrying R346K (Omicron-R346K). Data are representative of  $n = 2$  biologically independent experiments for most monoclonal antibodies; for sotrovimab against Omicron VSV  $n = 6$  and for Omicron authentic virus  $n = 3$ .

We compared the in vitro neutralizing activity of these therapeutic monoclonal antibodies side-by-side against Wuhan-Hu-1 and Omicron spike proteins using VSV pseudoviruses (Fig. 3). Although sotrovimab had a threefold-reduced potency against Omicron and Omicron-R346K variant VSV pseudoviruses, all of the other (RBM-specific) monoclonal antibodies completely lost their neutralizing activity—with the exception of the combination of COV2-2130 and COV2-2196, for which we determined an approximately 100-fold-reduced potency (Fig. 3b,c). Moreover, sotrovimab exhibited a reduction of less than twofold in neutralizing activity against authentic Omicron SARS-CoV-2 as compared to the WA1/2020 D614G virus (Fig. 3c, Extended Data Fig. 7), consistent with recent reports on S309, the parent of sotrovimab<sup>41,42</sup>. The threefold and less-than-twofold decrease in the neutralizing activity of sotrovimab against pseudoviruses and authentic virus, respectively, is within the currently defined threshold of ‘no change’ as defined by the US Food and Drug Administration (FDA; the FDA fact sheet for sotrovimab denotes no change as a reduction of less than fivefold in susceptibility<sup>43</sup>). Overall, our findings agree with two preliminary reports<sup>16,18</sup> and, together with serological data, support the conclusion that the Omicron VOC has undergone antigenic shift.

We next tested a larger panel of 36 neutralizing NTD- or RBD-specific monoclonal antibodies for which the epitopes have been characterized structurally or assigned to a given antigenic site through competition studies<sup>3,4,9,12,44,45</sup> (Fig. 4a, Extended Data Table 2, Extended Data Fig. 8). The four NTD-specific antibodies completely lost activity against Omicron, consistent with the presence of mutations and deletions in the NTD antigenic supersite<sup>21,45,46</sup>. Three out of the twenty-two monoclonal antibodies that target the RBD antigenic site I (RBM) retained potent neutralizing

activity against Omicron, including S2K146, which binds the RBD of SARS-CoV-2, SARS-CoV and other sarbecoviruses through ACE2 molecular mimicry<sup>1</sup>. Of the nine monoclonal antibodies that are specific for the conserved RBD site II (refs. [4,12](#)), only S2X259<sup>3</sup> retained activity against Omicron, whereas neutralization was decreased by more than tenfold or abolished for the remaining antibodies. Finally, the S2H97 monoclonal antibody retained neutralizing activity against Omicron through recognition of the highly conserved cryptic site V (ref. [4](#)). The panel of 44 monoclonal antibodies tested in this study includes members of each of the four classes of neutralizing monoclonal antibodies, defined by their cognate RBD-binding sites (sites I, II, IV and V)<sup>12</sup>. Our findings show that a member, or members, of each of the four classes can retain Omicron neutralization: S2K146, S2X324 and S2N28 targeting site I, S2X259 targeting site II, sotrovimab targeting site IV and S2H97 targeting site V (Fig. [4b](#)). Several of these monoclonal antibodies cross-react with and neutralize sarbecoviruses beyond the SARS-CoV-2 clade 1b<sup>[1,3,4](#)</sup>, indicating that targeting of conserved epitopes can lead to neutralization breadth and resilience to antigenic shift associated with viral evolution.

**Fig. 4: Neutralization of Omicron SARS-CoV-2 VSV pseudovirus by monoclonal antibodies.**

---

 **figure 4**

**a**, Top, mean IC<sub>50</sub> values for Omicron (coloured as in **b**) and Wuhan-Hu-1 (white). Bottom, mean fold change for 4 NTD monoclonal antibodies and 32 RBD monoclonal antibodies. Non-neutralizing IC<sub>50</sub> titres and fold change were set to 10<sup>4</sup> and 10<sup>3</sup>, respectively. Triangles for S2K146 indicate neutralization of Omicron carrying R346K. Vero E6 cells were used as target cells. Data are representative of  $n = 2$  biologically independent experiments (except for S2K146, for which  $n = 6$ ). **b**, The RBD sites targeted by four monoclonal antibodies that cross-neutralize Omicron are

annotated and representative antibodies (the Fv region) bound to spike proteins are shown as a composite. Coloured surfaces on the RBD depict the epitopes and the RBM is shown as a black outline.

## Discussion

The high number of substitutions present in the Omicron spike protein marks a pronounced shift in antigenicity and is associated with immune evasion of considerable magnitude for SARS-CoV-2. Antigenic shift of the influenza virus is defined as genetic reassortment of the RNA genome segments, but the mechanism for the abrupt appearance of a large number of mutations in SARS-CoV-2 Omicron spike protein remains to be determined. Although recombination events are a hallmark of coronaviruses<sup>47</sup>, we and others<sup>48</sup> propose that the Omicron shift may result from extensive viral replication in immunodeficient hosts<sup>47,49</sup>, although we cannot rule out the possibility of a contribution of inter-species ping-pong transmission<sup>5</sup> between humans and rodents, as previously described for minks<sup>50</sup>.

Consistent with the variable decrease in plasma neutralizing antibody titres, we found that only 6 out of a panel of 44 neutralizing monoclonal antibodies retained potent neutralizing activity against Omicron. The monoclonal antibodies that retain neutralization recognize RBD antigenic sites that are conserved in Omicron and other sarbecoviruses. Notably, three of these antibodies bind to the RBM, including one that is a molecular mimic of the ACE2 receptor (S2K146)<sup>1</sup>. Collectively, these data may guide future efforts to develop SARS-CoV-2 vaccines and therapies to counteract antigenic shift and future sarbecovirus zoonotic spillovers.

## Methods

### Cell lines

Cell lines used in this study were obtained from ATCC (HEK293T and Vero E6), Thermo Fisher Scientific (Expi-CHO-S cells, FreeStyle 293-F cells and Expi293F cells), Takara (Lenti-X 293T cells) or generated in-house (Vero E6-TMPRSS2)<sup>40</sup>. Vero-TMPRSS2<sup>51</sup> cells were cultured at 37 °C in Dulbecco's modified Eagle's medium (DMEM) supplemented with 10% fetal bovine serum (FBS), 10 mM HEPES pH 7.3 and 100 U ml<sup>-1</sup> of penicillin–streptomycin and supplemented with 5 µg ml<sup>-1</sup> of blasticidin. None of the cell lines used was authenticated. Cell lines were routinely tested for mycoplasma contamination.

### Omicron prevalence analysis

The viral sequences and the corresponding metadata were obtained from the GISAID EpiCoV project (<https://www.gisaid.org/>). Analysis was performed on sequences submitted to GISAID up to 20 December 2021. Spike protein sequences were obtained from the genomic sequences with the exonerate<sup>52</sup> 2.2.4.0-haf93ef1\_3 (<https://quay.io/repository/biocontainers/exonerate?tab=tags>) using protein to DNA alignment with parameters -m protein2dna –refine full –minintron 999999 –percent 20 and using accession YP\_009724390.1 as a reference. Multiple sequence alignment of all human spike proteins was performed with mafft<sup>53</sup> 7.475–h516909a\_0 (<https://quay.io/repository/biocontainers/mafft?tab=tags>) with parameters –auto –reorder –mapout –keeplength –addfragments using the same reference as above. The –mapout parameter was used to retrieve insertions. Spike sequences that contained more than 10% ambiguous amino acids or that were less than 80% of the canonical protein length were discarded. Figures were generated with R 4.0.2 (<https://cran.r-project.org/>) using the ggplot2 3.3.2 and sf 0.9-7 packages. To identify each mutation prevalence, missingness (or ambiguous amino acids) was taken into account in both nominator and denominator.

## Monoclonal antibodies

Sotrovimab and VIR-7832 (VIR-7832<sup>54</sup>) is derived from sotrovimab, Fc further engineered to carry GAALIE) were produced at WuXi Biologics. Antibody VH and VL sequences for the monoclonal antibodies COV2-2130 (Protein Data Bank (PDB) ID 7L7E), COV2-2196 (PDB ID 7L7E, 7L7D), REGN10933 (PDB ID 6XDG), REGN10987 (PDB ID 6XDG) and ADI-58125 (PCT application WO2021207597, seq. IDs 22301 and 22311) were subcloned into heavy chain (human IgG1) and the corresponding light chain (human Ig κ-chain, Ig λ-chain) expression vectors respectively and produced in transiently transfected ExpiCHO-S cells (Thermo Fisher Scientific, A29133) at 37 °C and 8% CO<sub>2</sub>. Cells were transfected using ExpiFectamine. Transfected cells were supplemented 1 day after transfection with ExpiCHO Feed and ExpiFectamine CHO Enhancer. Cell culture supernatant was collected eight days after transfection and filtered through a 0.2-μm filter. Recombinant antibodies were affinity purified on an ÄKTA Xpress FPLC device using 5 ml HiTrap MabSelect PrismA columns followed by buffer exchange to histidine buffer (20 mM histidine, 8% sucrose, pH 6) using HiPrep 26/10 desalting columns. Antibody VH and VL sequences for LY-CoV555, LY-CoV016 and CT-P59 were obtained from PDB IDs 7KMG, 7C01 and 7CM4, respectively, and monoclonal antibodies were produced as recombinant IgG1 by ATUM. The remaining monoclonal antibodies were discovered at VIR and have been produced as recombinant IgG1 in ExpiCHO-S cells as described above. The identity of the produced monoclonal antibodies was confirmed by liquid chromatography–mass spectrometry (LC–MS) analysis.

## IgG mass quantification by LC–MS intact protein mass analysis

Fc N-linked glycan from monoclonal antibodies was removed by PNGase F after overnight non-denaturing reaction at room temperature. Deglycosylated protein (4 µg) was injected to the LC–MS system to acquire intact MS signal. Thermo MS (Q Exactive Plus Orbitrap) was used to acquire intact protein mass under denaturing condition with *m/z* window from 1,000 to 6,000. BioPharma Finder 3.2 software was used to deconvolute the raw *m/z* data to protein average mass. The theoretical mass for each monoclonal antibody was calculated with GPMAW 10.10 software. Post-translational modifications such as N-terminal pyroglutamate cyclization, C-terminal lysine cleavage and formation of 16–18 disulfide bonds were added into the calculation.

## Sample donors

Samples were obtained from SARS-CoV-2 convalescent and vaccinated individuals under study protocols approved by the local institutional review boards (Canton Ticino Ethics Committee, Switzerland, Comitato Etico Milano Area 1). All donors provided written informed consent for the use of blood and blood derivatives (such as peripheral blood mononuclear cells, sera or plasma) for research. Plasma samples from convalescent individuals and individuals who had been vaccinated with Ad26.COV2.S, mRNA-1273 or BNT162b2 were obtained from the HAARVI study, approved by the University of Washington Human Subjects Division Institutional Review Board (STUDY00000959). Samples from individuals who had been vaccinated with AZD1222 were obtained from INGM, Ospedale Maggio Policlinico of Milan and approved by the local review board Study Polimmune. Samples from individuals who had been vaccinated with Sputnik V were obtained from healthcare workers at the hospital de Clínicas ‘José de San Martín’, Buenos Aires, Argentina. Samples from individuals who had been vaccinated with Sinopharm were enrolled from Aga Khan University under the institutional review board of the UWARN (United World Antivirus Research Network) study.

## Pseudovirus neutralization assays

### Generation of VSV pseudovirus used in Vero E6 cells

The plasmid encoding the Omicron SARS-CoV-2 spike variant was generated by overlap PCR mutagenesis of the wild-type plasmid, pcDNA3.1(+)-spike-D19<sup>55</sup>. Replication defective VSV pseudovirus expressing SARS-CoV-2 spike proteins corresponding to the ancestral Wuhan-Hu-1 virus and the Omicron VOC were generated as previously described<sup>46</sup> with some modifications. Lenti-X 293T cells

(Takara) were seeded in 15-cm<sup>2</sup> dishes at a density of  $10 \times 10^6$  cells per dish and the following day were transfected with 25 µg of spike expression plasmid with TransIT-Lenti (Mirus, 6600) according to the manufacturer's instructions. One day after transfection, cells were infected with VSV-luc (VSV-G) with a multiplicity of infection (MOI) of 3 for 1 h, rinsed three times with PBS containing Ca<sup>2+</sup> and Mg<sup>2+</sup>, then incubated for an additional 24 h in complete medium at 37 °C. The cell supernatant was clarified by centrifugation, aliquoted, and frozen at -80 °C.

### **Generation of VSV pseudovirus used in Vero E6-TMPRSS2 cells**

Comparison of Omicron SARS-CoV-2 spike VSV to SARS-CoV-2 G614 spike (YP 009724390.1) VSV and Beta spike VSV used pseudotyped particles prepared as described previously<sup>9,56</sup>. In brief, HEK293T cells in DMEM supplemented with 10% FBS, 1% penicillin–streptomycin seeded in 10-cm dishes were transfected with the plasmid encoding the corresponding spike glycoprotein using Lipofectamine 2000 (Life Technologies) following the manufacturer's instructions. One day after transfection, cells were infected with VSV(G\*ΔG-luciferase)<sup>57</sup> and after 2 h were washed five times with DMEM before adding medium supplemented with anti-VSV-G antibody (I1-mouse hybridoma supernatant, CRL-2700, ATCC). Virus pseudotypes were collected 18–24 h after inoculation, clarified by centrifugation at 2,500g for 5 min, filtered through a 0.45-µm cut-off membrane, concentrated 10 times with a 30-kDa cut-off membrane, aliquoted and stored at -80 °C.

### **VSV pseudovirus neutralization**

### **Assay performed using Vero E6 cells**

Vero E6 cells were grown in DMEM supplemented with 10% FBS and seeded into clear bottom white 96 well plates (PerkinElmer, 6005688) at a density of 20,000 cells per well. The next day, monoclonal antibodies or plasma were serially diluted in pre-warmed complete medium, mixed with pseudoviruses and incubated for 1 h at 37 °C in round bottom polypropylene plates. Medium from cells was aspirated and 50 µl of virus–monoclonal antibody–plasma complexes was added to cells, which were then incubated for 1 h at 37 °C. An additional 100 µl of prewarmed complete medium was then added on top of complexes and cells were incubated for an additional 16–24 h. Conditions were tested in duplicate wells on each plate and eight wells per plate contained untreated infected cells (defining the 0% of neutralization, 'MAX RLU' value) and infected cells in the presence of S309 and S2X259 at 20 µg ml<sup>-1</sup> each (defining the 100% of neutralization, 'MIN RLU' value). Virus–monoclonal antibody–plasma-containing medium was then aspirated from cells and 100 µl of a 1:2 dilution of SteadyLite Plus (PerkinElmer, 6066759) in PBS with Ca<sup>2+</sup> and Mg<sup>2+</sup> was added to

cells. Plates were incubated for 15 min at room temperature and then were analysed on the Synergy-H1 (Biotek). The average relative light units (RLUs) of untreated infected wells ( $\text{MAX RLU}_{\text{ave}}$ ) was subtracted by the average of MIN RLU ( $\text{MIN RLU}_{\text{ave}}$ ) and used to normalize percentage of neutralization of individual RLU values of experimental data according to the following formula:  $(1 - (\text{RLU}_x - \text{MIN RLU}_{\text{ave}})/(\text{MAX RLU}_{\text{ave}} - \text{MIN RLU}_{\text{ave}})) \times 100$ . Data were analysed and visualized with Prism (v.9.1.0).  $\text{IC}_{50}$  (monoclonal antibodies) and  $\text{ID}_{50}$  (plasma) values were calculated from the interpolated value from the log(inhibitor) versus response, using variable slope (four parameters) nonlinear regression with an upper constraint of  $\leq 100$ , and a lower constrain equal to 0. Each neutralization experiment was conducted on two independent experiments—that is, biological replicates—in which each biological replicate contains a technical duplicate.  $\text{IC}_{50}$  values across biological replicates are presented as arithmetic mean  $\pm$  s.d. The loss or gain of neutralization potency across spike variants was calculated by dividing the variant  $\text{IC}_{50}/\text{ID}_{50}$  by the parental  $\text{IC}_{50}/\text{ID}_{50}$  within each biological replicate, and then visualized as arithmetic mean  $\pm$  s.d.

### Assay performed using Vero E6-TMPRSS2 cells

VeroE6-TMPRSS2 cells were cultured in DMEM with 10% FBS (Hyclone), 1% penicillin–streptomycin and  $8 \mu\text{g ml}^{-1}$  puromycin (to ensure retention of TMPRSS2) with 5%  $\text{CO}_2$  in a 37 °C incubator (Thermo Fisher Scientific). Cells were trypsinized using 0.05% trypsin and plated to be at 90% confluence the following day. In an empty half-area 96-well plate, a 1:3 serial dilution of serum was made in DMEM and diluted pseudovirus was then added and incubated at room temperature for 30–60 min before addition of the serum–virus mixture to the cells at 37 °C. Two hours later, 40  $\mu\text{l}$  of a DMEM solution containing 20% FBS and 2% penicillin–streptomycin (Thermo Fisher Scientific, 10,000 units per ml of penicillin and 10,000  $\mu\text{g ml}^{-1}$  of streptomycin when undiluted) was added to each well. After 17–20 h, 40  $\mu\text{l}$  per well of One-Glo-EX substrate (Promega) was added to the cells and they were incubated in the dark for 5–10 min before reading on a BioTek plate reader. Measurements were done at least in duplicate using distinct batches of pseudoviruses and one representative experiment is shown. RLUs were plotted and normalized in Prism (GraphPad). Nonlinear regression of log(inhibitor) versus normalized response was used to determine  $\text{IC}_{50}$  values from curve fits. Normality was tested using the D'Agostino-Pearson test and in the absence of a normal distribution, Kruskal–Wallis tests were used to compare two groups to determine whether differences reached statistical significance. Fold changes were determined by comparing individual  $\text{IC}_{50}$  and then averaging the individual fold changes for reporting.

## Focus reduction neutralization test

The WA1/2020 strain with a D614G substitution was described previously<sup>58</sup>. The B.1.1.529 isolate (hCoV-19/USA/WI-WSLH-221686/2021) was obtained from a nasal swab and passaged on Vero-TMPRSS2 cells as described<sup>59</sup>. The B.1.1.529 isolate was sequenced (GISaid: EPI\_ISL\_7263803) to confirm the stability of substitutions. All virus experiments were performed in an approved biosafety level 3 (BSL-3) facility.

Serial dilutions of sotrovimab were incubated with  $10^2$  focus-forming units of SARS-CoV-2 (WA1/2020 D614G or B.1.1.529) for 1 h at 37 °C. Antibody–virus complexes were added to Vero-TMPRSS2 cell monolayers in 96-well plates and incubated at 37 °C for 1 h. Subsequently, cells were overlaid with 1% (w/v) methylcellulose in MEM. Plates were collected 30 h later (WA1/2020 D614G on Vero-TMPRSS2 cells) or 70 h later (B.1.1.529 on Vero-TMPRSS2 cells) by removal of overlays and fixation with 4% PFA in PBS for 20 min at room temperature. Plates with WA1/2020 D614G were washed and sequentially incubated with an oligoclonal pool of SARS2-2, SARS2-11, SARS2-16, SARS2-31, SARS2-38, SARS2-57 and SARS2-71<sup>60</sup> anti-S antibodies. Plates with B.1.1.529 were additionally incubated with a pool of monoclonal antibodies that cross-react with SARS-CoV-1 and bind a CR3022-competing epitope on the RBD<sup>61</sup>. All plates were subsequently stained with HRP-conjugated goat anti-mouse IgG (Sigma, A8924) in PBS supplemented with 0.1% saponin and 0.1% bovine serum albumin. SARS-CoV-2-infected cell foci were visualized using TrueBlue peroxidase substrate (KPL) and quantitated on an ImmunoSpot microanalyser (Cellular Technologies). Antibody dose response curves were analysed using nonlinear regression analysis with a variable slope (GraphPad Software), and the IC<sub>50</sub> was calculated.

## VSV pseudovirus entry assays using mouse ACE2

HEK293T (293T) cells (ATCC CRL-11268) were cultured in 10% FBS, 1% penicillin–streptomycin in DMEM at 37 °C in a humidified 8% CO<sub>2</sub> incubator. Transient transfection of mouse ACE2 in 293T cells was done 18–24 h before infection using Lipofectamine 2000 (Life Technologies) and an HDM plasmid containing full-length mouse ACE2 (GenBank: Q8R010, synthesized by GenScript) in Opti-MEM. After a 5-h incubation at 37 °C in a humidified 8% CO<sub>2</sub> incubator, DMEM with 10% FBS was added and cells were incubated at 37 °C in a humidified 8% CO<sub>2</sub> incubator for 18–24 h. Immediately before infection, 293T cells with transient expression of mouse ACE2 were washed with DMEM 1×, then plated with pseudovirus at a 1:75 dilution in DMEM. Infection in DMEM was done with cells between 60% and 80% confluence for 2.5 h before adding FBS and penicillin–streptomycin to final concentrations of 10% and 1%, respectively. After 18–24 h of

infection, One-Glo-EX (Promega) was added to the cells and they were incubated in the dark for 5 min before reading on a Synergy H1 Hybrid Multi-Mode plate reader (Bioteck). Cell entry levels of pseudovirus generated on different days (biological replicates) were plotted in GraphPad Prism as individual points, and average cell entry across biological replicates was calculated as the geometric mean.

## Production of recombinant RBD proteins

SARS-CoV-2 RBD proteins for SPR binding assays (residues 328–531 of the spike protein from GenBank NC\_045512.2 with N-terminal signal peptide and C-terminal thrombin cleavage site-TwinStrep-8×His-tag) were expressed in Expi293F (Thermo Fisher Scientific) cells at 37 °C and 8% CO<sub>2</sub>. Transfections were performed using the ExpiFectamine 293 Transfection Kit (Thermo Fisher Scientific). Cell culture supernatants were collected two to four days after transfection and supplemented with 10× PBS to a final concentration of 2.5× PBS (342.5 mM NaCl, 6.75 mM KCl and 29.75 mM phosphates). SARS-CoV-2 RBDs were purified using cobalt-based immobilized metal affinity chromatography followed by buffer exchange into PBS using a HiPrep 26/10 desalting column (Cytiva) or, for the second batch of Omicron RBD used for SPR, a Superdex 200 Increase 10/300 GL column (Cytiva).

The SARS-CoV-2 Wuhan-Hu-1 and Delta (B.1.617.2) RBD-Avi constructs were synthesized by GenScript into pcDNA3.1- with an N-terminal mu-phosphatase signal peptide and a C-terminal octa-histidine tag, flexible linker and avi tag (GHHHHHHHHGGSSGLNDIFEAQKIEWHE). The boundaries of the construct are N-<sub>328</sub>RFPN<sub>331</sub> and <sub>528</sub>KKST<sub>531</sub>-C (refs. [9](#)[14](#)). Proteins were produced in Expi293F cells (Thermo Fisher Scientific) grown in suspension using Expi293 Expression Medium (Thermo Fisher Scientific) at 37 °C in a humidified 8% CO<sub>2</sub> incubator rotating at 130 rpm. Cells grown to a density of 3 million cells per ml were transfected using the the ExpiFectamine 293 Transfection Kit (Thermo Fisher Scientific) and cultivated for 3–5 days. Proteins were purified from clarified supernatants using a nickel HisTrap HP affinity column (Cytiva) and washed with 10 column volumes of 20 mM imidazole, 25 mM sodium phosphate pH 8.0 and 300 mM NaCl before elution on a gradient to 500 mM imidazole. Proteins were biotinylated overnight using the BirA Biotin-Protein Ligase Kit (Avidity) and purified again using the HisTrapHP affinity column. After a wash and elution as before, proteins were buffer-exchanged into 20 mM sodium phosphate pH 8 and 100 mM NaCl, and concentrated using centrifugal filters (Amicon Ultra) before being flash-frozen.

## Recombinant production of ACE2 orthologues

Recombinant human ACE2 (residues 19–615 from Uniprot Q9BYF1 with a C-terminal AviTag-10×His-GGG-tag, and N-terminal signal peptide) was produced by

ATUM. Protein was purified via Ni Sepharose resin followed by isolation of the monomeric hACE2 by size-exclusion chromatography using a Superdex 200 Increase 10/300 GL column (Cytiva) pre-equilibrated with PBS. The mouse (*Mus musculus*) ACE2 ectodomain construct (GenBank: Q8R0I0) was synthesized by GenScript and placed into a pCMV plasmid. The domain boundaries for the ectodomain are residues 19–615. The native signal tag was identified using SignalP-5.0 (residues 1–18) and replaced with an N-terminal mu-phosphatase signal peptide. This construct was then fused to a sequence encoding a thrombin cleavage site and a human Fc fragment or an 8×His tag at the C terminus. ACE2-Fc and ACE2-His constructs were produced in Expi293 cells (Thermo Fisher Scientific, A14527) in Gibco Expi293 Expression Medium at 37 °C in a humidified 8% CO<sub>2</sub> incubator rotating at 130 rpm. The cultures were transfected using PEI-25K (Polyscience) with cells grown to a density of 3 million cells per ml and cultivated for 4–5 days. Proteins were purified from clarified supernatants using a 1-ml HiTrap Protein A HP affinity column (Cytiva) or a 1-ml HisTrap HP affinity column (Cytiva), concentrated and flash-frozen in 1× PBS, pH 7.4 (10 mM Na<sub>2</sub>HPO<sub>4</sub>, 1.8 mM KH<sub>2</sub>PO<sub>4</sub>, 2.7 mM KCl, 137 mM NaCl).

## ACE2-binding measurements using SPR

Measurements were performed using a Biacore T200 instrument, in triplicate for monomeric human and mouse ACE2 and duplicate for dimeric mouse ACE2. A CM5 chip covalently immobilized with StrepTactin XT (IBA LifeSciences) was used for surface capture of TwinStrepTag-containing RBDs (Wuhan-Hu-1, Alpha, Beta, Omicron, K417N) and a Cytiva Biotin CAPture Kit was used for surface capture of biotinylated RBDs (Delta and Wuhan-Hu-1 used for fold-change comparison to Delta). Two different batches of Omicron RBD were used for the experiments. Running buffer was HBS-EP+ pH 7.4 (Cytiva) and measurements were performed at 25 °C. Experiments were performed with a threefold dilution series of human ACE2 (300, 100, 33, 11 nM) or mouse ACE2 (900, 300, 100, 33 nM) and were run as single-cycle kinetics. Monomeric ACE2-binding data were double-reference-subtracted and fit to a 1:1 binding model using Biacore Evaluation software. High concentrations of dimeric mouse ACE2 exhibited significant binding to the CAP sensor chip reference flow cell.

## Statistical analysis

Neutralization measurements were performed in duplicate and RLU<sub>s</sub> were converted to per cent neutralization and plotted with a nonlinear regression model to determine IC<sub>50</sub>/ID<sub>50</sub> values using GraphPad Prism software (v.9.0.0). Comparisons between two groups of paired two-sided data were made with Wilcoxon rank test.

## Reporting summary

Further information on research design is available in the [Nature Research Reporting Summary](#) linked to this paper.

## Data availability

Materials generated in this study will be made available on request and may require a material transfer agreement. Access to GISAID ([www.gisaid.org](http://www.gisaid.org)) data requires registration. Note: after consulting with the local ethical authority, owing to health and data protection laws relating to the demographic and clinical information contained in the manuscript, we will not be able to fully comply with the requirement to share demographic and clinical data of individual patients and donors in this study.

## References

1. Park, Y. J. et al. Antibody-mediated broad sarbecovirus neutralization through ACE2 molecular mimicry. *Science* <https://doi.org/10.1126/science.abm8143> (2022).
2. Pinto, D. et al. Cross-neutralization of SARS-CoV-2 by a human monoclonal SARS-CoV antibody. *Nature* **583**, 290–295 (2020).
3. Tortorici, M. A. et al. Broad sarbecovirus neutralization by a human monoclonal antibody. *Nature* **597**, 103–108 (2021).
4. Starr, T. N. et al. SARS-CoV-2 RBD antibodies that maximize breadth and resistance to escape. *Nature* **597**, 97–102 (2021).
5. Telenti, A. et al. After the pandemic: perspectives on the future trajectory of COVID-19. *Nature* **596**, 495–504 (2021).
6. Wang, P. et al. Antibody resistance of SARS-CoV-2 variants B.1.351 and B.1.1.7. *Nature* **593**, 130–135 (2021).
7. Chen, R. E. et al. Resistance of SARS-CoV-2 variants to neutralization by monoclonal and serum-derived polyclonal antibodies. *Nat. Med.* **27**, 717–726 (2021).
8. Corti, D., Purcell, L. A., Snell, G. & Veesler, D. Tackling COVID-19 with neutralizing monoclonal antibodies. *Cell* **184**, 3086–3108 (2021).

9. McCallum, M. et al. Molecular basis of immune evasion by the Delta and Kappa SARS-CoV-2 variants. *Science* **374**, 1621–1626 (2021).
10. Mlcochova, P. et al. SARS-CoV-2 B.1.617.2 Delta variant replication and immune evasion. *Nature* **599**, 114–119 (2021).
11. Sheikh, A. et al. SARS-CoV-2 Delta VOC in Scotland: demographics, risk of hospital admission, and vaccine effectiveness. *Lancet* **397**, 2461–2462 (2021).
12. Piccoli, L. et al. Mapping neutralizing and immunodominant sites on the SARS-CoV-2 spike receptor-binding domain by structure-guided high-resolution serology. *Cell* **183**, 1024–1042 (2020).
13. Greaney, A. J. et al. Comprehensive mapping of mutations in the SARS-CoV-2 receptor-binding domain that affect recognition by polyclonal human plasma antibodies. *Cell Host Microbe* **29**, 463–476 (2021).
14. Walls, A. C. et al. Structure, function, and antigenicity of the SARS-CoV-2 spike glycoprotein. *Cell* **181**, 281–292 (2020).
15. Cele, S. et al. Omicron extensively but incompletely escapes Pfizer BNT162b2 neutralization. *Nature* <https://doi.org/10.1038/s41586-021-04387-1> (2021).
16. Wilhelm, A. et al. Reduced neutralization of SARS-CoV-2 Omicron variant by vaccine sera and monoclonal antibodies. Preprint at <https://doi.org/10.1101/2021.12.07.21267432> (2021).
17. Andrews, N. et al. Effectiveness of COVID-19 vaccines against the Omicron variant of concern. Preprint at <https://doi.org/10.1101/2021.12.14.21267615> (2021).
18. Cao, Y. et al. B.1.1.529 escapes the majority of existing SARS-CoV-2 neutralizing antibodies. *Nature* <https://doi.org/10.1038/s41586-021-04385-3> (2021).
19. Leist, S. R. et al. A mouse-adapted SARS-CoV-2 induces acute lung injury and mortality in standard laboratory mice. *Cell* **183**, 1070–1085 (2020).
20. Dinnon, K. H. III et al. A mouse-adapted model of SARS-CoV-2 to test COVID-19 countermeasures. *Nature* **586**, 560–566 (2020).
21. Collier, D. A. et al. Sensitivity of SARS-CoV-2 B.1.1.7 to mRNA vaccine-elicited antibodies. *Nature* **593**, 136–141 (2021).

22. Starr, T. N. et al. Deep mutational scanning of SARS-CoV-2 receptor binding domain reveals constraints on folding and ACE2 binding. *Cell* **182**, 1295–1310 (2020).
23. Shuai, H. et al. Emerging SARS-CoV-2 variants expand species tropism to murines. *EBioMedicine* **73**, 103643 (2021).
24. Pan, T. et al. Infection of wild-type mice by SARS-CoV-2 B.1.351 variant indicates a possible novel cross-species transmission route. *Sig. Transduct. Target Ther.* **6**, 420 (2021).
25. Hoffmann, M. et al. The Omicron variant is highly resistant against antibody-mediated neutralization—implications for control of the COVID-19 pandemic. *Cell* <https://doi.org/10.1016/j.cell.2021.12.032> (2021).
26. Nicholls, J. & Chan Chi-wai, M. HKUMed finds Omicron SARS-CoV-2 can infect faster and better than Delta in human bronchus but with less severe infection in lung. [www.med.hku.hk/en/news/press/20211215-omicron-sars-cov-2-infection](http://www.med.hku.hk/en/news/press/20211215-omicron-sars-cov-2-infection) (2021).
27. Bassi, J. et al. Poor neutralization and rapid decay of antibodies to SARS-CoV-2 variants in vaccinated dialysis patients. Preprint at <https://doi.org/10.1101/2021.10.05.21264054> (2021).
28. Khoury, D. S. et al. Neutralizing antibody levels are highly predictive of immune protection from symptomatic SARS-CoV-2 infection. *Nat. Med.* **27**, 1205–1211 (2021).
29. Stamatatos, L. et al. mRNA vaccination boosts cross-variant neutralizing antibodies elicited by SARS-CoV-2 infection. *Science* <https://doi.org/10.1126/science.abg9175> (2021).
30. Bergstrom, J. J., Xu, H. & Heyman, B. Epitope-specific suppression of IgG responses by passively administered specific IgG: evidence of epitope masking. *Front. Immunol.* **8**, 238 (2017).
31. Baum, A. et al. Antibody cocktail to SARS-CoV-2 spike protein prevents rapid mutational escape seen with individual antibodies. *Science* **369**, 1014–1018 (2020).
32. Hansen, J. et al. Studies in humanized mice and convalescent humans yield a SARS-CoV-2 antibody cocktail. *Science* **369**, 1010–1014 (2020).

33. Shi, R. et al. A human neutralizing antibody targets the receptor-binding site of SARS-CoV-2. *Nature* **584**, 120–124 (2020).
34. Gottlieb, R. L. et al. Effect of bamlanivimab as monotherapy or in combination with etesevimab on viral load in patients with mild to moderate COVID-19: a randomized clinical trial. *JAMA* **325**, 632–644 (2021).
35. Jones, B. E. et al. The neutralizing antibody, LY-CoV555, protects against SARS-CoV-2 infection in nonhuman primates. *Sci. Transl. Med.* **13**, eabf1906 (2021).
36. Dong, J. et al. Genetic and structural basis for SARS-CoV-2 variant neutralization by a two-antibody cocktail. *Nat. Microbiol.* **6**, 1233–1244 (2021).
37. Zost, S. J. et al. Potently neutralizing and protective human antibodies against SARS-CoV-2. *Nature* **584**, 443–449 (2020).
38. Thomson, E. C. et al. Circulating SARS-CoV-2 spike N439K variants maintain fitness while evading antibody-mediated immunity. *Cell* **184**, 1171–1187 (2021).
39. Starr, T. N. et al. ACE2 binding is an ancestral and evolvable trait of sarbecoviruses. Preprint at <https://doi.org/10.1101/2021.07.17.452804> (2021).
40. Lempp, F. A. et al. Lectins enhance SARS-CoV-2 infection and influence neutralizing antibodies. *Nature* **598**, 342–347 (2021).
41. VanBlargan, L. A. et al. An infectious SARS-CoV-2 B.1.1.529 Omicron virus escapes neutralization by therapeutic monoclonal antibodies. *Nat. Med.* <https://doi.org/10.1038/s41591-021-01678-y> (2022).
42. Aggarwal, A. et al. SARS-CoV-2 Omicron: evasion of potent humoral responses and resistance to clinical immunotherapeutics relative to viral variants of concern. Preprint at <https://doi.org/10.1101/2021.12.14.21267772> (2021).
43. FDA. Fact sheet for healthcare providers: emergency use authorization (EUA) of sotrovimab. <https://www.fda.gov/media/149534/download> (2021).
44. Tortorici, M. A. et al. Ultrapotent human antibodies protect against SARS-CoV-2 challenge via multiple mechanisms. *Science* **370**, 950–957 (2020).
45. McCallum, M. et al. N-terminal domain antigenic mapping reveals a site of vulnerability for SARS-CoV-2. *Cell* **184**, 2332–2347 (2021).
46. McCallum, M. et al. SARS-CoV-2 immune evasion by the B.1.427/B.1.429 variant of concern. *Science* **373**, 648–654 (2021).

47. Fischer, W. et al. HIV-1 and SARS-CoV-2: patterns in the evolution of two pandemic pathogens. *Cell Host Microbe* **29**, 1093–1110 (2021).
48. Kupferschmidt, K. Where did ‘weird’ Omicron come from? *Science* **374**, 1179 (2021).
49. Corey, L. et al. SARS-CoV-2 variants in patients with immunosuppression. *N. Engl. J. Med.* **385**, 562–566 (2021).
50. Oude Munnink, B. B. et al. Transmission of SARS-CoV-2 on mink farms between humans and mink and back to humans. *Science* **371**, 172–177 (2021).
51. Zang, R. et al. TMPRSS2 and TMPRSS4 promote SARS-CoV-2 infection of human small intestinal enterocytes. *Sci. Immunol.* **5**, eabc3582 (2020).
52. Maziarz, R. T. et al. Control of an outbreak of human parainfluenza virus 3 in hematopoietic stem cell transplant recipients. *Biol. Blood Marrow Transplant.* **16**, 192–198 (2010).
53. Katoh, K. & Standley, D. M. MAFFT multiple sequence alignment software version 7: improvements in performance and usability. *Mol. Biol. Evol.* **30**, 772–780 (2013).
54. Yamin, R. et al. Fc-engineered antibody therapeutics with improved anti-SARS-CoV-2 efficacy. *Nature* **599**, 465–470 (2021).
55. Giroglou, T. et al. Retroviral vectors pseudotyped with severe acute respiratory syndrome coronavirus S protein. *J. Virol.* **78**, 9007–9015 (2004).
56. Walls, A. C. et al. Elicitation of broadly protective sarbecovirus immunity by receptor-binding domain nanoparticle vaccines. *Cell* **184**, 5432–5447 (2021).
57. Kaname, Y. et al. Acquisition of complement resistance through incorporation of CD55/decay-accelerating factor into viral particles bearing baculovirus GP64. *J. Virol.* **84**, 3210–3219 (2010).
58. Plante, J. A. et al. Spike mutation D614G alters SARS-CoV-2 fitness. *Nature* **592**, 116–121 (2021).
59. Imai, M. et al. Syrian hamsters as a small animal model for SARS-CoV-2 infection and countermeasure development. *Proc. Natl Acad. Sci. USA* **117**, 16587–16595 (2020).

60. Liu, Z. et al. Identification of SARS-CoV-2 spike mutations that attenuate monoclonal and serum antibody neutralization. *Cell Host Microbe* **29**, 477–488 (2021).
61. VanBlargan, L. A. et al. A potently neutralizing SARS-CoV-2 antibody inhibits variants of concern by utilizing unique binding residues in a highly conserved epitope. *Immunity* **54**, 2399–2416 (2021).
62. Cathcart, A. L. et al. The dual function monoclonal antibodies VIR-7831 and VIR-7832 demonstrate potent in vitro and in vivo activity against SARS-CoV-2. Preprint at <https://doi.org/10.1101/2021.03.09.434607> (2021).
63. Gupta, A. et al. Early treatment for Covid-19 with SARS-CoV-2 neutralizing antibody sotrovimab. *N. Engl. J. Med.* **385**, 1941–1950 (2021).
64. Kim, C. et al. A therapeutic neutralizing antibody targeting receptor binding domain of SARS-CoV-2 spike protein. *Nat. Commun.* **12**, 288 (2021).
65. Ryu, D. K. et al. Therapeutic effect of CT-P59 against SARS-CoV-2 South African variant. *Biochem. Biophys. Res. Commun.* **566**, 135–140 (2021).
66. Baum, A. et al. REGN-COV2 antibodies prevent and treat SARS-CoV-2 infection in rhesus macaques and hamsters. *Science* **370**, 1110–1115 (2020).
67. Copin, R. et al. The monoclonal antibody combination REGEN-COV protects against SARS-CoV-2 mutational escape in preclinical and human studies. *Cell* **184**, 3949–3961 (2021).
68. Weinreich, D. M. et al. REGN-COV2, a neutralizing antibody cocktail, in outpatients with Covid-19. *N. Engl. J. Med.* **384**, 238–251 (2021).
69. Chen, P. et al. SARS-CoV-2 neutralizing antibody LY-CoV555 in outpatients with Covid-19. *N. Engl. J. Med.* **384**, 229–237 (2021).
70. Group, A.-T. L.-C. S. et al. A neutralizing monoclonal antibody for hospitalized patients with Covid-19. *N. Engl. J. Med.* **384**, 905–914 (2021).
71. Belk, J., Deveau, L. M., Rappazzo, C. G., Walker, L. & Wec, A. PCT application WO/2021/207597: Compounds specific to coronavirus S protein and uses thereof. (Adagio Therapeutics, 2021).

## Acknowledgements

We thank H. Tani for providing the reagents necessary for preparing VSV pseudotyped viruses. This study was supported by the National Institute of Allergy and Infectious Diseases (DP1AI158186 and HHSN272201700059C to D.V.), a Pew Biomedical Scholars Award (D.V.), an Investigators in the Pathogenesis of Infectious Disease Awards from the Burroughs Wellcome Fund (D.V.), Fast Grants (D.V.) and the National Institute of General Medical Sciences (5T32GM008268-32 to S.K.Z.). D.V. is an Investigator of the Howard Hughes Medical Institute. O.G. is funded by the Swiss Kidney Foundation. This work was supported, in part, by the National Institutes of Allergy and Infectious Diseases Center for Research on Influenza Pathogenesis (HHSN272201400008C), the Center for Research on Influenza Pathogenesis and Transmission (CRIPT) (75N93021C00014) and the Japan Program for Infectious Diseases Research and Infrastructure (JP21wm0125002) from the Japan Agency for Medical Research and Development (AMED). This work was supported in part through National Institutes of Health USA grant U01 AI151698 for the United World Antivirus Research Network (UWARN).

## Author information

### Author notes

1. These authors contributed equally: Elisabetta Cameroni, John E. Bowen, Laura E. Rosen, Christian Saliba
2. These authors jointly supervised this work: Herbert W. Virgin, Antonio Lanzavecchia, Gyorgy Snell, David Veesler, Davide Corti

### Affiliations

1. Humabs Biomed SA, a subsidiary of Vir Biotechnology, Bellinzona, Switzerland

Elisabetta Cameroni, Christian Saliba, Katja Culap, Dora Pinto, Anna De Marco, Fabrizia Zatta, Jessica Bassi, Chiara Silacci-Fregnini, Luca Piccoli, Matteo Samuele Pizzuto, Antonio Lanzavecchia & Davide Corti

2. Department of Biochemistry, University of Washington, Seattle, WA, USA

John E. Bowen, Samantha K. Zepeda, Kaitlin R. Sprouse, Alexandra C. Walls & David Veesler

3. Vir Biotechnology, San Francisco, CA, USA

Laura E. Rosen, Julia di Julio, Hannah Kaiser, Julia Noack, Nisar Farhat, Nadine Czudnochowski, Colin Havenar-Daughton, Josh R. Dillen, Abigail E.

Powell, Alex Chen, Cyrus Maher, Li Yin, David Sun, Leah Soriaga, Christy Hebner, Lisa A. Purcell, Amalio Telenti, Herbert W. Virgin & Gyorgy Snell

4. Department of Medicine, Washington University School of Medicine, St Louis, MO, USA

Laura A. VanBlargan & Michael S. Diamond

5. ATUM, Newark, CA, USA

Claes Gustafsson

6. Division of Allergy and Infectious Diseases, University of Washington, Seattle, WA, USA

Nicholas M. Franko, Jenni Logue & Helen Chu

7. Department of Paediatrics and Child Health, Aga Khan University, Karachi, Pakistan

Najeeha Talat Iqbal

8. Instituto de Investigaciones Biomédicas en Retrovirus y SIDA (INBIRS), Facultad de Medicina, Universidad de Buenos Aires, Buenos Aires, Argentina

Ignacio Mazzitelli & Jorge Geffner

9. National Institute of Molecular Genetics, Milan, Italy

Renata Grifantini & Antonio Lanzavecchia

10. Infectious Disease Unit, Fondazione IRCCS Ca' Granda, Ospedale Maggiore Policlinico, Milan, Italy

Andrea Gori

11. Department of Biomedical and Clinical Sciences ‘L.Sacco’ (DIBIC), Università di Milano, Milan, Italy

Agostino Riva

12. Faculty of Biomedical Sciences, Università della Svizzera italiana, Lugano, Switzerland

Olivier Giannini, Alessandro Ceschi & Paolo Ferrari

13. Department of Medicine, Ente Ospedaliero Cantonale, Bellinzona, Switzerland

Olivier Giannini & Pietro E. Cippà

14. Clinical Trial Unit, Ente Ospedaliero Cantonale, Lugano, Switzerland

Alessandro Ceschi

15. Division of Clinical Pharmacology and Toxicology, Institute of Pharmacological Sciences of Southern Switzerland, Ente Ospedaliero Cantonale, Lugano, Switzerland

Alessandro Ceschi

16. Department of Clinical Pharmacology and Toxicology, University Hospital Zurich, Zurich, Switzerland

Alessandro Ceschi

17. Division of Nephrology, Ente Ospedaliero Cantonale, Lugano, Switzerland

Paolo Ferrari & Pietro E. Cippà

18. Clinical School, University of New South Wales, Sydney, New South Wales, Australia

Paolo Ferrari

19. Faculty of Medicine, University of Zurich, Zurich, Switzerland

Pietro E. Cippà

20. Clinical Research Unit, Clinica Luganese Moncucco, Lugano, Switzerland

Alessandra Franzetti-Pellanda

21. Clinic of Internal Medicine and Infectious Diseases, Clinica Luganese Moncucco, Lugano, Switzerland

Christian Garzoni

22. Influenza Research Institute, Department of Pathobiological Sciences, School of Veterinary Medicine, University of Wisconsin–Madison, Madison, WI, USA

Peter J. Halfmann & Yoshihiro Kawaoka

23. Division of Virology, Department of Microbiology and Immunology, Institute of Medical Science, University of Tokyo, Tokyo, Japan

Yoshihiro Kawaoka

24. The Research Center for Global Viral Diseases, National Center for Global Health and Medicine Research Institute, Tokyo, Japan

Yoshihiro Kawaoka

25. Howard Hughes Medical Institute, Seattle, WA, USA

Alexandra C. Walls & David Veesler

26. Department of Pathology and Immunology, Washington University School of Medicine, St Louis, MO, USA

Michael S. Diamond & Herbert W. Virgin

27. Department of Molecular Microbiology, Washington University School of Medicine, St Louis, MO, USA

Michael S. Diamond

28. Department of Internal Medicine, UT Southwestern Medical Center, Dallas, TX, USA

Herbert W. Virgin

## Contributions

D.C., G.S., M.S.P., L.P. and D.V. conceived the research and designed the study. D.C., D.P., E.C., L.E.R., G.S., M.S.P., L.P., J.E.B., S.K.Z., A.C.W. and D.V. designed experiments. E.C. and K.C. designed and performed mutagenesis for the spike mutant expression plasmids. C.S., D.P., H.K., J.N., N.F., K.R.S. and S.K.Z. produced pseudoviruses. C.S., J.E.B., S.K.Z., D.P., F.Z., J.B., C.S.-F. and A.D.M. performed pseudovirus entry or neutralization assays. C.S., K.C. and E.C. expressed antibodies. L.A.V., P.J.H. and Y.K. isolated and propagated the SARS-CoV-2 Omicron live virus. L.A.V. performed authentic virus neutralization assays. M.S.D. supervised the research on authentic virus neutralization assays. L.E.R. performed binding assays. C. Gustafsson, S.K.Z., A.C.W., N.C., A.E.P. and J.R.D. synthesized expression plasmids and expressed and purified ACE2 and RBD proteins. C.S. and A.C. produced and performed quality control of monoclonal antibodies. J.d.I., C.M., L.Y., D.S. and L.S. performed bioinformatic and epidemiology analyses. C.S., D.P., L.P., L.E.R., M.S.P.

and A.D.M. interpreted data. E.C., C.S., F.Z., A.D.M., K.C., D.P., J.E.B., L.E.R., S.K.Z., A.C.W., D.V., A.T., G.S. and D.C. analysed data. A.R., O.G., C. Garzoni, A.C., P.F., A.F.-P., H.C., N.M.F., J.L., N.T.I., I.M., J.G., R.G., A.G., P.E.C. and C.H.-D. contributed to the recruitment of donors and collection of plasma samples. D.C., A.L., H.W.V., G.S., A.T., C.H., L.A.P. and D.V. wrote the manuscript with input from all authors.

## Corresponding authors

Correspondence to [Gyorgy Snell](#), [David Veesler](#) or [Davide Corti](#).

## Ethics declarations

### Competing interests

E.C., K.C., C.S., D.P., F.Z., A.D.M., A.L., L.P., M.S.P., D.C., H.K., J.N., N.F., J.d.I., L.E.R., N.C., C.H.-D., K.R.S., J.R.D., A.E.P., A.C., C.M., L.Y., D.S., L.S., L.A.P., C.H., A.T., H.W.V. and G.S. are employees of Vir Biotechnology and may hold shares in Vir Biotechnology. L.A.P. is a former employee and shareholder in Regeneron Pharmaceuticals. Regeneron provided no funding for this work. H.W.V. is a founder and holds shares in PierianDx and Casma Therapeutics. Neither company provided resources. The D.V. laboratory has received a sponsored research agreement from Vir Biotechnology. H.C. reported consulting with Ellume, Pfizer, the Bill and Melinda Gates Foundation, Glaxo Smith Kline and Merck. She has received research funding from Emergent Ventures, Gates Ventures, Sanofi Pasteur and the Bill and Melinda Gates Foundation, and support and reagents from Ellume and Cepheid outside of the submitted work. M.S.D. is a consultant for Inbios, Vir Biotechnology, Senda Biosciences and Carnival Corporation, and is on the Scientific Advisory Boards of Moderna and Immunome. The M.S.D. laboratory has received funding support in sponsored research agreements from Moderna, Vir Biotechnology and Emergent BioSolutions. The remaining authors declare that the research was conducted in the absence of any commercial or financial relationships that could be construed as a potential conflict of interest.

## Peer review

### Peer review information

*Nature* thanks the anonymous reviewers for their contribution to the peer review of this work.

## **Additional information**

**Publisher's note** Springer Nature remains neutral with regard to jurisdictional claims in published maps and institutional affiliations.

## **Extended data figures and tables**

### [Extended Data Fig. 1 Schematic of mutations landscape in SARS-CoV-2 VOCs, variants of interest and variants under monitoring.](#)

D, deletion; ins, insertion; VOI, variant of interest; VUM, variant under monitoring.

### [Extended Data Fig. 2 Amino acid substitutions and their prevalence in the Omicron RBD.](#)

**a**, SARS-CoV-2 spike protein in fully open conformation (PDB: 7K4N) with positions of mutated residues in Omicron highlighted on one protomer in green or red spheres in or outside the ACE2 footprint (ACE2), respectively. RBM is defined by a 6 Å cut-off in the RBD-ACE2 interface<sup>38</sup>. Not all Omicron mutations are shown. **b**, Substitutions and their prevalence in Omicron sequences reported in GISAID as of 20 December 2021 (ambiguous amino acid substitutions are indicated with strikethrough cells). Shown are also the prevalence in Omicron (%) and substitutions found in other variants. K417N mutation in Delta is found only in a fraction of sequences.

### [Extended Data Fig. 3 Amino acid substitutions and their prevalence in the Omicron NTD.](#)

Sequences reported in GISAID as of 20 December 2021 (ambiguous amino acid substitutions are marked with strikethrough cells). Shown are also the substitutions found in other variants.

### [Extended Data Fig. 4 Amino acid substitutions and their prevalence in Omicron S2.](#)

Sequences reported in GISAID as of 20 December 2021 (ambiguous amino acid substitutions are marked with strikethrough cells). Shown are also the substitutions found in other variants.

### [Extended Data Fig. 5 Characteristics of emergent mutations of Omicron.](#)

**a**, Shared mutations of Omicron with other sarbecovirus and with VOC. **b**, Since the beginning of the pandemic there is a progressive coalescence of Omicron-defining mutations into non-Omicron haplotypes that may carry as many as 10 of the Omicron-defining mutations. **c**, Pango lineages (dots) rarely carry more than 10-15 lineage-defining mutations. **d**, Exceptionally, some non-Omicron haplotypes may carry up to a maximum 19 Omicron-defining mutations. Shown are selected exceptional haplotypes. Spike G142D and Y145del may also be noted as G142del and Y145D.

**Extended Data Fig. 6 SPR analysis of human and mouse ACE2.**

**a**, Full fit results for one representative replicate from each quantifiable SPR dataset with a monomeric analyte (1:1 binding model). **b**, Single-cycle kinetics SPR analysis of dimeric mouse ACE2 binding to six RBD variants. Dimeric ACE2 is injected successively at 33, 100, 300, and 900 nM. White and grey stripes indicate association and dissociation phases, respectively. The asterisk indicates where high concentrations of dimeric mouse ACE2 are non-specifically binding to the sensor chip surface (Delta experiment was performed separately from the other RBD variants, with a different capture tag and chip surface).

**Extended Data Fig. 7 Neutralization of SARS-CoV-2 Omicron live virus by sotrovimab in Vero-TMPRSS2 cells.**

**a–f**, Neutralization curves in Vero-TMPRSS2 cells comparing the sensitivity of SARS-CoV-2 strains with sotrovimab with WA1/2020 D614G and hCoV-19/USA/WI-WSLH-221686/2021 (an infectious clinical isolate of Omicron from a symptomatic individual in the United States). Shown are three independent experiments performed in technical duplicate.

**Extended Data Fig. 8 Neutralization of WT (D614) and Omicron SARS-CoV-2 Spike pseudotyped virus by a panel of 36 monoclonal antibodies.**

**a–c**, Neutralization of SARS-CoV-2 VSV pseudoviruses carrying wild-type D614 (grey) or Omicron (orange) spike protein by NTD-targeting (**a**) and RBD-targeting (**b**, **c**) monoclonal antibodies (**b**, site I; **c**, sites II and V). Data are representative of two independent experiments. Shown is the mean of 2 technical replicates.

**Extended Data Table 1 Demographics of enrolled donors**

**Extended Data Table 2 Properties of tested monoclonal antibodies**

**Supplementary information**

## Supplementary Information

This Supplementary Information contains Supplementary Figs. 1–3, which show neutralization plots of individual plasma donor shown in Fig. 2, and Supplementary Table 1, which shows the effect of point mutations in RBD on its expression and binding to human ACE2 as measured by flow cytometry (FACS) and surface plasmon resonance (SPR).

## Reporting Summary

## Rights and permissions

### Reprints and Permissions

## About this article

### Cite this article

Cameroni, E., Bowen, J.E., Rosen, L.E. *et al.* Broadly neutralizing antibodies overcome SARS-CoV-2 Omicron antigenic shift. *Nature* **602**, 664–670 (2022). <https://doi.org/10.1038/s41586-021-04386-2>

- Received: 12 December 2021
- Accepted: 23 December 2021
- Published: 23 December 2021
- Issue Date: 24 February 2022
- DOI: <https://doi.org/10.1038/s41586-021-04386-2>

## Share this article

Anyone you share the following link with will be able to read this content:

[Get shareable link](#)

Sorry, a shareable link is not currently available for this article.

[Copy to clipboard](#)

## Further reading

- **Striking antibody evasion manifested by the Omicron variant of SARS-CoV-2**

- Lihong Liu
- Sho Iketani
- David D. Ho

*Nature* (2022)

- **An ultrapotent RBD-targeted biparatopic nanobody neutralizes broad SARS-CoV-2 variants**

- Xiaojing Chi
- Xinhui Zhang
- Wei Yang

*Signal Transduction and Targeted Therapy* (2022)

- **Considerable escape of SARS-CoV-2 Omicron to antibody neutralization**

- Delphine Planas
- Nell Saunders
- Olivier Schwartz

*Nature* (2022)

- **Activity of convalescent and vaccine serum against SARS-CoV-2 Omicron**

- Juan Manuel Carreño
- Hala Alshammary
- Florian Krammer

*Nature* (2022)

| [Section menu](#) | [Main menu](#) |

- Article
- [Published: 23 December 2021](#)

# Considerable escape of SARS-CoV-2 Omicron to antibody neutralization

- [Delphine Planas](#)<sup>1,2 na1</sup>,
- [Nell Saunders](#) ORCID: [orcid.org/0000-0002-0872-1529](https://orcid.org/0000-0002-0872-1529)<sup>1,3 na1</sup>,
- [Piet Maes](#) ORCID: [orcid.org/0000-0002-4571-5232](https://orcid.org/0000-0002-4571-5232)<sup>4 na1</sup>,
- [Florence Guivel-Benhassine](#)<sup>1</sup>,
- [Cyril Planchais](#)<sup>5</sup>,
- [Julian Buchrieser](#) ORCID: [orcid.org/0000-0003-4790-7577](https://orcid.org/0000-0003-4790-7577)<sup>1</sup>,
- [William-Henry Bolland](#)<sup>1,3</sup>,
- [Françoise Porrot](#) ORCID: [orcid.org/0000-0001-8995-3614](https://orcid.org/0000-0001-8995-3614)<sup>1</sup>,
- [Isabelle Staropoli](#)<sup>1</sup>,
- [Frederic Lemoine](#) ORCID: [orcid.org/0000-0001-9576-4449](https://orcid.org/0000-0001-9576-4449)<sup>6</sup>,
- [Hélène Pérez](#)<sup>7,8</sup>,
- [David Veyer](#)<sup>7,8</sup>,
- [Julien Puech](#)<sup>7</sup>,
- [Julien Rodary](#)<sup>7</sup>,
- [Guy Baele](#) ORCID: [orcid.org/0000-0002-1915-7732](https://orcid.org/0000-0002-1915-7732)<sup>4</sup>,
- [Simon Dellicour](#) ORCID: [orcid.org/0000-0001-9558-1052](https://orcid.org/0000-0001-9558-1052)<sup>4,9</sup>,
- [Joren Raymenants](#)<sup>10</sup>,
- [Sarah Gorissen](#)<sup>10</sup>,
- [Caspar Geenen](#) ORCID: [orcid.org/0000-0002-2778-6344](https://orcid.org/0000-0002-2778-6344)<sup>10</sup>,
- [Bert Vanmechelen](#)<sup>4</sup>,
- [Tony Wawina-Bokalanga](#)<sup>4</sup>,
- [Joan Martí-Carreras](#)<sup>4</sup>,
- [Lize Cuypers](#)<sup>11</sup>,
- [Aymeric Sève](#)<sup>12</sup>,
- [Laurent Hocqueloux](#) ORCID: [orcid.org/0000-0002-2264-4822](https://orcid.org/0000-0002-2264-4822)<sup>12</sup>,
- [Thierry Prazuck](#)<sup>12</sup>,
- [Félix A. Rey](#) ORCID: [orcid.org/0000-0002-9953-7988](https://orcid.org/0000-0002-9953-7988)<sup>13</sup>,
- [Etienne Simon-Loriere](#) ORCID: [orcid.org/0000-0001-8420-7743](https://orcid.org/0000-0001-8420-7743)<sup>14</sup>,
- [Timothée Bruel](#) ORCID: [orcid.org/0000-0002-3952-4261](https://orcid.org/0000-0002-3952-4261)<sup>1,2 na2</sup>,

- [Hugo Mouquet](#) <sup>5 na2</sup>,
- [Emmanuel André](#) <sup>10,11 na2</sup> &
- [Olivier Schwartz](#) <sup>ORCID: orcid.org/0000-0002-0729-1475<sup>1,2 na2</sup></sup>

*Nature* volume **602**, pages 671–675 (2022)

- 16k Accesses
- 15 Citations
- 144 Altmetric
- [Metrics details](#)

## Subjects

- [Antibodies](#)
- [SARS-CoV-2](#)
- [Vaccines](#)
- [Viral infection](#)

## Abstract

The SARS-CoV-2 Omicron variant was first identified in November 2021 in Botswana and South Africa<sup>1,2,3</sup>. It has since spread to many countries and is expected to rapidly become dominant worldwide. The lineage is characterized by the presence of around 32 mutations in spike—located mostly in the N-terminal domain and the receptor-binding domain—that may enhance viral fitness and enable antibody evasion. Here we isolated an infectious Omicron virus in Belgium from a traveller returning from Egypt. We examined its sensitivity to nine monoclonal antibodies that have been clinically approved or are in development<sup>4</sup>, and to antibodies present in 115 serum samples from COVID-19 vaccine recipients or individuals who have recovered from COVID-19. Omicron was completely or partially resistant to neutralization by all monoclonal antibodies tested. Sera from recipients of the Pfizer or AstraZeneca vaccine, sampled five months after complete vaccination, barely inhibited Omicron. Sera from COVID-19-convalescent patients collected 6 or 12 months after symptoms displayed low or no neutralizing activity against Omicron. Administration of a booster Pfizer dose as well as vaccination of previously infected individuals generated an anti-Omicron neutralizing response, with titres 6-fold to 23-fold lower against Omicron compared with those against Delta. Thus, Omicron escapes most therapeutic monoclonal antibodies and, to a large extent, vaccine-elicited antibodies. However, Omicron is neutralized by antibodies generated by a booster vaccine dose.

[Download PDF](#)

## Main

In less than three weeks after its discovery, the Omicron variant was detected in dozens of countries. The WHO classified this lineage (previously known as Pango lineage B.1.1.529) as a variant of concern (VOC) on 26 November 2021 (ref. [1](#)). Preliminary estimates of its doubling time range between 1.2 days and 3.6 days in populations with a high rate of SARS-CoV-2 immunity<sup>[2,5](#)</sup>. Omicron is expected to supplant the currently dominant Delta lineage during the next weeks or months. Little is known about its sensitivity to the humoral immune response. Recent reports indicated that Omicron has a reduced sensitivity to certain monoclonal and polyclonal antibodies<sup>[6,7,8,9,10](#)</sup>, and CD8<sup>+</sup> T cell epitopes that were previously characterized in other variants seem to be conserved in Omicron<sup>[11](#)</sup>.

## Isolation and characterization of an Omicron variant

We isolated an Omicron variant from a nasopharyngeal swab of an unvaccinated individual who developed moderate symptoms 11 days after returning to Belgium from Egypt. The virus was amplified by one passage in Vero E6 cells. The sequences of the swab and the outgrown virus were identical, and were identified as the Omicron variant (Pango lineage BA.1, GISAID: EPI\_ISL\_6794907 (swab) and EPI\_ISL\_7413964 (outgrown)) (Fig. [1a](#)). The spike protein contained 32 changes compared with the D614G strain (belonging to the basal B.1 lineage), which we used here as a reference, including 7 changes in the N-terminal domain (NTD), with substitutions, deletions and a 3-amino-acid insertion (A67V, Δ69–70, T95I, G142D, Δ141–143, Δ211L212I and Ins214EPE), 15 mutations in the receptor-binding domain (RBD) (G339D, S371L, S373P, S375F, K417N, N440K, G446S, S477N, T478K, E484A, Q493R, G496S, Q498R and N501Y, and Y505H), the T574K mutation, 3 mutations close to the furin cleavage site (H655Y, N679K and P681H) and 6 mutations in the S2 region (N764K, D796Y, N856K, Q954H, N969 and L981F) (Fig. [1a](#)). This extensive constellation of changes is unique, but includes at least 11 modifications that have been observed in other lineages and VOCs or at sites that are mutated in other variants (Fig. [1a](#)). Viral stocks were titrated using S-Fuse reporter cells and Vero cells. S-Fuse cells become GFP<sup>+</sup> after infection, enabling rapid assessment of infectivity and the measurement of neutralizing antibody levels<sup>[12,13,14](#)</sup>. Syncytia were observed in Omicron-infected S-Fuse cells (Extended Data Fig. [1](#)). Syncytia were smaller after infection with Omicron, relative to Delta (Extended Data Fig. [1](#)). Future experiments will help to determine whether the fusogenic potential of Omicron is different from that of other variants<sup>[15](#)</sup>.

**Fig. 1: Neutralization of SARS-CoV-2 variants Delta and Omicron by clinical and preclinical monoclonal antibodies.**

 figure 1

**a**, The mutational landscape of the Omicron spike protein. The amino acid modifications are indicated in comparison to the ancestral Wuhan-Hu-1 sequence (GenBank: [NC\\_045512](#)). Consensus sequences of the spike protein were built using the Sierra tool<sup>38</sup>. The Omicron sequence corresponds to the viral strain that was isolated in Belgium and used in the study (GISaid: EPI\_ISL\_6794907). Mutations are compared to some pre-existing VOCs and variants of interest. The filled circles indicate changes identical to Omicron. The open circles indicate different substitutions at the same position. **b**, Neutralization curves of monoclonal antibodies. Dose-response analysis of the neutralization by clinical or preclinical monoclonal antibodies (bamlanivimab, etesevimab, casirivimab, imdevimab, adintrevimab, cilgavimab, tixagevimab, regdanvimab and sotrovimab) and the indicated combinations (bamlanivimab + etesevimab, casirivimab + imdevimab (corresponding to monoclonal antibodies present in Ronapreve), cilgavimab + tixagevimab (corresponding to monoclonal antibodies present in Evusheld)) on Delta (blue dots) and Omicron (red dots) variants. Data are mean ± s.d. of three independent experiments. The IC<sub>50</sub> values for each antibody are presented in Extended Data Table 1.

## [Source data](#)

## Phylogenetic analysis of the Omicron lineage

We inferred a global phylogeny by subsampling SARS-CoV-2 sequences that are available on the GISAID EpiCoV database. To better contextualize the isolated virus genome, we performed a focused phylogenetic analysis using all of the Omicron samples deposited on GISAID on 6 December 2021 as background (Extended Data Fig. 2). The tree topology indicates that the Omicron lineage does not directly derive from any of the previously described VOCs. The very long branch of the Omicron lineage in the time-calibrated tree (Extended Data Fig. 2) might reflect a cryptic and potentially complex evolutionary history. At the time of writing, no Omicron genomic sequences from Egypt were available on GISAID, nor do we know of any sequences of travellers that used the same planes. The isolated strain genome showed no close connection to other Belgian Omicron infections. Follow-up analyses with additional genomic data will improve the phylogenetic resolution to determine whether the patient was infected before or after returning to Belgium.

## The mutational landscape of Omicron

We highlighted the 29 amino acid substitutions, the 3 amino-acid deletions and a 3-residue insertion that are present in the Omicron spike, with respect to the Wuhan strain, in a 3D model of the protein (Extended Data Fig. 3a). The 15 mutations in the RBD cluster around the trimer interface. The RBD is the target of the most potently neutralizing monoclonal antibodies against SARS-CoV-2, which have been divided into four classes depending of the location of their epitope<sup>4,16,17</sup> (Extended Data Fig. 3b). Monoclonal antibodies in classes 1 and 2 compete for binding to human ACE2 (hACE2), whereas those from classes 3 and 4 bind away from the hACE2 interaction surface (Extended Data Fig. 3b). The epitopes of the class 2 and 3 monoclonal antibodies are exposed irrespective of the conformation of the RBD on the spike ('up' or 'down' configuration<sup>18</sup>), whereas those of classes 1 and 4 require an RBD in the up conformation. Whereas the previous VOCs displayed mutations only in the region targeted by class 1 and 2 monoclonal antibodies, Omicron mutations are located within the epitopes of all four classes of monoclonal antibodies. The mutations, insertion and deletions in the NTD might also affect the recognition of this domain by antibodies.

## Neutralization of Omicron by monoclonal antibodies

We next assessed the sensitivity of Omicron to a panel of human monoclonal antibodies using the S-Fuse assay. We tested nine antibodies that are in clinical use or in development<sup>19,20,21,22,23,24,25</sup>. These monoclonal antibodies belong to the four main

classes of anti-RBD antibodies<sup>4,16,17</sup>. Bamlanivimab and etesevimab (class 2 and class 1, respectively) are mixed in the Lilly cocktail. Casirivimab and imdevimab (class 1 and class 3, respectively) form the REGN-COV2 cocktail from Regeneron and Roche (Ronapreve). Cilgavimab and tixagevimab (class 2 and class 1, respectively) from AstraZeneca are also used in combination (Evusheld). Regdanvimab (Regkirona; Celltrion) is a class 1 antibody. Sotrovimab (Xevudy) by GlaxoSmithKline and Vir Biotechnology is a class 3 antibody that displays activity against diverse coronaviruses. It targets an RBD epitope outside the receptor-binding motif that includes N343-linked glycans. Adintrevimab (ADG20), developed by Adagio, binds to an epitope that is located between the class 1 and class 4 sites.

We measured the activity of the nine antibodies described above against Omicron and included the Delta variant for comparison purposes (Fig. 1b). As previously reported, bamlanivimab did not neutralize Delta<sup>14,26,27</sup>. The other antibodies neutralized Delta with a 50% inhibitory concentration ( $IC_{50}$ ) varying from 3.1 to 325 ng ml<sup>-1</sup> (Fig. 1b and Extended Data Fig. 4). Five antibodies (bamlanivimab, etesevimab, casirivimab, imdevimab and regdanvimab) lost antiviral activity against Omicron. The four other antibodies displayed a 2.8-fold to 453-fold increase in  $IC_{50}$  (ranging from 403 to 8,305 ng ml<sup>-1</sup>) against Omicron. Sotrovimab was the only antibody that displayed a rather similar activity against both strains, with an  $IC_{50}$  of 325 and 917 ng ml<sup>-1</sup> against Delta and Omicron, respectively. We also tested the antibodies in combination to mimic the therapeutic cocktails. Bamlanivimab + etesevimab (Lilly) or casirivimab + imdevimab (Ronapreve) were inactive against Omicron. Cilgavimab + tixagevimab (Evusheld) neutralized Omicron with an  $IC_{50}$  of 773 ng ml<sup>-1</sup>, corresponding to a 58-fold increase relative to Delta (Fig. 1b and Extended Data Fig. 4).

Next, using flow cytometry, we examined the binding of each monoclonal antibody to Vero cells infected with the Delta and Omicron variants (Extended Data Fig. 4). The five clinical antibodies that lost antiviral activity (bamlanivimab, etesevimab, casirivimab, imdevimab and regdanvimab) displayed a strong reduction (8-fold to 47-fold and 11-fold to 242-fold at 1 and 0.1 µg ml<sup>-1</sup>, respectively) in their binding to Omicron-infected cells compared with Delta-infected cells, as measured by the median fluorescence intensity of the signal (Extended Data Fig. 4). Cilgavimab, sotrovimab, tixagevimab and adintrevimab, which remained partly active, were less impaired in their binding to Omicron-infected cells (2-fold to 9-fold and 1.6-fold to 11-fold decrease at 1 and 0.1 µg ml<sup>-1</sup>, respectively) (Extended Data Fig. 4).

Thus, Omicron completely or partially escapes neutralization by the tested antibodies. Our results are consistent with findings reported in recent preprints<sup>7,8,10</sup>. The neutralization escape is correlated with a decrease in the binding of the antibodies to Omicron spike.

## Sensitivity of Omicron to sera from vaccinees

We next examined whether vaccine-elicited antibodies neutralized Omicron. To achieve this, we randomly selected 54 individuals from a cohort established in the French city of Orléans, comprising vaccinated individuals who were not previously infected with SARS-CoV-2. The characteristics of the vaccinated individuals are shown in Extended Data Table 1. Sixteen individuals received the Pfizer two-dose vaccine regimen and 18 received the AstraZeneca two-dose vaccine regimen. Twenty individuals who were vaccinated with the Pfizer vaccine received a booster dose. We measured the potency of the sera of these individuals against the Delta and Omicron strains. We used the D614G ancestral strain (belonging to the basal B.1 lineage) as a control (Fig. 2a). We calculated the 50% effective dilution ( $ED_{50}$ ) for each combination of serum and virus. Sera were first sampled five months after the full two-dose vaccination. For the Pfizer vaccine, the levels of neutralizing antibodies were relatively low against D614G and Delta (median  $ED_{50}$  of neutralization of 329 and 91), reflecting the waning of the humoral response<sup>14</sup> (Fig. 2a). We did not detect any neutralization against the Omicron variant with these sera, except one, which displayed a low antiviral activity (Fig. 2a). The percentage of sera with detectable neutralizing activity is shown in Extended Data Fig. 5.

**Fig. 2: Sensitivity of the SARS-CoV-2 variants D614G, Delta and Omicron to sera from vaccinated, convalescent or infected-then-vaccinated individuals.**

 figure 2

Neutralization titres of the sera against the three indicated viral variants are expressed as  $ED_{50}$ . **a**, Neutralizing activity of sera from individuals who were vaccinated with the AstraZeneca ( $n = 18$ ; left) and Pfizer ( $n = 16$ ; right) vaccines, sampled at 5 months after the second dose. **b**, Neutralizing activity of sera from Pfizer-vaccinated recipients sampled one month (M1) after the third injection.  $n = 20$ . The dotted line indicates the limit of detection ( $ED_{50} = 30$ ). **c**, The neutralizing activity of sera from convalescent individuals ( $n = 16$ ), sampled at 6 months after the onset of symptoms (left). Middle, the neutralizing activity of sera from convalescent individuals ( $n = 23$ ), sampled at 12 months after the onset of symptoms. Right, the neutralizing activity of sera from individuals who were infected then vaccinated ( $n = 22$ ), sampled one month after the

first injection (right). In each panel, data are the mean values from two to three independent experiments. Two-sided Friedman tests with Dunn's multiple-comparison correction was performed to compare D614G and Omicron with the Delta variant; \* $P$  < 0.05, \*\* $P$  < 0.01, \*\*\* $P$  < 0.001.

### Source data

A similar pattern was observed for the AstraZeneca vaccine. Five months after vaccination, the levels of antibodies neutralizing Delta were low ( $ED_{50}$  of 187 and 68 against D614G and Delta, respectively). No antiviral activity was detected against Omicron in 90% of the sera (Fig. 2a and Extended Data Fig. 5).

We next examined the effect of a Pfizer booster dose, administrated seven months after Pfizer vaccination. The sera were collected one month after the third dose. The booster dose enhanced neutralization titres against D614G and Delta by 39-fold and 49-fold ( $ED_{50}$  of 12,739 and 4,489, respectively, compared with the sampling time 5 months after the full two-dose vaccination). The sera from 1 month after the booster dose were also associated with a strong increase in the neutralization activity against Omicron ( $ED_{50}$  of 722) (Fig. 2b). At this time point, 100% of the tested sera displayed neutralizing activity (Extended Data Fig. 5).

Taken together, these results indicate that Omicron is poorly or not neutralized by sera of vaccinated individuals sampled five months after vaccination. The booster dose triggered detectable cross-neutralization activity against Omicron. However, even after the booster dose, the variant displayed a decrease in  $ED_{50}$  of 18-fold and 6-fold compared with D614G and Delta, respectively.

## Sensitivity of Omicron to convalescent sera

We subsequently examined the neutralization ability of sera from convalescent individuals. We randomly selected 61 longitudinal samples from 40 donors in a cohort of infected individuals from Orléans. Individuals were diagnosed with SARS-CoV-2 infection by quantitative PCR with reverse transcription (RT-qPCR) (Extended Data Table 1b). We previously studied the potency of these sera against D614G, Alpha, Beta and Delta isolates<sup>13,14</sup>. We analysed individuals sampled at a median of 6 and 12 months (M6 and M12) after the onset of symptoms. For the D614G and Delta variants, the neutralization titres were stable or slightly decreased over time (569 and 580 for D614G, and 235 and 143 for Delta, at M6 and M12, respectively)<sup>13</sup> (Fig. 2c). The convalescent sera barely neutralized Omicron or did not inhibit Omicron at all at these time points. Only 36% and 39% of the samples displayed neutralizing activity against

Omicron at M6 and M12, respectively, whereas the majority (91–94%) were active against Delta (Extended Data Fig. 5).

Twenty-two individuals were vaccinated at M12 with a Pfizer dose. Sera sampled 1 month after vaccination showed a considerable increase in neutralizing antibody titres against the D614G and Delta variants, reaching a median ED<sub>50</sub> of 78,162 and 33,536, respectively (Fig. 2d). These sera also neutralized Omicron, with a median ED<sub>50</sub> of 1,466 (Fig. 2d). Thus, as shown for other variants<sup>13,28,29</sup>, a single dose of vaccine boosted cross-neutralizing antibody responses to Omicron in previously infected individuals. However, the neutralization titres were reduced by 53-fold and 23-fold compared with D614G and Delta, respectively.

## Discussion

Omicron has opened a new chapter in the COVID-19 pandemic<sup>2,30</sup>. The principal concerns about this variant include its high transmissibility, as underlined by its rapid spread in different countries, and the presence of more than 55 mutations spanning the whole viral genome. Omicron contains 32 mutations in its spike protein in the NTD, RBD and in vicinity of the furin cleavage site. Some mutations were already present in other VOCs and variants of interest, and have been extensively characterized<sup>30,31,32</sup>. Owing to their position, they are expected to affect the binding of natural or therapeutic antibodies, to increase affinity to ACE2 and to enhance the fusogenic activity of the spike. Future work will help to determine how this association of mutations affects viral fitness in culture systems and their contribution to the high transmissibility of the variant.

Here we studied the cross-reactivity of clinical or preclinical monoclonal antibodies, as well as of 115 sera from vaccine recipients and long-term convalescent individuals against an infectious Omicron isolate. We report that, among nine monoclonal antibodies in clinical use or in development, six (bamlanivimab, etesevimab, casirivimab, imdevimab, tixagevimab and regdanvimab) were inactive against Omicron. Two other antibodies (cilgavimab and adintrevimab) displayed about a 20-fold increase in IC<sub>50</sub>. Sotrovimab was less affected by Omicron's mutations, with an increase in IC<sub>50</sub> by only threefold. We also show that Omicron was barely neutralized by sera from vaccinated individuals who were sampled 5 months after the administration of two doses of the Pfizer or AstraZeneca vaccine. Sera from convalescent individuals at 6 or 12 months after infection barely neutralized or did not detectably neutralize Omicron.

The decrease in antibody efficacy helps to explain the high number of breakthrough infections and reinfection cases, and the spread of Omicron in both non-immune and

immune individuals<sup>33</sup>. There is currently no evidence of increased disease severity associated with Omicron compared with Delta, either among naive or immunized individuals. It is probable that, even if pre-existing SARS-CoV-2 antibodies may poorly prevent Omicron infection, anamnestic responses and cellular immunity will be operative to prevent severe forms of the disease<sup>34</sup>.

We further report that a booster dose of Pfizer vaccine, as well as vaccination of previously infected individuals, strongly increased overall levels of anti-SARS-CoV-2 neutralizing antibodies, well above a threshold allowing inhibition of Omicron.

Affinity maturation of antibodies is known to improve the efficacy of the humoral anti-SARS-CoV-2 response over time<sup>35,36</sup>. This process helps to explain the efficacy of booster doses. However, sera with high antibody levels displayed a 6-fold to 23-fold reduction in neutralization efficacy against Omicron compared with the currently predominant Delta strain.

Potential limitations of our work include the low number of sera analysed from vaccine recipients and convalescent individuals, and the lack of characterization of cellular immunity, which is known to be more cross-reactive than the humoral response. Our results may therefore partly underestimate the residual protection offered by vaccines and previous infections against Omicron infection, in particular with regard to the severity of disease. We analysed only sera sampled one month after the booster dose, or after vaccination of infected individuals. Future work with more individuals and longer survey periods will help to characterize the duration of the humoral response against Omicron. We focused on immune responses elicited by Pfizer and AstraZeneca vaccination. It will be worth determining the potency of other vaccines against this variant.

We focused our analyses on one single viral isolate, corresponding to the archetype Omicron variant sequence (Pango BA.1 lineage). Two related lineages with additional mutations (BA.2 and BA.3) have recently emerged and are less widely spread. It will be worth comparing the behaviour of viral isolates from these more recent lineages with the main BA.1 Omicron strain.

Our results have important public health consequences regarding the use of therapeutic monoclonal antibodies and vaccines. Clinical indications of monoclonal antibodies include pre-exposure prophylaxis in individuals who are unable to mount an immune response, as well as the prevention of COVID-19 in infected individuals who are at high risk for progressing towards severe disease. Antibody-based treatment strategies need to be rapidly adapted to Omicron. Experiments in preclinical models or clinical trials are warranted to assess whether the drops in IC<sub>50</sub> are translated into impaired clinical efficacy of the monoclonal antibodies that retain efficacy against Omicron. Most low-income countries display a low vaccination rate, a situation that probably

facilitates SARS-CoV-2 spread and continuous evolution. A booster dose improves the quality and the level of the humoral immune response, and is associated with a strong protection against severe forms of the disease<sup>[37](#)</sup>. An accelerated deployment of vaccines and boosters throughout the world is necessary to counteract viral spread. Our results also suggest that there is a need to update and complete the current pharmacopoeia, in particular with regard to vaccines and monoclonal antibodies.

## Methods

No statistical methods were used to predetermine sample size. The experiments were not randomized and the investigators were not blinded to allocation during experiments and outcome assessment. Our research complies with all relevant ethical regulation.

### Orléans Cohort of convalescent and vaccinated individuals

Since 27 August 2020, a prospective, monocentric, longitudinal, interventional cohort clinical study enrolling 170 individuals infected with SARS-CoV-2 with different disease severities, and 59 non-infected healthy control individuals is ongoing, aiming to describe the persistence of specific and neutralizing antibodies over a 24-month period. This study was approved by the ILE DE FRANCE IV ethical committee. At enrolment, written informed consent was collected and the participants completed a questionnaire that covered sociodemographic characteristics, virological findings (SARS-CoV-2 RT–PCR results, including date of testing), clinical data (date of symptoms onset, type of symptoms and hospitalization), and data related to anti-SARS-CoV-2 vaccination if ever (brand product, and date of first and second doses). The serological status of the participants was assessed every three months. Those who underwent anti-SARS-CoV-2 vaccination had regular blood sampling after first dose of vaccine (ClinicalTrials.gov: [NCT04750720](#)). The primary outcome was the presence of antibodies against the SARS-CoV-2 spike protein, as measured using the S-Flow assay. The secondary outcome was the presence of neutralizing antibodies as measured using the S-Fuse assay. For this study, we selected 61 convalescent and 54 vaccinated participants. Some individuals were sampled multiple times. We analysed a total of 115 sera. Study participants did not receive any compensation. The characteristics of each individual from the two cohorts are presented in Supplementary Table [2](#). The cohorts were constituted before the occurrence of the Omicron variant.

### Phylogenetic analysis

To contextualize the isolated Omicron genome, all SARS-CoV-2 sequences available on the GISAID EpiCov database as of 6 December 2021 were retrieved. A subset of

complete and high-coverage sequences, as indicated in GISAID, assigned to lineages B.1.529 or BA.1 and BA.2, were randomly subsampled. This subset was included in a global SARS-CoV-2 phylogeny reconstructed with augur and visualized with auspice as implemented in the Nextstrain pipeline (<https://github.com/nextstrain/ncov>, version from 6 May 2021)<sup>39</sup>. Within Nextstrain, a random subsampling approach capping a maximum number of sequences per global region was used. The acknowledgment of contributing and originating laboratories for all sequences used in the analysis is provided in Supplementary Table 1.

### 3D representation of mutations on the surface of spike of B1.617.2 and other variants

The panels in Extended Data Fig. 3 were prepared using The PyMOL Molecular Graphics System, v.2.1 (Schrödinger). The atomic model used (Protein Data Bank: [6XR8](#)) has previously been described<sup>40</sup>.

### S-Fuse neutralization assay

U2OS-ACE2 GFP1-10 or GFP 11 cells, also termed S-Fuse cells, become GFP<sup>+</sup> when they are productively infected by SARS-CoV-2 (refs. [12,13](#)). Cells tested negative for mycoplasma. Cells were mixed (ratio 1:1) and plated at  $8 \times 10^3$  per well in a μClear 96-well plate (Greiner Bio-One). The indicated SARS-CoV-2 strains were incubated with serially diluted monoclonal antibodies or sera for 15 min at room temperature and added to S-Fuse cells. The sera were heat-inactivated for 30 min at 56 °C before use. Then, 18 h later, cells were fixed with 2% PFA, washed and stained with Hoechst (dilution of 1:1,000, Invitrogen). Images were acquired using an Opera Phenix high-content confocal microscope (PerkinElmer). The GFP area and the number of nuclei were quantified using the Harmony software (PerkinElmer). The percentage of neutralization was calculated using the number of syncytia as value with the following formula:  $100 \times (1 - (\text{value with serum} - \text{value in 'non-infected'}) / (\text{value in 'no serum'} - \text{value in 'non-infected'}}))$ . Neutralizing activity of each serum was expressed as the half maximal effective dilution (ED<sub>50</sub>). ED<sub>50</sub> values (in  $\mu\text{g ml}^{-1}$  for monoclonal antibodies and in dilution values for sera) were calculated with a reconstructed curve using the percentage of the neutralization at the different concentrations.

### Characteristics of the patient infected with Omicron

The 32-year-old woman was unvaccinated and developed moderate symptoms on 22 November 2021, 11 days after returning to Belgium from Egypt via Turkey (stop-over to switch flights, without having left the airport). She did not display any risk factor for severe COVID-19 and rapidly recovered. She transmitted the virus to her husband

but not to their children. She provided informed written consent to use the swab for future studies. The nasopharyngeal swab tested positive for SARS-CoV-2 on this date. The leftover material of the sample was used in this study after performing routine diagnostics, within the context of the mandate that was provided to UZ/KU Leuven as National Reference Center (NRC) of respiratory pathogens, as described in detail in the Belgian Royal Decree of 09/02/2011.

## Virus strains

The reference D614G strain (hCoV-19/France/GE1973/2020) was supplied by the National Reference Centre for Respiratory Viruses hosted by Institut Pasteur and headed by S. van der Werf. This viral strain was supplied through the European Virus Archive goes Global (Evag) platform, a project that has received funding from the European Union's Horizon 2020 research and innovation program under grant agreement no 653316. The variant strains were isolated from nasal swabs using Vero E6 cells and amplified by one or two passages. Delta was isolated from a nasopharyngeal swab of a hospitalized patient returning from India<sup>14</sup>. The swab was provided and sequenced by the laboratory of Virology of Hopital Européen Georges Pompidou (Assistance Publique, Hopitaux de Paris). The Omicron-positive sample was cultured on Vero E6 cells as previously described<sup>41</sup>. Viral growth was confirmed by RT-qPCR three days after infection. At day 6 after infection, a cytopathic effect was detected and a full-length sequencing of the virus was performed. The Omicron strain was supplied and sequenced by the NRC UZ/KU Leuven. Both patients provided informed consent for the use of the biological materials. Titration of viral stocks was performed on Vero E6 cells, with a limiting dilution technique enabling the calculation of the median tissue culture infectious dose, or on S-Fuse cells. Viruses were sequenced directly on nasal swabs, and after one or two passages on Vero cells. The sequences were deposited on GISAID immediately after their generation (D614G: EPI\_ISL\_414631; Delta ID: EPI\_ISL\_2029113; Omicron ID: EPI\_ISL\_6794907).

## Flow cytometry

Vero cells were infected with the indicated viral strains at a multiplicity of infection of 0.01. Two days after, cells were detached using PBS-0.1% EDTA and transferred into U-bottom 96-well plates (50,000 cells per well). Cells were then incubated for 30 min at 4 °C with the indicated monoclonal antibodies (1 or 0.1 µg ml<sup>-1</sup>) in MACS buffer (PBS, 5 g l<sup>-1</sup> BSA, 2 mM EDTA). Cells were washed with PBS and stained using anti-IgG AF647 (1:600 dilution in MACS buffer) (Thermo Fisher Scientific). Stainings were also performed on control non-infected cells. Cells were then fixed in 4% PFA for 30 min at room temperature. Data were acquired on the Attune Nxt instrument using Attune Nxt Software v.3.2.1 (Life Technologies) and analysed using FlowJo v.10.7.1 (Becton Dickinson).

## Antibodies

Four clinically available antibodies (bamlanivimab, casirivimab, etesevimab and imdevimab) were provided by CHR Orleans. The other human SARS-CoV-2 anti-RBD neutralizing antibodies (ADG20 or adintrevimab, AZD1061 (COV2-2130) or cilgavimab, AZD8895 (COV2-2196) or tixagevimab, CT-P59 or regdanvimab, LY-CoV016 (CB6) or etesevimab, LY-CoV555 or bamlanivimab, REGN10933 or casirivimab, REGN10987 or imdevimab, and VIR-7831 (S309) or sotrovimab<sup>19,20,21,22,23,24,25</sup> were produced as follows. DNA fragments encoding their IgH and IgL variable domains were synthesized (Life Technologies, Thermo Fisher Scientific). Purified digested DNA fragments were cloned into human Ig $\gamma$ 1- and Ig $\kappa$ -/Ig $\lambda$ -expressing vectors<sup>42</sup> and recombinant IgG1 antibodies were produced by transient co-transfection of Freestyle 293-F suspension cells (Thermo Fisher Scientific) using the PEI-precipitation method as previously described<sup>43</sup>. IgG1 antibodies were purified by batch/gravity-flow affinity chromatography using protein G Sepharose 4 Fast Flow Beads (Cytivia) according to the manufacturer's instructions, dialysed against PBS using Slide-A-Lyzer dialysis cassettes (Thermo Fisher Scientific), quantified using the NanoDrop 2000 instrument (Thermo Fisher Scientific), and checked for purity and quality on a silver-stained SDS-PAGE gel (3–8% Tris-Acetate Novex, Thermo Fisher Scientific). The pan-coronavirus anti-S2 non-neutralizing antibody Ab-10 was previously described<sup>13,14</sup>.

## Statistical analysis

Flow cytometry data were analysed using FlowJo v.10 (TriStar). Calculations were performed using Excel 365 (Microsoft). Figures were generated using Prism 9 (GraphPad Software). Statistical analysis was conducted using GraphPad Prism 9. Statistical significance between different groups was calculated using the tests indicated in each figure legend.

## Reporting summary

Further information on research design is available in the [Nature Research Reporting Summary](#) linked to this paper.

## Data availability

All data supporting the findings of this study are available within the Article or from the corresponding authors on request. Viral sequences are available on request and were deposited at GISAID (<https://www.gisaid.org/>) under the following numbers:

D614G (EPI\_ISL\_414631), Delta ID (EPI\_ISL\_2029113) and Omicron ID (EPI\_ISL\_6794907). [Source data](#) are provided with this paper.

## References

1. Classification of Omicron (B.1.1.529): SARS-CoV-2 Variant of Concern, [https://www.who.int/news-room/detail/26-11-2021-classification-of-omicron-\(b.1.1.529\)-sars-cov-2-variant-of-concern](https://www.who.int/news-room/detail/26-11-2021-classification-of-omicron-(b.1.1.529)-sars-cov-2-variant-of-concern) (WHO, 2021).
2. Karim, S. S. A. & Karim, Q. A. Omicron SARS-CoV-2 variant: a new chapter in the COVID-19 pandemic. *Lancet* **398**, 2126–2128 (2021).
3. Viana, R. et al. Rapid epidemic expansion of the SARS-CoV-2 Omicron variant in southern Africa. *Nature*, <https://doi.org/10.1038/s41586-022-04411-y> (2022).
4. Taylor, P. C. et al. Neutralizing monoclonal antibodies for treatment of COVID-19. *Nat. Rev. Immunol.* **21**, 382–393 (2021).
5. Grabowski, F., Kochańczyk, M. & Lipniacki, T. Omicron strain spreads with the doubling time of 3.2–3.6 days in South Africa province of Gauteng that achieved herd immunity to Delta variant. Preprint at <https://doi.org/10.1101/2021.12.08.21267494> (2021).
6. Cele, S. et al. Omicron extensively but incompletely escapes Pfizer BNT162b2 neutralization. *Nature*, <https://doi.org/10.1038/s41586-021-04387-1> (2021).
7. Cao, Y. et al. Omicron escapes the majority of existing SARS-CoV-2 neutralizing antibodies. *Nature*, <https://doi.org/10.1038/s41586-021-04385-3> (2021).
8. Cameroni, E. et al. Broadly neutralizing antibodies overcome SARS-CoV-2 Omicron antigenic shift. *Nature*, <https://doi.org/10.1038/s41586-021-04386-2> (2021).
9. Dejnirattisai, W. et al. Reduced neutralisation of SARS-COV-2 Omicron-B.1.1.529 variant by post-immunisation serum. *Lancet* **399**, 234–236 (2021).
10. Aggarwal, A. et al. SARS-CoV-2 Omicron: evasion of potent humoral responses and resistance to clinical immunotherapeutics relative to viral variants of concern. Preprint at <https://doi.org/10.1101/2021.12.14.21267772> (2021).
11. Redd, A. D. et al. Minimal cross-over between mutations associated with Omicron variant of SARS-CoV-2 and CD8<sup>+</sup> T cell epitopes identified in COVID-

- 19 convalescent individuals. Preprint at <https://doi.org/10.1101/2021.12.06.471446> (2021).
12. Buchrieser, J. et al. Syncytia formation by SARS-CoV-2 infected cells. *EMBO J.* **39**, e106267 (2020).
  13. Planas, D. et al. Sensitivity of infectious SARS-CoV-2 B.1.1.7 and B.1.351 variants to neutralizing antibodies. *Nat. Med.* **27**, 917–924 (2021).
  14. Planas, D. et al. Reduced sensitivity of SARS-CoV-2 variant Delta to antibody neutralization. *Nature* **596**, 276–280 (2021).
  15. Rajah, M. M. et al. SARS-CoV-2 Alpha, Beta, and Delta variants display enhanced spike-mediated syncytia formation. *EMBO J.* **40**, e108944 (2021).
  16. Liu, L. et al. Potent neutralizing antibodies against multiple epitopes on SARS-CoV-2 spike. *Nature* **584**, 450–456 (2020).
  17. Barnes, C. O. et al. SARS-CoV-2 neutralizing antibody structures inform therapeutic strategies. *Nature* **588**, 682–687 (2020).
  18. Wrapp, D. et al. Cryo-EM structure of the 2019-nCoV spike in the prefusion conformation. *Science* **367**, 1260–1263 (2020).
  19. Rappazzo, C. G. et al. Broad and potent activity against SARS-like viruses by an engineered human monoclonal antibody. *Science* **371**, 823–829 (2021).
  20. Zost, S. J. et al. Potently neutralizing and protective human antibodies against SARS-CoV-2. *Nature* **584**, 443–449 (2020).
  21. Kim, C. et al. A therapeutic neutralizing antibody targeting receptor binding domain of SARS-CoV-2 spike protein. *Nat. Commun.* **12**, 288 (2021).
  22. Shi, R. et al. A human neutralizing antibody targets the receptor-binding site of SARS-CoV-2. *Nature* **584**, 120–124 (2020).
  23. Jones, B. E. et al. The neutralizing antibody, LY-CoV555, protects against SARS-CoV-2 infection in nonhuman primates. *Sci. Transl. Med.* **13**, eabf1906 (2021).
  24. Hansen, J. et al. Studies in humanized mice and convalescent humans yield a SARS-CoV-2 antibody cocktail. *Science* **369**, 1010–1014 (2020).
  25. Pinto, D. et al. Cross-neutralization of SARS-CoV-2 by a human monoclonal SARS-CoV antibody. *Nature* **583**, 290–295 (2020).

26. Liu, J. et al. BNT162b2-elicited neutralization of B.1.617 and other SARS-CoV-2 variants. *Nature* **596**, 273–275 (2021).
27. Lucas, C. et al. Impact of circulating SARS-CoV-2 variants on mRNA vaccine-induced immunity. *Nature* **600**, 523–529 (2021).
28. Gallais, F. et al. Evolution of antibody responses up to 13 months after SARS-CoV-2 infection and risk of reinfection. *EBioMedicine* **71**, 103561 (2021).
29. Krammer, F. et al. Antibody responses in seropositive persons after a single dose of SARS-CoV-2 mRNA vaccine. *New Engl. J. Med.* **384**, 1372–1374 (2021).
30. McCallum, M. et al. SARS-CoV-2 immune evasion by the B.1.427/B.1.429 variant of concern. *Science* **373**, 648–654 (2021).
31. Plante, J. A. et al. The variant gambit: COVID-19’s next move. *Cell Host Microbe* **29**, 508–515 (2021).
32. Starr, T. N. et al. Prospective mapping of viral mutations that escape antibodies used to treat COVID-19. *Science* **371**, 850–854 (2021).
33. Pulliam, J. R. C. et al. Increased risk of SARS-CoV-2 reinfection associated with emergence of the Omicron variant in South Africa. Preprint at <https://doi.org/10.1101/2021.11.11.21266068> (2021).
34. Gagne, M. et al. Protection from SARS-CoV-2 Delta one year after mRNA-1273 vaccination in rhesus macaques is coincident with anamnestic antibody response in the lung. *Cell* **185**, 113–130 (2021).
35. Gaebler, C. et al. Evolution of antibody immunity to SARS-CoV-2. *Nature* **591**, 639–644 (2021).
36. Wang, Z. et al. Naturally enhanced neutralizing breadth against SARS-CoV-2 one year after infection. *Nature* **595**, 426–431 (2021).
37. Barda, N. et al. Effectiveness of a third dose of the BNT162b2 mRNA COVID-19 vaccine for preventing severe outcomes in Israel: an observational study. *Lancet* **398**, 2093–2100 (2021).
38. Tzou, P. L. et al. Coronavirus Antiviral Research Database (CoV-RDB): an online database designed to facilitate comparisons between candidate anti-coronavirus compounds. *Viruses* **12**, 1006 (2020).

39. Hadfield, J. et al. Nextstrain: real-time tracking of pathogen evolution. *Bioinformatics* **34**, 4121–4123 (2018).
40. Cai, Y. et al. Distinct conformational states of SARS-CoV-2 spike protein. *Science* **369**, 1586–1592 (2020).
41. Van Cleemput, J. et al. Organ-specific genome diversity of replication-competent SARS-CoV-2. *Nat. Commun.* **12**, 6612 (2021).
42. Tiller, T. et al. Efficient generation of monoclonal antibodies from single human B cells by single cell RT-PCR and expression vector cloning. *J. Immunol. Methods* **329**, 112–124 (2008).
43. Lorin, V. & Mouquet, H. Efficient generation of human IgA monoclonal antibodies. *J. Immunol. Methods* **422**, 102–110 (2015).
44. Walls, A. C. et al. Structure, function, and antigenicity of the SARS-CoV-2 spike glycoprotein. *Cell* **181**, 281–292 (2020).

## Acknowledgements

We thank the staff at the European Health Emergency Preparedness and Response Authority (HERA) for their support; S. Cole for his help in initiating the collaboration between Institut Pasteur and KU Leuven through the HERA network; A. Baidaliuk and F. Gambaro for their help with the sequencing data analysis; the patients who participated to this study; the members of the Virus and Immunity Unit and other teams for discussions and help; N. Aulner and the staff at the UtechS Photonic BioImaging (UPBI) core facility (Institut Pasteur)—a member of the France BioImaging network—for image acquisition and analysis; the members of the KU Leuven University authorities, and J. Arnout, B. Lambrecht, C. Van Geet and L. Sels for their support; L. Belec, N. Robillard and M. Saliba for their help with sequencing; and F. Peira, V. Legros and L. Courtellemont for their help with the cohorts. The Opera system was co-funded by Institut Pasteur and the Région Ile de France (DIM1Health). Work in the O.S. laboratory is funded by Institut Pasteur, Urgence COVID-19 Fundraising Campaign of Institut Pasteur, Fondation pour la Recherche Médicale (FRM), ANRS, the Vaccine Research Institute (ANR-10-LABX-77), Labex IBEID (ANR-10-LABX-62-IBEID), ANR/FRM Flash Covid PROTEO-SARS-CoV-2 and IDISCOVR. Work in the UPBI is funded by grant ANR-10-INSB-04-01 and Région Ile-de-France program DIM1-Health. D.P. is supported by the Vaccine Research Institute. The H.M. laboratory is funded by the Institut Pasteur, the Milieu Intérieur Program (ANR-10-LABX-69-01), the INSERM, REACTing, EU (RECOVER) and Fondation de France (00106077) grants. The E.S.-L. laboratory is

funded by Institut Pasteur, the INCEPTION program (Investissements d’Avenir grant ANR-16-CONV-0005) and the French Government’s Investissement d’Avenir programme, Laboratoire d’Excellence ‘Integrative Biology of Emerging Infectious Diseases’ (grant no. ANR-10-LABX-62-IBEID). G.B. acknowledges support from the Internal Funds KU Leuven under grant agreement C14/18/094, and the Research Foundation–Flanders (Fonds voor Wetenschappelijk Onderzoek–Vlaanderen, G0E1420N, G098321N). P.M. acknowledges support from a COVID-19 research grant of ‘Fonds Wetenschappelijk Onderzoek’/Research Foundation–Flanders (grant no. G0H4420N). S.D. is supported by the Fonds National de la Recherche Scientifique (FNRS, Belgium) and also acknowledges support from the Research Foundation–Flanders (Fonds voor Wetenschappelijk Onderzoek–Vlaanderen, G098321N) and from the European Union Horizon 2020 project MOOD (grant no. 874850). The funders of this study had no role in study design, data collection, analysis and interpretation, or writing of the article.

## Author information

### Author notes

1. These authors contributed equally: Delphine Planas, Nell Saunders, Piet Maes
2. These authors jointly supervised this work: Timothée Bruel, Hugo Mouquet, Emmanuel André, Olivier Schwartz

### Affiliations

1. Virus and Immunity Unit, Institut Pasteur, Université de Paris, CNRS UMR3569, Paris, France

Delphine Planas, Nell Saunders, Florence Guivel-Benhassine, Julian Buchrieser, William-Henry Bolland, Françoise Porrot, Isabelle Staropoli, Timothée Bruel & Olivier Schwartz

2. Vaccine Research Institute, Créteil, France

Delphine Planas, Timothée Bruel & Olivier Schwartz

3. École Doctorale BioSPC 562, Université de Paris, Paris, France

Nell Saunders & William-Henry Bolland

4. Department of Microbiology, Laboratory of Clinical and Epidemiological Virology, Immunology and Transplantation, Rega Institute, KU Leuven, Leuven,

Belgium

Piet Maes, Guy Baele, Simon Dellicour, Bert Vanmechelen, Tony Wawina-Bokalanga & Joan Martí-Carreras

5. Humoral Immunology Laboratory, Institut Pasteur, Université de Paris, INSERM U1222, Paris, France

Cyril Planchais & Hugo Mouquet

6. Hub de Bioinformatique et Biostatistique, Institut Pasteur, Université de Paris, CNRS USR 3756, Paris, France

Frederic Lemoine

7. Laboratoire de Virologie, Service de Microbiologie, Hôpital Européen Georges Pompidou, Paris, France

Hélène Péré, David Veyer, Julien Puech & Julien Rodary

8. Functional Genomics of Solid Tumors (FunGeST), Centre de Recherche des Cordeliers, INSERM, Université de Paris, Sorbonne Université, Paris, France

Hélène Péré & David Veyer

9. Spatial Epidemiology Lab (SpELL), Université Libre de Bruxelles, Brussels, Belgium

Simon Dellicour

10. Laboratory of Clinical Microbiology, Department of Microbiology, Immunology and Transplantation, KU Leuven, Leuven, Belgium

Joren Raymenants, Sarah Gorissen, Caspar Geenen & Emmanuel André

11. Department of Laboratory Medicine, National Reference Centre for Respiratory Pathogens, University Hospitals Leuven, Leuven, Belgium

Lize Cuypers & Emmanuel André

12. Service de Maladies Infectieuses, CHR d'Orléans, Orléans, France

Aymeric Sève, Laurent Hocqueloux & Thierry Prazuck

13. Structural Virology Unit, Institut Pasteur, Université de Paris, CNRS UMR3569, Paris, France

Félix A. Rey

14. G5 Evolutionary Genomics of RNA Viruses, Institut Pasteur, Université de Paris, Paris, France

Etienne Simon-Loriere

## Contributions

Experimental strategy design, experiments: D.P., N.S., F.G.-B., C.P., J.B., W.-H.B., F.P., I.S., F.A.R., E.S.-L., T.B., H.M. and O.S. Vital materials: P.M., C.P., F.L., H.P., D.V., J.P., J. Rodary, G.B., S.D., J. Raymenants, S.G., C.G., B.V., T.W.-B., J.M.-C., L.C., A.S., L.H., T.P., H.M. and E.A. Phylogenetic analysis: G.B., E.S.-L., F.L. and S.D. Manuscript writing: D.P., F.A.R., E.S.-L., T.B., H.M., E.A. and O.S. Manuscript editing: D.P., N.S., P.M., G.B., L.C., F.A.R., E.S.-L., T.B., H.M., E.A. and O.S.

## Corresponding authors

Correspondence to [Timothée Bruel](#), [Hugo Mouquet](#), [Emmanuel André](#) or [Olivier Schwartz](#).

## Ethics declarations

## Competing interests

C.P., H.M., O.S, T.B. and F.A.R. have a pending patent application for an anti-RBD monoclonal antibody that was not used in this study (PCT/FR2021/070522).

## Peer review

## Peer review information

*Nature* thanks the anonymous reviewers for their contribution to the peer review of this work.

## Additional information

**Publisher's note** Springer Nature remains neutral with regard to jurisdictional claims in published maps and institutional affiliations.

## Extended data figures and tables

### Extended Data Fig. 1 SARS-CoV-2 variants induce syncytia in S-Fuse cells.

S-Fuse cells were exposed to the indicated SARS-CoV-2 strains, at a multiplicity of infection (MOI) of  $10^{-3}$ . The cells become GFP+ when they fuse together. After 20 h, infected cells were stained with Hoechst to visualize nuclei. Syncytia (green) and nuclei (blue) are shown. Representative images from three independent experiments are shown. Scale bar, 500  $\mu\text{m}$ .

### Extended Data Fig. 2 Global phylogeny of SARS-CoV-2 highlighting the Omicron lineage.

Time calibrated global SARS-CoV-2 phylogeny available from the Nextstrain platform (<https://nextstrain.org/ncov/gisaid/global>)<sup>39</sup>. The position of the isolated Omicron variant is highlighted, and the variants of concern (VOCs) (Alpha, Beta, Gamma, Delta and Omicron) and variants of interest (VOIs) (Lambda, Mu) are coloured as indicated.

### Extended Data Fig. 3 Mapping of the mutations present in Omicron to the spike's surface.

a. The spike shown in top (left panel) and in side view (middle and right panels). The spike trimer is shown in surface representation with the three protomers coloured in light grey, light blue and light green. N-terminal and the receptor-binding (NTD and RBD) domains are labelled for the protomer in green only. The represented spike (PDB: 6XR8) is in the closed conformation, i.e., with all three RBDs in the “Down” conformation<sup>44</sup>. The RBD surface of interaction with hACE2 (which is partially occluded in a closed spike) is coloured in yellow. The amino acid differences in the spike of the Omicron variant with respect to the initial Wuhan sequence are marked in red. In the right panel, the front subunit was removed to show changes in S2 and in the C-terminal segment of S1 (labelled) that map to the trimer interface, which could impact the stability of the spike trimer. b. The RBD view down the hACE2 binding surface (left panel) and in two other orthogonal orientations (middle and right panel), as indicated. The hACE2 binding surface is coloured in yellow and the residues altered in Omicron are in red. The RBD surfaces that are buried and exposed in a closed spike

are coloured in light cyan and white, respectively. The ovals outline the location of the epitopes of neutralizing antibodies of the various classes that have been described<sup>17</sup>.

#### Extended Data Fig. 4 Binding of anti-SARS-CoV-2 monoclonal antibodies to Vero cells infected with Delta and Omicron variants.

Vero cells were infected with the indicated variants at an MOI of 0.01. After 48 h, cells were stained with 1 or 0.1  $\mu\text{g ml}^{-1}$  of the indicated anti-SARS-CoV-2 monoclonal antibodies (Bamlanivimab, Etesevimab, Casirivimab, Imdevimab, Adintrevimab, Cilgavimab, Tixagevimab, Regdanvimab, Sotrovimab) and analysed by flow-cytometry. **a.** Gating strategy and example of gates on negative (non-infected) or positive (Delta-infected) samples. **b.** The anti-S2 pan-coronavirus mAb 10 was used to measure the percentage of infected cells. Histograms show binding of mAb 10 to Vero cells infected with the indicated variants. **c.** Radar charts represent for each antibody the logarithm of the median fluorescent intensity (MFI) of the staining. Data are representative of two or three independent experiments. **d.** Inhibitory Concentrations 50% (IC50) of mAbs against Delta and Omicron variants. The IC50 of the indicated mAbs and some of their combinations were calculated from the neutralization curves displayed in Fig. 1b. Results are in  $\text{ng ml}^{-1}$ . Colour code: Grey: inactive mAbs. Green: mAbs displaying a neutralizing activity. The binding activity was measured by flow cytometry on Vero cells infected with the indicated variants. Results are presented as the fold-decrease of binding to Omicron-infected cells relative to Delta-infected cells.

#### Source data

#### Extended Data Fig. 5 Fraction of neutralizers in the cohorts of vaccinated or convalescent individuals.

Individuals with an ED50 of neutralization above 30 were categorized as neutralizers and are indicated in pink. Non-neutralizers are in grey. The numbers indicate the percentage of neutralizers. **a.** Fraction of neutralizers in sera from Pfizer ( $n = 16$ ) (left panel) and AstraZeneca ( $n = 18$ ) (right panel) vaccinated recipients sampled 5 months after the second dose (results related to Fig. 2a). **b.** Fraction of neutralizers in sera from Pfizer vaccinated recipients sampled one month after the 3<sup>rd</sup> injection ( $n = 20$ ; (results related to Fig. 2b). **c.** Fraction of neutralizers in sera from convalescent individuals, sampled at 6 months post onset of symptoms (M6) ( $n = 16$ ) (right panel), at 12 months (M12) ( $n = 23$ ) (middle panel) and one month after the 1<sup>st</sup> injection ( $n = 22$ ) (right panel; results related to Fig. 2c). In each panel, data are mean from 2 to 3 independent experiments.

## **Extended Data Table 1 Characteristics of the two cohorts of vaccinated and convalescent individuals**

## **Supplementary information**

### **Supplementary Table 1**

GISAID Acknowledgements.

### **Reporting Summary**

### **Supplementary Table 2**

## **Source data**

### **Source Data Fig. 1**

### **Source Data Fig. 2**

### **Source Data Extended Data Fig. 4**

## **Rights and permissions**

### **Reprints and Permissions**

## **About this article**

### **Cite this article**

Planas, D., Saunders, N., Maes, P. *et al.* Considerable escape of SARS-CoV-2 Omicron to antibody neutralization. *Nature* **602**, 671–675 (2022).  
<https://doi.org/10.1038/s41586-021-04389-z>

- Received: 10 December 2021
- Accepted: 23 December 2021
- Published: 23 December 2021
- Issue Date: 24 February 2022

- DOI: <https://doi.org/10.1038/s41586-021-04389-z>

## Share this article

Anyone you share the following link with will be able to read this content:

[Get shareable link](#)

Sorry, a shareable link is not currently available for this article.

[Copy to clipboard](#)

Provided by the Springer Nature SharedIt content-sharing initiative

## Further reading

- [\*\*ACE2-Targeting antibody suppresses SARS-CoV-2 Omicron and Delta variants\*\*](#)

- Jianxia Ou
- Yanan Zhang
- Chunhe Wang

*Signal Transduction and Targeted Therapy* (2022)

- [\*\*Striking antibody evasion manifested by the Omicron variant of SARS-CoV-2\*\*](#)

- Lihong Liu
- Sho Iketani
- David D. Ho

*Nature* (2022)

- [\*\*Landscape of the RBD-specific IgG, IgM, and IgA responses triggered by the inactivated virus vaccine against the Omicron variant\*\*](#)

- Jun-biao Xue
- Dan-yun Lai
- Sheng-ce Tao

*Cell Discovery* (2022)

- **Impaired detection of omicron by SARS-CoV-2 rapid antigen tests**

- Andreas Osterman
- Irina Badell
- Oliver T. Keppler

*Medical Microbiology and Immunology* (2022)

---

This article was downloaded by **calibre** from <https://www.nature.com/articles/s41586-021-04389-z>

| [Section menu](#) | [Main menu](#) |

- Article
- [Published: 23 December 2021](#)

# Striking antibody evasion manifested by the Omicron variant of SARS-CoV-2

- [Lihong Liu<sup>1</sup> na1](#),
- [Sho Iketani<sup>1,2</sup> na1](#),
- [Yicheng Guo](#) [ORCID: orcid.org/0000-0001-5357-660X<sup>1</sup> na1](#),
- [Jasper F.-W. Chan](#) [ORCID: orcid.org/0000-0001-6336-6657<sup>3,4</sup> na1](#),
- [Maple Wang<sup>1</sup> na1](#),
- [Liyuan Liu<sup>5</sup> na1](#),
- [Yang Luo](#) [ORCID: orcid.org/0000-0003-3277-8792<sup>1</sup>](#),
- [Hin Chu](#) [ORCID: orcid.org/0000-0003-2855-9837<sup>3,4</sup>](#),
- [Yiming Huang<sup>5</sup>](#),
- [Manoj S. Nair](#) [ORCID: orcid.org/0000-0002-5994-3957<sup>1</sup>](#),
- [Jian Yu<sup>1</sup>](#),
- [Kenn K.-H. Chik<sup>4</sup>](#),
- [Terrence T.-T. Yuen<sup>3</sup>](#),
- [Chaemin Yoon<sup>3</sup>](#),
- [Kelvin K.-W. To](#) [ORCID: orcid.org/0000-0002-1921-5824<sup>3,4</sup>](#),
- [Honglin Chen](#) [ORCID: orcid.org/0000-0001-5108-8338<sup>3,4</sup>](#),
- [Michael T. Yin<sup>1,6</sup>](#),
- [Magdalena E. Sobieszczyk<sup>1,6</sup>](#),
- [Yaoxing Huang](#) [ORCID: orcid.org/0000-0001-6270-1644<sup>1</sup>](#),
- [Harris H. Wang](#) [ORCID: orcid.org/0000-0003-2164-4318<sup>5</sup>](#),
- [Zizhang Sheng<sup>1</sup>](#),
- [Kwok-Yung Yuen](#) [ORCID: orcid.org/0000-0002-2083-1552<sup>3,4</sup>](#) &
- [David D. Ho](#) [ORCID: orcid.org/0000-0003-1627-149X<sup>1,2,6</sup>](#)

*Nature* volume 602, pages 676–681 (2022)

- 23k Accesses
- 28 Citations

- 121 Altmetric
- [Metrics details](#)

## Subjects

- [SARS-CoV-2](#)
- [Vaccines](#)

## Abstract

The B.1.1.529/Omicron variant of SARS-CoV-2 was only recently detected in southern Africa, but its subsequent spread has been extensive, both regionally and globally<sup>1</sup>. It is expected to become dominant in the coming weeks<sup>2</sup>, probably due to enhanced transmissibility. A striking feature of this variant is the large number of spike mutations<sup>3</sup> that pose a threat to the efficacy of current COVID-19 vaccines and antibody therapies<sup>4</sup>. This concern is amplified by the findings of our study. Here we found that B.1.1.529 is markedly resistant to neutralization by serum not only from patients who recovered from COVID-19, but also from individuals who were vaccinated with one of the four widely used COVID-19 vaccines. Even serum from individuals who were vaccinated and received a booster dose of mRNA-based vaccines exhibited substantially diminished neutralizing activity against B.1.1.529. By evaluating a panel of monoclonal antibodies against all known epitope clusters on the spike protein, we noted that the activity of 17 out of the 19 antibodies tested were either abolished or impaired, including ones that are currently authorized or approved for use in patients. Moreover, we also identified four new spike mutations (S371L, N440K, G446S and Q493R) that confer greater antibody resistance on B.1.1.529. The Omicron variant presents a serious threat to many existing COVID-19 vaccines and therapies, compelling the development of new interventions that anticipate the evolutionary trajectory of SARS-CoV-2.

[Download PDF](#)

## Main

The COVID-19 pandemic continues as the causative agent SARS-CoV-2 continues to evolve. Many diverse viral variants have emerged (Fig. [1a](#)), each characterized by mutations in the spike protein that raise concerns of both antibody evasion and enhanced transmission. The B.1.351/Beta variant was found to be highly refractory to antibody neutralization<sup>4</sup> and therefore compromised the efficacy of vaccines<sup>[5,6,7](#)</sup> and therapeutic antibodies. The B.1.1.7/Alpha variant became dominant globally in early

2021 due to having an edge in transmission<sup>8</sup>, only to be replaced by the B.1.617.2/Delta variant, which exhibited an even greater propensity to spread coupled with a moderate level of antibody resistance<sup>9</sup>. Next came the B.1.1.529/Omicron variant, which was first detected in southern Africa in November 2021 (refs. [3](#),[10](#),[11](#)) (Fig. [1a](#)). Omicron has since spread rapidly in the region, as well as to over 60 countries, gaining traction even in regions in which the Delta variant is prevalent. The short doubling time (2–3 days) of Omicron cases suggests that it could soon become dominant<sup>2</sup>. Moreover, its spike protein contains an alarming number of mutations (>30) (Fig. [1b](#) and Extended Data Fig. [1](#)), including at least 15 in the receptor-binding domain (RBD), the principal target of neutralizing antibodies. These extensive spike mutations raise the possibility that current vaccines and therapeutic antibodies would be greatly compromised. This concern is amplified by the findings that we now report.

**Fig. 1: Resistance of B.1.1.529 to neutralization by sera.**

 [figure 1](#)

**a**, Unrooted phylogenetic tree of B.1.1.529 with other major SARS-CoV-2 variants. **b**, Key spike mutations found in the viruses isolated in the major lineage of B.1.1.529. Del, deletion; ins, insertion. **c**, Neutralization of D614G and B.1.1.529 pseudoviruses by convalescent patient sera. **d**, Neutralization of D614G and B.1.1.529 pseudoviruses

by vaccinee sera. Within the four standard vaccination groups, individuals who were vaccinated without documented infection are denoted as circles and individuals who were both vaccinated and infected are denoted as triangles. Within the boosted group, Moderna vaccinees are denoted as squares and Pfizer vaccinees are denoted as diamonds. **e**, Neutralization of authentic D614G and B.1.1.529 viruses by vaccinee sera. Moderna vaccinees are denoted as squares and Pfizer vaccinees are denoted as diamonds. Data represent one out of two independent experiments. For all of the panels, the values above the symbols denote the geometric mean titre and the numbers in parentheses denote the number of samples above the limit of detection. *P* values were determined by using two-tailed Wilcoxon matched-pairs signed-rank tests.

## Serum neutralization of B.1.1.529

We first examined the neutralizing activity of serum collected in spring 2020 from patients with COVID-19, who were presumably infected with the wild-type (WT) SARS-CoV-2 (9–120 days after symptoms) ([Methods](#) and Extended Data Table 1). Samples from ten individuals were tested for neutralization against both D614G (WT) and B.1.1.529 pseudoviruses. Although robust titres were observed against D614G, a significant drop (>32-fold) in 50% infectious dose ( $ID_{50}$ ) titres was observed against B.1.1.529, with only two samples showing titres above the limit of detection (LOD) (Fig. [1c](#) and Extended Data Fig. [2a](#)). We next assessed the neutralizing activity of sera from individuals who received one of the four widely used COVID-19 vaccines: BNT162b2 (Pfizer, 15–213 days after vaccination), mRNA-1273 (Moderna, 6–177 days after vaccination), Ad26.COV2.S (Johnson & Johnson, 50–186 days after vaccination) and ChAdOx1 nCoV-19 (AstraZeneca, 91–159 days after vaccination) ([Methods](#) and Extended Data Table 2). In all cases, a substantial loss in neutralizing potency was observed against B.1.1.529 (Fig. [1d](#) and Extended Data Fig. [2b–f](#)). For the two mRNA-based vaccines, BNT162b2 and mRNA-1273, a >21-fold and >8.6-fold decrease in  $ID_{50}$  was observed, respectively. Note that, for these two groups, we specifically chose samples with high titres so that the fold change in titre could be better quantified; the difference in the number of samples with titres above the LOD (6 out of 13 for BNT162b2 versus 11 out of 12 for mRNA-1273) may therefore be favourably biased. Within the Ad26.COV2.S and ChAdOx1 nCOV-19 groups, all of the samples were below the LOD against B.1.1.529, except for two Ad26.COV2.S samples from patients who had a previous history of SARS-CoV-2 infection (Fig. [1d](#)). Collectively, these results suggest that individuals who were previously infected or fully vaccinated remain at risk for B.1.1.529 infection.

Booster shots are now routinely administered in many countries 6 months after full vaccination. We therefore also examined the serum neutralizing activity of individuals who had received three homologous mRNA vaccinations (13 with BNT162b2 and 2 with mRNA-1273, 14–90 days after vaccination). Every sample showed lower activity

in neutralizing B.1.1.529, with a mean decrease of 6.5-fold compared with the WT (Fig. 1d). Although all of the samples had titres above the LOD, the substantial loss in activity may still pose a risk for B.1.1.529 infection despite the booster vaccination.

We next confirmed the above findings by testing a subset of the BNT162b2 and mRNA-1273 vaccinee serum samples using authentic SARS-CoV-2 isolates: WT and B.1.1.529. Again, a substantial decrease in the neutralization of B.1.1.529 was observed, with mean decreases of >6.0-fold and >4.1-fold for the fully vaccinated group and the boosted group, respectively (Fig. 1e).

## Antibody neutralization of B.1.1.529

To understand the types of antibodies in the serum that lost neutralizing activity against B.1.1.529, we assessed the neutralization profile of 19 well-characterized monoclonal antibodies against the spike protein, including 17 directed to the RBD and 2 directed to the N-terminal domain (NTD). We included the following monoclonal antibodies that have been authorized or approved for clinical use, either individually or in combination: REGN10987 (imdevimab)<sup>12</sup>, REGN10933 (casirivimab)<sup>12</sup>, COV2-2196 (tixagevimab)<sup>13</sup>, COV2-2130 (cilgavimab)<sup>13</sup>, LY-CoV555 (bamlanivimab)<sup>14</sup>, CB6 (etesevimab)<sup>15</sup>, Brii-196 (amubarvimab)<sup>16</sup>, Brii-198 (romlusevimab)<sup>16</sup> and S309 (sotrovimab)<sup>17</sup>. We also included other monoclonal antibodies of interest: 910-30 (ref. 18), ADG-2 (ref. 19), DH1047 (ref. 20), S2X259 (ref. 21) and our antibodies 1-20, 2-15, 2-7, 4-18, 5-7 and 10-40 (refs. 22,23,24). The footprints of monoclonal antibodies with structures available were drawn in relation to the mutations found in the B.1.1.529 RBD (Fig. 2a) and NTD (Fig. 2b). The risk to each of the four classes<sup>25</sup> of RBD monoclonal antibodies, as well as to the NTD monoclonal antibodies, was immediately apparent. Indeed, neutralization studies on B.1.1.529 pseudovirus showed that 17 out of the 19 monoclonal antibodies tested lost neutralizing activity completely or partially (Fig. 2c and Extended Data Fig. 3). The potency of class 1 and class 2 RBD monoclonal antibodies all decreased by more than 100-fold, as did the more potent monoclonal antibodies in RBD class 3 (REGN10987, COV2-2130 and 2-7). The activities of S309 and Brii-198 were spared. All of the monoclonal antibodies in RBD class 4 lost neutralization potency against B.1.1.529 by at least tenfold, as did monoclonal antibodies directed to the antigenic supersite<sup>26</sup> (4-18) or the alternative site<sup>23</sup> (5-7) on the NTD. Strikingly, all four combination monoclonal antibody drugs in clinical use lost substantial activity against B.1.1.529, probably abolishing or impairing their efficacy in patients.

**Fig. 2: Resistance of B.1.1.529 to neutralization by monoclonal antibodies.**

---

 **figure 2**

**a**, Footprints of RBD-directed antibodies. Mutations within B.1.1.529 are highlighted in cyan. Approved or authorized antibodies are shown in bold. The receptor-binding motif (RBM) residues are highlighted in yellow. **b**, Footprints of NTD-directed antibodies. Mutations within B.1.1.529 are highlighted in cyan. The NTD supersite residues are highlighted in light pink. **c**, Neutralization of D614G and B.1.1.529 pseudoviruses by RBD-directed and NTD-directed monoclonal antibodies (mAbs). **d**, Neutralization of D614G and B.1.1.529+R346K pseudoviruses by RBD-directed and NTD-directed monoclonal antibodies. Data represent one out of two independent experiments.

Approximately 10% of the B.1.1.529 viruses in the Global Initiative on Sharing All Influenza Data (GISAID)<sup>1</sup> also contain an additional RBD mutation, R346K, which is the defining mutation for the B.1.621/Mu variant<sup>27</sup>. We therefore constructed another pseudovirus (B.1.1.529+R346K) containing this mutation for additional testing using the same panel of monoclonal antibodies (Fig. [2d](#)). The overall findings resembled

those already shown in Fig. 2c, with the exception that the neutralizing activity of Brii-198 was abolished. In fact, nearly the entire panel of antibodies was essentially rendered inactive against this minor form of the Omicron variant.

The fold changes in IC<sub>50</sub> of the monoclonal antibodies against B.1.1.529 and B.1.1.529+R346K relative to D614G are summarized in the first two rows of Fig. 3a. The considerable loss of activity observed for all classes of monoclonal antibodies against B.1.1.529 suggests that perhaps the same is occurring in the serum of convalescent patients and vaccinated individuals.

**Fig. 3: Impact of individual mutations within B.1.1.529 against monoclonal antibodies.**

 figure 3



**a**, Neutralization of pseudoviruses containing single mutations found within B.1.1.529 by a panel of 19 monoclonal antibodies. The fold change relative to neutralization of D614G is denoted, with resistance coloured red and sensitization coloured green. **b**, Modelling of critical mutations in B.1.1.529 that affect antibody neutralization.

## Mutations conferring antibody resistance

To understand the specific B.1.1.529 mutations that confer antibody resistance, we next individually tested the same panel of 19 monoclonal antibodies against pseudoviruses for each of the 34 mutations (excluding D614G) found in B.1.1.529 or B.1.1.529+R346K. Our findings not only confirmed the role of known mutations at spike residues 142–145, 417, 484 and 501 in conferring resistance to NTD or RBD (class 1 or class 2) antibodies<sup>4</sup> but also revealed several mutations that were not previously known to have functional importance to neutralization (Fig. 3a and Extended Data Fig. 4). Q493R, which was previously shown to affect binding of CB6 and LY-CoV555 (ref. 28) as well as polyclonal sera<sup>29</sup>, mediated resistance to CB6 (class 1) as well as to LY-CoV555 and 2-15 (class 2), findings that could be explained by the abolishment of hydrogen bonds due to the long side chain of arginine and induced steric clashes with CDRH3 in these antibodies (Fig. 3b (left)). Both N440K and G446S mediated resistance to REGN10987 and 2-7 (class 3), observations that could also be explained by steric hindrance (Fig. 3b (middle)). The most striking and perhaps unexpected finding was that S371L broadly affected neutralization by monoclonal antibodies in all four RBD classes (Fig. 3a and Extended Data Fig. 4). Although the precise mechanism of this resistance is unknown, *in silico* modelling suggested two possibilities (Fig. 3b (right)). First, in the RBD-down state, mutating Ser to Leu results in an interference with the N343 glycan, thereby possibly altering its conformation and affecting class 3 antibodies that typically bind to this region. Second, in the RBD-up state, S371L may alter the local conformation of the loop consisting of Ser371-Ser373-Ser375, thereby affecting the binding of class 4 antibodies that generally target a portion of this loop<sup>24</sup>. It is not clear how class 1 and class 2 RBD monoclonal antibodies are affected by this mutation.

## Evolution of SARS-CoV-2 to antibodies

To gain insights into the antibody resistance of B.1.1.529 relative to previous SARS-CoV-2 variants, we evaluated the neutralizing activity of the same panel of neutralizing monoclonal antibodies against pseudoviruses for B.1.1.7 (ref. 8), B.1.526 (ref. 30), B.1.429 (ref. 31), B.1.617.2 (ref. 9), P.1 (ref. 32) and B.1.351 (ref. 33). It is evident from these results (Fig. 4 and Extended Data Fig. 5) that previous variants developed resistance to only NTD antibodies and class 1 and class 2 RBD antibodies. Here B.1.1.529, with or without R346K, has made a big mutational leap by becoming not only nearly completely resistant to class 1 and class 2 RBD antibodies, but also substantially resistant to both class 3 and class 4 RBD antibodies. B.1.1.529 is now the most complete ‘escapee’ from neutralization by currently available antibodies.

**Fig. 4: Evolution of antibody resistance across SARS-CoV-2 variants.**

---

 figure 4

Neutralization of SARS-CoV-2 variant pseudoviruses by a panel of 19 monoclonal antibodies. The fold change relative to neutralization of D614G is denoted.

## Discussion

The Omicron variant caused fear almost as soon as it was detected to be spreading in South Africa. The suggestion that this new variant would transmit more readily has come true in the ensuing weeks<sup>2</sup>. The extensive mutations found in its spike protein raised concerns that the efficacy of current COVID-19 vaccines and antibody therapies might be compromised. Indeed, in this study, sera from convalescent patients (Fig. 1c) and vaccinees (Fig. 1d,e) showed markedly reduced neutralizing activity against B.1.1.529. Other studies have found similar losses<sup>34,35,36,37,38</sup>. These findings are consistent with emerging clinical data on the Omicron variant demonstrating higher rates of reinfection<sup>11</sup> and vaccine breakthroughs. In fact, recent reports showed that the efficacy of two doses of BNT162b2 vaccine has dropped from over 90% against the original SARS-CoV-2 strain to approximately 40% and 33% against B.1.1.529 in the United Kingdom<sup>39</sup> and South Africa<sup>40</sup>, respectively. Even a third booster shot may not adequately protect against Omicron infection<sup>39,41</sup>, although the protection against disease still makes it advisable to administer booster vaccinations. Vaccines that elicited lower neutralizing titres<sup>35,42</sup> are expected to fare worse against B.1.1.529.

The nature of the loss in serum neutralizing activity against B.1.1.529 could be discerned from our findings on a panel of monoclonal antibodies directed to the viral spike. The neutralizing activities of all four major classes of RBD monoclonal antibodies and two distinct classes of NTD monoclonal antibodies are either abolished or impaired (Fig. 2c,d). In addition to previously identified mutations that confer antibody resistance<sup>4</sup>, we have uncovered four previously undescribed spike mutations with functional consequences. Q493R confers resistance to some class 1 and class 2 RBD monoclonal antibodies; N440K and G446S confer resistance to some class 3 RBD monoclonal antibodies; and S371L confers global resistance to many RBD monoclonal antibodies through mechanisms that are not yet apparent. While performing these monoclonal antibody studies, we also observed that nearly all of the currently authorized or approved monoclonal antibody drugs are rendered weak or inactive by B.1.1.529 (Figs. 2c and 3a). In fact, the Omicron variant that contains

R346K renders almost all current antibody therapy for COVID-19 ineffective (Figs. 2d and 3a).

The scientific community has chased after SARS-CoV-2 variants for a year. As more and more of them appeared, our interventions directed to the spike became increasingly ineffective. The Omicron variant has now put an exclamation mark on this point. It is not too farfetched to think that this SARS-CoV-2 is now only a mutation or two away from being pan-resistant to current antibodies, either monoclonal or polyclonal. We must devise strategies that anticipate the evolutionary direction of the virus and develop agents that target better-conserved viral elements.

## Methods

### Data reporting

No statistical methods were used to predetermine sample size. The experiments were not randomized and the investigators were not blinded to allocation during experiments and outcome assessment.

### Serum samples

Convalescent plasma samples were obtained from patients with documented SARS-CoV-2 infection. These samples were collected at the beginning of the pandemic in early 2020 at Columbia University Irving Medical Center and are therefore assumed to be infection by the WT strain of SARS-CoV-2 (ref. 4). Sera from individuals who received two or three doses of mRNA-1273 or BNT162b2 vaccine were collected at Columbia University Irving Medical Center at least two weeks after the final dose. Sera from individuals who received one dose of Ad26.COV2.S or two doses of ChAdOx1 nCov-19 were obtained from BEI Resources. Some individuals were also infected by SARS-CoV-2 in addition to the vaccinations they received. Note that, whenever possible, we specifically chose samples with high titres against the WT strain of SARS-CoV-2 such that the loss in activity against B.1.1.529 could be better quantified and the titres observed here should therefore be considered in that context. All collections were conducted under protocols reviewed and approved by the Institutional Review Board of Columbia University. All of the participants provided written informed consent. Additional information for the convalescent samples and vaccinee samples is provided in Extended Data Tables 1 and 2, respectively.

### Monoclonal antibodies

Antibodies were expressed as previously described<sup>22</sup> by synthesis of heavy chain variable (VH) and light chain variable (VL) genes (GenScript), transfection of Expi293 cells (Thermo Fisher Scientific) and affinity purification from the supernatant by rProtein A Sepharose (GE). REGN10987, REGN10933, COV2-2196 and COV2-2130 were provided by Regeneron Pharmaceuticals; Brii-196 and Brii-198 were provided by Brii Biosciences; CB6 was provided by B. Zhang and P. Kwong (NIH); and 910-30 was provided by B. DeKosky (MIT).

## Cell lines

Expi293 cells were obtained from Thermo Fisher Scientific (A14527); Vero E6 cells were obtained from the ATCC (CRL-1586); HEK293T cells were obtained from the ATCC (CRL-3216); and Vero-E6-TMPRSS2 cells were obtained from JCRB (JCRB1819). Cells were purchased from authenticated vendors and morphology was confirmed visually before use. All cell lines tested mycoplasma negative.

## Variant SARS-CoV-2 spike plasmid construction

An in-house high-throughput template-guide gene synthesis approach was used to generate spike genes with single or full mutations of B.1.1.529. In brief, 5'-phosphorylated oligos with designed mutations were annealed to the reverse strand of the WT spike gene construct and extended by DNA polymerase. Extension products (forward-stranded fragments) were then ligated together by Taq DNA ligase and subsequently amplified by PCR to generate variants of interest. To verify the sequences of variants, next-generation sequencing libraries were prepared according to a low-volume Nextera sequencing protocol<sup>43</sup> and sequenced on the Illumina MiSeq platform (single-end mode with 50 bp R1). Raw reads were processed using Cutadapt v.2.1<sup>44</sup> with the default settings to remove adapters, and were then aligned to reference variants sequences using Bowtie2 v.2.3.4<sup>45</sup> with the default settings. The resulting reads alignments were then visualized in the Integrative Genomics Viewer<sup>46</sup> and manually inspected to verify the fidelity of variants. The sequences of the oligos used in variants generation are provided in Extended Data Table 3.

## Pseudovirus production

Pseudoviruses were produced in the vesicular stomatitis virus (VSV) background, in which the native glycoprotein was replaced by that of SARS-CoV-2 and its variants, as previously described<sup>24</sup>. In brief, HEK293T cells were transfected with a spike expression construct with polyethylenimine (PEI) (1 mg ml<sup>-1</sup>) and cultured overnight at 37 °C under 5% CO<sub>2</sub>, and then infected with VSV-G pseudotyped ΔG-luciferase (G\*ΔG-luciferase, Kerafast) 1 day after transfection. After 2 h of infection, cells were

washed three times, changed to fresh medium and then cultured for approximately another 24 h before the supernatants were collected, centrifuged and aliquoted to use in assays.

### Pseudovirus neutralization assay

All viruses were first titrated to normalize the viral input between assays. Heat-inactivated sera or antibodies were first serially diluted in 96 well-plates in triplicate, starting at 1:100 dilution for sera and 10 µg ml<sup>-1</sup> for antibodies. Viruses were then added and the virus–sample mixture was incubated at 37 °C for 1 h. Vero-E6 cells (ATCC) were then added at a density of 3 × 10<sup>4</sup> cells per well and the plates were incubated at 37 °C for approximately 10 h. Luciferase activity was quantified using the Luciferase Assay System (Promega) according to the manufacturer’s instructions using SoftMax Pro v.7.0.2 (Molecular Devices). Neutralization curves and IC<sub>50</sub> values were derived by fitting a nonlinear five-parameter dose–response curve to the data in GraphPad Prism v.9.2.

### Authentic virus isolation and propagation

Authentic B.1.1.529 was isolated from a specimen from the respiratory tract of a patient with COVID-19 in Hong Kong by K.-Y. Yuen and colleagues at the Department of Microbiology, The University of Hong Kong. Isolation of WT SARS-CoV-2 was previously described<sup>47</sup>. Viruses were propagated in Vero-E6-TMPRSS2 cells and the sequence was confirmed by next-generation sequencing before use.

### Authentic virus neutralization assay

To measure neutralization of authentic SARS-CoV-2 viruses, Vero-E6-TMPRSS2 cells were first seeded in 96-well plates in cell culture medium (Dulbecco’s Modified Eagle Medium (DMEM) + 10% fetal bovine serum (FBS) + 1% penicillin–streptomycin) overnight at 37 °C under 5% CO<sub>2</sub> to establish a monolayer. The next day, sera or antibodies were serially diluted in 96-well plates in triplicate in DMEM + 2% FBS and then incubated with 0.01 multiplicity of infection of WT SARS-CoV-2 or B.1.1.529 at 37 °C for 1 h. Sera were diluted from 1:100 dilution and antibodies were diluted from 10 µg ml<sup>-1</sup>. Next, the mixture was overlaid onto cells and further incubated at 37 °C under 5% CO<sub>2</sub> for approximately 72 h. Cytopathic effects were then scored by plaque assay in a blinded manner. Neutralization curves and IC<sub>50</sub> values were derived by fitting a nonlinear five-parameter dose–response curve to the data in GraphPad Prism v.9.2.

### Antibody footprint analysis and RBD mutagenesis analysis

The SARS-CoV-2 spike structure used for displaying epitope footprints and mutations within emerging strains was downloaded from the Protein Data Bank (PDB: [6ZGE](#)). The structures of antibody-spike complexes were also obtained from PDB ([7L5B](#) (2-15), [6XDG](#) (REGN10933 and REGN10987), [7L2E](#) (4-18), [7RW2](#) (5-7), [7C01](#) (CB6), [7KMG](#) (LY-COV555), [7CDI](#) (Brii-196), [7KS9](#) (910-30), [7LD1](#) (DH1047), [7RAL](#) (S2X259), [7LSS](#) (2-7) and [6WPT](#) (S309)). Interface residues were identified using PISA<sup>48</sup> using the default parameters. The footprint for each antibody was defined by the boundaries of all epitope residues. The border for each footprint was then optimized by ImageMagick v.7.0.10-31 (<https://imagemagick.org>). PyMOL v.2.3.2 was used to perform mutagenesis and to generate structural plots (Schrödinger).

## Reporting summary

Further information on research design is available in the [Nature Research Reporting Summary](#) linked to this paper.

## Data availability

Materials used in this study will be made available under an appropriate Materials Transfer Agreement. All the data are provided in the paper. The structures used for analysis in this study are available from PDB under accession numbers [6ZGE](#), [7L5B](#), [6XDG](#), [7L2E](#), [7RW2](#), [7C01](#), [7KMG](#), [7CDI](#), [7KS9](#), [7LD1](#), [7RAL](#), [7LSS](#) and [6WPT](#).

## References

1. Shu, Y. & McCauley, J. GISAID: global initiative on sharing all influenza data—from vision to reality. *Euro Surveill.* **22**, 30494 (2017).
2. Grabowski, F., Kochańczyk, M. & Lipniacki, T. Omicron strain spreads with the doubling time of 3.2—3.6 days in South Africa province of Gauteng that achieved herd immunity to Delta variant. Preprint at <https://doi.org/10.1101/2021.12.08.21267494> (2021).
3. Scott, L. et al. Track Omicron’s spread with molecular data. *Science* **374**, 1454–1455 (2021).
4. Wang, P. et al. Antibody resistance of SARS-CoV-2 variants B.1.351 and B.1.1.7. *Nature* **593**, 130–135 (2021).
5. Abu-Raddad, L. J., Chemaitelly, H. & Butt, A. A. Effectiveness of the BNT162b2 COVID-19 vaccine against the B.1.1.7 and B.1.351 variants. *N. Engl. J. Med.* **385**, 187–189 (2021).

6. Madhi, S. A. et al. Efficacy of the ChAdOx1 nCoV-19 COVID-19 vaccine against the B.1.351 variant. *N. Engl. J. Med.* **384**, 1885–1898 (2021).
7. Sadoff, J. et al. Safety and efficacy of single-dose Ad26.COV2.S vaccine against COVID-19. *N. Engl. J. Med.* **384**, 2187–2201 (2021).
8. Davies, N. G. et al. Estimated transmissibility and impact of SARS-CoV-2 lineage B.1.1.7 in England. *Science* **372**, eabg3055 (2021).
9. Mlcochova, P. et al. SARS-CoV-2 B.1.617.2 Delta variant replication and immune evasion. *Nature* **599**, 114–119 (2021).
10. Hadfield, J. et al. Nextstrain: real-time tracking of pathogen evolution. *Bioinformatics* **34**, 4121–4123 (2018).
11. Pulliam, J. R. C. et al. Increased risk of SARS-CoV-2 reinfection associated with emergence of the Omicron variant in South Africa. Preprint at <https://doi.org/10.1101/2021.11.11.21266068> (2021).
12. Hansen, J. et al. Studies in humanized mice and convalescent humans yield a SARS-CoV-2 antibody cocktail. *Science* **369**, 1010–1014 (2020).
13. Zost, S. J. et al. Potently neutralizing and protective human antibodies against SARS-CoV-2. *Nature* **584**, 443–449 (2020).
14. Jones, B. E. et al. The neutralizing antibody, LY-CoV555, protects against SARS-CoV-2 infection in nonhuman primates. *Sci. Transl. Med.* **13**, eabf1906 (2021).
15. Shi, R. et al. A human neutralizing antibody targets the receptor-binding site of SARS-CoV-2. *Nature* **584**, 120–124 (2020).
16. Ju, B. et al. Human neutralizing antibodies elicited by SARS-CoV-2 infection. *Nature* **584**, 115–119 (2020).
17. Pinto, D. et al. Cross-neutralization of SARS-CoV-2 by a human monoclonal SARS-CoV antibody. *Nature* **583**, 290–295 (2020).
18. Banach, B. B. et al. Paired heavy- and light-chain signatures contribute to potent SARS-CoV-2 neutralization in public antibody responses. *Cell Rep* **37**, 109771 (2021).
19. Rappazzo, C. G. et al. Broad and potent activity against SARS-like viruses by an engineered human monoclonal antibody. *Science* **371**, 823–829 (2021).

20. Li, D. et al. In vitro and in vivo functions of SARS-CoV-2 infection-enhancing and neutralizing antibodies. *Cell* **184**, 4203–4219 (2021).
21. Tortorici, M. A. et al. Broad sarbecovirus neutralization by a human monoclonal antibody. *Nature* **597**, 103–108 (2021).
22. Liu, L. et al. Potent neutralizing antibodies against multiple epitopes on SARS-CoV-2 spike. *Nature* **584**, 450–456 (2020).
23. Cerutti, G. et al. Neutralizing antibody 5-7 defines a distinct site of vulnerability in SARS-CoV-2 spike N-terminal domain. *Cell Rep.* **37**, 109928 (2021).
24. Liu, L. et al. Isolation and comparative analysis of antibodies that broadly neutralize sarbecoviruses. Preprint at <https://doi.org/10.1101/2021.12.11.472236> (2021).
25. Barnes, C. O. et al. SARS-CoV-2 neutralizing antibody structures inform therapeutic strategies. *Nature* **588**, 682–687 (2020).
26. Cerutti, G. et al. Potent SARS-CoV-2 neutralizing antibodies directed against spike N-terminal domain target a single supersite. *Cell Host Microbe* **29**, 819–833 (2021).
27. Uriu, K. et al. Neutralization of the SARS-CoV-2 Mu variant by convalescent and vaccine serum. *N. Engl. J. Med.* **385**, 2397–2399 (2021).
28. Starr, T. N., Greaney, A. J., Dingens, A. S. & Bloom, J. D. Complete map of SARS-CoV-2 RBD mutations that escape the monoclonal antibody LY-CoV555 and its cocktail with LY-CoV016. *Cell Rep. Med.* **2**, 100255 (2021).
29. Amanat, F. et al. SARS-CoV-2 mRNA vaccination induces functionally diverse antibodies to NTD, RBD, and S2. *Cell* **184**, 3936–3948 (2021).
30. Annavajhala, M. K. et al. Emergence and expansion of SARS-CoV-2 B.1.526 after identification in New York. *Nature* **597**, 703–708 (2021).
31. Zhang, W. et al. Emergence of a novel SARS-CoV-2 variant in southern California. *JAMA* **325**, 1324–1326 (2021).
32. Faria, N. R. et al. Genomics and epidemiology of the P.1 SARS-CoV-2 lineage in Manaus, Brazil. *Science* **372**, 815–821 (2021).
33. Tegally, H. et al. Detection of a SARS-CoV-2 variant of concern in South Africa. *Nature* **592**, 438–443 (2021).

34. Schmidt, F. et al. Plasma neutralization of the SARS-CoV-2 Omicron variant. *New Engl. J. Med.* <https://doi.org/10.1056/NEJMc2119641> (2021).
35. Garcia-Beltran, W. F. et al. mRNA-based COVID-19 vaccine boosters induce neutralizing immunity against SARS-CoV-2 Omicron variant. *Cell*, <https://doi.org/10.1016/j.cell.2021.12.033> (2022).
36. Cameroni, E. et al. Broadly neutralizing antibodies overcome SARS-CoV-2 Omicron antigenic shift. *Nature* <https://doi.org/10.1038/s41586-021-04386-2> (2021).
37. Doria-Rose, N. A. et al. Booster of mRNA-1273 vaccine reduces SARS-CoV-2 Omicron escape from neutralizing antibodies. Preprint at <https://doi.org/10.1101/2021.12.15.21267805> (2021).
38. Planas, D. et al. Considerable escape of SARS-CoV-2 variant Omicron to antibody neutralization. *Nature* <https://doi.org/10.1038/s41586-021-04389-z> (2021).
39. Andrews, N. et al. Effectiveness of COVID-19 vaccines against the Omicron (B.1.1.529) variant of concern. Preprint at <https://doi.org/10.1101/2021.12.14.21267615> (2021).
40. Wroughton, L. Omicron variant more resistant to vaccine but causes less severe covid, major South African study concludes. *The Washington Post* (14 December 2021).
41. Kuhlmann, C. et al. Breakthrough infections with SARS-CoV-2 Omicron variant despite booster dose of mRNA vaccine. SSRN <https://doi.org/10.2139/ssrn.3981711> (2021).
42. Cromer, D. et al. Neutralising antibody titres as predictors of protection against SARS-CoV-2 variants and the impact of boosting: a meta-analysis. *Lancet Microbe* **3**, e52–e61 (2021).
43. Baym, M. et al. Inexpensive multiplexed library preparation for megabase-sized genomes. *PLoS ONE* **10**, e0128036 (2015).
44. Martin, M. Cutadapt removes adapter sequences from high-throughput sequencing reads. *EMBnet J.* **17**, 10–12 (2011).
45. Langmead, B. & Salzberg, S. L. Fast gapped-read alignment with Bowtie 2. *Nat. Methods* **9**, 357–359 (2012).

46. Robinson, J. T. et al. Integrative genomics viewer. *Nat. Biotechnol.* **29**, 24–26 (2011).
47. Chu, H. et al. Comparative tropism, replication kinetics, and cell damage profiling of SARS-CoV-2 and SARS-CoV with implications for clinical manifestations, transmissibility, and laboratory studies of COVID-19: an observational study. *Lancet Microbe* **1**, e14–e23 (2020).
48. Krissinel, E. & Henrick, K. Inference of macromolecular assemblies from crystalline state. *J. Mol. Biol.* **372**, 774–797 (2007).

## Acknowledgements

We thank the staff at Regeneron Pharmaceuticals, B. Zhang and P. Kwong (NIAID), and B. Dekosky (MIT) for antibodies. This study was supported by funding from the Gates Foundation, the JPB Foundation, A. and P. Cherng, S. Yin, C. Ludwig, D. and R. Wu, Health@InnoHK and the National Science Foundation (MCB-2032259).

## Author information

### Author notes

1. These authors contributed equally: Lihong Liu, Sho Iketani, Yicheng Guo, Jasper F.-W. Chan, Maple Wang, Liyuan Liu

### Affiliations

1. Aaron Diamond AIDS Research Center, Columbia University Vagelos College of Physicians and Surgeons, New York, NY, USA

Lihong Liu, Sho Iketani, Yicheng Guo, Maple Wang, Yang Luo, Manoj S. Nair, Jian Yu, Michael T. Yin, Magdalena E. Sobieszczyk, Yaoxing Huang, Zizhang Sheng & David D. Ho

2. Department of Microbiology and Immunology, Columbia University Vagelos College of Physicians and Surgeons, New York, NY, USA

Sho Iketani & David D. Ho

3. State Key Laboratory of Emerging Infectious Diseases, Carol Yu Centre for Infection, Department of Microbiology, Li Ka Shing Faculty of Medicine, The University of Hong Kong, Hong Kong Special Administrative Region, China

Jasper F.-W. Chan, Hin Chu, Terrence T.-T. Yuen, Chaemin Yoon, Kelvin K.-W. To, Honglin Chen & Kwok-Yung Yuen

4. Centre for Virology, Vaccinology and Therapeutics, Hong Kong Special Administrative Region, China

Jasper F.-W. Chan, Hin Chu, Kenn K.-H. Chik, Kelvin K.-W. To, Honglin Chen & Kwok-Yung Yuen

5. Department of Systems Biology, Columbia University Vagelos College of Physicians and Surgeons, New York, NY, USA

Liyuan Liu, Yiming Huang & Harris H. Wang

6. Division of Infectious Diseases, Department of Medicine, Columbia University Vagelos College of Physicians and Surgeons, New York, NY, USA

Michael T. Yin, Magdalena E. Sobieszczyk & David D. Ho

## Contributions

D.D.H. conceived this project. Lihong Liu, S.I. and M.W. conducted pseudovirus neutralization experiments. J.F.-W.C., H. Chu, K.K.-H.C., T.T.-T.Y., C.Y., K.K.-W.T. and H. Chen conducted authentic virus neutralization experiments. Y.G. and Z.S. conducted bioinformatic analyses. Liyuan Liu and Yiming Huang constructed the spike expression plasmids. Y.L. managed the project. J.Y. expressed and purified antibodies. M.T.Y. and M.E.S. provided clinical samples. M.S.N. and Yaoxing Huang contributed to discussions. H.H.W., K.-Y.Y. and D.D.H. directed and supervised the project. Lihong Liu, S.I. and D.D.H. analysed the results and wrote the manuscript.

## Corresponding author

Correspondence to [David D. Ho](#).

## Ethics declarations

## Competing interests

Lihong Liu, S.I., M.S.N., J.Y., Yaoxing Huang and D.D.H. are inventors on patent applications (WO2021236998) or provisional patent applications (63/271,627) filed by Columbia University for a number of SARS-CoV-2 neutralizing antibodies described in this manuscript. Both sets of applications are under review. D.D.H. is a co-founder

of TaiMed Biologics and RenBio, consultant to WuXi Biologics and Brii Biosciences, and board director for Vicarious Surgical.

## Peer review

### Peer review information

*Nature* thanks the anonymous reviewers for their contribution to the peer review of this work.

## Additional information

**Publisher's note** Springer Nature remains neutral with regard to jurisdictional claims in published maps and institutional affiliations.

## Extended data figures and tables

### [Extended Data Fig. 1 Mutations within B.1.1.529 denoted on the full SARS-CoV-2 spike trimer.](#)

The SARS-CoV-2 spike structure was downloaded from PDB 6ZGE.

### [Extended Data Fig. 2 Individual neutralization curves for pseudovirus neutralization assays by serum.](#)

Neutralization by **a**, convalescent sera. **b**, Pfizer (BNT162b2) vaccinee sera. **c**, Moderna (mRNA-1273) vaccinee sera. **d**, J&J (Ad26.COV2.S) vaccinee sera. **e**, AstraZeneca (ChAdOx1 nCoV-19) vaccinee sera. **f**, boosted (three homologous BNT162b2 or mRNA-1273 vaccinations) vaccinee sera. Error bars denote mean ± standard error of the mean (SEM) for three technical replicates.

### [Extended Data Fig. 3 Individual neutralization curves for pseudovirus neutralization assays by monoclonal antibodies.](#)

Error bars denote mean ± standard error of the mean (SEM) for three technical replicates.

### [Extended Data Fig. 4 Individual neutralization curves for pseudovirus neutralization assays by monoclonal antibodies against individual](#)

## SARS-CoV-2 mutations.

Error bars denote mean ± standard error of the mean (SEM) for three technical replicates.

## Extended Data Fig. 5 Individual neutralization curves for pseudovirus neutralization assays by monoclonal antibodies against SARS-CoV-2 variants.

Error bars denote mean ± standard error of the mean (SEM) for three technical replicates.

**Extended Data Table 1** Demographics and vaccination information for serum samples from convalescent patients used in this study

**Extended Data Table 2** Demographics and vaccination information for serum samples from vaccinated individuals used in this study

**Extended Data Table 3** Oligos used to construct spike expression plasmids

## Supplementary information

### Reporting Summary

### Rights and permissions

### Reprints and Permissions

### About this article

### Cite this article

Liu, L., Iketani, S., Guo, Y. *et al.* Striking antibody evasion manifested by the Omicron variant of SARS-CoV-2. *Nature* **602**, 676–681 (2022).

<https://doi.org/10.1038/s41586-021-04388-0>

- Received: 14 December 2021
- Accepted: 23 December 2021
- Published: 23 December 2021

- Issue Date: 24 February 2022
- DOI: <https://doi.org/10.1038/s41586-021-04388-0>

## Share this article

Anyone you share the following link with will be able to read this content:

[Get shareable link](#)

Sorry, a shareable link is not currently available for this article.

[Copy to clipboard](#)

Provided by the Springer Nature SharedIt content-sharing initiative

## Further reading

- [Nasal delivery of thermostable and broadly neutralizing antibodies protects mice against SARS-CoV-2 infection](#)

- Wenhui Fan
- Shanshan Sun
- Limin Yang

*Signal Transduction and Targeted Therapy* (2022)

- [ACE2-Targeting antibody suppresses SARS-CoV-2 Omicron and Delta variants](#)

- Jianxia Ou
- Yanan Zhang
- Chunhe Wang

*Signal Transduction and Targeted Therapy* (2022)

- [An ultrapotent RBD-targeted biparatopic nanobody neutralizes broad SARS-CoV-2 variants](#)

- Xiaojing Chi
- Xinhui Zhang
- Wei Yang

*Signal Transduction and Targeted Therapy* (2022)

- **Activity of convalescent and vaccine serum against SARS-CoV-2 Omicron**

- Juan Manuel Carreño
- Hala Alshammary
- Florian Krammer

*Nature* (2022)

---

This article was downloaded by **calibre** from <https://www.nature.com/articles/s41586-021-04388-0>

| [Section menu](#) | [Main menu](#) |

- Article
- [Published: 31 December 2021](#)

# Activity of convalescent and vaccine serum against SARS-CoV-2 Omicron

- [Juan Manuel Carreño<sup>1</sup>](#),
- [Hala Alshammary<sup>1</sup>](#),
- [Johnstone Tcheou<sup>1</sup>](#),
- [Gagandeep Singh<sup>1</sup>](#),
- [Ariel J. Raskin<sup>1</sup>](#),
- [Hisaki Kawabata<sup>1</sup>](#),
- [Levy A. Sominsky<sup>1</sup>](#),
- [Jordan J. Clark<sup>1</sup>](#),
- [Daniel C. Adelsberg ORCID: orcid.org/0000-0003-0591-7136<sup>1</sup>](#),
- [Dominika A. Bielak<sup>1</sup>](#),
- [Ana Silvia Gonzalez-Reiche ORCID: orcid.org/0000-0003-3583-4497<sup>2</sup>](#),
- [Nicholas Dambrauskas<sup>4</sup>](#),
- [Vladimir Vigdorovich ORCID: orcid.org/0000-0003-4195-4858<sup>4</sup>](#),
- [PSP-PARIS Study Group](#),
- [Komal Srivastava<sup>1</sup>](#),
- [D. Noah Sather<sup>4,5</sup>](#),
- [Emilia Mia Sordillo ORCID: orcid.org/0000-0001-7787-3051<sup>6 na1</sup>](#),
- [Goran Bajic ORCID: orcid.org/0000-0003-0480-4324<sup>1 na1</sup>](#),
- [Harm van Bakel ORCID: orcid.org/0000-0002-1376-6916<sup>2,3,6 na1</sup>](#),
- [Viviana Simon ORCID: orcid.org/0000-0002-6416-5096<sup>1,6,7,8 na1</sup>](#) &
- [Florian Krammer ORCID: orcid.org/0000-0003-4121-776X<sup>1,6 na1</sup>](#)

[Nature](#) volume **602**, pages 682–688 (2022)

- 13k Accesses
- 6 Citations
- 155 Altmetric
- [Metrics details](#)

## Subjects

- [RNA vaccines](#)
- [SARS-CoV-2](#)

## Abstract

The Omicron (B.1.1.529) variant of severe acute respiratory syndrome coronavirus 2 (SARS-CoV-2) was initially identified in November 2021 in South Africa and Botswana, as well as in a sample from a traveller from South Africa in Hong Kong<sup>1,2</sup>. Since then, Omicron has been detected globally. This variant appears to be at least as infectious as Delta (B.1.617.2), has already caused superspreader events<sup>3</sup>, and has outcompeted Delta within weeks in several countries and metropolitan areas. Omicron hosts an unprecedented number of mutations in its spike gene and early reports have provided evidence for extensive immune escape and reduced vaccine effectiveness<sup>2,4,5,6</sup>. Here we investigated the virus-neutralizing and spike protein-binding activity of sera from convalescent, double mRNA-vaccinated, mRNA-boosted, convalescent double-vaccinated and convalescent boosted individuals against wild-type, Beta (B.1.351) and Omicron SARS-CoV-2 isolates and spike proteins. Neutralizing activity of sera from convalescent and double-vaccinated participants was undetectable or very low against Omicron compared with the wild-type virus, whereas neutralizing activity of sera from individuals who had been exposed to spike three or four times through infection and vaccination was maintained, although at significantly reduced levels. Binding to the receptor-binding and N-terminal domains of the Omicron spike protein was reduced compared with binding to the wild type in convalescent unvaccinated individuals, but was mostly retained in vaccinated individuals.

[Download PDF](#)

## Main

SARS-CoV-2 was first detected in Wuhan, China, in late 2019 and has since caused the coronavirus disease 2019 (COVID-19) pandemic. Although SARS-CoV-2 was antigenically relatively stable during its first few months of circulation, the first antigenically distinct variants—Alpha (B.1.1.7), Beta and Gamma (P.1)—emerged in late 2020. Other variants of interest and variants of concern followed. So far, Beta has shown the most antigenic drift in terms of reduction of in vitro neutralization, rivalled only by Mu<sup>7</sup> (B.1.621). Delta, which emerged in early 2021, has been the most consequential variant, since it is more infectious than the viruses circulating in the beginning of the pandemic and also partially escapes neutralization in vitro<sup>8</sup>. Omicron

was first detected in South Africa, Botswana and in a traveller from South Africa in Hong Kong<sup>1,2</sup>. The variant hosts a large number of mutations in its spike protein including at least 15 amino acid changes in the receptor-binding domain (RBD) and extensive changes in the N-terminal domain (NTD). These mutations are predicted to affect most neutralizing antibody epitopes. In addition, Omicron seems to be fit and highly transmissible<sup>3</sup> and has spread rapidly across the globe, outcompeting Delta within weeks to become the dominant circulating variant in several countries and urban areas.

Immunity to SARS-CoV-2 in human populations is highly variable and probably differs in individuals with infection induced immunity, double vaccinated individuals, boosted individuals, and individuals with hybrid immunity owing to the combination of infection followed by vaccination. Understanding residual neutralizing and binding activity against highly antigenically distinct viral variants such as Omicron in these distinct groups is essential to gauge the level of protection that a specific community has against infection and mild or severe COVID-19.

## Neutralization of Omicron

To address these questions, we determined differences in in vitro neutralizing and binding activity for Omicron (Pango lineage BA.1) compared with other variants in sera from individuals with different levels of immunity. We included samples from individuals who had recovered from SARS-CoV-2 infection (convalescent individuals) ( $n = 15$ ), individuals vaccinated twice with BNT162b2 (Pfizer–BioNTech mRNA vaccine;  $n = 10$ ), individuals vaccinated twice with mRNA-1273 (Moderna mRNA vaccine;  $n = 10$ ), individuals vaccinated three times (boosted) with BNT162b2 (boosted individuals) ( $n = 10$ ), individuals vaccinated three times with mRNA-1273 ( $n = 10$ ), convalescent individuals who had received two doses of BNT162b2 ( $n = 10$ ), convalescent individuals who had received two doses of mRNA-1273 ( $n = 10$ ), and convalescent individuals who had received three doses of BNT162b2 ( $n = 10$ ) (Fig. 1a, Extended Data Tables 1, 2). First, we tested the in vitro neutralizing activity of the sera against wild type SARS-CoV-2 (USA-WA1/2020; as a reference for ancestral strains), Beta (as a reference for the most pronounced in vitro escape phenotype) and Omicron (isolated from one of the first cases identified in New York City in late November 2021) (Extended Data Table 3). The neutralization assay that we used is performed with authentic SARS-CoV-2 in a multicycle replication setting in which serum and antibody are present at all times, similar to the situation in a seropositive individual. Across all 85 samples, the reduction in neutralization of Omicron compared with wild type was greater than 14.5-fold (the actual fold reduction could not be calculated since many samples were below the limit of detection) (Fig. 1b). By comparison, there was a fourfold reduction of Beta neutralization compared with wild type in the same sample set. Indeed, 16.5% of samples did not show neutralizing activity against

Omicron. Comparing the different groups, we noted that convalescent individuals had lower neutralizing antibody titres against wild-type and Beta, with the majority (73.3%) of samples exhibiting no measurable neutralizing activity for Omicron (Fig. [1c](#)). Sera from individuals double vaccinated with either BNT162b2 or mRNA-1273 showed a reduction in neutralization of Omicron compared with wild-type of more than 23-fold or 42-fold, respectively (Fig. [1d,e](#)). However, most individuals showed low but detectable neutralizing activity against Omicron. Boosted individuals showed smaller differences in neutralizing activity with a 7.5-fold reduction in neutralization of Omicron compared with wild type for BNT162b2-boosted individuals and a 16.7-fold reduction in mRNA-1273-boosted individuals (Fig. [1f,g](#)). Of note, the smaller fold change and higher initial neutralization titres against wild-type virus led to substantial neutralizing activity against Omicron in sera from boosted individuals. Convalescent individuals who received 2 BNT162b2, 2 mRNA-1272 or 3 BNT162b2 vaccine doses showed reductions in Omicron neutralization compared with wild type of 14-fold, 11-fold and 13-fold, respectively (Fig. [1h–j](#)). However, all individuals in these groups maintained relatively robust neutralization activity against Omicron. These data indicate that convalescent individuals greatly benefit from vaccination, an observation that is of considerable importance to public health.

**Fig. 1: Sera from convalescent and vaccinated individuals exhibit strongly reduced neutralizing activity against Omicron compared with wild type SARS-CoV-2.**

---

 **figure 1**

---

**a**, Overview of different exposure groups from whom samples were obtained. Further details are provided in Supplementary Tables 1, 2. **b**, Absolute titres (left) and fold reduction (right) for neutralization by all serum samples of wild-type (WA1 (WT)), Beta and Omicron SARS-CoV-2 variants. **c–j**, Neutralization of wild-type (WA1

(WT)), Beta and Omicron SARS-CoV-2 variants by sera from convalescent individuals (**c**), after two BNT162b2 vaccinations (**d**), after two mRNA-1273 vaccinations (**e**), after three BNT162b2 vaccinations (**f**), after three mRNA-1273 vaccinations (**g**), from convalescent individuals after two BNT162b2 vaccinations (**h**), from convalescent individuals after two mRNA-1273 vaccinations (**i**) and from convalescent individuals after three BNT162b2 vaccinations (**j**). One-way ANOVA with Tukey's multiple comparisons test was used to compare the neutralization titres;  $P < 0.05$  indicated.  $n = 85$  (**b**), 15 (**c**), or 10 (**d–j**) samples. The dotted line represents the limit of detection (10); negative samples were assigned half the limit of detection (5). Each dot represents a biological replicate and the assays were performed once. Fold change is defined as the geometric mean fold change.

[Source data](#)

## Binding to RBD, NTD and spike

In vitro neutralization is a key function of the antibody response; however, antibody binding—even in the absence of detectable neutralizing activity—can also provide protection through Fc-mediated effector functions. This type of protection has been described in detail for influenza virus<sup>9,10,11</sup>, but binding antibody titres also represent a correlate of protection from SARS-CoV-2<sup>12,13</sup>. Furthermore, retention of binding to a highly mutated RBD or NTD, even if it is reduced, indicates that cognate B cells are present. These B cells could probably be rapidly recalled during infection with variants or by variant-specific vaccination, producing a strong plasmablast response leading to rapid control of viral spread. In addition, B cells with low-affinity binding to antigenically drifted variant proteins may enter lymph nodes and engage in germinal centre reactions, leading to production of antibodies that may regain neutralizing activity through affinity maturation.

To investigate the reduction in binding, we expressed a recombinant Omicron RBD and compared binding of sera to this RBD with binding to wild-type (Wuhan-1) and Beta RBD (Fig. 2a). Overall, the reduction in binding to Omicron RBD compared with wild-type was much less pronounced than the reduction in neutralization (Fig. 2b). However, this reduction in binding to Omicron RBD was significantly greater than the reduction in binding to Beta RBD observed here and previously<sup>8</sup>. This reduced binding to Omicron RBD was most pronounced for convalescent individuals (Fig. 2c), with a difference of more than 7.5-fold compared with wild-type RBD and undetectable reactivity by enzyme-linked immunosorbent assay (ELISA) in two-thirds of the convalescent individuals who were infected early in the pandemic before the circulation of viral variants of concern. In all other groups, there was a smaller difference in binding to Omicron RBD compared with wild type, with reductions

ranging from 2.9-fold in individuals who had received two vaccinations with mRNA-1273 to 1.5-fold in individuals boosted with BNT162b2 (Fig. [2d–j](#)).

**Fig. 2: Sera from vaccinated individuals mostly retain binding to the Omicron RBD.**

 figure 2

**a**, A model of the Omicron spike protein in complex with the angiotensin converting enzyme 2 (ACE2) receptor with Omicron-specific mutations indicated. The model is based on Protein Data Bank 6M0J<sup>25</sup> and 7C2L<sup>15</sup> and the figure was made in PyMOL. **b**, Absolute titres (left) and fold reduction (right) in binding to wild-type, Beta and Omicron spike RBDs for all serum samples. **c–j**, Binding to wild-type, Beta and Omicron RBDs by sera from convalescent individuals (**c**), after two BNT162b2 vaccinations (**d**), after two mRNA-1273 vaccinations (**e**), after three BNT162b2 vaccinations (**f**), after three mRNA-1273 vaccinations (**g**), from convalescent individuals after two BNT162b2 vaccinations (**h**), from convalescent individuals after two mRNA-1273 vaccinations (**i**) and from convalescent individuals after three BNT162b2 vaccinations (**j**). One-way ANOVA with Tukey's multiple comparisons test was used to compare the binding, except in **b**, **d**, where a mixed-effects model was used owing to a missing data point;  $P < 0.05$  indicated.  $n = 85$  (**b**), 15 (**c**), or 10 (**d–j**) samples, except in **d**, where one data point for Beta is missing. The dotted line represents the limit of detection (10), negative samples were assigned half the limit of detection (5). Each dot represents a biological replicate and the assays were performed twice. Fold change is defined as the geometric mean fold change.

#### Source data

In addition to the RBD, the spike NTD is a prime target for B cells following COVID-19 mRNA vaccination<sup>14</sup>. The NTD also hosts neutralizing epitopes inside and outside of the immunodominant ‘super site’<sup>15,16,17,18</sup>. The NTD of Omicron spike carries a large number of amino acid substitutions, three deletions and one three-amino-acid-long insertion (Fig. 2a, Extended Data Table 4); collectively, these mutations are predicted to substantially change the neutralizing epitopes inside and outside the super site. To determine whether infection-induced and vaccine-induced antibodies retain binding to the Omicron NTD, we expressed both wild-type and variant NTDs and probed them by ELISA using the same 85 samples tested for neutralization. Surprisingly, the sera retained binding to the Omicron NTD, with relatively minor reductions (maximum 1.9-fold) compared with the wild type, suggesting that binding to the super site was retained (for example, at lower affinity), or the presence of a large number of unchanged epitopes within this domain but outside the super site (Fig. 3).

**Fig. 3: Serum of vaccinated individuals retains binding to the Omicron NTD.**

---

 **figure 3**

**a**, Absolute titres (left) and fold reduction (right) in binding to wild-type and Omicron NTDs for all serum samples. **b–i**, Binding to wild-type and Omicron spike NTDs by sera from convalescent individuals (**b**), after two BNT162b2 vaccinations (**c**), after two mRNA-1273 vaccinations (**d**), after three BNT162b2 vaccinations (**e**), after three

mRNA-1273 vaccinations (**f**), from convalescent individuals after two BNT162b2 vaccinations (**g**), from convalescent individuals after two mRNA-1273 vaccinations (**h**) and from convalescent individuals after three BNT162b2 vaccinations (**i**).

Student's *t*-test was used to compare the binding;  $P < 0.05$  indicated.  $n = 85$  (**a**), 15 (**b**), or 10 (**c–i**) samples. The dotted line represents the limit of detection (10), negative samples were assigned half the limit of detection (5). Each dot represents a biological replicate and the assays were performed once. Fold change is defined as the geometric mean fold change.

#### [Source data](#)

Finally, we also measured antibody binding to the wild-type (Wuhan-1), Beta and Omicron spike protein ectodomains. Overall, there was a 5.2-fold decrease in the binding to Omicron spike and a 2.7-fold decrease in binding to Beta spike, compared with wild-type spike (Fig. 4a). Sera from all convalescent individuals bound to Omicron spike and there was no significant difference in binding between Beta and Omicron spike, with some low-titre sera showing better binding to Omicron spike than to Beta spike (Fig. 4b). However, in sera from vaccinated individuals and from convalescent plus vaccinated individuals, which typically showed strong binding to spike protein, the difference in binding to Omicron spike compared with wild type (ranging from 4.4- to 8.3-fold) was consistently larger than for Beta (ranging from 2- to 3.8-fold) (Fig. 4c–i). Of note, all proteins used were histidine-tagged, to enable control of the coating concentration. Probing with an anti-His antibody showed that the variant spike proteins exhibited similar binding to the ELISA plates (Extended Data Fig. 1).

**Fig. 4: Sera from vaccinated individuals mostly retain binding to Omicron spike protein.**

---

 **figure 4**

**a**, Absolute titres (left) and fold reduction (right) in binding to wild-type and Omicron spike protein ectodomain for all serum samples. **b–i**, Binding to wild-type and Omicron spike protein ectodomain by sera from convalescent individuals (**b**), after two BNT162b2 vaccinations (**c**), after two mRNA-1273 vaccinations (**d**), after three

---

BNT162b2 vaccinations (**e**), after three mRNA-1273 vaccinations (**f**), from convalescent individuals after two BNT162b2 vaccinations (**g**), from convalescent individuals after two mRNA-1273 vaccinations (**h**) and from convalescent individuals after three BNT162b2 vaccinations (**i**). One-way ANOVA with Tukey's multiple comparisons test was used to compare the binding;  $P < 0.05$  indicated.  $n = 85$  (**a**), 15 (**b**), or 10 (**c–i**) samples. The dotted line represents the limit of detection (10), negative samples were assigned half the limit of detection (5). Each dot represents a biological replicate and the assays were performed once. Fold change is defined as the geometric mean fold change.

[Source data](#)

## Discussion

The data presented here align well with initial reports on the impact of Omicron on in vitro neutralizing activity of serum from convalescent and vaccinated individuals and expand on these initial reports by including subcohorts with divergent histories of SARS-CoV-2 exposure, including infection-induced, primary vaccination-induced, booster vaccination-induced and hybrid immunity<sup>2,5,6</sup>. We found that neutralizing activity against Omicron is weakest in unvaccinated, convalescent individuals and in naive individuals who acquired immunity through two mRNA COVID-19 vaccine doses. Our findings support recent reports describing significantly reduced protection from reinfection<sup>19</sup> and almost non-existent vaccine effectiveness against symptomatic disease after two BNT162b2 vaccinations<sup>4</sup>. However, boosted individuals have shown—at least within a short time after a booster dose—significant protection against symptomatic disease<sup>4</sup> in the range of 75%. Although it is unclear how long this protection lasts, we observed neutralizing titres similar to those in boosted individuals in convalescent vaccinated individuals, suggesting that those individuals may experience significant protection. With regard to neutralization, we made some interesting additional observations. It has been reported that in some vaccine effectiveness studies protection from infection is better maintained after mRNA-1273 vaccination as compared with BNT162b2 vaccination<sup>20</sup>. We did not observe obvious differences in residual Omicron-neutralizing activity between the two vaccines in naive individuals who were vaccinated two or three times, but there was a trend towards higher titres in convalescent individuals after mRNA-1273 vaccination compared with BNT162b2 vaccination. However, the failure to observe differences may be owing to the small sample size per group, which is a major limitation of our study. Further, individuals with low neutralizing activity against wild-type SARS-CoV-2 often showed neutralization against Omicron only at the highest tested concentration, resulting in titres just above the limit of detection. Whether this was an artefact of the assay or bona fide neutralization is unclear. It is currently unclear which

epitopes are targeted by the antibodies responsible for the residual neutralizing activity against Omicron. On the basis of recent reports with data for monoclonal antibodies, it is likely that most of the residual activity comes from antibodies binding to epitopes outside the receptor binding motif (sites IV and V), but rare antibodies binding to sites I and II (which completely or partially overlap with the RBD) may also contribute<sup>21,22</sup>.

This study also provides insights into Omicron RBD-, NTD- and spike-specific binding changes. Compared with the changes in neutralizing activities, binding was relatively well preserved, especially against the NTD in general and against the RBD in vaccinated, boosted and convalescent vaccinated individuals. Notably, reductions in binding to the full Omicron spike ectodomain were somewhat larger than against the RBD and the NTD, despite there being fewer mutations outside of these two domains. A possible explanation for this finding could be that more epitopes—and more conserved epitopes—are accessible in recombinant RBD and NTD, whereas it is mostly the mutated epitopes that are accessible in the full-length ectodomain.

Conversely, in some instances, sera from convalescent individuals with low titres exhibited greater reactivity to Omicron spike than to Beta spike. Although differences at such low levels of binding should not be over-interpreted, this phenomenon could be driven by slight differences in spike conformation, which could lead to exposure of additional epitopes owing either to differences in sequence or differences in the spike preparations. However, no such phenomenon was seen in the other groups that had higher titres against wild-type spike. Based on conservation, we assume that most of the cross-reactive anti-spike antibodies do in fact bind to the S2 subunit<sup>14</sup>.

It is conceivable that these binding antibodies—which frequently have non-neutralizing phenotypes in cell culture—contribute to protection from disease, as has been seen for other viral infections<sup>9,10,11</sup>. In concert with T cell-based immunity<sup>23</sup>, these non-neutralizing but binding antibodies—which frequently target S2 but also the RBD and NTD<sup>14</sup>—could be responsible for the protection from severe disease that has been observed against Omicron in individuals with pre-existing immunity. In addition, the presence of strong binding antibodies suggests that, although some antibodies may have lost affinity for the drifted epitopes, B cells may be recalled when encountering Omicron spike through infection or vaccination. This could lead to a strong anamnestic response, which could have a positive effect against COVID-19 progression. It could also lead to the recruitment of these B cells into germinal centres for further affinity maturation resulting in potent, high-affinity neutralizing antibodies against Omicron<sup>24</sup>. Our data add to the growing body of evidence suggesting that Omicron-specific vaccines are urgently needed.

## Methods

## **Human serum samples**

Convalescent and post-vaccine sera were collected from participants in the longitudinal observational PARIS (Protection Associated with Rapid Immunity to SARS-CoV-2) study<sup>8,26</sup>. This cohort follows health care workers longitudinally since April 2020. The study was reviewed and approved by the Mount Sinai Hospital Institutional Review Board (IRB-20-03374). All participants signed written consent forms prior to sample and data collection. All participants provided permission for sample banking and sharing. Serum samples from the PARIS cohort are unique to this study and are not publicly available.

For the antigenic characterization of the Omicron variant, we selected 85 serum samples from 54 participants. Twenty out of 54 participants were seronegative prior to vaccination while 34/54 had COVID-19 prior to vaccination (see Supplementary Tables 1, 2 for demographics and vaccine information). All participants with pre-vaccination immunity were infected in 2020 when only ancestral SARS-CoV-2 strains circulated in the New York metropolitan area. Convalescent samples ( $n = 15$ ) were obtained within three months of SARS-CoV-2 infection (average: 58 days, range: 23–87 days) whereas the post-vaccination samples were collected on average 23 days (range: 14–39 days) after the second dose ( $n = 40$ , 20 Pfizer 2× and 20 Moderna 2×) or 19 days (range: 14–33 days) after the third booster ( $n = 30$ , 20 Pfizer 3× and 10 Moderna 3×) vaccine dose.

## **Cells**

Vero.E6 cells expressing TMPRSS2 (BPS Biosciences, catalogue (cat.) no. 78081) were cultured in Dulbecco's modified Eagles medium (DMEM; Corning, cat. no. 10-013-CV) containing 10% heat-inactivated fetal bovine serum (FBS; GeminiBio, cat. no. 100–106) and 1% minimum essential medium (MEM) amino acids solution (Gibco, cat. no. 11130051), supplemented with 100 U ml<sup>-1</sup> penicillin and 100 µg ml<sup>-1</sup> streptomycin (Gibco, cat. no. 15140122), 100 µg ml<sup>-1</sup> normocin (InvivoGen, cat. no. ant-nr), and 3 µg ml<sup>-1</sup> puromycin (InvivoGen, cat. no. ant-pr). FreeStyle 293-F cells (Gibco, cat. no. R79007) were cultured in ESF-SFM medium (Expression Systems, cat. no. 98-001) supplemented with 100 U ml<sup>-1</sup> penicillin and 100 µg ml<sup>-1</sup> streptomycin (Gibco, cat. no. 15140122). Expi293F cells (Gibco, cat. no. A14527) were cultured in Expi293 Expression Medium (Gibco, cat. no. A1435102) supplemented with 100 U ml<sup>-1</sup> penicillin and 100 µg ml<sup>-1</sup> streptomycin (Gibco, cat. no. 15140122). Cell lines were authenticated by supplier. No other authentication at the laboratory level was performed. Cell lines are tested on a regular basis for mycoplasma and are mycoplasma-free.

## **Selection and culture of replication competent SARS-CoV-2 isolates**

The Mount Sinai Pathogen Surveillance program (IRB approved, HS no. 13-00981) actively screens nasopharyngeal swab specimens from patients seeking care at the Mount Sinai Health System for emerging viral variants. After completion of the diagnostics, de-identified biospecimen were sequenced either using an established complete virus genome sequencing approach<sup>27</sup> (for example, Beta isolate USA/NY-MSHSPSP-PV27007/2021, EPI\_ISL\_1708926) or based on the spike S1 mutational profile determined by Spike-ID (Omicron, manuscript in preparation). The B.1.1.529 isolate USA/NY-MSHSPSP-PV44488/2021 (BA.1, EPI\_ISL\_7908059) represents one of the first cases diagnosed in New York State (female, age bracket: 30–40 years, mild COVID-19 symptoms, vaccinated and boosted) in late November 2021. The SARS-CoV-2 isolate USA-WA1/2020 was used as wild-type reference (BEI Resources, NR-52281). Supplementary Table 3 summarizes the amino acid substitutions, insertions and deletions in the spike region of each of the three viral isolates.

Viruses were grown by adding 200 µl of viral transport media from the nasopharyngeal swabs to Vero.E6-TMPRSS2 cells in culture media supplemented with 0.5 µg ml<sup>-1</sup> amphotericin B (Gibco, cat. no. 15290-018). Cytopathic effects appeared within 4–6 days at which point the culture supernatants were clarified by centrifugation at 4,000g for 5 min. Expanded viral stocks used were sequence-verified and titred by the 50% tissue culture infectious dose (TCID<sub>50</sub>) method on Vero.E6-TMPRSS2 cells before use in microneutralization assays.

## **Generation of recombinant variant RBD, NTD and spike proteins**

The recombinant RBD proteins were produced using Expi293F cells (Life Technologies). The coding sequences for the proteins were cloned into a mammalian expression vector, pCAGGS as described earlier<sup>28,29</sup> and purified after transient transfections with each respective plasmid. Six-hundred-million Expi293F cells were transfected using the ExpiFectamine 293 Transfection Kit and purified DNA. Supernatants were collected on day four post transfection, centrifuged at 4,000g for 20 min and finally filtered using a 0.22-µm filter. Ni-nitrilotriacetic acid (Ni-NTA) agarose (Qiagen) was used to purify the proteins via gravity flow and proteins were eluted as previously described<sup>28,29</sup>. The buffer was exchanged using Amicon centrifugal units (EMD Millipore) and all recombinant proteins were finally re-suspended in phosphate buffered saline (PBS). Proteins were also run on a sodium dodecyl sulphate (SDS) polyacrylamide gels (5–20% gradient; Bio-Rad) to check for purity<sup>30,31</sup>. The NTD protein constructs (residues 1–306) were cloned into pVRC8400 expression vector between SalI and NotI endonuclease restriction sites yielding an NTD with a human rhinovirus (HRV) 3C protease-cleavable C-terminal hexahistidine

and streptavidin-binding protein tags. The NTDs were transiently expressed in FreeStyle 293-F cells. Four days after transfection, supernatants were collected by centrifugation and further purified using immobilized metal affinity chromatography (IMAC) with cobalt-TALON resin (Takara) followed by a Superdex 200 Increase 10/300 GL size exclusion column (GE Healthcare). Spike proteins were expressed as described before<sup>8</sup>.

### Enzyme-linked immunosorbent assay

Antibody titres in sera from convalescent individuals and vaccinees were measured by a research-grade ELISA using recombinant versions of the RBD, NTD and spike of wild-type SARS-CoV-2 as well as B.1.351 (Beta) and B.1.1.529 (Omicron) (see Supplementary Table 4 for specific substitutions in each variant). All samples were analysed in a blinded manner. In brief, 96-well microtitre plates (Corning, cat. no. 353227) were coated with 50 µl per well of recombinant protein (2 µg ml<sup>-1</sup>) overnight at 4 °C. Plates were washed 3 times with phosphate-buffered saline (PBS; Gibco, cat. no. 10010-031) supplemented with 0.1% Tween-20 (PBS-T; Fisher Scientific ref. 202666) using an automatic plate washer (BioTek 405TS microplate washer). For blocking, PBS-T containing 3% milk powder (American Bio, cat. no. AB1010901000) was used. After 1 h of incubation at room temperature, blocking solution was removed and initial dilutions (1:100) of heat-inactivated sera (in PBS-T 1%-milk powder) were added to the plates, followed by twofold serial dilutions. After 2 h of incubation, plates were washed three times with PBS-T and 50 µl per well of the pre-diluted secondary anti-human IgG (Fab-specific) horseradish peroxidase (HRP) antibody (produced in goat; Sigma-Aldrich, cat. no. A0293, RRID: AB\_257875) diluted 1:3,000 in PBS-T containing 1% milk powder were added. After 1 h of incubation at room temperature, plates were washed three times with PBS-T and SigmaFast O-phenylenediamine dihydrochloride (Sigmafast OPD; Sigma-Aldrich, Ref. P9187-50SET) was added (100 µl per well) for 10 min, followed by addition of 50 µl per well of 3 M hydrochloric acid (Thermo Fisher, Ref. S25856) to stop the reaction. Optical density was measured at a wavelength of 490 nm using a plate reader (BioTek, SYNERGY H1 microplate reader). The area under the curve (AUC) values were calculated and plotted using Prism 9 software (GraphPad).

### SARS-CoV-2 multi-cycle microneutralization assay

Sera from vaccinees were used to assess the neutralization of wild type (WA1), B.1.351 (Beta) and B.1.1.529 (Omicron) SARS-CoV-2 isolates (Supplementary Table 3). All procedures were performed in a biosafety level 3 (BSL-3) facility at the Icahn School of Medicine at Mount Sinai following standard safety guidelines. Vero.E6-TMPRSS2 cells were seeded in 96-well high binding cell culture plates (Costar, cat. no. 07620009) at a density of 20,000 cells per well in complete Dulbecco's modified

Eagle medium (cDMEM) one day before the infection. Heat inactivated serum samples (56 °C for 1 h) were serially diluted (threefold) in minimum essential media (MEM; Gibco, cat. no. 11430-030) supplemented with 2 mM l-glutamine (Gibco, cat. no. 25030081), 0.1% sodium bicarbonate (w/v) (HyClone, cat. no. SH30033.01), 10 mM 4-(2-hydroxyethyl)-1-piperazineethanesulfonic acid (HEPES; Gibco, cat. no. 15630080), 100 U ml<sup>-1</sup> penicillin, 100 µg ml<sup>-1</sup> streptomycin (Gibco, cat. no. 15140122) and 0.2% bovine serum albumin (BSA) (MP Biomedicals, cat. no. 810063) starting at 1:10. Remdesivir (Medkoo Bioscience inc., cat. no. 329511) was included as a control to monitor assay variation. Serially diluted sera were incubated with 10,000 TCID<sub>50</sub> of WT USA-WA1/2020 SARS-CoV-2, MSHSPSP-PV27007/2021 (B.1.351, Beta) or USA/NY-MSHSPSP-PV44488/2021 (B.1.1.529, Omicron) for one hour at room temperature, followed by the transfer of 120 µl of the virus–serum mix to Vero.E6-TMPRSS2 plates. Infection proceeded for 1 h at 37 °C and inoculum was removed. One-hundred microlitres per well of the corresponding antibody dilutions plus 100 µl per well of infection media supplemented with 2% fetal bovine serum (FBS; Gibco, cat. no. 10082-147) were added to the cells. Plates were incubated for 48 h at 37 °C followed by fixation overnight at 4 °C in 200 µl per well of a 10% formaldehyde solution. For staining of the nucleoprotein, formaldehyde solution was removed, and cells were washed with PBS (pH 7.4) (Gibco, cat. no. 10010-031) and permeabilized by adding 150 µl per well of PBS with 0.1% Triton X-100 (Fisher Bioreagents, cat. no. BP151-100) for 15 min at room temperature. Permeabilization solution was removed, plates were washed with 200 µl per well of PBS (Gibco, cat. no. 10010-031) twice and blocked with PBS, 3% BSA for 1 h at room temperature. Blocking solution was removed and 100 µl per well of biotinylated monoclonal antibody 1C7C7<sup>32</sup>, a mouse anti-SARS nucleoprotein monoclonal antibody generated at the Center for Therapeutic Antibody Development at The Icahn School of Medicine at Mount Sinai ISMMS (Millipore Sigma, cat. no. ZMS1075) at a concentration of 1 µg ml<sup>-1</sup> in PBS, 1% BSA was added for 1 h at room temperature. Cells were washed with 200 µl per well of PBS twice and 100 µl per well of HRP-conjugated streptavidin (Thermo Fisher Scientific) diluted in PBS, 1% BSA were added at a 1:2,000 dilution for 1 h at room temperature. Cells were washed twice with PBS, and 100 µl per well of *O*-phenylenediamine dihydrochloride (Sigmafast OPD; Sigma-Aldrich) were added for 10 min at room temperature, followed by addition of 50 µl per well of a 3 M HCl solution (Thermo Fisher Scientific). Optical density (OD) was measured (490 nm) using a microplate reader (Synergy H1; Biotek). Analysis was performed using Prism 7 software (GraphPad). After subtraction of background and calculation of the percentage of neutralization with respect to the ‘virus-only’ control, a nonlinear regression curve fit analysis was performed to calculate the 50% inhibitory dilution (ID<sub>50</sub>), with top and bottom constraints set to 100% and 0% respectively. All samples were analysed in a blinded manner.

## Statistics

A one-way ANOVA with Tukey's multiple comparisons test was used to compare the neutralization and RBD-binding antibody titres. The exception is the 2 $\times$  BNT162b2 RBD ELISA group, where a mixed-effects model had to be used owing to a missing data point. A Student's *t*-test was used for comparing wild-type and Omicron NTD-binding data. Statistical analyses were performed using Prism 9 software (GraphPad).

## Reporting summary

Further information on research design is available in the [Nature Research Reporting Summary](#) linked to this paper.

## Data availability

Complete genome sequences for the viral isolates cultured from nasal swabs (B.1.351 and B.1.1.529) were deposited to GISAID. [Source data](#) are provided with this paper.

## References

1. Gu, H. et al. Probable transmission of SARS-CoV-2 Omicron variant in quarantine hotel, Hong Kong, China, November 2021. *Emerg. Infect. Dis.* **28**, 460–462 (2021).
2. Cele, S. et al. Omicron extensively but incompletely escapes Pfizer BNT162b2 neutralization. *Nature* <https://doi.org/10.1038/s41586-021-04387-1> (2021).
3. Brandal, L. T. et al. Outbreak caused by the SARS-CoV-2 Omicron variant in Norway, November to December 2021. *Eurosurveillance* **26**, 2101147 (2021).
4. Andrews, N. et al. Effectiveness of COVID-19 vaccines against the Omicron (B.1.1.529) variant of concern. Preprint at <https://doi.org/10.1101/2021.12.14.21267615> (2021).
5. Wilhelm, A. et al. Reduced neutralization of SARS-CoV-2 Omicron variant by vaccine sera and monoclonal antibodies. Preprint at <https://doi.org/10.1101/2021.12.07.21267432> (2021).
6. Rössler, A., Riepler, L., Bante, D., Laer, D. V. & Kimpel, J. SARS-CoV-2 Omicron variant neutralization in serum from vaccinated and convalescent persons. *N. Eng. J. Med.* <https://doi.org/10.1056/NEJMc2119236> (2022).

7. Uriu, K. et al. Neutralization of the SARS-CoV-2 Mu variant by convalescent and vaccine serum. *N. Engl. J. Med.* **385**, 2397–2399 (2021).
8. Carreño, J. M. et al. Evidence for retained spike-binding and neutralizing activity against emerging SARS-CoV-2 variants in serum of COVID-19 mRNA vaccine recipients. *eBioMedicine* **73**, 103626 (2021).
9. Dilillo, D. J., Tan, G. S., Palese, P. & Ravetch, J. V. Broadly neutralizing hemagglutinin stalk-specific antibodies require Fc $\gamma$ R interactions for protection against influenza virus in vivo. *Nat. Med.* **20**, 143–151 (2014).
10. Asthagiri Arunkumar, G. et al. Broadly cross-reactive, nonneutralizing antibodies against influenza B virus hemagglutinin demonstrate effector function-dependent protection against lethal viral challenge in mice. *J. Virol.* **93**, e01696–18 (2019).
11. Ng, S. et al. Novel correlates of protection against pandemic H1N1 influenza A virus infection. *Nat. Med.* **25**, 962–967 (2019).
12. Gilbert, P. B. et al. Immune correlates analysis of the mRNA-1273 COVID-19 vaccine efficacy clinical trial. *Science* eab3435 (2021).
13. Earle, K. A. et al. Evidence for antibody as a protective correlate for COVID-19 vaccines. *Vaccine* **39**, 4423–4428 (2021).
14. Amanat, F. et al. SARS-CoV-2 mRNA vaccination induces functionally diverse antibodies to NTD, RBD, and S2. *Cell* **184**, 3936–3948.e10 (2021).
15. Chi, X. et al. A neutralizing human antibody binds to the N-terminal domain of the spike protein of SARS-CoV-2. *Science* **369**, 650–655 (2020).
16. Voss, W. N. et al. Prevalent, protective, and convergent IgG recognition of SARS-CoV-2 non-RBD spike epitopes. *Science* **372**, 1108–1112 (2021).
17. Cerutti, G. et al. Potent SARS-CoV-2 neutralizing antibodies directed against spike N-terminal domain target a single supersite. *Cell Host Microbe* **29**, 819–833.e817 (2021).
18. Rosa, A. et al. SARS-CoV-2 can recruit a heme metabolite to evade antibody immunity. *Sci. Adv.* **7**, eabg7607 (2021).
19. Pulliam, J. R. C. et al. Increased risk of SARS-CoV-2 reinfection associated with emergence of the Omicron variant in South Africa. Preprint at <https://doi.org/10.1101/2021.11.11.21266068> (2021).

20. Rosenberg, E. S. et al. Covid-19 vaccine effectiveness in New York state. *N. Engl. J. Med.* **386**, 116–127 (2021).
21. Cameroni, E. et al. Broadly neutralizing antibodies overcome SARS-CoV-2 Omicron antigenic shift. *Nature* <https://doi.org/10.1038/s41586-021-04386-2> (2021).
22. Liu, L. et al. Striking antibody evasion manifested by the Omicron variant of SARS-CoV-2. *Nature* <https://doi.org/10.1038/s41586-021-04388-0> (2021).
23. GeurtsvanKessel, C. H. et al. Divergent SARS CoV-2 Omicron-specific T- and B-cell responses in COVID-19 vaccine recipients. Preprint at <https://doi.org/10.1101/2021.12.27.21268416> (2021).
24. Turner, J. S. et al. SARS-CoV-2 mRNA vaccines induce persistent human germinal centre responses. *Nature* **596**, 109–113 (2021).
25. Lan, J. et al. Structure of the SARS-CoV-2 spike receptor-binding domain bound to the ACE2 receptor. *Nature* **581**, 215–220 (2020).
26. Krammer, F. et al. Antibody responses in seropositive persons after a single dose of SARS-CoV-2 mRNA vaccine. *N. Engl. J. Med.* **384**, 1372–1374 (2021).
27. Gonzalez-Reiche, A. S. et al. Introductions and early spread of SARS-CoV-2 in the New York City area. *Science* **369**, 297–301 (2020).
28. Amanat, F. et al. A serological assay to detect SARS-CoV-2 seroconversion in humans. *Nat. Med.* **26**, 1033–1036 (2020).
29. Stadlbauer, D. et al. SARS-CoV-2 seroconversion in humans: a detailed protocol for a serological assay, antigen production, and test setup. *Curr. Protoc. Microbiol.* **57**, e100 (2020).
30. Margine, I., Palese, P. & Krammer, F. Expression of functional recombinant hemagglutinin and neuraminidase proteins from the novel H7N9 influenza virus using the baculovirus expression system. *J. Vis. Exp.* **81**, e51112 (2013).
31. Amanat, F. et al. Antibodies to the glycoprotein GP2 subunit cross-react between old and new world arenaviruses. *mSphere* **3**, e00189–18 (2018).
32. Amanat, F. et al. An in vitro microneutralization assay for SARS-CoV-2 serology and drug screening. *Curr. Protoc. Microbiol.* **58**, e108 (2020).

## Acknowledgements

We thank the study participants for their generosity and willingness to participate in longitudinal COVID-19 research studies. We thank the Rapid Response Laboratories and the Molecular Microbiology Laboratory of the Mount Sinai Health System for their assistance in the expeditious transfer of SARS-CoV-2 positive diagnostic specimen; R. A. Albrecht for oversight of the conventional BSL3 biocontainment facility; J. Kimpel and D. von Laer for sharing B.1.1.529 virus isolates (even though they could not be included in this work); P. Palese, C. Cordon-Cardo, D. Charney, D. Reich and K. Davis for their leadership and support throughout the COVID-19 pandemic; and D. Caughey for expert administrative assistance. This work is part of the PARIS/SPARTA studies funded by the NIAID Collaborative Influenza Vaccine Innovation Centers (CIVIC) contract 75N93019C00051. In addition, this work was also partially funded by the NIAID Centers of Excellence for Influenza Research and Response (CEIRR) contract and 75N93021C00014 by anonymous donors. The Mount Sinai Pathogen Surveillance Program is supported by institutional School of Medicine and Hospital funds. This work is part of the NIAID SARS-CoV-2 Assessment of Viral Evolution (SAVE) program.

## Author information

### Author notes

1. These authors jointly supervised this work: Emilia Mia Sordillo, Goran Bajic, Harm van Bakel, Viviana Simon, Florian Krammer

### Affiliations

1. Department of Microbiology, Icahn School of Medicine at Mount Sinai (ISMMS), New York, NY, USA

Juan Manuel Carreño, Hala Alshammary, Johnstone Tcheou, Gagandeep Singh, Ariel J. Raskin, Hisaaki Kawabata, Levy A. Sominsky, Jordan J. Clark, Daniel C. Adelsberg, Dominika A. Bielak, B. Alburquerque, A. A. Amoako, R. Banu, K. F. Beach, M. C. Bermúdez-González, G. Y. Cai, I. Ceglia, C. Cognigni, K. Farrugia, C. R. Gleason, A. van de Guchte, G. Kleiner, Z. Khalil, N. Lytle, W. A. Mendez, L. C. F. Mulder, A. Oostenink, A. Rooker, A. T. Salimbangon, M. Saksena, A. E. Paniz-Mondolfi, J. Polanco, Komal Srivastava, Goran Bajic, Viviana Simon & Florian Krammer

2. Department of Genetics and Genomic Sciences, ISMMS, New York, NY, USA

Ana Silvia Gonzalez-Reiche & Harm van Bakel

3. Icahn Genomics Institute, ISMMS, New York, NY, USA

Harm van Bakel

4. Center for Global Infectious Disease Research, Seattle Children's Research Institute, University of Washington, Seattle, WA, USA

Nicholas Dambrauskas, Vladimir Vigdorovich & D. Noah Sather

5. Department of Pediatrics, University of Washington, Seattle, Washington, USA

D. Noah Sather

6. Department of Pathology, Molecular and Cell-Based Medicine, ISMMS, New York, NY, USA

Emilia Mia Sordillo, Harm van Bakel, Viviana Simon & Florian Krammer

7. Division of Infectious Diseases, Department of Medicine, ISMMS, New York, NY, USA

Viviana Simon

8. The Global Health and Emerging Pathogens Institute, ISMMS, New York, NY, USA

Viviana Simon

## Consortia

### PSP-PARIS Study Group

- B. Alburquerque
- , A. A. Amoako
- , R. Banu
- , K. F. Beach
- , M. C. Bermúdez-González
- , G. Y. Cai
- , I. Ceglia
- , C. Cognigni
- , K. Farrugia
- , C. R. Gleason

- , A. van de Guchte
- , G. Kleiner
- , Z. Khalil
- , N. Lyttle
- , W. A. Mendez
- , L. C. F. Mulder
- , A. Oostenink
- , A. Rooker
- , A. T. Salimbangon
- , M. Saksena
- , A. E. Paniz-Mondolfi
- & J. Polanco

## **Contributions**

Conceptualization: J.M.C., H.A., E.M.S., G.B., H.v.B., V.S. and F.K. Methodology: J.M.C., H.A., D.C.A. and A.S.G.-R. Investigation: J.M.C., H.A., J.T., G.S., A.J.R., H.K., L.A.S., J.J.C., D.C.A., D.A.B., A.S.G.-R., N.D. and V.V. and the PSP-PARIS Study Group. Visualization: G.B. and F.K. Funding acquisition: V.S., H.v.B. and F.K. Project administration: K.S., D.N.S., E.M.S., G.B., H.v.B., V.S. and F.K. Supervision: J.M.C., D.N.S., E.M.S., G.B., H.v.B., V.S. and F.K. Writing, first draft: F.K. Writing, review and editing: J.M.C., H.A., J.T., G.S., A.J.R., H.K., L.A.S., J.J.C., D.C.A., D.A.B., A.S.G.-R., N.D., V.V., PSP-PARIS Study Group, K.S., D.N.S., E.M.S., G.B., H.v.B., V.S. and F.K.

## **Corresponding authors**

Correspondence to [Emilia Mia Sordillo](#), [Goran Bajic](#), [Harm van Bakel](#), [Viviana Simon](#) or [Florian Krammer](#).

## **Ethics declarations**

## **Competing interests**

The Icahn School of Medicine at Mount Sinai has filed patent applications relating to SARS-CoV-2 serological assays (US provisional application numbers: 62/994,252, 63/018,457, 63/020,503 and 63/024,436) and NDV-based SARS-CoV-2 vaccines (US provisional application number: 63/251,020) which list F.K. as co-inventor. V.S. is also listed on the serological assay patent application as co-inventor. Patent applications were submitted by the Icahn School of Medicine at Mount Sinai. Mount Sinai has spun out a company, Kantaro, to market serological tests for SARS-CoV-2. F.K. has

consulted for Merck and Pfizer (before 2020), and is currently consulting for Pfizer, Third Rock Ventures, Seqirus and Avimex. The F.K. laboratory is also collaborating with Pfizer on animal models of SARS-CoV-2.

## Peer review

### Peer review information

*Nature* thanks the anonymous reviewers for their contribution to the peer review of this work.

## Additional information

**Publisher's note** Springer Nature remains neutral with regard to jurisdictional claims in published maps and institutional affiliations.

## Extended data figures and tables

### [Extended Data Fig. 1 ELISA coating control data.](#)

All recombinant proteins used were his tagged which allows to control for coating efficiency by using an anti-his antibody. **A** shows endpoint titers of an anti-his mouse antibody to wild type, B.1.351 and B.1.1.529 spike. **B** shows the same for RBD. **C** shows binding of the anti-his antibody to NTDs from wild type and B.1.1529. **D–F** shows the same graphed as AUC. The assays were performed once. Data shown is based on three technical replicates.

**Extended Data Table 1 Overall description of samples used**

**Extended Data Table 2 Detailed description of samples used**

**Extended Data Table 3 Information on the viral isolates used in neutralization assays**

**Extended Data Table 4 Overview of the mutations encoded in the RBD and NTD proteins used for the binding assays**

## Supplementary information

### [Reporting Summary](#)

## Source data

[Source Data Fig. 1](#)

[Source Data Fig. 2](#)

[Source Data Fig. 3](#)

[Source Data Fig. 4](#)

## Rights and permissions

[Reprints and Permissions](#)

## About this article

### Cite this article

Carreño, J.M., Alshammary, H., Tcheou, J. *et al.* Activity of convalescent and vaccine serum against SARS-CoV-2 Omicron. *Nature* **602**, 682–688 (2022).  
<https://doi.org/10.1038/s41586-022-04399-5>

- Received: 20 December 2021
- Accepted: 31 December 2021
- Published: 31 December 2021
- Issue Date: 24 February 2022
- DOI: <https://doi.org/10.1038/s41586-022-04399-5>

### Share this article

Anyone you share the following link with will be able to read this content:

[Get shareable link](#)

Sorry, a shareable link is not currently available for this article.

[Copy to clipboard](#)

Provided by the Springer Nature SharedIt content-sharing initiative

This article was downloaded by **calibre** from <https://www.nature.com/articles/s41586-022-04399-5>

| [Section menu](#) | [Main menu](#) |

- Article
- Open Access
- [Published: 09 February 2022](#)

# Early prediction of preeclampsia in pregnancy with cell-free RNA

- [Mira N. Moufarrej](#) ORCID: [orcid.org/0000-0001-8953-4057<sup>1</sup>](https://orcid.org/0000-0001-8953-4057),
- [Sevahn K. Vorperian](#) ORCID: [orcid.org/0000-0003-0418-5260<sup>2</sup>](https://orcid.org/0000-0003-0418-5260),
- [Ronald J. Wong](#) ORCID: [orcid.org/0000-0003-1205-6936<sup>3</sup>](https://orcid.org/0000-0003-1205-6936),
- [Ana A. Campos<sup>3</sup>](#),
- [Cecele C. Quaintance<sup>3</sup>](#),
- [Rene V. Sit<sup>4</sup>](#),
- [Michelle Tan<sup>4</sup>](#),
- [Angela M. Detweiler<sup>4</sup>](#),
- [Honey Mekonen<sup>4</sup>](#),
- [Norma F. Neff](#) ORCID: [orcid.org/0000-0001-7141-5420<sup>4</sup>](https://orcid.org/0000-0001-7141-5420),
- [Courtney Baruch-Gravett<sup>5</sup>](#),
- [James A. Litch](#) ORCID: [orcid.org/0000-0003-0570-0308<sup>5</sup>](https://orcid.org/0000-0003-0570-0308),
- [Maurice L. Druzin<sup>6</sup>](#),
- [Virginia D. Winn](#) ORCID: [orcid.org/0000-0003-1136-2907<sup>6</sup>](https://orcid.org/0000-0003-1136-2907),
- [Gary M. Shaw<sup>3</sup>](#),
- [David K. Stevenson<sup>3</sup>](#) &
- [Stephen R. Quake](#) ORCID: [orcid.org/0000-0002-1613-0809<sup>1,4,7</sup>](https://orcid.org/0000-0002-1613-0809)

[Nature](#) volume 602, pages 689–694 (2022)

- 11k Accesses
- 115 Altmetric
- [Metrics details](#)

## Subjects

- [Gene expression profiling](#)
- [Machine learning](#)

- [Personalized medicine](#)
- [Predictive markers](#)

## Abstract

Liquid biopsies that measure circulating cell-free RNA (cfRNA) offer an opportunity to study the development of pregnancy-related complications in a non-invasive manner and to bridge gaps in clinical care<sup>1,2,3,4</sup>. Here we used 404 blood samples from 199 pregnant mothers to identify and validate cfRNA transcriptomic changes that are associated with preeclampsia, a multi-organ syndrome that is the second largest cause of maternal death globally<sup>5</sup>. We find that changes in cfRNA gene expression between normotensive and preeclamptic mothers are marked and stable early in gestation, well before the onset of symptoms. These changes are enriched for genes specific to neuromuscular, endothelial and immune cell types and tissues that reflect key aspects of preeclampsia physiology<sup>6,7,8,9</sup>, suggest new hypotheses for disease progression and correlate with maternal organ health. This enabled the identification and independent validation of a panel of 18 genes that when measured between 5 and 16 weeks of gestation can form the basis of a liquid biopsy test that would identify mothers at risk of preeclampsia long before clinical symptoms manifest themselves. Tests based on these observations could help predict and manage who is at risk for preeclampsia—an important objective for obstetric care<sup>10,11</sup>.

[Download PDF](#)

## Main

Advances in obstetrics and neonatology have substantially mitigated many of the adverse pregnancy outcomes related to preterm birth and preeclampsia<sup>3</sup>. Nonetheless, the standard of care implemented today focuses on how to treat a mother and child once a complication has been diagnosed, which proves both insufficient and costly<sup>1,2,4,12</sup>. Preeclampsia and related hypertensive disorders cause 14% of maternal deaths each year globally, second only to haemorrhage<sup>5</sup>, and cost nearly US\$2 billion in care in the first year following delivery<sup>2</sup>. Worse, three out of five maternal deaths in the USA are preventable and often associated with a missed or delayed diagnosis<sup>13</sup>. Such outcomes highlight the need for tools that would aid in identifying which mothers are at risk for preeclampsia before clinical presentation<sup>10,11</sup>.

Formally defined as new-onset hypertension with proteinuria or other organ damage (for example, renal, liver or brain) occurring after 20 weeks of gestation<sup>14</sup>, preeclampsia can clinically manifest anytime thereafter, including into the post-partum

period<sup>15</sup>. So far, no recommended test exists that can predict the future onset of preeclampsia early in pregnancy<sup>10</sup>. Liquid biopsies that measure plasma cfRNA suggest a means to achieve this<sup>16</sup>; there have been promising results both in the confirmation of preeclampsia at clinical diagnosis<sup>17,18</sup> and earlier in pregnancy<sup>19</sup>. The prediction of preeclampsia early in gestation, before symptoms present, could guide the prophylactic use of potential therapeutic agents<sup>10</sup> such as low-dose aspirin<sup>11</sup>.

Preeclampsia is specific to humans<sup>6</sup> and a few non-human primates<sup>7</sup>, and consequently, elucidating its pathogenesis has proven challenging. Broadly, it is accepted that preeclampsia occurs in two stages—abnormal placentation early in pregnancy followed by systemic endothelial dysfunction<sup>6,8,9</sup>. Preeclampsia can present with a diversity of symptoms and efforts to subclassify the disease on the basis of the timing of onset<sup>20</sup> have had mixed success<sup>6,9,21,22</sup>. Separate efforts have focused on subtyping preeclampsia molecularly using placental gene expression and histology<sup>23,24</sup>. As cfRNA is derived from many tissues in the body<sup>25,26</sup>, liquid biopsies present a potential means to indirectly observe pathogenesis in real time and to identify physiological changes associated with preeclampsia for proposed subtypes.

Here we report that cfRNA transcriptomic changes can distinguish between normotensive and preeclampsia pregnancies throughout the course of pregnancy, irrespective of preeclampsia subtype. The majority of these cfRNA changes are most marked early in pregnancy—well before the onset of symptoms. Neuromuscular, endothelial and immune cell types and tissues contribute to these cfRNA changes, consistent with important aspects of the pathogenesis of preeclampsia and also suggesting new approaches to stratify the disease. These observations enabled us to identify and independently validate a panel of 18 genes that when measured between 5 and 16 weeks of gestation form a predictive signature of preeclampsia risk. cfRNA measurements also reflect the multifactorial nature of preeclampsia and provide a means to monitor maternal organ health in a non-invasive manner. Together, these results show that cfRNA measurements can form the basis for clinically relevant tests that would predict preeclampsia months before presentation, manage who is at risk for specific organ damage and help to characterize the pathogenesis of preeclampsia in real time.

## Clinical study design

To identify changes associated with preeclampsia well before traditional diagnosis, we designed a prospective study and recruited pregnant mothers at their first clinical visit to Stanford’s Lucile Packard Children’s Hospital. For each participant, we analysed cfRNA for samples collected before or at 12 weeks, between 13 and 20 weeks, at or after 23 weeks of gestation and post-partum. We then split this larger group into discovery ( $n = 73$ , (49 normotensive, 24 with preeclampsia)) and validation 1 ( $n = 39$ ,

(32 normotensive, 7 with preeclampsia) cohorts. We also obtained samples from an independent cohort of 87 mothers (validation 2); these samples were collected at several separate institutions before 16 weeks of gestation (61 normotensive, 26 with preeclampsia) (Fig. [1a](#)).

**Fig. 1: Comparing sample, maternal and pregnancy characteristics for normotensive and preeclampsia groups across cohorts.**

---

 **figure 1**

- a**, Matched sample collection time both across gestation (left) and after delivery (right). **b**, Maternal characteristics ( $P = 0.02$  comparing BMI in the discovery cohort). **c**, Matched gestational age at preeclampsia onset regardless of preeclampsia symptom severity. **d**, Gestational age at delivery ( $P = 6 \times 10^{-7}, 0.04, 8 \times 10^{-9}$ ) for the discovery

( $n = 49$  normotensive [37, 36, 39, 30];  $n = 24$  with preeclampsia [13, 17, 20, 17]), validation 1 ( $n = 32$  normotensive [19, 27, 19, 19];  $n = 7$  with preeclampsia [3, 8, 6, 5]) and validation 2 ( $n = 61$  normotensive [61]; 26 with preeclampsia [28]) cohorts.

Square brackets indicate the sample number per collection group. For **a**, statistics were calculated by sample group. For **b–d**, statistics were calculated by cohort group (NS = not significant,  $*P < 0.05$ ,  $**P \leq 10^{-7}$ ; two-sided (**a–c**) and one-sided (**d**) Mann–Whitney rank test).

All cohorts included individuals of diverse racial and ethnic backgrounds in approximately matched proportions across normotensive and preeclampsia groups (Extended Data Table 1). A pregnancy was considered to be normotensive if it was both uncomplicated and went to full-term (37 or more weeks), or as preeclampsia with or without severe features on the basis of current guidelines (see [Methods](#)). For mothers who developed preeclampsia, all antenatal blood samples were collected before diagnosis. Our final analysis included a subset of those samples that passed predefined quality metrics (Extended Data Fig. 1, Supplementary Note 1, Supplementary Table 1, [Methods](#)).

Across gestational time points in all cohorts, we found no significant difference in sampling time between preeclampsia and normotensive groups ( $P \geq 0.26, 0.11, 0.46$ ) (values are reported as discovery, validation 1, validation 2; two-sided Mann–Whitney rank test unless otherwise specified). Known risk factors for preeclampsia, such as pre-pregnancy maternal body mass index (BMI), maternal age and gravidity followed expected trends. BMI was significantly different between preeclampsia and normotensive groups in the discovery cohort alone ( $P = 0.02, 0.45$ , not available), whereas maternal age and gravidity were not ( $P \geq 0.29, 0.16, 0.2$ ) (Fig. 1b, Extended Data Table 1). In validation 2, history of preterm birth and mode of delivery were significantly different between normotensive and preeclampsia groups. Other demographic factors such as race, ethnicity and nulliparity differed across cohorts but not between case groups within each cohort ( $P \leq 0.05$ , two-sided chi-squared test for categorical or ANOVA for continuous variables with Bonferroni correction; Extended Data Table 1, Supplementary Table 2).

In mothers who later developed preeclampsia, we observed no significant difference ( $P = 0.14, 1.0, 0.4$ ) in gestational age at onset between those who did not experience severe symptoms ( $n = 11, 4, 3^*$ ) and those who did experience severe symptoms ( $n = 13, 3, 13^*$ ) (\*denotes incomplete data for the specified cohort) (Fig. 1c). Furthermore, 21 mothers who developed preeclampsia also delivered preterm ( $n = 9, 1, 11$ ) as compared with no mothers in the normotensive group; this was reflected by significantly different gestational ages at delivery ( $P = 10^{-7}, 0.04, 10^{-9}$ ; one-sided Mann–Whitney rank test) (Fig. 1d) and lower fetal weight at delivery (Extended Data

Table 1), which is consistent with epidemiological evidence that preeclampsia increases the risk of spontaneous or indicated preterm delivery<sup>2,27</sup>.

## Identifying preeclampsia-related cfRNA changes

A total of 544 differentially expressed genes (DEGs) were altered across gestation and post-partum between mothers who later developed preeclampsia with or without severe features and normotensive mothers who did not experience complications ( $P \leq 0.05$ ; see [Methods](#)). Most DEGs were annotated as protein-coding and a small fraction (43; 8%) were other types, including 11 mitochondrial transfer RNAs, 6 long non-coding RNAs, 8 pseudogenes and 1 small nucleolar RNA (snoRNA). These changes in gene expression occurred most notably before 20 weeks of gestation, as indicated by a clear bimodal distribution with two peaks centred around a  $\log_2$ -transformed fold change ( $\log_2(\text{FC})$ ) of +0.8 and -0.6 (Fig. 2a). Changes in gene expression were also most stable before 20 weeks of gestation, at which point over 50% of genes had a coefficient of variation (CV) < 1 as compared to 31% of genes at or after 23 weeks of gestation and 36% at post-partum (Extended Data Fig. 2a).

**Fig. 2: Before 20 weeks of gestation, cfRNA measurements segregate preeclampsia and normotensive samples and are enriched for neuromuscular, endothelial and immune cell types and tissues.**

 [figure 2](#)

**a**, Distribution of  $\log_2(\text{FC})$  for DEGs ( $n = 544$ ) with dashed lines at  $\log_2(\text{FC}) = \pm 1$ . **b**, Before 20 weeks of gestation, a subset of DEGs can separate preeclampsia (PE) and normotensive samples despite differences in symptom severity, preeclampsia onset subtype and gestational age (GA) at delivery. *HIST2H2BE* is also known as *H2BC21*. See Supplementary Table 3 for more information on genes included in

heatmaps. **c**, Comparison of  $\log_2(\text{FC})$  for DEGs between the discovery and the validation 2 cohorts reveals strong agreement. **d**, DEGs for preeclampsia as compared to normotensive samples can be described as either increased (orange) or decreased (dark blue) in preeclampsia over gestation. Points indicate median per trend and shaded region indicates 95% CI. **e**, Approximately 13% of DEGs are tissue- or cell-type-specific when compared with the Human Protein Atlas (HPA) and an augmented Tabula Sapiens (TSP+) atlas.

We then asked whether a subset of genes approximately proportional in number to the total sample number ( $n = 49, 49, 57, 46$  for 12 weeks or less, 13–20 weeks, 23 weeks or more of gestation, and post-partum, respectively) was sufficient to segregate preeclampsia ( $n = 13, 16, 20, 17$ ) and normotensive ( $n = 36, 33, 37, 29$ ) samples across gestation. We found that 24–32 genes were sufficient to separate preeclampsia and normotensive samples across gestation and at post-partum with good specificity (86% [75–93%], 79% [66–88%], 97% [90–100%] and 90% [78–96%]) and sensitivity (85% [64–95%], 88% [69–96%], 65% [47–80%] and 71% [51–86%]) (values in square brackets are 90% confidence intervals (CI); Fig. 2b, Extended Data Fig. 2b). See also Extended Data Fig. 3, Supplementary Table 3.

Nearly all 544 DEG changes showed strong agreement in both validation cohorts as compared to the discovery cohort across gestation but not post-partum. Specifically, more than 82% and 92% of genes across gestation had the same  $\log_2(\text{FC})$  sign, with a Spearman correlation of at least 0.67 and 0.71 for validation 1 and validation 2 respectively ( $P < 10^{-15}$ ; two-sided  $t$ -test) as compared with 60% and 0.35 post-partum (Fig. 2c, Extended Data Fig. 2c). Finally, we asked whether symptom severity correlated with  $\log_2(\text{FC})$  magnitude for these 544 DEGs common to both preeclampsia subtypes. We found that on average, symptom severity did not influence  $\log_2(\text{FC})$  magnitude as reflected by a slope of nearly one across gestation (Extended Data Fig. 2e).

## cfRNA changes reflect preeclampsia pathophysiology

The 544 identified DEGs could be well categorized into two longitudinal trends (Fig. 2d, Extended Data Fig. 4a,c). Resembling a V shape, the first trend (group 1) described the longitudinal behaviour of 216 genes (40%), for which measured levels were reduced in preeclampsia samples ( $-1.3\times$  to  $-1.5\times$ ) across gestation with a minimum between 13 and 20 weeks. Peaking in early gestation before 20 weeks ( $1.75\times$ ), the second trend (group 2) described the behaviour of 328 genes (60%) that had significantly increased levels in preeclampsia samples before 20 weeks and to a lesser extent after 23 weeks of gestation ( $1.3\times$ ). For group 1 but not group 2, gene changes were far less evident post-partum and tended towards no difference between preeclampsia and normotensive, which may reflect a placental contribution. DEGs

were also enriched for genes previously implicated in preeclampsia<sup>28</sup> broadly (30 gene overlap,  $P = 0.006$ ; one-sided hypergeometric test) and more specifically through placental biopsies<sup>23,24</sup> (two of nine previously identified genes overlap, *PIK3CB*, *TAPI*) (Extended Data Table 2).

Approximately 13% of DEGs were tissue- or cell-type-specific (Fig. 2e). Genes that were decreased in preeclampsia across gestation (group 1) were broadly enriched for the immune system, whereas those genes increased in preeclampsia across gestation (group 2) were enriched for nervous, muscular, endothelial and immune contributions as reflected by cell type and pathway enrichment ( $P \leq 0.05$ ; one-sided hypergeometric test with multiple hypothesis correction, see [Methods](#)) (Extended Data Fig. 2e, Extended Data Table 2, [Supplementary Table 4](#)). Consistent with the known pathogenesis of preeclampsia, we identified a strong endothelial-linked signal underscored by contributions from capillary aerocytes ( $P = 0.03$ ), an endothelial cell type specific to the lungs<sup>29</sup>, platelets ( $P = 10^{-33}$ ) and several platelet-related pathways like platelet degranulation ( $P = 10^{-9}$ ) and platelet activation, signalling and aggregation ( $P = 10^{-8}$ ) among others. We also identified a small, borderline-significant placental contribution ( $P = 0.16$ ) from two genes (*IGF2*, *TGM2*) in group 1 with established roles in trophoblast development<sup>30,31</sup>.

We found increased nervous and muscular contributions for preeclampsia as emphasized by contributions from excitatory neurons ( $P = 0.02$ ), oligodendrocytes ( $P = 0.005$ ) and smooth muscle ( $P = 0.0003$ ), and terms like muscle contraction ( $P = 0.02$ ) and dilated cardiomyopathy ( $P = 0.01$ ). The immune system also contributes to both increased (for example, mesenchymal stem cells, total peripheral blood mononuclear cells) and decreased (granulocytes, T cells) changes across gestation. Genes in both groups were enriched for signalling pathways (that is, secretion by cell, integrin-mediated signalling pathway, regulation of I $\kappa$ B kinase, NF- $\kappa$ B signalling). Group 2 was also enriched for cellular compartments such as the cell periphery, cell junctions and extracellular space, consistent with reports that preeclampsia may be associated with signalling from the fetoplacental complex<sup>32</sup>.

## Risk prediction early in gestation

As gene expression changes associated with preeclampsia pathogenesis across gestation were readily detected irrespective of symptom severity, we sought to build a classifier that could identify mothers at risk of preeclampsia at or before 16 weeks of gestation (Extended Data Fig. 2e, [Supplementary Note 2](#)). We trained a logistic regression model on the discovery cohort ( $n = 61$  normotensive, 24 with preeclampsia). After training, the final model performed well, with a near-perfect area under the receiver operating characteristic curve (AUROC) (0.99 [0.99–0.99]), good specificity (85% [77–91%]) and perfect sensitivity (100% [92–100%]) (Fig. 3a,

Extended Data Table 3). We then tested this model on validation 1 ( $n = 35$  normotensive, 8 preeclampsia) and two other independent cohorts, which were collected at separate institutions: validation 2 ( $n = 61$  normotensive, 28 preeclampsia) and the cohort used by Del Vecchio and colleagues<sup>19</sup> ( $n = 8$  normotensive, 5 with preeclampsia, 7 with gestational diabetes, 2 with chronic hypertension). Across these cohorts, the final model once again performed well, with consistent AUROC (0.71 [0.70–0.72], 0.72 [0.71–0.72], 0.74 [0.73–0.75]), sensitivity (75% [46–92%], 56% [42–72%], 60% [26–87%]) and specificity (56% [43–70%], 69% [59–78%], 100% [89–100%]) (all reported as validation 1, validation 2, Del Vecchio, value [90% CI]) (Fig. 3a, Extended Data Table 3).

**Fig. 3: A subset of cfRNA changes can predict risk of preeclampsia early in gestation.**

 figure 3

**a**, Classifier performance as quantified by receiver operator characteristic curve (ROC) for samples collected in early gestation between 5 and 16 weeks, with AUROC and corresponding 90% CI noted per cohort. **b**, Prediction of preeclampsia incorporates cfRNA levels for 18 genes for which normalized centred  $\log_2(\text{FC})$  trends hold across the discovery ( $n = 61$  normotensive, 24 preeclampsia), validation 1 ( $n = 35$  normotensive, 8 preeclampsia), validation 2 ( $n = 61$  normotensive, 28 preeclampsia) and Del Vecchio ( $n = 17$  normotensive or other complication, 5 preeclampsia) cohorts as confirmed using univariate analysis (\* $P \leq 0.05$ , \*\* $P \leq 0.01$ , \*\*\* $P \leq 0.005$ ; one-sided Mann–Whitney rank test with Benjamini–Hochberg correction). See Supplementary Table 5 for exact  $P$  values. For box plots, centre line, box limits, whiskers and outliers represent the median, upper and lower quartiles, 1.5 $\times$  interquartile range and any outliers outside that distribution, respectively. Plot limits are –8 to 4 to better visualize the main distribution.  $\log_2(\text{CPM})$ ,  $\log_2$ -transformed counts per million reads.

Misclassified individuals did not predominantly belong to one racial or ethnic group; rather, the fraction of misclassified individuals for each race and ethnicity matched the cohort distribution as a whole. Notably, this holds true even for a group not included in the discovery cohort (American Indian or Alaskan Native) which made up 23% of both case and control for the validation 2 cohort. For false negatives in validation 2 and Del Vecchio, we find a shift to later gestational ages at collection ( $13.5 \pm 2$ ,  $12.5 \pm$

2 weeks) as compared to preeclampsia samples that were correctly classified ( $12 \pm 2$ ,  $12 \pm 0$  weeks; mean  $\pm$  s.d. for validation 2, Del Vecchio) (Extended Data Fig. 5a). This suggests that in practice, there may be an optimal collection window to reduce false negatives. Indeed, if we only consider samples before 14 weeks of gestation, we observe a 9% and a 15% increase in sensitivity, with corresponding AUROC values of 0.73 and 0.90 for validation 2 and Del Vecchio, respectively. There were no false positives from the Del Vecchio cohort, suggesting that the model can distinguish between preeclampsia and other risks like chronic hypertension or gestational diabetes. The model also proved well-calibrated, estimating a slightly increased probability of preeclampsia for gestational diabetes ( $0.15 \pm 0.08$ ) and chronic hypertension ( $0.18 \pm 0.13$ )—known preeclampsia risk factors<sup>33,34</sup>—as compared to the estimate for normotensive samples ( $0.1 \pm 0.08$ ) (mean  $\pm$  s.d., Extended Data Fig. 5b). These increased probabilities for other risk factors affected the AUROC of the test (0.74 [0.73–0.75] as compared to 0.8 [0.79–0.81] for only preeclampsia versus normotensive samples, Extended Data Table 3) (all reported as value [90% CI]).

Finally, we inspected the 18 genes (Fig. 3b, Extended Data Table 4) used by the model to yield probability estimates. Eight genes were annotated in the Human Protein Atlas (HPA, v.19)<sup>35</sup> as enhanced or enriched in the placenta (*TENT5A* (also known as *FAM46A*) and *MYLIP*), neuromuscular (*CAMK2G*, *NDUFV3*, *PI4KA* and *PRTFDC1*) and immune system (*RNF149* and *TRIM21*). Univariate analysis further confirmed that nine of the gene trends (that is, decreased or increased gene levels in preeclampsia) observed in the discovery dataset are upheld in validation 2 ( $P \leq 0.05$ ; one-sided Mann–Whitney rank test with Benjamini–Hochberg correction) (Fig. 3b, Supplementary Table 5). We also found that most models trained using a subset of the 18 initial genes can predict future preeclampsia onset with varying performance. Notably, performance improved across all metrics (sensitivity, specificity and AUROC) as we increased the number of genes included for model training (Supplementary Table 6, Extended Data Fig. 5c).

## Preeclampsia as a multifactorial disease

By comparing mothers who later developed preeclampsia with or without severe symptoms, we identified 503 DEGs ( $P \leq 0.05$ ). As there were no significant differences in symptom severity as related to the timing of preeclampsia onset (Fig. 1c), we believe that our observations contrasting preeclampsia with and without severe symptoms are not obscured by differences in preeclampsia-onset type. DEGs could be well categorized into four longitudinal trends (Fig. 4a, Extended Data Fig. 4b,d). Two groups (groups 1 and 3) described the temporal behaviour of 217 genes (44%), for which measured levels were either consistently increased (group 1) or reduced (group 3) in preeclampsia with as compared to without severe symptoms ( $\pm 1.8\times$ ) across gestation and trended towards no change post-partum. By contrast, groups 2 and 4

(286 genes, 56%) changed signs in mid-gestation, beginning as slightly increased (group 2,  $1.2\times$ ) or decreased (group 4,  $-1.2\times$ ) in severe preeclampsia and then moving to decreased (group 2,  $-1.4\times$ ) or unchanged (Group 4,  $1\times$ ) at 23 weeks or more of gestation.

**Fig. 4: cfRNA measurements reflect the multifactorial nature and pathogenesis of preeclampsia over pregnancy before diagnosis.**

 figure 4

**a**, DEGs for preeclampsia with as compared to without severe features ( $n = 503$ ) can be described by four longitudinal trends. **b**, Comparison of organ and cell-type changes over gestation for eight organ systems reflects the multifactorial nature of preeclampsia and provides a possible means to comprehensively monitor maternal organ health. Points indicate median per sample group and shaded region indicates 95% CI in **a** and 75% CI in **b**. LSECs, liver sinusoidal endothelial cells; NK cells, natural killer cells.

Analysis of the enriched cell types and tissues of origin for each of these groups revealed that increased gene differences in severe preeclampsia were driven by contributions from endothelial cells and the adaptive immune system (bone marrow). By contrast, genes that changed signs over gestation were enriched for innate immune cell types (for example, granulocytes and neutrophils for group 2, thymus for group 4) (Extended Data Table 5). Quantifying the total cfRNA signal confirmed an increased bone marrow signal for only severe preeclampsia across gestation and a decreased granulocyte signal for only preeclampsia without severe features at 12 weeks or less of gestation (Fig. 4b). Functional enrichment analysis further revealed pathways specific to genes that were only decreased for severe preeclampsia in early gestation (group 4); for example, axon guidance, nervous development and metabolism of RNA ( $P < 0.05$ ; one-sided hypergeometric test with multiple hypothesis correction; see [Methods](#)).

## cfRNA reflects maternal organ health

We then investigated the possibility of monitoring organ health in a non-invasive manner. We focused on eight organ systems (Fig. 4b) relevant to

preeclampsia presentation with consequences such as proteinuria, impaired liver function, renal insufficiency and epilepsy. We found substantial shifts in total contributions for all systems. We observed an increased astrocyte signal before 20 weeks of gestation and decreased oligodendrocytes and excitatory neurons at 23 or more weeks of gestation for all preeclampsia relative to normotensive (Fig. 4b). Although placental contributions increased over pregnancy with a peak in late gestation as expected, placental tissue and syncytiotrophoblast contributions were reduced for preeclampsia pregnancies before 20 weeks of gestation. Finally, we observed a decreased signal in hepatocyte, kidney, endothelial cell and smooth muscle signatures across gestation and an increased platelet signal before 12 weeks of gestation for preeclampsia. These tissue- and cell-type-specific changes are consistent both with common preeclampsia pathogenesis and with the specific, prominent diagnoses in our cohort (for example, thrombocytopenia, proteinuria, impaired liver function and renal insufficiency).

## Discussion

Our findings provide molecular evidence that supports the present physiological understanding of preeclampsia pathogenesis: early abnormal placentation and systemic endothelial dysfunction<sup>6</sup>. Early in gestation, we observe a reduced placental signal for preeclampsia, regardless of onset type or symptom severity. Concurrently, platelets and endothelial cells drive changes in cfRNA in preeclampsia samples regardless of symptom severity as compared to normotensive samples and between individuals with preeclampsia with and without severe symptoms, especially before 20 weeks of gestation. Increases in cell-type-specific cfRNA may occur in part through signalling and secretion by cells, as underscored by functional enrichment analysis. The innate and adaptive immune system also heavily contribute to cfRNA changes in preeclampsia, with marked shifts related to bone marrow, T cells, B cells, granulocytes and neutrophils—consistent with previous studies on the maternal–placental interface and preeclampsia<sup>6,36,37,38,39</sup>.

Given the diversity of clinical presentations in preeclampsia, we propose a non-invasive means of monitoring a mother’s risk of specific organ damage. The cfRNA changes that we characterized here reflect dysfunction in at least five organ systems (brain, liver, kidney, muscle and bone marrow), and can in some cases further distinguish between preeclampsia with and without severe symptoms. As a molecular lens into maternal health, liquid biopsies present an opportunity both as a research and clinical tool to learn about the pathogenesis of a human disease in humans and as a predictor of maternal health. Here we have shown proof of principle that cfRNA measurements can form the basis for a robust liquid biopsy test, which predicts preeclampsia very early in gestation. If validated in controlled clinical studies of suitably large, racially and ethnically diverse populations, such tests could help to

discover and manage individuals who are at risk for preeclampsia, complementing recent efforts based on clinical and laboratory data<sup>40</sup>. We have also shown here that cfRNA measurements reflect who is at risk for specific organ damage. Together, these results form the basis for a series of clinical tests that can be used to help to characterize and stratify the pathogenesis of preeclampsia in real time, and thereby to meet key objectives for obstetric care.

## Methods

### Clinical study design

The discovery and validation 1 cohorts were collected as part of a longitudinal, prospective study. We enrolled pregnant mothers (aged 18 years or older) receiving routine antenatal care on or before 12 weeks of gestation at Lucile Packard Children's Hospital at Stanford University, following study review and approval by the Institutional Review Board (IRB) at Stanford University (21956). All individuals signed informed consent before enrolment. Whole-blood samples for plasma isolation were then collected at three distinct time points during their pregnancy course and once (or twice for two individuals) post-partum. To split the larger Stanford cohort into Discovery and Validation 1, we first allocated samples using sequencing batches of which there were three. We allocated the sequencing batch with the most preeclampsia samples to Discovery to ensure sufficient statistical power and the second most preeclampsia samples to Validation 1. Sequencing batches themselves contained randomly allocated samples based on the individual such that all samples from the same individual were in the same batch. For the final sequencing batch, we randomly allocated individuals to either Discovery or Validation 1 such that all samples from 1 individual were part of the same group (either Discovery or Validation 1) and we maintained at least a 1–2 case to control ratio in both groups.

The validation 2 cohort was collected as part of the Global Alliance to Prevent Prematurity and Stillbirth (GAPPS) Pregnancy Biorepository at Yakima Valley Memorial Hospital, Swedish Medical Center and the University of Washington Medical Center under review and approval by Advarra IRB (CR00195799). Samples were processed and sequenced at Stanford under the same IRB as above (21956). All individuals signed informed consent before enrolment. Whole-blood samples for plasma isolation were collected at a single time point (or two time points in the case of two individuals with preeclampsia) before or at 16 weeks of gestation.

For all three cohorts, we chose a case to control ratio of approximately 1–2 to increase statistical power. We also ensured that case and control groups were matched for race and ethnicity, and that all included individuals did not have chronic hypertension or gestational diabetes. No other matching or exclusion criterion were used; we

performed no further sample selection prior to sample processing. Mothers were defined as having preeclampsia on the basis of current American College of Obstetrics and Gynecology (ACOG) guidelines (see below). Mothers were defined as controls if they had uncomplicated term pregnancies and either normal spontaneous vaginal or caesarean deliveries. For mothers who developed preeclampsia, all antenatal samples included in this study were collected before clinical diagnosis.

We processed samples from 88 individuals (60 normotensive, 28 with preeclampsia) in the discovery cohort, 43 individuals (34 normotensive, 9 with preeclampsia) in the validation 1 cohort and 87 individuals (61 normotensive, 26 with preeclampsia) in the validation 2 cohort. For some cohorts, only a subset of these individuals was included in the final analysis after filtering samples on the basis of pre-defined quality metrics (see ‘Sample quality filtering’, Supplementary Note 1, Supplementary Table 1)

We tested for within-cohort (normotensive versus preeclampsia) and across-cohort differences in demographic variables using a two-sided chi-squared test and ANOVA for categorical and continuous variables, respectively. We then applied Bonferroni correction and reported any differences as significant if adjusted  $P \leq$  0.05. Investigators were blinded during data collection as pregnancy outcomes were not known yet. Investigators were not blinded during data analysis as analysis methods required knowledge of outcome (that is, supervised learning).

## Definition of preeclampsia

Preeclampsia was defined per the ACOG guidelines<sup>27</sup> on the basis of two diagnostic criteria: (1) new-onset hypertension developing on or after 20 weeks of gestation; and (2) new-onset proteinuria or in its absence, thrombocytopenia, impaired liver function, renal insufficiency, pulmonary oedema or cerebral or visual disturbances.

New-onset hypertension was defined when the systolic and/or diastolic blood pressure were at least 140 or 90 mmHg, respectively, on at least two separate occasions between four hours and one week apart. Proteinuria was defined when either 300 mg protein was present within a 24-h urine collection or an individual urine sample contained a protein/creatinine ratio of 0.3 mg dl<sup>-1</sup>, or if these were not available, a random urine specimen had more than 1 mg protein as measured by dipstick. Thrombocytopenia, impaired liver function and renal insufficiency were defined as a platelet count of less than 100,000 per µl, liver transaminase levels two or more times higher than normal and serum creatinine level of higher than 1.1 mg dl<sup>-1</sup>, respectively.

Symptoms were defined as severe per the ACOG guidelines. Specifically, preeclampsia was defined as severe if any of the following symptoms were present and diagnosed as described above: new-onset hypertension with systolic and/or

diastolic blood pressure of at least 160 and/or 110 mmHg, respectively, thrombocytopenia, impaired liver function, renal insufficiency, pulmonary oedema, new-onset headache unresponsive to medication and unaccounted for otherwise or visual disturbances.

Finally, a pregnant mother was considered to have early-onset preeclampsia if onset occurred before 34 weeks of gestation and late onset thereafter.

## Sample preparation

### Plasma processing

At Lucile Packard Children's Hospital, blood samples were collected in either EDTA-coated (368661, Becton-Dickinson) or Streck cfRNA BCT (218976, Streck) tubes at  $\leq 12$ , 13–20 and  $\geq 23$  weeks of gestation, and post-partum for each participant. Within 30 min, tubes were then centrifuged at 1,600g for 30 min at room temperature. Plasma was transferred to 2-ml microfuge tubes and centrifuged at 13,000g for another 10 min in a microfuge. One-millilitre aliquots were then transferred to 2-ml Sarstedt screw cap microtubes (50809242, Thermo Fisher Scientific) and stored at  $-80^{\circ}\text{C}$  until analysis.

At GAPPS, blood samples were collected in EDTA-coated tubes at  $\leq 16$  weeks of gestation from a network of collection sites. Per standard operating procedure, tubes were then centrifuged within 2 h of collection at 2,500 rpm for 10 min at room temperature in a swinging bucket rotor. Plasma was transferred to 2-ml cryovials in at most 1-ml aliquots and stored at  $-80^{\circ}\text{C}$  until analysis. Sample volume was also recorded.

### cfRNA isolation

In 96-sample batches, cfRNA from 1-ml plasma samples was extracted in a semi-automated manner using the Opentrons 1.0 system and Norgen Plasma/Serum Circulating and Exosomal RNA Purification 96-Well Kit (Slurry Format) (29500, Norgen). Samples were subsequently treated with Baseline-ZERO DNase (DB0715K, Lucigen) for 20 min at  $37^{\circ}\text{C}$ . DNase-treated cfRNA was then cleaned and concentrated into 12  $\mu\text{l}$  using Zymo RNA Clean and Concentrator-96 kits (R1080).

After cfRNA extraction from plasma samples, isolated RNA concentrations were estimated for a randomly selected 11 samples per batch using the Bioanalyzer RNA 6000 Pico Kit (5067-1513, Agilent) per the manufacturer's instructions.

### Sequencing library preparation

cRNA sequencing libraries were prepared with the SMARTer Stranded Total RNAseq Kit v2 - Pico Input Mammalian Components (634419, Takara) from 4 µl of eluted cRNA according to the manufacturer's instructions. Samples were barcoded using the SMARTer RNA Unique Dual Index Kit – 96U Set A (634452, Takara), and then pooled in an equimolar manner and sequenced on Illumina's NovaSeq platform ( $2 \times 75$  bp) to a mean depth of 54, 33 and 38 million reads per sample for discovery, validation 1, and validation 2 cohorts, respectively. Some samples (12, 61 and 0 for discovery, validation 1 and validation 2 cohorts) were not sequenced owing to failed library preparation.

## Bioinformatic processing

For each sample, raw sequencing reads were trimmed using Trimmomatic (v.0.36) and then mapped to the human reference genome (hg38) with STAR (v.2.7.3a). Duplicate reads were then removed by GATK's (v.4.1.1) MarkDuplicates tool. Finally, mapped reads were sorted and quantified using htseq-count (v.0.11.1) generating a counts table (genes × samples). Read statistics were estimated using FastQC (v.0.11.8).

Across samples, the bioinformatic pipeline was managed using Snakemake (v.5.8.1). Read and tool performance statistics were aggregated across samples and steps using MultiQC (v.1.7). After sample quality and gene filtering, all gene counts were adjusted to log<sub>2</sub>-transformed counts per million reads (CPM) with trimmed mean of M values (TMM) normalization<sup>41</sup>.

## Sample quality filtering

For every sequenced sample, we estimated three quality parameters as previously described<sup>42,43</sup>. To estimate RNA degradation in each sample, we first counted the number of reads per exon and then annotated each exon with its corresponding gene ID and exon number using htseq-count. Using these annotations, we measured the frequency of genes for which all reads mapped exclusively to the 3'-most exon as compared to the total number of genes detected. RNA degradation for a given sample can then be approximated as the fraction of genes in which all reads mapped to the 3'-most exon. To estimate the number of reads that mapped to genes, we summed counts for all genes per sample using the counts table generated from bioinformatic processing above. To estimate DNA contamination, we quantified the ratio of reads that mapped to intronic as compared to exonic regions of the genome.

After measuring these metrics across nearly 700 samples, we empirically estimated RNA degradation and DNA contamination's 95th percentile bound. We considered any given sample an outlier, low-quality sample if its value for at least one of these

metrics was greater than or equal to the 95th percentile bound or if no reads were assigned to genes.

Once values for each metric were estimated across the entire dataset, we visualized: (1) whether low-quality samples clustered separately using hierarchical clustering (average linkage, Euclidean distance metric); and (2) whether sample quality drove variance in gene measurements using principal component analysis (PCA). These analyses were performed in Python (v.3.6) using Scikit-learn for PCA (v.0.23.2), Scipy for hierarchical clustering (v.1.5.1) and heatmap for heat map and clustering visualization (v.0.1.4).

After confirming sample quality, 404 samples from 199 mothers (142 normotensive, 57 with preeclampsia) were included in the final analysis (Supplementary Table 1). Specifically, 209, 106 and 89 samples from 73, 39 and 87 participants (49, 32 and 61 normotensive; 24, 7 and 26 with preeclampsia) were included in discovery, validation 1 and validation 2, respectively.

## Gene filtering

We performed filtering to identify well-detected genes across the entire cohort. Specifically, we used a basic cut-off that required a given gene be detected at a level of at least 0.5 CPM in at least 75% of discovery samples after removing outlier samples. Following this step, we retain 7,160 genes for differential expression analysis.

## Differential expression analysis

Differential expression analysis was performed in R using Limma (v.3.38.3). To identify gene changes associated with preeclampsia across gestation and post-partum, we used a mixed-effects model. We performed differential expression analysis using two design matrices: (1) examine the interaction between time to preeclampsia onset or delivery for normotensive and preeclampsia symptoms (that is, preeclampsia with or without severe symptoms); and (2) examine the interaction between time to preeclampsia onset or delivery for normotensive and preeclampsia broadly. In both design matrices, we included time to preeclampsia onset or delivery for normotensive (continuous variable), whether a sample was collected post-partum (binary variable), the interaction between time and preeclampsia symptoms for (1) or preeclampsia for (2), the interaction between whether a sample is post-partum and preeclampsia symptoms for (1) and preeclampsia for (2), and 7–8 confounding factors.

In (1), we defined preeclampsia symptoms categorically using three levels—normotensive, preeclampsia without severe symptoms, preeclampsia with severe symptoms. In (2), we defined whether a sample was preeclampsia using a binary,

indicator variable (0 = normotensive, 1 = preeclampsia). The 7–8 confounding variables included were maternal race (categorical variable), maternal ethnicity (binary variable), fetal sex (binary variable), maternal pre-pregnancy BMI group (categorical variable), maternal age (continuous variable, only included in design 1), and sequencing batch (categorical variable). We defined time to preeclampsia onset or delivery as the difference between gestational age at onset or delivery and gestational age at sample collection. We defined BMI group as follows: obese ( $BMI \geq 30$ ), overweight ( $25 \leq BMI < 30$ ), healthy ( $18.5 \leq BMI < 25$ ), underweight ( $BMI < 18.5$ ). We chose to model time to preeclampsia onset or delivery as a continuous variable, specifically a natural cubic spline with four degrees of freedom to account for the range across which samples were collected (one to three months per collection period). We also blocked for participant identity (categorical variable), modelling it as a random effect to account for auto-correlation between samples from the same person.

Per the Limma-Voom guide, to account for sample auto-correlation over time, we ran the function `voomWithQualityWeights` twice. We first ran it without any blocking on participant identity, and used this base estimation to approximate sample auto-correlation on the basis of participant identity using the function `duplicateCorrelation`. After estimating correlation, `voomWithQualityWeights` was run again, this time blocking for participant identity and including the estimated auto-correlation level. A linear model was then fit for each gene using `lmFit` and differential expression statistics were approximated using Empirical Bayes (eBayes) methods. For comparing preeclampsia with versus without severe symptoms, we contrasted the relevant coefficients (`makeContrasts`) and then applied Empirical Bayes as opposed to directly after `lmFit`.

DEGs were then identified using the relevant design matrix coefficients with Benjamini–Hochberg multiple hypothesis correction at a significance level of 0.05. For design 1, we identified DEGs related to three comparisons: preeclampsia without severe symptoms versus normotensive (1,759 DEGs); severe preeclampsia versus normotensive (1,198 DEGs); and preeclampsia with versus without severe symptoms (503 DEGs). We find 544 genes in common for preeclampsia without and with severe symptoms versus normotensive. These 544 DEGs are examined in Fig. 2 and the related main text. For design 2, we identified DEGs related to preeclampsia versus normotensive alone (330 DEGs), which we used as the initial gene set for building a logistic regression model (see Supplementary Note 2). Finally, we removed the effect of sequencing batch on estimated logCPM values with TMM normalization for the discovery cohort using the limma-voom function, `removeBatchEffect`.

## **log<sub>2</sub>-transformed fold change and CV estimation**

We define  $\log_2$ -transformed fold-change ( $\log_2(\text{FC})$ ) as the difference between the median gene level ( $\text{logCPM}$ ; see ‘Bioinformatic processing’) between preeclampsia and normotensive samples for a given sample collection period (that is,  $\leq 12$ , 13–20 and  $\geq 23$  weeks of gestation, or post-partum). In the case in which a given person had multiple samples included into a specific collection period, we only used the values associated with the first collected sample to avoid artificially reducing within-group (preeclampsia or normotensive) variance due to auto-correlation among samples from the same person.

We then quantified the relative dispersion around the estimated  $\log_2(\text{FC})$  for each gene using an approximation for CV. Specifically, we consider CV to be the ratio between an error bound,  $\partial$ , and the estimated  $\log_2(\text{FC})$ . We defined the error bound,  $\partial$ , as the one-sided error bound associated with the lower (or upper in the case of negative  $\log_2(\text{FC})$  values) 95% CI as estimated by bootstrapping. This definition of  $\partial$  as a one-sided bound that approaches 0 (equivalent to no FC) allowed us to explore how confident we could be in an estimated  $\log_2(\text{FC})$ . For instance, a  $\text{CV} = 1$  would indicate that at the boundary of proposed values, the  $\log_2(\text{FC})$  for a given gene becomes effectively 0. Similarly, a  $\text{CV} > 1$  would indicate even less confidence in a proposed average  $\log_2(\text{FC})$  and indicate that at the boundary, the estimated  $\log_2(\text{FC})$  changes signs (that is, a negative  $\log_2(\text{FC})$  becomes a positive one or vice versa).

## Hierarchical clustering analysis

For each sample collection period, hierarchical clustering was performed using DEGs with an  $|\log_2(\text{FC})| \geq 1$  and  $\text{CV} < 0.5$  or 0.4 in the case of the 13–20 weeks of gestation time point so that the number of genes used did not exceed the number of samples. For each gene that passed these thresholds, we calculated a  $z$ -score across all samples (at most 1 per individual, the earliest collected sample in a given group) in each sample collection period using the function StandardScaler in Scikit-learn (v.0.23.2). Average linkage hierarchical clustering with a Euclidean distance metric was then performed for both rows (gene  $z$ -scores) and columns (samples in same collection group) for a given matrix in Python using Scipy (v.1.5.1). Clustering and corresponding heat maps were visualized using nheatmap (v.0.1.4).

## Longitudinal dynamics analysis

To group gene changes by longitudinal behaviour, we performed  $k$ -means clustering on a matrix in which each row was a DEG and each column was the estimated  $\log_2(\text{FC})$  for a given sample collection period ( $N$  genes  $\times$  4 time points). We measured the sum of squared distances for every ‘ $k$ ’ between 1 and 16 ( $4^2$ ), in which 16

represents the maximum possible  $k$  (4 time points with 2 possibilities each,  $\log_2(\text{FC}) > 0$  or  $\log_2(\text{FC}) < 0$ ). We then identified the optimal  $k$  clusters by using the well-established elbow method to identify the smallest ‘ $k$ ’ that best explained the data, visually described as the elbow (or knee) of a convex plot like that for the sum of squared distances versus  $k$  (Extended Data Fig. 4a,c). To do so, we either visually inspected and identified the elbow (Fig. 2d) or used the function KneeLocator as implemented in the package Kneed (v.0.7.0) (Fig. 4a). We used visual inspection for Fig. 2d as we observed that given two  $k$ -values (for example,  $k = 2, 3$ ) with a similar sum of squared distances, KneeLocator would choose the larger value, whereas we preferred a simpler model. Having identified the optimal number of clusters,  $k$ , we labelled every DEG with its assigned cluster and visualized average behaviour (median) and the 95% CI (bootstrapped using 1,000 iterations) per cluster using Seaborn line plot (v.0.10.0).

To confirm that the identified patterns were not spurious (that is, an artifact of the  $k$ -means clustering algorithm), we permuted the data columns ( $\log_2(\text{FC})$  per time point) for each gene thereby scrambling any time-related structure while preserving its overall distribution. We then visualized the result using Seaborn line plot as described above. After permutation, we observed no longitudinal patterns, which were instead replaced by nearly flat, uninformative trends (Extended Data Fig. 4b,d).

## Correlation analysis

To verify DEGs identified in the discovery cohort, we compared  $\log_2(\text{FC})$  values for the discovery cohort as compared to both validation 1 and validation 2 cohorts. We calculated the percentage of genes for which the  $\log_2(\text{FC})$  had the same sign across cohorts (that is, both positive or both negative) and the Spearman correlation using the function scipy.stats.spearmanr. We did not calculate  $\log_2(\text{FC})$  values for DEGs at  $\leq 12$  weeks of gestation in validation 1 because of small sample numbers (3 preeclampsia samples before 12 weeks).

We also sought to compare whether symptom severity (without or with severe preeclampsia) correlated with  $\log_2(\text{FC})$  magnitude for 544 DEGs identified as common to all preeclampsia in design 1. To do so, we calculated the slope of a best-fit line in which  $x$  and  $y$  were defined as  $\log_2(\text{FC})$  values for preeclampsia without ( $x$ ) and with ( $y$ ) severe features versus normotensive. We would expect a slope  $> 1$  and  $< 1$  if  $\log_2(\text{FC})$  magnitudes for preeclampsia with as compared to without severe symptoms were larger or smaller on average, respectively. Similarly, a slope = 1 would reflect that symptom severity did not correlate with  $\log_2(\text{FC})$  magnitude for the 544 DEGs tested.

Finally, to confirm that the identified correlations were significant, we permuted the data columns ( $\log_2(\text{FC})$  per cohort) for each gene, thereby scrambling any structure while preserving its overall distribution. We then calculated the same statistics. After permutation, we observe about 50–55%  $\log_2(\text{FC})$  agreement, as expected at random, a Spearman correlation of 0 and a slope of 0.

## Defining cell-type- and tissue-specific gene profiles

Cell-type gene profiles were identified as previously described<sup>26</sup> and briefly summarized below. We also briefly describe an adapted, similar method to derive tissue gene profiles.

On the tissue level, for genes and tissues (and some blood and immune cell types) measured in the HPA (v.19)<sup>35</sup>, we calculated a Gini coefficient per gene as a measure of tissue specificity. As a measure of inequality, Gini coefficient values closer to 1 represent genes that are tissue-specific. We defined a given gene  $Y$  as specific to tissue  $X$  included in the HPA if  $\text{Gini}(Y) \geq 0.6$  and max expression for  $Y$  is in tissue  $X$ . The aforementioned method can identify genes that are expressed in several tissues (for example, group-enriched) as opposed to only one. Specifically, it is possible to have a gene  $Y$  where  $\text{Gini}(Y) \geq 0.6$  and the gene is expressed in more than 1 tissue (for example, enrichment in placenta and muscle). To this end, when tracking a single cell type or tissue's trajectory over gestation (for example, Fig. 4b), where the specificity of a given gene profile is especially important, we imposed a further constraint to ensure that any gene signal only reflects the named tissue (for example, any gene named placenta-specific is specific to the placenta alone). Specifically, we required that genes be annotated by HPA as ‘Tissue-enriched’ or ‘Tissue-enhanced’ and term this reference ‘HPA strict’.

On the cell-type level, we identified cell-type-specific gene profiles using both Tabula Sapiens v.1.0 (TSP) and individual cell atlases. We used individual cell atlases to identify gene profiles for cell types from missing tissues in TSP (for example, placenta, brain) or tissues that are known to be important in preeclampsia with additional annotations in individual single-cell atlases (for example, liver, kidney). First, for genes and cell types measured in TSP, we defined a given gene  $Y$  as specific to cell type  $X$  included in TSP if  $\text{Gini}(Y) \geq 0.8$  and max mean expression for  $Y$  is in cell type  $X$ . We combined subtype annotations for neutrophil and endothelial cells into single parent categories called ‘neutrophil’ and ‘endothelial cell’ respectively; as subtype annotations were based on manifold clustering, it was unclear whether they were truly distinct enough to be distinguished at a whole-body level for our purposes. Next, for genes and cell types described in individual tissue single-cell atlases, we required that a gene be differentially expressed in the specific single-cell atlases and

tissue-specific per the HPA (Gini  $\geq 0.6$ ). The following single-cell atlases were used for each organ: (1) placenta<sup>44,45</sup>; (2) liver<sup>46</sup>; (3) kidney<sup>47</sup>; (4) heart<sup>48</sup>; and (5) brain<sup>49</sup>.

We then created an augmented reference, which we term TSP+. For TSP+, we took the union of TSP and individual atlas gene annotations. A small number of genes had conflicting double annotations in TSP as compared to at most one individual tissue single-cell atlas. In these rare instances, which most often occurred for genes related to cell types missing in TSP (for example, placental or brain cell types), we used the individual single-cell atlas label.

## Determining cell type and tissue of origin

We determined whether a given cell type or tissue was enriched in preeclampsia by comparing preeclampsia DEGs with cell-type and tissue gene profiles using a one-sided hypergeometric test. For every tissue (HPA) or cell type (TSP+) with at least two DEGs specific to it, we performed the following. First, we defined a hypergeometric distribution (`scipy.stats.hypergeom`, (v.1.5.1)) with the following parameters, where category refers to tissue when using HPA and cell type when using TSP+:  $M$  = number of genes specific to any category;  $n$  = number of genes specific to this category;  $N$  = number of DEGs in this  $k$ -means longitudinal cluster specific to this category. Next, we estimated a  $P$  value using the survival function (1 – cumulative distribution function (CDF)) for the specified distribution. Specifically, a  $P$  value is defined as the cumulative probability,  $P(X > (n\_DEGs\_specific\_to\_this\_category - 1))$ , that the distribution takes a value greater than the number of DEGs specific to this category – 1. Finally, once we estimated a  $P$  value for every cell type (TSP+) or tissue (HPA) identified in each DEG  $k$ -means longitudinal cluster, we adjusted for multiple hypotheses using Benjamini–Hochberg with a significance threshold of 0.05.

## Defining relative signature score per cell type or tissue

We define a signature score as the sum of logCPM values over all genes in a given tissue or cell-type gene profile<sup>26</sup>. We required that a cell-type or tissue gene profile have at least five specified genes to be considered for signature scoring in cfRNA. Genes were defined as specific to a given tissue on the basis of the reference HPA strict, and to a given cell type on the basis of the reference TSP+ (see ‘Defining cell-type- and tissue-specific gene profiles’ for details).

To account for our previous observation that baseline cfRNA levels vary between individuals—the consequence of biological and technical (for example, sample processing) factors, we chose to calculate relative as opposed to absolute signature scores. For each individual whose post-partum sample passed sample quality control (QC) (see ‘Sample quality filtering’ for details), we estimated a relative signature

score, which was defined as the difference between the signature score at a given gestational time point and the post-partum sample. For both the discovery cohort and the validation 1 cohort, 49 normotensive individuals and 24 individuals with preeclampsia had a post-partum sample that survived sample QC. After normalization, all samples at post-partum had a similar baseline (0). We note that one can define a relative signature score based on any sampled time point for a given person. We chose the post-partum sample because we were interested in tracking maternal organ health over gestation.

Finally, we scaled (that is, z-score) the relative signature scores for a given cell type or tissue by dividing by the interquartile range, a robust alternative to standard deviation, using the `sklearn.preprocessing` class, `RobustScaler`. This accounted for differing gene profile lengths and gene expression levels, and allowed us to compare both different cell-type and tissue contributions and case groups per cell type or tissue.

Having defined a relative signature score per cell type and tissue, we visualized average behaviour (median) and the 75% CI, a non-parametric estimation of standard deviation, (bootstrapped relative signature score per case group and time point using 1,000 iterations) using Seaborn line plot (v.0.10.0).

## Functional enrichment analysis

Functional enrichment analysis was performed using the tool GProfiler (v.1.0.0) for the following data sources: Gene Ontology: biological processes and cellular compartments (GO:BP, GO:CC, released 1 May 2021, 2021-05-01), Reactome (REAC, released 7 May 2021, 2021-05-07) and Kyoto Encyclopedia of Genes and Genomes (KEGG FTP, released 3 May 2021, 2021-05-03). To identify GO terms, we excluded electronic GO annotations (IEA) and used a custom background of only the 7,160 genes that were included in the differential expression analysis. We then performed the recommended multiple hypothesis correction (g:SCS) with an experiment-wide significance threshold of  $\alpha = 0.05$  (ref. [50](#)).

## Logistic regression feature selection and training

To build a robust classifier that can identify mothers at risk of preeclampsia at or before 16 weeks of gestation, we first pre-selected features using the set of 330 DEGs when contrasting preeclampsia versus normotensive (see design 2 in ‘Differential expression analysis’ and Supplementary Note [2](#)) as a starting point.

We normalized gene measurements using a series of steps. First, to correct for batch effect, in which we define batch as a set of samples processed at the same time by a distinct group (for example, discovery cohort = batch, Del Vecchio cohort = batch), we

centred the data by subtracting the median logCPM per gene for a given cohort. Next, we scaled gene values for each cohort using its corresponding interquartile range in the discovery cohort. Finally, to account for sampling differences across samples, we used an approach similar to when analysing quantitative PCR with reverse transcription (RT–qPCR) data, and normalized data using multiple internal control (that is, housekeeping) genes. On a per-sample basis, we subtracted the median, normalized logCPM value (centred and scaled) for all internal control genes, which we define as 66 genes for which the measured value did not change across preeclampsia versus normotensive comparisons (all genes with adjusted  $P > 0.99$  for preeclampsia versus normotensive; design 2). When calculating the median value for all internal control genes, we excluded any 0 logCPM values as these are likely to have been the consequence of technical dropout.

Model training then used the discovery cohort alone split into 80% for hyperparameter tuning and 20% for model selection and consisted of two stages—further feature pre-selection based on two metrics followed by the construction of a logistic regression model with an elastic net penalty. Using a split discovery cohort for training mitigated overfitting even though all discovery samples were used for differential expression, which defined the initial feature set.

For feature pre-selection, we calculated logFC values using the 80% discovery split for all 330 genes for preeclampsia versus normotensive. We focused on 2 practical metrics measured across the 80% split of discovery samples collected on or before 16 weeks of gestation: gene change size ( $|\log_2(\text{FC})|$ ) and gene change stability (CV). All model hyperparameters were then tuned using AUROC as the outcome metric and fivefold cross validation. Next, we selected the best model including tuned feature pre-selection cut-offs again using AUROC. Specifically, we calculated an AUROC score for both the 80% and the 20% discovery splits separately, and the selected model achieved the best score on both splits.

Finally, we tuned the probability threshold,  $P$ , at which a sample is labelled as at risk of preeclampsia if  $P(\text{PE}) \geq P$  using the entire discovery cohort. To do so, we constructed a receiver operator characteristic curve (ROC) and calculated the false positive rate (FPR) and true positive rate (TPR) at different thresholds,  $P_i$ . We identified the threshold,  $P_i$ , at which  $\text{FPR} = 10\%$ , and round to the nearest 5 (for example, 0.37 would become 0.35). This yielded a tuned threshold of  $P = 0.35$ . All classifications as negative or positive were then made based on this threshold.

To understand the importance of each gene feature, we trained a separate logistic regression model for a subset of all possible feature subsets (307 combinations out of a total of 262,143 for 1–17 genes). No feature pre-selection was performed for this sub-analysis. All model hyperparameters were tuned as previously described. We defined a

gene subset as weakly predictive if the model yielded an AUROC > 0.5 on the test set (validation 2).

In all cases, performance metrics were assessed as described below (see next section) and used Scikit-learn (v.0.23.2).

## Performance metric analysis

Model performance was assessed using several statistics including sensitivity, specificity, positive predictive value (PPV), negative predictive value (NPV) and AUROC. Given a  $2 \times 2$  confusion matrix in which rows 1 and 2 represent true negatives and positives and columns 1 and 2 represent negative and positive predictions, respectively, we can define the values in row 1, column 1 as true negatives (TN), row 1, column 2 as false positives (FP), row 2, column 1 as false negatives (FN), and row 2, column 2 as true positives (TP). We can then define the following proportions: (1) sensitivity = TP/(TP + FN); (2) specificity = TN/(TN + FP); (3) PPV = TP/(TP + FP); (4) NPV = TN/(TN + FN). For each proportion, we calculated 90% CIs using Jeffrey's interval<sup>51</sup> and the function, proportion\_confint, from statsmodels.stats.proportion. We also approximated AUC and its corresponding 90% CI using the Scikit-learn function, roc\_auc\_score, and the binormal approximation, respectively.

## Statistical analyses

All  $P$  values reported herein were calculated using the non-parametric Mann–Whitney rank test unless otherwise stated. One-sided tests were performed where required based on the hypothesis tested.

## Reporting summary

Further information on research design is available in the [Nature Research Reporting Summary](#) linked to this paper.

## Data availability

Raw and processed sequencing data (BioProject PRJNA792450) are available through the Sequence Read Archive (SRA, SRP352519) and the Gene Expression Omnibus (GEO, GSE192902), respectively. Data were mapped using the human reference genome (hg38) and annotated using ENSEMBL v.82. We used publicly available data from the HPA (v.19; <https://v19.proteinatlas.org/>); TSP (v.1.0; <https://tabula-sapiens-portal.ds.czbiohub.org/>); Gene Ontology: biological processes and cellular

compartments (GO:BP, GO:CC, released 1 May 2021, 2021-05-01); Reactome (REAC, released 7 May 2021, 2021-05-07); Kyoto Encyclopedia of Genes and Genomes (KEGG, released 3 May 2021, 2021-05-03); and several previous publications<sup>44,45,46,47,48,49</sup>.

## Code availability

All computational analyses were performed using Python 3.6 or R 3.5, and are available on Github at [https://github.com/miramou/pe\\_cfrna](https://github.com/miramou/pe_cfrna).

## References

1. Blencowe, H. et al. Born too soon: the global epidemiology of 15 million preterm births. *Reprod. Health* **10**, S2 (2013).
2. Stevens, W. et al. Short-term costs of preeclampsia to the United States health care system. *Am. J. Obstet. Gynecol.* **217**, 237–248 (2017).
3. Basso, O. et al. Trends in fetal and infant survival following preeclampsia. *JAMA* **296**, 1357–1362 (2006).
4. Beam, A. L. et al. Estimates of healthcare spending for preterm and low-birthweight infants in a commercially insured population: 2008–2016. *J. Perinatol.* **40**, 1091–1099 (2020).
5. Say, L. et al. Global causes of maternal death: a WHO systematic analysis. *Lancet Glob. Health* **2**, e323–e333 (2014).
6. Phipps, E. A., Thadhani, R., Benzing, T. & Karumanchi, S. A. Pre-eclampsia: pathogenesis, novel diagnostics and therapies. *Nat. Rev. Nephrol.* **15**, 275–289 (2019).
7. Pennington, K. A., Schlitt, J. M., Jackson, D. L., Schulz, L. C. & Schust, D. J. Preeclampsia: multiple approaches for a multifactorial disease. *Dis. Model. Mech.* **5**, 9–18 (2012).
8. Steegers, E. A. P., von Dadelszen, P., Duvekot, J. J. & Pijnenborg, R. Pre-eclampsia. *Lancet* **376**, 631–644 (2010).
9. Burton, G. J., Redman, C. W., Roberts, J. M. & Moffett, A. Pre-eclampsia: pathophysiology and clinical implications. *BMJ* **366**, l2381 (2019).

10. McCarthy, F. P., Ryan, R. M. & Chappell, L. C. Prospective biomarkers in preterm preeclampsia: a review. *Pregnancy Hypertens.* **14**, 72–78 (2018).
11. Henderson, J. T., Vesco, K. K., Senger, C. A., Thomas, R. G. & Redmond, N. Aspirin use to prevent preeclampsia and related morbidity and mortality: updated evidence report and systematic review for the US preventive services task force. *JAMA* **326**, 1192–1206 (2021).
12. Behrman, R. E. & Butler, A. S. in *Preterm Birth: Causes, Consequences, and Prevention* (eds Berhman, R. E. & Butler, A. S.) Ch. 12 (National Academic Press, 2007).
13. Petersen, E. E. et al. Vital signs: pregnancy-related deaths, United States, 2011–2015, and strategies for prevention, 13 states, 2013–2017. *MMWR Morb. Mortal. Wkly Rep.* **68**, 423–429 (2019).
14. The American College of Obstetricians and Gynecologists. Hypertension in pregnancy. Report of the American College of Obstetricians and Gynecologists' Task Force on Hypertension in Pregnancy. *Obstet. Gynecol.* **122**, 1122–1131 (2013).
15. Goel, A. et al. Epidemiology and mechanisms of de novo and persistent hypertension in the postpartum period. *Circulation* **132**, 1726–1733 (2015).
16. Whitehead, C. L., Walker, S. P. & Tong, S. Measuring circulating placental RNAs to non-invasively assess the placental transcriptome and to predict pregnancy complications. *Prenat. Diagn.* **36**, 997–1008 (2016).
17. Munchel, S. et al. Circulating transcripts in maternal blood reflect a molecular signature of early-onset preeclampsia. *Sci. Transl. Med.* **12**, eaaz0131 (2020).
18. Tsang, J. C. H. et al. Integrative single-cell and cell-free plasma RNA transcriptomics elucidates placental cellular dynamics. *Proc. Natl Acad. Sci. USA* **114**, E7786–E7795(2017).
19. Del Vecchio, G. et al. Cell-free DNA methylation and transcriptomic signature prediction of pregnancies with adverse outcomes. *Epigenetics* **16**, 642–661 (2021).
20. von Dadelszen, P., Magee, L. A. & Roberts, J. M. Subclassification of preeclampsia. *Hypertens. Pregnancy* **22**, 143–148 (2003).
21. Raymond, D. & Peterson, E. A critical review of early-onset and late-onset preeclampsia. *Obstet. Gynecol. Surv.* **66**, 497–506 (2011).

22. Chaiworapongsa, T. et al. Differences and similarities in the transcriptional profile of peripheral whole blood in early and late-onset preeclampsia: insights into the molecular basis of the phenotype of preeclampsia. *J. Perinat. Med.* **41**, 485–504 (2013).
23. Leavey, K. et al. Unsupervised placental gene expression profiling identifies clinically relevant subclasses of human preeclampsia. *Hypertension* **68**, 137–147 (2016).
24. Benton, S. J., Leavey, K., Grynspan, D., Cox, B. J. & Bainbridge, S. A. The clinical heterogeneity of preeclampsia is related to both placental gene expression and placental histopathology. *Am. J. Obstet. Gynecol.* **219**, 604.e1–604.e25 (2018).
25. Koh, W. et al. Noninvasive in vivo monitoring of tissue-specific global gene expression in humans. *Proc. Natl Acad. Sci. USA* **111**, 7361–7366 (2014).
26. Vorperian, S. K., Moufarrej, M. N., Tabula Sapiens Consortium & Quake, S. R. Cell types of origin in the cell free transcriptome in human health and disease. Preprint at *bioRxiv* <https://doi.org/10.1101/2021.05.05.441859> (2021).
27. The American College of Obstetricians and Gynecologists. Gestational hypertension and preeclampsia: ACOG practice bulletin, number 222. *Obstet. Gynecol.* **135**, e237–e260 (2020).
28. Uzun, A., Triche, E. W., Schuster, J., Dewan, A. T. & Padbury, J. F. dbPEC: a comprehensive literature-based database for preeclampsia related genes and phenotypes. *Database* **2016**, baw006 (2016).
29. Gillich, A. et al. Capillary cell-type specialization in the alveolus. *Nature* **586**, 785–789 (2020).
30. Harris, L. K., Crocker, I. P., Baker, P. N., Aplin, J. D. & Westwood, M. IGF2 actions on trophoblast in human placenta are regulated by the insulin-like growth factor 2 receptor, which can function as both a signaling and clearance receptor. *Biol. Reprod.* **84**, 440–446 (2011).
31. Robinson, N. J., Baker, P. N., Jones, C. J. P. & Aplin, J. D. A role for tissue transglutaminase in stabilization of membrane-cytoskeletal particles shed from the human placenta. *Biol. Reprod.* **77**, 648–657 (2007).
32. Arck, P. C. & Hecher, K. Fetomaternal immune cross-talk and its consequences for maternal and offspring's health. *Nat. Med.* **19**, 548–556 (2013).

33. Weissgerber, T. L. & Mudd, L. M. Preeclampsia and diabetes. *Curr. Diab. Rep.* **15**, 9 (2015).
34. Sibai, B. M. et al. The impact of prior preeclampsia on the risk of superimposed preeclampsia and other adverse pregnancy outcomes in patients with chronic hypertension. *Am. J. Obstet. Gynecol.* **204**, 345.e1–345.e6 (2011).
35. Uhlen, M. et al. A genome-wide transcriptomic analysis of protein-coding genes in human blood cells. *Science* **366** eaax9198 (2019).
36. Han, X. et al. Differential dynamics of the maternal immune system in healthy pregnancy and preeclampsia. *Front. Immunol.* **10**, 1305 (2019).
37. Ander, S. E., Diamond, M. S. & Coyne, C. B. Immune responses at the maternal–fetal interface. *Sci. Immunol.* **4**, eaat6114 (2019).
38. Szarka, A., Rigó, J., Lázár, L., Beko, G. & Molvarec, A. Circulating cytokines, chemokines and adhesion molecules in normal pregnancy and preeclampsia determined by multiplex suspension array. *BMC Immunol.* **11**, 59 (2010).
39. Ibarra, A. et al. Non-invasive characterization of human bone marrow stimulation and reconstitution by cell-free messenger RNA sequencing. *Nat. Commun.* **11**, 400 (2020).
40. Marić, I. et al. Early prediction of preeclampsia via machine learning. *Am. J. Obstet. Gynecol. MFM* **2**, 100100 (2020).
41. Robinson, M. D. & Oshlack, A. A scaling normalization method for differential expression analysis of RNA-seq data. *Genome Biol.* **11**, R25 (2010).
42. Pan, W. *Development of Diagnostic Methods Using Cell-free Nucleic Acids* (Stanford University, 2016).
43. Moufarrej, M. N., Wong, R. J., Shaw, G. M., Stevenson, D. K. & Quake, S. R. Investigating pregnancy and its complications using circulating cell-free RNA in women’s blood during gestation. *Front. Pediatr.* **8**, 605219 (2020).
44. Vento-Tormo, R. et al. Single-cell reconstruction of the early maternal–fetal interface in humans. *Nature* **563**, 347–353 (2018).
45. Suryawanshi, H. et al. A single-cell survey of the human first-trimester placenta and decidua. *Sci. Adv.* **4**, eaau4788 (2018).

46. Aizarani, N. et al. A human liver cell atlas reveals heterogeneity and epithelial progenitors. *Nature* **572**, 199–204 (2019).
47. Stewart, B. J. et al. Spatiotemporal immune zonation of the human kidney. *Science* **365**, 1461–1466 (2019).
48. Litviňuková, M. et al. Cells of the adult human heart. *Nature* **588**, 466–472 (2020).
49. Mathys, H. et al. Single-cell transcriptomic analysis of Alzheimer's disease. *Nature* **570**, 332–337 (2019).
50. Raudvere, U. et al. gProfiler: a web server for functional enrichment analysis and conversions of gene lists (2019 update). *Nucleic Acids Res.* **47**, W191–W198 (2019).
51. Brown, L. D., Cai, T. T. & DasGupta, A. Interval estimation for a binomial proportion. *Stat. Sci.* **16**, 101–133 (2001).

## Acknowledgements

We thank N. Aghaeepour and I. Maric for discussions and data analysis suggestions; the many researchers and clinicians affiliated with the March of Dimes Prematurity Research Center at Stanford University for feedback after oral presentations; the Hess Research Fund for financial support; and the participants in this study for their contribution. This research was conducted using specimens and data collected and stored on behalf of the GAPS repository. The schematics in Fig. 4b were created with BioRender. This work was supported by the Chan Zuckerberg Biohub, GAPS and the March of Dimes Foundation. M.N.M. is supported by the Stanford Bio-X Bowes Fellowship; S.K.V. is supported by a NSF Graduate Research Fellowship (grant no. DGE 1656518), the Benchmark Stanford Graduate Fellowship, and the Stanford ChEM-H Chemistry Biology Interface (CBI) training program; and V.D.W. is supported by the H&H Evergreen Fund.

## Author information

### Affiliations

1. Department of Bioengineering, Stanford University, Stanford, CA, USA

Mira N. Moufarrej & Stephen R. Quake

2. ChEM-H and Department of Chemical Engineering, Stanford University, Stanford, CA, USA

Sevahn K. Vorperian

3. Department of Pediatrics, Stanford University School of Medicine, Stanford, CA, USA

Ronald J. Wong, Ana A. Campos, Cecele C. Quaintance, Gary M. Shaw & David K. Stevenson

4. Chan Zuckerberg Biohub, San Francisco, CA, USA

Rene V. Sit, Michelle Tan, Angela M. Detweiler, Honey Mekonen, Norma F. Neff & Stephen R. Quake

5. Global Alliance to Prevent Prematurity and Stillbirth (GAPPS), Lynnwood, WA, USA

Courtney Baruch-Gravett & James A. Litch

6. Department of Obstetrics and Gynecology, Stanford University School of Medicine, Stanford, CA, USA

Maurice L. Druzin & Virginia D. Winn

7. Department of Applied Physics, Stanford University, Stanford, CA, USA

Stephen R. Quake

## Contributions

M.N.M., G.M.S., D.K.S. and S.R.Q. conceptualized and designed the study. M.L.D., V.D.W., G.M.S. and D.K.S. designed the cohort study at Lucile Packard Children's Hospital. R.J.W., A.A.C. and C.C.Q. collected and processed whole-blood samples and corresponding sample and participant metadata. C.B.-G. and J.A.L. oversaw whole-blood sample and corresponding sample and participant metadata collection at GAPPS. M.N.M. developed experimental protocols for cfRNA extraction and data generation and processed all samples from cfRNA extraction up to and including library generation for RNA sequencing. R.V.S., M.T., A.M.D., H.M. and N.F.N. developed and executed experimental protocols for RNA sequencing and computational protocols for raw sequencing data transfer. S.K.V. developed computational methods to define genes as cell-type- and tissue-specific in the context of the whole body. M.N.M. and S.K.V. designed the analyses to characterize tissue and

cell-type contributions. M.N.M. conceptualized and developed computational analyses, analysed the data and wrote the initial manuscript draft in collaboration with S.R.Q. All authors contributed to writing and editing the manuscript.

## Corresponding author

Correspondence to [Stephen R. Quake](#).

## Ethics declarations

## Competing interests

M.N.M., S.K.V., G.M.S., D.K.S. and S.R.Q. are inventors on a patent application submitted by the Chan Zuckerberg Biohub and Stanford University that covers non-invasive early prediction of preeclampsia and monitoring maternal organ health over pregnancy (USPTO application number 63/159,400 filed on 10 March 2021 and 63/276,467 filed on 5 November 2021). S.R.Q. is a founder, consultant and shareholder of Mirvie. M.N.M. is also a shareholder of Mirvie.

## Peer review

### Peer review information

*Nature* thanks the anonymous reviewers for their contribution to the peer review of this work.

## Additional information

**Publisher's note** Springer Nature remains neutral with regard to jurisdictional claims in published maps and institutional affiliations.

## Extended data figures and tables

### [Extended Data Fig. 1 Samples with outlier values for at least one QC metric cluster separately from most non-outlier samples.](#)

**a–c**, For discovery (**a**), validation 1 (**b**), and validation 2 (**c**), hierarchical clustering (left) and PCA (right) reveals that most outlier samples cluster with negative control (NC) samples and separately from non-outlier samples. **d, e**, Visualization of other QC metrics like the amount of cfRNA extracted (**d**) and the percent of reads that align

uniquely to the human genome (**e**) ( $n = 209, 106, 89$  samples for discovery, validation 1, and validation 2, respectively). For PCA in **a–c**, sample outliers and poorly detected genes drive PCA and serve as leverage points. The top two principal components are visualized when performed using all samples and all genes (leftmost PCA) or only samples that pass QC metrics (middle PCA) reveals that certain samples can act as leverage points. Once sample outliers and lowly detected genes are removed from the cfRNA gene matrix (rightmost PCA), the top two principal components reflect natural variance in the data and are no longer driven by a few leverage points. For box plots, centre line, box limits, whiskers and outliers represent the median, upper and lower quartiles,  $1.5 \times$  interquartile range and any outliers outside that distribution, respectively.

**Extended Data Fig. 2 Across gestation before diagnosis, changes in the cfRNA transcriptome segregate preeclampsia and normotensive samples and reflect known preeclampsia biology.**

**a**, Distribution of CVs with dashed line at  $CV = 1$  for all DEGs ( $n = 544$ ) between preeclampsia as compared to normotensive samples across gestation. **b**, At  $\geq 23$  weeks of gestation and post-partum, a subset of DEGs can separate preeclampsia ( $n = 20, 17$ ) and normotensive ( $n = 37, 29$ ) samples despite differences in symptom severity, preeclampsia onset subtype, and GA at delivery. **c**, Comparison of  $\log_2(FC)$  for DEGs for preeclampsia as compared to normotensive between discovery and validation 1 reveals good agreement across gestation but not post-partum. **d**, The genes in each longitudinal trend group reflect known preeclampsia aetiology as highlighted across four databases (GO biological processes, KEGG, the reactome, and GO cellular compartment). Some preeclampsia associated terms are emphasized in bold, coloured text that corresponds to group colour from Fig. [2d](#) (Dark blue and orange indicate decreased and increased in preeclampsia versus normotensive, respectively) ( $p \leq 0.05$ ; one-sided hypergeometric test with multiple hypothesis correction, see [Methods](#)). **e**, Comparison of  $\log_2(FC)$  for DEGs for preeclampsia without severe features versus normotensive and preeclampsia with severe features versus normotensive in the discovery cohort reveals good agreement along the  $y=x$  axis with a slope of 0.93, 1.03, 0.77, and 0.86 at  $\leq 12$  weeks, 13–20,  $\geq 23$  weeks, and post-partum, respectively.

**Extended Data Fig. 3 Across gestation and before diagnosis, changes in the cfRNA transcriptome identified at one time point can moderately segregate preeclampsia and normotensive samples at other time points.**

DEGs with  $|\log_2(FC)| \geq 1$  and  $CV < 0.5$  or 0.4 for the 13–20 week time point were identified at each time point across gestation. Each row visualizes how well a specific DEG subset from a given sample collection period can separate preeclampsia ( $n = 13$ ,

16, 20, 17) and normotensive ( $n = 36, 33, 37, 29$ ) samples in all other collection periods ( $\leq 12, 13\text{--}20, \geq 23$  weeks of gestation and post-partum respectively). The number of genes identified per sample collection period is highlighted along the main diagonal.

**Extended Data Fig. 4 *k*-means clustering reveals meaningful longitudinal patterns.**

**a, c**, The chosen  $k$  clusters (dashed line) comparing a performance metric, the sum of squared distances, and values of  $k$  for clustering of DEGs for preeclampsia versus normotensive related to Fig. 2d (a) and DEGs for preeclampsia with versus without severe features related to Fig. 4a (c). **b, d**, Following permutation of the data matrix prior to  $k$ -means clustering, longitudinal changes over gestation are replaced by 2 flat lines for clustering of  $\log_2(\text{FC})$  for preeclampsia versus normotensive (**b**) and 4 uninformative lines for clustering of  $\log_2(\text{FC})$  for preeclampsia with versus without severe features (**d**). For **b, d**, points indicate median per trend and shaded region indicates 95% CI.

**Extended Data Fig. 5 Examining the logistic regression model used to predict risk of preeclampsia early in gestation.**

**a**, Comparison of gestational age at sample collection (weeks) for incorrectly predicted (yellow) or correctly predicted (green) samples across normotensive and preeclampsia groups in the discovery, validation 1, validation 2 and Del Vecchio cohorts shows that incorrectly predicted preeclampsia samples (false negatives) are collected at later gestational ages. **b**, Estimated probability of preeclampsia as outputted by logistic regression for both preeclampsia and normotensive samples shows that the model is well-calibrated across most predictions. Dashed line at 0.35 indicates classifier cut-off where  $P(\text{PE}) \geq 0.35$  constitutes a sample predicted as preeclampsia. **c**, Logistic regression models trained on subsets of 1–18 genes of the initial 18 genes can moderately predict future preeclampsia onset in the validation 2 cohort with improving performance as subset size increases and as characterized by PPV, NPV, sensitivity, specificity and AUROC (left to right).

**Extended Data Table 1 Participant, pregnancy and preeclampsia characteristics across both discovery and validation cohorts**

**Extended Data Table 2 Tissue, cell types, and genes previously implicated in preeclampsia enriched in 544 DEGs identified when comparing preeclampsia with or without severe features and normotensive pregnancies**

**Extended Data Table 3 Preeclampsia prediction performance metrics for samples collected early in gestation (5–16 weeks)**

**Extended Data Table 4** Preeclampsia prediction relies on the cfRNA levels of 18 genes

**Extended Data Table 5** Tissue and cell types enriched in 503 DEGs identified when comparing preeclampsia with as compared to without severe features

## Supplementary information

### Supplementary Information

This file contains Supplementary Notes 1 and 2; Supplementary Tables 1, 2, 5 and 6 and legends for Supplementary Tables 3 and 4.

### Reporting Summary

### Supplementary Table 3

See Supplementary Information file for description.

### Supplementary Table 4

See Supplementary Information file for description.

## Rights and permissions

**Open Access** This article is licensed under a Creative Commons Attribution 4.0 International License, which permits use, sharing, adaptation, distribution and reproduction in any medium or format, as long as you give appropriate credit to the original author(s) and the source, provide a link to the Creative Commons license, and indicate if changes were made. The images or other third party material in this article are included in the article's Creative Commons license, unless indicated otherwise in a credit line to the material. If material is not included in the article's Creative Commons license and your intended use is not permitted by statutory regulation or exceeds the permitted use, you will need to obtain permission directly from the copyright holder. To view a copy of this license, visit <http://creativecommons.org/licenses/by/4.0/>.

### Reprints and Permissions

## About this article

### Cite this article

Moufarrej, M.N., Vorperian, S.K., Wong, R.J. *et al.* Early prediction of preeclampsia in pregnancy with cell-free RNA. *Nature* **602**, 689–694 (2022).  
<https://doi.org/10.1038/s41586-022-04410-z>

- Received: 10 March 2021
- Accepted: 06 January 2022
- Published: 09 February 2022
- Issue Date: 24 February 2022
- DOI: <https://doi.org/10.1038/s41586-022-04410-z>

## Share this article

Anyone you share the following link with will be able to read this content:

[Get shareable link](#)

Sorry, a shareable link is not currently available for this article.

[Copy to clipboard](#)

Provided by the Springer Nature SharedIt content-sharing initiative

## [RNA test detects deadly pregnancy disorder early](#)

- Nick Petrić Howe
- Shamini Bundell

Nature Podcast 09 Feb 2022

---

This article was downloaded by **calibre** from <https://www.nature.com/articles/s41586-022-04410-z>

- Article
- Open Access
- [Published: 16 February 2022](#)

# Visualizing protein breathing motions associated with aromatic ring flipping

- [Laura Mariño Pérez](#) ORCID: [orcid.org/0000-0003-1658-7179<sup>1,2</sup>](https://orcid.org/0000-0003-1658-7179),
- [Francesco S. Ielasi](#) ORCID: [orcid.org/0000-0002-5272-0865<sup>3</sup>](https://orcid.org/0000-0002-5272-0865),
- [Luiza M. Bessa](#) ORCID: [orcid.org/0000-0002-1993-3105<sup>1</sup>](https://orcid.org/0000-0002-1993-3105),
- [Damien Maurin<sup>1</sup>](#),
- [Jaka Kragelj<sup>1</sup>](#) nAff<sup>5</sup>,
- [Martin Blackledge](#) ORCID: [orcid.org/0000-0003-0935-721X<sup>1</sup>](https://orcid.org/0000-0003-0935-721X),
- [Nicola Salvi](#) ORCID: [orcid.org/0000-0003-1515-6908<sup>1</sup>](https://orcid.org/0000-0003-1515-6908),
- [Guillaume Bouvignies](#) ORCID: [orcid.org/0000-0003-4398-0320<sup>4</sup>](https://orcid.org/0000-0003-4398-0320),
- [Andrés Palencia](#) ORCID: [orcid.org/0000-0002-1805-319X<sup>3</sup>](https://orcid.org/0000-0002-1805-319X) &
- [Malene Ringkjøbing Jensen](#) ORCID: [orcid.org/0000-0003-0419-2196<sup>1</sup>](https://orcid.org/0000-0003-0419-2196)

*Nature* volume 602, pages 695–700 (2022)

- 10k Accesses
- 95 Altmetric
- [Metrics details](#)

## Subjects

- [Solution-state NMR](#)
- [X-ray crystallography](#)

## Abstract

Aromatic residues cluster in the core of folded proteins, where they stabilize the structure through multiple interactions. Nuclear magnetic resonance (NMR) studies in the 1970s showed that aromatic side chains can undergo ring flips—that is, 180° rotations—despite their role in maintaining the protein fold<sup>1,2,3</sup>. It was suggested that

large-scale ‘breathing’ motions of the surrounding protein environment would be necessary to accommodate these ring flipping events<sup>1</sup>. However, the structural details of these motions have remained unclear. Here we uncover the structural rearrangements that accompany ring flipping of a buried tyrosine residue in an SH3 domain. Using NMR, we show that the tyrosine side chain flips to a low-populated, minor state and, through a proteome-wide sequence analysis, we design mutants that stabilize this state, which allows us to capture its high-resolution structure by X-ray crystallography. A void volume is generated around the tyrosine ring during the structural transition between the major and minor state, and this allows fast flipping to take place. Our results provide structural insights into the protein breathing motions that are associated with ring flipping. More generally, our study has implications for protein design and structure prediction by showing how the local protein environment influences amino acid side chain conformations and vice versa.

[Download PDF](#)

## Main

Aromatic residues make up a considerable fraction of the hydrophobic core of folded proteins, where they stabilize the structure through CH–π (refs. [4,5,6](#)), π–π (refs. [7,8](#)) and cation–π (refs. [9,10](#)) interactions as well as hydrogen bonds. NMR studies in the 1970s demonstrated that aromatic side chains can undergo ring flips—that is, 180° rotations of the  $\chi_2$  dihedral angle (Cβ–Cγ axis)—even when engaged in stabilizing interactions in the hydrophobic core<sup>[1,2,3](#)</sup>. These ring flips require concerted movements of the surrounding residues (large-amplitude protein breathing motions), and ring flipping rates as a function of temperature and pressure have been used to report on these motions by deriving activation energies and volumes<sup>[11,12,13,14,15,16,17,18,19,20,21](#)</sup>. However, the structural details of ring flipping and the associated breathing motions have remained unknown, probably owing to difficulties in stabilizing ring flipping transition states or intermediates that are amenable to structure elucidation.

Here we capture ring flipping events of a buried tyrosine residue in the SH3 domain of the JNK-interacting protein 1 (JIP1). We show using NMR relaxation dispersion that the aromatic ring of this tyrosine residue populates a minor-state conformation (3%), and we design single point mutations to stabilize this conformation and capture its high-resolution structure using X-ray crystallography. The structure reveals how the intricate network of hydrogen bonds and CH–π interactions is rearranged in the minor state. We show how a substantial void volume is generated around the tyrosine ring during the structural transition from the major to the minor state, which can be associated with the breathing motions that allow fast-timescale ring flipping events to

take place. Our results provide structural insights into aromatic ring flipping and its associated protein breathing motions.

## Protein dynamics induced by a tyrosine residue

The SH3 domain of JIP1 undergoes exchange between two distinct conformations, as evidenced by  $^{15}\text{N}$  NMR relaxation measured at multiple temperatures (Extended Data Figs. 1, 2, Supplementary Discussion). To analyse the observed dynamics in detail, we acquired  $^{15}\text{N}$  and  $^1\text{H}^\text{N}$  Carr–Purcell–Meiboom–Gill (CPMG) relaxation dispersion experiments at 15 °C (refs. 22,23,24,25). These experiments quantify the kinetics of exchange processes and provide the difference in chemical shift between a major and a minor state, together with their relative populations<sup>26,27,28,29,30</sup>. The data confirm that exchange contributions to the transverse relaxation are present for residues within three regions of the protein (Extended Data Fig. 1d,e, Supplementary Table 1). These residues are located spatially close to tyrosine 526 (Y526) (Extended Data Fig. 1f). A mutation of Y526 to alanine (Y526A) shows no conformational exchange (Extended Data Fig. 1d,e), and conserves the protein backbone conformation, as evidenced from its crystal structure that we obtained at 1.5-Å resolution (Extended Data Fig. 3, Extended Data Tables 1, 2). These results show that the relaxation dispersion that affects around 40% of the residues in the SH3 domain arises from a single exchange process, with Y526 being the origin of the observed exchange.

The  $^{15}\text{N}$  and  $^1\text{H}^\text{N}$  relaxation dispersion data were analysed simultaneously according to a two-site exchange model in which a highly populated major state interconverts with a low-populated minor state (Extended Data Fig. 4a,b, Supplementary Discussion). The analysis of the data gives a population of the minor state of  $p_{\text{minor}} = 2.8 \pm 0.1\%$  and an exchange rate constant of  $k_{\text{EX}} = 2,600 \pm 70 \text{ s}^{-1}$ . The derived chemical shift differences,  $\Delta\delta_{\text{CPMG}}$ , span a range of 4.7 ppm for  $^{15}\text{N}$  and 1.1 ppm for  $^1\text{H}^\text{N}$  suggesting that there are substantial structural changes between the major and the minor state (Extended Data Fig. 4c,d).

The side chain of Y526 is found in an unusual conformation in the crystal structure (Protein Data Bank (PDB) code 2FPE (ref. 31), Extended Data Table 1), characterized by a  $\chi_2$  dihedral angle of 2° (Fig. 1a). Normally, this eclipsed conformation is energetically unfavourable because of steric interactions with the backbone (Fig. 1b), and it is rarely found in proteins as  $\chi_2$  angles are preferred where  $\text{C}\delta_1$  and  $\text{C}\delta_2$  are staggered with respect to  $\text{C}\alpha$  (ref. 32). However, the eclipsed conformation of the aromatic ring of Y526 is stabilized by CH–π interactions from V517, Q520 and A541 and by π–π interactions with H493 (Fig. 1a).

**Fig. 1: The side chain conformation of Y526 is determined by steric interactions with the surrounding amino acids.**

 figure 1

**a**, Crystal structure of wild-type JIP1-SH3, showing the conformation of Y526 and its stabilizing interactions with H493, V517, Q520 and A541. Dashed lines indicate CH–

$\pi$  (black) and  $\pi-\pi$  (red) interactions. **b**, Side chain conformation of Y526 in JIP1-SH3, illustrating the steric interactions between the  $\delta_1$  nuclei of the aromatic ring and the backbone. **c**, PCA of a dataset comprising the size of the amino acid side chains at positions 493, 517 and 541 within SH3 domains that contain Y or F at position 526 (Extended Data Fig. 5b). Two groups are observed, which correspond to eclipsed (group 1) or staggered (group 2) conformations of the aromatic ring. JIP1-SH3 is indicated in blue; POSH-SH3-1 and POSH-SH3-4 are indicated in green; and SH3 domains for which crystal structures have been determined previously are shown in red. **d**, Crystal structure of POSH-SH3-1, showing a staggered conformation of Y172. **e**, Unbiased electron density maps (Fo–Fc) of Y172 and the surrounding residues in POSH-SH3-1. **f**, Crystal structure of POSH-SH3-4, showing an eclipsed conformation of F867. **g**, Unbiased electron density maps (Fo–Fc) of F867 and the surrounding residues in POSH-SH3-4. **h**, **i**, Results of the PCA, illustrating the size and nature of the residues that surround the aromatic ring in position 526 in group 1 (**h**) and group 2 (**i**) SH3 domains. The size of the spheres in each position is proportional to the average size ( $n_{av}$ ) of the amino acid side chain across group members.

## Proteome-wide SH3 sequence analysis

To investigate the contribution from the surrounding residues in stabilizing the eclipsed conformation of Y526, we analysed the sequences of all identified human SH3 domains<sup>33</sup>. We categorized the sequences according to the identity of the amino acid at the position of Y526 in the JIP1 SH3 domain (JIP1-SH3) (Extended Data Fig. 5a), and we retained the sequences carrying a phenyl-based amino acid (Tyr or Phe) at this position, amounting to 33 SH3 domains. Sequence alignments reveal a large variation in the size of the amino acids at positions 493, 517 and 541, whereas at position 520 most sequences contain Gln, Arg or Lys (72%) (Extended Data Fig. 5b, c). To study the size correlation between the amino acids at positions 493, 517 and 541 and their influence on the conformation of the aromatic residue at position 526, we carried out a principal component analysis (PCA) by assigning a size score ( $n$ ) to each amino acid according to the number of heavy atoms in their side chains. This analysis reveals two well-separated groups, with the SH3 domain of JIP1 belonging to group 1 (Fig. 1c). In group 2, five SH3 domains are found for which high-resolution crystal structures are available; these include three SH3 domains of the sorbin and SH3 domain-containing proteins 1 and 2 (SORBS1 and SORBS2)<sup>34</sup>, and the SH3 domains of the dedicator of cytokinesis protein 2 (DOCK2)<sup>35</sup> and of the tyrosine protein kinase CSK<sup>36</sup> (Extended Data Fig. 5b). Notably, all group 2 structures show a favourable, staggered side chain conformation (of C $\delta_1$ /C $\delta_2$  with respect to C $\alpha$ ) of the corresponding tyrosine, with the  $\chi_2$  dihedral angle ranging from  $-40^\circ$  to  $-64^\circ$  (Fig. 1c). We therefore hypothesized that SH3 domains of group 1 have eclipsed conformations, whereas group 2 have staggered conformations. To test our hypothesis,

we determined two crystal structures of SH3 domains of the scaffold protein POSH ('plenty of SH3 domains'), for which the first SH3 domain belongs to group 2 and the fourth SH3 domain belongs to group 1 (Extended Data Table 2, Fig. 1c). Consistent with the PCA, the crystal structure of the first SH3 domain of POSH (POSH-SH3-1) shows a staggered conformation of the corresponding tyrosine residue (Y172), which is stabilized by CH–π interactions from L163 (position 517) and T185 (position 541) (Fig. 1d,e). POSH-SH3-4 shows a similar structure to JIP1-SH3, with an eclipsed conformation of the corresponding phenylalanine residue (F867) stabilized by CH–π interactions from V858 (position 517), K861 (position 520) and G882 (position 541), and by π–π interactions with H834 (position 493) (Fig. 1f,g). Our data therefore suggest that the conformation of the aromatic ring at position 526 is determined by steric interactions dictated by the size of the surrounding amino acids.

## Structure of the minor state

Next, we investigated whether the minor state detected by NMR corresponds to a staggered conformation of the side chain of Y526. We sought to stabilize the minor state relative to the major state by introducing single point mutations. The PCA suggests that a staggered conformation in group 2 is favoured over an eclipsed conformation in group 1 when residues with larger side chains are found in position 541, when isoleucine or leucine are occupying position 517 and when smaller residues are found in position 493 (Fig. 1h,i). Accordingly, we designed four different mutants of JIP1-SH3 (H493A, V517A, V517L and A541L) and obtained their high-resolution structures by X-ray crystallography (Extended Data Tables 1, 2). Of note, three mutants (H493A, V517A and A541L) induce a staggered conformation of Y526, with  $\chi_2$  dihedral angles ranging from  $-41^\circ$  to  $-75^\circ$ , whereas V517L shows an eclipsed conformation of Y526 and an almost identical structure to the wild-type protein (Fig. 2, Extended Data Fig. 6a). The high resolution of these structures, ranging from 1.4 to 1.9 Å, allows unambiguous determination of the conformation of Y526 and the surrounding residues, as demonstrated by their unbiased electron density maps (Fig. 2).

**Fig. 2: High-resolution crystal structures of JIP1-SH3 variants.**

---

 **figure 2**

**a–d**, Crystal structures showing the conformation of Y526, the corresponding unbiased electron density maps ( $F_o - F_c$ ) of Y526 and its surrounding residues, and the Newman projection along the  $C\beta - C\gamma$  bond of Y526 in the V517L (**a**), A541L (**b**), H493A (**c**) and V517A (**d**) variants of JIP1-SH3. Dashed lines indicate  $CH - \pi$  (black) and  $\pi - \pi$  (red) interactions. Residue numbers in red indicate the site of mutation. The wild-type JIP1-SH3 structure is shown as a reference in the centre.

## Structural details of breathing motions

The two variants H493A and V517A show almost identical crystal structures (Extended Data Fig. 6b) and an equivalent stabilization mechanism of the aromatic ring of Y526. Whereas the wild-type structure exhibits a classic  $\beta$ -bulge at residue 518

(ref. [37](#)), the transition from the eclipsed to the staggered conformation induces a local inversion (in-out) at residues 518–520, which leads to the formation of a canonical  $\beta$ -strand, as observed in the structures of the H493A and V517A variants (Fig. [3a–c](#)). This transition allows the side chain of L519 to rearrange and form CH– $\pi$  interactions with the ring of Y526 (Fig. [2c,d](#)); and, at the same time, large-scale movements of E518, Q520, E522 and Y524 are observed (Fig. [3a](#)). We note that SH3 domains in both group 1 and group 2 of the PCA show classic  $\beta$ -bulges at position 518 (Extended Data Fig. [5d](#)), which suggests that the presence of this structural motif is not determinant of the side chain conformation of the phenyl ring in position 526.

**Fig. 3: Crystal structures capture large-scale protein breathing motions.**

---

 **figure 3**

**a**, Structural changes associated with the transition from the eclipsed (green) to the staggered (grey) conformation of Y526. **b**, Illustration of the backbone conformation of the  $\beta$ -sheet formed between the 516–521 and 524–529 regions in the wild-type (WT) protein (left), and in the H493A (middle) and V517A (right) variants. Dashed

lines indicate hydrogen bonds. **c**, Schematic representation of the conformation of the  $\beta$ -strand encompassing residues 516–521, showing the orientation of the carbonyl group ('out', carbonyl group surface exposed; 'in', carbonyl group pointing towards the  $\beta$ -strand encompassing residues 524–529) in the wild-type protein (left) and in the H493A (middle) and V517A (right) variants. **d, e**, Two examples of linear correlations between the chemical shifts of wild-type JIP1-SH3 (blue spectrum) and the two variants H493A (grey spectrum) and V517A (red spectrum) as observed in  $^1\text{H}$ – $^{15}\text{N}$  HSQC spectra acquired at 35 °C (**d**, residue E522; **e**, residue D524). **f**, Energy landscapes illustrating the effect of single point mutations on the exchange rate constants and fractional populations of the major (eclipsed) and minor (staggered) conformations as determined by relaxation dispersion experiments acquired at 15 °C.

The A541L mutation also triggers a staggered conformation of Y526 and a rearrangement of the 517–522 region; however, the stabilization mechanism of the aromatic ring is different. A looping out of the  $\beta$ -strand between residues 517 and 522 is observed (Extended Data Fig. [6c–e](#)), which allows the side chain of A521 to reorient and to stabilize the staggered conformation of the ring through CH– $\pi$  interactions together with L541 and V517 (Fig. [2b](#)). At the same time, the side chains of L519, Q520 and E522 and D523 undergo large-scale movements to accommodate the flipped ring within the pocket (Extended Data Fig. [6c](#)).

Altogether, the different mutants show that the dynamics of the region encompassing residues 517–522 are key for the formation of the minor state. The experimental  $^{13}\text{C}$  chemical shifts for residues in this region are characteristic of random coil conformations (Extended Data Fig. [1b](#)) and, compared to other regions of secondary structure, the relaxation-derived order parameters ( $S^2$ ) are lower (Extended Data Fig. [2g](#)) and the crystallographic *B*-factors are higher. This supports the idea of the 517–522 region being intrinsically dynamic, with a fluctuating hydrogen-bonding network that is prone to structural transitions.

Next, we sought to determine which of the two crystal structures (H493A/V517A-like or A541L-like) best capture the conformation of the wild-type minor state detected by NMR relaxation dispersion. The H493A and V517A variants show almost identical crystal structures and for a subset of residues, the chemical shifts of which are unaffected by the mutations, the resonances of the two variants fall on a straight line together with the resonances of the wild-type protein (Fig. [3d, e](#)). This suggests that they are in fast–intermediate exchange between two conformations represented by the crystal structures of the wild-type protein and of the H493A/V517A variants. In agreement with this, both variants show line broadening and chemical exchange contributions as detected by  $^{15}\text{N}$  and  $^1\text{H}^N$  relaxation dispersion (Extended Data Figs. [7a–c](#), [8a–c](#)). Analysis of these data (Extended Data Figs. [7d, e](#), [8d, e](#)) shows that the structural features of the minor state of the wild-type protein are captured by the

H493A/V517A crystal structures, as shown by the excellent agreement between the  $\Delta\delta_{\text{CPMG}}$  values for the wild-type protein and the two variants (Extended Data Figs. 7f, g, 8f, g). In addition, the analysis yields exchange rates between the staggered (canonical  $\beta$ -strand) and the eclipsed (classic  $\beta$ -bulge) conformation of  $k_{\text{EX}} = 2,830 \pm 70 \text{ s}^{-1}$  (H493A) and  $k_{\text{EX}} = 6,800 \pm 300 \text{ s}^{-1}$  (V517A), compared to  $k_{\text{EX}} = 2,600 \pm 70 \text{ s}^{-1}$  determined for the wild-type protein. Finally, the observable chemical shifts of the two variants (Fig. 3d, e), in conjunction with analysis of the relaxation dispersion data ([Supplementary Discussion](#)), show that the H493A mutation slightly stabilizes the minor state relatively to the major state, whereas the V517A mutation almost inverts the relative populations of the major and minor states (Fig. 3f). For completeness, we note that the A541L crystal structure is not representative of the minor state conformation (Extended Data Fig. 9), although it shares structural features that are necessary for fast ring flipping of Y526 (see below).

## Void volume enables ring flipping

Aromatic  $^1\text{H}$ – $^{13}\text{C}$  heteronuclear single quantum coherence (HSQC) spectra show averaging of the NMR signals of the tyrosine  $\epsilon_1/\epsilon_2$  nuclei of Y526 (Fig. 4a, Extended Data Fig. 10a, Supplementary Fig. 1), which shows that full  $180^\circ$  ring flipping occurs. This poses the question of the timescale of the full ring flipping and its relation to the observed minor state. To answer this question, we acquired L-optimized TROSY-selected aromatic side chain  $^{13}\text{C}\epsilon$  CPMG (ref. 38) and on-resonance  $R_{1\rho}$  (ref. 39) relaxation dispersion data of Y526. These data are entirely explained by the exchange process between the major and minor state, with a negligible contribution from the full ring flipping event (Fig. 4b, c), demonstrating that ring flipping of Y526 is fast ( $k_{\text{EX}} > 50,000 \text{ s}^{-1}$ ) ([Supplementary Discussion](#)). This observation agrees with a 1- $\mu\text{s}$  molecular dynamics (MD) simulation that shows several  $180^\circ$  ring flipping events of Y526 (Fig. 4d, Extended Data Fig. 10b, c).

**Fig. 4: Void volume creation enables fast aromatic ring flipping of Y526.**

---

 figure 4

**a**,  $^1\text{H}$ - $^{13}\text{C}$  HSQC spectrum of JIP1-SH3 at 15 °C showing tyrosine epsilon correlations. **b**,  $^{13}\text{C}\epsilon$  CPMG relaxation dispersion profiles of Y526 obtained at 15 °C (red, 600 MHz; green, 700 MHz; blue, 850 MHz). The data were analysed simultaneously according to a two-site exchange model (full-drawn lines). Error bars represent one s.d. derived from Monte Carlo simulations of experimental uncertainty.

**c**,  $^{13}\text{C}\varepsilon$  on-resonance  $R_{1\rho}$  relaxation dispersion profile of Y526 at 15 °C and 700 MHz. The full-drawn line corresponds to the calculated  $R_{1\rho}$  profile from the exchange parameters ( $k_{\text{EX}}$ ,  $p_{\text{minor}}$  and  $\Delta\delta_{\text{CPMG}}$ ) obtained from the analysis of the CPMG data in **b**. Error bars represent one s.d. and were derived as in **b**. **d**, The dihedral angle  $\chi_2$  of Y526 as a function of simulation time in a 1-μs MD simulation of the dimeric JIP1-SH3. **e**, Volume of the pocket of Y526 across the structural trajectory between the major and minor state. **f**, Surface representation of JIP1-SH3 in three different states corresponding to the major state, an intermediate state on the structural trajectory and the minor state. The Y526 pocket is highlighted in pink (major), blue (intermediate) and yellow (minor). The rearrangements along the structural trajectory between the major and the minor state generate a void volume around Y526, thereby lowering the transition-state energy of ring flipping. **g**, Illustration of the protein breathing motions along the structural trajectory from the major to the minor state. A void volume is created around Y526, which allows fast ring flipping to take place. The ring flipping is occasionally interrupted by trapping of Y526 in a staggered conformation through formation of CH–π interactions with L519 enabled by the β-bulge to β-sheet transition.

During the structural transition between the major and the minor state (Supplementary Video 1), a void volume is created around the ring of Y526 that corresponds to a pocket expansion of 65 Å<sup>3</sup>; this is mainly due to the structural reorganization of the side chain of Q520 (Fig. 4e,f). This cavity expansion is in agreement with previous studies that have reported activation volumes between 40 and 85 Å<sup>3</sup> for ring flipping events of aromatic residues in other proteins<sup>12,14,21,40,41</sup>. The expansion is followed by a compaction of the surrounding protein environment as the ring becomes stabilized by CH–π interactions from L519 (Fig. 4e,f).

Collectively, our results are consistent with a model in which fast protein breathing motions along the structural trajectory between the major and the minor state generate the necessary void volume for ring flipping to take place by lowering the energy of the transition state (Fig. 4e–g, Supplementary Video 2). Occasionally, the β-bulge to β-sheet transition is completed and the aromatic ring becomes trapped in a staggered conformation that is stabilized by CH–π interactions with L519—a process that gives rise to the observed relaxation dispersion. These events are rare and occur on a slow timescale (Figs. 3f, 4g), but they constitute an important tool for observing the trajectory of the protein breathing motions coupled to aromatic ring flipping. The initial generation of void volume around the ring is almost identical along the structural trajectory between the major state (wild type) and the A541L crystal structure (Extended Data Fig. 6f). Thus, all mutants—including A541L, which stabilizes Y526 in a staggered conformation by a different mechanism—share the same initial structural trajectory and report on identical breathing motions.

## Conclusions

Our results provide structural insights into the protein breathing motions that are associated with aromatic ring flipping. We reveal how the dynamics of the region encompassing residues 517 to 522 are key for accommodating the ring flipping process of Y526. Notably, the transition from the eclipsed, major conformation to the staggered, minor conformation is associated with a structural change from a rare, classic  $\beta$ -bulge to a common, canonical  $\beta$ -strand conformation (Supplementary Video 1, Fig. 3a–c). Breathing motions along the structural trajectory between the major and the minor state generate the necessary void volume for fast ring flipping of Y526 to take place (Supplementary Video 2). Although a recent NMR study suggested extensive local unfolding as the source of cavity creation<sup>41</sup>, our study provides an alternative view by showing how a substantial void volume can be generated through distinct structural rearrangements, while maintaining the overall protein fold.

More generally, our study shows how the local environment in the protein core can lead to a priori energetically unfavourable conformations of amino acid side chains, and how subtle changes in this environment can lead to major structural rearrangements to revert to preferred amino acid conformations. Our results therefore have implications for protein design and structure prediction, and for how novel biological functions can be acquired during the course of evolution; for example, by altering the delicate balance between hydrogen bonds and CH– $\pi$  interactions. Finally, the combination of sensitive NMR methods to detect low-populated states, protein design using proteome-wide sequence analyses and high-resolution crystallography could be a strategy to further discover the structural details of sparsely populated protein states and their link to function.

## Methods

### Expression and purification of JIP1-SH3, POSH-SH3-1 and POSH-SH3-4

JIP1-SH3, corresponding to residues 490–549 of human JIP1 (Uniprot Q9UQF2), was subcloned into a pET28a vector, and two of the four SH3 domains of the E3 ubiquitin-protein ligase SH3RF1 (Uniprot Q7Z6J0; also known as ‘plenty of SH3 domains’ (POSH)), SH3-1 (135–194) and SH3-4 (829–888), were subcloned into a pESPRIT vector<sup>42</sup>. The constructs therefore contained an N-terminal hexahistidine tag followed by a tobacco etch virus (TEV) cleavage site. The final proteins after protease cleavage contain N-terminal GRR (POSH) or GHM extensions (JIP1).

To obtain unlabelled proteins, *Escherichia coli* BL21(DE3) cells transformed with one of the constructs were grown in lysogeny broth (LB) medium at 37 °C until the optical density at 600 nm reached 0.7. Protein expression was induced by the addition of isopropyl β-D-1-thiogalactopyranoside (IPTG) to a final concentration of 1 mM. The cultures were grown for an additional 15 h at 20 °C (POSH-SH3s) or 4 h at 37 °C (JIP1-SH3). The cells were collected by centrifugation and frozen at -20 °C or -80 °C. Isotopically <sup>15</sup>N/<sup>13</sup>C- and <sup>15</sup>N-labelled proteins were produced by growing transformed *E. coli* BL21(DE3) cells in M9 minimal medium containing 1 g l<sup>-1</sup> of <sup>15</sup>N-NH<sub>4</sub>Cl and 2 g l<sup>-1</sup> of <sup>13</sup>C<sub>6</sub>-D-glucose or <sup>12</sup>C<sub>6</sub>-D-glucose. To obtain <sup>15</sup>N-labelled protein with tyrosine residues site-selectively labelled at the ε position with <sup>13</sup>C, transformed *E. coli* BL21(DE3) cells were grown in M9 minimal medium containing 1 g l<sup>-1</sup> of <sup>15</sup>N-NH<sub>4</sub>Cl, 2 g l<sup>-1</sup> of NaH<sup>13</sup>CO<sub>3</sub> and 2 g l<sup>-1</sup> of [2-<sup>13</sup>C]-glycerol<sup>43</sup>.

All SH3 domains were purified by Ni affinity chromatography followed by size-exclusion chromatography. Cell lysis was carried out by sonication using purification buffer (POSH: 50 mM Tris pH 7.0/8.0, 500 mM NaCl, 1 mM β-mercaptoethanol; JIP1: 50 mM HEPES pH 7.0, 150 mM NaCl) supplemented with protease inhibitor tablets (Roche). The washing buffer used for Ni affinity chromatography was the same as the purification buffer with the addition of 20 mM imidazole. The elution buffer was the same as the purification buffer with the addition of 500 mM (POSH) or 300 mM (JIP1) imidazole. Nickel affinity chromatography was followed by cleavage by the TEV protease, a second Ni affinity column and size-exclusion chromatography on a Superdex 75 (GE Healthcare). This column was equilibrated with 50 mM HEPES pH 8.0, 500 mM NaCl, 2 mM DTT for POSH-SH3-1, 50 mM HEPES pH 7.0, 500 mM NaCl, 2 mM DTT for POSH-SH3-4 and 50 mM HEPES pH 7.0, 150 mM NaCl for JIP1-SH3.

## Expression and purification of JIP1-SH3 variants

Expression and purification of the JIP1-SH3 variants (Y526A, V517A, V517L, A541L and H493A) were performed following the same protocol as for JIP1-SH3, except that the cultures were grown for 15 h after induction at 20 °C (instead of 4 h at 37 °C).

## Thermal stability measurements of JIP1-SH3

The stability of JIP1-SH3 was measured by differential scanning fluorimetry using a Prometheus NT.48 (Nanotemper) instrument with the emission wavelengths set to 330 and 350 nm and an excitation power of 10%. The melting curve for wild-type JIP1-SH3 was measured at a protein concentration of 4 mg ml<sup>-1</sup> in 50 mM HEPES, 150 mM NaCl at pH 7.0 by using Prometheus Standard Capillaries (PR-C002). The temperature scan rate was fixed at 1 °C per min from 20 °C to 95 °C. The melting temperature ( $T_m$ )

was calculated from the peak of the first derivative of the intrinsic protein fluorescence intensity ratio at 350 nm and 330 nm throughout the duration of the temperature ramp.

## NMR spectral assignment of JIP1-SH3 and its variants

The NMR assignment experiments were acquired in 50 mM HEPES, 150 mM NaCl, pH 7.0 at a protein concentration of 0.94 mM (JIP1-SH3), 1.06 mM (JIP1-SH3(Y526A)), 1.10 mM (JIP1-SH3(A541L)), 2 mM (JIP1-SH3(V517A)) and 0.90 mM (JIP1-SH3(H493A)). The NMR spectral assignments of JIP1-SH3 were performed at 25 °C using a set of BEST-TROSY triple resonance experiments (HNCO, intra-residue HNCACO, HNCOCA, intra-residue HNCA, HNCOCACB and intra-residue HNCACB) acquired at a <sup>1</sup>H frequency of 600 MHz (Bruker, operated with TopSpin v.3.5)<sup>44</sup>. The NMR spectral assignments of JIP1-SH3(Y526A) were obtained at 25 °C at a <sup>1</sup>H frequency of 700 MHz (Bruker) using BEST-TROSY HNCO, HNCOCACB and intra-residue HNCACB experiments. The NMR spectral assignments of JIP1-SH3(A541L) (at 25 °C), JIP1-SH3(V517A) (at 35 °C) and JIP1-SH3(H493A) (at 35 °C) were obtained at a <sup>1</sup>H frequency of 700 MHz (Bruker) using a BEST-TROSY HNCACB experiment. The spectra were manually peak-picked using NMRFAM-Sparky<sup>45</sup> and sequential connectivities were identified manually or by using the assignment program MARS<sup>46</sup>. Secondary structure propensities were calculated using SSP on the basis of the experimental Cα and Cβ chemical shifts<sup>47</sup>.

## <sup>15</sup>N relaxation measurements of JIP1-SH3

Measurements of <sup>15</sup>N relaxation rates ( $R_1$ ,  $R_2$  and heteronuclear NOEs) of JIP1-SH3 were obtained using standard HSQC-type pulse sequences<sup>48</sup> at a <sup>1</sup>H frequency of 600 MHz (Agilent, operated with VnmrJ v.3.1). The relaxation rates were measured at four different temperatures: 15, 25, 35 and 45 °C. The magnetization decay was sampled at (0, 100, 200, 400, 600, 800, 1,100, 1,500 and 1,900) milliseconds (ms) for longitudinal and at (10, 30, 50, 70, 90, 130, 170, 210 and 250) ms for transverse relaxation. Technical replicates of one or two of these delays were acquired to estimate the uncertainty on the relaxation rates using a Monte Carlo approach. Details of the Lipari–Szabo model free analysis can be found in the [Supplementary Discussion](#).

## <sup>15</sup>N and <sup>1</sup>H<sup>N</sup> CPMG relaxation dispersion of JIP1-SH3 and its variants

All <sup>15</sup>N CPMG relaxation dispersion experiments<sup>24</sup> were carried out at 15 °C using a constant-time relaxation delay of 32 ms with CPMG frequencies ( $v_{CPMG}$ ) ranging from 31.25 to 1,000 Hz and a <sup>1</sup>H decoupling field of 11 kHz. The <sup>1</sup>H<sup>N</sup> relaxation dispersion experiments were carried out at 15 °C using the published pulse sequence<sup>25</sup> with a

constant-time relaxation delay of 20 ms and CPMG frequencies ranging from 50 to 2,000 Hz. Uncertainties on peak intensities extracted from the relaxation dispersion experiments were estimated using the pooled s.d. calculated from repeat measurements (technical replicates of one to three  $v_{\text{CPMG}}$  values), each pool being the set of repeat points per  $v_{\text{CPMG}}$  and per peak. Uncertainties on  $R_{2\text{eff}}$  values were propagated from the peak intensity uncertainty using a Monte Carlo approach. The following relaxation dispersion experiments were acquired: JIP1-SH3:  $^{15}\text{N}$  (600 MHz, Agilent),  $^{15}\text{N}$  (850 MHz, Bruker),  $^1\text{H}^{\text{N}}$  (600 MHz, Bruker),  $^1\text{H}^{\text{N}}$  (950 MHz, Bruker); JIP1-SH3(H493A) and JIP1-SH3(V517A):  $^{15}\text{N}$  (600 MHz, Bruker),  $^{15}\text{N}$  (950 MHz, Bruker),  $^1\text{H}^{\text{N}}$  (600 MHz, Bruker),  $^1\text{H}^{\text{N}}$  (950 MHz, Bruker); JIP1-SH3(Y526A):  $^{15}\text{N}$  (700 MHz, Bruker) and  $^1\text{H}^{\text{N}}$  (600 MHz, Bruker); JIP1-SH3(A541L):  $^{15}\text{N}$  (700 MHz, Bruker). All relaxation dispersion data were analysed using the program ChemEx (<https://github.com/gbouvignies/ChemEx>)<sup>49</sup> as described in the Supplementary Discussion.

## Tyrosine assignments and $^{13}\text{C}$ CPMG relaxation dispersion of Y526

The  $^{13}\text{C}\epsilon-\text{H}\epsilon$  tyrosine resonances were assigned at 45 °C by acquiring a two-dimensional (2D) plane of a BEST-TROSY intra-residue HNCACB experiment<sup>44</sup>, an aromatic BEST constant-time  $^1\text{H}-^{13}\text{C}$  HSQC experiment<sup>50</sup> and a  $(\text{H}\beta)\text{C}\beta(\text{C}\gamma\text{C}\delta\text{C}\epsilon)\text{H}\epsilon$  experiment<sup>51</sup> linking the  $\text{C}\beta$  chemical shifts directly to the  $\text{H}\epsilon$  chemical shifts. The spectra were manually peak-picked using NMRFAM-Sparky<sup>45</sup> and  $^{13}\text{C}\epsilon-\text{H}\epsilon$  tyrosine resonances were assigned manually (Supplementary Fig. 1). The acquisition of aromatic BEST constant-time  $^1\text{H}-^{13}\text{C}$  HSQC experiments at different temperatures (between 5 and 45 °C) enabled the final assignment at 15 °C.

Aromatic L-optimized TROSY-selected  $^{13}\text{C}$  CPMG<sup>38</sup> and  $R_{1\rho}$ <sup>39</sup> relaxation dispersion experiments were carried out at 15 °C on a 1 mM uniformly  $^{15}\text{N}$  and site-selective  $^{13}\text{C}$ -labelled JIP1-SH3 sample in 50 mM HEPES, 150 mM NaCl at pH 7.0. CPMG relaxation dispersion experiments were carried out at magnetic field strengths of 600 MHz, 700 MHz and 850 MHz (Bruker) using a constant-time relaxation delay of 20 ms with CPMG frequencies ranging from 100 to 1,000 Hz. The  $R_{1\rho}$  relaxation dispersion experiment was recorded on-resonance with Y526 at 700 MHz (Bruker) using  $B_1$  field strengths ranging from 700 to 10,000 Hz with a 20 ms relaxation delay. Error bars were derived from repeat measurements as described above for the  $^{15}\text{N}$  and  $^1\text{H}^{\text{N}}$  relaxation dispersion experiments. Analysis of the  $^{13}\text{C}$  data was carried out using ChemEx or using available analytical expressions for  $R_{1\rho}$  relaxation in the presence of two-site exchange<sup>52</sup> (Supplementary Discussion).

## **Comparison of JIP1-SH3 to other human SH3 domains**

The sequences of 320 human SH3 domains were obtained<sup>33</sup>, aligned using Clustal Omega<sup>53</sup> and categorized according to the identity of the amino acid at the position of Y526 in JIP1-SH3. A new alignment was performed using only the sequences that carry Y or F at this position, amounting to a total of 33 human SH3 domains. The sequences of the SH3 domains of the RIMS-binding proteins 1, 2 and 3 and the metastasis-associated in colon cancer protein 1 (MACC1) were not included in this alignment, as they contain longer insertions compared to the JIP1-SH3 sequence. For each SH3 domain, the amino acids corresponding to residues 493, 517 and 541 of JIP1-SH3 were assigned a size score according to the number of heavy atoms in their side chains (A: 1, C: 2, D: 4, E: 5, F: 7, G: 0, H: 6, I: 4, K: 5, L: 4, M: 4, N: 4, P: 3, Q: 5, R: 7, S: 2, T: 3, V: 3, Y: 8, W: 10). A PCA was carried out to reveal potential correlations between the sizes of the amino acids in position 493, 517 and 541 using the ClustVis webtool<sup>54</sup>.

## **Crystallization of JIP1-SH3 and the variants Y526A, V517A, V517L, A541L and H493A**

JIP1-SH3 and its variants were concentrated to a final concentration of 20 mg ml<sup>-1</sup> (JIP1-SH3, JIP1-SH3(V517A), JIP1-SH3(A541L) and JIP1-SH3(V517L)), 10 mg ml<sup>-1</sup> (JIP1-SH3(Y526A)) and 4 mg ml<sup>-1</sup> (JIP1-SH3(H493A)) after size-exclusion chromatography by using Amicon Ultra-4 3.0-kDa centrifugal filters (Merck). All crystals were obtained in 0.1 M HEPES pH 7.5, 1–5% PEG 400 and 2–2.5 M ammonium sulfate at 20 °C by the hanging-drop vapour diffusion method in 24-well plates (Hampton research)<sup>55</sup>. Drops of 2–3 µl consisting of 1:1 or 2:1 parts of protein solution and reservoir solution were vapour-equilibrated against 500 µl of reservoir solution. All crystals appeared after two days and were collected by transferring them to a mother liquor solution containing 20–30% trehalose, frozen and kept in liquid nitrogen.

## **Crystallization of POSH-SH3-1 and POSH-SH3-4**

Purified POSH-SH3-1 and POSH-SH3-4 were directly concentrated after size-exclusion chromatography to 3.4 and 5.0 mg ml<sup>-1</sup>, respectively, using Amicon Ultra-4 3.5-kDa centrifugal filters (Merck). Initial crystallization conditions were identified using the high-throughput crystallization platform (EMBL).

The initial condition identified for POSH-SH3-1 was 0.2 M NaF, 20% PEG 3350 from the PEGs-I screen (Qiagen) at 4 °C. Needles appeared after 3 to 7 days. Further optimization was done using the hanging-drop vapour diffusion method at 4 °C in 24-

well plates. Drops of 2 µl consisting of equal parts protein solution at 2.5 mg ml<sup>-1</sup> and reservoir solution (0.2 M NaF, 22% PEG 3350) were vapour-equilibrated against 500 µl of reservoir solution. Hexagonal crystals appeared after three days and were collected after five days by transferring them to a mother liquor solution containing 5% ethylene glycol as cryoprotectant, frozen and kept in liquid nitrogen.

The initial screen of POSH-SH3-4 identified two crystallization conditions: 0.1 M MES pH 6.5, 25% PEG 3000 (condition 1) and 0.1 M MES pH 6.5, 25% PEG 4000 (condition 2) from the PEGs-I screen (Qiagen) at 4 °C. Diffraction-quality needles (condition 1, 0.1 M MES pH 6.5, 26% PEG 3000) or three-dimensional crystals (condition 2, 0.1 M MES pH 6.5, 23% PEG 4000) were obtained after four days using the same vapour-diffusion set-up as for POSH-SH3-1. These were collected after seven days with 10% ethylene glycol as cryoprotectant, frozen and kept in liquid nitrogen.

## Structure determination

Crystal diffraction was performed at the ESRF beamlines ID30A, ID23-1, ID23-2 using the MXCube software<sup>56,57</sup>, at the automated beamline MASSIF-1<sup>58</sup> or at the Diamond beamlines I04 and I04-1, all equipped with Pilatus detectors (Dectris). Indexing and integration was performed using the XDS<sup>59</sup>, the autoProc<sup>60</sup> or GrenADeS<sup>61</sup> program suites. Data reduction for JIP1-SH3(H493A) was carried out with Pointless and Aimless<sup>62,63</sup>. Molecular replacement of the wild-type JIP1-SH3 structure was carried out in Phaser<sup>64</sup> using the PDB code 2FPE (chains A–B) as a search model. The structures of JIP1-SH3 mutants were obtained by using our wild-type JIP1-SH3 structure as a search model. The initial solutions were improved through cycles of manual adjusting in Coot<sup>65</sup> and refined by using Refmac5<sup>66</sup>. Aimless, Phaser and Refmac were all used as programs of the CCP4 suite<sup>67</sup>.

The structure of POSH-SH3-4 was determined by molecular replacement using a homology model that was built on the basis of the SH3 domain structure of SORBS1 (PDB code: 2LJ1, chain A), which has 45% sequence identity. The structure of POSH-SH3-1 was determined by molecular replacement using as a search model the SH3 domain of human tyrosine protein kinase C-Src (PDB code: 2SRC). Crystallography applications were compiled and configured by SBGrid<sup>68</sup>.

## Structural trajectory and void volume calculations

The structural trajectory between the major and minor conformation was generated with Chimera<sup>69</sup> by morphing between the wild-type JIP1-SH3 structure (PDB 7NYK) and the structures of the two variants JIP1-SH3(H493A) (7NYL) and JIP1-

SH3(V517A) (7NYM). To calculate changes in the volume of the Y526 pocket, protons were added to all structures of the trajectory and Y526 was replaced by glycine to allow calculation of the complete pocket volume by POVME 3.0 using a distance cut-off of 1.09 Å, corresponding to the van der Waals radius of a hydrogen atom<sup>70</sup>. A similar strategy was used to generate the structural trajectory between the wild-type JIP1-SH3 structure (PDB 7NYK) and the structure of the JIP1-SH3(A541L) variant (7NYO).

## MD simulations of JIP1-SH3

MD simulations were carried out using ACEMD v.3.3.0<sup>71</sup> and the Charmm36m force field parameters<sup>72</sup>. Using VMD<sup>73</sup>, coordinates of the dimer from PDB 2FPE were inserted in the box of dimensions with a minimum distance of 2 Å in each direction between each atom and any box side. The box was then filled with water molecules and an amount of Na<sup>+</sup> and Cl<sup>-</sup> corresponding to [NaCl] = 0.1 M. Electrostatic interactions were evaluated using Particle-Mesh Ewald (PME) electrostatics with a cut-off distance of 9 Å. Van der Waals forces were calculated with a cut-off of 9 Å and a switching function active from 7.5 Å to smoothly reduce the potential to zero. An integration step of 2 fs and holonomic constraints on all hydrogen-heavy atom bond terms were used. The energy of the system was minimized using conjugate-gradient minimization for 500 steps. Random velocities from a Maxwell distribution with  $T = 298.15\text{ K}$  were assigned to atoms. Then, the system was equilibrated first for 100 ps in the NVE ensemble and then for 1 ns in the NPT ensemble. In the latter case, temperature and pressure were controlled using the Langevin thermostat with a damping constant of 1 ps<sup>-1</sup> and Berendsen barostat with a relaxation time of 400 fs, respectively. Finally, a 1 μs trajectory was calculated in the NVT ensemble using the Langevin thermostat with a damping constant of 0.1 ps<sup>-1</sup>. Trajectories were processed and analysed using the MDAnalysis Python package<sup>74</sup>.

## Reporting summary

Further information on research design is available in the [Nature Research Reporting Summary](#) linked to this paper.

## Data availability

Protein structure data have been deposited in the PDB with accession codes: [7NYK](#) (JIP1-SH3), [7NZB](#) (JIP1-SH3(V517L)), [7NYO](#) (JIP1-SH3(A541L)), [7NYL](#) (JIP1-SH3(H493A)), [7NYM](#) (JIP1-SH3(V517A)), [7NZC](#) (POSH-SH3-1) and [7NZD](#) (POSH-SH3-4). The <sup>1</sup>H, <sup>13</sup>C and <sup>15</sup>N chemical shifts of JIP1-SH3 have been deposited in the Biological Magnetic Resonance Data Bank with accession codes: [50814](#) (JIP1-

SH3), [50817](#) (JIP1-SH3(Y526A)), [50816](#) (JIP1-SH3(V517A)), [50818](#) (JIP1-SH3(H493A)) and [50815](#) (JIP1-SH3(A541L)). SH3 domain structures for molecular replacement were retrieved from the PDB (<https://www.ebi.ac.uk/pdbe/>) with accession codes: [2FPE](#) (JIP1), [2LJ1](#) (SORBS1) and [2SRC](#) (tyrosine protein kinase C-Src). Structures for the proteome-wide SH3 sequence analysis were retrieved from the PDB with accession codes: [1CSK](#), [3A98](#), [2O9S](#), [5VEI](#) and [4LNP](#).

## References

1. Campbell, I. D., Dobson, C. M. & Williams, R. J. Proton magnetic resonance studies of the tyrosine residues of hen lysozyme-assignment and detection of conformational mobility. *Proc. R. Soc. B.* **189**, 503–509 (1975).
2. Wüthrich, K. & Wagner, G. NMR investigations of the dynamics of the aromatic amino acid residues in the basic pancreatic trypsin inhibitor. *FEBS Lett.* **50**, 265–268 (1975).
3. Wagner, G., DeMarco, A. & Wüthrich, K. Dynamics of the aromatic amino acid residues in the globular conformation of the basic pancreatic trypsin inhibitor (BPTI). I.  $^1\text{H}$  NMR studies. *Biophys. Struct. Mech.* **2**, 139–158 (1976).
4. Perutz, M. F. The role of aromatic rings as hydrogen-bond acceptors in molecular recognition. *Philos. Trans. R. Soc. A* **345**, 105–112 (1993).
5. Brandl, M., Weiss, M. S., Jabs, A., Sühnel, J. & Hilgenfeld, R. C–H... $\pi$ -interactions in proteins. *J. Mol. Biol.* **307**, 357–377 (2001).
6. Steiner, T. & Koellner, G. Hydrogen bonds with  $\pi$ -acceptors in proteins: frequencies and role in stabilizing local 3D structures. *J. Mol. Biol.* **305**, 535–557 (2001).
7. Burley, S. K. & Petsko, G. A. Aromatic–aromatic interaction: a mechanism of protein structure stabilization. *Science* **229**, 23–28 (1985).
8. McGaughey, G. B., Gagné, M. & Rappé, A. K.  $\pi$ -Stacking interactions. Alive and well in proteins. *J. Biol. Chem.* **273**, 15458–15463 (1998).
9. Dougherty, D. A. Cation– $\pi$  interactions in chemistry and biology: a new view of benzene, Phe, Tyr, and Trp. *Science* **271**, 163–168 (1996).
10. Ma, J. C. & Dougherty, D. A. The cation– $\pi$  interaction. *Chem. Rev.* **97**, 1303–1324 (1997).

11. Wagner, G. & Wüthrich, K. Dynamic model of globular protein conformations based on NMR studies in solution. *Nature* **275**, 247–248 (1978).
12. Wagner, G. Activation volumes for the rotational motion of interior aromatic rings in globular proteins determined by high resolution  $^1\text{H}$  NMR at variable pressure. *FEBS Lett.* **112**, 280–284 (1980).
13. Skalicky, J. J., Mills, J. L., Sharma, S. & Szyperski, T. Aromatic ring-flipping in supercooled water: implications for NMR-based structural biology of proteins. *J. Am. Chem. Soc.* **123**, 388–397 (2001).
14. Hattori, M. et al. Infrequent cavity-forming fluctuations in HPr from *Staphylococcus carnosus* revealed by pressure- and temperature-dependent tyrosine ring flips. *Protein Sci.* **13**, 3104–3114 (2004).
15. Rao, D. K. & Bhuyan, A. K. Complexity of aromatic ring-flip motions in proteins: Y97 ring dynamics in cytochrome c observed by cross-relaxation suppressed exchange NMR spectroscopy. *J. Biomol. NMR* **39**, 187–196 (2007).
16. Weininger, U., Respondek, M., Löw, C. & Akke, M. Slow aromatic ring flips detected despite near-degenerate NMR frequencies of the exchanging nuclei. *J. Phys. Chem. B* **117**, 9241–9247 (2013).
17. Weininger, U., Modig, K. & Akke, M. Ring flips revisited:  $^{13}\text{C}$  relaxation dispersion measurements of aromatic side chain dynamics and activation barriers in basic pancreatic trypsin inhibitor. *Biochemistry* **53**, 4519–4525 (2014).
18. Yang, C.-J., Takeda, M., Terauchi, T., Jee, J. & Kainosho, M. Differential large-amplitude breathing motions in the interface of FKBP12–drug complexes. *Biochemistry* **54**, 6983–6995 (2015).
19. Kasinath, V., Fu, Y., Sharp, K. A. & Wand, A. J. A sharp thermal transition of fast aromatic-ring dynamics in ubiquitin. *Angew. Chem. Int. Ed.* **54**, 102–107 (2015).
20. Gauto, D. F. et al. Aromatic ring dynamics, thermal activation, and transient conformations of a 468 kDa enzyme by specific  $^1\text{H}$ - $^{13}\text{C}$  labeling and fast magic-angle spinning NMR. *J. Am. Chem. Soc.* **141**, 11183–11195 (2019).
21. Dreydoppel, M., Raum, H. N. & Weininger, U. Slow ring flips in aromatic cluster of GB1 studied by aromatic  $^{13}\text{C}$  relaxation dispersion methods. *J. Biomol. NMR* **74**, 183–191 (2020).

22. Loria, J. P., Rance, M. & Palmer, A. G. A relaxation-compensated Carr–Purcell–Meiboom–Gill sequence for characterizing chemical exchange by NMR spectroscopy. *J. Am. Chem. Soc.* **121**, 2331–2332 (1999).
23. Ishima, R. & Torchia, D. A. Extending the range of amide proton relaxation dispersion experiments in proteins using a constant-time relaxation-compensated CPMG approach. *J. Biomol. NMR* **25**, 243–248 (2003).
24. Hansen, D. F., Vallurupalli, P. & Kay, L. E. An improved  $^{15}\text{N}$  relaxation dispersion experiment for the measurement of millisecond time-scale dynamics in proteins. *J. Phys. Chem. B* **112**, 5898–5904 (2008).
25. Yuwen, T. & Kay, L. E. Revisiting  $^1\text{H}$  CPMG relaxation dispersion experiments: a simple modification can eliminate large artifacts. *J. Biomol. NMR* **73**, 641–650 (2019).
26. Sugase, K., Dyson, H. J. & Wright, P. E. Mechanism of coupled folding and binding of an intrinsically disordered protein. *Nature* **447**, 1021–1025 (2007).
27. Baldwin, A. J. & Kay, L. E. NMR spectroscopy brings invisible protein states into focus. *Nat. Chem. Biol.* **5**, 808–814 (2009).
28. Bouvignies, G. et al. Solution structure of a minor and transiently formed state of a T4 lysozyme mutant. *Nature* **477**, 111–114 (2011).
29. Neudecker, P. et al. Structure of an intermediate state in protein folding and aggregation. *Science* **336**, 362–366 (2012).
30. Alderson, T. R. & Kay, L. E. Unveiling invisible protein states with NMR spectroscopy. *Curr. Opin. Struct. Biol.* **60**, 39–49 (2020).
31. Kristensen, O. et al. A unique set of SH3–SH3 interactions controls IB1 homodimerization. *EMBO J.* **25**, 785–797 (2006).
32. Dunbrack, R. L. & Karplus, M. Conformational analysis of the backbone-dependent rotamer preferences of protein sidechains. *Nat. Struct. Biol.* **1**, 334–340 (1994).
33. Teyra, J. et al. Comprehensive analysis of the human SH3 domain family reveals a wide variety of non-canonical specificities. *Structure* **25**, 1598–1610 (2017).
34. Gehmlich, K. et al. Paxillin and ponsin interact in nascent costameres of muscle cells. *J. Mol. Biol.* **369**, 665–682 (2007).

35. Hanawa-Suetsugu, K. et al. Structural basis for mutual relief of the Rac guanine nucleotide exchange factor DOCK2 and its partner ELMO1 from their autoinhibited forms. *Proc. Natl Acad. Sci. USA* **109**, 3305–3310 (2012).
36. Borchert, T. V., Mathieu, M., Zeelen, J. P., Courtneidge, S. A. & Wierenga, R. K. The crystal structure of human CskSH3: structural diversity near the RT-Src and n-Src loop. *FEBS Lett.* **341**, 79–85 (1994).
37. Chan, A. W. E., Hutchinson, E. G., Harris, D. & Thornton, J. M. Identification, classification, and analysis of  $\beta$ -bulges in proteins. *Protein Sci.* **2**, 1574–1590 (1993).
38. Weininger, U., Respondek, M. & Akke, M. Conformational exchange of aromatic side chains characterized by L-optimized TROSY-selected  $^{13}\text{C}$  CPMG relaxation dispersion. *J. Biomol. NMR* **54**, 9–14 (2012).
39. Weininger, U., Brath, U., Modig, K., Teilum, K. & Akke, M. Off-resonance rotating-frame relaxation dispersion experiment for  $^{13}\text{C}$  in aromatic side chains using L-optimized TROSY-selection. *J. Biomol. NMR* **59**, 23–29 (2014).
40. Li, H., Yamada, H. & Akasaka, K. Effect of pressure on the tertiary structure and dynamics of folded basic pancreatic trypsin inhibitor. *Biophys. J.* **77**, 2801–2812 (1999).
41. Dreydoppel, M., Dorn, B., Modig, K., Akke, M. & Weininger, U. Transition-state compressibility and activation volume of transient protein conformational fluctuations. *JACS Au* **1**, 833–842 (2021).
42. Hart, D. J. & Tarendreau, F. Combinatorial library approaches for improving soluble protein expression in *Escherichia coli*. *Acta Crystallogr. D* **62**, 19–26 (2006).
43. LeMaster, D. M. & Kushlan, D. M. Dynamical mapping of *E. coli* thioredoxin via  $^{13}\text{C}$  NMR relaxation analysis. *J. Am. Chem. Soc.* **118**, 9255–9264 (1996).
44. Solyom, Z. et al. BEST-TROSY experiments for time-efficient sequential resonance assignment of large disordered proteins. *J. Biomol. NMR* **55**, 311–321 (2013).
45. Lee, W., Tonelli, M. & Markley, J. L. NMRFAM-SPARKY: enhanced software for biomolecular NMR spectroscopy. *Bioinformatics* **31**, 1325–1327 (2015).

46. Jung, Y.-S. & Zweckstetter, M. Mars—robust automatic backbone assignment of proteins. *J. Biomol. NMR* **30**, 11–23 (2004).
47. Marsh, J. A., Singh, V. K., Jia, Z. & Forman-Kay, J. D. Sensitivity of secondary structure propensities to sequence differences between alpha- and gamma-synuclein: implications for fibrillation. *Protein Sci.* **15**, 2795–2804 (2006).
48. Farrow, N. A. et al. Backbone dynamics of a free and phosphopeptide-complexed Src homology 2 domain studied by  $^{15}\text{N}$  NMR relaxation. *Biochemistry* **33**, 5984–6003 (1994).
49. Vallurupalli, P., Bouvignies, G. & Kay, L. E. Studying ‘invisible’ excited protein states in slow exchange with a major state conformation. *J. Am. Chem. Soc.* **134**, 8148–8161 (2012).
50. Christou, N. E. & Brutscher, B. BEST and SOFAST experiments for resonance assignment of histidine and tyrosine side chains in  $^{13}\text{C}/^{15}\text{N}$  labeled proteins. *J. Biomol. NMR* **72**, 115–124 (2018).
51. Yamazaki, T., Forman-Kay, J. D. & Kay, L. E. Two-dimensional NMR experiments for correlating  $^{13}\text{C}\beta$  and  $^1\text{H}\delta/\epsilon$  chemical shifts of aromatic residues in  $^{13}\text{C}$ -labeled proteins via scalar couplings. *J. Am. Chem. Soc.* **115**, 11054–11055 (1993).
52. Miloushev, V. Z. & Palmer, A. G.  $R_{1\rho}$  relaxation for two-site chemical exchange: general approximations and some exact solutions. *J. Magn. Reson.* **177**, 221–227 (2005).
53. Madeira, F. et al. The EMBL-EBI search and sequence analysis tools APIs in 2019. *Nucleic Acids Res.* **47**, W636–W641 (2019).
54. Metsalu, T. & Vilo, J. ClustVis: a web tool for visualizing clustering of multivariate data using principal component analysis and heatmap. *Nucleic Acids Res.* **43**, W566–W570 (2015).
55. Dar, I., Bonny, C., Pedersen, J. T., Gajhede, M. & Kristensen, O. Crystallization and preliminary crystallographic characterization of an SH3 domain from the IB1 scaffold protein. *Acta Crystallogr. D* **59**, 2300–2302 (2003).
56. Gabadinho, J. et al. MxCuBE: a synchrotron beamline control environment customized for macromolecular crystallography experiments. *J. Synchrotron Radiat.* **17**, 700–707 (2010).

57. Oscarsson, M. et al. MXCuBE2: the dawn of MXCuBE collaboration. *J. Synchrotron Radiat.* **26**, 393–405 (2019).
58. Svensson, O., Malbet-Monaco, S., Popov, A., Nurizzo, D. & Bowler, M. W. Fully automatic characterization and data collection from crystals of biological macromolecules. *Acta Crystallogr. D* **71**, 1757–1767 (2015).
59. Kabsch, W. XDS. *Acta Crystallogr. D* **66**, 125–132 (2010).
60. Vonrhein, C. et al. Data processing and analysis with the autoPROC toolbox. *Acta Crystallogr. D* **67**, 293–302 (2011).
61. Monaco, S. et al. Automatic processing of macromolecular crystallography X-ray diffraction data at the ESRF. *J. Appl. Crystallogr.* **46**, 804–810 (2013).
62. Evans, P. R. An introduction to data reduction: space-group determination, scaling and intensity statistics. *Acta Crystallogr. D* **67**, 282–292 (2011).
63. Evans, P. R. & Murshudov, G. N. How good are my data and what is the resolution? *Acta Crystallogr. D* **69**, 1204–1214 (2013).
64. McCoy, A. J. et al. Phaser crystallographic software. *J. Appl. Crystallogr.* **40**, 658–674 (2007).
65. Emsley, P., Lohkamp, B., Scott, W. G. & Cowtan, K. Features and development of Coot. *Acta Crystallogr. D* **66**, 486–501 (2010).
66. Murshudov, G. N. et al. REFMAC5 for the refinement of macromolecular crystal structures. *Acta Crystallogr. D* **67**, 355–367 (2011).
67. Winn, M. D. et al. Overview of the CCP4 suite and current developments. *Acta Crystallogr. D* **67**, 235–242 (2011).
68. Morin, A. et al. Collaboration gets the most out of software. *eLife* **2**, e01456 (2013).
69. Pettersen, E. F. et al. UCSF Chimera—a visualization system for exploratory research and analysis. *J. Comput. Chem.* **25**, 1605–1612 (2004).
70. Wagner, J. R. et al. POVME 3.0: software for mapping binding pocket flexibility. *J. Chem. Theory Comput.* **13**, 4584–4592 (2017).
71. Harvey, M. J., Giupponi, G. & Fabritiis, G. D. ACEMD: accelerating biomolecular dynamics in the microsecond time scale. *J. Chem. Theory Comput.*

**5**, 1632–1639 (2009).

72. Huang, J. et al. CHARMM36m: an improved force field for folded and intrinsically disordered proteins. *Nat. Methods* **14**, 71–73 (2017).
73. Humphrey, W., Dalke, A. & Schulten, K. VMD: visual molecular dynamics. *J. Mol. Graph.* **14**, 27–28 (1996).
74. Michaud-Agrawal, N., Denning, E. J., Woolf, T. B. & Beckstein, O. MDAnalysis: a toolkit for the analysis of molecular dynamics simulations. *J. Comput. Chem.* **32**, 2319–2327 (2011).
75. Dosset, P., Hus, J. C., Blackledge, M. & Marion, D. Efficient analysis of macromolecular rotational diffusion from heteronuclear relaxation data. *J. Biomol. NMR* **16**, 23–28 (2000).
76. Krissinel, E. & Henrick, K. Inference of macromolecular assemblies from crystalline state. *J. Mol. Biol.* **372**, 774–797 (2007).

## Acknowledgements

We thank W. Adamski, S. Milles and T. Herrmann for discussions. We acknowledge the platforms of the Grenoble Instruct European Research Infrastructure Consortium (Integrated Structural Biology Grenoble; UAR 3518 CNRS-CEA-UGA-EMBL) within the Grenoble Partnership for Structural Biology. Platform access was supported by French Infrastructure for Integrated Structural Biology (ANR-10-INBS-05-02) and the Grenoble Alliance for Integrated Structural and Cell Biology, a project of the University Grenoble Alpes graduate school (Ecole Universitaire de Recherche) CBH-EUR-GS (ANR-17-EURE-0003). The Institut de Biologie Structurale acknowledges integration into the Interdisciplinary Research Institute of Grenoble. The authors thank the Diamond Light Source and the European Synchrotron Radiation Facility for beamtime access and technical support. This work was funded by the Fondation pour la Recherche Medicale through a postdoctoral fellowship to L.M.P. (contract SPF201909009258) and by a PhD fellowship to J.K. from the IDPbyNMR Marie Curie action of the European commission (contract no. 264257). Funding is also acknowledged from the Agence National de la Recherche (ANR) through ANR T-ERC MAPKassembly (to M.R.J.), ANR ScaffoldDisorder (to M.R.J. and A.P.) and ANR JCJC RC18114CC NovoTargetParasite (to A.P.).

## Author information

Author notes

## 1. Jaka Kragelj

Present address: Department of Biophysics, University of Texas Southwestern Medical Center, Dallas, TX, USA

## Affiliations

### 1. Université Grenoble Alpes, CEA, CNRS, IBS, Grenoble, France

Laura Mariño Pérez, Luiza M. Bessa, Damien Maurin, Jaka Kragelj, Martin Blackledge, Nicola Salvi & Malene Ringkjøbing Jensen

### 2. Departament de Química, Universitat de les Illes Balears, Palma de Mallorca, Spain

Laura Mariño Pérez

### 3. Institute for Advanced Biosciences (IAB), Structural Biology of Novel Targets in Human Diseases, INSERM U1209, CNRS UMR5309, Université Grenoble Alpes, Grenoble, France

Francesco S. Ielasi & Andrés Palencia

### 4. Laboratoire des Biomolécules (LBM), Département de Chimie, École normale supérieure, PSL University, Sorbonne Université, CNRS, Paris, France

Guillaume Bouvignies

## Contributions

L.M.P., M.R.J. and A.P. conceived the study. L.M.P., L.M.B., D.M. and J.K. made samples. L.M.B. and A.P. solved the structures of the POSH SH3 domains. L.M.P., F.S.I. and A.P. solved the structures of JIP1-SH3 and its variants. L.M.P., J.K. and M.R.J. designed and performed all NMR experiments. L.M.P., G.B. and M.R.J. analysed and interpreted the NMR data. M.B. and N.S. performed and analysed the MD simulation. M.R.J. and A.P. wrote the paper with input from all authors.

## Corresponding authors

Correspondence to [Andrés Palencia](#) or [Malene Ringkjøbing Jensen](#).

## Ethics declarations

## Competing interests

The authors declare no competing interests.

## Peer review

### Peer review information

*Nature* thanks Hashim Al-Hashimi and the other, anonymous, reviewers for their contribution to the peer review of this work. Peer reviewer reports are available.

## Additional information

**Publisher's note** Springer Nature remains neutral with regard to jurisdictional claims in published maps and institutional affiliations.

## Extended data figures and tables

### [Extended Data Fig. 1 Structural propensities and conformational exchange in JIP1-SH3.](#)

**a**,  $^1\text{H}$ - $^{15}\text{N}$  HSQC spectrum of JIP1-SH3 at 25 °C with labels indicating assignments. Horizontal lines connect side chain resonances. **b**, Secondary structure propensities of JIP1-SH3 calculated from experimental  $^{13}\text{C}\alpha$  and  $^{13}\text{C}\beta$  chemical shifts at 25 °C. The position of secondary structure elements is indicated, as observed in the crystal structure of JIP1-SH3 (PDB: 2FPE). **c**, Differential scanning fluorimetry (DSF) melting curve for JIP1-SH3 (RFU – relative fluorescence unit). **d**, Conformational exchange contributions,  $R_{\text{EX}}$ , extracted from  $^{15}\text{N}$  CPMG relaxation dispersion data acquired at 15 °C of JIP1-SH3 (blue – 850 MHz, red – 600 MHz) and JIP1-SH3(Y526A) (orange – 700 MHz) as the difference between  $R_{2\text{eff}}$  at low (31 Hz) and high (1 kHz) CPMG frequencies. **e**, Exchange contributions,  $R_{\text{EX}}$ , extracted from  $^1\text{H}^{\text{N}}$  CPMG relaxation dispersion data acquired at 15 °C of JIP1-SH3 (blue – 950 MHz, red – 600 MHz) and JIP1-SH3(Y526A) (orange – 600 MHz) as the difference between  $R_{2\text{eff}}$  at low (50 Hz) and high (2 kHz) CPMG frequencies. **f**, Structure of the dimeric SH3 domain of JIP1 with Y526 shown in cyan. Residues with exchange contributions ( $^{15}\text{N }R_{\text{EX}} > 3 \text{ s}^{-1}$  and  $^1\text{H}^{\text{N}} R_{\text{EX}} > 10 \text{ s}^{-1}$ ) are shown as spheres with colours indicating their position in the primary sequence (region 1 – green, region 2 – red, region 3 – blue). The residues showing  $^{15}\text{N}$  and  $^1\text{H}^{\text{N}}$  exchange contributions are represented separately on each monomer.

## Extended Data Fig. 2 Lipari–Szabo model-free analysis of $^{15}\text{N}$ relaxation data of JIP1-SH3.

**a**, Region of the  $^1\text{H}$ - $^{15}\text{N}$  HSQC spectrum of JIP1-SH3 at temperatures ranging from 5 to 46 °C. **b**, Experimental  $^{15}\text{N} R_2$  (CPMG) relaxation rates at a  $^1\text{H}$  frequency of 600 MHz and four different temperatures. **c**, Experimental  $^{15}\text{N} R_1$  relaxation rates at a  $^1\text{H}$  frequency of 600 MHz and four different temperatures. **d**, Experimental  $\{^1\text{H}\}$ - $^{15}\text{N}$  heteronuclear NOEs acquired at a  $^1\text{H}$  frequency of 600 MHz and 25 °C. Error bars in **b–d** represent one standard deviation (s.d.) derived from Monte Carlo simulations of experimental uncertainty. **e**, A model-free analysis of  $^{15}\text{N} R_1$ ,  $R_2$  and heteronuclear NOEs at 25 °C was carried out providing an axially symmetric diffusion tensor (Supplementary Discussion). The diffusion tensor is represented relative to the dimeric structure of JIP1-SH3. Distributions of axis orientations are shown as red dots and were determined from Monte Carlo simulations using Tensor2<sup>75</sup>. **f**, Angular dependence of the  $R_2/R_1$  ratios relative to the main axis of the diffusion tensor of JIP1-SH3. Only residues without exchange contributions to the transverse relaxation and for which the  $\{^1\text{H}\}$ - $^{15}\text{N}$  NOE is above 0.7 were included in the analysis. Error bars are centred at experimental values and were propagated from the experimental uncertainty on  $R_2$  and  $R_1$ . Orange squares are back-calculated values using the optimal tensor. **g**, Order parameters,  $S^2$ , derived from the model-free analysis of the relaxation data at 25 °C. Error bars represent one standard deviation (s.d.) derived from Monte Carlo simulations as implemented in Tensor2. **h**, Conformational exchange contributions,  $R_{\text{EX}}$ , derived from the model-free analysis of the relaxation data at 25 °C. Green bars indicate residues that are located in the dimer interface of the SH3 domain as detected by the PISA server<sup>76</sup>.

## Extended Data Fig. 3 Structure and dynamics of the Y526A variant of JIP1-SH3.

**a**, Comparison of the crystal structure of JIP1-SH3(Y526A) (green) with the WT structure (grey) showing an almost identical backbone conformation of the two proteins. The zoom highlights a minor structural difference at the level of the side chain of Q520 which reorients in the variant to take up the position normally occupied by Y526 in the WT protein. **b**, Superposition of  $^1\text{H}$ - $^{15}\text{N}$  HSQC spectra of JIP1-SH3(Y526A) (red) and JIP1-SH3(WT) (blue) acquired at 25 °C. **c**, Comparison of dihedral angles in JIP1-SH3(WT) (grey spheres) and JIP1-SH3(Y526A) (red lines). Dashed lines correspond to the backbone  $\phi$  angle and full drawn lines to the backbone  $\psi$  angle. **d**, Conformational exchange contributions,  $R_{\text{EX}}$ , extracted from  $^{15}\text{N}$  CPMG relaxation dispersion data as the difference between  $R_{2\text{eff}}$  at low (31 Hz) and high (1

kHz) CPMG frequencies. The exchange contributions are compared for WT JIP1-SH3 (grey, at 600 MHz) and the Y526A variant (red, at 700 MHz). **e**, Conformational exchange contributions,  $R_{\text{EX}}$ , extracted from  $^1\text{H}^{\text{N}}$  CPMG relaxation dispersion data as the difference between  $R_{2\text{eff}}$  at low (50 Hz) and high (2 kHz) CPMG frequencies. The exchange contributions are compared for the WT JIP1-SH3 (grey, at 600 MHz) and the Y526A variant (red, at 600 MHz). **f–i**, Chemical shift differences between the Y526A variant and WT JIP1-SH3 for  $^1\text{H}^{\text{N}}$  (**f**),  $^{15}\text{N}$  (**g**),  $^{13}\text{C}\alpha$  (**h**) and  $^{13}\text{C}\beta$  (**i**).

**Extended Data Fig. 4 Analysis of  $^{15}\text{N}$  and  $^1\text{H}^{\text{N}}$  relaxation dispersion data of JIP1-SH3.**

**a**, Examples of  $^{15}\text{N}$  CPMG relaxation dispersion profiles for JIP1-SH3 obtained at two magnetic field strengths (red – 600 MHz, blue – 850 MHz) at 15 °C. **b**, Examples of  $^1\text{H}^{\text{N}}$  CPMG relaxation dispersion profiles for JIP1-SH3 obtained at two magnetic field strengths (red – 600 MHz, blue – 950 MHz) at 15 °C. The  $^{15}\text{N}$  and  $^1\text{H}^{\text{N}}$  data were analysed simultaneously for all residues according to a two-site exchange model (full-drawn lines in **a** and **b**). Error bars in **a** and **b** represent one standard deviation (s.d.) derived from Monte Carlo simulations of experimental uncertainty. **c**, **d**, Chemical shift differences between the major and minor state extracted from a simultaneous analysis of the relaxation dispersion data at 15 °C for  $^{15}\text{N}$  (**c**) and  $^1\text{H}^{\text{N}}$  (**d**).

**Extended Data Fig. 5 Analysis of the sequence composition of 320 human SH3 domains.**

**a**, Distribution of amino acid types at the position of Y526 of JIP1-SH3 following a sequence alignment of all 320 SH3 domains. **b**, Sequence alignment of all identified SH3 domains carrying either a phenylalanine (F) or tyrosine (Y) at the position of Y526 in JIP1-SH3. For each sequence the PCA group is indicated along with the PDB code and resolution of available crystal structures. **c**, Pie charts showing the distribution of amino acid types in the different SH3 domains at positions corresponding to residue 493, 517, 520 and 541 in JIP1-SH3. The pie charts are colour-coded according to the size score assigned to each amino acid type corresponding to the number of heavy atoms in their side chains (see online [Methods](#)). **d**, Illustration of the backbone conformation of the β-sheet formed between the 516–521 and 524–529 regions in SH3 domains with tyrosine or phenylalanine at position 526. The β-bulge conformation observed in WT JIP1-SH3 is observed in all SH3 domains for which high-resolution crystal structures are available.

**Extended Data Fig. 6 Comparison of the structures of JIP1-SH3 and different variants.**

**a**, Comparison of the crystal structures of JIP1-SH3(WT) (grey) and its V517L variant (green). The backbone conformation is entirely conserved with only minor rearrangements of protein side chains. **b**, Comparison of the crystal structures of the H493A (grey) and V517A (green) variants of JIP1-SH3. Structural features are conserved including similar side chain conformations. **c**, Comparison of the crystal structures of JIP1-SH3(WT) (grey) and its A541L variant (green) with arrows indicating the major conformational rearrangements between the WT protein and the variant. **d**, Illustration of the backbone conformation of the  $\beta$ -sheet formed between the 516–521 and 524–529 regions in the WT protein (left), and in the A541L variant (right). Dashed lines indicate hydrogen bonds. The A541L variant does not adopt a  $\beta$ -sheet conformation owing to the absence of several hydrogen bonds between the two  $\beta$ -strands. **e**, Schematic representation of the conformation of the  $\beta$ -strand encompassing residues 516 to 521 showing the orientation of the carbonyl group (“out” – carbonyl group surface exposed, “in” – carbonyl group pointing towards the  $\beta$ -strand encompassing residues 524 to 529) in the WT protein (left) and in the A541L variant (right). **f**, Volume of the Y526 pocket along the structural trajectory between the WT conformation and the conformations of the H493A/V517A mutants (grey) or A541L mutant (green). Conformations from the two structural trajectories at the maximum pocket volume are superimposed and shown in cartoon representation. The initial pocket expansion and its associated structural features are shared among all mutants.

### Extended Data Fig. 7 Analysis of CPMG relaxation dispersion data of the H493A variant of JIP1-SH3.

**a**, Region of the  $^1\text{H}$ – $^{15}\text{N}$  HSQC of the H493A variant at three different temperatures (green - 15 °C, blue - 25 °C and red - 35 °C). **b**, Conformational exchange contributions,  $R_{\text{EX}}$ , extracted from  $^{15}\text{N}$  CPMG relaxation dispersion data of the H493A variant as the difference between  $R_{2\text{eff}}$  at low (31 Hz) and high (1 kHz) CPMG frequencies (600 MHz and 15 °C). **c**, Conformational exchange contributions,  $R_{\text{EX}}$ , extracted from  $^1\text{H}^{\text{N}}$  CPMG relaxation dispersion data of the H493A variant as the difference between  $R_{2\text{eff}}$  at low (50 Hz) and high (2 kHz) CPMG frequencies (600 MHz and 15 °C). **d**, **e**, Examples of  $^{15}\text{N}$  (**d**) and  $^1\text{H}^{\text{N}}$  (**e**) CPMG relaxation dispersion profiles of the H493A variant of JIP1-SH3 obtained at two magnetic field strengths (red – 600 MHz, blue – 950 MHz) at 15 °C. The  $^{15}\text{N}$  and  $^1\text{H}^{\text{N}}$  data were analysed simultaneously for all residues according to a two-site exchange model (full-drawn lines in **d** and **e**) using a population of the minor state fixed to 10%. Error bars represent one standard deviation (s.d.) derived from Monte Carlo simulations of experimental uncertainty. **f**, **g**, Comparison of the chemical shift differences between the major and minor state extracted from relaxation dispersion experiments for WT

JIP1-SH3 (red) and its H493A variant (blue). Data are shown for both  $^{15}\text{N}$  (f) and  $^1\text{H}^{\text{N}}$  (g) chemical shifts.

**Extended Data Fig. 8 Analysis of CPMG relaxation dispersion data of the V517A variant of JIP1-SH3.**

**a**, Region of the  $^1\text{H}-^{15}\text{N}$  HSQC of the V517A variant at three different temperatures (green - 15 °C, blue - 25 °C and red - 35 °C). **b**, Conformational exchange contributions,  $R_{\text{EX}}$ , extracted from  $^{15}\text{N}$  CPMG relaxation dispersion data of the V517A variant as the difference between  $R_{2\text{eff}}$  at low (31 Hz) and high (1 kHz) CPMG frequencies (600 MHz and 15 °C). **c**, Conformational exchange contributions,  $R_{\text{EX}}$ , extracted from  $^1\text{H}^{\text{N}}$  CPMG relaxation dispersion data of the V517A variant as the difference between  $R_{2\text{eff}}$  at low (50 Hz) and high (2 kHz) CPMG frequencies (600 MHz and 15 °C). **d, e**, Examples of  $^{15}\text{N}$  (**d**) and  $^1\text{H}^{\text{N}}$  (**e**) CPMG relaxation dispersion profiles of the V517A variant of JIP1-SH3 obtained at two magnetic field strengths (red – 600 MHz, blue – 950 MHz) at 15 °C. The  $^{15}\text{N}$  and  $^1\text{H}^{\text{N}}$  data were analysed simultaneously for all residues according to a two-site exchange model (full-drawn lines in **d** and **e**) using a population of the minor state fixed to 11%. Error bars represent one standard deviation (s.d.) derived from Monte Carlo simulations of experimental uncertainty. **f, g**, Comparison of the chemical shift differences between the major and minor state extracted from relaxation dispersion experiments for WT JIP1-SH3 (red) and its V517A variant (blue). Data are shown for both  $^{15}\text{N}$  (**f**) and  $^1\text{H}^{\text{N}}$  (**g**) chemical shifts.

**Extended Data Fig. 9 The A541L variant does not capture the structural details of the minor state detected by CPMG relaxation dispersion in JIP1-SH3.**

**a**, Superposition of  $^1\text{H}-^{15}\text{N}$  HSQC spectra of JIP1-SH3(A541L) (red) and WT JIP1-SH3 (blue) acquired at 15 °C. **b**, Conformational exchange contributions,  $R_{\text{EX}}$ , extracted from  $^{15}\text{N}$  CPMG relaxation dispersion data of the A541L variant as the difference between  $R_{2\text{eff}}$  at low (31 Hz) and high (1 kHz) CPMG frequencies at 700 MHz and 15 °C. Only modest  $^{15}\text{N}$  conformational exchange contributions are observed suggesting that this variant is populating a single conformation in solution represented by the determined crystal structure. **c, d**, Comparison of the chemical shift differences between the major and minor states extracted from relaxation dispersion experiments of WT JIP1-SH3 (blue) and the chemical shift differences between the observed chemical shifts of the A541L variant and WT JIP1-SH3 (red). Data are shown for  $^{15}\text{N}$  (**c**) and for  $^1\text{H}^{\text{N}}$  (**d**) nuclei. The poor agreement between the two

datasets show that the A541L crystal structure is not representative of the conformation of the minor state detected by NMR relaxation dispersion. **e**, **f**, Chemical shift differences between the A541L variant and WT JIP1-SH3 for  $^{13}\text{C}\alpha$  (**e**) and  $^{13}\text{C}\beta$  (**f**).

### **Extended Data Fig. 10 The aromatic ring of Y526 undergoes fast flipping.**

**a**,  $^1\text{H}$ - $^{13}\text{C}$  HSQC spectra of JIP1-SH3 showing the region of tyrosine epsilon correlations. A sample of JIP1-SH3 site-selectively labelled at the epsilon positions was used, and spectra at four different temperatures were acquired in the range from 5 to 45 °C. **b**, Per-residue root-mean square fluctuation (RMSF) of  $\text{C}\alpha$  atoms during the MD simulation. **c**, Residue-specific Ramachandran plots showing the conformational sampling of  $\beta$ -strand residues during the MD simulation. The MD values are colour-coded from white to black according to simulation time. Blue regions indicate the allowed and marginally allowed regions. Red points indicate the starting conformation (one for each monomer of JIP1-SH3). Panels **b** and **c** demonstrate that the protein maintains a stable conformation throughout the MD simulation, while displaying several 180° ring flipping events of Y526 (Fig. [4d](#)).

**Extended Data Table 1 Data collection and refinement statistics for the JIP1-SH3 structures**

**Extended Data Table 2 Data collection and refinement statistics for the JIP1-SH3 and POSH-SH3 structures**

## **Supplementary information**

### **Supplementary Information**

This file contains the Supplementary Discussion (sections 1–3), Supplementary Fig. 1 and Supplementary Table 1.

### **Reporting Summary**

### **Peer Review File**

### **Supplementary Video 1**

Structural rearrangements associated with the transition between the major and minor state of JIP1-SH3. The animation shows how the major state of Y526 is stabilized by CH- $\pi$  interactions from V517, Q520 and A541 and  $\pi$ - $\pi$  interactions from H493. The

transition to the minor state is associated with major structural rearrangements in the region encompassing residues 517 to 522. In particular, a classic  $\beta$ -bulge conformation is observed at residue 518 in the major state, which transitions to a canonical  $\beta$ -strand in the minor state. The video shows how these structural changes allow L519 to stabilize the ring of Y526 through CH– $\pi$  interactions in the minor state.

## **Supplementary Video 2**

Protein breathing motions generate a void volume around Y526 allowing fast ring flipping. The animation (surface representation) shows how a substantial void volume is generated around the tyrosine ring of Y526 through protein breathing motions along the structural trajectory from the major to the minor state. This cavity expansion allows fast time-scale ring flipping events of Y526 before closing the pocket of Y526.

## **Rights and permissions**

**Open Access** This article is licensed under a Creative Commons Attribution 4.0 International License, which permits use, sharing, adaptation, distribution and reproduction in any medium or format, as long as you give appropriate credit to the original author(s) and the source, provide a link to the Creative Commons license, and indicate if changes were made. The images or other third party material in this article are included in the article's Creative Commons license, unless indicated otherwise in a credit line to the material. If material is not included in the article's Creative Commons license and your intended use is not permitted by statutory regulation or exceeds the permitted use, you will need to obtain permission directly from the copyright holder. To view a copy of this license, visit <http://creativecommons.org/licenses/by/4.0/>.

## Reprints and Permissions

## **About this article**

### **Cite this article**

Mariño Pérez, L., Ielasi, F.S., Bessa, L.M. *et al.* Visualizing protein breathing motions associated with aromatic ring flipping. *Nature* **602**, 695–700 (2022).  
<https://doi.org/10.1038/s41586-022-04417-6>

- Received: 30 April 2021
- Accepted: 07 January 2022
- Published: 16 February 2022

- Issue Date: 24 February 2022
- DOI: <https://doi.org/10.1038/s41586-022-04417-6>

## Share this article

Anyone you share the following link with will be able to read this content:

[Get shareable link](#)

Sorry, a shareable link is not currently available for this article.

[Copy to clipboard](#)

Provided by the Springer Nature SharedIt content-sharing initiative

---

This article was downloaded by **calibre** from <https://www.nature.com/articles/s41586-022-04417-6>

| [Section menu](#) | [Main menu](#) |

- Article
- Open Access
- [Published: 16 February 2022](#)

# Mechanism-based traps enable protease and hydrolase substrate discovery

- [Shan Tang](#) [ORCID: orcid.org/0000-0003-4483-1108<sup>1</sup>](#),
- [Adam T. Beattie<sup>1</sup>](#),
- [Lucie Kafkova<sup>2</sup>](#),
- [Gianluca Petris](#) [ORCID: orcid.org/0000-0002-2420-6359<sup>1</sup>](#),
- [Nicolas Huguenin-Dezot](#) [ORCID: orcid.org/0000-0001-8816-2159<sup>1</sup>](#),
- [Marc Fiedler](#) [ORCID: orcid.org/0000-0003-4269-7873<sup>1</sup>](#),
- [Matthew Freeman](#) [ORCID: orcid.org/0000-0003-0410-5451<sup>2</sup>](#) &
- [Jason W. Chin](#) [ORCID: orcid.org/0000-0003-1219-4757<sup>1</sup>](#)

[Nature](#) volume 602, pages 701–707 (2022)

- 7792 Accesses
- 61 Altmetric
- [Metrics details](#)

## Subjects

- [Chemical tools](#)
- [Enzymes](#)

## Abstract

Hydrolase enzymes, including proteases, are encoded by 2–3% of the genes in the human genome and 14% of these enzymes are active drug targets<sup>1</sup>. However, the activities and substrate specificities of many proteases—especially those embedded in membranes—and other hydrolases remain unknown. Here we report a strategy for creating mechanism-based, light-activated protease and hydrolase substrate traps in complex mixtures and live mammalian cells. The traps capture substrates of

hydrolases, which normally use a serine or cysteine nucleophile. Replacing the catalytic nucleophile with genetically encoded 2,3-diaminopropionic acid allows the first step reaction to form an acyl-enzyme intermediate in which a substrate fragment is covalently linked to the enzyme through a stable amide bond<sup>2</sup>; this enables stringent purification and identification of substrates. We identify new substrates for proteases, including an intramembrane mammalian rhomboid protease RHBDL4 (refs. <sup>3,4</sup>). We demonstrate that RHBDL4 can shed luminal fragments of endoplasmic reticulum-resident type I transmembrane proteins to the extracellular space, as well as promoting non-canonical secretion of endogenous soluble endoplasmic reticulum-resident chaperones. We also discover that the putative serine hydrolase retinoblastoma binding protein 9 (ref. <sup>5</sup>) is an aminopeptidase with a preference for removing aromatic amino acids in human cells. Our results exemplify a powerful paradigm for identifying the substrates and activities of hydrolase enzymes.

[Download PDF](#)

## Main

Activity-based probes have confirmed the presence and selective reactivity of the catalytic serine or cysteine nucleophile for many hydrolase proteins in cells<sup>6,7,8</sup>. Efforts to define hydrolase specificity have captured non-covalent interactors with hydrolases and investigated the substrates that accumulate in the absence of a hydrolase or the products that accumulate in the presence of a hydrolase<sup>9</sup>. Current approaches to identifying protease substrates mostly aim to either co-immunoprecipitate substrates that are non-covalently bound to catalytically inactive protease variants<sup>10,11,12</sup>, or identify the peptides resulting from the action of the protease from experiments with and without the protease<sup>13,14,15</sup>. In the first approach, substrates may be lost in the washing steps, and bound proteins may not be substrates. The second approach typically underestimates the number of substrates, and the cleavages identified may be indirect<sup>16,17</sup>. The identification of intramembrane protease substrates by current approaches is particularly challenging<sup>18,19</sup>. The methodological challenges in defining hydrolase and protease specificity mean that the substrates of many proteases remain unknown or incomplete, and many hydrolases remain orphans—with unknown substrates and uncharacterized specificity.

We previously demonstrated the genetically encoded, site-specific incorporation of photocaged Dap ((2S)-2-amino-3-{{(2-{{[1-(6-nitrobenzo[d][1,3]dioxol-5-yl)ethyl]thio}ethoxy)carbonyl]amino}propanoic acid) (pc-Dap) into proteins expressed in *Escherichia coli*<sup>2,20</sup>. We converted pc-Dap to Dap (2,3-diaminopropionic acid) in proteins in vitro by illuminating purified proteins followed by incubation for up to 2 days at pH 8. By incubating purified proteases or thioesterases—in which we had

replaced the catalytic cysteine or serine with Dap—with known substrates, we captured the otherwise transient thioester or ester intermediates—resulting from the first step of the reaction of these enzymes with their substrates—as their stable amide analogues. We demonstrated the utility of this approach for structural studies of acyl-enzyme intermediates<sup>2</sup>.

Here we demonstrate that genetically encoded pc-Dap coupled to mass spectrometry provides a powerful approach for discovering hydrolase substrates in complex mixtures and in live mammalian cells (Extended Data Fig. 1). We first demonstrate that recombinant proteases containing Dap in place of their catalytic nucleophile can be used to covalently link the N-terminal fragment of substrates to the protease, via a stable amide bond, in cell lysates. Through stringent purification of substrates linked to high-temperature requirement protein A2 (HtrA2) protease in combination with a mass spectrometry workflow we identify more than 200 new substrates for this protease. We then demonstrate that pc-Dap can be genetically encoded into proteins in mammalian cells. Illumination effects the rapid, post-translational conversion of pc-Dap to Dap in live cells and enables the specific covalent capture of the N-terminal fragments of protease substrates in cells. We identify new substrates for the mammalian rhomboid protease RHBDL4, an intramembrane protease that resides in the endoplasmic reticulum (ER). Our results demonstrate that RHBDL4 can shed luminal fragments of type I transmembrane proteins to the extracellular space. Upon removal of the ER retention motif, RHBDL4 promotes the secretion of a wide range of ER chaperones from cells. Finally, we develop a pipeline to directly identify the branched peptides formed between a substrate fragment and Dap and thereby reveal that the putative serine hydrolase retinoblastoma binding protein 9 (RBBP9) is an aminopeptidase with a preference for removing aromatic amino acids in mammalian cells.

## Trapping substrates in complex mixtures

We demonstrated that recombinant Tobacco etch virus (TEV) protease containing Dap in place of its catalytic cysteine (TEV(C151Dap)) formed a specific conjugate with GFP with a TEV protease cleavage site appended at its C-terminus (GFP-s) when the two proteins were incubated together in human cell lysate (Extended Data Fig. 2). Although GFP-s was present in the lysate at comparable levels to many other proteins, TEV(C151Dap) formed a specific conjugate, observed by immunoblotting, with its substrate partner and not with any other proteins in the lysate. Control experiments demonstrated that conjugate formation was dependent on both the presence of Dap in the protease and the presence of the TEV cleavage site in the substrate. Replacing the catalytic cysteine of other proteases (UL36<sup>USP</sup> and SCoV2-PLpro) with Dap also led to the selective capture of their known substrates (Extended Data Fig. 3). We conclude

that replacing the active site nucleophile with Dap allows the specific covalent capture of substrates.

## Profiling HtrA2 substrates

Next, we demonstrated the utility of Dap-containing proteases for the capture and identification of protease substrates from cell lysate. We focussed on the mature cytosolic form of HtrA2, which is released from the mitochondrial intermembrane space and relocated to the cytosol upon stress<sup>21,22</sup>. Several substrates have been identified for cytosolic HtrA2, including caspase inhibitors<sup>21</sup> (for example, XIAP and cIAP1/2). HtrA2 contains a PDZ domain and chymotrypsin-like protease domain; since PDZ domains bind a wide range of proteins and chymotrypsin-like domains commonly have broad specificity<sup>23</sup>, we hypothesized that there may be undiscovered substrates of HtrA2.

We replaced the catalytic serine of HtrA2 with Dap, creating HtrA2(S306Dap)–HA–Strep (Supplementary Fig. 2). We incubated this protein with human cell lysate and enriched covalent conjugates to the protease by immunoprecipitation followed by stringent washing. The conjugates were eluted and immunoblotting against the Strep-tag on Dap-containing HtrA2 revealed numerous species with a higher apparent molecular mass (Fig. 1a). These species were not observed in the control experiments and are primarily covalent conjugates to Dap-containing HtrA2.

**Fig. 1: Dap-mediated HtrA2 substrate identification in mammalian cell lysate.**

---

 **figure 1**

**a**, HtrA2(S306Dap)–HA–Strep and its conjugates were enriched from cell lysate with anti-HA beads and detected with an anti-Strep antibody. Control experiments were performed with wild-type (WT) HtrA2 and the catalytically inactive S306A mutant. Input: HtrA2 variants in cell lysates before incubation. **b**, Venn diagram showing the number of proteins identified in HtrA2(S306Dap) elution compared with controls. Proteins identified in at least two of the three replicates were considered as positively identified. **c**, Volcano plot based on label-free quantification (LFQ) values for the proteins identified in HtrA2(S306Dap) and wild-type HtrA2 samples. The black line represents the cut-off curve for significance ( $S_0 = 1$ , FDR < 0.01). Each data point is calculated in Perseus using  $n = 4$  for each HtrA2 variant. The dot representing ornithine aminotransferase (OAT) is labelled in red. **d**, Wild-type HtrA2 or HtrA2(S306A) (1  $\mu$ M) was added into Expi293 cell lysate and incubated for the indicated time at 37 °C. Red arrowhead, full-length OAT; blue arrowhead, wild-type HtrA2-dependent proteolytic fragments. GAPDH was used as a loading control. The experiment in **a** was performed in biological triplicate, and the experiment in **d** was performed in two biological replicates, both with similar results. For gel source data, see Supplementary Fig. 1.

Proteomic analysis identified 274 proteins that were specifically captured by HtrA2(S306Dap); 237 of these proteins were not found in control experiments (Fig. [1b](#), Supplementary Data File [1](#)) and 37 proteins were significantly enriched (minimum fold change ( $S_0$ ) = 1, false discovery rate (FDR) < 0.01) in the HtrA2(S306Dap) elution with respect to controls (Fig. [1c](#), Supplementary Fig. [2](#)). Our study identified 17 times more potential HtrA2 substrates than previous work, and this approach identified the majority of the proteins previously identified as HtrA2 substrates by N-terminal proteomics<sup>[24](#)</sup> (Supplementary Table [1](#)).

We tested 29 of the newly identified potential substrates for proteolysis with wild-type HtrA2. Eighty-six percent of the candidates showed a decrease in the abundance of full-length protein or the generation of defined proteolytic fragments over time upon addition of the wild-type protease (Fig. [1d](#), Supplementary Fig. [3](#), Supplementary Tables [2](#), [3](#)). Overall, our results demonstrate that we have developed an approach for the efficient and specific identification of protease substrates in complex mixtures.

**Fig. 2: Optical activation of a Protease(Dap) substrate trap in human cells.**

---

 **figure 2**

**a**, The mass of TEV(C151pc-Dap) before and after illumination of human cells expressing the protein. TEV containing pc-Dap was produced using the DapRS–tRNA<sub>CUA</sub> pair and a TEV gene bearing the amber codon (TAG) at position 151 in the presence of pc-Dap. The grey trace shows proteins purified before illumination. Fully protected TEV(C151pc-Dap) bearing an acetyl group ([Ac-TEV(C151pc-Dap)]: expected 39,245.4 Da, observed 39,244.4 Da). The blue trace shows proteins purified immediately after illumination of cells. The fully deprotected product ([Ac-TEV(C151Dap)]: expected 38,948.2 Da, observed 38,945.2 Da); the deprotection intermediate ([Ac-TEV(C151Dap<sub>inter</sub>)]: expected 39,052.2 Da, observed 39,054.0 Da). The brown trace shows proteins purified 6 h after illumination of cells. **b**, TEV variants and GFP-s were co-expressed in HEK293T cells for 48 h. Total lysate was analysed by anti-Strep (for TEV) and anti-GFP antibodies. Wild-type TEV

quantitatively cleaved GFP-s to GFP.  $\beta$ -Tubulin was used as a loading control. **c**, Detection of TEV(Dap)–GFP conjugate after Strep-tag enrichment. Samples, not illuminated (lane 4) or after UV illumination (lanes 1–3 and 5–10) were collected at indicated time points. Input, cell lysates before immunoprecipitation probed with anti-Strep and anti-GFP antibodies.  $\beta$ -Tubulin was used as a loading control. Experiments in **a–c** were performed in two biological replicates with similar results. For gel source data, see Supplementary Fig. 1.

## Trapping substrates in live human cells

Next, we set out to extend our approach to capturing and identifying protease substrates in human cells (Extended Data Fig. 4a). It was unclear—on the basis of previous work<sup>2</sup>—whether pc-Dap could be converted to Dap in live cells to activate protease substrate traps. We set out to: encode pc-Dap in human cells, investigate the activation of a protease substrate trap through deprotection of pc-Dap to Dap in human cells, and demonstrate the covalent capture of protease substrates in human cells.

We demonstrated the efficient, site-specific, genetically directed incorporation of pc-Dap into proteins in human cells (Supplementary Figs. 4, 5). We produced TEV protease in which the catalytic cysteine was replaced by pc-Dap (TEV(C151pc-Dap)) in human cells (Supplementary Fig. 6). To deprotect pc-Dap we illuminated cells<sup>25,26</sup> expressing TEV(C151pc-Dap) for 2 min. Mass spectrometry revealed that more than 60% of the TEV purified from cells immediately after illumination was fully deprotected to TEV(C151Dap); the remaining 40% of TEV contained the deprotection intermediate. Six hours after illumination, we detected only TEV(C151Dap) (Fig. 2a); this demonstrated that deprotection, from pc-Dap to Dap—to activate the protease substrate trap—proceeds rapidly in live cells.

To demonstrate that we can capture protease substrates in human cells, we co-expressed TEV(C151pc-Dap) and GFP-s (Fig. 2b). We illuminated HEK293T cells to generate TEV(C151Dap) and followed the formation of the TEV(Dap)–GFP conjugate in cells by immunoblotting (Fig. 2c, Supplementary Fig. 7). The conjugate was observed 30 min after illumination of cells and accumulated over time. We did not detect the conjugate by immunoblotting from cells expressing wild-type TEV, TEV(C151A) or cells expressing TEV(C151pc-Dap) before illumination. No other conjugates were observed, further confirming the specificity of the approach. Tandem mass spectrometry (MS/MS) explicitly demonstrated the formation of an amide bond between TEV(C151Dap) and GFP in cells (Supplementary Fig. 8). Additional experiments confirmed that replacing the catalytic residue with Dap in other cysteine proteases (UL36<sup>USP</sup> and SCoV2-PLpro) led to the covalent capture of their known substrates in human cells (Extended Data Fig. 4b, c). Overall, these experiments demonstrated that: pc-Dap can be site-specifically incorporated into soluble proteases

in human cells, protease substrate traps can be rapidly activated by illumination of human cells, and activated protease substrate traps can be used to specifically and covalently capture protease substrates in human cells.

## Trapping a model substrate of RHBDL4

Intramembrane proteases have diverse and important roles in biological regulation<sup>27,28</sup>. However, defining the physiological substrates of intramembrane proteases in mammalian cells has proved exceptionally challenging<sup>18,29,30</sup>. Rhomboid proteases are an important class of intramembrane protease that use a catalytic serine for catalysis<sup>31,32</sup>. We focused on RHBDL4, a rhomboid protease located in the ER membrane of mammalian cells, which has been associated with multiple cellular pathways<sup>4,12,33,34,35</sup>, and potentially Alzheimer disease pathology<sup>36</sup>. However, physiologically relevant substrates of RHBDL4 remain essentially unknown. We set out to: encode pc-Dap in place of the catalytic serine in RHBDL4, activate the rhomboid protease substrate trap by illuminating cells, and demonstrate the covalent capture and identification of substrates for RHBDL4.

We produced RHBDL4(S144pc-Dap) at a similar level to a wild-type control, and confirmed that the protein localized predominantly in the ER membrane (Supplementary Fig. 9), as expected<sup>4,35</sup>. We co-expressed a model substrate pT $\alpha$ , which is efficiently cleaved by wild-type RHBDL4 at multiple sites<sup>4</sup> (Extended Data Fig. 5a, b). We illuminated cells containing RHBDL4(S144pc-Dap) and pT $\alpha$  to activate the protease substrate trap and followed conjugate formation by immunoblot against the N-terminal Flag tag on pT $\alpha$  after affinity purification using the twin-Strep-tag on RHBDL4 (Extended Data Fig. 5c). We detected Dap-specific conjugates 15 min after illumination of cells expressing RHBDL4(S144pc-Dap); these conjugates rapidly accumulated within 4 h (Extended Data Fig. 5d, Supplementary Fig. 10). Overall, these experiments demonstrated that we can express and optically activate a protease substrate trap for RHBDL4, and that the trap efficiently captures its model substrate.

## Identifying RHBDL4 substrates

To identify RHBDL4 substrates, we illuminated human cells producing RHBDL4(S144pc-Dap). We collected the membrane fraction and purified the protease conjugates by Strep-tag affinity enrichment. Anti-Strep analysis of the affinity-enriched samples showed several bands of higher apparent molecular mass in the RHBDL4(S144Dap) experiments that were not observed in control experiments (Fig. 3a); this suggested that the Dap-containing protease had covalently captured RHBDL4 substrates.

**Fig. 3: Discovery of RHBDL4 substrates.**

 figure 3

**a**, RHBDL4 variants were expressed in Expi293 cells. Immunoblotting analysis of RHBDL4 variants enriched from an equal number of cells after optical activation and substrate capture. Ala, RHBDL4(S144A); Dap, RHBDL4(S144Dap). Red arrows, RHBDL4(S144Dap)-specific higher molecular mass bands. **b**, Venn diagram showing the number of proteins identified in RHBDL4(S144Dap) elution with respect to controls. Proteins found in at least two of the three replicates were considered to be positively identified. **c, d**, Volcano plots based on the LFQ values for the identified proteins for RHBDL4(S144Dap) versus wild-type RHBDL4 (**c**;  $S_0 = 1$ , FDR < 0.01) and RHBDL4(S144Dap) versus RHBDL4(S144A) (**d**;  $S_0 = 1.5$ , FDR < 0.05). Black lines represent the cut-off curve for significance. Each point was calculated in Perseus using  $n = 3$  for each RHBDL4 variant. ER-resident candidates are marked in red and select candidates are also labelled. **e**, RHBDL4 cleaves CCDC47. SP, signal peptide; V5, V5-tag; TMH, transmembrane helix; HA, HA-tag; red arrows, RHBDL4 cleavage sites; black circles, full-length CCDC47; blue triangles, N-terminal proteolytic fragments; red triangles, C-terminal proteolytic fragments; asterisk, bands present without RHBDL4. **f**, RHBDL4(S144Dap) conjugates to endogenous BiP and the cleavage of endogenous BiP by wild-type RHBDL4. Cell lysates before immunoprecipitation (input) and the conjugates were directly visualized by anti-BiP and anti-Strep antibodies after Strep-tag enrichment. Red arrow, the proteolytic fragment of endogenous BiP cleaved by wild-type RHBDL4. **g**, Cleaved BiP is secreted into the medium. The medium was separated into supernatant (SN) and microvesicles (MV). Red arrow, the proteolytic fragment. Whereas full-length BiP was detected by both anti-BiP and anti-KDEL antibodies, cleaved BiP can only be detected with an anti-BiP antibody. Asterisk indicates non-specific bands. Revert 700 total protein stain was used as a loading control. Experiments in **a, f**, were performed in biological triplicate; the experiment in **e** was repeated in three biological

replicates; the experiment in **g** was repeated in two biological replicates; all with similar results. For gel source data, see Supplementary Fig. [1](#).

Proteomic analysis identified 43 potential RHBDL4 substrates; 24 of these proteins were detected only in the RHBDL4(S144Dap) elution (Fig. [3b](#)) and 19 of them were significantly enriched in the RHBDL4(S144Dap) samples relative to controls (Fig. [3c](#), [d](#)). We note that proteins enriched or uniquely identified in both the RHBDL4(S144Dap) and RHBDL4(S144A) samples with respect to the wild-type control may also be substrates (Supplementary Data File [2](#)), but these were not investigated in our subsequent analysis. Twenty-five of the candidate substrates are ER-associated proteins, including 15 ER-resident proteins (5 of which are transmembrane proteins), 2 nuclear transmembrane proteins, and 8 proteins in secretory pathways (Supplementary Table [4](#)). We also identified non-ER-associated proteins, primarily nuclear proteins (Supplementary Fig. [11](#), Supplementary Note [1](#)). We investigated the RHBDL4-mediated cleavage of a subset of the ER-associated candidate substrates.

We first validated transmembrane protein candidates—the protein class that is conventionally considered as rhomboid protease substrates—using a cell-based rhomboid gain-of-function cleavage assay<sup>4</sup>. Over-expressed wild-type RHBDL4, but not the catalytically inactive S144A mutant, cleaved all tested transmembrane proteins identified by Dap conjugation (Fig. [3e](#), Extended Data Fig. [6a–c](#)). RHBDL4 cleaved CCDC47 (ref. [37](#)) at three positions in the luminal domain, and the ectodomains resulting from proteolysis were secreted into extracellular media (Fig. [3e](#) and Extended Data Fig. [6d, e](#)). In addition, endogenous CCDC47 was cleaved by exogenously expressed wild-type RHBDL4 (Extended Data Fig. [6f](#)). Our data collectively demonstrated that RHBDL4 can proteolyze the transmembrane proteins identified by our approach and, upon cleavage by RHBDL4, luminal fragments of CCDC47 are released into the extracellular medium.

Soluble proteins have not been reported as endogenous RHBDL4 substrates. However, a substantial percentage (67%) of the ER-resident proteins that we identified are soluble; the majority of these proteins (90%) are chaperones (Supplementary Table [4](#)). We therefore focussed on further investigating the cleavage of ER soluble chaperones by RHBDL4.

We identified binding immunoglobulin protein (BiP) (encoded by *HSPA5*) as a potential substrate using our approach (Fig. [3c, d](#)). We directly visualized the conjugates of RHBDL4(Dap) and endogenous BiP in human cells (Fig. [3f](#), Supplementary Fig. [12](#)). The RHBDL4 cleavage assay confirmed that BiP can be cleaved at its interdomain linker region and C-terminus by wild-type RHBDL4. The N-terminal fragments generated by these cleavages—which do not possess the ER retention motif<sup>38</sup> (KDEL sequence from the C-terminus of BiP)—were secreted

into the medium (Fig. 3g and Supplementary Fig. 13). Endogenous BiP was cleaved by exogenously expressed WT RHBDL4, and secretion of the proteolytic fragment into the medium was Brefeldin A (BFA) sensitive (Extended Data Fig. 7a), consistent with secretion by the conventional pathway. Importantly, the proteolytic fragment from endogenous BiP was detected in the extracellular medium from WT cells, but not from an RHBDL4 knockout cells (Extended Data Fig. 7b), confirming the cleavage of endogenous BiP by endogenous RHBDL4. Collectively, our data demonstrate that a fraction of the soluble BiP present in cells is a physiological substrate of endogenous RHBDL4.

RHBDL4-mediated removal of the C-terminal ER retention motif from soluble ER-resident protein candidates was also validated for protein disulfide-isomerases (protein disulfide-isomerase A6 (gene name: *PDIA6*) and ER protein 44 (gene name: *ERP44*) and calcium-binding chaperone Calreticulin (gene name: *CALR*), which were identified as potential substrates through our approach (Extended Data Fig. 8a–e). The secretion of proteolytic fragments of endogenous PDIA6 and Calreticulin was BFA sensitive (Extended Data Fig. 8f,g). The cleavage of a fraction of endogenous Calreticulin by endogenous RHBDL4 was detected in extracellular medium by an anti-Calreticulin antibody in wild-type but not in RHBDL4 knockout cells (Extended Data Fig. 8h).

Additional tests confirmed that RHBDL4 also cleaved other ER-resident soluble chaperones which were identified through our approach, including Calumenin, peptidyl-prolyl cis-trans isomerase FKBP9, Glucosidase 2 subunit  $\alpha$  and  $\beta$ ; in each case the cleavage led to secretion of the resulting N-terminal fragments into extracellular media (Supplementary Fig. 14). However, RHBDL4 did not cleave Calnexin, an abundant ER-resident chaperone, which was not identified as a potential substrate by our approach (Supplementary Figs. 12 and 14); this observation is consistent with our approach specifically capturing RHBDL4 substrates.

Collectively, our results demonstrate that we can capture and identify substrates for an intramembrane protease. Moreover, we have discovered that RHBDL4 can act as a non-canonical secretase. Unlike conventional secretases—which cleave transmembrane substrates in transmembrane domains or juxtamembrane domains to release ectodomains<sup>16,18</sup>—cleavage by RHBDL4 has the effect of removing the C-terminal ER-retention motif from a proportion of physiological substrate molecules, allowing the release of their N-terminal proteolytic fragments into the extracellular space.

## Determining enzymatic function of RBBP9

Many serine hydrolases have been defined on the basis of their reactivity with activity-based probes, but their enzymatic function remains unknown<sup>39</sup>. Defining the activity of these orphan hydrolases remains an outstanding challenge. We set out to address this challenge using Dap-mediated substrate trapping. We focussed on RBBP9, a tumour-associated putative serine hydrolase<sup>5</sup>. RBBP9 possesses a classical  $\alpha/\beta$  hydrolase superfamily fold<sup>40</sup>, and its hydrolase activity promoted tumour cell proliferation during pancreatic neoplasia<sup>41</sup>. Despite multiple efforts to characterize the cellular activity of RBBP9, its enzymatic function in cells has remained enigmatic.

Initial experiments suggested that RBBP9 is unlikely to function as an endopeptidase (Supplementary Fig. 15). We developed an approach to directly identify any entities (which we designated ‘X’), conjugated to RBBP9(S75Dap), in which the catalytic serine of RBBP9 has been replaced by Dap (Fig. 4a). We first expressed RBBP9(S75Dap) in human cells and enriched any conjugates that it formed (RBBP9(Dap75-X)) in the cells, digested with trypsin, then performed LC–MS/MS on the resulting peptide pool. We then developed a computational pipeline to search for the tryptic peptides of RBBP9 containing Dap and conjugated to X (Pept(Dap-X)), based on the prediction that they should have MS2 spectra related to the corresponding non-conjugated peptide (Pept(Dap)), in which certain fragmentation peaks are shifted by the mass of X (or the mass of a tryptic fragment of X) ( $mx$ ) (Fig. 4a,b).

**Fig. 4: Identifying RBBP9(Dap75) conjugates.**

 figure 4

**a**, The Dap-containing tryptic peptide sequence (Pept(Dap-X)) of RBBP9 with certain b and y ion masses of Pept(Dap) modified by  $mx$ . **b**, Pipeline to identify  $mx$  in live cells. RBBP9(Dap75-X) conjugates were affinity purified and trypsinized. The resulting peptide pool was analysed by LC–MS/MS and peptides with molecular mass no less than MS(Pept(Dap)) were individually selected for  $mx$  calculation (for

example, the blue peak represents Pept(Dap),  $mx = 0$ . The experimental MS2 peaks were compared to theoretical MS2 peaks for scoring as described in [Methods](#). In the example shown, the peaks are colour coded as b, y, b+ $mx$  or y+ $mx$  ions, using the colour scheme in **a**. **c**,  $mx$  obtained from the top-scoring spectra were plotted. Each dot represents the mass shift of the observed peptide relative to the parental peptide. +113 (Leu/Ile), +131 (Met), +147 (Phe), +163 (Tyr), +186 (Trp), +297 (pc-Dap), +42 and +77 (consistent with near cognate suppression of this amber codon in mammalian cells with Gln and Tyr, respectively). **d**, The entire mass of RBBP9 variants and Dap conjugates purified from human cells. Green trace (i): wild-type RBBP9 ([Ac-(RBBP9-Met)]): expected 23,995 Da, observed 23,994.5 Da); black trace (ii): RBBP9(S75A) ([Ac-(RBBP9(S75A)-Met)]): expected 23,979 Da, observed 23,978.5 Da); brown trace (iii): RBBP9(S75pc-Dap) before illumination ([Ac-(RBBP9(S75pc-Dap)-Met)]): expected 24,291 Da, observed 24,290.5 Da); purple dashed trace (iv): RBBP9(S75Dap) deprotected from RBBP9(S75pc-Dap) in vitro ([Ac-(RBBP9(S75Dap)-Met)]): expected 23,994 Da, observed 23,993.5 Da); multicolour trace (v): RBBP9(S75pc-Dap) purified from cells after illumination and substrate trapping for 3 h ([Ac-(RBBP9(S75Dap<sub>inter</sub>)-Met)]): expected 24,098 Da, observed 24,097 Da; [Ac-(RBBP9(Dap-L/I)-Met)]): expected 24,107 Da, observed 24,108 Da; [Ac-(RBBP9(Dap-F)-Met]): expected 24,141 Da, observed 24,140.5 Da; [Ac-(RBBP9(Dap-Y)-Met]): expected 24,157 Da, observed 24,156 Da; [Ac-(RBBP9(Dap-W)-Met]): expected 24,180 Da, observed 24,179 Da). The experiment in **c** was performed in biological triplicate. In **d**, the entire mass acquisition of trace (v) was performed in two biological replicates with similar results, the other traces were acquired once.

Our analysis revealed mass shifts of +113 Da, +131 Da, +147 Da, +163 Da and +186 Da, with respect to the mass of Pept(Dap) (Fig. [4c](#), Supplementary Fig. [16](#)). These masses correspond to the amino acids leucine/isoleucine (Leu/Ile), methionine (Met), phenylalanine (Phe), tyrosine (Tyr) or tryptophan (Trp), respectively, after condensation on Dap (Supplementary Fig. [17](#)). Additionally, we characterized the entire mass of RBBP9(Dap75-X) and further confirmed the conjugation of Leu/Ile, Phe, Tyr or Trp to RBBP9(S75Dap) (Fig. [4d](#)).

Collectively, we demonstrated that RBBP9(S75Dap) preferentially forms conjugates with individual hydrophobic amino acids. We conclude that RBBP9 is likely to cleave amide (or ester or thioester) bonds to these hydrophobic amino acids in human cells. Amino acid sequence analysis suggested that RBBP9 belongs to DUF1234 hydrolase superfamily<sup>[40](#)</sup>, which includes the acylpeptide hydrolase-like protein<sup>[42](#)</sup> from *Arabidopsis thaliana* (AHLP; Uniprot ID: Q9FG66); this protein possesses a similar  $\alpha/\beta$  hydrolase fold to RBBP9 and removes N-terminal hydrophobic residues—especially aromatic amino acids—from peptides. We therefore postulated that RBBP9 may have aminopeptidase activity in human cells.

## RBBP9 is an aromatic aminopeptidase

To investigate the aminopeptidase activity of RBBP9, we performed a fluorescence-based hydrolysis assay for 19 amino acid 7-amino-4-methylcoumarin (AA–AMC) compounds (Fig. 5a, Supplementary Fig. 18). RBBP9 showed a clear preference for hydrolysing aromatic residues, especially Phe and Tyr; this is generally consistent with the mass adducts identified on Dap from live cells. Moreover, RBBP9-mediated hydrolysis required a free  $\alpha$ -amine, as acetylated Met–AMC (AcMet–AMC) and the dipeptide Glu-Phe–AMC were not hydrolysed; this explains why the aminopeptidase activity was not detected even though a subset of protease substrates (for example, Pro–pNA and Suc–Phe–pNA) were screened in previous studies<sup>40</sup>.

**Fig. 5: Characterization of RBBP9 aminopeptidase activity.**

 figure 5



**a**, RBBP9 is specific for aromatic amino acids. The graph shows the catalytic efficiency of RBBP9 on 19 AA–AMCs relative to its catalytic efficiency on Phe–AMC. The bar graph represents the mean of  $n = 2$  independent measurements. **b, c**, RBBP9 cleaves aromatic amino acids from the N terminus of peptide hormones (nociceptin or MENK). The full-length (FL) peptides and the products (DePhe<sup>1</sup> or DeTyr<sup>1</sup>) after incubating with wild-type RBBP9 or RBBP9(S75A) were determined by mass spectrometry. Black solid line shows detection of product after incubating with WT RBBP9; brown solid line shows detection of product after incubating with RBBP9(S75A); black dashed line shows detection of full-length peptide after incubating with wild-type RBBP9; brown dashed line shows detection of full-length peptide after incubating with RBBP9(S75A). **d, e**, The crystal structure of RBBP9 in complex with Phe. **d**, surface view of RBBP9 and sphere representation of Phe (purple). The surface of Tyr99, Leu103, Phe140 and Leu141 is shown in yellow. **e**, Ribbon diagram of RBBP9 with key residues shown as sticks. Side chains of Tyr99, Leu103, Phe140 and Leu141 are shown in yellow; side chains of Glu108 and Ser76 are shown in green. The hydrogen bond between the  $\alpha$ -amine group of Phe and the side chain of Glu108 (2.7 Å) is represented by a red dashed line. The side chain of Ser76 or Tyr99 may also form hydrogen bonds with the  $\alpha$ -amine group of Phe (dashed brown lines, bond distances of 2.8 Å or 2.9 Å, respectively).

#### Source data

The aminopeptidase activity and selectivity of RBBP9 was further validated on peptides. As expected, wild-type RBBP9 but not the catalytically inactive S75A mutant removed the first Phe (Phe<sup>1</sup>) from neuropeptide nociceptin (Fig. 5b), the first Tyr (Tyr<sup>1</sup>) from enkephalin (MENK) (Fig. 5c), and the first Trp (Trp<sup>1</sup>) from fibronectin adhesion-promoting peptide, but not the first glycine (Gly<sup>1</sup>) from a tetrapeptide (Supplementary Fig. 19, Supplementary Table 5).

To understand the preference shown by RBBP9 towards aromatic residues, we solved the crystal structure of RBBP9 in complex with Phe (Extended Data Table 1). The overall structure of this complex is almost identical (root mean squared deviation = 0.17 Å) to that of RBBP9 alone<sup>40</sup>. Phe sits in the RBBP9 catalytic pocket (Fig. 5d). Tyr99, Leu103, Phe140 and Leu141 form a hydrophobic cage that holds the bulky aromatic ring of Phe in position (Fig. 5d). In addition, the hydrogen bond formed between the  $\alpha$ -amine of Phe and the side chain of Glu108 (or Ser76 or Tyr99) anchors the amino group at this position (Fig. 5e); this explains why a free  $\alpha$ -amine is required on the N terminus of RBBP9 substrates. Overall, our results demonstrate that RBBP9 is an aminopeptidase with a preference for removing aromatic residues from the N terminus in human cells. To our knowledge, this is the first reported aminopeptidase in mammals that uses a catalytic serine nucleophile to remove the N-terminal amino acid from polypeptides. Future work should aim to identify the C-terminal portion of

RBBP9 substrates and understand how the hydrolase activity we have discovered relates to tumour cell proliferation.

## Discussion

We have demonstrated that adding a Dap-containing protease to a complex mixture facilitates discovery of protease substrates. Extensions of this approach should facilitate substrate discovery in systems where genetic manipulation is challenging, including primary tissue samples. We have demonstrated that we can directly express and rapidly optically activate hydrolase substrate traps in live mammalian cells. As the genetic code expansion methods used to express caged hydrolase substrate traps have now been developed in several model organisms<sup>43,44</sup>, including mice, future work may extend our approach to diverse physiological settings.

Hydrolases have arisen independently multiple times in evolution<sup>45,46</sup>. Proteases that proceed through an acyl-enzyme intermediate naturally divide into two classes on the basis of the stereochemistry of nucleophilic attack<sup>46</sup>. We have exemplified our approach for serine and cysteine proteases from both mechanistic classes. Proteases have also been classified into clans that have a common ancestry, as identified by structural homology<sup>47</sup>. We have exemplified our approach for cysteine proteases from the major clan within animals (Clan PA, 66%) and viruses (Clan CA and PA, 72%), and for the major serine proteases and hydrolase clans within animals (Clans PA and SC, 70%) and viruses (Clan PA, 48%)<sup>47</sup> (Extended Data Fig. 9); we have also exemplified our approach for both soluble and intramembrane proteases, and provided biological insights (Supplementary Note 2). Thus, our results cover many classes of protease reaction that proceed through an acyl-enzyme intermediate and the majority of protease structural classes; this suggests that our approach will be broadly applicable.

Finally, we have demonstrated the utility of combining hydrolase substrate traps with the direct identification of Dap conjugates to define the molecular function of an orphan hydrolase. We anticipate that future work will extend the approaches we have developed to identify the activities and substrates of many other hydrolases.

## Methods

### Plasmid construction

Standard molecular biology techniques, including PCR, restriction cloning, Gibson assembly, Golden gate assembly, and quik-change mutagenesis were applied to assemble plasmids. To generate plasmids for protein expression in *E. coli*, the DNA

fragment encoding human HtrA2(134–458), RBBP9 or SCoV2-PLpro was synthesized as a double stranded DNA (Integrated DNA Technologies (IDT)), and UL36<sup>USP</sup> (UL36(39–285)) and UL36<sup>USP</sup>(C65S) were amplified from UL36<sup>USP</sup> containing plasmids<sup>48</sup>. The encoding sequence was cloned into pNHD vector<sup>2</sup> with a C-terminal HA–Strep-tag for HtrA2 and RBBP9, and a C-terminal twin-Strep-tag for UL36<sup>USP</sup> and SCoV2-PLpro. To convert catalytic serine/cysteine to alanine or amber stop codon, site directed mutagenesis was completed using quik-change primers (Agilent primer design). To generate vectors for protein expression in mammalian cells, DapRST<sup>2</sup>, TEV<sup>2</sup>, human RHBDL4 (ref. <sup>49</sup>) or RBBP9 encoding sequence was amplified and introduced into the previously reported pcDNA3.1 plasmid backbone<sup>50</sup> with  $4 \times [U6\text{-}^{\text{Py}}\text{l}\text{tRNA}_{\text{CUA}}]$ . A C-terminal HA–Strep-tag was introduced to TEV, and a twin-Strep-tag was introduced at the C-terminus of RHBDL4, RBBP9, UL36<sup>USP</sup> or SCoV2-PLpro. The DNA fragments encoding ER-resident proteins—human CCDC47, PDIA6, CALR, GANAB, ERP44, CALU, PRKCSH, FKBP9, DNAJC3 and CANX—were amplified from HEK293T cDNA and cloned into a previously reported pcDNA3.1-based BiP expressing plasmid<sup>51</sup>, in which an ER leader peptide was followed by a V5-tag and BiP encoding sequence. An additional HA-tag was introduced at the C-terminus of CCDC47, or before the ER retention motif sequence of ERP44. The DNA fragments encoding MFN2, LEMD2, EMD, HNRNPH1 and HNRNPM were amplified from HEK293T cDNA and cloned into a pcDNA3.1 plasmid. An HA-tag was placed at the C-terminus of MFN2, LEMD2 or HNRNPM, while a GFP-tag was introduced at the C-terminus of Emerin or HNRNPH1 for better detection of the proteolytic fragments. The guide RNA (gRNA) for RHBDL4 knockout was introduced into pX330-puro plasmid with the optimized scaffold<sup>52</sup> via Golden gate assembly.

## Western blot

Samples were separated by SDS–PAGE (note that NuPAGE 4–12%, 10% Bis-Tris or 3–8% Tris-Acetate gels running in MES or MOPS buffer were applied to achieve the optimal separation of proteins (protein fragments) of interest) and transferred to polyvinylidene difluoride (PVDF) membrane by iBlot 2 dry blotting system (Thermo Fisher Scientific). Membrane was blocked by Odyssey blocking buffer in PBS (catalogue (cat.) no. 927-40000, Li-Cor) at room temperature for 30 min. Membrane was incubated in primary antibody solution (dilution according to manufacturer's instructions in Odyssey T20 (PBS) antibody diluent (927-75001, Li-Cor)) at 4 °C overnight. All incubations were carried out on a platform shaker. The membrane was washed three time with PBST (PBS supplemented with 0.1% Tween-20 (v/v)), and incubated with the secondary antibody solution (1: 15,000 (v/v) in PBS blocking buffer supplemented with 0.2% Tween-20 (v/v), and 0.01% SDS) at room temperature for 1 h. After washing 3 times with PBST and once with PBS, the immunoreactive

proteins were visualized by the Odyssey CLx imaging system (Li-Cor) by scanning at 700 nm and/or 800 nm channels. Revert 700 Total Protein Stain (926–11015, Li-Cor) was used for total protein staining. The data were analysed by Image Studio Lite (version 5.2.5). For primary and secondary antibodies used in this study, see ‘Antibodies’ in [Supplementary Methods](#).

## Deprotection of pc-Dap containing proteins in buffer

To activate protease(pc-Dap), proteins were illuminated (365 nm, 4 mW cm<sup>-2</sup>) for 1 min in Tris buffer (5 mM DTT, pH 8.0) and incubated at 4 °C or 37 °C overnight to generate protease(Dap). MIC-LED-365 (500 mA, Prizmatix collimated modular MIC-LED light source, Supplementary Fig. 2) was used for illuminating proteins in solution. This apparatus was also used for illuminating suspension cells (Expi293 cells) in tissue culture hood.

## HtrA2 substrate trapping in cell lysate

Thirty micrograms HtrA2–HA–Strep variant (wild type, Ala or Dap) was added to 1 ml of Expi293 cell lysate (3 µg µl<sup>-1</sup>) and incubated at 30 °C for 3 h. The reaction was shaken 10 s every 10 min. Fifty microlitres of anti-HA agarose slurry (A2095, Merck) was added to the reaction and mixed at 4 °C on an end-over-end rocker for 2 h. The mixture was transferred to a Bio-spin column. The resin was washed with RIPA buffer 3 times and PBST buffer 3 times using a vacuum pump, followed by centrifugation at 5,000g for 1 min to remove the residual buffer. Then, beads were incubated in 100 µl 1× LDS loading buffer and boiled at 95 °C for 5 min. Twenty microlitres of the eluate was analysed by SDS–PAGE or western blot. Twenty microlitres of eluate was separated in a Bolt 10% Bis-Tris Plus gel for 3 min at 200 V. Gel slices containing all proteins were cut and analysed by LC–MS/MS as described in ‘Electrospray ionization tandem mass spectrometry’.

## Validation of HtrA2 substrates in cell lysate

Wild-type HtrA2 or HtrA2(S306A) (1 µM) was added to 1.2 ml Expi293 cell lysate. At indicated time points, 300 µl of reaction was quenched by mixing with 100 µl 4 × LDS loading buffer and boiled at 95 °C for 5 min. The samples were analysed by western blot with primary antibodies listed in Supplementary Tables 2, 3. GAPDH was used as a loading control.

## Incorporation of pc-Dap in HEK293T cells

HEK293T cells were purchased from European Collection of Cell Cultures (authenticated by STR DNA profiling) and were tested negative for *Mycoplasma*

contamination.

HEK293T cells were cultured in Dulbecco's Modified Eagle Medium (DMEM) (Gibco) supplemented with 10% fetal bovine serum (FBS) (Gibco) and Penicillin-Streptomycin (Pen/Strep, 100 IU ml<sup>-1</sup> penicillin and 100 µg ml<sup>-1</sup> streptomycin) at 37 °C in a humidified incubator supplied with 5% CO<sub>2</sub>. Cells were passaged every 2–3 days by detaching with trypsin–EDTA solution, resuspended in DMEM with 10% FBS, and seeded into cell culture flasks.

For transfection in a 24-well plate: 0.75 µl of Lipofectamine 3000 (Thermo Fisher) was diluted in 25 µl Opti-MEM (Gibco) and vortexed briefly. DNA solution was prepared by mixing 500 ng DNA mixture (substrate:DapRST:protease, 1:1:3 or empty vector:DapRST:Protease, 1:1:3) in 25 µl Opti-MEM, followed by adding 1 µl of P3000 reagent. Then, diluted Lipofectamine was added to DNA solution (1:1 v/v). The mixture was incubated at room temperature for 10 min and the DNA–lipid complexes were added to cells. Indicated concentrations in figure legends (or 0.5 mM) of pc-Dap was added to the culture medium 30 min after transfection to achieve pc-Dap incorporation. Cells were incubated at 37 °C for 40–48 h before further analysis.

## Incorporation of pc-Dap in Expi293 cells

Expi293 cells were purchased from Thermo Fisher (authenticated by STR DNA profiling) and were tested negative for *Mycoplasma* contamination.

Expi293 cells were cultured in Expi293 media (Gibco) and shaken at 125 rpm in incubator at 37 °C with 8% CO<sub>2</sub>. Cells were passaged every 2–3 days, starting with the cell density around 0.5 × 10<sup>6</sup> cells per ml. Transfection was performed at cell density around 2.5 × 10<sup>6</sup> cells per ml.

Transfection of 100 ml Expi293 cells: 300 µl of polyethyleneimine molecular mass 40,000 (PEI, 1 mg ml<sup>-1</sup>, Polysciences) was diluted in 3.3 ml Expi293 medium. 100 µg DNA mixture (substrate:DapRST:protease, 1:1:3 or empty vector:DapRST:protease, 1:1:3) was diluted in 3.3 mL Expi293 media. Diluted DNA and PEI solution were mixed and incubated at room temperature for 15 min before adding to the cell culture. 0.5 mM (or indicated concentrations in figure legends) of pc-Dap was added 30 min after transfection for pc-Dap incorporation. Forty to forty-eight hours after transfection, the cells were collected and photoactivated for further analysis.

## Photoactivation of protease(pc-Dap) and substrate trapping in mammalian cells

Forty to forty-eight hours after transfection, cell culture medium was replaced with fresh medium, and cells were illuminated for 2 min. The apparatus for illuminating adherent mammalian cells was built in-house (Supplementary Fig. 7). LuxiGen 365 nm UV LED Emitter (LZ4-04UV0R-0000, Mouser Electronics) was used for illumination. The UV intensity at the well plate was set at  $4 \text{ mW cm}^{-2}$ . After illumination, cells were incubated at  $37^\circ\text{C}$  for indicated period of time (Proteasome inhibitor MG132 (2  $\mu\text{M}$ ) was added if needed). For adherent cells, at each time point, cells in a 6-well plate were washed with PBS and lysed in 400  $\mu\text{l}$  RIPA lysis buffer (89900, Thermo) supplemented with Halt Protease Inhibitor Cocktail (78429, Thermo Fisher) and the Universal Nuclease (88702, Thermo Fisher). The lysate was cleared by centrifuging at 21,000g for 5 min and the supernatant was flash frozen and stored at  $-80^\circ\text{C}$ . For suspension cells, at each indicated time point, 5 ml cell culture was centrifuged at 650g for 5 min and the cell pellet was flash frozen and kept at  $-80^\circ\text{C}$ . Then, cell pellets were lysed in 1 ml RIPA lysis buffer supplemented with protease inhibitors and the Universal Nuclease at  $4^\circ\text{C}$ . Cell lysates were centrifuged at 21,000g for 5 min. The cleared lysates were used for SDS–PAGE and western blot analysis or affinity enrichment by MagStrep type3 XT beads (2-4090-002, IBA).

### Trapping endogenous substrates to RHBDL4(S144Dap)

RHBDL4 variants were expressed in Expi293 cells as described in ‘Incorporation of pc-Dap in Expi293 cells’. Forty hours after transfection, 50 ml cell culture was resuspended in fresh Expi293 media and illuminated (365 nm,  $4 \text{ mW cm}^{-2}$ ) for 2 min. Cells were incubated at  $37^\circ\text{C}$  for 4 h in the presence of 2  $\mu\text{M}$  MG132 before collection. After pelleting, cells were resuspended in HEPES buffer (50 mM HEPES, pH 7.4, 150 mM NaCl, 1 mM MgCl<sub>2</sub>, 5% glycerol, 1 mM DTT) supplemented with protease inhibitors and the Universal Nuclease. The suspension was lysed by passing twice through an Avestin Emulsiflex C3 homogenizer (ATA Scientific) at 3,000–5,000 psi. The lysate was centrifuged at 1,000g for 5 min twice and the supernatant was further centrifuged at 100,000g for 1 h. The pellet was washed with Na<sub>2</sub>CO<sub>3</sub> (100 mM, pH 11.3) at  $4^\circ\text{C}$  for 20 min and then centrifuged at 140,000g for 1 h. The membrane fraction was dissolved in 2% SDS buffer (50 mM Tris, pH 8, 150 mM NaCl, 1 mM DTT and protease inhibitors). The solution was diluted by 10% NP40 to generate a final concentration of 0.1% SDS and 1% NP40. One-hundred microlitres MagStrep type3 XT beads were added to the solution and incubated at room temperature for 1 h. The beads were washed with RIPA and PBST three times each. Proteins attached to the beads were eluted in 1× LDS loading buffer by heating at  $65^\circ\text{C}$  for 15 min. The eluates were separated in a Bolt 10% Bis-Tris Plus gel for 3 min. Gel slices containing proteins were cut and analysed by LC–MS/MS.

### RHBDL4 cleavage assay

Empty vector, wild-type (WT) RHBDL4 or RHBDL4(S144A) plasmid was co-transfected with candidate substrate containing plasmid or empty vector (for endogenous substrates) into HEK293T or Expi293 cells. The amount of candidate substrate-containing plasmid was optimized for expression level. Forty to forty-eight hours after transfection, cells were collected and lysed in RIPA buffer supplemented with protease inhibitors and the Universal Nuclease. The lysate was cleared and analysed by western blot.

To analyse proteins in the extracellular medium, FBS-containing medium for HEK293T cells was replaced with hybridoma serum free medium (12045076, Thermo Fisher) 24 h before collection. Expi293 medium, which is serum-free and protein-free, can be directly collected for further analysis. The medium was collected and filtered through a 0.22 µm polyethersulfone membrane. To obtain total proteins in the medium, 1/10 volume of 100% ice-cold TCA solution (T0699, Sigma) was added at 4 °C for protein precipitation. To obtain proteins in the supernatant, the medium was centrifuged at 200,000g for 1 h to separate supernatant from microvesicles. The SN was collected and added 1/10 volume of ice-cold TCA to precipitate proteins. After centrifuging at 21,000g for 10 min, the precipitate was washed once with acetone, and dissolved in 1× LDS loading buffer. The microvesicles pellet after ultra-centrifugation was washed with PBS once and dissolved in equal volume of 1× LDS loading buffer.

Deglycosylation was performed by adding 1/10 volume of 10% NP40 and PNGase (P0704S, NEB) or DeGlycosylation mix II (P6044S, NEB) to proteins dissolved in the 1× LDS loading buffer. The reaction was incubated at 37 °C for 1 h before analysis.

### Brefeldin A inhibitory assay

Twenty-four hours after transfection, Expi293 cells were split into two halves treated separately with DMSO or BFA (5 µg ml<sup>-1</sup>). The BFA treatment was performed in two ways: (1) BFA was directly added into medium culture; (2) the medium culture was replaced with fresh medium supplemented with BFA. Sixteen hours after BFA treatment, the cells and extracellular medium were collected and analysed as described in ‘RHBDL4 cleavage assay’.

### Knockout of RHBDL4

HCT116 cells were purchased from American Type Culture Collection (authenticated by STR DNA profiling) and were tested negative for *Mycoplasma* contamination.

HCT116 cells were cultured in McCoy’s 5A (modified) Media (Gibco) supplemented with 10% fetal bovine serum (FBS) (Gibco) and Pen/Strep at 37 °C in humidified incubator with 5% CO<sub>2</sub>. Cells were passaged every 2–3 days.

HCT116 cells in 6-well plates were transfected by Lipofectamine LTX (15338100, Thermo Fisher) with 2.5 µg of pX330-puro plasmid containing gRNA (5'-TCCAGTAAGTACAGAAAATG-3') and Cas9 for RHBDL4 knockout. Twenty-four hours after transfection, cells were trypsinized and plated in a 10 cm petri dish. After 24 h, the cells were treated with puromycin (1 µg ml<sup>-1</sup>). The puromycin selection stopped after 48 h. Cells were trypsinized and limited dilution was performed to generate single clones, which were expanded and analysed by western blot (anti-RHBDL4) and genotyped by sequencing the genomic DNA region targeted by the gRNA.

To detect the proteolytic fragments from endogenous substrates generated by endogenous RHBDL4, 10 million wild-type or RHBDL4 knockout HCT116 cells were cultured in hybridoma serum free medium for 40 h. The medium was collected, filtered and concentrated by a 30 kDa cut-off concentrator. Proteins were precipitated by TCA and dissolved in 1× LDS loading buffer for immunoblotting analysis.

## Trapping endogenous substrates to RBBP9(S75Dap)

To identify X attached to Pept(Dap), RBBP9 variants were expressed in HEK293T cells as described in ‘Incorporation of pc-Dap in HEK293T cells’. pc-Dap (0.1 mM) was added to cells to produce RBBP9(S75pc-Dap). To characterize the entire masses of RBBP9 variants, RBBP9 variants were produced in 100 ml Expi293 cells as described in ‘Incorporation of pc-Dap in Expi293 cells’. RBBP9(S75pc-Dap) was expressed in the presence of 0.5 mM pc-Dap. 40 h after transfection, cells were illuminated (365 nm, 4 mW cm<sup>-2</sup>) for 2 min, and incubated at 37 °C for 3 h. Cells were then collected and lysed in Tris buffer (50 mM Tris, pH 8.0, 150 mM NaCl, 1 mM EDTA and Universal Nuclease) by sonication. Note that protease inhibitors were not added in lysis buffer. The lysate was cleared by centrifuging at 21,000g for 20 min. RBBP9 species in the supernatant were enriched using MagStrep type3 XT beads. Proteins attached to beads were eluted in 50 mM Biotin in Tris buffer for mass characterization.

## Aminopeptidase assay of RBBP9

### Fluorescence-based assay

Two micromolar RBBP9 was incubated with each AA–AMC over a range of different substrate concentrations in Tris buffer (100 mM Tris, 150 mM NaCl, pH 7.3). Fluorescence intensity (due to the release of the AMC fluorophore by hydrolysis of AA–AMC by RBBP9) was measured every 20 s over a 10-min period (MARS Data Analysis Software (version 3.20 R2)). For each substrate, the rate of fluorescence increase was converted to rate of product formation using standard curves. At

substrate concentrations of greater than 10 µM, intermolecular quenching of AMC fluorescence by AA-AMC was found to be significant. Therefore, for all substrates other than Phe-AMC and Tyr-AMC, AA-AMC concentrations between 0 and 4 µM were used, and pseudo-first order kinetics were employed to calculate specificity constants. For Phe-AMC and Tyr-AMC, which showed significantly faster rates of hydrolysis when compared to the other substrates, a concentration range of 0 to 160 µM was used and converted rates were fitted to Michaelis–Menten kinetics in order to obtain specificity constants.

### Peptide-based assay

Peptides (100 µM) were dissolved in Tris buffer (100 mM Tris pH 7.4, 150 mM NaCl, 1 mM EDTA). Two micromolar wild-type RBBP9 or RBBP9(S75A) was added to start the hydrolysis reaction. The reaction was stopped by quenching with acetic acid and monitored by mass spectrometry. Selected ion mass (SIM) mode was applied for detection of peptide substrates and the desired products.

### Protein crystallization and data collection

Human RBBP9 with a C-terminal His-tag<sup>40</sup> (LEHHHHHH) was expressed in BL21(DE3) cells and purified by a two-step protocol consisting of HisTrap enrichment and gel filtration (Superdex 75) chromatography. Pure fractions of RBBP9 (> 98% purity determined by SDS-PAGE) were concentrated with a 10 kD MWCO Vivaspin 20 concentrator (Sartorius) to 10 mg ml<sup>-1</sup> in buffer containing 10 mM Tris (pH 7.5), 100 mM NaCl, 5 mM DTT and 5 mM Phe. Prior to crystallization, samples were cleared by centrifugation for 15 min at 10,000g. Crystallization trials with multiple commercial crystallization kits were performed in 96-well sitting-drop vapor diffusion plates (Molecular Dimensions) at 18 °C and set up with a mosquito HTS robot (TTP Labtech). Drop ratios of 0.2 µl protein solution plus 0.2 µl reservoir solution were used for coarse and fine screening. Initial hits were obtained under multiple conditions and required no further optimization. Data was collected from crystals collected from following conditions: 30% w/v PEG 4K, 0.1 M MES sodium salt, pH 6.5.

To ensure cryo-protection, crystal-containing drops were mixed with 25% glycerol in reservoir solution prior to picking and flash frozen in liquid nitrogen. Diffraction data was collected at the Diamond Light Source (DLS, UK) on beamline I04. Datasets were auto-processed with XIA2 DIALS (version 0.7.90), scaled using Aimless and Refmac5 (version 5.8.0258) in the CCP4 suite (version 7.0.078) of programs. Structure refinement and manual model building were performed with Refmac5 and COOT (version 0.8.9.2). Colour figures were prepared with PyMol (version 2.5).

### Mass characterization

## **Electrospray ionization mass spectrometry**

Mass spectra of all protein samples were acquired on an Agilent 1200 LC-MS system equipped with a 6130 Quadrupole spectrometer. A Phenomenex Jupiter C4 column ( $150 \times 2$  mm,  $5 \mu\text{m}$ ) was used to elute proteins. Buffer A (0.2% formic acid in  $\text{H}_2\text{O}$ ) and buffer B (0.2% formic acid in acetonitrile) was used for RP-HPLC. Mass spectra were acquired in the positive mode and analysed by the MS Chemstation software (Rev.C.01.06[61], Agilent Technologies). The deconvolution program provided in the software was used to obtain the entire mass spectra. Theoretical molecular mass of proteins with non-canonical amino acids was calculated by correcting the calculated molecular mass of wild-type protein (<http://www.peptidesynthetics.co.uk/tools/>) with the molecular mass of non-canonical amino acids.

## **Electrospray ionization tandem mass spectrometry**

Proteins (including TEV-GFP conjugate, substrates trapped to HtrA2 or RHBDL4) in polyacrylamide gel slices (1–2 mm) were enzymatically digested *in situ* for LC–MS/MS analysis. In brief, the excised protein gel pieces were placed in a 96-well microtitre plate and destained with 50% v/v acetonitrile and 50 mM ammonium bicarbonate, followed by reduction with 10 mM DTT and alkylation with 55 mM iodoacetamide. RBBP9 eluates in solution were treated in two ways: (1) incubation at room temperature overnight in the presence of 10 mM DTT without alkylation; (2) reduction with 10 mM DTT for 30 min and alkylation with 55 mM iodoacetamide. Then, proteins were digested with trypsin/LysC (Promega) overnight at 37 °C. The resulting peptides were extracted in 2% v/v formic acid, 2% v/v acetonitrile and analyzed by nanoscale capillary LC-MS/MS, which uses an Ultimate U3000 HPLC (ThermoScientific Dionex) with a flow rate of  $300 \text{ nl min}^{-1}$ . A C18 Acclaim PepMap100  $5 \mu\text{m}$ ,  $100 \mu\text{m} \times 20 \text{ mm}$  nanoViper (ThermoScientific Dionex) was used to trap the peptides before separation on a C18 Acclaim PepMap100  $3 \mu\text{m}$ ,  $75 \mu\text{m} \times 150 \text{ mm}$  nanoViper (ThermoScientific Dionex). Peptides were eluted with a gradient of acetonitrile. The eluate was directly introduced to a modified nanoflow ESI source with a hybrid dual pressure linear ion trap mass spectrometer (Orbitrap Velos, ThermoScientific). Data-dependent analysis was carried out using a resolution of 30,000 for the full MS spectrum, followed by ten MS/MS spectra in the linear ion trap. MS spectra were collected over an  $m/z$  range of 100–2,000.

## **LC–MS/MS data analysis by Venn diagram**

LC–MS/MS data were searched against an in-house protein sequence database containing Swiss-Prot and the protein constructs specific to the experiment, using the Mascot search engine program (Matrix Science, version 2.4). Database search

parameters were set with a precursor tolerance of 5 p.p.m. and a fragment ion mass tolerance of 0.8 Da. Variable modifications for oxidized methionine, carbamidomethyl cysteine, pyroglutamic acid, and deamination of glutamine/asparagine were included. MS/MS data were validated using the Scaffold program (version 5, Proteome Software Inc.).

### LC-MS/MS data analysis by volcano plot

For quantitative analysis, MS raw files were processed by MaxQuant software (version 1.6.3.4) and searched with the embedded Andromeda search engine against the corresponding database (Uniprot). The required FDR was set to 1% or 5% at peptide and protein levels. The maximum number of allowed missed cleavages was set to two. Protein quantification was done by LFQ with default settings. The MaxQuant ProteinGroups output file was further processed with Perseus (version 1.6.2.3)<sup>53</sup>. Contaminations and reverse hits were removed by filtering. The remaining protein quantifications were log<sub>2</sub>-transformed.

### Determination of X attached to Dap in RBBP9

LC-MS/MS files (in RAW format) were first converted to mzML format<sup>54</sup> using ProteoWizard (version 3.0.11252)<sup>55</sup>. Data preparation and processing were then performed using custom Python (version 3.8.1) scripts written with the pyOpenMS package (version 2.4.0)<sup>56</sup>. In brief, collected spectra were centroided and all MS2 spectra with a precursor mass lower than that of the unconjugated Dap-containing tryptic peptide from RBBP9 (Pept(Dap)) were filtered out. For each filtered MS2 spectrum, the ten most abundant peaks in each 100 Th mass interval were extracted.

Based on the peptide sequence of Pept(Dap) and the precursor mass for each MS2 spectrum, a list of theoretical ion masses was calculated; these corresponded to the MS2 fragmentation of a substrate-conjugated Pept(Dap), (Pept(Dap-X)). This list contained the monocationic b- and y-ions, the dicatonic b- and y- ions, and ions corresponding to water or ammonium losses from the side-chains of b- or y- ions. Peaks in the MS2 spectrum were matched against this list, and a score for this matching was calculated as previously described<sup>57</sup>. This score was ten times the negative logarithm of the approximate probability that at least  $k$  out of  $n$  masses have been matched by chance, where  $k$  is the number of matches and  $n$  is the number of masses in the list.

To extract the top-scoring spectra, the family-wise error rate for the probability values was controlled at 0.05 using the Bonferroni correction. The mass difference between Pept(Dap) and the precursor ion for each Pept(Dap-X) spectrum was calculated to

determine the molecular mass of each conjugate. For each mass shift, representative top-scoring spectra were manually interrogated to verify the assignment.

## Reporting summary

Further information on research design is available in the [Nature Research Reporting Summary](#) linked to this paper.

## Data availability

The structure of RBBP9 in complex with Phe is available in the Protein Data Bank under accession code [7OEX](#). The mass spectrometry proteomics data have been deposited to the ProteomeXchange Consortium via the PRIDE partner repository with the accession number PDX030381. All other datasets and materials generated or analysed in this study are available from the corresponding authors upon reasonable request. The data used to analyse serine and cysteine proteases clans were downloaded from the MEROPS database (<https://www.ebi.ac.uk/merops/>). [Source data](#) are provided with this paper.

## Code availability

The code used for RBBP9 substrate identification by proteomic analysis is available at <https://doi.org/10.5281/zenodo.5768340>.

## References

1. Klebe, G. in *Drug Design: Methodology, Concepts, and Mode-of-Action* (ed. Klebe, G.) 493–532 (Springer, 2013).
2. Huguenin-Dezot, N. et al. Trapping biosynthetic acyl-enzyme intermediates with encoded 2,3-diaminopropionic acid. *Nature* **565**, 112–117 (2019).
3. Freeman, M. The rhomboid-like superfamily: molecular mechanisms and biological roles. *Annu. Rev. Cell Dev. Biol.* **30**, 235–254 (2014).
4. Fleig, L. et al. Ubiquitin-dependent intramembrane rhomboid protease promotes ERAD of membrane proteins. *Mol. Cell* **47**, 558–569 (2012).
5. Woitach, J. T., Zhang, M., Niu, C. H. & Thorgeirsson, S. S. A retinoblastoma-binding protein that affects cell-cycle control and confers transforming ability. *Nat. Genet.* **19**, 371–374 (1998).

6. Niphakis, M. J. & Cravatt, B. F. Enzyme inhibitor discovery by activity-based protein profiling. *Annu. Rev. Biochem.* **83**, 341–377 (2014).
7. Sanman, L. E. & Bogyo, M. Activity-based profiling of proteases. *Annu. Rev. Biochem.* **83**, 249–273 (2014).
8. De Cesare, V. et al. Deubiquitinating enzyme amino acid profiling reveals a class of ubiquitin esterases. *Proc. Natl Acad. Sci. USA* **118**, e2006947118 (2021).
9. Lopez-Otin, C. & Overall, C. M. Protease degradomics: a new challenge for proteomics. *Nat. Rev. Mol. Cell Biol.* **3**, 509–519 (2002).
10. Rei Liao, J. Y. & van Wijk, K. J. Discovery of AAA+ protease substrates through trapping approaches. *Trends Biochem. Sci.* **44**, 528–545 (2019).
11. Saita, S. et al. PARL mediates Smac proteolytic maturation in mitochondria to promote apoptosis. *Nat. Cell Biol.* **19**, 318–328 (2017).
12. Knopf, J. D. et al. Intramembrane protease RHBDL4 cleaves oligosaccharyltransferase subunits to target them for ER-associated degradation. *J. Cell Sci.* **133**, jcs243790 (2020).
13. Dix, M. M., Simon, G. M. & Cravatt, B. F. Global mapping of the topography and magnitude of proteolytic events in apoptosis. *Cell* **134**, 679–691 (2008).
14. Zhou, J. et al. Deep profiling of protease substrate specificity enabled by dual random and scanned human proteome substrate phage libraries. *Proc. Natl Acad. Sci. USA* **117**, 25464–25475 (2020).
15. Luo, S. Y., Araya, L. E. & Julien, O. Protease substrate identification using N-terminomics. *ACS Chem. Biol.* **14**, 2361–2371 (2019).
16. O'Brien, R. J. & Wong, P. C. Amyloid precursor protein processing and Alzheimer's disease. *Annu. Rev. Neurosci.* **34**, 185–204 (2011).
17. Crawford, E. D. & Wells, J. A. Caspase substrates and cellular remodeling. *Annu. Rev. Biochem.* **80**, 1055–1087 (2011).
18. Wolfe, M. S. Intramembrane proteolysis. *Chem. Rev.* **109**, 1599–1612 (2009).
19. Beard, H. A., Barniol-Xicota, M., Yang, J. & Verhelst, S. H. L. Discovery of cellular roles of intramembrane proteases. *ACS Chem. Biol.* **14**, 2372–2388 (2019).

20. Tinzl, M. & Hilvert, D. Trapping transient protein species by genetic code expansion. *ChemBioChem* **22**, 92–99 (2021).
21. Suzuki, Y. et al. A serine protease, HtrA2, is released from the mitochondria and interacts with XIAP, inducing cell death. *Mol. Cell.* **8**, 613–621 (2001).
22. Chao, J. R. et al. Hax1-mediated processing of HtrA2 by Parl allows survival of lymphocytes and neurons. *Nature* **452**, 98–102 (2008).
23. Martins, L. M. et al. Binding specificity and regulation of the serine protease and PDZ domains of HtrA2/Omi. *J. Biol. Chem.* **278**, 49417–49427 (2003).
24. Vande Walle, L. et al. Proteome-wide identification of HtrA2/Omi substrates. *J. Proteome Res.* **6**, 1006–1015 (2007).
25. Courtney, T. & Deiters, A. Recent advances in the optical control of protein function through genetic code expansion. *Curr. Opin. Chem. Biol.* **46**, 99–107 (2018).
26. Wang, J. et al. Time-resolved protein activation by proximal decaging in living systems. *Nature* **569**, 509–513 (2019).
27. Brown, M. S., Ye, J., Rawson, R. B. & Goldstein, J. L. Regulated intramembrane proteolysis: a control mechanism conserved from bacteria to humans. *Cell* **100**, 391–398 (2000).
28. Wolfe, M. S. & Kopan, R. Intramembrane proteolysis: theme and variations. *Science* **305**, 1119–1123 (2004).
29. Muller, S. A., Scilabria, S. D. & Lichtenthaler, S. F. Proteomic substrate identification for membrane proteases in the brain. *Front. Mol. Neurosci.* **9**, 96 (2016).
30. Dickey, S. W., Baker, R. P., Cho, S. & Urban, S. Proteolysis inside the membrane is a rate-governed reaction not driven by substrate affinity. *Cell* **155**, 1270–1281 (2013).
31. Urban, S., Lee, J. R. & Freeman, M. *Drosophila* rhomboid-1 defines a family of putative intramembrane serine proteases. *Cell* **107**, 173–182 (2001).
32. Lemberg, M. K. & Freeman, M. Functional and evolutionary implications of enhanced genomic analysis of rhomboid intramembrane proteases. *Genome Res.* **17**, 1634–1646 (2007).

33. Song, W. et al. Rhomboid domain containing 1 promotes colorectal cancer growth through activation of the EGFR signalling pathway. *Nat. Commun.* **6**, 8022 (2015).
34. Wan, C. et al. Exosome-related multi-pass transmembrane protein TSAP6 is a target of rhomboid protease RHBDD1-induced proteolysis. *PLoS ONE* **7**, e37452 (2012).
35. Wunderle, L. et al. Rhomboid intramembrane protease RHBDL4 triggers ER-export and non-canonical secretion of membrane-anchored TGF $\alpha$ . *Sci. Rep.* **6**, 27342 (2016).
36. Paschkowsky, S., Hamze, M., Oestereich, F. & Munter, L. M. Alternative processing of the amyloid precursor protein family by rhomboid protease RHBDL4. *J. Biol. Chem.* **291**, 21903–21912 (2016).
37. Chitwood, P. J. & Hegde, R. S. An intramembrane chaperone complex facilitates membrane protein biogenesis. *Nature* **584**, 630–634 (2020).
38. Munro, S. & Pelham, H. R. A C-terminal signal prevents secretion of luminal ER proteins. *Cell* **48**, 899–907 (1987).
39. Jessani, N. et al. A streamlined platform for high-content functional proteomics of primary human specimens. *Nat. Methods* **2**, 691–697 (2005).
40. Vorobiev, S. M. et al. Crystal structure of human retinoblastoma binding protein 9. *Proteins* **74**, 526–529 (2009).
41. Shields, D. J. et al. RBBP9: a tumor-associated serine hydrolase activity required for pancreatic neoplasia. *Proc. Natl Acad. Sci. USA* **107**, 2189–2194 (2010).
42. Tsuji, A., Fujisawa, Y., Mino, T. & Yuasa, K. Identification of a plant aminopeptidase with preference for aromatic amino acid residues as a novel member of the prolyl oligopeptidase family of serine proteases. *J. Biochem.* **150**, 525–534 (2011).
43. Chin, J. W. Expanding and reprogramming the genetic code of cells and animals. *Annu. Rev. Biochem.* **83**, 379–408 (2014).
44. Brown, W., Liu, J. & Deiters, A. Genetic code expansion in animals. *ACS Chem. Biol.* **13**, 2375–2386 (2018).
45. Dodson, G. & Wlodawer, A. Catalytic triads and their relatives. *Trends Biochem. Sci.* **23**, 347–352 (1998).

46. Buller, A. R. & Townsend, C. A. Intrinsic evolutionary constraints on protease structure, enzyme acylation, and the identity of the catalytic triad. *Proc. Natl Acad. Sci. USA* **110**, E653–E661 (2013).
47. Rawlings, N. D., Waller, M., Barrett, A. J. & Bateman, A. MEROPS: the database of proteolytic enzymes, their substrates and inhibitors. *Nucleic Acids Res.* **42**, D503–D509 (2014).
48. MacDonald, C., Winistorfer, S., Pope, R. M., Wright, M. E. & Piper, R. C. Enzyme reversal to explore the function of yeast E3 ubiquitin-ligases. *Traffic* **18**, 465–484 (2017).
49. Ikeda, K. N. & Freeman, M. Spatial proteomics reveal that the protein phosphatase PTP1B interacts with and may modify tyrosine phosphorylation of the rhomboid protease RHBDL4. *J. Biol. Chem.* **294**, 11486–11497 (2019).
50. Schmied, W. H., Elsasser, S. J., Uttamapinant, C. & Chin, J. W. Efficient multisite unnatural amino acid incorporation in mammalian cells via optimized pyrrolysyl tRNA synthetase/tRNA expression and engineered eRF1. *J. Am. Chem. Soc.* **136**, 15577–15583 (2014).
51. Cesaratto, F. et al. BiP/GRP78 mediates ERAD targeting of proteins produced by membrane-bound ribosomes stalled at the STOP-codon. *J. Mol. Biol.* **431**, 123–141 (2019).
52. Maule, G. et al. Allele specific repair of splicing mutations in cystic fibrosis through AsCas12a genome editing. *Nat. Commun.* **10**, 3556 (2019).
53. Tyanova, S. et al. The Perseus computational platform for comprehensive analysis of (prote)omics data. *Nat. Methods* **13**, 731–740 (2016).
54. Martens, L. et al. mzML-a community standard for mass spectrometry data. *Mol. Cell Proteomics* **10**, R110.000133 (2011).
55. Chambers, M. C. et al. A cross-platform toolkit for mass spectrometry and proteomics. *Nat. Biotechnol.* **30**, 918–920 (2012).
56. Rost, H. L., Schmitt, U., Aebersold, R. & Malmstrom, L. pyOpenMS: a Python-based interface to the OpenMS mass-spectrometry algorithm library. *Proteomics* **14**, 74–77 (2014).
57. Cox, J. et al. Andromeda: a peptide search engine integrated into the MaxQuant environment. *J. Proteome Res.* **10**, 1794–1805 (2011).

58. Kattenhorn, L. M., Korbel, G. A., Kessler, B. M., Spooner, E. & Ploegh, H. L. A deubiquitinating enzyme encoded by HSV-1 belongs to a family of cysteine proteases that is conserved across the family Herpesviridae. *Mol. Cell* **19**, 547–557 (2005).
59. Shin, D. et al. Papain-like protease regulates SARS-CoV-2 viral spread and innate immunity. *Nature* **587**, 657–662 (2020).
60. Patchett, S. et al. A molecular sensor determines the ubiquitin substrate specificity of SARS-CoV-2 papain-like protease. *Cell Rep.* **36**, 109754 (2021).
61. Klemm, T. et al. Mechanism and inhibition of the papain-like protease, PLpro, of SARS-CoV-2. *EMBO J.* **39**, e106275 (2020).
62. Liu, G. et al. ISG15-dependent activation of the sensor MDA5 is antagonized by the SARS-CoV-2 papain-like protease to evade host innate immunity. *Nat Microbiol.* **6**, 467–478 (2021).

## Acknowledgements

This work was supported by the UK Medical Research Council (MRC; MC\_U105181009 and MC\_UP\_A024\_1008) to J.W.C.; MC\_U105192713 to M. Bienz (M. Fiedler's supervisor), and Wellcome Trust Investigator Awards (101035/Z/13/Z and 220887/Z/20/Z) to M. Freeman. S.T. was supported by a European Molecular Biology Organization Long-Term Fellowship (ALTF 825-2016). L.K. (no. 884511) and G.P. (no. 897663) were supported by Marie Skłodowska-Curie European Postdoctoral Fellowships. We thank M. K. Lemberg for providing the pT $\alpha$  construct; N. Gomez-Navarro for sharing the UL36<sup>USP</sup> containing plasmids; O. R. Burrone for providing the BiP expressing plasmid; R. Hegde and S. Munro (MRC-LMB) for helpful comments on previous versions of the manuscript; O. Perisic, Y. Christova, S. Grazioli, C. Morgan and M. Spinck for helpful discussions; K. Lilley for advice on RHBDL4 proteomics analysis; the FACS facility (MRC-LMB); K. Heesom, M. Skehel, F. Begum, M. Kyte and A. Howe and the MRC-LMB Mechanical Workshop for support; and B. Cravatt (Scripps Research) for suggesting RBBP9 as a target for investigation.

## Author information

### Affiliations

1. Medical Research Council Laboratory of Molecular Biology, Cambridge, UK

Shan Tang, Adam T. Beattie, Gianluca Petris, Nicolas Huguenin-Dezot, Marc Fiedler & Jason W. Chin

2. Sir William Dunn School of Pathology, University of Oxford, Oxford, UK

Lucie Kafkova & Matthew Freeman

## Contributions

S.T. and J.W.C. wrote the paper. J.W.C. set the overall direction of research. S.T. and N.H.-D. developed the hydrolase substrate identification approaches in cell lysate (for TEV and HtrA2), and S.T. established the hydrolase substrate discovery approaches in mammalian cells (for TEV, UL36<sup>USP</sup>, SCoV2-PLpro, RHBDL4 and RBBP9). N.H.-D. expressed and purified TEV and HtrA2 variants from *E. coli*. S.T. expressed and purified UL36<sup>USP</sup> and SCoV2-PLpro variants from *E. coli* and performed the conjugation assays with UBL-AMC molecules. S.T. performed HtrA2 substrate validation. S.T. developed the capture of RHBDL4 model substrates with contributions from L.K. S.T. performed RHBDL4 substrate capture and identification experiments. S.T., L.K. and G.P. performed RHBDL4 substrate validation. S.T. and G.P. generated the RHBDL4 knockout cell line. M. Freeman supervised L.K. and contributed to the planning and interpretation of the RHBDL4 experiments. A.T.B. developed the computational pipeline for identifying the conjugates on RBBP9(S75Dap). A.T.B. and S.T. characterized the aminopeptidase activity of RBBP9. S.T. and M. Fiedler solved the structure of RBBP9 in complex with Phe. All authors provided critical feedback and helped shape the research, analysis and manuscript.

## Corresponding authors

Correspondence to [Shan Tang](#) or [Jason W. Chin](#).

## Ethics declarations

## Competing interests

The authors declare no competing interests.

## Peer review

## Peer review information

*Nature* thanks Michael Bollong and the other, anonymous reviewers for their contribution to the peer review of this work.

## Additional information

**Publisher's note** Springer Nature remains neutral with regard to jurisdictional claims in published maps and institutional affiliations.

## Extended data figures and tables

### [Extended Data Fig. 1 Strategies for Dap-mediated hydrolase substrate discovery.](#)

Genetically encoded pc-Dap in place of the catalytic serine or cysteine in the active site of a hydrolase enables the deprotection of pc-Dap to Dap and the activation of a hydrolase substrate trap that can covalently capture substrates. Purified recombinant and pre-activated Dap-containing hydrolase can be added to lysate or extract and used to capture substrates. Hydrolase containing pc-Dap can also be expressed directly in mammalian cells. The hydrolase substrate trap can then be optically activated in live cells to capture substrates. Covalent conjugates can be enriched by immunoprecipitation with stringent washing to remove non-covalent binders and the conjugates can be visualized and identified by immunoblot and mass spectrometry-based methods. Control experiments use the wild-type (WT) enzyme that does not form a stable covalent acyl-enzyme conjugate and the catalytically inactive mutant (Ala, catalytic serine/cysteine is mutated to alanine) of the hydrolase that does not react with substrates. We note that not all the Dap-containing hydrolase will necessarily be found in conjugates; in general, we expect the fraction of Dap-containing hydrolase in conjugates to be a function of hydrolase abundance, substrate abundance, effects on the rate of acyl-intermediate formation resulting from replacing the catalytic nucleophile with Dap, and the stability of the acyl-intermediate.

### [Extended Data Fig. 2 TEV\(C151Dap\) specifically traps its substrate in Expi293 cell lysate.](#)

TEV variants (WT, Ala, Dap, 1 μM) were incubated with control GFP-c (a polypeptide “Gly-Gly-Gly-Ser-Gly-Gly-His6” was attached at the C-terminus of GFP) or substrate GFP-s (a TEV cleavage sequence “Glu-Asn-Leu-Tyr-Phe-Gln-Gly-His6” was attached at the C-terminus of GFP. The cleavage between Gln and Gly is underlined) in Expi293 cell lysate at 37 °C for 3 h. The concentration of GFP-s or GFP-c was (a) 1 μM or (b) 5 μM. Dap\*: reaction of TEV(C151Dap) with GFP-s in Tris buffer. The input (reaction before IP) and Strep-tag enriched TEV species were

analyzed by SDS-PAGE (Coomassie staining) and WB (anti-Strep for TEV and anti-GFP). (a) and (b) were repeated in three biological replicates with similar results. For gel source data, see Supplementary Fig. 1.

### Extended Data Fig. 3 Dap-containing proteases selectively capture known substrates of their parent enzymes.

(a) The change of AMC fluorescence resulting from cleavage from the C-terminus of Ubiquitin (Ub) or ubiquitin-like molecules (SUMO, NEDD8, ISG15) was followed upon mixing with UL36<sup>USP</sup>. WT UL36<sup>USP</sup> from human herpesvirus 1 specifically hydrolyses Ub-AMC, but not other ubiquitin-like protein-AMC (UBL-AMC) molecules. The deubiquitination activity of UL36<sup>USP</sup> is lost when Cys65 is mutated to Ser. This data is consistent with the previously reported specificity of UL36<sup>USP</sup><sup>58</sup>. (b) UL36<sup>USP</sup>(C65Dap) specifically reacts with Ub-AMC to form the UL36<sup>USP</sup>(Dap)-Ub conjugate. In contrast, no conjugates were observed between UL36<sup>USP</sup>(Dap) and SUMO1, NEDD8 or ISG15. (c) WT SCoV2-PLpro selectively hydrolyses ISG15-AMC in preference to other Ub/UBL-AMC molecules; this data is consistent with the previously reported specificity of SCoV2-PLpro<sup>59</sup>. The hydrolysis of ISG15-AMC is abrogated when the catalytic Cys111 of SCoV2-PLpro is mutated to Ala. (d) SCoV2-PLpro(C111Dap) specifically reacts with ISG15-AMC, generating the SCoV2-PLpro(Dap)-ISG15 conjugate. \*: UBL-AMC independent higher MW bands resulting from PLpro(C111Dap) self-reaction. (a) and (c) were generated using n = 3 independent measurements. The line represents the means of three measurements. (b) was repeated twice and (d) was performed in three biological replicates with similar results. For gel source data, see Supplementary Fig. 1.

[Source data](#)

### Extended Data Fig. 4 UL36<sup>USP</sup>(C65Dap) and SCoV2-PLpro(C111Dap) form conjugates with endogenous ubiquitin in live cells.

(a) A protease containing pc-Dap in place of its catalytic serine or cysteine is produced in mammalian cells by genetic code expansion, creating a photocaged protease trap. The trap is activated by illuminating cells. The activated trap covalently and specifically captures substrate fragments in acyl-enzyme complexes linked through stable amide bonds. (b) Immunoblotting analysis of UL36<sup>USP</sup> variants enriched from an equal number of cells after optical activation and substrate capture. The conjugates formed between UL36<sup>USP</sup>(C65Dap) and endogenous proteins were detected by an anti-Strep antibody and an anti-Ub antibody; this demonstrates that UL36<sup>USP</sup>(C65Dap) captures Ub and di-ubiquitin (Ub<sub>2</sub>) in cells. Catalytically inactive

UL36<sup>USP</sup>(C65S) non-covalently associated with Ub chains to co-IP them (lanes 2 and 6), while UL36<sup>USP</sup>(C65Dap) formed conjugates with endogenous Ub molecules (lanes 7–9). Input: cell lysates before IP probed with an anti-Strep antibody. These data are consistent with previous work demonstrating that UL36<sup>USP</sup> is a deubiquitinase in cells<sup>58</sup>. **(c)** Immunoblotting analysis of SCoV2-PLpro(C111Dap) variants enriched from an equal number of cells after optical activation and substrate capture. The conjugates formed between SCoV2-PLpro(C111Dap) and endogenous proteins were detected by an anti-Strep antibody and an anti-Ub antibody; this demonstrates that SCoV2-PLpro(C111Dap) captures Ub and Ub<sub>2</sub> in cells. Catalytically inactive SCoV2-PLpro(C111A) and SCoV2-PLpro(C111pc-Dap) without illumination non-covalently associated with Ub chains to co-IP them (lanes 2, 4 and 6), while SCoV2-PLpro(C111Dap) also formed conjugates with endogenous Ub molecules (lanes 8 and 9). Input: cell lysates before IP probed with an anti-Strep antibody. Note that SCoV2-PLpro has previously been shown to cleave poly-Ub chains in cells<sup>59,60</sup>. While SCoV2-PLpro will also cleave ISG15, this protein is not expressed in Expi293 cells without stimulation<sup>61,62</sup>. **(b)** and **(c)** were repeated in two biological replicates with similar results. For gel source data, see Supplementary Fig. 1.

### **Extended Data Fig. 5 Formation of RHBDL4(Dap)-pT $\alpha$ conjugates in Expi293 cells.**

**(a)** Schematic representation of the model substrate pT $\alpha$ . SP: signal peptide; FLAG: FLAG-tag; TMH: transmembrane helix; V5: V5-tag. Red arrows: RHBDL4 cleavage sites; black arrow: SPase cleavage site. **(b)** Co-expression of C-terminal Strep-tagged RHBDL4 variants and pT $\alpha$  in Expi293 cells for 40 h. pc-Dap was added to produce full-length RHBDL4(S144pc-Dap). Cell lysates were analysed by anti-Strep (for RHBDL4), anti-FLAG and anti-V5 antibodies. Blue triangles: N-terminal proteolytic fragments of pT $\alpha$ ; Red triangles: C-terminal proteolytic fragments of pT $\alpha$ . **(c)** Detection of RHBDL4(Dap)-pT $\alpha$  conjugates after Strep-tag enrichment. Samples without illumination (lane 4) and with illumination (lanes 1–3 and 5–11) were collected at indicated time points. Input: cell lysate before IP analysed by anti-Strep and anti-FLAG antibodies. **(d)** The formation of conjugates was monitored for a longer period of time. RHBDL4(Dap)-pT $\alpha$  conjugates were gradually degraded 4 h after UV irradiation. RHBDL4 variants were also gradually degraded over time pT $\alpha$ <sup>\*</sup>, the deglycosylated form of pT $\alpha$ . The experiments were repeated in two biological replicates with similar results. For gel source data, see Supplementary Fig. 1.

### **Extended Data Fig. 6 RHBDL4 cleaves transmembrane substrate candidates.**

RHBDL4 cleavage assays for (a) MFN2, (b) EMD, (c) LEMD2 and (d) CCDC47. The putative cleavage sites – the approximate positions of which were estimated based on the MW of the proteolytic bands – are indicated by red arrows in schematic representations. HA: HA-tag; GFP: GFP-tag; SP: signal peptide; V5: V5-tag. The transmembrane helices are labeled in grey. (a) WT RHBDL4 cleaved MFN2, a multiple membrane-spanning protein resident in mitochondria or the ER. Red triangle: the C-terminal proteolytic fragment. (b) WT RHBDL4 cleaved EMD, a type II transmembrane protein in the nuclear inner membrane. Red triangle: the C-terminal proteolytic fragment. (c) WT RHBDL4 cleaved LEMD2, a multiple membrane-spanning protein in the nuclear inner membrane. Two minor cleavages (red triangles) would be in the perinuclear space, but the major cleavage site (blue triangle) in the domain resident in nucleus might be cut by the inverted RHBDL4 (see Supplementary Note 1). (d) RHBDL4 cleaved both full-length (FL) CCDC47 and CCDC47(21–135), generating the same MW N-terminal proteolytic fragment (lanes 2 and 5, blue triangle); this suggested that RHBDL4-mediated cleavage is independent of the transmembrane helix of CCDC47. Blue triangle: the N-terminal fragment; Red triangles: C-terminal proteolytic fragments. (e) Comparison of the proteolytic fragments to truncated CCDC47 standards confirmed that the cleavages are in the luminal domain of CCDC47. WT + FL: FL CCDC47 cleaved by WT RHBDL4. (f) Over-expressed WT RHBDL4 cleaved endogenous CCDC47. Red triangles: proteolytic fragments detected by an anti-CCDC47 antibody. The C-terminal proteolytic fragments of MFN2, LEMD2 and CCDC47 were probed with an anti-HA antibody, while the proteolytic fragment of EMD was detected by an anti-GFP antibody. The N-terminal proteolytic fragments were probed with an anti-V5 antibody. RHBDL4 variants were detected by an anti-Strep antibody. (a-d) were repeated in three biological replicates with similar results. (e) was performed once. (f) was repeated in two biological replicates with similar results. For gel source data, see Supplementary Fig. 1.

### **Extended Data Fig. 7 RHBDL4 cleaves endogenous BiP in mammalian cells and facilitates the secretion of N-terminal proteolytic fragments.**

(a) BFA inhibitory assay was performed for endogenous BiP. The secretion of BiP proteolytic fragment into extracellular media was inhibited by Brefeldin A (BFA) compared to cells treated with DMSO (lanes 5 vs 2, 11 vs 8, anti-BiP). Especially when the medium was changed, no BiP proteolytic fragment was detected in the medium (lane 11, dashed red arrow). Treatment of BFA greatly increased the endogenous level of BiP (lanes 4–6 vs 1–3, anti-BiP in cell lysate). In comparison, the expression of endogenous BiP was slightly increased when WT RHBDL4 or RHBDL4(S144A) was expressed (lanes 2 and 3 vs 1, anti-BiP in cell lysate). BFA treatment or RHBDL4 variant expression facilitated the secretion of full-length BiP (lane 4 vs 1 or 2 vs 1), but not the proteolytic fragment generated by RHBDL4

cleavage. RHBDL4 expression was detected by an anti-Strep antibody in cell lysate. Revert 700 total protein staining was used as loading control. (b) Endogenous BiP was cleaved by endogenously expressed RHBDL4. WT RHBDL4-dependent BiP proteolytic fragment in the media was detected by an anti-BiP antibody in WT HCT116 cells (red arrow), but not in RHBDL4 knockout HCT116 cells. Transferrin: loading control; additionally, the same samples run in different lanes were stained by Revert 700 for total protein loading control. Endogenous BiP was detected by an anti-BiP antibody and RHBDL4 was detected by an anti-RHBDL4 antibody in the cell lysate. All experiments were repeated in two biological replicates with similar results. For gel source data, see Supplementary Fig. 1.

### **Extended Data Fig. 8 RHBDL4 cleaves other ER-resident proteins before ER retention motifs and facilitates the secretion of N-terminal proteolytic fragments.**

RHBDL4 cleavage assays for V5-tagged (a) PDIA6, (b) Calreticulin and (c) ERP44. The putative cleavage sites are indicated by blue arrows in the schematic representations. (a) WT RHBDL4 cleaved PDIA6 at the C-terminus, resulting in secretion of the N-terminal fragment (blue arrow) into the medium. (b) WT RHBDL4 cleaved Calreticulin at the internal region (minor cleavage) and the C-terminus (major cleavage), resulting in secretion of the N-terminal fragments (blue arrows) into the SN. (c) WT RHBDL4 cleaved ERP44 before RDEL sequence. The secreted proteins were deglycosylation mix II sensitive. Because we could not source an antibody to specifically detect the RDEL sequence, we inserted an HA-tag four amino acids before the RDEL sequence for detection. Anti-V5 detected proteolytic fragments 1 and 2 (p1 and p2), and p1 was also detected by the anti-HA antibody, indicating that one cleavage might happen after the HA-tag. The expression of RHBDL4 was detected by an anti-Strep antibody. RHBDL4 cleavage assays for (d) endogenous PDIA6 and (e) endogenous Calreticulin. (d) WT RHBDL4 cleaved endogenous PDIA6. The proteolytic fragment of PDIA6 (red arrow) without the KDEL sequence was secreted into the SN. (e) WT RHBDL4 cleaved endogenous Calreticulin. The proteolytic fragment of Calreticulin (red arrow) without the KDEL sequence was secreted into the SN. Expression of RHBDL4 did not increase the endogenous level of PDIA6 and Calreticulin (lanes 2 and 3 vs 1). The expression of RHBDL4 is shown in Fig. 3g. BFA inhibitory assays for (f) PDIA6 and (g) Calreticulin. The secretion of proteolytic fragments of PDIA6 and Calreticulin was inhibited compared to cells treated with DMSO (lanes 5 vs 2, 11 vs 8). Endogenous PDIA6 and Calreticulin were detected by an anti-PDIA6 and an anti-CALR antibody, respectively. The expression of RHBDL4 is shown in Extended Data Fig. 7a. (h) Endogenous RHBDL4 cleaves endogenous Calreticulin. WT RHBDL4-dependent Calreticulin proteolytic fragments in the extracellular media were detected by an anti-CALR antibody in WT HCT116 cells (red arrows), but not in RHBDL4 KO HCT116 cells. The secretion of the major

proteolytic fragment (near full-length Calreticulin, low intensity) and the minor proteolytic fragment (high intensity) were both detected. Transferrin: loading control. The endogenous RHBDL4 is shown in Extended Data Fig. 7b. (a-h) were repeated in two biological replicates with similar results. For gel source data, see Supplementary Fig. 1.

### **Extended Data Fig. 9 The distribution of cysteine and serine protease clans.**

The clan distribution of cysteine proteases from (a) animals and (b) viruses. The clan distribution of serine proteases from (c) animals and (d) viruses. We have demonstrated the Dap-mediated protease substrate capture method for multiple cysteine proteases (TEV (Clan PA), UL36<sup>USP</sup> (Clan CA) and SCoV2-PLpro (Clan CA)) and serine proteases (HtrA2 (Clan PA), RHBDL4 (Clan ST) and RBBP9 (Note that RBBP9 has not been included in the MEROPS database by September 30, 2021. RBBP9 possesses the “alpha-beta hydrolase” fold<sup>40</sup>, suggesting that it belongs to Clan SC). The data used to generate this figure were downloaded from the MEROPS database<sup>47</sup>.

### **Source data**

### **Extended Data Table 1 Summary of crystallographic information**

## **Supplementary information**

### **Supplementary Information**

The Supplementary Information contains Supplementary Notes 1 and 2, Supplementary Figures 1-19 (in which the Supplementary Fig. 1 contains all uncropped SDS-PAGE and western blots), Supplementary Tables 1-5, Supplementary Methods and Supplementary Data Files 1 and 2.

### **Reporting Summary**

## **Source data**

### **Source Data Fig. 5**

### **Source Data Extended Data Fig. 3**

## Source Data Extended Data Fig. 9

### Rights and permissions

**Open Access** This article is licensed under a Creative Commons Attribution 4.0 International License, which permits use, sharing, adaptation, distribution and reproduction in any medium or format, as long as you give appropriate credit to the original author(s) and the source, provide a link to the Creative Commons license, and indicate if changes were made. The images or other third party material in this article are included in the article's Creative Commons license, unless indicated otherwise in a credit line to the material. If material is not included in the article's Creative Commons license and your intended use is not permitted by statutory regulation or exceeds the permitted use, you will need to obtain permission directly from the copyright holder. To view a copy of this license, visit <http://creativecommons.org/licenses/by/4.0/>.

### Reprints and Permissions

### About this article

#### Cite this article

Tang, S., Beattie, A.T., Kafkova, L. *et al.* Mechanism-based traps enable protease and hydrolase substrate discovery. *Nature* **602**, 701–707 (2022).  
<https://doi.org/10.1038/s41586-022-04414-9>

- Received: 12 June 2021
- Accepted: 07 January 2022
- Published: 16 February 2022
- Issue Date: 24 February 2022
- DOI: <https://doi.org/10.1038/s41586-022-04414-9>

#### Share this article

Anyone you share the following link with will be able to read this content:

[Get shareable link](#)

Sorry, a shareable link is not currently available for this article.

[Copy to clipboard](#)

Provided by the Springer Nature SharedIt content-sharing initiative

---

This article was downloaded by **calibre** from <https://www.nature.com/articles/s41586-022-04414-9>

| [Section menu](#) | [Main menu](#) |

# Amendments & Corrections

- [\*\*Author Correction: Structures of the HER2–HER3–NRG1 \$\beta\$  complex reveal a dynamic dimer interface\*\*](#) [ 07 ]

February 2022]

Author Correction •

- Author Correction
- [Published: 07 February 2022](#)

# Author Correction: Structures of the HER2–HER3–NRG1 $\beta$ complex reveal a dynamic dimer interface

- [Devan Diwanji](#)<sup>1,2</sup> na1,
- [Raphael Trenker](#) [ORCID: orcid.org/0000-0003-1748-0517](#)<sup>1</sup> na1,
- [Tarjani M. Thaker](#)<sup>1,3</sup>,
- [Feng Wang](#)<sup>4</sup>,
- [David A. Agard](#) [ORCID: orcid.org/0000-0003-3512-695X](#)<sup>4</sup>,
- [Kliment A. Verba](#) [ORCID: orcid.org/0000-0002-2238-8590](#)<sup>5,6</sup> &
- [Natalia Jura](#) [ORCID: orcid.org/0000-0001-5129-641X](#)<sup>1,7</sup>

[Nature](#) volume **602**, page E26 (2022)

- 834 Accesses
- 1 Altmetric
- [Metrics details](#)

## Subjects

- [Breast cancer](#)
- [Cryoelectron microscopy](#)

The [Original Article](#) was published on 10 November 2021

[Download PDF](#)

Correction to: *Nature* <https://doi.org/10.1038/s41586-021-04084-z>

Published online 10 November 2021

In the version of this article initially published, there were several labelling errors. In Fig. 1c, the rotation shown at right for the inset structure reading “90°” initially read “180°.” In Extended Data Figs. 2f and 7d, “MotionCor2” replaces “Motioncorr2,” while in Extended Data Fig. 8d, “Trastuzumab” replaces “Pertuzumab.” In Extended Data Fig. 8f, HER2 in the heading has been replaced by HER2-S310F. In Extended Data Fig. 4, the numbering of the EGFR sequence has been changed to include the signal sequence and is consistent with Uniprot numbering. Consequently, in Extended Data Fig. 4a, H-bond 18 has been relabelled as C307; in Extended Data Fig. 4c, H-bond 1 has been relabelled as K248; and in Extended Data Fig. 4e, H-bond 1 has been relabelled as K248.

## Author information

### Author notes

1. These authors contributed equally: Devan Diwanji, Raphael Trenker

## Affiliations

1. Cardiovascular Research Institute, University of California San Francisco, San Francisco, CA, USA

Devan Diwanji, Raphael Trenker, Tarjani M. Thaker & Natalia Jura

2. Medical Scientist Training Program, University of California San Francisco, San Francisco, CA, USA

Devan Diwanji

3. Department of Chemistry and Biochemistry, The University of Arizona, Tucson, AZ, USA

Tarjani M. Thaker

4. Department of Biochemistry and Biophysics, University of California San Francisco, San Francisco, CA, USA

Feng Wang & David A. Agard

5. Quantitative Biosciences Institute (QBI), University of California San Francisco, San Francisco, CA, USA

Kliment A. Verba

6. Department of Pharmaceutical Chemistry, University of California San Francisco, San Francisco, CA, USA

Kliment A. Verba

7. Department of Cellular and Molecular Pharmacology, University of California San Francisco, San Francisco, CA, USA

Natalia Jura

## Corresponding authors

Correspondence to [Kliment A. Verba](#) or [Natalia Jura](#).

## Rights and permissions

[Reprints and Permissions](#)

## About this article

### Cite this article

Diwanji, D., Trenker, R., Thaker, T.M. *et al.* Author Correction: Structures of the HER2–HER3–NRG1 $\beta$  complex reveal a dynamic dimer interface.

*Nature* **602**, E26 (2022). <https://doi.org/10.1038/s41586-021-04299-0>

- Published: 07 February 2022
- Issue Date: 24 February 2022
- DOI: <https://doi.org/10.1038/s41586-021-04299-0>

## Share this article

Anyone you share the following link with will be able to read this content:

[Get shareable link](#)

Sorry, a shareable link is not currently available for this article.

[Copy to clipboard](#)

Provided by the Springer Nature SharedIt content-sharing initiative

---

This article was downloaded by **calibre** from <https://www.nature.com/articles/s41586-021-04299-0>

| [Section menu](#) | [Main menu](#) |